frontiers | Research Topics

Trapped charge dating and its application in geomorphological, geological and archaeological studies in east asia

Edited by
Hui Zhao, Bo Li, Yuxin Fan and Hao Long

Published in
Frontiers in Earth Science

ISSN 1664-8714
ISBN 978-2-83251-492-4
DOI 10.3389/978-2-83251-492-4

About Frontiers

Frontiers is more than just an open access publisher of scholarly articles: it is a pioneering approach to the world of academia, radically improving the way scholarly research is managed. The grand vision of Frontiers is a world where all people have an equal opportunity to seek, share and generate knowledge. Frontiers provides immediate and permanent online open access to all its publications, but this alone is not enough to realize our grand goals.

Frontiers journal series

The Frontiers journal series is a multi-tier and interdisciplinary set of open-access, online journals, promising a paradigm shift from the current review, selection and dissemination processes in academic publishing. All Frontiers journals are driven by researchers for researchers; therefore, they constitute a service to the scholarly community. At the same time, the *Frontiers journal series* operates on a revolutionary invention, the tiered publishing system, initially addressing specific communities of scholars, and gradually climbing up to broader public understanding, thus serving the interests of the lay society, too.

Dedication to quality

Each Frontiers article is a landmark of the highest quality, thanks to genuinely collaborative interactions between authors and review editors, who include some of the world's best academicians. Research must be certified by peers before entering a stream of knowledge that may eventually reach the public - and shape society; therefore, Frontiers only applies the most rigorous and unbiased reviews. Frontiers revolutionizes research publishing by freely delivering the most outstanding research, evaluated with no bias from both the academic and social point of view. By applying the most advanced information technologies, Frontiers is catapulting scholarly publishing into a new generation.

What are Frontiers Research Topics?

Frontiers Research Topics are very popular trademarks of the *Frontiers journals series*: they are collections of at least ten articles, all centered on a particular subject. With their unique mix of varied contributions from Original Research to Review Articles, Frontiers Research Topics unify the most influential researchers, the latest key findings and historical advances in a hot research area.

Find out more on how to host your own Frontiers Research Topic or contribute to one as an author by contacting the Frontiers editorial office: frontiersin.org/about/contact

Trapped charge dating and its application in geomorphological, geological and archaeological studies in east asia

Topic editors

Hui Zhao — Chinese Academy of Sciences (CAS), China

Bo Li — University of Wollongong, Australia

Yuxin Fan — Lanzhou University, China

Hao Long — Nanjing Institute of Geography and Limnology, Chinese Academy of Sciences (CAS), China

Citation

Zhao, H., Li, B., Fan, Y., Long, H., eds. (2023). *Trapped charge dating and its application in geomorphological, geological and archaeological studies in east asia*. Lausanne: Frontiers Media SA. doi: 10.3389/978-2-83251-492-4

Table of contents

frontiers | Frontiers in Earth Science

TYPE Editorial
PUBLISHED 16 January 2023
DOI 10.3389/feart.2022.1057341

OPEN ACCESS

EDITED AND REVIEWED BY
János Kovács,
University of Pécs, Hungary

*CORRESPONDENCE
Hui Zhao,
hzhao@lzb.ac.cn

SPECIALTY SECTION
This article was submitted to Quaternary Science, Geomorphology and Paleoenvironment, a section of the journal Frontiers in Earth Science

RECEIVED 29 September 2022
ACCEPTED 21 October 2022
PUBLISHED 16 January 2023

CITATION
Zhao H, Long H, Fan Y and Li B (2023), Editorial: Trapped charge dating and its application in geomorphological, geological and archaeological studies in East Asia.
Front. Earth Sci. 10:1057341.
doi: 10.3389/feart.2022.1057341

Editorial: Trapped charge dating and its application in geomorphological, geological and archaeological studies in East Asia

Hui Zhao[1]*, Hao Long[2], Yuxin Fan[3] and Bo Li[4]

[1]Key Laboratory of Desert and Desertification, Northwest Institute of Eco-Environment and Resources, Chinese Academy of Science, Lanzhou, China, [2]State Key Laboratory of Lake Science and Environment, Nanjing Institute of Geography and Limnology, Chinese Academy of Sciences, Nanjing, China, [3]School of Earth Sciences and Key Laboratory of Mineral Resources in Western China (Gansu Province), Lanzhou University, Lanzhou, China, [4]Centre for Archaeological Science, School of Earth, Atmospheric and Life Sciences, University of Wollongong, Wollongong, NSW, Australia

KEYWORDS

luminescence and ESR dating, geomorphological process, aeolian process, human migration, Quaternary, East Asia

Editorial on the Research Topic
Trapped charge dating and its application in geomorphological, geological and archaeological studies in East Asia

Trapped charge dating refers to two main techniques, luminescence (OSL/IRSL) dating and electron spin resonance (ESR) dating, and both based on the time-dependent storage of energy from natural radioactivity in crystal materials. Luminescence dating is commonly used to date the last time since quartz or feldspar grains in rocks or sediments were exposed to sunlight or heating, as well as the exposure age of rock surface. ESR is mainly applied for dating biogenic materials such as fossil tooth, but can also be used to date quartz. Given its wide dating range (from decades up to more than one million years) and availability of materials (quartz and feldspars, more than 70% of Earth's crust), trapped charge dating has become one of the most important dating tools for studying Earth and its inhabitants during the Quaternary. The techniques have been successfully applied to various geological context and geomorphological processes, including aeolian, fluvial, alluvial and lacustrine deposits which recorded paleoclimatic and paleoenvironmental changes, provenance of sediments, tectonic activities, accumulation and erosion; and human migration etc.

This Research Topic focuses on new advances in trapped charge dating and its application to various deposit contexts. This collection includes 14 papers covering the studies of the characteristic of the luminescence signals; reconstruction of fluvial geomorphological process, aeolian processes in deserts and sandy lands, and human migration history in East Asia.

Six papers in this Research Topic focused on the applications of the luminescence dating to the paleoshorelines or the fluvial terraces to explore the lake level variability, and the geomorphological process etc. Wu et al. studied the late Quaternary lake shrinkage of Dagze Co in central Tibetan Plateau. Based on OSL dating and differential GPS measurement, it is found that a high lake level (+55 m) occurred at 9.1–9.6 ka followed by two abrupt drops (9–8 ka and after 5 ka). It was proposed that the long-term decreasing trend of Asian monsoon precipitation could be the main reason for this major drop of lake level. Several studies have documented recent rapid incision events in northeastern Tibet that are probably linked to global climate change. However, it is unclear whether the incision process occurs in vast areas to upper reaches or is restricted in lower reach of the rivers. Cao et al. dated the Quaternary fluvial terraces of the rivers in Northeastern Tibet. They suggest that the adjustment of the climate-induced longitudinal river profile is limited to the downstream reach. Tamura et al. applied K-feldspar pIRIR dating to identify the sedimentary sequences in an uplifted coast since the Middle Pleistocene, eastern Japan. This study provides a valuable and comprehensive case study of feldspar pIRIR dating application to the coastal stratigraphy and shows how useful the resultant chronology is for defining sedimentary sequence formed in response to glacial-interglacial sea-level oscillations. The eastern margin of the Tibetan Plateau experienced extensive tectonic activities in the form of earthquakes and landslides. To further understand the timing of the activities, Zhang et al. selected the strath terraces of the Minjiang River in the region for luminescence dating. Seven strath terraces (T1 to T7) were recognized, and 16 sedimentary samples were collected from the terraces. Quartz OSL dating results show that the terraces T1-T6 formed during the intervals of 13–63 ka. Liu et al. applied the quartz OSL dating to the alluvial fan deposits from the Helan Mountain, North China. They found that the dating results were affected by the aliquot-size with different age model. This research makes the dose dependency of aliquot sizes and age models more definite and shows a possibility of dating paleo-alluvial deposits to establish a chronological framework. Li et al. applied K-feldspar $pIRIR_{150}$ signals to date the Late Pleistocene sediments in the NW Khangai Mountains (Mongolia) using a standardized dose response curves (sDRC) approach. The sDRCs and DRC of individual samples yield consistent age, supporting that the sDRCs are applicable for luminescence dating with improvement of measurement efficiency. However, a comparison between the radiocarbon dates, the fading corrected $pIRIR_{150}$ and IR_{50} ages may be overestimated due to fading over-correction.

Three articles in the Research Topic applied the ESR dating or luminescence dating to the archeological sites to obtain the history of the human migration in the East Asia. Han et al. obtained the chronology of early human settlement in Three Gorges Region (TGR), China, by using the ESR and Uranium-series dating methods. TGR is a probable migration corridor for hominins and other mammals between South and North China. Seven important Early and Middle Pleistocene hominin settlement sites were studied, and hominins were proposed to be settled in TGR probably from ~2.5–2.2 Ma at the Longgupo site, and to the Yumidong site at ~274–14 ka and likely to spread to other parts of East Asia during this time period. Guo et al. re-dated the Zhuwobu Paleolithic site, a part of the "generalized" Nihewan Basin, in the Huailai basin, North China, using the MET-pIRIR procedure on both single and multiple aliquots of K-feldspars. The results suggest that the cultural layer at this site was deposited about 280 ± 13 ka ago, ~220 ka younger than the previous ESR age (504 ± 76 ka) which might be overestimated due to poor bleaching before burial. In contrast, the ESR age of 346 ± 32 ka for the sample collected from same cultural-layer might be more reliable due to higher-quality bleaching before burial. Pottery and burnt clay are the most abundant dating material available in neolithic archaeological sites. Wang et al. reported the OSL and TL dating application to heated quartz grains extracted from pottery and burnt clay excavated from the archaeological site of Lingjiatan, China. The study provided new insights on the luminescence characteristics of heated quartz, including sensitivity, components, fast ratio, thermal stability, recuperation, etc., and explored their effects on luminescence ages. Two types of quartz signals were distinguished in terms of their component and sensitivity characteristics. They highlighted that a modified measurement procedure should be used for the type of samples that decay slowly to obtain accurate optical ages. Compared with ^{14}C dates from charcoal chips extracted from the burnt clay, OSL dating provides a robust method to obtain the accurate time since the last archaeological heating event.

Methodological studies of luminescence characteristics of the OSL/IRSL signals are important for the application of the optical dating. Five articles in this Research Topic focus on the sensitivity and bleaching condition of OSL or the IRSL signals. Zhang et al. studied the bleaching limits of IRSL signals at various stimulation temperatures and their potential inference of the pre-burial light exposure duration. They conducted comprehensive bleaching experiments of IRSL and pIRIR signals, demonstrating that a non-bleachable component exists in the IR (and possibly pIRIR) signals, and positively correlated with preheat/stimulation temperature. It is noteworthy that the relative residual signal level is consistent between the IR_{50} and pIRIR signals for the same preheat temperature. Subsequently, authors proposed a novel approach to explore the pre-burial light exposure history of sediment utilizing multiple feldspar pIRIR signals. Mo et al. focused their study on the bleaching degree of multi-grain coarse quartz OSL signal of near-surface aeolian sediments collected around the margin of the Tengger Desert. In this

study, methods of empirical investigation and numerical validation were applied to assess the bleaching degree of the coarse-grain fraction of near-surface aeolian sediments. The results reveal that the limitation of traditional methods in the identification of heterogeneous bleaching for aeolian sediments measured from multi-grain aliquots. It concludes that the wind-driven erosion/reworking of the stationary near-surface sediments and/or the absence of severe aggregation leads to the fully bleaching of the investigated multi-grain samples. The quartz luminescence sensitivity (QLS) has been used as one proxy in the provenance investigation of Quaternary sediments. Liu et al. studied the luminescence sensitivity of quartz grains in five typical loess sequences obtained from the eastern Tibetan Plateau. Their results show significant spatiotemporal variations in the quartz luminescence sensitivity at different locations, indicating that the dust sources have played an important role in the variation of the QLS and the QLS can be used for tracing the loess in the Tibetan Plateau. However, the study of eight samples from Permian biotite monzogranite in Cao et al. indicates further research is required to apply the thermal activation curves in the study of provenance, though the degree of chemical weathering does not correspond with the QLS values of samples that have undergone varying degrees of *in situ* weathering and that quartz from the same source with varying degrees of *in situ* chemical weathering has a constant response to irradiation-bleaching cycles. Rui et al. tested the reliability of using the continental standardized growth curves (SGCs) by using coarse quartz grains from Lake Woods in Northern Australia. They applied full SAR procedure to individual quartz grains, and built regional SGCs for Lake Woods. With the obtained data, they calculated SAR D_e, regional SGC D_e and continental SGC D_e for the studied samples, and found that D_e values obtained by continental SGCs are consistent with D_e values obtained by regional SGCs and by the SAR procedure. It was proposed that the continental SGC can be successfully applied to coarse quartz grains from Lake Woods, and large instrument time can be saved by using this method.

Author contributions

All authors listed have made a substantial, direct, and intellectual contribution to the work and approved it for publication.

Funding

We acknowledge the supports from the Second Tibetan Plateau Scientific Expedition and Research Program (2019QZKK0202).

Acknowledgments

We appreciate the Editorial office of Frontiers in Earth Science for their timely support during organizing and managing the topic and all the reviewers for their selfless contributions during the reviewing processes that substantially improved the qualities of the published papers.

Conflict of interest

The authors declare that the research was conducted in the absence of any commercial or financial relationships that could be construed as a potential conflict of interest.

Publisher's note

frontiers | Frontiers in Earth Science

ORIGINAL RESEARCH
published: 16 June 2022
doi: 10.3389/feart.2022.922692

On the Bleaching Degree of Multi-Grain Coarse Quartz OSL Signal of Near-Surface Aeolian Sediments Around the Tengger Desert: Empirical Investigation and Numerical Validation

Hongwei Mo, Jun Peng, Zhenguo Li, Yan Song and Teng Feng*

School of Earth Sciences and Spatial Information Engineering, Hunan University of Science and Technology, Xiangtan, China

In this study, the degree of bleaching of multi-grain coarse quartz optically stimulated luminescence (OSL) signal of near-surface aeolian samples collected around the Tengger Desert is assessed. The single-aliquot regenerative dose (SAR) protocol and the standardized growth curve (SGC) method are applied to measure the equivalent dose (D_e) of these samples. The bleaching degree of the samples is assessed by investigating 1) the relationship between L_n/T_n and SAR D_e and 2) the SGC D_e distribution. Various degrees of heterogeneously-bleached multi-grain dose distributions synthetized with a numerical simulation method is further used to validate the bleaching performance of the samples. It demonstrates that the investigated samples are characterized by tight D_e distributions and the maximum D_e estimate is smaller than 1.1 Gy. The numerical simulation method which uses as input a large proportion of fully-bleached grains and a small baseline dose is able to reproduce multi-grain D_e distributions similar to the measured ones. We conclude that OSL signals of multi-grain coarse quartz extracted from most of the investigated aeolian samples are fully bleached before deposition.

Keywords: quartz OSL dating, multi-grain aliquots, aeolian sediments, bleaching degree, tengger desert

OPEN ACCESS

Edited by:
Hao Long,
Nanjing Institute of Geography and Limnology (CAS), China

Reviewed by:
Shuangwen Yi,
Nanjing University, China
Xue Rui,
Jilin University, China

****Correspondence:***
Jun Peng
pengjun10@mails.ucas.ac.cn

Specialty section:
This article was submitted to Quaternary Science, Geomorphology and Paleoenvironment, a section of the journal Frontiers in Earth Science

Received: *18 April 2022*
Accepted: *24 May 2022*
Published: *16 June 2022*

Citation:
Mo H, Peng J, Li Z, Song Y and Feng T (2022) On the Bleaching Degree of Multi-Grain Coarse Quartz OSL Signal of Near-Surface Aeolian Sediments Around the Tengger Desert: Empirical Investigation and Numerical Validation. Front. Earth Sci. 10:922692. doi: 10.3389/feart.2022.922692

INTRODUCTION

Optically simulated luminescence (OSL) dating techniques are widely used for the determination of the burial ages of Quaternary sediments (e.g., Li et al., 2002, 2014; Zhao et al., 2007; Yi et al., 2015; Peng et al., 2022). To obtain accurate OSL ages, optically sensitive charges that were previously accumulated in the mineral (quartz and feldspar) grain should be completed zeroed (or bleached) by sunlight prior to the last deposition of sediments (Godfrey-Smith et al., 1988; Peng et al., 2020). However, heterogeneous bleaching of quartz OSL signals has been frequently reported in the literature, especially for younger sediments with smaller equivalent dose (D_e) values (e.g., Lian and Huntley, 1999; Li, 2001; Zhang et al., 2003; Olley et al., 2004; Arnold et al., 2009; Pietsch, 2009; Hu et al., 2010; Costas et al., 2012; Ou et al., 2015; Mahadev et al., 2019).

Aeolian sediments are the most readily available materials for OSL dating in semi-arid/arid regions (Peng et al., 2022), and are thought to be the most unlikely influenced by heterogeneous bleaching (Wintle, 1993) due to their longer time of exposure to sunlight before deposition compared to water-lain sediments. Although many authors reported that their aeolian samples under analyzed were fully bleached before deposition (e.g., Bailey et al., 2001; Ballarini et al., 2003; Stokes et al., 2004;

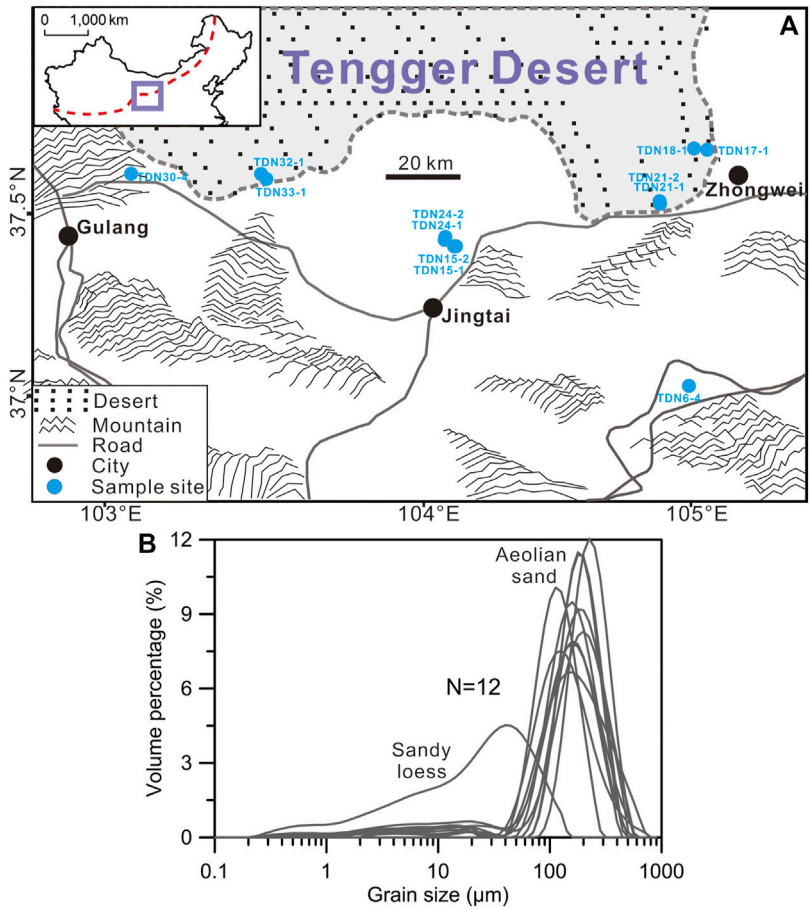

FIGURE 1 | (A) Site locations of the investigated samples. The bold rectangle in the inset indicates the studied region and the dashed red line indicates the border of the East Asia summer Monsoon. **(B)** Grain-size distributions of the investigated samples.

Singarayer et al., 2005; Zhao et al., 2012; Gong et al., 2013; Fu et al., 2015; Long et al., 2019; Yang et al., 2020), there is a growing lines of evidence indicating that it is not a sufficient guarantee that aeolian sediments under all deposition environments were fully bleached (e.g., Lian and Huntley, 1999; Spooner et al., 2001; Goble et al., 2004; Olley et al., 2004; Tissoux et al., 2010; Costas et al., 2012; Fan et al., 2013, 2022; Buckland et al., 2019). Accordingly, it is important to assess the bleaching degree of aeolian sediments in a region-specific scale to obtain accurate OSL ages for young samples to establish reliable geochronological framework on a century to decadal time scale.

Tengger Desert is a major proximal desert upwind to the Chinese Loess Plateau and aeolian dust released therein has significantly influenced region- and hemisphere-scale environments (Peng et al., 2022). Fan et al. (2013) assessed the bleaching degree of fine-grained quartz (11–63 μm) OSL signals near the Lanzhou city 200 km south to the Tengger Desert and indicated that most (but not all) the investigated samples were fully bleached. Fan et al. (2022) investigated the bleaching degree of coarse-grained quartz (90–125 μm) OSL signal of dune sands from the hinterland of the Tengger Desert and suggested that approximately a half of the studied samples were heterogeneously bleached. However, the bleaching characteristics of coarse-grained quartz OSL signals of aeolian sediments along the margin of the Tengger Desert have not been formally assessed yet, although a growing number of chronostratigraphic records from the desert margin were dated using coarse-grained quartz OSL (e.g., Qiang et al., 2010; Yin et al., 2013; Peng et al., 2016, 2022). In this study, near-surface coarse aeolian samples collected around the margin of the Tengger Desert were investigated to assess their multi-grain quartz OSL signal bleaching degrees using both empirical and numerical simulation methods.

SAMPLES AND METHODS

Twelve aeolian samples collected from nine different sites around the margin of the Tengger Desert were investigated (**Figure 1A**). The maximum distance between these sites and the mobile sand sea of the desert are smaller than 60 km. Samples were collected at the near-surface of the outcrops (with an average depth of ~0.86 m) and were expected to have D_e values approaching zero. Sample TDN6-4 is sandy loess and the remaining samples are aeolian sand. The results of grain-size analysis

demonstrate that most samples are dominant by coarse fractions with particle diameters greater than 63 μm (**Figure 1B**). The reader is referred to Peng et al. (2022) for further information on the samples.

Raw samples were processed with the standard procedure (see Peng et al., 2022 and reference therein) to extract the 90–125 μm (or 63–90 μm, i.e., sample TDN6-4) quartz fractions which were subsequently contained in the inner part (four to five mm in diameter) of the discs for OSL measurements. Post-IR OSL signals were measured with a Risø-TL/OSL-DA-20 reader equipped with IR LEDs (870 nm, 48 mW/cm^2) and blue LEDs (470 nm, 48 mW/cm^2) to suppress the contribution of feldspar luminescence (e.g., Banerjee et al., 2001). Post-IR OSL signals were collected at 130°C for 40 s (with 400 channels). The preheat temperatures before the natural and regenerative OSL measurements were 260 and 220°C, respectively. The test dose used for sensitivity correction was 7.9 Gy throughout the measurements. D_e measurements were conducted using the single-aliquot regenerative-dose (SAR) (Murray and Wintle, 2000) and the standardized growth curve (SGC) (Roberts and Duller, 2004) methods. SAR D_e was determined by a full protocol with one natural cycle and six regenerative cycles. SGC D_e was determined by projecting the sensitivity-corrected natural OSL signal (L_n/T_n) onto a pre-determined SGC. OSL data analysis was performed using the R package "numOSL" (Peng et al., 2013; Peng and Li, 2017).

Numerical simulations were performed to generate heterogeneously-bleached D_e distributions (e.g., Peng, 2021) so as to validate the bleaching performance of the measured multi-grain aliquots. Single-grain OSL sensitivities were simulated from the empirical distribution of a measured sand dune sample according to the method of Rhodes (2007). OSL signals were generated using a pre-determined dose-response curve (DRC) described by a single saturating exponential function (e.g., Li et al., 2017). The heterogeneous bleaching process of the single-grain quartz OSL was simulated by assuming that the fast-component OSL signal decays exponentially with sunlight exposure duration with a bleaching rate of 0.4 s^{-1} which allows the OSL signal to decay to less than 2% of its initial level after a bleaching duration of 10 s (Peng et al., 2020). This is consistent with the sunlight bleaching experiment work carried out by Godfrey-Smith et al. (1988) who predicted that 90% of the natural optical signal should be erased following a 10 s exposure to sunlight. The methodologies and terminologies used to simulate the baseline doses, baseline signals, residual signals, residual doses, burial doses, and natural doses were consistent with those of Peng et al. (2020). To synthetize multi-grain D_e distributions, a random sampling protocol (without replacement) was used to draw subsets from 1,000 simulated noise-free single-grain OSL datasets, and each subset containing OSL signals from N_g heterogeneously-bleached grains were superposed and noised to generate a "measured" multi-grain D_e value (and associated standard errors). The process was implemented repeatedly to generated "measured" multi-grain D_e distributions. The "measured" OSL signal was simulated by taking into account the counting statistics, instrument irreproducibility, and intrinsic over-dispersion (e.g., Li et al., 2017; Peng et al., 2020; Peng, 2021).

RESULTS

Measured Results

Typical natural OSL decay curves are presented in **Figure 2**, for samples TDN6-4 and TDN15-1. A detectable natural OSL signal is presented in certain aliquots of TDN6-4 but absent in all aliquots of TDN15-1. **Figure 3A** shows typical SAR D_e calculation for a sample (TDN15-1). Due to the low signal-to-noise ratios of the measured decay curves, the SAR D_e calculations were characterized by very large uncertainties. **Figure 4** shows the variation of the SAR D_e with the sensitivity-corrected natural OSL signal (e.g., Li, 2001) for eleven out of twelve samples (except TDN33-1). It shows that for certain samples (such as TDN6-4, TDN15-1, TDN17-1, and TDN30-4) positive correlations are observed between D_e and L_n/T_n values.

We applied the SGC method to these young aeolian sediments to improve the precision of D_e determination and to rapid explore their potential burial dose distributions (e.g., Hu and Li, 2019; Yang et al., 2020). The common DRC used for SGC D_e calculation (i.e., Peng et al., 2022) is shown in **Figure 3B** and a comparison of SAR and SGC D_e estimates for eleven samples is shown in **Figure 3C**. The two different methods yield D_e estimates that are broadly consistent with each other after accounting for associated errors. The calculated SGC D_e distributions are shown in **Figure 5** as radial plots (Galbraith, 1988). Since negative D_e values present in most SGC D_e

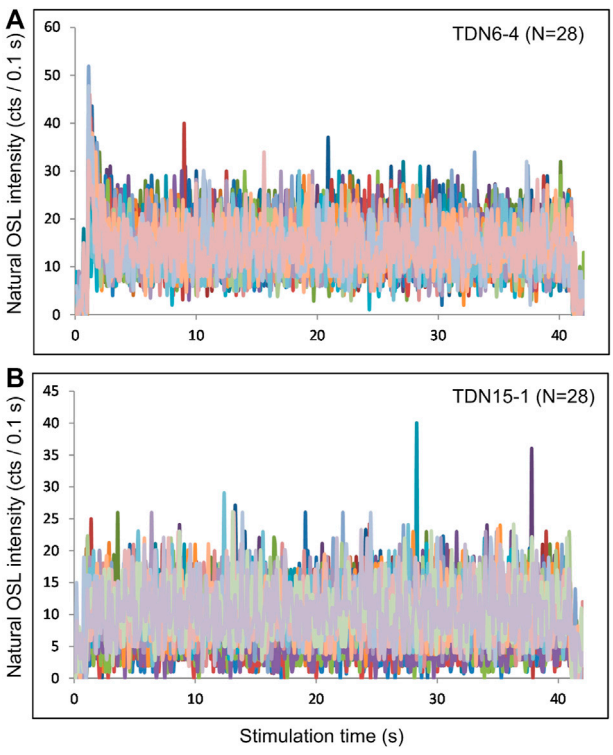

FIGURE 2 | Natural post-IR OSL decay curves of samples TDN6-4 and TDN15-1.

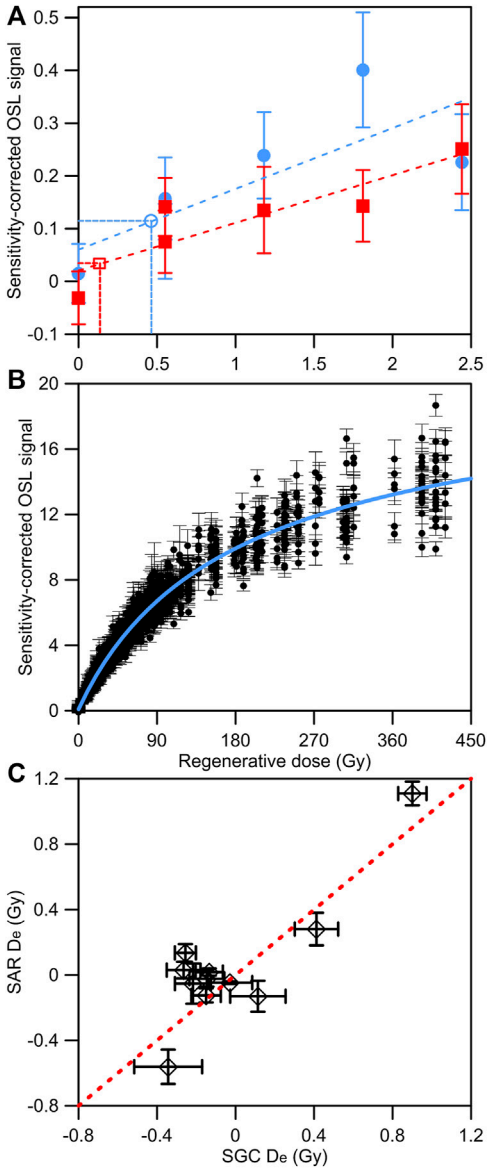

FIGURE 3 | (A) shows SAR D_e determination for two different aliquots of sample TDN15-1. The dashed lines indicate the fitted DRCs. **(B)** shows the sensitivity-corrected regenerative post-IR OSL signals used for establishing the SGC. The blue line indicates the established SGC. **(C)** compares SAR and SGC D_e estimates for eleven samples. For each sample, the SAR D_e estimate were based on twelve aliquots and the SGC ones were based on at least twenty-three aliquots. The dashed red line indicates y = x.

distributions due to poor counting statistics, a linear transformation (rather than a logarithmic transformation) as suggested by Vermeesch (2009) was used to draw the radial plots. It demonstrates that the SGC D_e distributions fall into narrow ranges and most D_e values are within the two-sigma range. The final D_e estimates were determined using an unlogged version of the central age model (Galbraith et al., 1999). The max final D_e estimate was calculated as 1.09 ± 0.15 Gy (i.e., sample TDN6-4) and ten samples (i.e., TDN15-1, TDN15-2, TDN17-1, TDN18-1, TDN21-1, TDN21-2, TDN24-1, TDN24-2, TDN32-1, TDN33-1) yield D_e estimates ranging between -0.26 ± 0.05 Gy and 0.2 ± 0.23 Gy.

Simulated Results

Considering that each of the above measured multi-grain aliquots contains at least 200 quartz grains (i.e., according to Duller, 2008) and therefore the results may be influenced by the "averaging" effect which may obscure the results and the effect amplifies as the number of grains within an aliquots (N_g) increases (e.g., Wallinga, 2002; Rhodes, 2007; Buckland et al., 2019), we explored the possible influences of this effect on the resultant multi-grain D_e distributions measured from aeolian samples with weak OSL intensities by numerical simulation of heterogeneously-bleached dose distributions (e.g., Peng et al., 2020; Peng, 2021). The mean burial dose absorbed by the grains since their last exposure to sunlight (μ_a) was fixed as 0.1 Gy (i.e., close to the average CAM D_e determined in **Figure 5**), the mean baseline doses (μ_q) accumulated in the quartz grains prior to their last transport and depositional events was either 10 or 50 Gy, and the proportion of fully-bleached grains (p) was either 0.05, 0.5, or 0.95. The simulated D_e distributions with N_g values of 1, 10, and 200 are presented in **Figures 6**, **7**, respectively, for two scenarios with μ_q values of 10 and 50 Gy.

We demonstrated in both scenarios that the standard errors of D_e values decrease dramatically while the CAM D_e estimates increase gradually as N_g increases (**Figures 6**, **7**). In addition, in the cases of $p = 0.05$ and $p = 0.5$, the increase in CAM D_e estimates is more significant when N_g increases from 1 to 10 (compared to the situation of N_g increases from 10 to 200). By contrast, in the cases of $p = 0.95$, the increase in CAM D_e estimates is insignificant among N_g values of 1, 10, and 200. These demonstrate the non-linear variation of the "averaging" effect with p and N_g values. In both scenarios, the CAM D_e estimate decreases as p increases (**Figures 6**, **7**). In the scenario of μ_q = 10 Gy, the single-grain CAM D_e estimate (**Figure 6G**) is consistent with multi-grain ones (**Figures 6H,I**) when $p = 0.95$. By contrast, in the scenario of μ_q = 50 Gy, the CAM D_e estimate increases slightly as N_g increases from 1 to 200 when p = 0.95 (**Figures 7G–I**). In addition, the CAM D_e estimates obtained from a smaller baseline dose are obviously lower than those obtained from a larger baseline dose; the maximum CAM D_e estimates are 2.22 ± 0.013 Gy and 10.37 ± 0.047 Gy, when μ_q = 10 Gy and μ_q = 50 Gy, respectively. These results demonstrate the strong influences of the baseline doses and the proportion of fully-bleached grains on the simulated dose distributions (Peng et al., 2020).

DISCUSSION

A positive correlation was identified between L_n/T_n and corresponding SAR D_e in several samples (**Figure 4**), suggesting that these multi-grain aliquots might have been influenced by heterogeneous bleaching (e.g., Fan et al., 2013). However, we noted that it is improper to diagnose them as heterogeneously-bleached samples based solely on the L_n/T_n versus D_e plot. For example, although the natural OSL

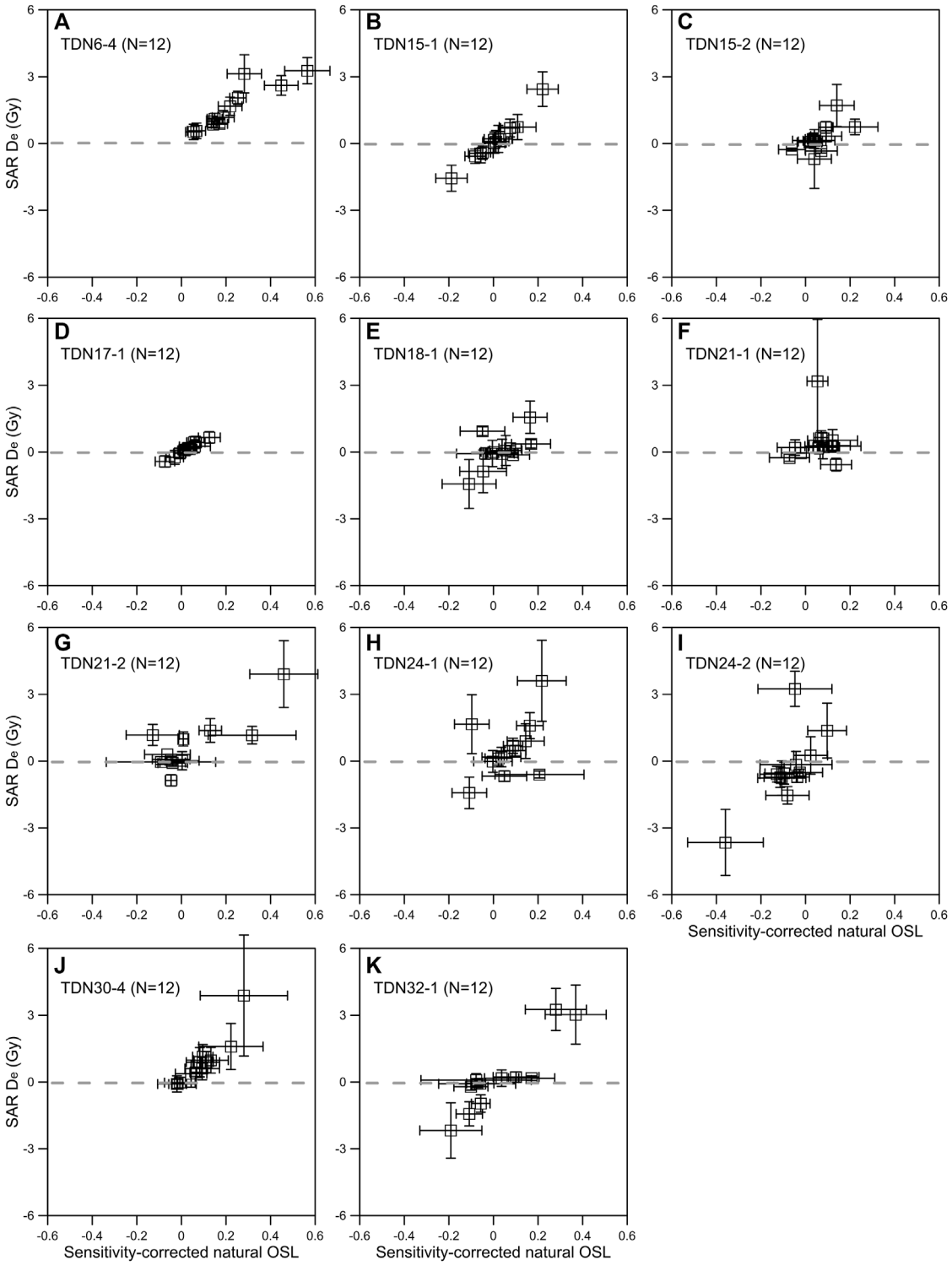

FIGURE 4 | Variations of SAR D_e values as a function of the sensitivity-corrected natural OSL signals for different aeolian samples.

intensity of sample TDN15-1 is close to the background level (**Figure 2B**), an obvious positive relationship is observed between L_n/T_n and D_e (**Figure 4B**), suggesting the diagnosis method is inapplicable. This may because 1) the huge uncertainty of the calculated SAR D_e caused by poor counting statistics and 2) the "averaging" effect arising from the multi-grain results discount the usefulness of the L_n/T_n versus D_e plot; In the first situation, L_n/T_n and D_e values have large uncertainties and in the second

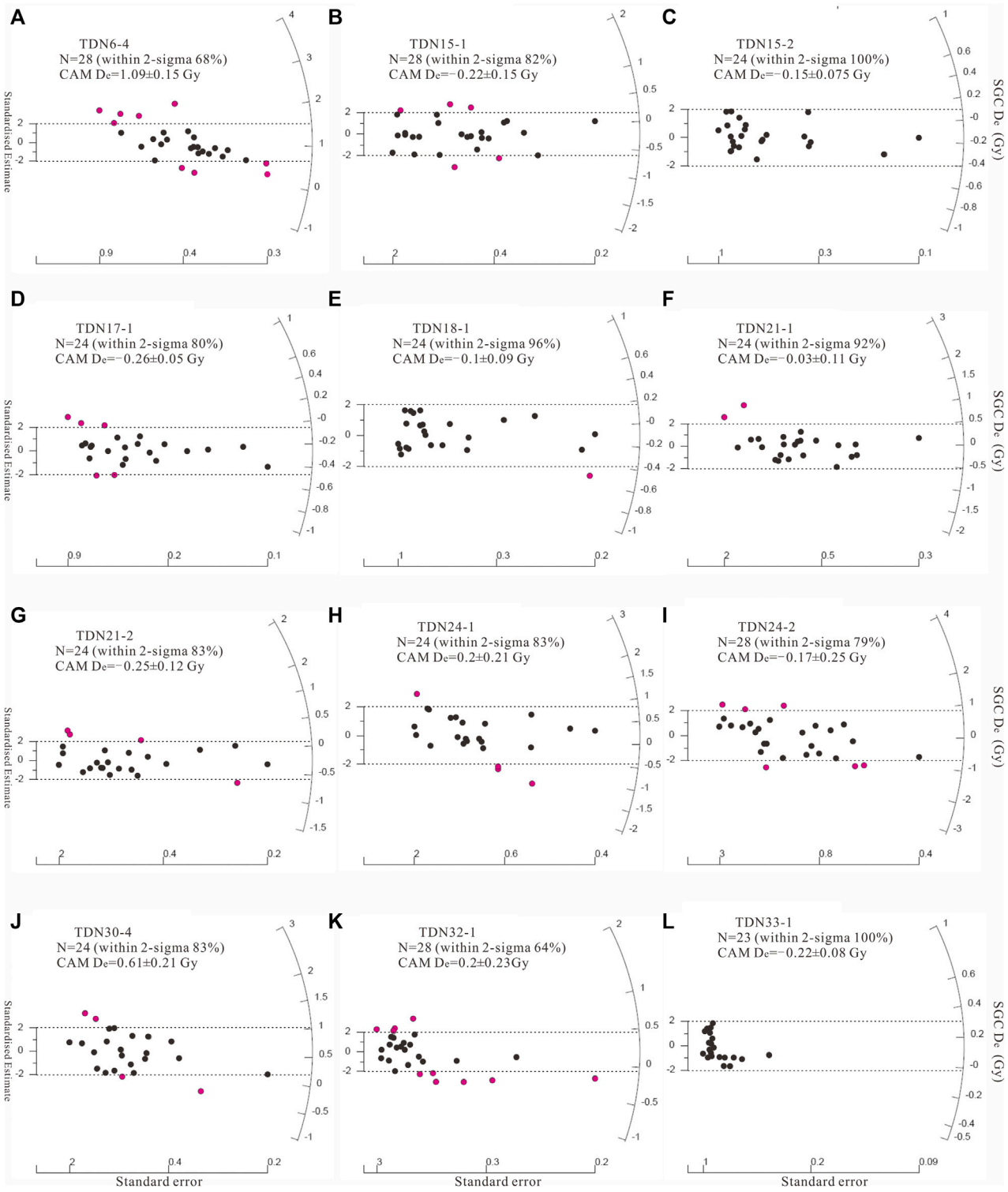

FIGURE 5 | Radial plot showing calculated SGC D_e distributions of different aeolian samples. The dashed lines indicate the two sigma range of the distribution.

situation, an increase of D_e as a function of L_n/T_n may merely result from the superposition of signals originated from different grains. Wallinga (2002) demonstrated that a correlation between natural OSL and associated D_e should only be expected for heterogeneously-bleached multi-grain samples when the OSL sensitivity of individual grains is similar. In addition, Fan et al.

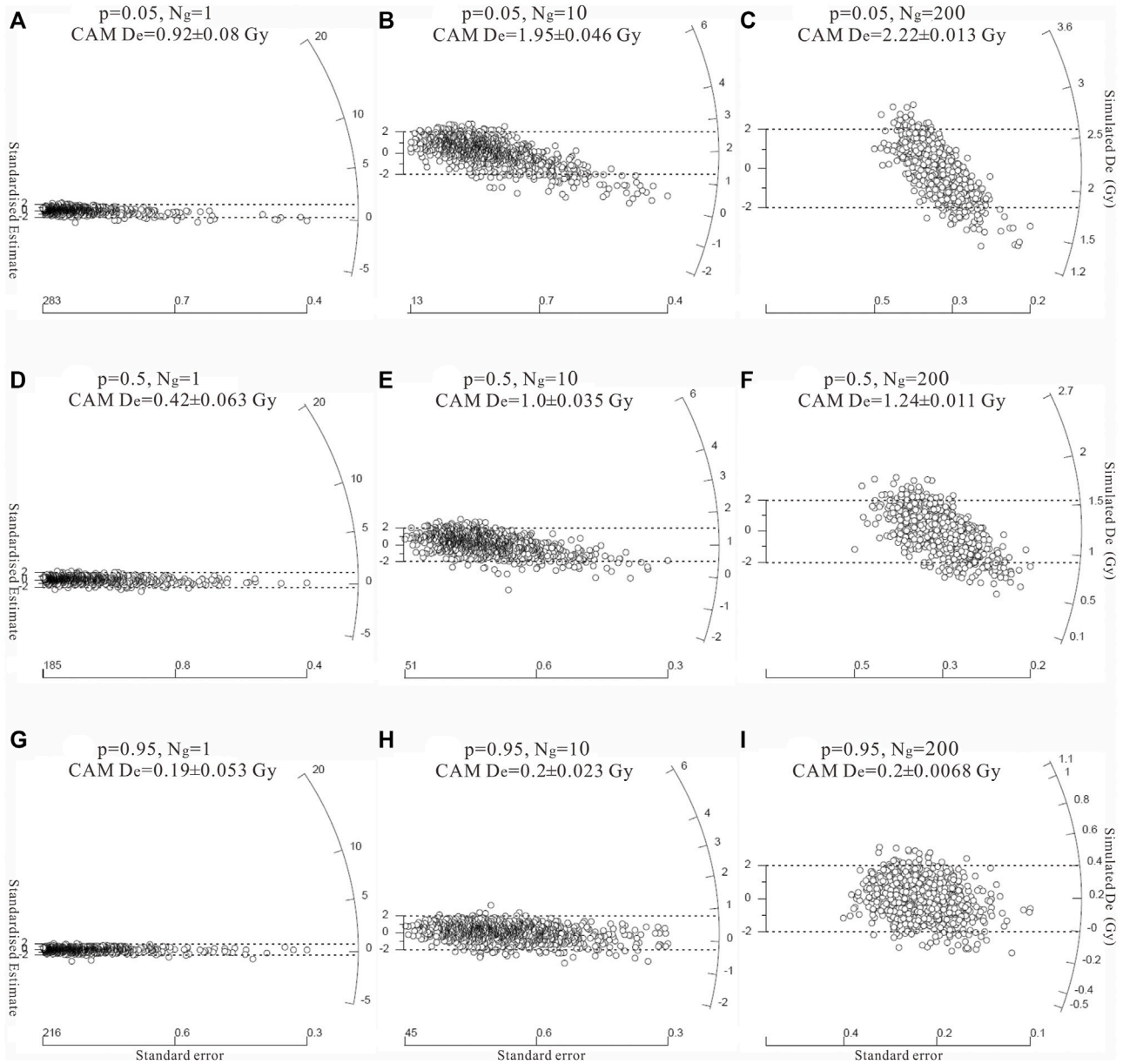

FIGURE 6 | D_e distributions simulated using a burial dose of μ_a = 0.1 Gy and a baseline dose of μ_q = 10 Gy, for different proportions of fully-bleached grains (p) and different numbers of grains contained in an aliquot (N_g). Each subplot consists of 1,000 D_e values. The dashed lines indicate the two sigma range of the distribution.

(2013) suggested that the L_n/T_n versus D_e plot is only applicable for the portion of the plot containing only positive D_e values. An alternative method for bleaching degree diagnosis is inspecting the D_e distribution, that is, tight D_e distributions are expected for undisturbed and fully-bleached samples (e.g., Olley et al., 2004; Arnold et al., 2009). The D_e distributions obtained using the SGC method demonstrate small between-aliquot variations and the resultant CAM D_e estimates are very small (**Figure 5**). However, it has been pointed out that the detection of heterogeneous bleaching based solely on this method may fail if a large number of grains are presented within an aliquot (e.g., Wallinga, 2002; Duller, 2008). Accordingly, it is best that the bleaching degree of OSL signals of multi-grain aliquots can be assessed using multiple methods.

Considering the abovementioned concerns on the detection of heterogeneous bleaching based on the multi-grain results presented here, we further applied a simulation approach to validate the bleaching degree of these samples. When a grain number of 200 (i.e., the expected minimum grain numbers for the measured aliquots of **Figure 5**) and a small baseline dose (10 Gy) were applied, the CAM D_e calculated using the simulated multi-grain aliquots were 2.22 ± 0.013 Gy (**Figure 6C**), 1.24 ± 0.011 Gy (**Figure 6F**), and 0.2 ± 0.0068 Gy (**Figure 6I**), respectively, if the proportion of fully-bleached grains are small (5%), moderate

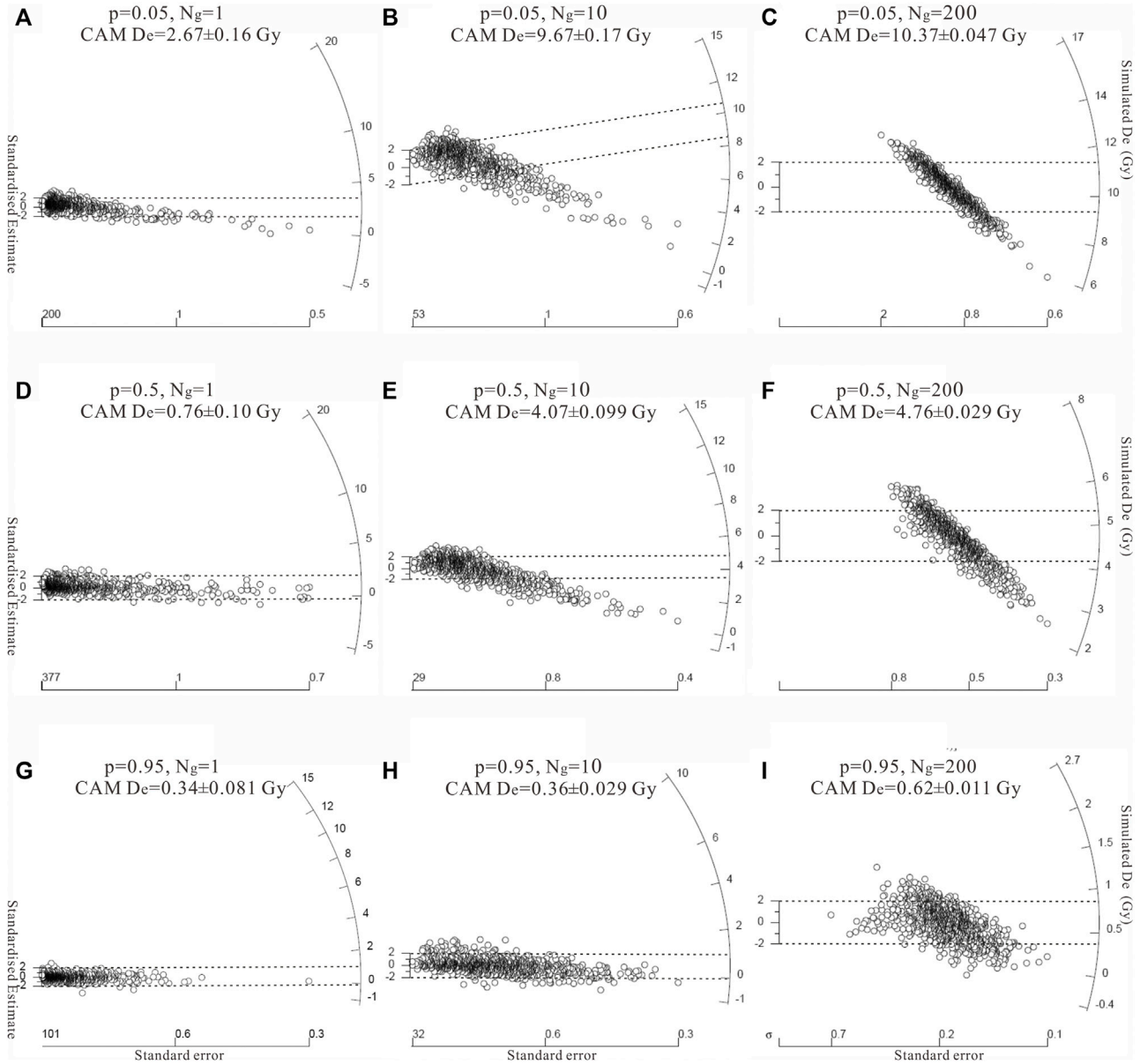

FIGURE 7 | D_e distributions simulated using a burial dose of μ_a = 0.1 Gy and a baseline dose of μ_q = 50 Gy, for different proportions of fully-bleached grains (p) and different numbers of grains contained in an aliquot (N_g). Each subplot consists of 1,000 D_e values. The dashed lines indicate the two sigma range of the distribution.

(50%), and large (95%). When a grain number of 200 and a relatively large baseline dose (50 Gy) were applied, the CAM D_e estimates were 10.37 ± 0.047 Gy (**Figure 7C**), 4.76 ± 0.029 Gy (**Figure 7F**), and 0.62 ± 0.011 Gy (**Figure 7I**), respectively. The measured D_e distributions containing both positive and negative D_e values and tight dose distributions (**Figure 5B**–l) are more similar to the one of **Figure 6I** simulated with a large proportion of fully-bleached grains and a small baseline dose. In addition, a small baselined dose and a proportion of fully-bleached grains of 50% (i.e., **Figure 6F**) yield a CAM D_e similar to the measured sample TDN6-4 (**Figure 5A**). These results validate that the measured multi-grain aliquots of **Figure 5** (except TDN6-4) had small residual doses before the last exposure to sunlight and most of their grains (at least 95%) were fully bleached before deposition. Yang et al. (2020) reached a similar conclusion for their coarse-grained aeolian samples collected from the middle Hexi Corridor to the west of the Tengger Desert.

The bleaching of optically sensitive electrons within a quartz grain depends on both the transport medium and the deposition mechanism. The distance or time duration of transport (Spooner et al., 2001; Singhvi and Porat, 2008) and the deposition process (Rhodes, 2011; Fan et al., 2013) are two major factors influencing the bleaching degree of aeolian sediments, that is, a longer transport distance and a slower deposition rate enable higher

degree of bleaching. Since most of the investigated aeolian samples were collected along the margin of the Tengger Desert (with relatively short transport distance), transport distance should not be a critical factor responsible for the good bleaching performance. A possible mechanism prompting a high degree of bleaching is that these near-surface samples have experienced strong wind-driven erosion/reworking processes before their final deposition. This is likely to occur in relatively high-energy environments characterized by intermittent strong winds such as the Tengger Desert (e.g., Fan et al., 2002; Lv et al., 2009; Zhang et al., 2014). The extremely high volume abundances in the uppermost part of the grain-size distributions (see **Figure 1B**) suggest that almost samples acquired their sorting characteristics in a high-energy environment. An already halted/deposited quartz grain will have a chance to be exposed to sunlight if it subsequently suffers from at least one cycle of erosion/reworking, which explains why the measured multi-grain D_e distributions can be successfully reproduced by the simulation model fed with a small baseline dose. Rhodes (2011) emphasized the importance of total transport time and the repeated burst of movement interspersed with temporary shallow burial or halts on the bleaching of grains and pointed out that the last transport event before the final deposition is not necessarily the most important if the grain has been exposed for sufficient duration during previous movement/rework. In addition, the negligible volume abundances of fine particles contained within almost aeolian samples (**Figure 1B**) suggest that the bleaching of these coarse grains might have not been severely influenced by the phenomena of aggregation (or the adhering of fine particles to coarser ones) (e.g., Derbyshire et al., 1998) which impedes the bleaching of aggregated grains by attenuating of sunlight during transportation.

CONCLUSION

The bleaching degree of multi-grain coarse quartz OSL signals from the margin of the Tengger Dessert was investigated by both empirical analysis and numerical validation. The tight D_e distributions and small D_e values indicate that these multi-grain aliquots may have been fully bleached before deposition. A numerical modelling method is able to reproduce multi-grain D_e distributions similar to the measured ones only if the vast majority of the grains within an aliquot are fully bleached and the baseline dose is relatively small during the simulation. These results reassure us to strengthen the conclusion that most investigated samples are fully bleached before deposition, which may be explained by the wind-driven erosion/reworking of the already stopped near-surface sediments and/or the absence of severe aggregation of grains.

DATA AVAILABILITY STATEMENT

The raw data supporting the conclusions of this article will be made available by the authors, without undue reservation.

AUTHOR CONTRIBUTIONS

HM conceptualized the study, conducted the investigation and visualization, and wrote the original draft. JP conducted the investigation and visualization, performed the numerical simulation, and edited the manuscript. ZL conducted the investigation and visualization, reviewed the manuscript. YS conducted the investigation and visualization, and performed the formal analysis. TF edited and reviewed the manuscript.

FUNDING

This study was supported by the National Natural Science Foundation of China (Grant No. 41701004) and the Natural Science Foundation of Hunan Province, China (Grant No. 2020JJ5162).

ACKNOWLEDGMENTS

We appreciate both reviewers for their valuable comments which allow us to improve the quality of the manuscript.

REFERENCES

Arnold, L. J., Roberts, R. G., Galbraith, R. F., and DeLong, S. B. (2009). A Revised Burial Dose Estimation Procedure for Optical Dating of Youngand Modern-Age Sediments. *Quat. Geochronol.* 4 (4), 306–325. doi:10.1016/j.quageo.2009.02.017

Bailey, S. D., Wintle, A. G., Duller, G. A. T., and Bristow, C. S. (2001). Sand Deposition during the Last Millennium at Aberffraw, Anglesey, North Wales as Determined by OSL Dating of Quartz. *Quat. Sci. Rev.* 20 (5–9), 701–704. doi:10.1016/s0277-3791(00)00053-6

Ballarini, M., Wallinga, J., Murray, A. S., van Heteren, S., Oost, A. P., Bos, A. J. J., et al. (2003). Optical Dating of Young Coastal Dunes on a Decadal Time Scale. *Quat. Sci. Rev.* 22 (10–13), 1011–1017. doi:10.1016/s0277-3791(03)00043-x

Banerjee, D., Murray, A. S., Bøtter-Jensen, L., and Lang, A. (2001). Equivalent Dose Estimation Using a Single Aliquot of Polymineral Fine Grains. *Radiat. Meas.* 33 (1), 73–94. doi:10.1016/s1350-4487(00)00101-3

Buckland, C. E., Bailey, R. M., and Thomas, D. S. G. (2019). Using Post-IR IRSL and OSL to Date Young (< 200 Yrs) Dryland Aeolian Dune Deposits. *Radiat. Meas.* 126, 106131. doi:10.1016/j.radmeas.2019.106131

Costas, I., Reimann, T., Tsukamoto, S., Ludwig, J., Lindhorst, S., Frechen, M., et al. (2012). Comparison of OSL Ages from Young Dune Sediments with a High-Resolution Independent Age Model. *Quat. Geochronol.* 10, 16–23. doi:10.1016/j.quageo.2012.03.007

Derbyshire, E., Meng, X., and Kemp, R. A. (1998). Provenance, Transport and Characteristics of Modern Aeolian Dust in Western Gansu Province, China, and Interpretation of the Quaternary Loess Record. *J. Arid Environ.* 39 (3), 497–516. doi:10.1006/jare.1997.0369

Duller, G. A. T. (2008). Single-grain Optical Dating of Quaternary Sediments: Why Aliquot Size Matters in Luminescence Dating. *Boreas* 37 (4), 589–612. doi:10.1111/j.1502-3885.2008.00051.x

Fan, H. W., Xiao, H. L., Duan, Z. H., Li, X. R., Li, T., and Li, J. G. (2002). Dustfall Characteristics and Affect Factors in Chinese Desert Region. *J. Desert Res.* 22 (6), 559–565. (In Chinese).

Fan, T. L., Fan, Y. X., Zhao, H., Chen, F. H., and Lai, Z. P. (2013). Investigations on the Degree of Bleaching of Quartz OSL Signals Using Modern Aeolian Dust from Western Loess Plateau, China. *Geochronometria* 40 (3), 165–176. doi:10.2478/s13386-013-0112-y

Fan, Y. X., Zhang, Q. S., Cai, Q. S., Gao, M. M., Yan, X. Y., and Yang, G. L. (2022). OSL Chronology of Sediments in the Tengger Sandy Desert and its Indication to Aeolian Sand Source and Desertification Mechanism. *Quat. Sci.* 42 (2), 350–367. (In Chinese). doi:10.11928/j.issn.1001-7410.2022.02.03

Fu, X., Li, S. H., and Li, B. (2015). Optical Dating of Aeolian and Fluvial Sediments in North Tian Shan Range, China: Luminescence Characteristics and Methodological Aspects. *Quat. Geochronol.* 30, 161–167. doi:10.1016/j.quageo.2015.03.001

Galbraith, R. F. (1988). Graphical Display of Estimates Having Differing Standard Errors. *Technometrics* 30 (3), 271–281. doi:10.1080/00401706.1988.10488400

Galbraith, R. F., Roberts, R. G., Laslett, G. M., Yoshida, H., and Olley, J. M. (1999). Optical Dating of Single and Multiple Grains of Quartz from Jinmium Rock Shelter, Northern Australia: Part I, Experimental Design and Statistical Models. *Archaeometry* 41 (2), 339–364. doi:10.1111/j.1475-4754.1999.tb00987.x

Goble, R. J., Mason, J. A., Loope, D. B., and Swinehart, J. B. (2004). Optical and Radiocarbon Ages of Stacked Paleosols and Dune Sands in the Nebraska Sand Hills, USA. *Quat. Sci. Rev.* 23 (9–10), 1173–1182. doi:10.1016/j.quascirev.2003.09.009

Godfrey-Smith, D. I., Huntley, D. J., and Chen, W. H. (1988). Optical Dating Studies of Quartz and Feldspar Sediment Extracts. *Quat. Sci. Rev.* 7 (3–4), 373–380. doi:10.1016/0277-3791(88)90032-7

Gong, Z. J., Li, S. H., Sun, J. M., and Xue, L. (2013). Environmental Changes in Hunshandake (Otindag) Sandy Land Revealed by Optical Dating and Multi-Proxy Study of Dune Sands. *J. Asian Earth Sci.* 76, 30–36. doi:10.1016/j.jseaes.2013.07.035

Hu, G. M., and Li, S. H. (2019). Simplified Procedures for Optical Dating of Young Sediments Using Quartz. *Quat. Geochronol.* 49, 31–38. doi:10.1016/j.quageo.2018.03.009

Hu, G., Zhang, J. F., Qiu, W. L., and Zhou, L. P. (2010). Residual OSL Signals in Modern Fluvial Sediments from the Yellow River (HuangHe) and the Implications for Dating Young Sediments. *Quat. Geochronol.* 5 (2–3), 187–193. doi:10.1016/j.quageo.2009.05.003

Li, S. H., Sun, J. M., and Zhao, H. (2002). Optical Dating of Dune Sands in the Northeastern Deserts of China. *Palaeogeogr. Palaeoclimatol. Palaeoecol.* 181 (4), 419–429. doi:10.1016/s0031-0182(01)00443-6

Li, G. Q., Jin, M., Wen, L. J., Zhao, H., Madsen, D., Liu, X. K., et al. (2014). Quartz and K-Feldspar Optical Dating Chronology of Eolian Sand and Lacustrine Sequence from the Southern Ulan Buh Desert, NW China: Implications for Reconstructing Late Pleistocene Environmental Evolution. *Palaeogeogr. Palaeoclimatol. Palaeoecol.* 393, 111–121. doi:10.1016/j.palaeo.2013.11.003

Li, B., Jacobs, Z., Roberts, R. G., Galbraith, R., and Peng, J. (2017). Variability in Quartz OSL Signals Caused by Measurement Uncertainties: Problems and Solutions. *Quat. Geochronol.* 41, 11–25. doi:10.1016/j.quageo.2017.05.006

Li, S. H. (2001). Identification of Well-Bleached Grains in the Optical Dating of Quartz. *Quat. Sci. Rev.* 20 (12), 1365–1370. doi:10.1016/s0277-3791(00)00156-6

Lian, O. B., and Huntley, D. J. (1999). Optical Dating Studies of Postglacial Aeolian Deposits from the South-Central Interior of British Columbia, Canada. *Quat. Sci. Rev.* 18 (13), 1453–1466. doi:10.1016/s0277-3791(98)00085-7

Long, H., Tsukamoto, S., Buylaert, J.-P., Murray, A. S., Jain, M., and Frechen, M. (2019). Late Quaternary OSL Chronologies from the Qinghai Lake (NE Tibetan Plateau): Inter-comparison of Quartz and K-Feldspar Ages to Assess the Pre-depositional Bleaching. *Quat. Geochronol.* 49, 159–164. doi:10.1016/j.quageo.2018.05.003

Lv, P., Dong, Z. B., Zhang, Z. C., and Zhao, A. G. (2009). Characteristics of Wind Velocity, Temperature and Humidity Profiles of Near-Surface Layer in Tengger Desert. *J. Desert Res.* 29 (5), 977–981. (In Chinese).

Mahadev, R., Singh, A. K., and Jaiswal, M. K. (2019). Application of Luminescence Age Models to Heterogeneously Bleached Quartz Grains from Flood Deposits in Tamilnadu, Southern India: Reconstruction of Past Flooding. *Quat. Int.* 513, 95–106. doi:10.1016/j.quaint.2019.02.037

Murray, A. S., and Wintle, A. G. (2000). Luminescence Dating of Quartz Using an Improved Single-Aliquot Regenerative-Dose Protocol. *Radiat. Meas.* 32 (1), 57–73. doi:10.1016/s1350-4487(99)00253-x

Olley, J. M., Pietsch, T., and Roberts, R. G. (2004). Optical Dating of Holocene Sediments from a Variety of Geomorphic Settings Using Single Grains of Quartz. *Geomorphology* 60 (3–4), 337–358. doi:10.1016/j.geomorph.2003.09.020

Ou, X. J., Duller, G. A. T., Roberts, H. M., Zhou, S. Z., Lai, Z. P., Chen, R., et al. (2015). Single Grain Optically Stimulated Luminescence Dating of Glacial Sediments from the Baiyu Valley, Southeastern Tibet. *Quat. Geochronol.* 30, 314–319. doi:10.1016/j.quageo.2015.02.018

Peng, J. (2021). Analyzing Statistical Age Models to Determine the Equivalent Dose and Burial Age Using a Markov Chain Monte Carlo Method. *Geochronometria* 48, 147–160. doi:10.1515/geochr-2015-0114

Peng, J., Dong, Z. B., Han, F. Q., Long, H., and Liu, X. J. (2013). R Package numOSL: Numeric Routines for Optically Stimulated Luminescence Dating. *Anc. TL* 31 (2), 41–48. Available at: https://CRAN.R-project.org/package=numOSL.

Peng, J., Dong, Z. B., Han, F. Q., and Gao, L. (2016). Aeolian Activity in the South Margin of the Tengger Desert in Northern China since the Late Glacial Period Revealed by Luminescence Chronology. *Palaeogeogr. Palaeoclimatol. Palaeoecol.* 457, 330–341. doi:10.1016/j.palaeo.2016.06.028

Peng, J., Li, B., and Jacobs, Z. (2020). Modelling Heterogeneously Bleached Single-Grain Equivalent Dose Distributions: Implications for the Reliability of Burial Dose Determination. *Quat. Geochronol.* 60, 101108. doi:10.1016/j.quageo.2020.101108

Peng, J., and Li, B. (2017). Single-aliquot Regenerative-Dose (SAR) and Standardised Growth Curve (SGC) Equivalent Dose Determination in a Batch Model Using the R Package "numOSL". *Anc. TL* 35 (2), 32–53.

Peng, J., Wang, X. L., Yin, G. M., Adamiec, G., Du, J. H., Zhao, H., et al. (2022). Accumulation of Aeolian Sediments Around the Tengger Desert during the Late Quaternary and its Implications on Interpreting Chronostratigraphic Records from Drylands in North China. *Quat. Sci. Rev.* 275, 107288. doi:10.1016/j.quascirev.2021.107288

Pietsch, T. J. (2009). Optically Stimulated Luminescence Dating of Young (<500 Years Old) Sediments: Testing Estimates of Burial Dose. *Quat. Geochronol.* 4 (5), 406–422. doi:10.1016/j.quageo.2009.05.013

Qiang, M. R., Chen, F. H., Wang, Z. T., Niu, G. M., and Song, L. (2010). Aeolian Deposits at the Southeastern Margin of the Tengger Desert (China): Implications for Surface Wind Strength in the Asian Dust Source Area over the Past 20,000 Years. *Palaeogeogr. Palaeoclimatol. Palaeoecol.* 286 (1–2), 66–80. doi:10.1016/j.palaeo.2009.12.005

Rhodes, E. (2007). Quartz Single Grain OSL Sensitivity Distributions: Implications for Multiple Grain Single Aliquot Dating. *Geochronometria* 26, 19–29. doi:10.2478/v10003-007-0002-5

Rhodes, E. J. (2011). Optically Stimulated Luminescence Dating of Sediments over the Past 200,000 Years. *Annu. Rev. Earth Planet. Sci.* 39, 461–488. doi:10.1146/annurev-earth-040610-133425

Roberts, H. M., and Duller, G. A. T. (2004). Standardised Growth Curves for Optical Dating of Sediment Using Multiple-Grain Aliquots. *Radiat. Meas.* 38 (2), 241–252. doi:10.1016/j.radmeas.2003.10.001

Singarayer, J. S., Bailey, R. M., Ward, S., and Stokes, S. (2005). Assessing the Completeness of Optical Resetting of Quartz OSL in the Natural Environment. *Radiat. Meas.* 40 (1), 13–25. doi:10.1016/j.radmeas.2005.02.005

Singhvi, A. K., and Porat, N. (2008). Impact of Luminescence Dating on Geomorphological and Palaeoclimate Research in Drylands. *Boreas* 37 (4), 536–558. doi:10.1111/j.1502-3885.2008.00058.x

Spooner, N. A., Olley, J. M., Questiaux, D. G., and Chen, X. Y. (2001). Optical Dating of an Aeolian Deposit on the Murrumbidgee Floodplain. *Quat. Sci. Rev.* 20 (5–9), 835–840. doi:10.1016/s0277-3791(00)00032-9

Stokes, S., Bailey, R. M., Fedoroff, N., and O'Marah, K. E. (2004). Optical Dating of Aeolian Dynamism on the West African Sahelian Margin. *Geomorphology* 59 (1–4), 281–291. doi:10.1016/j.geomorph.2003.07.021

Tissoux, H., Valladas, H., Voinchet, P., Reyss, J. L., Mercier, N., Falguères, C., et al. (2010). OSL and ESR Studies of Aeolian Quartz from the Upper Pleistocene Loess Sequence of Nussloch (Germany). *Quat. Geochronol.* 5 (2–3), 131–136. doi:10.1016/j.quageo.2009.03.009

Vermeesch, P. (2009). RadialPlotter: A Java Application for Fission Track, Luminescence and Other Radial Plots. *Radiat. Meas.* 44 (4), 409–410. doi:10.1016/j.radmeas.2009.05.003

Wallinga, J. (2002). On the Detection of OSL Age Overestimation Using Single-Aliquot Techniques. *Geochronometria* 21, 17–26.

Wintle, A. G. (1993). Luminescence Dating of Aeolian Sands: An Overview. *Geol. Soc. Lond. Spec. Publ.* 72 (1), 49–58. doi:10.1144/gsl.sp.1993.072.01.06

Yang, L. H., Long, H., Cheng, H. Y., Hu, G. Y., Duan, H. C., and Zhao, H. (2020). Historical Settlement Abandonment in the Middle Hexi Corridor Linked to Human-Induced Desertification. *Palaeogeogr. Palaeoclimatol. Palaeoecol.* 545, 10963. doi:10.1016/j.palaeo.2020.109634

Yi, S. W., Buylaert, J. P., Murray, A. S., Thiel, C., Zeng, L., and Lu, H. Y. (2015). High Resolution OSL and Post-IR IRSL Dating of the Last Interglacial-Glacial Cycle at the Sanbahuo Loess Site (Northeastern China). *Quat. Geochronol.* 30, 200–206. doi:10.1016/j.quageo.2015.02.013

Yin, G. M., Wang, X. L., and Han, F. (2013). The Age of the Shapotou Desert Expansion Based on OSL Ages of Aeolian Sediments in the Yellow River Terraces, Ningxia Hui Autonomous Region, Northern China. *Quat. Sci.* 33 (2), 269–275. (In Chinese).

Zhang, J. F., Zhou, L. P., and Yue, S. Y. (2003). Dating Fluvial Sediments by Optically Stimulated Luminescence: Selection of Equivalent Doses for Age Calculation. *Quat. Sci. Rev.* 22 (10–13), 1123–1129. doi:10.1016/s0277-3791(03)00054-4

Zhang, Z. C., Dong, Z. B., Wen, Q., and Jiang, C. W. (2014). Wind Regimes and Aeolian Geomorphology in the Western and Southwestern Tengger Desert, NW China. *Geol. J.* 50 (6), 707–719. doi:10.1002/gj.2586

Zhao, H., Chen, F. H., Li, S. H., Wintle, A. G., Fan, Y. X., and Xia, D. S. (2007). A Record of Holocene Climate Change in the Guanzhong Basin, China, Based on Optical Dating of a Loess-Palaeosol Sequence. *Holocene* 17 (7), 1015–1022. doi:10.1177/0959683607080530

Zhao, H., Li, G. Q., Sheng, Y. W., Jin, M., and Chen, F. H. (2012). Early-middle Holocene Lake-Desert Evolution in Northern Ulan Buh Desert, China. *Palaeogeogr. Palaeoclimatol. Palaeoecol.* 331-332, 31–38. doi:10.1016/j.palaeo.2012.02.027

Conflict of Interest: The authors declare that the research was conducted in the absence of any commercial or financial relationships that could be construed as a potential conflict of interest.

Publisher's Note: All claims expressed in this article are solely those of the authors and do not necessarily represent those of their affiliated organizations, or those of the publisher, the editors and the reviewers. Any product that may be evaluated in this article, or claim that may be made by its manufacturer, is not guaranteed or endorsed by the publisher.

frontiers | Frontiers in Earth Science

ORIGINAL RESEARCH
published: 30 June 2022
doi: 10.3389/feart.2022.939539

Optical Dating of Quartz Grains From the Minjiang Fluvial Terraces in the Sonpan Area on the Eastern Margin of the Tibetan Plateau

Ye-Song Han, Jia-Fu Zhang, Geng-Nian Liu and Zhi-Jiu Cui*

MOE Laboratory for Earth Surface Processes, Department of Geography, College of Urban and Environmental Sciences, Peking University, Beijing, China

The fluvial terraces along the banks of the Minjiang River are very important for understanding the tectonic activities of the eastern margin of the Tibetan Plateau and have been widely investigated. However, the reliability of the ages previously reported for the terraces needs further evaluation. In this study, the Minjiang River terraces in the Sonpan area from Hongqiaoguan to the Songpan town were investigated and dated using optically stimulated luminescence (OSL) techniques on quartz grains. Seven strath terraces (T1–T7) were recognized based on the exposures of fluvial sediment and the elevation of bedrock strath, and two of them have been reported by previous studies. The terrace deposits and overlying loess were sampled for OSL dating. The samples exhibited a large scatter in D_e, even for loess samples, which could be attributed to poor bleaching at deposition. However, the OSL ages obtained using the minimum age model were underestimated, and those obtained using the central age model are considered relatively reliable based on stratigraphic and geomorphological consistency and the comparison of the ages between stratigraphically parallel samples. The results show that the loess samples overlying fluvial terrace sediments were deposited later than terrace formation and their OSL ages cannot represent the terrace formation ages. The T1, T3, T4, T5, and T6 terraces were dated to 13.5 ± 0.6, 29.0 ± 1.7, 48.0 ± 3.3, 44.3 ± 5.2 and 63.8 ± 4.7 ka, respectively. The T4 and T5 terraces may be the same terrace with a weighted mean age of 46.9 ± 2.8 ka. The ages of the T2 and T7 terraces were inferred to be ~20 and ~80 ka, respectively, based on the relationship between strath ages and elevations of the other terraces. The mean bedrock river incision rates were calculated to be 1.2 ± 0.1 mm/a for the time period of 64 ka for the T6 terrace—14 ka for the T1 terrace, and 0.15 mm/a for the past 14 ka.

Keywords: quartz OSL dating, fluvial terraces, incision rate, Minjiang River, Tibetan Plateau

OPEN ACCESS

Edited by:
Hao Long,
Nanjing Institute of Geography and Limnology (CAS), China

Reviewed by:
Yuji Ishii,
National Institute of Advanced Industrial Science and Technology (AIST), Japan
Xiaodong Miao,
Linyi University, China

****Correspondence:***
Jia-Fu Zhang
jfzhang@pku.edu.cn

Specialty section:
This article was submitted to Quaternary Science, Geomorphology and Paleoenvironment, a section of the journal Frontiers in Earth Science

Received: *09 May 2022*
Accepted: *24 May 2022*
Published: *30 June 2022*

Citation:
Han Y-S, Zhang J-F, Liu G-N and Cui Z-J (2022) Optical Dating of Quartz Grains From the Minjiang Fluvial Terraces in the Sonpan Area on the Eastern Margin of the Tibetan Plateau. Front. Earth Sci. 10:939539. doi: 10.3389/feart.2022.939539

1 INTRODUCTION

The eastern margin of the Tibetan Plateau has been an active tectonic zone, where tectonic movements such as fault activities and earthquakes have been widely investigated in order to understand regional crustal deformation (Li, 1991; Tang et al., 1991; Harrison et al., 1992; Chen et al., 1994; Zhao et al., 1994; Burcheiel et al., 1995; Arne et al., 1997; Clark and Royden, 2000; Kirby et al.,

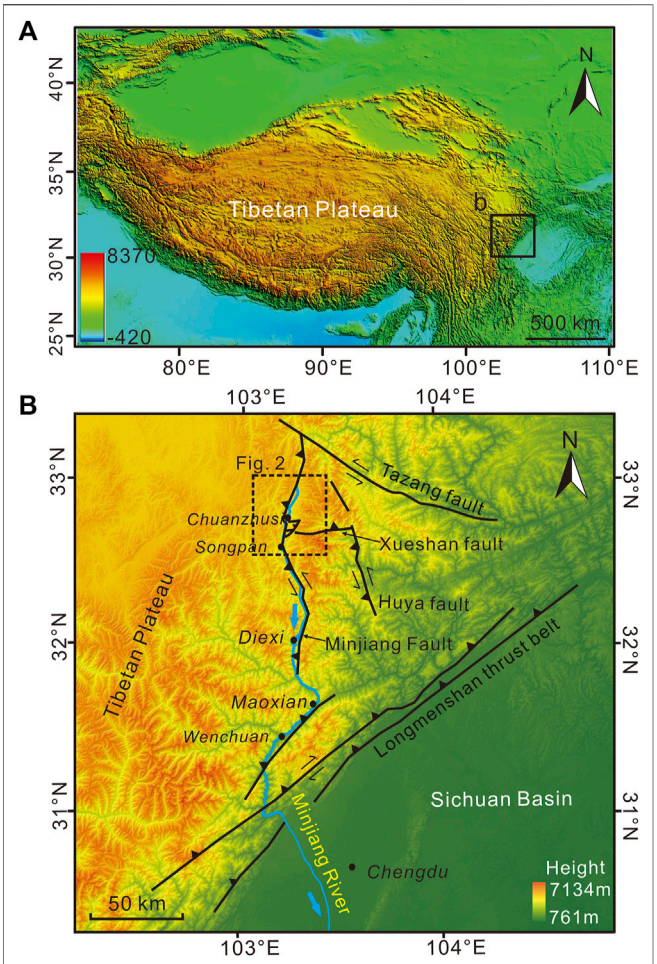

FIGURE 1 | DEM showing the location of the study area. **(A)** The Minjiang River is situated on the eastern margin of the Tibetan Plateau close to the Sichuan Basin, and **(B)** the enlarged image showing the reaches of the Minjiang River between its source and the basin, and the faults in the study area which are from Kirby et al. (2000) and Tan et al. (2019).

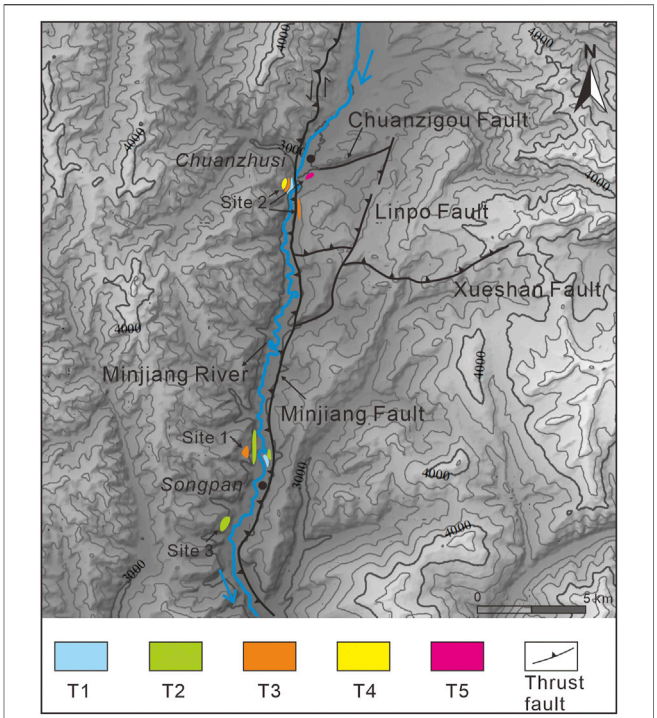

FIGURE 2 | DEM image showing the sites (marked as sites 1–3) investigated in the Songpan area, and the distribution of the seven fluvial terraces and the faults (Kirby et al., 2000).

2000, 2002; Zhou et al., 2000; Li et al., 2001; Toda et al., 2008; Royden et al., 2008). Tectonic activities like uplift could be recorded by a flight of fluvial strath terraces on river banks (Cunha et al., 2008; Gong et al., 2014; Fu et al., 2016), especially in the Tibetan Plateau and nearby regions (e.g., Lavé and Avouac, 2001; Vance et al., 2003). The Minjiang River situated at the eastern margin of the Tibetan Plateau (**Figure 1**) is the main tributary of the Yangtze River and has been widely investigated to understand the relationship between river erosion and tectonic movements (**Figure 1**; Tang et al., 1991; Chen et al., 1994; Zhao et al., 1994; Kirby et al., 2000; Zhou et al., 2000; Yang et al., 2003; Li et al., 2005; Ma et al., 2005; Gao and Li, 2006; Wu et al., 2009; Liu et al., 2013). On the other hand, fluvial incisions along the banks of the Minjiang River and its tributary have also induced a number of large rockslides (Kirby et al., 2002; Wang et al., 2011; Wang et al., 2012; Zhao et al., 2019; Wu et al., 2020). This means that the fluvial sediments and terraces of the Minjiang River can be archives of change in geomorphology and tectonic conditions of the region and can provide temporal information.

In the previous studies, the formation ages of the Minjiang River terraces were determined using various dating techniques including radiocarbon (Kirby et al., 2000), thermoluminescence (TL) (Tang, et al., 1991; Chen et al., 1994; Zhao et al., 1994; Zhou et al., 2000; Li et al., 2005; Ma et al., 2005; Gao and Li, 2006), infrared stimulated luminescence (IRSL, Kirby et al., 2000) and electron-spin resonance (ESR, Yang et al., 2003; Liu et al., 2013). However, the reliability of some of the ages obtained using these techniques requires further assessment. This is because 1) charcoal fragments within fluvial deposits might be from reworked sediments and re-deposited, and the upper age limit of radiocarbon dating is usually less than 40 ka; 2) TL and ESR signals from sediments are generally difficult to bleach, especially for those from fluvial sediments; 3) feldspar IRSL signals usually suffer from anomalous fading (Spooner, 1994). The former two could result in age overestimation, and the third in age underestimation. Additionally, loess deposits overlying fluvial sediments were sampled for TL dating (Chen et al., 1994; Kirby et al., 2000), the loesses may be much younger than the underlying fluvial sediments (Yan et al., 2018; Zhang et al., 2020). But their OSL ages can represent the minimum ages of terrace-tread formation. On the other hand, the published age data for the Minjiang River terraces are not enough to build a robust chronological frame for the terrace sequence of the whole river. Recently, optically stimulated luminescence (OSL) signals of quartz have been widely and successfully used to date fluvial sediments

because quartz OSL signals are more easily reset by light exposure (Perkins and Rhodes, 1994; Aitken, 1998; Wallinga, 2002; Rittenour, 2008; Rhodes, 2011; Zhang et al., 2003; Zhang et al., 2009).

In this study, we investigated the fluvial terraces of the Minjiang River in the Songpan area from Hongqiaoguan to the Songpan town in the upper reaches of the river (**Figures 1B**, **2**), where fluvial sediments and bedrock strath can be observed in exposures. In the field, we first found the exposures of fluvial layers on the banks of the river and their bottoms (bedrock straths), and measured the elevations of the straths above the modern river level (amrl), and sampled fluvial sediments and loess deposits on terraces for OSL dating. The strath terraces were mainly defined by the elevations of bedrock straths and their dated ages. The samples were OSL dated on quartz grains. The reliability of the OSL ages obtained for all samples was evaluated first by analyzing luminescence properties and next by stratigraphic and geomorphological consistency. The age values obtained for some terraces were used to calculate river incision.

2 GEOLOGICAL AND GEOMORPHOLOGICAL SETTINGS

The eastward extrusion of the Tibetan Plateau during the Indo-Asian collision results in upper crustal shortening at the eastern margin of the plateau and the formation of the Min Shan and Longmen Shan (Chinese "shan" = mountain) to the north of the Sichuan Basin during the Cenozoic (**Figure 1**; Kirby et al., 2000, 2002; Hubbard and Shaw, 2009; Hetzel, 2013). The marginal region is characterized by greater topographic relief than anywhere else on the Tibetan plateau (Hubbard and Shaw, 2009), as demonstrated by a series of rugged high mountain peaks, steep ridges, and narrow and deep valleys. The topographic elevation ranges from ~5,000 m above sea level (asl) for mountains in the eastern Tibetan Plateau to ~600 m asl for the Chengdu Plain within the Sichuan Basin within the horizontal distance of 50–60 km. The Min Shan (its main peak (Mount Xuebaoding) with an altitude of 5,588 m asl) is a north-south-trending mountain that extends 150 km long and 50–60 km wide (Zhao et al., 1994; Zhou et al., 2000; Zhang et al., 2006a; Zhang et al., 2006b). Landslides occur in large numbers along the Minjiang River, resulting in the formation and failure of landslide dams on the river (Wang and Meng, 2009; Chigira et al., 2010; Gorum et al., 2011; Luo et al., 2019; Zhao et al., 2019), which strongly influence fluvial processes of the river.

The Minjiang River along the eastern margin of the Tibetan Plateau originates from the Gongga watershed, runs through the Min Shan, and enters into the Sichuan Basin. A large number of sediments have been brought to the basin, where the sediments reach up to 500 m in thickness (Wang and Meng, 2009). The elevation of the mountains in the catchment of the river varies between ~5,000 m asl and ~1,000 m asl. This transition zone between plateau and basin belongs to the transitional belt between the Songpan-Ganzi orogenic belt and Longmen Shan tectonic belt (Tang et al., 1991; Chen et al., 1994; Li et al., 2005). In the Songpan area, as mentioned above, fluvial terraces have been wildly studied. However, different numbers of terraces have been reported: five terraces (Tang et al., 1991), three terraces (Zhao et al., 1994), or two terraces (Chen et al., 1994; Kirby et al., 2000), suggesting the complicated geomorphological situation of the study area and the need for further investigations.

3 METHODOLOGY

3.1 Field Work and Sampling

The original stair-stepped topography of fluvial terraces in the study area is not directly observed on topographic maps, satellite images, or air photos, because the terraces were found as isolated and local remnants, and not continually distributed along the two steep banks of the river. The identification of terraces was conducted by observing fluvial sediments exposed on natural outcrops or road cuts and the bottom of the sediment overlying bedrock surface (strath). The elevations of terrace straths and treads (here the "tread" is referred to as the near-horizontal top surface of fluvial deposits, including channel or overbank facies resting on terrace straths) above the modern river level and the thickness of the terrace deposits were measured using a laser rangefinder (TruPulse 200X, distance accuracy: 4–30 cm) and a tape measure. The precise locations and altitude of the exposures were recorded using a hand-held global positioning system (GPS) receiver with a barometric altimeter (Garmin GPSmap 60CSx) with an accuracy of ±~3 m in altitude. The stratigraphy and lithology of the exposures were described in detail. Here, three localities in the area were carefully investigated and the terrace remnants were mapped on a 1:50,000 topographic map (**Figure 2**).

In order to constrain the formation ages of the terraces, loess and fluvial sediments atop terrace straths were taken for OSL dating. The OSL dating of the loess samples is twofold: 1) the luminescence properties of the quartz grains from the loess samples can be used to evaluate the luminescence behaviors of fluvial sediments, and 2) the OSL ages of the loess samples can be regarded as the minimum age estimates of terrace formation. It is noted that some stratigraphically parallel samples (from the same depth, and the horizontal distance between the sampling holes is less than 30 cm) were collected for assessing the validity of OSL ages obtained. Sampling was done by hammering 3.5-cm-diameter and 20-cm-long stainless-steel tubes horizontally into freshly cleaned sections. The tubes were filled completely and wrapped with aluminum foil and adhesive tape in order to avoid the risk of sediment mixing and prevent further exposure to light and moisture loss during transport.

3.2 Luminescence Dating

Sample preparation was carried out in a dark room with subdued red light at Peking University. The 2-cm-thick materials at the ends of each sample tube, which may have been exposed to daylight, were removed and used for water

TABLE 1 | Dose rates of the samples from the Minjiang River.

Lab No.	Field No.	Terrace	Depth, m	Sediment	Grain size, μm	U, ppm	Th, ppm	K, %	Rb, ppm	Water content[a], %	Beta dose rate, Gy/ka	Gamma dose rate, Gy/ka	Cosmic dose rate, Gy/ka	Total dose rate, Gy/ka
Site 1														
Section A	103°36.093′E 32°39.623′N													
L2658	MJOSL-01A	T2	2.7	Loess	90–125	3.11 ± 0.12	16.40 ± 0.43	1.82 ± 0.05	86.20 ± 5.52	20 (15.2)	1.72 ± 0.09	1.29 ± 0.06	0.23 ± 0.02	3.24 ± 0.12
L2659	MJOSL-01B	T2	2.7	Loess	63–90	3.06 ± 0.12	14.70 ± 0.38	1.98 ± 0.06	103.00 ± 5.77	20 (20.1)	1.82 ± 0.10	1.25 ± 0.06	0.23 ± 0.02	3.30 ± 0.12
Section B	103°36.060′E 32°39.691′N													
L2660	MJOSL-02A	T5	7.0	Loess	63–90	3.15 ± 0.12	14.50 ± 0.39	2.18 ± 0.06	106.00 ± 5.94	15 (5.3)	2.05 ± 0.09	1.36 ± 0.06	0.14 ± 0.01	3.55 ± 0.11
L2661	MJOSL-02B	T5	7.0	Loess	63–90	3.10 ± 0.11	15.90 ± 0.41	2.50 ± 0.06	140.00 ± 6.44	15 (6.7)	2.29 ± 0.10	1.48 ± 0.06	0.14 ± 0.01	3.91 ± 0.12
Section C	103°36.289′E 32°39.517′N													
L2662	MJOSL-03	T1	5.5	Fluvial sand	90–125	2.08 ± 0.09	6.92 ± 0.22	1.39 ± 0.05	69.60 ± 5.22	5 (4.8)	1.4 ± 0.05	0.86 ± 0.02	0.17 ± 0.02	2.43 ± 0.05
L2663	MJOSL-04	T1	5.8	Fluvial sand	90–150	1.73 ± 0.07	4.92 ± 0.17	1.03 ± 0.04	52.20 ± 4.54	5 (2.7)	1.05 ± 0.04	0.65 ± 0.02	0.16 ± 0.02	1.86 ± 0.04
Section D	103°36.353′E 32°39.786′N													
L2680	MJOSL-17A	T2	2.12	Floodplain silt	90–125	2.16 ± 0.09	9.36 ± 0.27	1.39 ± 0.05	73.50 ± 5.22	15 (14.1)	1.31 ± 0.06	0.88 ± 0.04	0.25 ± 0.03	2.44 ± 0.08
L2681	MJOSL-17B	T2	2.12	Floodplain silt	90–125	2.10 ± 0.08	9.11 ± 0.27	1.36 ± 0.04	70.30 ± 5.13	15 (14.7)	1.28 ± 0.06	0.86 ± 0.04	0.25 ± 0.03	2.38 ± 0.07
Site 2														
Section E	103°37.134′E 32°46.085′N													
L2664	MJOSL-05	T1	2.1	Fluvial sand	90–125	2.42 ± 0.10	10.70 ± 0.30	1.94 ± 0.06	86.50 ± 5.71	10 (8.7)	1.81 ± 0.07	1.14 ± 0.04	0.25 ± 0.03	3.20 ± 0.08
L2665	MJOSL-06	T1	2.6	Fluvial sand	90–125	2.38 ± 0.10	10.60 ± 0.30	1.72 ± 0.06	91.00 ± 5.73	15 (12.5)	1.57 ± 0.08	1.03 ± 0.04	0.24 ± 0.02	2.83 ± 0.09
Section F	103°37.175′E 32°46.126′N													
L2666	MJOSL-07A	T5	0.6	Fluvial sand	90–150	1.85 ± 0.07	5.90 ± 0.20	1.01 ± 0.04	52.10 ± 4.53	5 (4.1)	1.07 ± 0.04	0.7 ± 0.02	0.32 ± 0.03	2.08 ± 0.05
Section G	103°37.046′E 32°46.170′N													
L2669	MJOSL-08B	T6	1.0	Fluvial sand	90–125	1.90 ± 0.08	8.76 ± 0.26	1.44 ± 0.05	86.20 ± 5.69	5 (5.1)	1.46 ± 0.05	0.94 ± 0.02	0.29 ± 0.03	2.68 ± 0.06
Section H	103°37.815′E 32°46.450′N													
L2670	MJOSL-09	T7	0.8	Fluvial sand	90–125	1.62 ± 0.08	8.86 ± 0.27	1.48 ± 0.05	72.90 ± 5.32	5 (6.6)	1.45 ± 0.05	0.92 ± 0.02	0.30 ± 0.03	2.67 ± 0.06
Section I	103°37.049′E 32°45.795′N													
L2675	MJOSL-13A	T4	5.3	Fluvial sand	90–125	2.07 ± 0.08	7.94 ± 0.24	1.37 ± 0.05	71.80 ± 5.17	15 (14.1)	1.26 ± 0.06	0.81 ± 0.03	0.18 ± 0.02	2.25 ± 0.07
Site 3														
Section J	103°35.239′E 32°37.689′E													
L3169	SP16-15	T3	4.2	Floodplain silt	90–150	2.43 ± 0.10	10.80 ± 0.30	1.80 ± 0.06	93.70 ± 5.25	15 (8.6)	1.62 ± 0.08	1.06 ± 0.04	0.19 ± 0.02	2.87 ± 0.09
L3170	SP16-16	T3	7.8	Fluvial sand	150–200	2.08 ± 0.09	4.57 ± 0.16	0.85 ± 0.04	40.90 ± 3.68	5 (0.5)	0.92 ± 0.03	0.63 ± 0.02	0.13 ± 0.01	1.68 ± 0.04
L1370[b]	SP16-16#[b]	T3	7.8	Fluvial gravels		1.67 ± 0.08	4.28 ± 0.15	0.66 ± 0.03	31.30 ± 3.04		0.74 ± 0.03	0.53 ± 0.02	0.13 ± 0.01	1.40 ± 0.03

[a]*The assumed water contents were used for dose rate calculation, and the relative uncertainty of 25% was assigned. The numbers in the brackets are the water contents measured at the laboratory. Note that the water contents of the same type of sediments are different, the loess samples are assigned to different water contents because of different geomorphological positions of the sampling sections (see text for details).*

[b]*The sample from surrounding of the OSL sampling position was used to determine the effect of its gamma dose rate on that of sample SP16-16 (see text for details).*

content and dose rate measurements. The remaining interior part of the tube was treated with 10% HCl to dissolve carbonates, and 30% H_2O_2 to remove organic matters, respectively. The samples were then dried and sieved to select the fractions of coarse (>90 μm in diameter) or medium (63–90 μm) grains. The fractions were then immersed in 40% HF for 40 min to remove feldspar contaminants and the outer layer of quartz grains affected by alpha radiation, followed by a wash in warm 10% HCl and deionized water. The extracts were then sieved again to remove grains <90 μm or 63 μm in diameter, respectively. The purity of the quartz fractions was tested by infrared stimulation (Duller, 2003). Negligible IRSL signals were detected, indicating that the feldspar contaminants were successfully removed. Finally, the chemically purified quartz extracts were mounted as a 2 mm diameter (small aliquot, Duller, 2008) monolayer of grains on an aluminum disc (9.8 mm diameter) using silicone oil as an adhesive.

All luminescence measurements, beta irradiation and preheat treatments were carried out in an automated Risø TL/OSL-15 luminescence reader equipped with a $^{90}Sr/^{90}Y$ beta source (Bøtter-Jensen et al., 1999). Blue light (470 ± 30 nm) LED stimulation (90% of 50 mW/cm^2 full power) was used for OSL measurements. Luminescence was detected by an EMI 9235QA photomultiplier tube with a 7.5 mm Hoya U-340 filter (290–370 nm) in front of it.

The improved single-aliquot regenerative-dose (SAR) procedure was applied to measure the equivalent dose (D_e) of the quartz extracts (Murray and Wintle, 2000, 2003). The procedure employed at least five regeneration doses including a zero dose (to check recuperation), and two doses of the same magnitude at the beginning and end (to check sensitivity correction). The preheat and cut heat temperatures were set to 200°C and 160°C for 10 s, respectively, which were determined by preheat plateau and dose recovery tests (see following section). OSL signals were measured for 40 s at the sample temperature of 125°C, and 40 s bleaching at the sample temperature of 280°C at the end of each cycle was performed to reduce recuperation. The net initial OSL signals were derived from the decay curve, taking the first 0.64 s integral of the initial OSL signal, minus a background estimated from the last 3.2 s integral of a 40 s stimulation. The value of D_e was estimated by interpolating the sensitivity-corrected natural OSL onto the dose-response curve using the Analyst software (Duller, 2007). The error on individual D_e values was calculated using the counting statistics and an instrumental uncertainty of 1.0%.

The uranium, thorium and potassium contents of all samples were determined by neutron activation analysis (NAA). Water contents (mass of moisture/dry mass) were measured in the laboratory and are listed in **Table 1**. We consider that these as-sampled water contents cannot represent the in-situ water contents of the samples. The water contents used for dose rate calculation were assumed for each sample, and the relative uncertainty of 25% was assigned (see below, **Section 6.1**). The elemental concentrations were converted into effective dose rates, and ages were calculated using the online dose rate and age calculator DRAC v1.2 (Durcan et al., 2015), in which cosmic ray contribution and dose-rate conversation factors (Guerin et al., 2011) are involved, the alpha (Brennan et al., 1991) and beta (Guerin et al., 2012) grain attenuation factors were used.

4 RIVER TERRACES AND OPTICALLY STIMULATED LUMINESCENCE SAMPLES

A total of ten exposures (Sections, numbered A to J) were carefully investigated in the three sites (**Figure 2**, numbered 1 to 3) in the study area, and two of them are displayed in **Figure 3**. Here the sediments overlying fluvial gravels are divided into loess and floodplain deposits. The loesses are characterized by a massive, loose, and porous structure with vertical joints (**Figure 3A**). They spread out continuously over the terraces, hillslopes, and mountains. The thickness is locally more than 10 m. The floodplain deposits are characterized by horizontal bedding structures, and they are distributed locally on the terraces. Combined with the elevations of straths, a series of fluvial terraces were identified and numbered from T1 youngest to T7 oldest (**Figures 4A–D**), they are described below, although fluvial terraces may suffer from the deformation or displacement in the active tectonic region.

4.1 Site 1

Four exposures (Sections A–D) at site 1 located in the north of the Songpan town were found on the two banks of the river (**Figures 2**, **4B**), and represent the T1, T2, and T5 terrace sections, respectively. The first terrace (T1) can be observed on the two banks of the river, and the elevation of strath above river bed is about 2.1 m (**Figure 4B**). This paired strath terrace is characterized by different deposits on the straths of the west and east banks and a broad and flat tread. The strath on the west bank is overlain by a thin veneer of fluvial gravels, but the deposits on the east bank are more complicated and this terrace reaches the thickness of about 9.8 m (Section C). The bottom layer mantling the strath in Section C is composed of the same well-rounded sandy gravels as in the west bank. The gravel layer is overlain by diamicton, which is sandy with significant contents of clay, silt, and some gravels. The diamicton exhibits weakly bedding and is poorly sorted, within which the gravels are well-rounded and matrix-supported. Lenses of laminated sand are found and sampled for OSL dating (samples MJOSL-03 and 04). The diamicton may be interpreted as solifluction sediment, which was deposited after the formation of the terrace. It is noted that solifluction is widespread on the hillslopes in the study area.

The remnants of the second terrace (T2) at site 1 were also found in the two banks (**Figure 4B**), and the terrace deposits are represented by Section A on the west bank and Section D on the east bank. Section A shows that the terrace deposits consist of channel gravels directly overlying bedrock (the elevation of the bedrock strath is about 9.8 m amrl), this gravel layer with a thickness of 2.5 m is overlain by 3-m-thick loess deposits (**Figure 3A**). The gravel deposits are clast-supported and matrix poorly sorted, and mainly composed of well-rounded

FIGURE 3 | Photographs showing Section A at site 1 **(A)** and Section J at site 3 **(B)**, which represent two terrace sections. Enlarged views of the loess deposits in Section A and gravel deposits in Section J on the right showing details of their sedimentary characteristics.

limestone pebbles and cobbles. Section D on the east bank is composed of gravels and overlying grey mud. The bottom of the gravel layer was not seen and measured. The mud (floodplain silt) is 2.1 m thick, and note that it is difficult to understand the origin of this grey mud in the field. The elevation of the terrace tread for Section D is ~14.9 m amrl. The remnant of the T5 terrace was found on the west bank of the river, with an elevation of ~45 m amrl, and the terrace deposits shown in Section B are the same as those for the T2 terrace. The thicknesses of the gravel and loess layers are 2.7 and 8.1 m, respectively. No sand lenses in these three sections and floodplain silt were found within the gravel layers. In this case, three sets of parallel loess or mud samples for OSL dating for the three sections were taken from positions ~40 cm above the gravel layer (**Table 1**; **Figure 4B**).

4.2 Site 2

Five exposures (Sections E, F, G, I, and H) on the two banks of the river were observed at site 2 located at Hongqiaoguan, and represent the remnants of four terraces named T1, T4, T5, T6, and T7 (**Figure 4A**). The remnants indicate the very narrow treads of the terraces. The deposits on the T1 terrace are composed of channel gravel unit, floodplain silt/fine sand unit, and slopewash deposits on top of the fluvial sediments. The yellow floodplain silt/fine sands are well sorted, and horizontal or nearly horizontal beddings can be observed on the fresh section surface, from which two samples for OSL dating were collected. It is noted that the boundary between the gravel and floodplain silt/fine sand units was not seen due to road construction. The elevation of the bedrock strath is about 2.3 m amrl. The other four sections are mainly composed of sandy gravels that are similar to those for Section A, sand lenses within gravel layers were found and sampled for OSL dating. For Section I, 0.5 m-thick slopewash deposits overlie the gravel unit. The elevations of the terrace straths are shown in **Figure 4A**.

4.3 Site 3

A complete section (Section J) was exposed in a sand pit at site 3 on the west bank of the river on the south of the Songpan town (**Figures 3B**, **4C**), and shows sediments on the T3 terrace. It can be seen that the sandy gravel layer overlying slate bedrock strath is ~12.6 m thick and exhibits horizontal bedding. The clast-supported gravels with interstitial matrix of poorly sorted sand are mainly composed of well-rounded limestone pebbles and cobbles and a few slate cobbles with weak clast long-axis imbrication. The coarse sand matrix is slightly cemented. The gravels in the middle of the layer are intercalated by a 0.3-m-thick sand horizon from which sample SP16-16 was taken. The 0.7-m-thick floodplain sandy silt layer overlying the gravel layer shows well-developed horizontal bedding, from this layer sample SP16-15 was collected. The upper layer consists of a 3.8-m-thick loess and slopewash deposits within which there are some slate fragments. The height of the bedrock strath is about 14.1 m arml.

5 DATING RESULTS

5.1 Luminescence Properties

An example of the dose-response and decay curves for our samples is shown in **Figure 5**. The decay curve for sample MJOSL-13A shows that the quartz OSL signal is reduced rapidly within the first 2 s of stimulation. The comparison of the signal with that from a standard calibrated quartz sample from Risø National Laboratory indicates that, although the reduction of the signal from sample MJOSL-13A during stimulation is much less complete than that of the signal from the standard sample, the intensity of the OSL signal from sample MJOSL-13A is relatively stable after 5 s stimulation than the signal from the standard sample. This implies that the quartz OSL signals from our samples are dominated by the fast component,

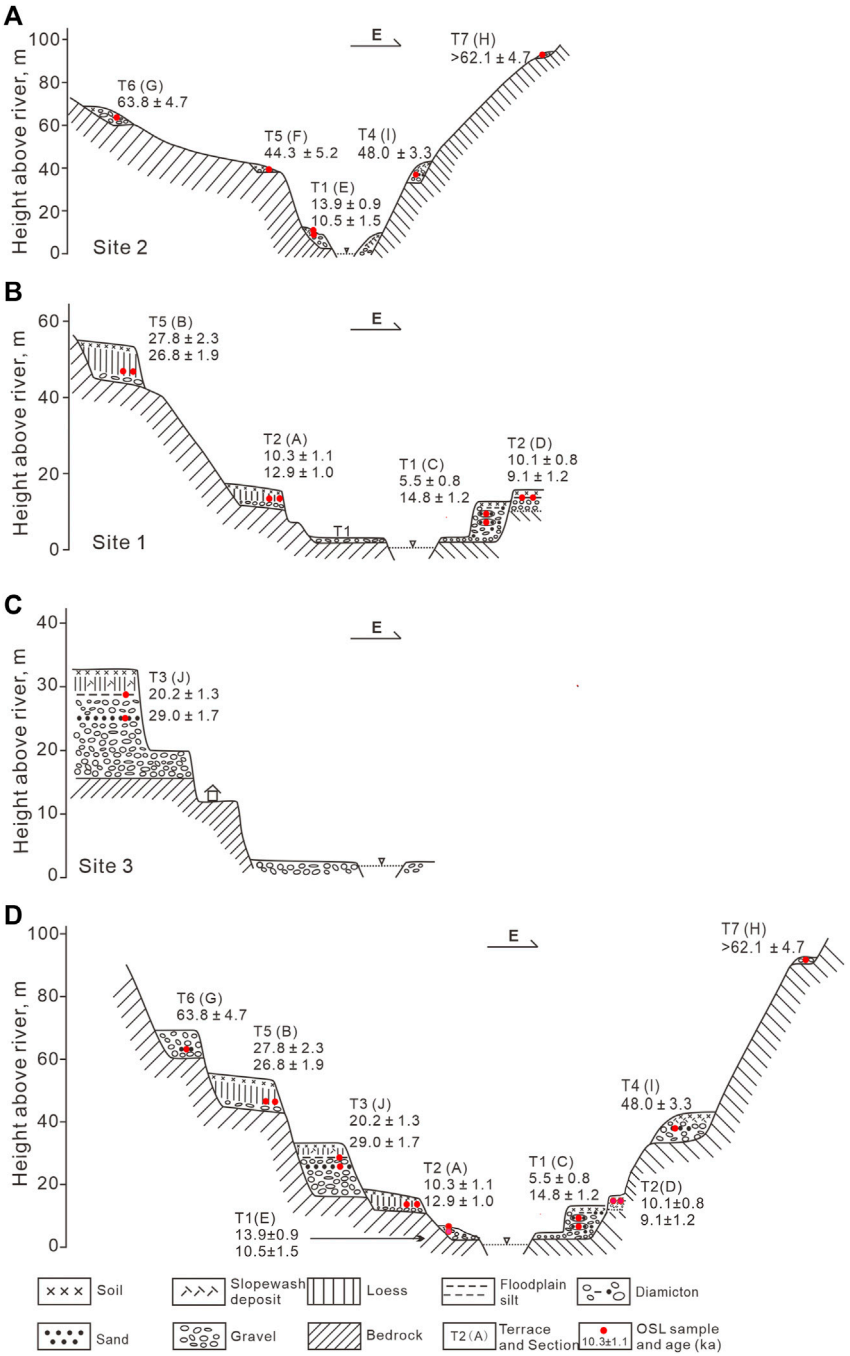

FIGURE 4 | Terrace profiles of the Minjiang River in the Songpan area. The localities of sites 2 **(A)**, 1 **(B)** and 3 **(C)** and the sections (letters in brackets) on the terraces are shown in **Figure 2**. The CAM ages obtained for the samples are displayed (see text for details). **(D)** Composite section showing all terraces found in the study area.

and were easily bleached prior to burial, indicating that the signals can be used for D_e measurement with the SAR protocol (Wintle and Murray, 2006). The dose-response curve in **Figure 5** is well fitted by a single saturation exponential function. The repeat point is in good agreement with the first regenerated dose point, suggesting that the correction for sensitivity change is successful. The sensitivity-corrected OSL signal produced by a zero dose is close to zero, indicating that thermal transfer (recuperation) during D_e measurement is negligible. It is noted that all the dose-response curves

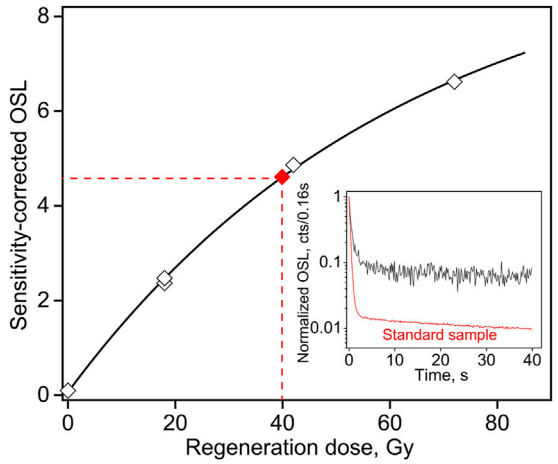

FIGURE 5 | Dose-response curve for a quartz aliquot of sample MJOSL-13A. The regenerated sensitivity-corrected and the natural OSL signals are displayed as open and red solid diamonds, respectively. The regeneration data are fitted using a saturation exponential function. Inset shows a natural OSL decay curve for the aliquot, and a decay curve for a standard calibrated quartz sample from Risø is presented for comparison.

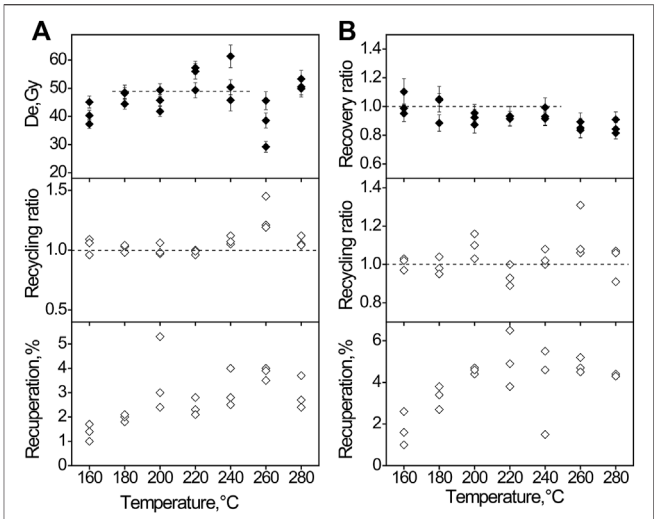

FIGURE 6 | The results of preheat plateau tests **(A)** and dose recovery tests **(B)** for sample MJOSL-13A.

demonstrate that all the measured aliquots are not saturated. However, some aliquots exhibited large thermal transfer (recuperation ratios are >5%), and/or have recycling ratios (the ratio between two duplicate regenerative dose points) beyond the range of 0.9–1.1, these aliquots were excluded for further analyses.

To determine an appropriate preheat temperature for our samples, preheat plateau tests were performed on sample MJOSL-13A using the SAR procedure with the preheat temperatures ranging from 160 to 280°C at 20°C intervals. Three aliquots were measured for each preheat temperature. The D_e values shown in **Figure 6A** indicate no dependence on preheat temperatures from 180 to 240°C when errors are considered. The recycling ratios are close to unity at temperatures from 160 to 220°C, and the recuperation ratios are less than 5% except for one aliquot for all preheat temperatures. To further confirm the D_e plateau, dose recovery tests were carried out on the same sample (MJOSL-13A) as used in the preheat tests. In the dose recovery tests, the nature OSL signals in quartz aliquots were first removed by exposure to the blue light within the OSL reader for 100 s at room temperature. After 18,000 s, the aliquots were then stimulated for 40 s by the blue light to check residual signals, and no detectable luminescence signals were observed. The aliquots were given a beta dose of 46.2 Gy equivalent to the average equivalent dose of the sample. This given dose was taken as a natural dose for the following D_e measurements. The aliquots were then measured using the same SAR procedure as used in the preheat plateau tests to measure the "equivalent dose". The results displayed in **Figure 6B** show that the dose recovery ratios (measured "equivalent dose"/given dose) are close to unity within errors in the temperature range of 160–240°C. The recycling ratios for most of the aliquots are close to unity, and have the recuperation ratios <5% for the whole preheat temperatures. Based on the results of the preheat plateau and dose recovery tests, a preheat of 200°C for 10 s was applied in the SAR procedure for D_e measurements.

5.2 D_e Distribution

Twenty–forty-six aliquots (**Table 2**, number in brackets) of each sample were measured, and 12–36 of them passed the SAR rejection criteria (recycling ratios of 0.9–1.1, recuperation <5%) for each sample and were accepted for final D_e analysis. The D_e distributions are displayed in **Figure 7** and **Supplementary Figure S1** and the degree of scatter in D_e values is evaluated by overdispersion (OD) values calculated using the central age model (CAM) (Galbraith et al., 1999). The results show that the studied samples have the OD values of 23%–56%, with an average of 36.9% ± 2.5%, which are much larger than the global average values of 14% ± 1% and 9% ± 1% published for well-bleached medium-sized aliquots (100–1,000 grains per aliquot) and large-sized aliquots (>1,000 grains per aliquot), respectively (Arnold and Roberts, 2009). Large OD values may indicate the heterogeneous bleaching of sediments at the time of deposition. In this case, the simplified minimum age model (MAM-3) of Galbraith et al. (1999) was used to obtain the "true" burial doses of the samples with the "luminescence package" program (Kreutzer et al., 2012). The σ_b parameter, representing the D_e scatter that cannot be explained by heterogeneous bleaching of quartz grains, should be determined before the D_e analysis using the MAM model. OD values obtained from dose recovery tests are generally considered to represent those of well-bleached samples from the same sources. Therefore, the OD value obtained from the dose recovery tests is generally used as the σ_b value in the MAM model (Galbraith and Roberts, 2012). In this study, the OD value

TABLE 2 | OSL dating results of the samples from the Minjiang River.

Lab No.	Field No.	Terrace	Depth, m	Sediment	Grain size, μm	Total dose rate, Gy/ka	Number of aliquots*	OD, %	CAM De, Gy	CAM age, ka	MAM De, Gy	MAM age, ka	MAM/CAM
Site 1													
Section A													
L2658	MJOSL-01A	T2	2.7	Loess	90–125	3.24 ± 0.12	30 (33)	52 ± 7	33.40 ± 3.27	10.3 ± 1.1	14.85 ± 2.88	4.6 ± 0.9	0.44 ± 0.10
L2659	MJOSL-01B	T2	2.7	Loess	63–90	3.30 ± 0.12	16 (20)	26 ± 5	42.76 ± 2.94	12.9 ± 1.0	36.63 ± 3.75	11.1 ± 1.2	0.86 ± 0.11
Section B													
L2660	MJOSL-02A	T5	7.0	Loess	63–90	3.55 ± 0.09	26 (37)	35 ± 6	98.97 ± 7.67	27.8 ± 2.3	59.84 ± 9.12	16.8 ± 2.6	0.60 ± 0.11
L2661	MJOSL-02B	T5	7.0	Loess	63–90	3.91 ± 0.10	27 (34)	32 ± 5	104.66 ± 6.79	26.8 ± 1.9	67.46 ± 11.53	17.2 ± 3.0	0.64 ± 0.12
Section C													
L2662	MJOSL-03	T1	5.5	Fluvial sand	90–125	2.43 ± 0.05	15 (31)	52 ± 10	13.30 ± 1.82	5.5 ± 0.8	4.63 ± 1.03	1.9 ± 0.4	0.35 ± 0.09
L2663	MJOSL-04	T1	5.8	Fluvial sand	90–150	1.86 ± 0.04	19 (30)	32 ± 6	27.52 ± 2.08	14.8 ± 1.2	20.81 ± 2.64	11.2 ± 1.4	0.76 ± 0.12
Section D													
L2680	MJOSL-17A	T2	2.12	Floodplain silt	90–125	2.44 ± 0.08	25 (30)	35 ± 5	24.52 ± 1.80	10.1 ± 0.8	21.22 ± 2.26	8.7 ± 1.0	0.86 ± 0.12
L2681	MJOSL-17B	T2	2.12	Floodplain silt	90–125	2.38 ± 0.07	21 (32)	56 ± 9	21.60 ± 2.72	9.1 ± 1.2	8.98 ± 2.26	3.8 ± 1.0	0.41 ± 0.12
Site 2													
Section E													
L2664	MJOSL-05	T1	2.0	Fluvial sand	90–125	3.20 ± 0.08	36 (46)	36 ± 4	44.55 ± 2.71	13.9 ± 0.9	28.13 ± 3.87	8.8 ± 1.2	0.63 ± 0.10
L2665	MJOSL-06	T1	2.6	Fluvial sand	90–125	2.83 ± 0.09	12 (30)	44 ± 10	29.77 ± 4.12	10.5 ± 1.5	16.39 ± 3.09	5.8 ± 1.1	0.55 ± 0.13
Section F													
L2666	MJOSL-07A	T5	0.6	Fluvial sand	90–150	2.08 ± 0.05	17 (35)	43 ± 9	92.27 ± 10.55	44.3 ± 5.2	49.71 ± 9.92	23.9 ± 4.8	0.54 ± 0.13
Section G													
L2669	MJOSL-08B	T6	1.0	Fluvial sand	90–125	2.68 ± 0.06	21 (30)	32 ± 5	170.86 ± 12.12	63.8 ± 4.7	107.45 ± 24.35	40.1 ± 9.1	0.63 ± 0.15
Section H													
L2670	MJOSL-09	T7	0.8	Fluvial sand	90–125	2.67 ± 0.06	14 (46)	25 ± 6	166.12 ± 11.96	62.1 ± 4.7	144.07 ± 14.08	53.9 ± 5.4	0.87 ± 0.11
Section I													
L2675	MJOSL-13A	T4	5.3	Fluvial sand	90–125	2.25 ± 0.07	30 (30)	30 ± 5	107.73 ± 6.66	48.0 ± 3.3	81.86 ± 9.64	36.5 ± 4.5	0.76 ± 0.11
Site 3													
Section J													
L3169	SP16-15	T3	4.2	Floodplain silt	90–150	2.87 ± 0.09	19 (23)	24 ± 4	57.78 ± 3.26	20.2 ± 1.3	48.41 ± 6.05	16.9 ± 2.2	0.84 ± 0.12
L3170	SP16-16	T3	7.8	Fluvial sand	150–200	1.68 ± 0.04	20 (23)	23 ± 4	48.82 ± 2.58	29.0 ± 1.7	46.22 ± 1.97	27.5 ± 1.3	0.95 ± 0.07

**The number of accepted aliquots were used for De statistical analysis, and the total number of the aliquots (in brackets) were measured for each sample.*

from the dose recovery test on sample MJOSL-13A is 5% ± 2%. Considering beta-dose heterogeneity (Jankowski and Jacobs, 2018; Fu et al., 2022), published OD values for small aliquots of fluvial sediments (Arnold and Roberts, 2009), and the values from the experiments and modeling for multi-grain analyses (Rodnight et al., 2006; Cunningham et al., 2011), σ_b = 0.15 ± 0.05 was used in our MAM calculation. Additionally, CAM D_e values were also calculated (Galbraith et al., 1999). The calculated CAM D_e values (**Table 2**) range from 13.3 to 170.9 Gy with relative errors from 5.3% to 13.8%, with a mean value of 8.4% ± 0.7%, and the MAM D_e values from 4.6 to 144.1 Gy with relative errors from 4.3% to 25.2%, with a mean value of 15.4% ± 1.4%.

5.3 Optically Stimulated Luminescence Ages

The U, Th, and K contents, water contents, and calculated dose rates of the samples are summarized in **Table 1**. It shows that the U, Th, and K contents are about 1.62–3.15 ppm, 4.57–16.4 ppm, and 0.85%–2.50%, respectively, the large ranges of the content indicate the chemical heterogeneity of the samples. The total dose rates were calculated to be about 1.68–3.91 Gy/ka. The beta and gamma contributions are about 54%–59% and 34%–40% of the total dose rates, respectively. It is noted that the cosmic dose rate is up to 0.32 Gy/ka due to the high altitude. Both CAM and MAM ages for a sample were calculated by dividing the CAM and MAM D_e values by the total dose rates, and the ages obtained for all the samples are presented in **Table 2**. The CAM ages are from about 6 to 64 ka, and the MAM ages from about 2 to 54 ka which are much smaller than the corresponding CAM ages.

6 DISCUSSION

6.1 Reliability of Optically Stimulated Luminescence Ages

6.1.1 Dosimetry

The internal consistency of the calculated dose rates between parallel samples for the three sets of parallel samples (MJOSL-01A and 01B, 02A and 02B, 17A and 17B) gives us confidence in our NAA analysis. However, particular attention is needed to the measured water contents, which (0.5%–20.1%) (**Table 1**, values in brackets) vary significantly from sample to sample, even for the parallel samples or the same type of sediments. It is obvious for some of the samples that their true long-term water contents were significantly underestimated if the measured water contents were used. This may be attributed to the following factors: 1) sediments near section surface had been partly dried up when sampling, 2) the water contents of some samples are associated with their geomorphological positions as suggested by field observation, and 3) the as-sampled water contents are influenced by local weather several days before

sampling. In this case, reasonable water contents are assumed for different samples according to the as-sampled water contents, geomorphological positions, and sediment types, and the assumed relative uncertainty of 25% (1σ) is large enough to cover water content fluctuations through time at a 2σ confidence level. Additionally, it is noted for sample SP16-16 that the sampled sand layer is only 0.3 m in thickness. In this case, the contribution of gamma from the overlying and underlying sediments needs to be considered, because of the possible difference in the radionuclide concentrations between the sampled layer and the overlying and underlying sediments. Usually, an at least a 30 cm distance between the sampling position and a stratigraphic boundary is required when using the U, Th, and K contents of the dated sample to calculate its infinite-matrix dose rate, because the contribution of gamma to dose rate is from a sphere with a radius of about 30 cm in sediments, whereas beta particle has a range of several millimeters. For this sample, the contributions of the beta, gamma, and cosmic dose rates obtained from its U, Th, and K contents to the total dose rate are 54.8%, 37.5%, and 7.8%, respectively. To evaluate the effect of gamma from the overlying and underlying sediments, a sample (SP16-16#) (a large amount of sandy gravels) was collected from the overlying and underlying layers and analyzed for its U, Th, and K contents. The results shown in **Table 1** indicate a slight difference in radioactive concentrations between samples SP16-16 and -16#. In this case, the true gamma dose rate for this sample was evaluated using the model described by Aitken (1998: appendix H). The modeling dry gamma dose rate of 0.65 ± 0.02 Gy/ka obtained for sample SP16-16 was transferred to the wet dose rate of 0.61 ± 0.02 Gy/ka, which is consistent with the gamma dose rate of 0.63 ± 0.02 Gy/ka within errors calculated

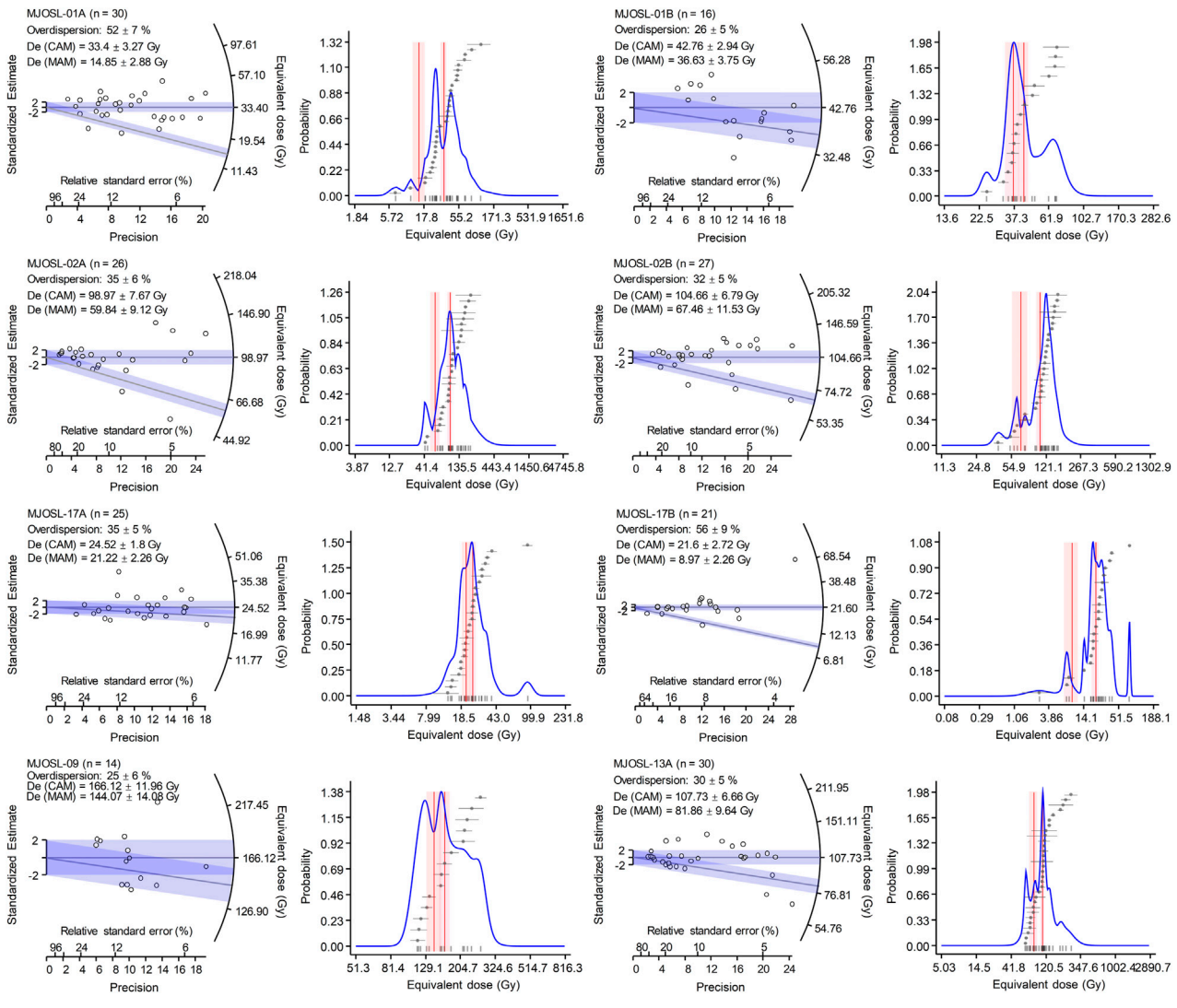

FIGURE 7 | Radial plots and probability density function (pdf) plots showing the D_e distributions, which were produced by the LDAC program (V1.0) provided by Liang and Forman (2019). The two shaded areas refer to the 2σ range for the CAM and MAM D_e values.

from the U, Th and K contents of sample SP16-16. This suggests that the effect of the gamma from the overlying and underlying sediments on sample SP16-16 is negligible when errors are considered. For consistency, the gamma dose rate of 0. 63 ± 0.02 Gy/ka was used for age calculation.

6.1.2 Comparison of Central Age Model and Minimum Age Model Ages

As mentioned above, some aliquots were rejected for failing the SAR rejection criteria (Wintle and Murray, 2006). The D_e values of the aliquots demonstrating luminesce properties suitable for the application of the SAR protocol were used for further analysis. The largest CAM D_e value obtained for our samples is 170.9 ± 12.1 Gy for sample MJOSL-08B from the T6 terrace, corresponding to the OSL age of about 64 ka. The D_e distribution of this sample is shown in **Supplementary Figure S1**, the single aliquot D_e value of 256 ± 27 Gy is the largest among the aliquots measured for this sample. The characteristic saturation dose (D_0) of the dose-response curve for this aliquot was calculated to be 190 Gy, showing that the age of the sample is within the maximum range of quartz luminescence dating (Wintle and Murray, 2006).

It is well known that dating fluvial sediments may encounter a partial bleaching problem, especially for young samples. Poorly bleached samples often show a wide, asymmetric distribution in D_e when small aliquots are analyzed (e.g., Duller, 1994; Murray et al., 1995; Olley et al., 1998; Olley et al., 1999; Lepper and McKeever, 2002; Wallinga, 2002; Spencer et al., 2003). For such partially bleached samples, their MAM ages are generally considered to represent the true burial ages of well-bleached grains (Galbraith et al., 1999). However, the application of the MAM to some samples may result in significant age underestimation (e.g., Thomsen et al., 2016; Singh et al., 2017; Murray et al., 2021). In this study, the samples exhibit large OD values ranging from 23% to 56%, even for the four loess samples (grain size of 63–90 μm was used for three samples) with an average OD value of 36.3% ± 5.6%. For the application of MAM (Galbraith et al., 1999), the appropriate value of σ_b is needed, this σ_b represents the expected overdispersion caused by factors such as counting statistics and instrument reproducibility except for incomplete bleaching. It is known that the D_e overdispersion is caused by many factors such as partial bleaching, post-depositional mixing, and microdosimetry except for measurement errors. In reality, it is difficult to identify and quantify the factors, among which one contributes to the size of the overdispersion. Galbraith and Roberts (2012) suggest the use of a well-bleached sample of similar origin and age with which to measure OD. Here the average OD value of the four loess samples is not used as σ_b required in MAM for the fluvial samples because of their different origins. The OD value of 36.3% ± 5.6% for loess samples is larger than those of most of the fluvial samples. If it is used as σ_b in the MAM calculation for our fluvial samples, the CAM and MAM ages obtained will be similar. In this study, the MAM ages obtained using the σ_b of 0.15 are compared with the CAM ages in **Figure 8**. It shows that the MAM underestimates the CAM by 5.3%–65.3% with an average of 33.2% ± 4.5% for all the samples including the loess samples (**Figure 8A**). The figure also demonstrates that the D_e difference (CAM-MAM) broadly increases with the CAM ages (inset in

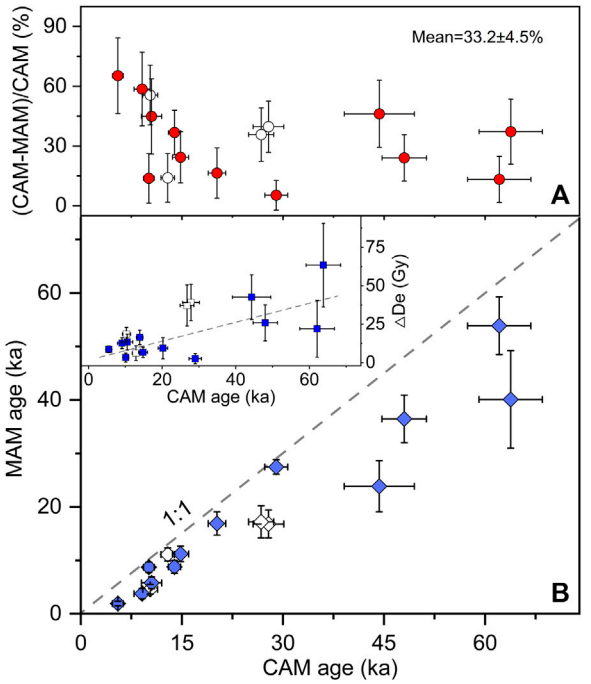

FIGURE 8 | (A) Plot of the relative difference between MAM and CAM ages as a function of the CAM ages, **(B)** comparison of the MAM and CAM ages, and the inset shows the difference (ΔD_e) between MAM and CAM D_e values. The open points refer to loess samples.

Figure 8B). The trend of an increasing difference with increasing CAM age is difficult to interpret using the degree of bleaching of OSL signals at the time of deposition (residual doses). This is supported by the fact that published residual doses of sand-sized quartz from modern fluvial sediments at the time of deposition are generally less than several Gy (e.g., Jain et al., 2004; Alexanderson, 2007; Hu et al., 2010; Hu et al., 2015; Toth et al., 2017; Chamberlain and Wallinga, 2019; Yan et al., 2021). For this case, as suggested by Thomsen et al. (2016) and Singh et al. (2017), the CAM ages may be more reliable.

The validity of the CAM and MAM ages is further checked using lithostratigraphic and geomorphological consistency. Three sets of parallel samples (MJOSL-01A and 01B, 02A and 02B, 17A and 17B) were measured to assess the reliability of the dating results. The OSL ages of parallel samples should have similar OSL ages. This is because each set of parallel samples was collected from the same depth, and the horizontal distance between the sampling holes is less than 30 cm. The results show that the loess parallel samples (MJOSL-01A and 01B) from Section A were measured using different grain sizes of quartz, their CAM ages are consistent within 2σ uncertainty level errors but their MAM ages are completely inconsistent. This is also the case for the fluvial parallel samples (MJOSL-17A and 17B). The other loess parallel samples (MJOSL-02A and 02B) from Section B have similar CAM and MAM ages, respectively. This comparison implies that the CAM ages appear to be more reliable. All these indicate that the CAM ages are more reasonable. Accordingly,

we consider the CAM ages to be relatively more reliable and used for further analyses.

6.2 Terrace Ages

6.2.1 Terrace T1

As shown in **Figure 4**, the four samples from the T1 terrace at sites 1 and 2 were, respectively, dated to 14.8 ± 1.2 and 5.5 ± 0.8 ka for Section C and 10.5 ± 1.5 and 13.9 ± 0.9 ka for Section E. The comparison shows that the value of 5.5 ± 0.8 ka cannot represent the formation age of the terrace. The other values are consistent within errors, although sample MJOSL-04 (14.8 ± 1.2 ka) from a sand lens within the diamicton overlying the fluvial gravel layer. The age consistency also suggests that deposition of the diamicton was contemporaneous with the formation of the terrace. In this case, these consistent ages were combined to obtain a single weighted mean age estimate, it was calculated to be 13.5 ± 0.6 ka. Thus, we consider that the formation age of the terrace is 13.5 ± 0.6 ka.

6.2.2 Terrace T2

The remnants of the T2 terrace were found on the east and west bank of the river at site 1, and four samples were collected from Sections A and D. The two loess samples from Section A yielded the OSL ages of 12.9 ± 1.0 and 10.3 ± 1.1 ka, and the two mud samples from Section D the ages of 9.1 ± 1.2 and 10.1 ± 0.8 ka, respectively. These four ages are consistent within errors and similar to the ages for the T1 terrace, suggesting that the loess and mud sediments overlying gravels on the two banks (Sections A and D) were deposited simultaneously and much later than the formation of the terrace. The terrace age should be older than the burial ages of the loess or mud samples. Based on the river incision rate (see below), the age of this terrace is deduced to be about 20 ka (**Figure 9**).

6.2.3 Terrace T3

At site 3, one overbank sample (SP16-15) and one sand sample (SP16-16) from the sand lens within the gravel layer from Section J were, respectively, dated to 20.2 ± 1.3 and 29.0 ± 1.7 ka, which are stratigraphically consistent. It is noted that the channel gravel layer at this site is very thick (up to 12.6 m). The vertical distance from the strath surface to the sampling point is about 9.3 m. The thick terrace deposits may lead to the difference in ages among the dated samples, the terrace tread and strath (Zhang et al., 2020). If the deposition of the gravels and overbank silts at this site were rapid, the ages of the terrace tread and strath are approximately equal to those (20.2 ± 1.3 and 29.0 ± 1.7 ka) of samples SP16-16 from the overbank silt layer and -17 from the gravel layer, respectively. On the other hand, if the deposition rate is relatively slow, the age of the dated sample could not directly represent the strath age, which is defined as the end of an interval of strath formation (Bull, 1991; Bull, 2007). Alternatively, tread and strath ages can be obtained by calculating a deposition rate for these sediments using an age-depth model (Zhang et al., 2020). We assumed an average deposition rate for the fluvial sediments and no hiatus between the two sedimentary facies, a deposition rate of 0.4 ± 0.1 m/ka was calculated based on the relationship between the ages and depths of the two fluvial samples. The terrace tread (top of floodplain silts) and strath (base of the gravels) were extrapolated to ~19.2 and ~51.7 ka, respectively. It is obvious that the extrapolated age of 51.7 ka for the strath is unreasonable because it is older than the age (~47 ka) of the higher terrace (T4 and T5) (see below). In this case, we deduce that the measured age of 29.0 ± 1.7 ka is closer to the true strath age than that obtained from the age-depth model.

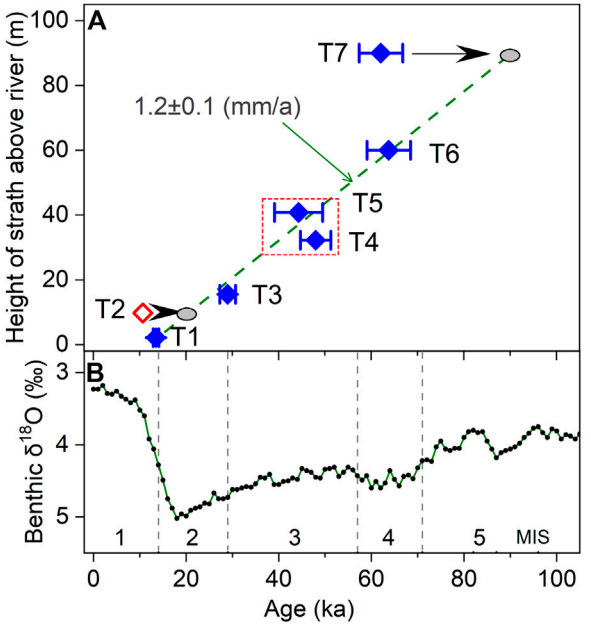

FIGURE 9 | (A) Plot of terrace heights above modern river against terrace ages. The slope of the regression line represents the long-term incision rate derived from the T1, T3, T5, and T6 terraces. The measured ages of the T2 and T7 were underestimated, the true ages may be inferred from the regression line. The T4 and T5 terrace may be the same terrace. The open diamond refers to loess samples. **(B)** The oxygen isotope curve for comparison to terrace ages, MIS refers to the marine oxygen isotope stages (Lisecki and Raymo, 2005).

6.2.4 Terraces T4 and T5

The remnants of the T4 terrace were found on the east bank of the river at site 2. One sample from Section I was dated to 48.0 ± 3.3 ka (**Figure 4A**). The remnants of the T5 terrace were found at sites 1 and 2 (**Figures 4A,B**), and the two parallel loess samples (MSOSL-02A and 02B) overlying gravels from Section B at site 1 were, respectively, dated to 26.8 ± 1.9 and 27.8 ± 2.3 ka, which are much younger than the fluvial sand sample from Section F at site 2 which yielded the age of 44.3 ± 5.2 ka. This indicates that loess was deposited much later than the formation of the terrace. It is noted that the ages of the two samples from Sections I for T4 and F for T5 at site 2 are statistically consistent with errors, which may indicate that they are actually one terrace with the weighted mean age of 46.9 ± 2.8 ka, although they have slightly different elevations of bedrock strath. This needs further investigation.

6.2.5 Terraces T6 and T7

The remnants of the T6 and T7 terraces were found on the west and east banks of the river at site 2 (**Figure 4A**). The two fluvial

sand samples from Section G for T6 and Section H for T7 were dated to 63.8 ± 4.7 and 62.1 ± 4.7 ka, respectively. Geomorphologically, the age consistency of these two samples is difficult to explain. This is because, for a series of strath terraces with different heights along a river valley, higher terraces usually formed earlier than lower terraces due to river incision if no tectonic activities had taken place. The elevation of the T7 bedrock strath is 90 m amrl, much higher than the T6 terrace strath (its elevation is 60 m amrl). The two terraces cannot form simultaneously. The most likely explanation for this situation is that the OSL age of the sample from T7 was underestimated, which cannot be explained by luminescence properties such as the shape of the dose-response curve, as shown by OSL dating of Yellow River terraces (Zhang et al., 2020; Yan et al., 2021). Based on the river incision rate (see below), the T7 terrace should be about 80 ka old (**Figure 9**).

6.2.6 Comparison With Previous Studies

Previous studies have reported that there are two fluvial terraces between Hongqiaoquan and the Songpan town: the lower terrace [called "the second terrace" by Chen et al. (1994) or "the Q3 terrace" by Kirby et al. (2000)] and the higher terrace [called "the third terrace' by Chen et al. (1994) or "the Q2 terrace" by Kirby et al. (2000)]. The higher terrace is discontinuous, and its elevation (for tread or strath?) is 40 m at Hongqiaoquan and 25 m at Gaotunzi located at the middle position between Hongqiaouuqn and the Songpan town (Chen et al., 1994), it was deduced to be 25.4 ± 0.5 cal. ka BP, based on the radiocarbon dating of one charcoal sample from associated sediments (not terrace deposits) (Kirby et al., 2000). The lower terrace is a continuous strath terrace, and its elevation (tread or strath?) varies from 20 m at Hongqiaoquan in the north to 5 m in the south (Chen et al., 1994) or its tread ranges from 5 to 10 m (Kirby et al., 2000). It was TL dated to 23.6 ± 2 or 15.3 ± 1.2 ka (two sediment samples) (Chen et al., 1994), or radiocarbon dated to >14.0–6.6 cal. ka BP (two charcoal and one wood sample). Based on the elevation of the lower terrace tread, the lower terrace should correspond to the T1 terrace in this study. It is obvious that the quartz OSL dating in this study provides a more precise age for this terrace than radiocarbon or TL dating. The higher terrace may correspond to the T3 or T4 terrace in this study, but its inferred age of 25.4 ± 0.5 cal. ka BP is obviously underestimated compared with the ages of the T3 or T4 terrace in this study. Additionally, the recognition of the reported two terraces in this area is not supported by the ages obtained in this study.

6.3 Incision Rate and Its Implication

Elevations of terrace strath above a modern river level and strath ages are often used for calculating mean bedrock river incision rates (Maddy, 1997; Maddy et al., 2000), which are then used as proxies for rock-uplift rates (Merritts et al., 1994). Here, the strath ages and elevations above the modern river level of the T1, T3, T5, and T6 terraces were used for calculating the average incision rate between 14 ka for T1 and 64 ka for T6 (**Figure 9**). It can be seen that the regression defines a mean incision rate of 1.2 ± 0.1 mm/a for the time range of 14–64 ka. This calculated rate is similar to the inferred mean incision rate of ~1.5 mm/a for the past ~160 ka reported for this region (Kirby et al., 2000). Compared with the mean incision rates (~0.35 mm/a for the past 70 ka) of the Yellow River in its middle reaches in the eastern Ordos Block (Guo et al., 2012; Zhang et al., 2020; Yan et al., 2021), the incision rate of 1.2 ± 0.1 mm/a implies that the studied tectonically active region has much larger incision or uplift rate during the Late Pleistocene than the stable Ordos Block in the northeastern margin of the Tibetan Plateau. Additionally, based on the mean incision rate of 1.2 ± 0.1 mm/a, we deduce that the T2 and T7 terraces were formed at ~20 and ~80 ka ago, respectively. It is interesting to note that the incision rate of ~0.15 mm/a for the past 14 ka terrace was calculated based on the ages and heights of the T1 terrace, this rate is much smaller than that for the time period of 14–64 ka. The most likely explanation is that the river was dammed nearby by landslides triggered by river erosion or earthquakes (Zhao et al., 2019; Wu et al., 2020) during the Holocene, resulting in the rise of local base level and reduction of the incision.

Figures 2, **4D** show that it is difficult to evaluate the effect of the activity of the Minjiang fault on the terraces. This is because there is no systematic difference in strath elevation and age between the two banks of the river or both sides of the fault. **Figure 9** demonstrates that the T3 terrace was formed during the transition from marine oxygen isotope stages (MIS) 3 to 2, and the T1 terrace from MIS 2 to 1. The other terraces were formed at MISs 5, 4, and 3, implying that it is difficult to infer a simple relationship between terrace formation and climate conditions for all the terraces. Mount Xuebaoding, the highest mountain in the Min Shan region, has been occupied by glaciers. Four glacier events were recognized, and their time periods are >14.1, 15.6–11.2, 9.1–6.7, and 2.5–1.5 ka, respectively (Liu et al., 2018). The T1 terrace was formed in the glacier period of 15.6–11.2 ka. As pointed out by Vandenberghe (1995), any climate change can result in river incisions, which induces terrace formation in constantly uplifting areas (Ruszkiczay-Rüdiger et al., 2005; Pan et al., 2009). Therefore, we induce that for these terraces, the joint effect of the two driving forces (tectonics and climate) may be responsible for their formation.

7 CONCLUSION

Seven Minjiang River strath terraces were identified in the Songpan area from Hongqiaoguan to the Songpan town based on fluvial sediments and the elevation of bedrock strath. Fluvial samples and overlying loess samples on the terraces have large scatter in D_e . However, the MAM ages are considered unreliable, and the CAM ages are reliable based on the comparison of the ages between parallel samples, and stratigraphic and geomorphological consistency. The loess samples overlying fluvial sediments were deposited much later than the terrace formation. The T1, T3, T4, T5, and T6 terraces were dated to 13.5 ± 0.6, 29.0 ± 1.7, 48.0 ± 3.3, 44.3 ± 5.2, and 63.8 ± 4.7 ka, respectively. The T4 and T5 terraces may be the same terrace with a weighted mean age of 46.9 ± 2.8 ka. The ages of the T2 and T7 terraces were inferred

to be ~20 and ~80 ka, respectively. The mean bedrock river incision rates are 1.2 ± 0.1 mm/a for the time period of 64 ka for the T6 terrace—14 ka for the T1 terrace, and 0.15 mm/a for the past 14 ka.

DATA AVAILABILITY STATEMENT

The original contributions presented in the study are included in the article/**Supplementary Material**, further inquiries can be directed to the corresponding author.

AUTHOR CONTRIBUTIONS

Z-JC, G-NL, and J-FZ contributed to the conception and design of the study. Y-SH carried out the OSL dating. Y-SH and J-FZ organized the data and wrote the first draft of the manuscript. All authors took part in the field work and contributed to manuscript revision, read, and approved the submitted version.

FUNDING

The work was supported by the National Natural Science Foundation of China (Nos.:41230743 and 42071003).

ACKNOWLEDGMENTS

We thank Professors Wei Zhang, Jie Wang and Jingdong Zhao and all other participants for their help in field work and OSL sampling. We appreciate the comments made by Dr. YI and Dr. XM.

SUPPLEMENTARY MATERIAL

The Supplementary Material for this article can be found online at: https://www.frontiersin.org/articles/10.3389/feart.2022.939539/full#supplementary-material

REFERENCES

Aitken, M. J. (1998). *An Introduction to Optical Dating*. New York: Oxford University Press.

Alexanderson, H. (2007). Residual OSL Signals from Modern Greenlandic River Sediments. *Geochronometria* 26, 1–9. doi:10.2478/v10003-007-0001-6

Arne, D., Worley, B., Wilson, C., Chen, S. F., Foster, D., Luo, Z. L., et al. (1997). Differential Exhumation in Response to Episodic Thrusting Along the Eastern Margin of the Tibetan Plateau. *Tectonophysics* 280, 239–256. doi:10.1016/s0040-1951(97)00040-1

Arnold, L. J., Roberts, R. G., Galbraith, R. F., and DeLong, S. B. (2009). A Revised Burial Dose Estimation Procedure for Optical Dating of Youngand Modern-Age Sediments. *Quat. Geochronol.* 4, 306–325. doi:10.1016/j.quageo.2009.02.017

Bøtter-Jensen, L., Mejdahl, V., and Murray, A. S. (1999). New Light on OSL. *Quat. Sci. Rev.* 18, 303–309. doi:10.1016/S0277-3791(98)00063-8

Brennan, B. J., Lyons, R. G., and Phillips, S. W. (1991). Attenuation of Alpha Particle Track Dose for Spherical Grains. *Int. J. Radiat. Appl. Instrum. Part D. Nucl. Tracks Radiat. Meas.* 18, 249–253. doi:10.1016/1359-0189(91)90119-3

Bull, W. B. (1991). *Geomorphic Responses to Climate Change*. Oxford, UK: Oxford University Press.

Bull, W. B. (2007). *Tectonic Geomorphology of Mountains: A New Approach to Paleoseismology*. Oxford: Wiley-Blackwell, 45.

Burchfiel, B. C., Zhiliang, C., Yupinc, L., and Royden, L. H. (1995). Tectonics of the Longmen Shan and Adjacent Regions, Central China. *Int. Geol. Rev.* 37, 661–735. doi:10.1080/00206819509465424

Chamberlain, E. L., and Wallinga, J. (2019). Seeking Enlightenment of Fluvial Sediment Pathways by Optically Stimulated Luminescence Signal Bleaching of River Sediments and Deltaic Deposits. *Earth Surf. Dynam.* 7, 723–736. doi:10.5194/esurf-7-723-2019

Chen, S. F., Wilson, C. J. L., Deng, Q. D., Zhao, X. L., and Zhi, L. L. (1994). Active Faulting and Block Movement Associated with Large Earthquakes in the Min Shan and Longmen Mountains, Northeastern Tibetan Plateau. *J. Geophys. Res.* 99, 24025–24038. doi:10.1029/94jb02132

Chigira, M., Wu, X., Inokuchi, T., and Wang, G. (2010). Landslides Induced by the 2008 Wenchuan Earthquake, Sichuan, China. *Geomorphology* 118, 225–238. doi:10.1016/j.geomorph.2010.01.003

Clark, K. M., and Royden, H. L. (2000). Topographic Ooze: Building the Eastern Margin of Tibet by Lower Crustal Flow. *Geology* 28, 703–706. doi:10.1130/0091-7613(2000)028<0703:tobtem>2.3.co;2

Cunha, P. P., Martins, A. A., Huot, S., Murray, A., and Raposo, L. (2008). Dating the Tejo River Lower Terraces in the Ródão Area (Portugal) to Assess the Role of Tectonics and Uplift. *Geomorphology* 102, 43–54. doi:10.1016/j.geomorph.2007.05.019

Cunningham, A., Wallinga, J., and Minderhoud, P. (2011). Expectations of Scatter in Equivalent-Dose Distributions When Using Multi-Grain Aliquots for OSL Dating. *Geochronometria* 38, 424–431. doi:10.2478/s13386-011-0048-z

Duller, G. A. T. (2007). Assessing the Error on Equivalent Dose Estimates Derived from Single Aliquot Regenerative Dose Measurements. *Anc. TL* 25, 15–24.

Duller, G. A. T. (2003). Distinguishing Quartz and Feldspar in Single Grain Luminescence Measurements. *Radiat. Meas.* 37, 161–165. doi:10.1016/s1350-4487(02)00170-1

Duller, G. A. T. (1994). Luminescence Dating of Poorly Bleached Sediments from Scotland. *Quat. Sci. Rev.* 13, 521–524. doi:10.1016/0277-3791(94)90070-1

Duller, G. A. T. (2008). Single-Grain Optical Dating of Quaternary Sediments: Why Aliquot Size Matters in Luminescence Dating. *Boreas* 37, 589–612. doi:10.1111/j.1502-3885.2008.00051.x

Durcan, J. A., King, G. E., and Duller, G. A. T. (2015). DRAC: Dose Rate and Age Calculator for Trapped Charge Dating. *Quat. Geochronol.* 28, 54–61. doi:10.1016/j.quageo.2015.03.012

Fu, X., Li, S. H., Li, B., and Fu, B. H. (2016). A Fluvial Terrace Record of Late Quaternary Folding Rate of the Anjihai Anticline in the Northern Piedmont of Tian Shan, China. *Geomorphology* 278, 91–104. doi:10.1016/j.geomorph.2016.10.034

Fu, X., Romanyukha, A. A., Li, B., Jankowski, N. R., Lachlan, T. J., Jacobs, Z., et al. (2022). Beta Dose Heterogeneity in Sediment Samples Measured Using a Timepix Pixelated Detector and its Implications for Optical Dating of Individual Mineral Grains. *Quat. Geochronol.* 68, 101254. doi:10.1016/j.quageo.2022.101254

Galbraith, R. F., Roberts, R. G., Laslett, G. M., Yoshida, H., and Olley, J. M. (1999). Optical Dating of Single and Multiple Grains of Quartz from Jinmium Rock Shelter, Northern Australia: Part I, Experimental Design and Statistical Models. *Archaeometry* 41, 339–364. doi:10.1111/j.1475-4754.1999.tb00987.x

Galbraith, R. F., and Roberts, R. G. (2012). Statistical Aspects of Equivalent Dose and Error Calculation and Display in OSL Dating: An Overview and Some Recommendations. *Quat. Geochronol.* 11, 1–27. doi:10.1016/j.quageo.2012.04.020

Gao, X. Y., and Li, Y. (2006). Comparison on the Incision Rate in the Upper and Middle Reaches of Minjiang River. *Resour. Environ. Yangtze Basin* 15, 517–521. (In Chinese with English Abstract).

Gong, Z., Li, S.-H., and Li, B. (2014). The Evolution of a Terrace Sequence Along the Manas River in the Northern Foreland Basin of Tian Shan, China, as Inferred from Optical Dating. *Geomorphology* 213, 201–212. doi:10.1016/j.geomorph.2014.01.009

Gorum, T., Fan, X., van Westen, C. J., Huang, R., Xu, Q., Tang, C., et al. (2011). Distribution Pattern of Earthquake-Induced Landslides Triggered by the 12 May 2008 Wenchuan Earthquake. *Geomorphology* 133, 152. doi:10.1016/j.geomorph.2010.12.030

Guerin, G., Mercier, N., and Adamiec, G. (2011). Dose-Rate Conversion Factors: Update. *Anc. TL* 29, 5–8.

Guérin, G., Mercier, N., Nathan, R., Adamiec, G., and Lefrais, Y. (2012). On the Use of the Infinite Matrix Assumption and Associated Concepts: A Critical Reviewfinite Matrix Assumption and Associated Concepts: A Critical Review. *Radiat. Meas.* 47, 778–785. doi:10.1016/j.radmeas.2012.04.004

Guo, Y.-J., Zhang, J.-F., Qiu, W.-L., Hu, G., Zhuang, M.-G., and Zhou, L.-P. (2012). Luminescence Dating of the Yellow River Terraces in the Hukou Area, China. *Quat. Geochronol.* 10, 129–135. doi:10.1016/j.quageo.2012.03.002

Harrison, T. M., Copeland, P., Kidd, W. S. F., and Yin, A. (1992). Raising Tibet. *Science* 255, 1663–1670. doi:10.1126/science.255.5052.1663

Hetzel, R. (2013). Active Faulting, Mountain Growth, and Erosion at the Margins of the Tibetan Plateau Constrained by In Situ-Produced Cosmogenic Nuclides. *Tectonophysics* 582, 1–24. doi:10.1016/j.tecto.2012.10.027

Hu, G., Yi, C.-L., Zhang, J.-F., Liu, J.-H., and Jiang, T. (2015). Luminescence Dating of Glacial Deposits Near the Eastern Himalayan Syntaxis Using Different Grain-Size Fractions. *Quat. Sci. Rev.* 124, 124–144. doi:10.1016/j.quascirev.2015.07.018

Hu, G., Zhang, J.-F., Qiu, W.-L., and Zhou, L.-P. (2010). Residual OSL Signals in Modern Fluvial Sediments from the Yellow River (HuangHe) and the Implications for Dating Young Sediments. *Quat. Geochronol.* 5, 187–193. doi:10.1016/j.quageo.2009.05.003

Hubbard, J., and Shaw, J. H. (2009). Uplift of the Longmen Shan and Tibetan Plateau, and the 2008 Wenchuan (M = 7.9) Earthquake. *Nature* 458, 194–197. doi:10.1038/nature07837

Jain, M., Murray, A. S., and Botter-Jensen, L. (2004). Optically Stimulated Luminescence Dating: How Significant Is Incomplete Light Exposure in Fluvial Environments? *Quaternaire* 15, 143–157. doi:10.3406/quate.2004.1762

Jankowski, N. R., and Jacobs, Z. (2018). Beta Dose Variability and its Spatial Contextualisation in Samples Used for Optical Dating: An Empirical Approach to Examining Beta Microdosimetry. *Quat. Geochronol.* 44, 23–37. doi:10.1016/j.quageo.2017.08.005

Kirby, E., Reiners, P. W., Krol, M. A., Whipple, K. X., Hodges, K. V., Farley, K. A., et al. (2002). Late Cenozoic Evolution of the Eastern Margin of the Tibetan Plateau: Inferences from $^{40}Ar/^{39}Ar$ and (U-Th)/He Thermochronology. *Tectonics* 21, 1. doi:10.1029/2000tc001246

Kirby, E., Whipple, K. X., Burchfiel, B. C., Tang, W., Berger, G., Sun, Z., et al. (2000). Neotectonics of the Min Shan, China: Implications for Mechanisms Driving Quaternary Deformation Aong the Eastern Margin of the Tibetan Plateau. *Geol. Soc. Am. Bull.* 112, 375–393. doi:10.1130/0016-7606(2000)112<375:notmsc>2.0.co;2

Kreutzer, S., Schmidt, C., Fuchs, M. C., Dietze, M., Fischer, M., and Fuchs, M. (2012). Introducing an R Package for Luminescence Dating Analysis. *Anc. TL* 30, 1–8.

Lavé, J., and Avouac, J. P. (2001). Fluvial Incision and Tectonic Uplift Across the Himalaya of Central Nepal. *J. Geophys. Res.* 106, 26561–26591. doi:10.1029/2001JB000359

Lepper, K., and McKeever, S. W. S. (2002). An Objective Methodology for Dose Distribution Analysis. *Radiat. Prot. Dosim.* 101, 349–352. doi:10.1093/oxfordjournals.rpd.a005999

Li, J. J., Fang, X. M., Pan, B. T., Zhao, Z. J., and Song, Y. G. (2001). Late Cenozoic Intensive Uplift of Qinghai-Xizang Plateau and its Impacts on Environments in Surrounding Area. *Quat. Sci.* 21, 381–391. (In Chinese with English Abstract).

Li, J. J. (1991). The Environmental Effects of the Uplift of the Qinghai-Xizang Plateau. *Quat. Sci. Rev.* 10, 479–483. doi:10.1016/0277-3791(91)90041-r

Li, Y., Cao, S. Y., Zhou, R. J., Densmore, A. L., and Ellis, M. A. (2005). Late Cenozoic Minjiang Incision Rate and its Constraint on the Uplift of the Eastern Margin of the Tibetan Plateau. *Acta Geol. Sin.* 79, 28–37. (In Chinese with English Abstract).

Liang, P., and Forman, S. L. (2019). LDAC: An Excel-Based Program for Luminescence Equivalent Dose and Burial Age Calculations. *Anc. TL* 37, 21e40.

Lisiecki, L. E., and Raymo, M. E. (2005). A Pliocene–Pleistocene Stack of 57 Globally Distributed Benthic $\delta^{18}O$ Records. *Paleoceanography* 20, PA1003. doi:10.1029/2004pa001071

Liu, B., Cui, Z., Peng, X., Han, Y., and Liu, G. (2018). Using 10Be Exposure Dating to Constrain Glacial Advances During the Late Glacial and Holocene on Mount Xuebaoding, Eastern Tibetan Plateau. *Quat. Res.* 90, 348–359. doi:10.1017/qua.2018.33

Liu, C.-R., Yin, G.-M., Zhang, H.-P., Zheng, W.-J., Voinchet, P., Han, F., et al. (2013). ESR Geochronology of the Minjiang River Terraces at Wenchuan, Eastern Margin of Tibetan Plateau, China. *Geochronometria* 40, 360–367. doi:10.2478/s13386-013-0129-2

Luo, X., Ying, Z., and Yang, L. (2019). Preliminary Analysis on the Development Characteristics of River Terraces and Their Relationship with Ancient Landslides in the Upper Reaches of Minjinag River. Quarter. *Sci.* 39, 391–398. (Chinese with English abstract).

Ma, B. Q., Su, G., Hou, Z. H., and Shu, S. B. (2005). Late Quaternary Slip Rate in the Central Part of the Longmenshan Fault Zone from Terrace Deformation Along the Minjiang River. *Seismol. Geol.* 27, 234–242. (In Chinese with English Abstract).

Maddy, D., Bridgland, D. R., and Green, C. P. (2000). Crustal Uplift in Southern England: Evidence from the River Terrace Records. *Geomorphology* 33, 167–181. doi:10.1016/s0169-555x(99)00120-8

Maddy, D. (1997). Uplift-Driven Valley Incision and River Terrace Formation in Southern England. *J. Quat. Sci.* 12, 539–545. doi:10.1002/(sici)1099-1417(199711/12)12:6<539:aid-jqs350>3.0.co;2-t

Merritts, D. J., Vincent, K. R., and Wohl, E. E. (1994). Long River Profiles, Tectonism, and Eustasy: A Guide to Interpreting Fluvial Terraces. *J. Geophys. Res.* 99, 14031–14050. doi:10.1029/94jb00857

Murray, A., Arnold, L. J., Buylaert, J. P., Guérin, G., Qin, J., Singhvi, A. K., et al. (2021). Optically Stimulated Luminescence Dating Using Quartz. *Nat. Rev. Methods Prim.* 1, 1–31. doi:10.1038/s43586-021-00068-5

Murray, A. S., Olley, J. M., and Caitcheon, G. G. (1995). Measurement of Equivalent Doses in Quartz from Contemporary Water-Lain Sediments Using Optically Stimulated Luminescence. *Quat. Sci. Rev.* 14, 365–371. doi:10.1016/0277-3791(95)00030-5

Murray, A. S., and Wintle, A. G. (2000). Luminescence Dating of Quartz Using an Improved Single-Aliquot Regenerative-Dose Protocol. *Radiat. Meas.* 32, 57–73. doi:10.1016/s1350-4487(99)00253-x

Murray, A. S., and Wintle, A. G. (2003). The Single Aliquot Regenerative Dose Protocol: Potential for Improvements in Reliability. *Radiat. Meas.* 37, 377–381. doi:10.1016/s1350-4487(03)00053-2

Olley, J., Caitcheon, G., and Murray, A. (1998). The Distribution of Apparent Dose as Determined by Optically Stimulated Luminescence in Small Aliquots of Fluvial Quartz: Implications for Dating Young Sediments. *Quat. Sci. Rev.* 17, 1033–1040. doi:10.1016/s0277-3791(97)00090-5

Olley, J. M., Caitcheon, G. G., and Roberts, R. G. (1999). The Origin of Dose Distributions in Fluvial Sediments, and the Prospect of Dating Single Grains from Fluvial Deposits Using Optically Stimulated Luminescencefluvial Sediments, and the Prospect of Dating Single Grains from Fluvial Deposits Using Optically Stimulated Luminescence. *Radiat. Meas.* 30, 207–217. doi:10.1016/s1350-4487(99)00040-2

Pan, B., Su, H., Hu, Z., Hu, X., Gao, H., Li, J., et al. (2009). Evaluating the Role of Climate and Tectonics During Non-Steady Incision of the Yellow River: Evidence from a 1.24 Ma Terrace Record Near Lanzhou, China. *Quat. Sci. Rev.* 28, 3281–3290. doi:10.1016/j.quascirev.2009.09.003

Perkins, N. K., and Rhodes, E. J. (1994). Optical Dating of Fluvial Sediments from Tattershall, U.K. *Quat. Sci. Rev.* 13, 517–520. doi:10.1016/0277-3791(94)90069-8

Rhodes, E. J. (2011). Optically Stimulated Luminescence Dating of Sediments Over the Past 200,000 Years. *Annu. Rev. Earth Planet. Sci.* 39, 461–488. doi:10.1146/annurev-earth-040610-133425

Rittenour, T. M. (2008). Luminescence Dating of Fluvial Deposits: Applications to Geomorphic, Palaeoseismic and Archaeological Research. *Boreas* 37, 613–635. doi:10.1111/j.1502-3885.2008.00056.x

Rodnight, H., Duller, G. A. T., Wintle, A. G., and Tooth, S. (2006). Assessing the Reproducibility and Accuracy of Optical Dating of Fluvial Deposits. *Quat. Geochronol.* 1, 109–120. doi:10.1016/j.quageo.2006.05.017

Royden, L. H., Burchfiel, B. C., and Van Der Hilst, R. D. (2008). The Geological Evolution of the Tibetan Plateau. *Science* 321, 1054–1058. doi:10.1126/science.1155371

Ruszkiczay-Rüdiger, Z., Fodor, L., Bada, G., Leél-Össy, S., Horváth, E., and Dunai, T. J. (2005). Quantification of Quaternary Vertical Movements in the Central Pannonian Basin: A Review of Chronologic Data Along the Danube River, Hungary. *Tectonophysics* 410, 157–172. doi:10.1016/j.tecto.2005.05.048

Singh, A., Thomsen, K. J., Sinha, R., Buylaert, J. P., Carter, A., Mark, D. F., et al. (2017). Counter-Intuitive Influence of Himalayan River Morphodynamics on Indus Civilisation Urban Settlementsfluence of Himalayan River Morphodynamics on Indus Civilisation Urban Settlements. *Nat. Commun.* 8, 1617. doi:10.1038/s41467-017-01643-9

Spencer, J. Q., Sanderson, D. C. W., Deckers, K., and Sommerville, A. A. (2003). Assessing Mixed Dose Distributions in Young Sediments Identified Using Small Aliquots and a Simple Two-Step SAR Procedure: The F-Statistic as a Diagnostic Tool. *Radiat. Meas.* 37, 425–431. doi:10.1016/s1350-4487(03)00064-7

Spooner, N. A. (1994). The Anomalous Fading of Infrared-Stimulated Luminescence from Feldspars. *Radiat. Meas.* 23, 625–632. doi:10.1016/1350-4487(94)90111-2

Tan, X., Liu, Y., Lee, Y.-H., Lu, R., Xu, X., Suppe, J., et al. (2019). Parallelism Between the Maximum Exhumation Belt and the Moho Ramp Along the Eastern Tibetan Plateau Margin: Coincidence or Consequence? *Earth Planet. Sci. Lett.* 507, 73–84. doi:10.1016/j.epsl.2018.12.001

Tang, R. C., Wen, D. H., Huang, Z. Z., Wu, X. G., Lin, W. F., Chen, G. X., et al. (1991). The Quaternary Activity Characteristics of Several Major Active Faults in the Songpan-Longmenshan Region. *Earthq. Res. China* 7, 64–71. (in Chinese with English abstract).

Thomsen, K. J., Murray, A. S., Buylaert, J. P., Jain, M., Hansen, J. H., and Aubry, T. (2016). Testing Single-Grain Quartz OSL Methods Using Sediment Samples with Independent Age Control from the Bordes-Fitte Rockshelter (Roches d'Abilly Site, Central France). *Quat. Geochronol.* 31, 77–96. doi:10.1016/j.quageo.2015.11.002

Toda, S., Lin, J., Meghraoui, M., and Stein, R. S. (2008). 12 May 2008 M = 7.9 Wenchuan, China, Earthquake Calculated to Increase Failure Stress and Seismicity Rate on Three Major Fault Systems. *Geophys. Res. Lett.* 35, L17305. doi:10.1029/2008gl034903

Tóth, O., Sipos, G., Kiss, T., and Bartyik, T. (2017). Variation of OSL Residual Doses in Terms of Coarse and Fine Grain Modern Sediments Along the Hungarian Section of the Danube. *Geochronometria* 44, 319–330. doi:10.1515/geochr-2015-0079

Vance, D., Bickle, M., Ivy-Ochs, S., and Kubik, P. W. (2003). Erosion and Exhumation in the Himalaya from Cosmogenic Isotope Inventories of River Sediments. *Earth Planet. Sci. Lett.* 206, 273–288. doi:10.1016/s0012-821x(02)01102-0

Vandenberghe, J. (1995). Timescales, Climate and River Development. *Quat. Sci. Rev.* 14, 631–638. doi:10.1016/0277-3791(95)00043-o

Wallinga, J. (2002). Optically Stimulated Luminescence Dating of Fluvial Deposits: A Review. *Boreas* 31, 303–322. doi:10.1080/030948023209425 36

Wang, E., and Meng, Q. (2009). Mesozoic and Cenozoic Tectonic Evolution of the Longmenshan Fault Belt. *Sci. China Ser. D-Earth Sci.* 52, 579–592. doi:10.1007/s11430-009-0053-8

Wang, L. S., Wang, X. Q., Xu, X. N., Cui, J., Sheng, J. H., and Zhang, Z. L. (2012). Significances of Studying the Diexi Paleo-Dammed Lake at the Upstream of Minjiang River, Sichuan, China. *Quat. Sci.* 32, 998–1010. (In Chinese with English Abstract).

Wang, P., Zhang, B., Qiu, W., and Wang, J. (2011). Soft-Sediment Deformation Structures from the Diexi Paleo-Dammed Lakes in the Upper Reaches of the Minjiang River, East Tibet. *J. Asian Earth Sci.* 40, 865–872. doi:10.1016/j.jseaes.2010.04.006

Wintle, A. G., and Murray, A. S. (2006). A Review of Quartz Optically Stimulated Luminescence Characteristics and Their Relevance in Single-Aliquot Regeneration Dating Protocols. *Radiat. Meas.* 41, 369–391. doi:10.1016/j.radmeas.2005.11.001

Wu, L. Z., Zhao, D. J., Zhu, J. D., Peng, J. B., and Zhou, Y. (2020). A Late Pleistocene River-Damming Landslide, Minjiang River, China. *Landslides* 17, 433–444. doi:10.1007/s10346-019-01305-5

Wu, X. P., and Hu, J. Z. (2009). Features of Neotectonic Movement in the Source Area of the Minjiang River. *Geoscience* 23, 430–439. (In Chinese with English).

Yan, Y.-Y., Zhang, J.-F., Hu, G., and Zhou, L.-P. (2021). Luminescence Chronology of the Yellow River Terraces in the Heiyukou Area, China, and its Implication for the Uplift Rate of the Ordos Plateau. *Geochronometria* 48, 325–338. doi:10.2478/geochr-2020-0008

Yan, Y. Y., Zhang, J. F., Hu, G., and Zhou, L. P. (2018). Comparison of Various Luminescence Dating Procedures on Sediments from One of the Strath Terraces of the Yellow River in the Jinshaan Canyon. *Quat. Sci.* 38, 594–610. (in Chinese with English abstract).

Yang, N., Zhang, Y. Q., Meng, H., and Zhang, H. P. (2003). Study of the Minjiang River Terraces in the Western Sichuan Plateau. *J. Geomechanics* 9, 363–370. (In Chinese with English Abstract).

Zhang, H.-P., Liu, S.-F., Yang, N., Zhang, Y.-Q., and Zhang, G.-W. (2006a). Geomorphic Characteristics of the Minjiang Drainage Basin (Eastern Tibetan Plateau) and its Tectonic Implications: New Insights from a Digital Elevation Model Study. *Isl. Arc.* 15, 239–250. doi:10.1111/j.1440-1738.2006.00524.x

Zhang, H. P., Yang, N., Zhang, Y. Q., and Meng, H. (2006b). Geomorphology of the Minjiang Drainage System (Sichuan, China) and its Structural Implications. *Quat. Sci.* 26, 126–135. (In Chinese with English Abstract).

Zhang, J.-F., Qiu, W.-L., Hu, G., and Zhou, L.-P. (2020). Determining the Age of Terrace Formation Using Luminescence Dating-A Case of the Yellow River Terraces in the Baode Area, China. *MPs* 3, 17. doi:10.3390/mps3010017

Zhang, J.-F., Qiu, W.-L., Li, R.-Q., and Zhou, L.-P. (2009). The Evolution of a Terrace Sequence Along the Yellow River (Huang He) in Hequ, Shanxi, China, as Inferred from Optical Dating. *Geomorphology* 109, 54–65. doi:10.1016/j.geomorph.2008.08.024

Zhang, J. F., Zhou, L. P., and Yue, S. Y. (2003). Dating Fluvial Sediments by Optically Stimulated Luminescence: Selection of Equivalent Doses for Age Calculationfluvial Sediments by Optically Stimulated Luminescence: Selection of Equivalent Doses for Age Calculation. *Quat. Sci. Rev.* 22, 1123–1129. doi:10.1016/s0277-3791(03)00054-4

Zhao, S., Chigira, M., and Wu, X. (2019). Gigantic Rockslides Induced by Fluvial Incision in the Diexi Area Along the Eastern Margin of the Tibetan Plateau. *Geomorphology* 338, 27–42. doi:10.1016/j.geomorph.2019.04.008

Zhao, X. L., Deng, Q. D., and Chen, S. F. (1994). Tectonic Geomorphology of the Minshan Uplift in the Western Sichuan, Southwestern China. *Seismol. Geol.* 16, 429–439. (In Chinese with English Abstract).

Zhou, R. J., Pu, X. H., He, Y. L., Li, X. G., and Ge, T. Y. (2000). Recent Activity of Minjiang Fault Zone, Uplift of Minshan Block and Their Relationship with Seismicity of Sichuan. *Seismol. Geol.* 22, 285–294. (In Chinese with English Abstract).

Conflict of Interest: The authors declare that the research was conducted in the absence of any commercial or financial relationships that could be construed as a potential conflict of interest.

frontiers | Frontiers in Earth Science

ORIGINAL RESEARCH
published: 11 July 2022
doi: 10.3389/feart.2022.940013

OSL Dating of Paleo-Shorelines at Dagze Co, Central Tibetan Plateau

Yang Wu[1,2,3,4], *Yiwei Chen*[1,2,3]*, *Long Huang*[1,2,3,4], *Ping Ding*[1,2,3], *Hao Cui*[1,2,3,4] and *Gangjian Wei*[1,2,3]

[1]State Key Laboratory of Isotope Geochemistry, Guangzhou Institute of Geochemistry, Chinese Academy of Sciences, Guangzhou, China, [2]CAS Center for Excellence in Deep Earth Science, Guangzhou, China, [3]Southern Marine Science and Engineering Guangdong Laboratory (Guangzhou), Guangzhou, China, [4]College of Earth and Planetary Sciences, University of Chinese Academy of Sciences, Beijing, China

Well-preserved paleo-shoreline systems suggest lake shrinkage occurred in a vast region of the Tibetan Plateau, indicating dramatic paleo-environmental changes that linked closely to variations in Asian monsoon precipitation, glacial meltwater, and evaporation. The elevation and chronology of these shoreline features can be used to reconstruct lake level fluctuation history and regional paleo-climate. Here, we report optically stimulated luminescence (OSL) dating of 14 sediment samples from three of seven paleo-shorelines at south of Dagze Co, central Tibetan Plateau, using coarse-grained quartz and K-feldspar. Two fine grain silt samples were also measured. The results suggest the following: 1) The highest paleo-shoreline for Dagze Co has an elevation around 4,525 m (+55 m above modern lake). Its age is estimated to be 9.1 ± 0.5 to 9.6 ± 0.6 ka, suggesting a relative humid condition in the early Holocene. 2) After that, the lake level dropped ~20 m and remained relatively stable (+35 m) from ~8 to 5 ka, implying a dry condition with reduced runoff. Lake level further declined for ~40 m since about 5 ka. 3) The general trend of shrinkage for Dagze Co broadly matches studies from adjacent lakes, suggesting a common pattern of lake's evolution on the south/central plateau in the late Quaternary. The long-term decreasing trend of Asian monsoon precipitation should be the main reason.

Keywords: paleo-shoreline, OSL dating, Dagze Co, lake level change, Tibetan Plateau

OPEN ACCESS

Edited by:
Bo Li,
University of Wollongong, Australia

Reviewed by:
Xiangjun Liu,
Northwest Normal University, China
Jifeng Zhang,
Institute of Tibetan Plateau Research (CAS), China

***Correspondence:**
Yiwei Chen
chenyw@gig.ac.cn

Specialty section:
This article was submitted to Quaternary Science, Geomorphology and Paleoenvironment, a section of the journal Frontiers in Earth Science

Received: *09 May 2022*
Accepted: *01 June 2022*
Published: *11 July 2022*

Citation:
Wu Y, Chen Y, Huang L, Ding P, Cui H and Wei G (2022) OSL Dating of Paleo-Shorelines at Dagze Co, Central Tibetan Plateau. Front. Earth Sci. 10:940013. doi: 10.3389/feart.2022.940013

INTRODUCTION

The Tibetan Plateau (TP) has a profound impact on global atmospheric circulations and the Asian monsoon system (e.g., An, 2000; Chen et al., 2020). Known as "the water tower of Asia," it is the origin of Asia's many great rivers, supplying runoffs for over 1 billion people (Krause et al., 2010; Song et al., 2013; Jonell et al., 2020; Wei et al., 2020). With a total area of more than 40,000 km^2, more than 1,000 lakes (>1 km^2 area) are widely distributed across the plateau, comprising an important component of water resources in the TP (Ma et al., 2011; Zhang et al., 2013; Liu et al., 2018). The evolution of lakes is closely linked to variations in climatic controls. Many studies have been carried out using lake core sediment with proxy analysis to reconstruct paleo-environment change (e.g., Zhu et al., 2008; Wang et al., 2009; Hou et al., 2017). Lake level and water volume are among the most important features to study the evolution of lakes. Paleo-shorelines are geomorphic features formed in the interaction of lake water, aerodynamics, and land, representing a temporary stationary state of the lake level due to precipitation–evaporation balance (e.g., Otvos, 2000), i.e., paleo-shorelines can provide ideal records for studying lake level fluctuation history.

The presence of a large number of paleo-shorelines 10–200 m above the modern lake in TP indicates that lake shrinkage occurred in a vast region (Li et al., 2009; Hudson and Quade, 2013). The

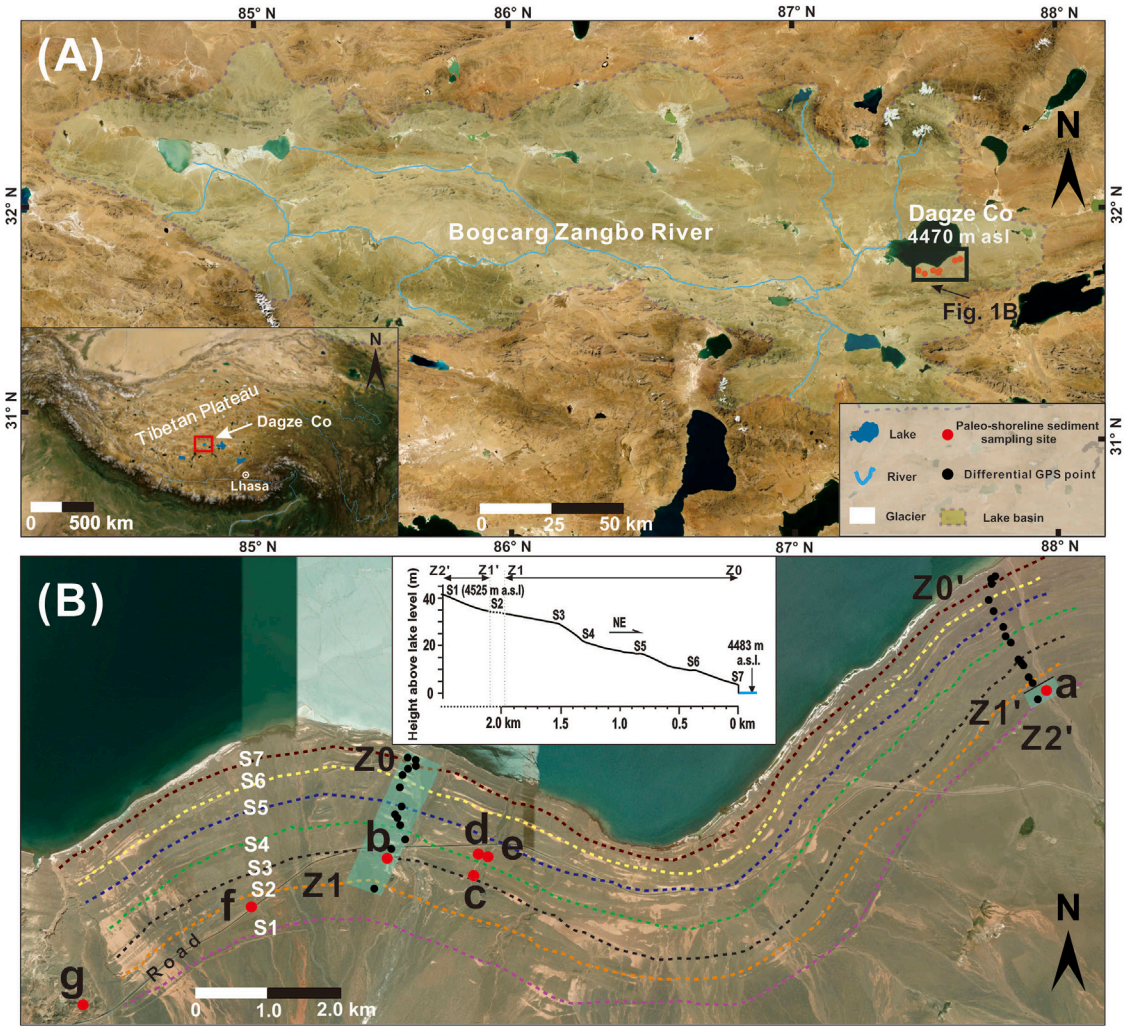

FIGURE 1 | Study region of Dagze Co. **(A)** The catchment area and main rivers of Dagze Co; **(B)** satellite image of the paleo-shorelines of Dagze Co. Red full circles in **(A,B)** represent sample locations, and black spots represent sites for differential GPS measurement. Satellite images are from the Google Earth.

timing for lake highstands and their relationship with climatic controls have been discussed in several recent studies (Chen et al., 2013; Liu et al., 2013b; Lai et al., 2014; Yan and Wünnemann, 2014; Zhou et al., 2020; Hou et al., 2021; Feng et al., 2022). Some researchers have pointed out that the spatiotemporal complexity for the timing of the recent highest lake levels in TP mainly follows such a pattern: many lakes in northwestern TP reached their maximum extents during the latest Pleistocene (Kong et al., 2007; Liu et al., 2016; Zhang et al., 2022), while many lakes in the southern/southwestern TP reach their highest levels in the early Holocene (Chen et al., 2013; Rades et al., 2013; Ahlborn et al., 2015; Hudson et al., 2015; Huth et al., 2015; Rades et al., 2015). Lake highstands in the MIS 5 mainly occur for lakes in the northeastern TP (see reviews and references in Zhang et al., 2020), while mid-Holocene expansions were also reported (e.g., Liu et al., 2015). The controlling climatic mechanism behind this pattern needs further investigation. However, there is still a lack of research for a comprehensive understanding of the history of lake level changes in TP, especially for small/medium-sized lake basins.

Dagze Co is a small lake in a closed basin in central TP (**Figure 1A**). It is surrounded by a well-preserved paleo-shoreline system. In this work, a detailed field survey was conducted using a differential GPS and a drone to identify and measure the relative elevations of paleo-shorelines. These shorelines were optically dated using quartz/K-feldspar grains to establish a detailed chronology for lake level fluctuations.

SAMPLE COLLECTION AND METHOD

Study Area

Dagze Co (31.82°–31.98°N, 87.42°–87.65°E) is situated in a fractured basin in central TP. Well-preserved paleo-shorelines can be observed at the east and south sides of the lake (**Figure 1A**). The lake has a surface area of 245 km^2 and a

TABLE 1 | General geographical, climatological, and limnological data for Dagze Co.

Altitude	**4,470 m a.s.l.**
E–W length	~21 km
N–S length	~17 km
Area	~245 km^2
Maximum water depth	~38 m
Catchment area	~10,885 km^2
Annual precipitation on-lake	~316 mm
Annual evaporation on-lake	~2,302 mm
Annual average temperature	0.55°C
Salinity	14.7–21.4 g/L
pH	9.9
Dissolved oxygen	5.42 mg/L

Modified after Wang and Dou (1998), Liu et al., (2013a), Hou et al. (2017), and Li et al. (2021). Modern lake level is based on Google Earth.

catchment area of 10,885 km^2 (Wang and Dou, 1998; Hou et al., 2017). As a carbonate-type saltwater lake, Dagze Co has an annual evaporation of about 2,302 mm, which is much higher than the average annual precipitation of ~ 316 mm (**Table 1**). Bogcarg Zangbo is the major infilling river.

Sampling and Altitude Measurement

According to satellite image and fieldwork, seven paleo-shorelines were identified, and they were named as S1–S7 (**Figure 1B**). We selected three shorelines to take samples at the south of the lake (S1, S3, and S4). This region mainly consists of an alluvial fan with a gentle slope, and the slope gradually flattened near the lakeshore. Seasonal rivers/gullies flow northward and cut through several paleo-shorelines, exposing sediment profiles. S1 seems the highest one (+55 m) with an

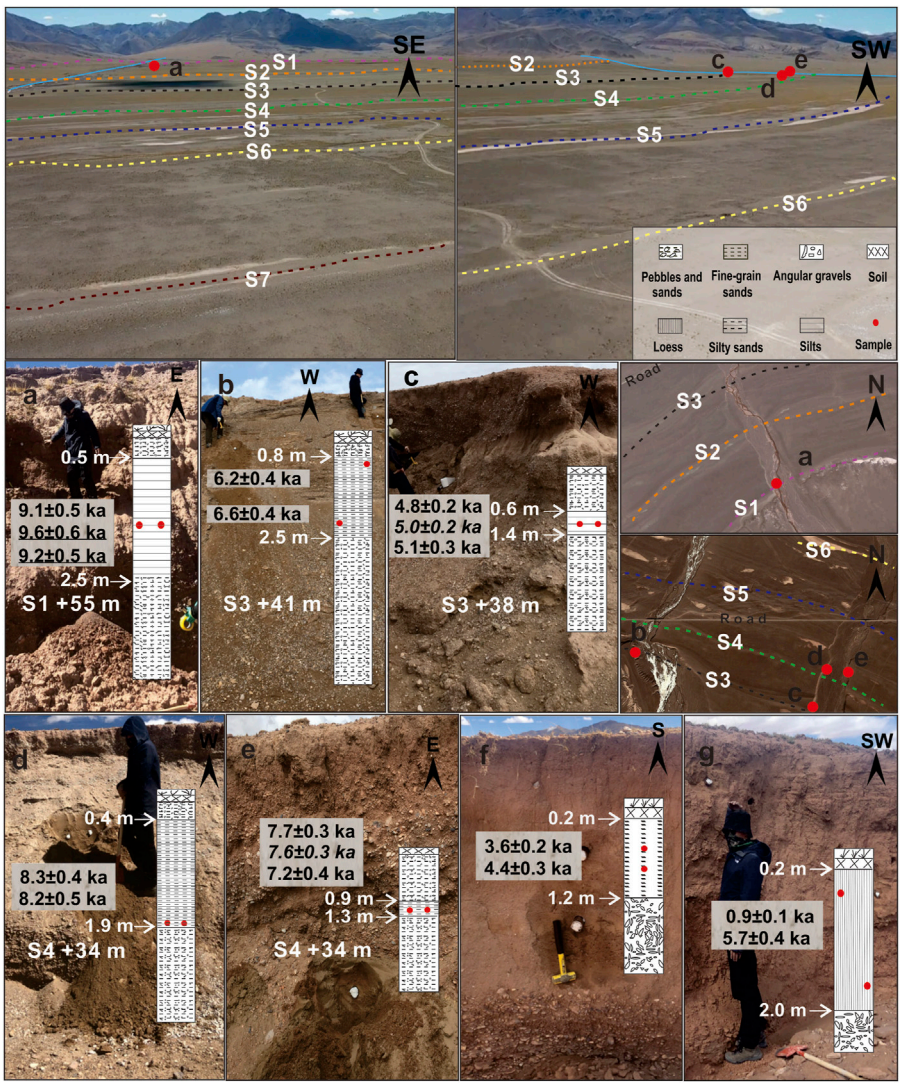

FIGURE 2 | Field photos, sampling profiles, and OSL ages. The fieldwork was carried out in 2019 and 2021. Note that ages in italics refer to pIRIR 225°C results from K-feldspar, while underlined ages refer to fine-grained quartz (4–11 μm) results.

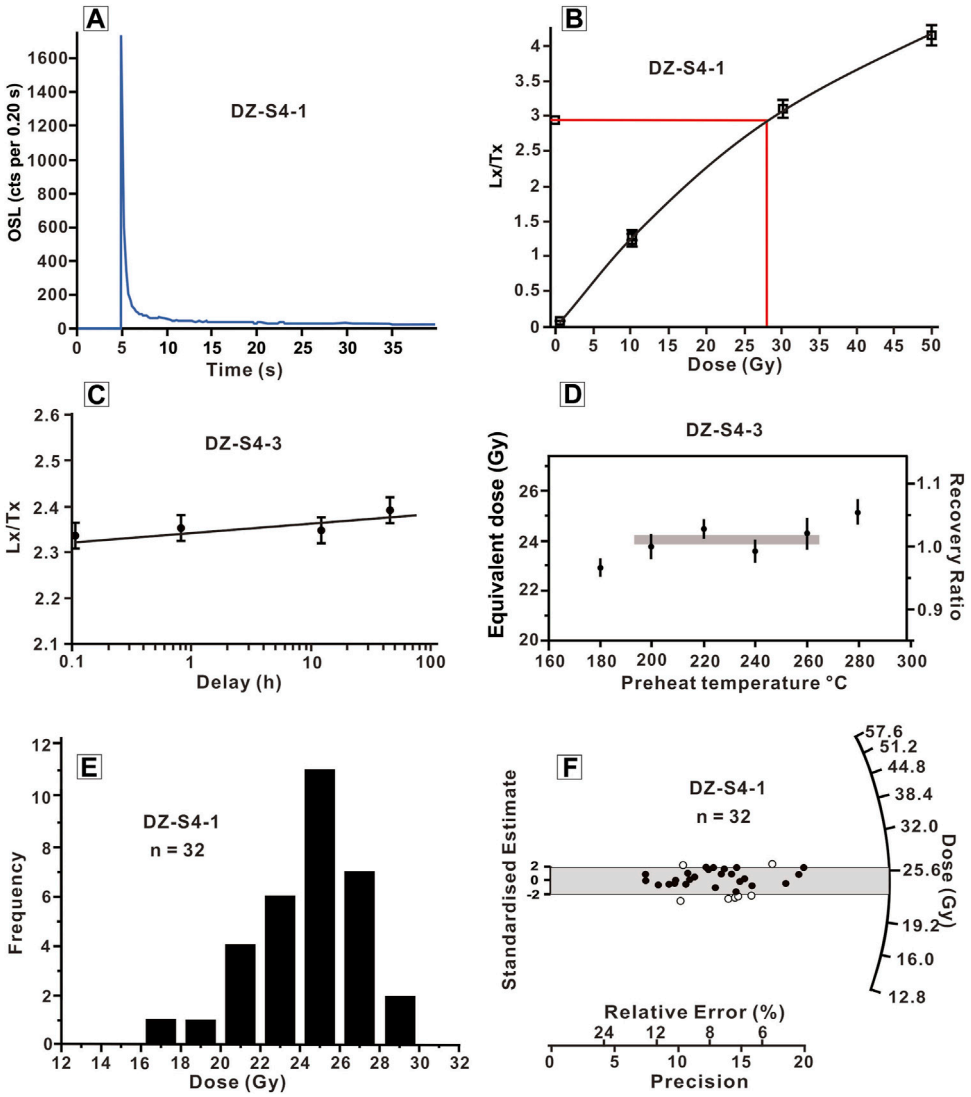

FIGURE 3 | OSL decay curve and dose–response curve for the sample of DZ-S4-1 **(A,B)**, fading test of quartz from sample DZ-S4-3 **(C)**, preheat plateau tests for DZ-S4-3, **(D)** and D_e distributions in histograms and radial plots for sample DZ-S4-1 **(E,F)**.

apparent ridge feature (~2 m in height), although there may be a higher one, but owing to a flat surface topography from thick alluvium aggradation, we were not able to locate it in the field. S3 is the most developed one and extends several kilometers (**Figure 1B**). One river cuts through S1, and a good profile was exposed. Under a coverage of alluvial gravels and surface soil (0.5 m), a thick and well-sorted silty–sandy layer was found (2 m). Beneath the sandy layer were massive poorly sorted pebbles and coarse sands, probably related to fluvial conditions in a high-energy sedimentary environment. Two samples were collected from the thick layer of silty sands (**Figure 2A**). Because these samples were taken from the location of S1, and they are typical near-shore sediment, we believe their optically stimulated luminescence (OSL) ages can be used to represent the age of S1. Likewise, four samples were taken from two rivers where they cut through S3 (**Figures 2B, C**). For S4, four samples were collected from one river at its both sides where it cuts through S4 (**Figures 2D, E**). In addition, two surface samples near the road between S1 and S2 (**Figure 1B**, **Figure 2F**) were collected, and two others were collected from a silt, loess-like profile (**Figure 1B**, **Figure 2G**). We think these samples should be later sediment after the formation of paleo-shorelines, so their ages may provide a conservative estimation. A stainless tube (5 cm in diameter and 25 cm in length) was inserted into the sand layer with the open side of the tube being sealed. After the tube was removed from sediment, the other end was also sealed from sunlight.

A differential GPS was used to determine the relative elevation of paleo-shorelines, with an error of centimeter scale. We set up the base station at the modern lake shore and took the portable station for shoreline elevation measurement (Z1–Z0 and Z2′–Z0′ sections in **Figure 1B**). In particular, we were not able to yield

TABLE 2 | OSL dating results for samples from Dagze Co.

Samples	K Content (%)	Th Content (ppm)	U Content (ppm)	Burial depth, m	Cosmic ray[a] (Gy/ka)	Water content[b] (%)	Aliquot Number	Equivalent Dose (Gy)	Dose Rate (Gy/ka)	Age (Ka)	$pIRIR_{225\ °C}$ ages (ka)
DZ-S1-1	1.81	9.03	2.15	1.8	0.338	5	18	28.67 ± 1.00	3.14 ± 0.12	9.1 ± 0.5	—
DZ-S1-1[c]	1.81	9.03	2.15	1.8	0.338	5	18	35.79 ± 1.88	3.72 ± 0.15	9.6 ± 0.6	—
DZ-S1-2[c]	2.06	10.8	2.41	1.8	0.338	5	18	39.01 ± 1.69	4.22 ± 0.15	9.2 ± 0.5	—
DZ-S3-1	1.74	10.1	2.07	1.1	0.370	5	19	19.61 ± 0.81	3.16 ± 0.12	6.2 ± 0.4	—
DZ-S3-2	1.49	7.57	2.58	2.2	0.320	5	20	18.47 ± 0.75	2.82 ± 0.11	6.6 ± 0.4	—
DZ-S3-3	1.59	6.50	1.93	1.0	0.375	5	35	13.32 ± 0.41	2.75 ± 0.11	4.8 ± 0.2	5.0 ± 0.2
DZ-S3-4	1.61	6.30	1.91	1.0	0.375	5	24	13.87 ± 0.57	2.74 ± 0.11	5.1 ± 0.3	—
DZ-S4-1	1.74	7.90	1.80	1.7	0.341	5	32	24.21 ± 0.78	2.92 ± 0.11	8.3 ± 0.4	—
DZ-S4-2	1.88	8.42	1.76	1.7	0.341	5	20	25.31 ± 0.99	3.07 ± 0.12	8.2 ± 0.5	—
DZ-S4-3	1.99	9.48	1.99	1.2	0.365	5	36	25.52 ± 0.52	3.33 ± 0.13	7.7 ± 0.3	7.6 ± 0.3
DZ-S4-4	1.77	9.59	1.97	1.2	0.365	5	19	22.60 ± 0.98	3.12 ± 0.12	7.2 ± 0.4	—
DZ-TR-1	1.87	8.92	2.20	0.5	0.403	5	20	11.70 ± 0.52	3.26 ± 0.13	3.6 ± 0.2	—
DZ-TR-2	1.69	8.45	2.21	0.9	0.381	5	20	13.44 ± 0.54	3.04 ± 0.12	4.4 ± 0.3	—
DZ-TL-1	1.94	7.63	1.72	0.5	0.403	5	18	2.89 ± 0.18	3.13 ± 0.12	0.9 ± 0.1	—
DZ-TL-2	1.77	8.81	2.02	1.8	0.338	5	18	17.45 ± 1.05	3.05 ± 0.12	5.7 ± 0.4	—

[a]*The error for the cosmic rays dose rate is estimated at ±0.02 Gy/ka.*

[b]*The error for the water content is estimated at ±5%.*

[c]*DZ-S1-2 was measured using fine-grained quartz (4–11 μm) since not enough coarse grains could be separated. To compare with quartz ages from coarse grains, sample DZ-S1-1 were measured using both coarse- and fine-grained quartz.*

absolute elevations because of the lack of geodetic surveying dataset in this region. The relative height of shorelines is shown in **Figure 1B**, and the results suggest a total gap of 44.8 m above the modern lake level. The elevation of 4,470 m from Google Earth (GE) was used as the modern lake level, and further calculations (area and volume) were all based on this elevation. In particular, S1 in GE has an elevation of 4,525 m, i.e., 55 m above 4,470 m; on the contrary, our differential GPS suggests that S1 is 44.8 m above the modern lake level. Given that the differential GPS can yield accurate relative elevations (centimeter scale error), the possible reason should be that the lake level has raised ~10 m, implying a recent lake expansion for Dagze Co (e.g., Zhang et al., 2019).

In summary, 10 samples from three shorelines were collected, while four other surface deposits were also collected.

Sample Preparation and Measurement

OSL dating was conducted in the Luminescence Dating Laboratory of Guangzhou Institute of Geochemistry, Chinese Academy of Sciences (GIG-CAS). Sediment at two ends of the tube was separated for uranium (U), U), thorium (Th), and potassium (K) concentration analysis. Under a subdued red-light condition, a series of physical/chemical treatments were applied to obtain coarse grains of quartz and K-feldspar (Aitken, 1998). Samples were treated with 10% hydrochloric acid (HCl) and 10% hydrogen peroxide (H_2O_2) to remove carbonates and organic materials, respectively. Then grains went through dry sieving to obtain the fraction between 90 and 125 μm, from which K-feldspar and quartz grains were separated successively by sodium polytungstate heavy liquid with densities of 2.58 and 2.75 g/cm^3, respectively. The K-feldspar grains were etched with 10% hydrofluoric (HF) acid for more than 10 min, and the quartz grains were etched with 40% HF acid for more than 45 min to remove the outer part and possible feldspar contaminant. Moreover, 10% HCl and distilled water were used to wash quartz and K-feldspar grains, before being dried for D_e measurement. For samples of DZ-S1-1 and DZ-S1-2, the 4- to 11-μm polymineral grains were separated according to Stokes' law. Then these grains were immersed in 30% hydrofluorosilicic (H_2SiF_6) for 3–4 days in an ultrasonic bath to extract the fine-grained quartz component.

Equivalent dose was determined using the SAR protocol (Murray and Wintle, 2000; Wintle and Murray, 2006). OSL and IRSL measurements were carried out using an automated Risø TL-DA-20 reader equipped with a $^{90}Sr/^{90}Y$ beta source (0.10 Gy/s on aluminum discs). Quartz and K-feldspar signals were stimulated by blue LED (470 ± 30 nm) and infrared light (870 ± 40 nm) and detected through two 3-mm Hoya U-340 glass filter and a package of Schott BG-39 with Corning 7–59 filters, respectively. Small aliquots were used all through D_e measurement (Duller, 2008), and 20–40 discs were tested for each sample. To perform cross-checking from the multi-dating method (e.g., Long et al., 2015), two samples from S3 and S4 were also dated using coarse-grained K-feldspar, based on the protocol of $pIRIR_{225}$ (Buylaert et al., 2009). For quartz, OSL stimulation was carried out for 40 s at 110°C, and the initial 0.4 s of signal was integrated for growth curve construction after subtracting the last 10-s signals. IRSL stimulation was carried out for 110 s at 50°C, while the second IRSL was measured at 225°C for 110 s.

Dose rate was determined based on the calculation of radiation from U, Th, K, and cosmic rays. K content was determined using an X-ray fluorescence spectrometer in GIG-CAS. The concentration of U and Th was measured by inductively coupled plasma–mass spectrometry (ICP-MS). Cosmic ray contributions were estimated for each sample as a function of burial depth, altitude, and geomagnetic latitude (Prescott and

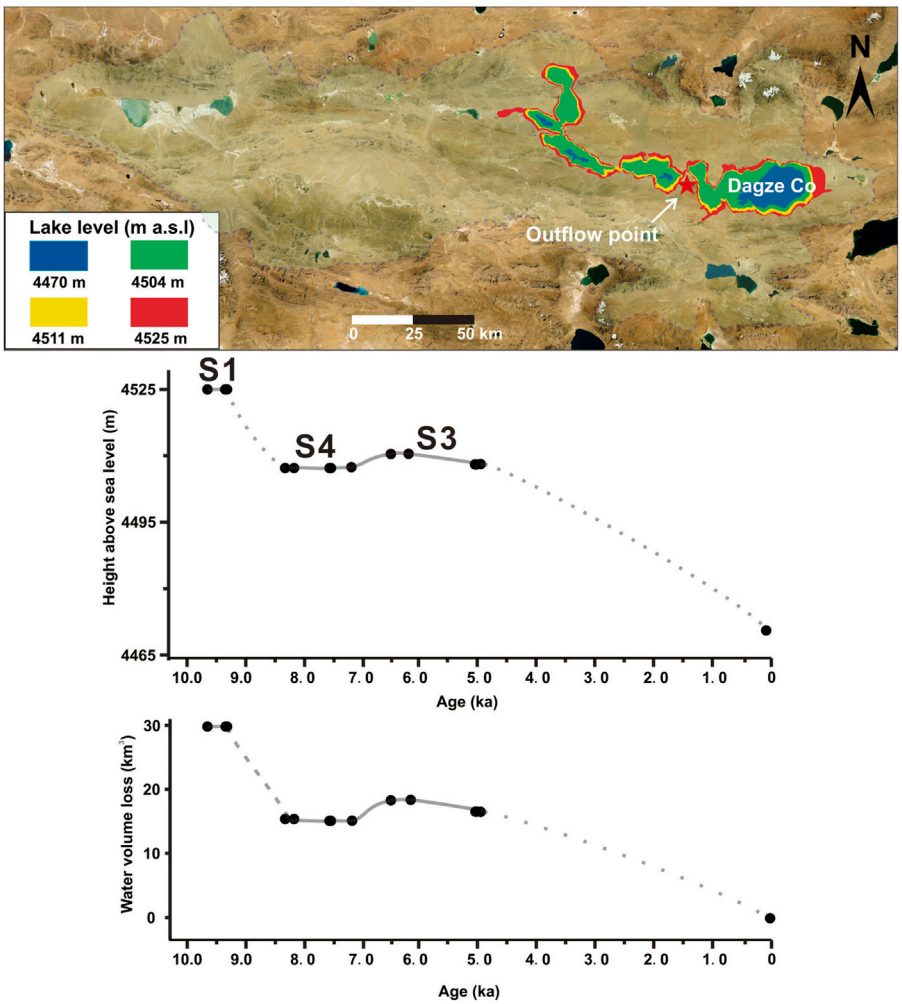

FIGURE 4 | Reconstruction of coverage areas for paleo-Dagze Co, and lake level fluctuation history and water volume loss of Dagze Co since the early Holocene.

Hutton, 1994). Water content was estimated to be 5 ± 5% (e.g., Chen et al., 2016).

Luminescence Behaviors

The preheat plateau test was carried out on the sample of DZ-S4-3, with preheating temperature varying from 180 to 280°C with a 20°C increment (**Figure 3D**). Under each preheating temperatures, six aliquots were measured. A plateau was observed between 200 and 260°C (**Figure 3D**), and we selected a preheat condition of 240°C (10 s) for natural/regenerative dose measurement and a cut heat of 200°C for test dose measurement. Dose recovery tests were also performed on the same sample, and the results indicated that the ratio of measured to given dose was in the range of 1.0 ± 0.1 (**Figure 3D**). Aliquots with recycling ratios outside 1.0 ± 0.1 and recuperations higher than 5% were excluded from the D_e calculation. Quartz grains in this study mainly show good luminescence features such as bright signal, fast component dominance (**Figures 3A, B**), normal distribution, and concentrated single peak for D_e values (**Figures 3E, F**), indicating that these samples were well reset and the SAR protocol was reliable for our samples.

Some recent studies reported very weak natural quartz signals from Tibetan lakes or even anomalously fading (e.g., Tsukamoto and Rades, 2016; Hou et al., 2021). To compare with the quartz results, two samples from S3 and S4 were dated using the $pIRIR_{225}$ procedure (Buylaert et al., 2009). Their K-feldspar results agree well with quartz ages (**Table 2**), suggesting that the OSL chronology for the samples in the study is reliable. The fading test was also conducted on the quartz grains of a sample DZ-S4-3, and the results suggest that no evident fading was observed (**Figure 3C**).

The results of OSL ages are summarized in **Table 2**.

RESULTS AND DISCUSSION

OSL Chronology

Two samples were collected from the well-sorted silty–sandy layer of S1, DZ-S1-1, and S1-2. For sample S1-1, its coarse-

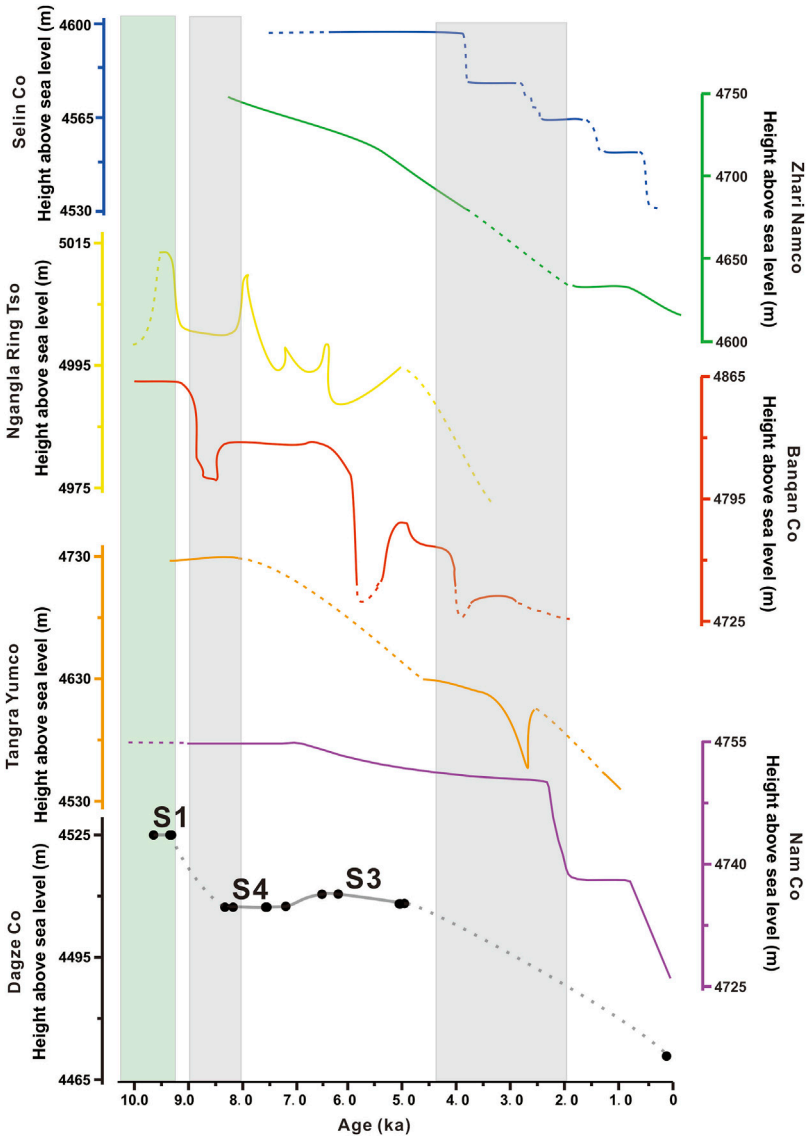

FIGURE 5 | Comparison of lake level changes in Dagze Co with those of other lakes in southern plateau in the Holocene: Selin Co (Shi et al., 2017; Hou et al., 2021), Zhari Namco (Chen et al., 2013), Ngangla Ring Tso (Huth et al., 2015), Banqan Co (Hudson et al., 2015), Tangra Yumco (Ahlborn et al., 2015), and Nam Co (Zhou et al., 2020; Huang et al., 2022).

grained quartz age (9.1 ± 0.5 ka) agrees well with its fine grain result (9.6 ± 0.6 ka). Since not enough coarse grains could be separated from the sample S1-2, we measured its fine-grained quartz, and an age of 9.2 ± 0.5 ka was obtained. These three results agree well with each other and suggest that S1 has an age of ~9.3 ka, indicating that Dagze Co had a lake highstand of +55 m in the early Holocene. Climate records from proxy studies of Dagze Co also suggest a relatively moist climate with intense runoff during 19–12 ka (Hou et al., 2017). Massive pebbles beneath the sand layer in S1 also confirm a strong river runoff before 9.3 ka. The age gap between 9.3 to 12 ka might because of the following: 1) uncertainties arising from different dating method (e.g., reservoir effect of C-14) and, 2) after water infill reached its peak, the lake might have maintained at this level for a period and began to decline with a time lag. It is noted that a similar paleo-shoreline to S1 was dated as the middle Holocene (Liu et al., 2020; Liu et al., 2021). The difference may because our samples of S1 were taken from the 2-m-thick well-sorted sand layer, which was typical near-shore sediment. In particular, the overlying and underlying massive gravels/pebbles are more related to diluvial/fluvial conditions, and quartz/K-feldspar grains within these pebble layers are also harder to be fully bleached prior to burial.

Four samples from S3 have an age of 4.8 ± 0.2, 5.1 ± 0.3, 6.2 ± 0.4, and 6.6 ± 0.4 ka. These four samples were taken from two sites where two seasonal rivers cut through S3, and their elevations vary slightly from 4,511 to 4,508 m. One K-feldspar sample from DZ-S3-3 yields an age of 5.0 ± 0.2 ka, which is consistent with its quartz

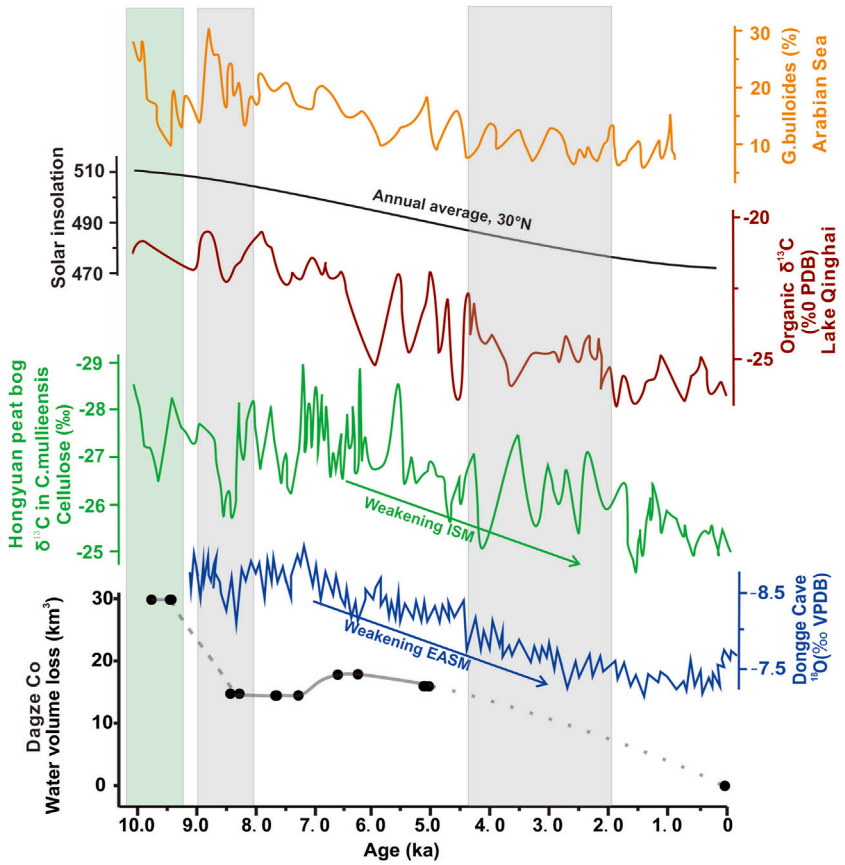

FIGURE 6 | Changes in lake volume of Dagze Co since the early Holocene and other related climatic proxies: *G. bulloides* proxy record from Arabian Sea (Gupta et al., 2003), summer solar insolation at 30°N (Berger and Loutre, 1991), proxy records from Qinghai Lake (Ji et al., 2005), $\delta^{13}C$ records from Hongyuan peat bog (Hong et al., 2003), and oxygen isotope records in the stalagmite from Dongge Cave (Wang et al., 2005).

age of 4.8 ± 0.2 ka. The results of these four samples suggest a high lake level of +40 m in the middle Holocene. Compared with those of S1, the results clearly show that lake level rapidly dropped about 20 m since 9.2 to 5–6 ka. A proxy study from Dagze Co also suggests relatively high lake water salinity, reduced runoff, and a dry environment during the early to middle Holocene (Hou et al., 2017).

For S4, four samples yield ages of 7.2 ± 0.4, 7.7 ± 0.3, 8.2 ± 0.5, and 8.3 ± 0.4 ka. Combining with one K-feldspar result of 7.6 ± 0.3 ka of DZ-S4-3, these results agree well with each other and suggest that S4 has an age of 7.2–8.3 ka. Notably, this lake level is slightly higher than that of S3, suggesting a wetter condition. A slightly increased runoff was also found in proxy signals from Dagze Co, implying a relatively humid climate during the middle to late Holocene (Hou et al., 2017). In addition, our results also suggest that the lake level of Dagze Co probably remained stable for a considerable duration between 8 ka and about 5 ka, with some slight fluctuations.

The DZ-TR profile (**Figure 2F**) was collected from the road near surface between S1 and S2. Their ages are 3.6 ± 0.2 and 4.4 ± 0.3 ka. Since these sediments are deposits near the alluvium, their ages imply the aggradation of sediments atop of S2 was still active until about 4 ka. The DZ-TL profile was loess-like silt atop of S2, and two samples yield ages of 0.9 ± 0.1 and 5.7 ± 0.4 ka, from top down. In the field, this profile occurred as massive loess-like materials with occasional appearance of inter-bedded gravels. We tend to attribute it to a combination of aeolian activity with occasional alluviums.

Lake Level and Water Volume Reconstruction

Based on the elevation of S1, S3, and S4, the past lake area was reconstructed using DEM data in **Figure 4** (source: Shuttle Radar Topography Mission data, ~90-m resolution). There is a watershed with a height of 4,527 m to the west. If Dagze Co can reach that level, it might have connected to a dry basin to its west (the red areas in **Figure 4**). If so, at the highest lake level of 4,525 m (+55 m), the extent of Dagze Co was estimated as 1,639 km^2, which was more than six times its present size.

From S1 to about S4, the lake area has shrunk from 1,639 to 1,141 km^2, and the volume of water decreased from 29.93 to 14.29 km^3. The lake probably remained at a stable level of 4,504–4,511 m at 8–5 ka with slight fluctuations. A further decline of ~ 40 m since about 5 ka was observed. In summary, the lake level of Dagze Co dropped by 55 m, with a total water loss of about 29.93 km^3.

Comparison With Other Lakes and Climate Records

In **Figure 5**, the lake fluctuation history of Dagze Co was compared to those of several adjacent Tibetan lakes such as Selin Co (Shi et al., 2017; Hou et al., 2021), Nam Co (Zhou et al., 2020; Huang et al., 2022), Baqan Tso (Huth et al., 2015), Zhari Namco (Chen et al., 2013), and Ngangla Ring Tso (Hudson et al., 2015). In general, lakes from the southern TP have their highest levels mainly occurred in the early Holocene, which follows well with the enhanced Indian summer monsoon precipitation in the early Holocene (**Figure 6**, Berger and Loutre, 1991; Hong et al., 2003; Ji et al., 2005; Wang et al., 2005), while the highest levels of lakes from the northwestern TP mainly occur in the latest Pleistocene, probably related to the strong glacier meltwater by then (e.g., Liu et al., 2016; Zhang et al., 2022). From lake sediments and ice-core records on the plateau, an early Holocene wet/warm phase with substantial precipitation has been widely described (Thompson et al., 1989; Thompson et al., 1997; Wang et al., 2002). $\delta^{18}O$ values from lacustrine carbonate in five lakes in western China show a rapid intensification of monsoon rainfall at about 12–11 ka (Wei and Gasse, 1999). A rainy episode at about 8 ka (Van Campo and Gasse, 1993) and a high lake level around 9 ka (Gasse et al., 1991) shown in the pollen record from Sumxi Co also suggest a long-term trend toward aridity since about 7 ka.

Given the lack of evidence of glacial activity in Dagze Co, we attribute that the loss of water volume is mainly related to the net balance between Asian monsoon precipitation and evaporation. According to DEM analysis, Dagze Co has lost a total of 29.93 km^3 of water and coincided with the general weakening trend of Asian monsoon since the early Holocene (**Figure 6**). Our findings from Dagze Co generally follow a similar pattern to those climatic records from Qinghai Lake (Ji et al., 2005), Dongge Cave (Wang et al., 2005), and the Arabian Sea (Gupta et al., 2003) (**Figure 6**). It is also noted that the strongest Indian monsoon precipitation occurred in the early Holocene, whereas the east Asian monsoon reached its peak in the early/middle Holocene; accordingly, lakes in southern TP have their highest levels occurred in the early Holocene, while lakes in northeastern TP reached their recent maximum in the middle Holocene (e.g., Chen et al., 2020; Zhang et al., 2020). Dagze Co lies within the region of Asian monsoon; its input of lake water should be under a joint control of ISM and EASM. This study shows that monsoonal precipitation has penetrated the basin of Dagze Co in the interior of the plateau during the early Holocene. Compared with records of the westerlies (see reviews and references in Chen et al., 2020), our result from Dagze Co implies that impact from westerlies in this region was not apparent during the early/middle Holocene. Notably, it is also possible that a lowered evaporation caused by low temperature could also lead to lake level rise, and such possibility should also be considered (e.g., Hou et al., 2021).

CONCLUSION

1) A lake highstand of Dagze Co (+55 m) occurred at 9.1 ± 0.5 to 9.6 ± 0.6 ka, suggesting a relatively humid period in the early Holocene. Intensified Asian monsoon precipitation in the early Holocene should be the main reason for the high lake level.
2) Lake level subsequently dropped about 20 m since 9.2 ka and probably remained at this level (+35 m) from about 8 to 5 ka, with slight fluctuations. A dry condition and reduced runoff should be the main reason for lake shrinkage. Lake level further dropped another 40 m in the late Holocene.
3) The shrinkage of Dagze Co generally follows a similar pattern to the evolution process of adjacent Tibetan lakes and the trend of Asian monsoon intensity, suggesting a long-term control of monsoon precipitation.

DATA AVAILABILITY STATEMENT

The original contributions presented in the study are included in the article/Supplementary Material, and further inquiries can be directed to the corresponding author.

AUTHOR CONTRIBUTIONS

YW: conducted the experiment and field trip, performed data analysis, and wrote the draft; YC: conducted the field trip, performed data analysis, and organized/revised the draft; LH: helped with the experiment and sample collection; PD: helped with sample collection and discussion; HC: helped with sample collection and discussion; and GW: organized the scientific framework.

FUNDING

This work was financially supported by the Second Tibetan Plateau Scientific Expedition and Research Program (STEP) (2019QZKK0202), the National Natural Science Foundation of China (41772176 and 41402150), the Key Special Project for Introduced Talents Team of Southern Marine Science and Engineering Guangdong Laboratory (Guangzhou) (GML2019ZD0308) and the Youth Innovation Promotion Association of the Chinese Academy of Sciences (2017403).

ACKNOWLEDGMENTS

Kai Kong and Xijie Wang are acknowledged for their assistance in the fieldwork.

REFERENCES

Ahlborn, M., Haberzettl, T., Wang, J., Fürstenberg, S., Mäusbacher, R., Mazzocco, J., et al. (2015). Holocene Lake Level History of the Tangra Yumco Lake System, Southern-Central Tibetan Plateau. *Holocene* 26 (2), 176–187. doi:10.1177/0959683615596840

Aitken, M. J. (1998). *Introduction to Optical Dating: The Dating of Quaternary Sediments by the Use of Photon-Stimulated Luminescence*. Oxford: Oxford University Press.

An, Z. S. (2000). The History and Variability of the East Asian Paleomonsoon Climate. *Quat. Sci. Rev.* 19 (1-5), 171–187. doi:10.1016/S0277-3791(99)00060-8

Berger, A., and Loutre, M. F. (1991). Insolation Values for the Climate of the Last 10 Million Years. *Quat. Sci. Rev.* 10 (4), 297–317. doi:10.1016/0277-3791(91)90033-Q

Buylaert, J. P., Murray, A. S., Thomsen, K. J., and Jain, M. (2009). Testing the Potential of an Elevated Temperature IRSL Signal from K-Feldspar. *Radiat. Meas.* 44 (5), 560–565. doi:10.1016/j.radmeas.2009.02.007

Chen, F., Zhang, J., Liu, J., Cao, X., Hou, J., Zhu, L., et al. (2020). Climate Change, Vegetation History, and Landscape Responses on the Tibetan Plateau during the Holocene: A Comprehensive Review. *Quat. Sci. Rev.* 243, 106444. doi:10.1016/j.quascirev.2020.106444

Chen, Y., Aitchison, J. C., Zong, Y., and Li, S.-H. (2016). OSL Dating of Past Lake Levels for a Large Dammed Lake in Southern Tibet and Determination of Possible Controls on Lake Evolution. *Earth Surf. Process. Landforms* 41 (11), 1467–1476. doi:10.1002/esp.3907

Chen, Y., Zong, Y., Li, B., Li, S., and Aitchison, J. C. (2013). Shrinking Lakes in Tibet Linked to the Weakening Asian Monsoon in the Past 8.2 ka. *Quat. Res.* 80 (2), 189–198. doi:10.1016/j.yqres.2013.06.008

Duller, G. A. T. (2008). Single-Grain Optical Dating of Quaternary Sediments: Why Aliquot Size Matters in Luminescence Dating. *Boreas* 37 (4), 589–612. doi:10.1111/j.1502-3885.2008.00051.x

Feng, Y., Hou, Y., Zhang, J., Yang, N., Cai, Y., Yang, F., et al. (2022). Timing of Holocene Lake Highstands Around Dawa Co in Inner Tibetan Plateau: Comparison of Quartz and Feldspar Luminescence Dating with Radiocarbon Age. *Quat. Geochronol.* 69, 101267. doi:10.1016/j.quageo.2022.101267

Gasse, F., Arnold, M., Fontes, J. C., Fort, M., Gibert, E., Huc, A., et al. (1991). A 13,000-Year Climate Record from Western Tibet. *Nature* 353 (6346), 742–745. doi:10.1038/353742a0

Gupta, A. K., Anderson, D. M., and Overpeck, J. T. (2003). Abrupt Changes in the Asian Southwest Monsoon during the Holocene and Their Links to the North Atlantic Ocean. *Nature* 421 (6921), 354–357. doi:10.1038/nature01340

Hong, Y. T., Hong, B., Lin, Q. H., Zhu, Y. X., Shibata, Y., Hirota, M., et al. (2003). Correlation between Indian Ocean Summer Monsoon and North Atlantic Climate during the Holocene. *Earth Planet. Sci. Lett.* 211 (3), 371–380. doi:10.1016/S0012-821X(03)00207-3

Hou, J., Tian, Q., Liang, J., Wang, M., and He, Y. (2017). Climatic Implications of Hydrologic Changes in Two Lake Catchments on the Central Tibetan Plateau Since the Last Glacial. *J. Paleolimnol.* 58 (2), 257–273. doi:10.1007/s10933-017-9976-9

Hou, Y., Long, H., Shen, J., and Gao, L. (2021). Holocene Lake-Level Fluctuations of Selin Co on the Central Tibetan Plateau: Regulated by Monsoonal Precipitation or Meltwater? *Quat. Sci. Rev.* 261, 106919. doi:10.1016/j.quascirev.2021.106919

Huang, L., Chen, Y., Wu, Y., Zeng, T., and Wei, G. (2022). Lake Level Changes of Nam Co since 25 ka as Revealed by OSL Dating of Paleo-Shorelines. *Quat. Geochronol.* 70, 101274. doi:10.1016/j.quageo.2022.101274

Hudson, A. M., Quade, J., Huth, T. E., Lei, G., Cheng, H., Edwards, L. R., et al. (2015). Lake Level Reconstruction for 12.8-2.3 ka of the Ngangla Ring Tso Closed-Basin Lake System, Southwest Tibetan Plateau. *Quat. Res.* 83 (1), 66–79. doi:10.1016/j.yqres.2014.07.012

Hudson, A. M., and Quade, J. (2013). Long-Term East-West Asymmetry in Monsoon Rainfall on the Tibetan Plateau. *Geology* 41 (3), 351–354. doi:10.1130/G34548C.110.1130/g33837.1

Huth, T., Hudson, A. M., Quade, J., Guoliang, L., and Hucai, Z. (2015). Constraints on Paleoclimate from 11.5 to 5.0 ka from Shoreline Dating and Hydrologic Budget Modeling of Baqan Tso, Southwestern Tibetan Plateau. *Quat. Res.* 83 (1), 80–93. doi:10.1016/j.yqres.2014.07.011

Ji, S., Xingqi, L., Sumin, W., and Matsumoto, R. (2005). Palaeoclimatic Changes in the Qinghai Lake Area during the Last 18,000 Years. *Quat. Int.* 136 (1), 131–140. doi:10.1016/j.quaint.2004.11.014

Jonell, T. N., Aitchison, J. C., Li, G., Shulmeister, J., Zhou, R., and Zhang, H. (2020). Revisiting Growth and Decline of Late Quaternary Mega-Lakes across the South-Central Tibetan Plateau. *Quat. Sci. Rev.* 248 (15), 106475. doi:10.1016/j.quascirev.2020.106475

Kong, P., Na, C., Fink, D., Huang, F., and Ding, L. (2007). Cosmogenic 10Be Inferred Lake-Level Changes in Sumxi Co Basin, Western Tibet. *J. Asian Earth Sci.* 29 (5), 698–703. doi:10.1016/j.jseaes.2006.04.010

Krause, P., Biskop, S., Helmschrot, J., Flügel, W.-A., Kang, S., and Gao, T. (2010). Hydrological System Analysis and Modelling of the Nam Co Basin in Tibet. *Adv. Geosci.* 27, 29–36. doi:10.5194/adgeo-27-29-2010

Lai, Z., Mischke, S., and Madsen, D. (2014). Paleoenvironmental Implications of New OSL Dates on the Formation of the "Shell Bar" in the Qaidam Basin, Northeastern Qinghai-Tibetan Plateau. *J. Paleolimnol.* 51 (2), 197–210. doi:10.1007/s10933-013-9710-1

Li, D., Li, Y., Ma, B., Dong, G., Wang, L., and Zhao, J. (2009). Lake-Level Fluctuations since the Last Glaciation in Selin Co (Lake), Central Tibet, Investigated Using Optically Stimulated Luminescence Dating of Beach Ridges. *Environ. Res. Lett.* 4 (4), 045204. doi:10.1088/1748-9326/4/4/045204

Li, X., Hou, J., Wang, M., and Xu, L. (2021). Ecolosystem Changes and Possible Mechanisms of Dagze Co in the Tibetan Plateau During the Past 1000 Years. *J. Lake Sci.* 33 (4), 1276–1288. doi:10.18307/2021.0427

Liu, S., Jia, Q., Liu, X., Zheng, M., and Liu, L. (2013a). The Depositional Environment and Organic Sediment Component of Dagze Co, a Saline Lake in Tibet, China. *Acta Ecol. Sin.(Engl. Ed.)* 33 (18), 5785–5793.

Liu, W., Sun, F., Li, Y., Zhang, G., Sang, Y.-F., Lim, W. H., et al. (2018). Investigating Water Budget Dynamics in 18 River Basins across the Tibetan Plateau through Multiple Datasets. *Hydrol. Earth Syst. Sci.* 22 (1), 351–371. doi:10.5194/hess-22-351-2018

Liu, X.-J., Lai, Z.-P., Zeng, F.-M., Madsen, D. B., and E, C.-Y. (2013b). Holocene Lake Level Variations on the Qinghai-Tibetan Plateau. *Int. J. Earth Sci.* 102 (7), 2007–2016. doi:10.1007/s00531-013-0896-2

Liu, X.-J., Lai, Z., Madsen, D., and Zeng, F. (2015). Last Deglacial and Holocene Lake Level Variations of Qinghai Lake, North-Eastern Qinghai-Tibetan Plateau. *J. Quat. Sci.* 30 (3), 245–257. doi:10.1002/jqs.2777

Liu, X.-J., Madsen, D. B., Liu, R., Sun, Y., and Wang, Y. (2016). Holocene Lake Level Variations of Longmu Co, Western Qinghai-Tibetan Plateau. *Environ. Earth Sci.* 75 (4), 301. doi:10.1007/s12665-015-5188-7

Liu, X., Cong, L., Li, X., Madsen, D., Wang, Y., Liu, Y., et al. (2020). Climate Conditions on the Tibetan Plateau during the Last Glacial Maximum and Implications for the Survival of Paleolithic Foragers. *Front. Earth Sci.* 8, 549. doi:10.3389/feart.2020.606051

Liu, X., Madsen, D., and Zhang, X. (2021). The Driving Forces Underlying Spatiotemporal Lake Extent Changes in the Inner Tibetan Plateau during the Holocene. *Front. Earth Sci.* 9, 1–17. doi:10.3389/feart.2021.685928

Long, H., Shen, J., Wang, Y., Gao, L., and Frechen, M. (2015). High-Resolution OSL Dating of a Late Quaternary Sequence from Xingkai Lake (NE Asia): Chronological Challenge of the "MIS 3a Mega-Paleolake" Hypothesis in China. *Earth Planet. Sci. Lett.* 428, 281–292. doi:10.1016/j.epsl.2015.07.003

Ma, R., Yang, G., Duan, H., Jiang, J., Wang, S., Feng, X., et al. (2011). China's Lakes at Present: Number, Area and Spatial Distribution. *Sci. China Earth Sci.* 54 (2), 283–289. doi:10.1007/s11430-010-4052-6

Murray, A. S., and Wintle, A. G. (2000). Luminescence Dating of Quartz Using an Improved Single-Aliquot Regenerative-Dose Protocol. *Radiat. Meas.* 32 (1), 57–73. doi:10.1016/S1350-4487(99)00253-X

Otvos, E. G. (2000). Beach Ridges — Definitions and Significance. *Geomorphology* 32 (1), 83–108. doi:10.1016/S0169-555X(99)00075-6

Prescott, J. R., and Hutton, J. T. (1994). Cosmic Ray Contributions to Dose Rates for Luminescence and ESR Dating: Large Depths and Long-Term Time Variations. *Radiat. Meas.* 23 (2), 497–500. doi:10.1016/1350-4487(94)90086-8

Rades, E. F., Hetzel, R., Xu, Q., and Ding, L. (2013). Constraining Holocene Lake-Level Highstands on the Tibetan Plateau by 10Be Exposure Dating: A Case Study at Tangra Yumco, Southern Tibet. *Quat. Sci. Rev.* 82, 68–77. doi:10.1016/j.quascirev.2013.09.016

Rades, E. F., Tsukamoto, S., Frechen, M., Xu, Q., and Ding, L. (2015). A Lake-Level Chronology Based on Feldspar Luminescence Dating of Beach Ridges at Tangra Yum Co (Southern Tibet). *Quat. Res.* 83 (3), 469–478. doi:10.1016/j.yqres.2015.03.002

Shi, X., Kirby, E., Furlong, K. P., Meng, K., Robinson, R., Lu, H., et al. (2017). Rapid and Punctuated Late Holocene Recession of Siling Co, Central Tibet. *Quat. Sci. Rev.* 172, 15–31. doi:10.1016/j.quascirev.2017.07.017

Song, C., Huang, B., and Ke, L. (2013). Modeling and Analysis of Lake Water Storage Changes on the Tibetan Plateau Using Multi-Mission Satellite Data. *Remote. Sens. Environ.* 135, 25–35. doi:10.1016/j.rse.2013.03.013

Thompson, L. G., Mosley-Thompson, E., Davis, M. E., Bolzan, J. F., Dai, J., Klein, L., et al. (1989). Holocene-Late Pleistocene Climatic Ice Core Records from Qinghai-Tibetan Plateau. *Science* 246 (4929), 474–477. doi:10.1126/science.246.4929.474

Thompson, L. G., Yao, T., Davis, M. E., Henderson, K. A., Mosley-Thompson, E., Lin, P.-N., et al. (1997). Tropical Climate Instability: The Last Glacial Cycle from a Qinghai-Tibetan Ice Core. *Science* 276 (5320), 1821–1825. doi:10.1126/science.276.5320.1821

Tsukamoto, S., and Rades, E. F. (2016). Performance of Pulsed OSL Stimulation for Minimising the Feldspar Signal Contamination in Quartz Samples. *Radiat. Meas.* 84, 26–33. doi:10.1016/j.radmeas.2015.11.007

Van Campo, E., and Gasse, F. (1993). Pollen- and Diatom-Inferred Climatic and Hydrological Changes in Sumxi Co Basin (Western Tibet) since 13,000 Yr B.P. *Quat. Res.* 39 (3), 300–313. doi:10.1006/qres.1993.1037

Wang, J., Zhu, L., Nishimura, M., Nakamura, T., Ju, J., Xie, M., et al. (2009). Spatial Variability and Correlation of Environmental Proxies during the Past 18,000 Years Among Multiple Cores from Lake Pumoyum Co, Tibet, China. *J. Paleolimnol.* 42 (3), 303–315. doi:10.1007/s10933-008-9277-4

Wang, N., Yao, T., Thompson, L. G., Henderson, K. A., and Davis, M. E. (2002). Evidence for Cold Events in the Early Holocene from the Guliya Ice Core, Tibetan Plateau, China. *Sci. Bull.* 47 (17), 1422–1427. doi:10.1360/02tb9313

Wang, S., and Dou, H. (1998). *Records of Lakes in China*. Beijing: Science Press.

Wang, Y., Cheng, H., Edwards, R. L., He, Y., Kong, X., An, Z., et al. (2005). The Holocene Asian Monsoon: Links to Solar Changes and North Atlantic Climate. *Science* 308 (5723), 854–857. doi:10.1126/science.1106296

Wei, K., and Gasse, F. (1999). Oxygen Isotopes in Lacustrine Carbonates of West China Revisited: Implications for Post Glacial Changes in Summer Monsoon Circulation. *Quat. Sci. Rev.* 18 (12), 1315–1334. doi:10.1016/S0277-3791(98)00115-2

Wei, K., Ouyang, C., Duan, H., Li, Y., Chen, M., Ma, J., et al. (2020). Reflections on the Catastrophic 2020 Yangtze River Basin Flooding in Southern China. *Innovation* 1 (2), 100038. doi:10.1016/j.xinn.2020.100038

Wintle, A. G., and Murray, A. S. (2006). A Review of Quartz Optically Stimulated Luminescence Characteristics and Their Relevance in Single-Aliquot Regeneration Dating Protocols. *Radiat. Meas.* 41 (4), 369–391. doi:10.1016/j.radmeas.2005.11.001

Yan, D., and Wünnemann, B. (2014). Late Quaternary Water Depth Changes in Hala Lake, Northeastern Tibetan Plateau, Derived from Ostracod Assemblages and Sediment Properties in Multiple Sediment Records. *Quat. Sci. Rev.* 95, 95–114. doi:10.1016/j.quascirev.2014.04.030

Zhang, G., Yao, T., Chen, W., Zheng, G., Shum, C. K., Yang, K., et al. (2019). Regional Differences of Lake Evolution across China during 1960s-2015 and its Natural and Anthropogenic Causes. *Remote Sens. Environ.* 221, 386–404. doi:10.1016/j.rse.2018.11.038

Zhang, L., Su, F., Yang, D., Hao, Z., and Tong, K. (2013). Discharge Regime and Simulation for the Upstream of Major Rivers over Tibetan Plateau. *J. Geophys. Res. Atmos.* 118 (15), 8500–8518. doi:10.1002/jgrd.50665

Zhang, S., Zhang, J., Zhao, H., Liu, X., and Chen, F. (2020). Spatiotemporal Complexity of the "Greatest Lake Period" in the Tibetan Plateau. *Sci. Bull.* 65 (16), 1317–1319. doi:10.1016/j.scib.2020.05.004

Zhang, S., Zhao, H., Sheng, Y., Zhang, J., Zhang, J., Sun, A., et al. (2022). Mega-Lakes in the Northwestern Tibetan Plateau Formed by Melting Glaciers during the Last Deglacial. *Quat. Sci. Rev.* 285, 107528. doi:10.1016/j.quascirev.2022.107528

Zhou, J., Zhou, W., Dong, G., Hou, Y., Xian, F., Zhang, L., et al. (2020). Cosmogenic ^{10}Be and ^{26}Al Exposure Dating of Nam Co Lake Terraces since MIS 5, Southern Tibetan Plateau. *Quat. Sci. Rev.* 231, 106175. doi:10.1016/j.quascirev.2020.106175

Zhu, L., Wu, Y., Wang, J., Lin, X., Ju, J., Xie, M., et al. (2008). Environmental Changes since 8.4 ka Reflected in the Lacustrine Core Sediments from Nam Co, Central Tibetan Plateau, China. *Holocene* 18 (5), 831–839. doi:10.1177/0959683608091801

Conflict of Interest: The authors declare that the research was conducted in the absence of any commercial or financial relationships that could be construed as a potential conflict of interest.

Publisher's Note: All claims expressed in this article are solely those of the authors and do not necessarily represent those of their affiliated organizations or those of the publisher, the editors, and the reviewers. Any product that may be evaluated in this article, or claim that may be made by its manufacturer, is not guaranteed or endorsed by the publisher.

frontiers | Frontiers in Earth Science

ORIGINAL RESEARCH
published: 14 July 2022
doi: 10.3389/feart.2022.929599

Spatiotemporal Variation of Late Quaternary River Incision Along the Heihe River in the Northeastern Tibetan Plateau, Constrained by Dating Fluvial Terraces

Xilin Cao[1,2], *Xiaofei Hu*[2]*, *Baotian Pan*[2] and *Zhijun Zhao*[1]

[1]Jiangsu Center for Collaborative Innovation in Geographical Information Resource Development and Application, School of Geography, Nanjing Normal University, Nanjing, China, [2]Key Laboratory of Western China's Environmental Systems (Ministry of Education), College of Earth and Environmental Sciences, Lanzhou University, Lanzhou, China

Rates of river incision are widely used to track changes in rock uplift rate and climate over time and space. However, the relationship between the spatiotemporal variation of river incision and past tectonic or climatic processes is still unclear. Here, we focus on the spatial patterns of river incision in the interior and front of the Qilian Shan in the northeastern Tibetan Plateau. A sequence of late Quaternary terraces is well preserved along the Heihe River across the central Qilian Shan. We complement existing chronologic data with five new optically stimulated luminescence ages and one cosmogenic radionuclide ^{10}Be exposure age of terrace abandonment. At the mountain front, the river incision rate was ~1 mm/yr over the past 100 kyr, while the range was from 2 to 7 mm/yr during the Holocene. We attribute the fast incision rates during the Holocene to the progressive decrease of the river gradient induced by the warm and wet Holocene climate. In the interior of the mountains (the Qilian basin site), the river incision rates were close to 1 mm/yr since ~53 ka, suggesting that the upstream incision rate remained stable from the late Pleistocene to the Holocene. This observation further suggests that the adjustment of the climate-induced longitudinal river profile is limited to the downstream reach, especially along the front of the mountain range. We conclude that the long-term incision rate (during the late Pleistocene) is explained by ongoing uplift driven by fault activity, which determines the background rate of fluvial incision (~1 mm/yr). On the other hand, denudation rates on the millennial timescale estimated by previous studies in this region are < 1 mm/yr, suggesting that landscape-scale erosion lags behind trunk river incision.

Keywords: fluvial terrace, river incision, Heihe River, Qilian Shan, northeastern Tibet

OPEN ACCESS

Edited by:
Hao Long,
Nanjing Institute of Geography and Limnology (CAS), China

Reviewed by:
Honghua Lu,
East China Normal University, China
Yiquan Li,
Nanjing University, China

***Correspondence:**
Xiaofei Hu
feixhu@lzu.edu.cn

Specialty section:
This article was submitted to Quaternary Science, Geomorphology and Paleoenvironment, a section of the journal Frontiers in Earth Science

Received: *27 April 2022*
Accepted: *22 June 2022*
Published: *14 July 2022*

Citation:
Cao X, Hu X, Pan B and Zhao Z (2022) Spatiotemporal Variation of Late Quaternary River Incision Along the Heihe River in the Northeastern Tibetan Plateau, Constrained by Dating Fluvial Terraces. Front. Earth Sci. 10:929599. doi: 10.3389/feart.2022.929599

1 INTRODUCTION

Average river incision rates are closely related to specific spatial and temporal scales (Daniels, 2008; Finnegan et al., 2014). On the timescale of millions of years (Myr), river incision is sensitive to the rock uplift rate, modified by tectonic or isostatic processes (Pan et al., 2003; Kirby and Whipple, 2012). On the timescale of several thousand years (kyr), river incision can vary with the ratio of sediment flux to water flux, as well with the vegetation cover, modified by glacial or interglacial cycles

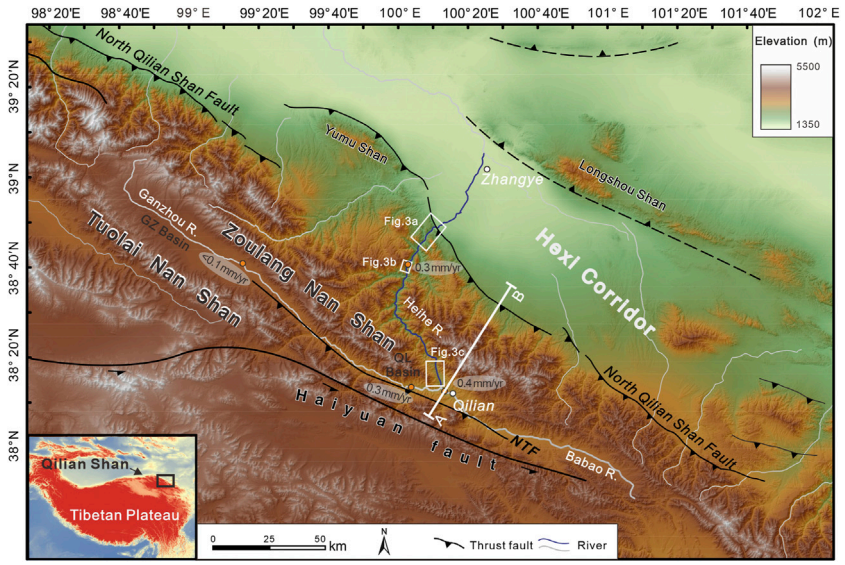

FIGURE 1 | Topographic map of the northeastern Tibetan Plateau (derived from 90 m SRTM data). The blue line indicates the fluvial reach shown in **Figure 2B**. The orange dots represent partial erosion rates estimated from cosmogenic ^{10}Be concentrations in river sediments (Palumbo et al., 2011; Hetzel, 2013; Hu et al., 2015a). NTF, North Tuolai Shan Fault; GZ Basin, Ganzhou River Basin; QL Basin, Qilian Basin.

(Ferrier et al., 2013). Moreover, a major river always flows through different tectonic zones, which complicates the relationship between river incision and tectonic or climatic processes (Craddock et al., 2010).

Over the past few decades, several studies have documented recent rapid incision rate events in northeastern Tibet that are probably linked to global climate change. For example, along the mountain front of the Qilian Shan and the Tien Shan, the deeply entrenched piedmont and the fast river incision are largely related to the warm and wet climate of the Holocene, rather than to tectonic forcing, which was shown to account for only 10% of the total incision (Poisson and Avouac, 2004; Hetzel et al., 2006; Lu et al., 2020). These authors further attributed the fast river incision to the progressive reduction of the river gradient along the mountain front. However, it is unclear whether the incision process continues to expand upstream, or if it restricted to the downstream reach. Quantifying changes in river incision rate over time and space is the primary method used for reconstructing this process.

In this study, we combined field observations, digital topographic analysis, and optically stimulated luminescence and cosmogenic radionuclide dating of multiple levels of fluvial terraces preserved along the Heihe River to quantify the spatial and temporal variation of river incision in northeastern Tibet during the Quaternary (**Figure 1**). We focus on the terraces located in the interior and the front of the Qilian Shan. These terraces provide average incision rates of the trunk valley of the Heihe River on timescales of 100–10 kyr. Furthermore, the distribution of the fluvial terraces and the spatial variation of their height above the river provide important information on the spatiotemporal pattern of river incision, which may help differentiate between tectonic and climatic forcing of river incision (Burbank et al., 1996).

2 STUDY AREA

Along the northeastern margin of the Tibetan Plateau, the Qilian Mountains are composed of several parallel NW-SE-trending ranges (e.g., the Zoulang Nan Shan and Tuolai Nan Shan, **Figures 1**, **2**), separated by thrust-fold systems. From the Hexi Corridor to the Qaidam Basin, the mountain ranges have a width of ~300 km. Multiple lines of evidence indicate that the uplift of the Qilian Mountains was caused by the extrusion of the Tibetan Plateau from the Early Miocene (Bovet et al., 2009; Zheng et al., 2010). The North Qilian Shan Fault (NQF, **Figure 1**) separates the mountain range and the foreland basin (Hexi Corridor) and dominates the uplift of the Qilian Mountains. The vertical slip rate of this boundary fault is estimated as 0.7–1.5 mm/yr, based on studies of late Quaternary geomorphic surfaces (e.g., Yang et al., 2018; Cao et al., 2021).

Our study area is in the northernmost range of the Qilian Shan and Zoulang Nan Shan, between the longitudes of 99°30′E and 100°20′E (**Figure 1**). The Heihe River drains the Zoulang Nan Shan and enters the Hexi Corridor (**Figure 2**). The segment up to the NQF is treated as the upstream reach, located in the mountain area with an average elevation of ~4,000 m. The upstream reach has two large tributaries: the Ganzhou River and the Babao River (**Figure 1**). The Ganzhou River drains eastward, joining the smaller and westward-flowing Babao River near the city of Qilian. The combined river then turns northward, and cross-cuts the NW-SE-oriented range of the Zoulang Nan Shan, producing a transverse drainage pattern. Specifically, the upper Ganzhou River valley is located at a piggy-back basin filled with Late Mesozoic and Quaternary deposits, with the thickness of the Quaternary deposits exceeding 400 m (Li, 1994). Cosmogenic nuclide data from the southern Zoulang Nan Shan show that

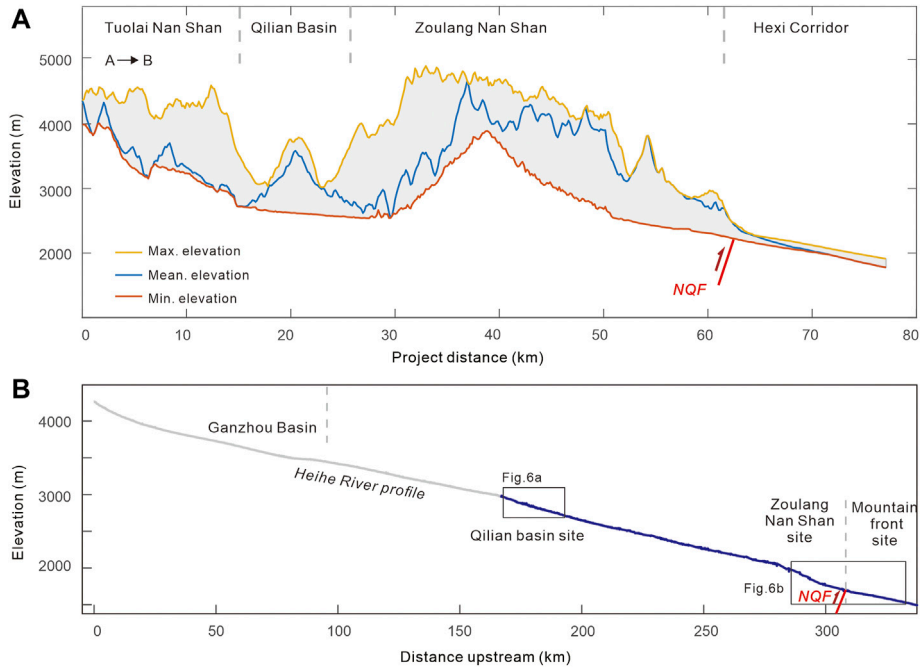

FIGURE 2 | (A) Swath profile (10 km × 10 km) across the Tuolai Nan Shan-Hexi Corridor. **(B)** Longitudinal profile of the Heihe River. Terraces along the blue reach are divided into three segments: Qilian basin site, Zoulang Nan Shan site, and mountain front site. Locations of the swath profile and the blue reach are shown in **Figure 1**. NQF, North Qilian Shan Fault.

millennial-scale erosion rates are as low as ~0.02 mm/yr, owing to the deposition of Quaternary sediments in the Ganzhou basin (upper Heihe River valley, Hetzel, 2013).

3 METHODS

3.1 Correlating and Classifying the Terraces

The terraces of the Heihe River have been extensively studied (Li et al., 1995; Li et al., 1999; Ren et al., 2019; Hu et al., 2021). Here, we use the labels Y-T1 to Y-T6 for the major terraces at the Zoulang Nan Shan–Mountain front sites (**Figure 2B**), and Q-T1 to Q-T6 for the major terraces of the Qilian basin site. We first mapped the terrace distribution on three segments along the Heihe River (the mountain front site, the Zoulang Nan Shan site, and the Qilian basin site; **Figures 2B**, **3**) using satellite imagery from Google Earth and detailed field surveys. Field investigations validated the terrace level, height, location, and extent of each mapped terrace, in addition to verifying the relative terrace ages based on geometric and topographic relationships. Correlation of terraces was primarily based on the continuity of the surface, the relative height of the terrace above the riverbed, and the terrace ages. The terraces were numbered in ascending order, from low to high: e.g., Y-T1 to Y-T6 at the mountain front and Zoulang Nan Shan sites. Note that the Qilian reach is one of the sites documented in our previous study (Hu et al., 2021), which used the labels T1 to T6 for the major terraces at the Qilian basin site. In the present study, we have modified the previous nomenclature because we identified new lower terraces. Adjacent to the river, three lower terraces were named Q-T1a, Q-T1b and Q-T1c. Through detailed field investigations (**Figure 3B**), the terrace numbers Q-T1b, Q-T2 to Q-T6 in this study respectively correspond to terraces T1 to T6 in Hu et al. (2021).

The elevations of the terrace surfaces (mainly the top of the fluvial gravels), strath surfaces, and the modern riverbed were surveyed using differential GPS (Trimble 5800), with uncertainties of less than 10 cm in the vertical direction. The higher terrace levels in the Qilian basin site were investigated in our previous study (Hu et al., 2021), and thus we adopted the survey data in the present study. For the Zoulang Nan Shan site, the terraces are discontinuous and thus several transects were established (**Figure 4**). Y-T4 and Y-T3, specifically, are widely spaced and extend for several kilometers in the foreland basin. Therefore, the terrace elevations were determined by both GPS surveying and DEM extraction (12.5-m ALOS PALSAR data, https://search.asf.alaska.edu/#/).

3.2 Dating the Terraces

The river incision rate is the ratio between the height of the terrace tread above the modern river level and the age of terrace formation (Burbank and Anderson, 2011). We determined the abandonment ages of the fluvial terraces based on previous work, as well as with our new data. The new terrace ages were determined using optically stimulated luminescence (OSL) and *in-situ* terrestrial cosmogenic nuclide (TCN) dating methods.

Floodplain sediments are deposited above the fluvial gravels on each terrace, and thus the dating was conducted on these floodplain sediments. Five new OSL samples were collected in this study.

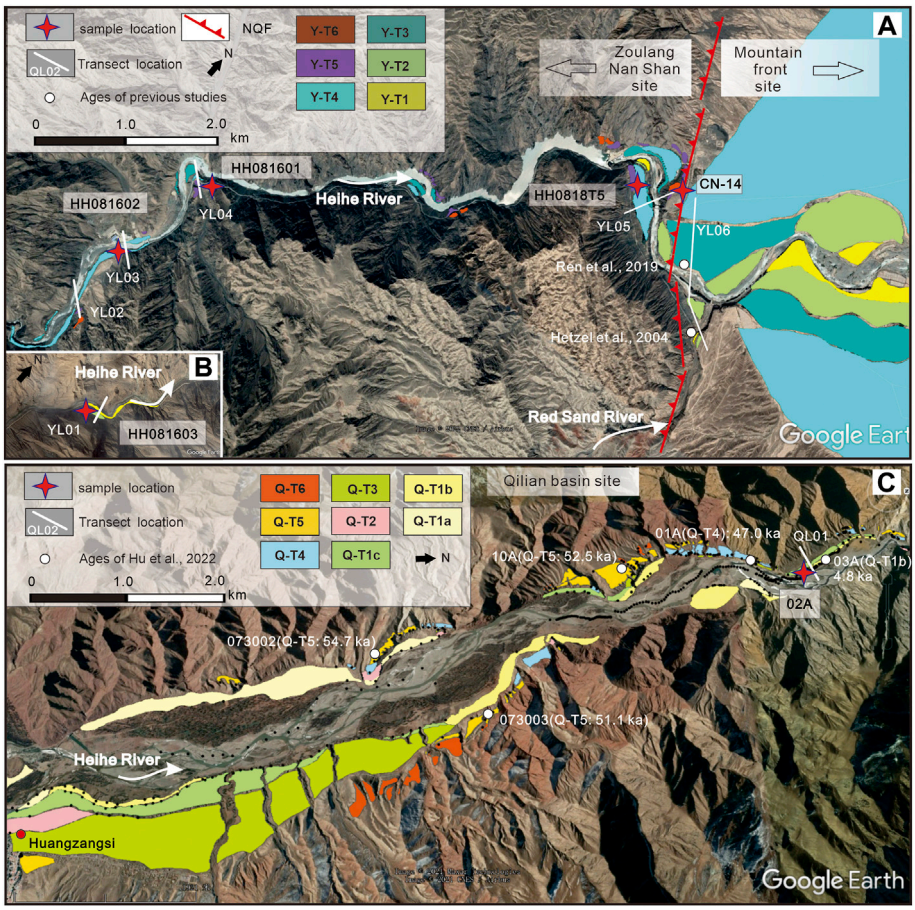

FIGURE 3 | Terrace distributions at the Zoulang Nan Shan site, mountain front site **(A)** and Qilian basin site **(B)**, with samples and transect positions. The background is from Google Earth (Map data: Image © 2019 CNES/Airbus) and the location is shown in **Figure 1**.

Stainless steel tubes were hammered into the freshly-cleaned sections, and after extraction the tubes were sealed with aluminum foil and plastic tape. OSL sample preparation and measurements were conducted in the laboratory of the Qinghai Institute of Salt Lakes, Chinese Academy of Sciences (Xining). Quartz grains (~38–63 μm) were extracted and cleaned following the procedures of Lai and Wintle (2006) and Lai et al. (2007). De was determined using the combination of the SAR protocol (Murray and Wintle, 2000) and the standardized growth curve (SGC) (Roberts and Duller, 2004). For each sample, six aliquots were measured by the SAR protocol to construct an SGC growth curve, and 11–12 additional aliquots were then measured for natural luminescence (Ln) and luminescence induced by the test dose (Tn). Sensitivity-corrected natural OSL (Ln/Tn) was projected on the SGC to yield a De. The characteristics of the De distributions for the samples are presented in **Figure 5**, and the average De was used for age calculation (**Table 1**). The decay curves, growth curves of individual aliquots, and the SGC for a representative sample (1A) are shown in **Figure 5**. The OSL signals decayed significantly during the first 1 s of stimulation (**Figure 5D**), suggesting that the OSL signal is dominated by fast components. Information on the dated samples and the age results are presented in **Table 1**.

For the highest terrace (Y-T6) along the river mouth, we collected one sample from fluvial gravels for surface exposure dating (CN-14, **Figure 3A**). Pits were excavated down to the gravel surface below the loess deposit (~45 cm). Quartz-rich clasts with diameters of 1–3 cm were selected from the gravel surface with the thickness of ~5 cm. To correct for differences in the inherited cosmogenic nuclide component, more than 30 quartz-rich pebbles were collected (Anderson et al., 1996; Niedermann and Niedermann, 2002). The quartz samples were physically and chemically purified in the Mineral Separation Laboratory of Purdue University. After target preparation, the ^{10}Be concentration was measured by accelerator mass spectrometry (AMS) at the Purdue Rare Isotope Measurement Laboratory. The two major sources of uncertainty of the cosmogenic age are the loess cover and the inheritance. Based on the ^{10}Be concentration in the Heihe trunk, we used the inheritance of $(1.15 \pm 0.06) \times 10^5$ atoms g^{-1} (Palumbo et al., 2011) for age correction, following the approach of Anderson et al. (1996). To account for the loess shielding effect, we followed the approach of Hetzel et al. (2004), with the assumption that the loess accumulated since 12 ± 2 ka and was removed only recently. ^{10}Be sample information and dating results are presented in **Table 2**.

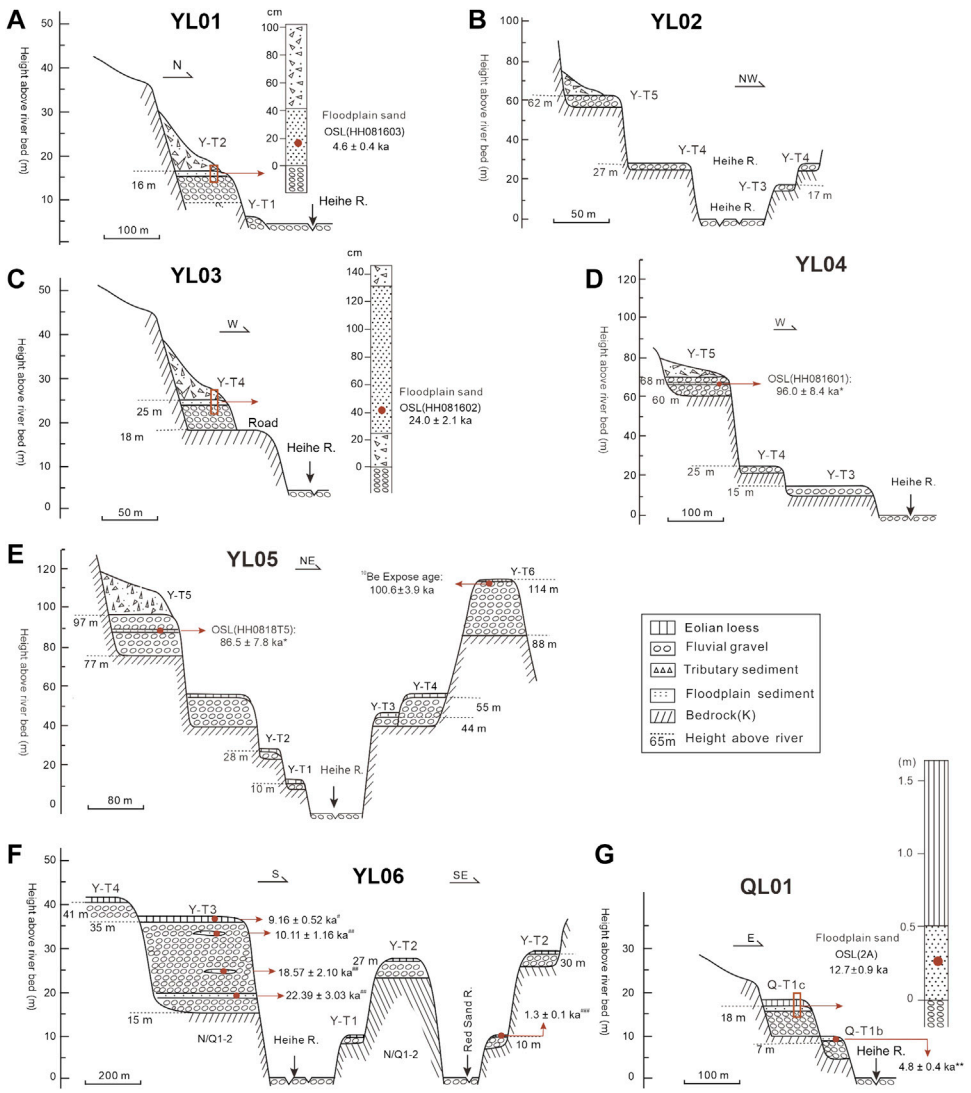

FIGURE 4 | Geomorphic transects along the Heihe River, showing the terrace staircases, the composition of each terrace level, and the locations of the samples used for terrace dating. YL01-YL05 are located in the Zoulang Nan Shan site, YL06 is located in the mountain front site and QL01 is located in the Qilian basin site. The locations of the transects are shown in **Figure 3**. Note: * indicates the excluded ages of terrace deposits; ** indicates ages from Hu et al. (2021); # indicates ages from Li et al. (1999); ## indicates ages from Ren et al. (2019) and ### indicates ages from Hetzel et al. (2004).

4 RESULTS

4.1 Fluvial Terraces Along the Heihe River

Several terraces are well preserved along the valley where the river flows through the Qilian basin, the Zoulang Nan Shan and the mountain front. By combining the previous work and the new fluvial geomorphological data of this work, we will describe the sequences of fluvial terraces along the different parts of the Heihe River.

4.1.1 Mountain Front Site

The mountain front site extends from the NQF to Zhangye city (**Figure 1**), and there are four levels of terraces along this reach (**Figure 3A**). Along transect YL06 (**Figure 4F**), GPS measurements in the field suggest that the four terraces (Y-T1 to Y-T4) are 10, 27, 35, and 41 m above the modern riverbed, respectively. For all terraces, the fluvial gravels consist mainly of rounded cobbles of sandstone, conglomerate, granite, diorite, and several metamorphic rocks. Most terrace treads are capped by 1-m-thick aeolian loess and the onset of loess deposition was in the early Holocene (Hetzel et al., 2004). Terrace profiles extracted from the DEM were consistent with the GPS measurements (**Figure 6B**). Profiles Y-T3 and Y-T4 indicate the progressive reduction of the river gradient and a decrease of the terrace spacing (**Figure 6B**). River incision decreases downstream from a maximum where the river exits the NQF to zero in the foreland.

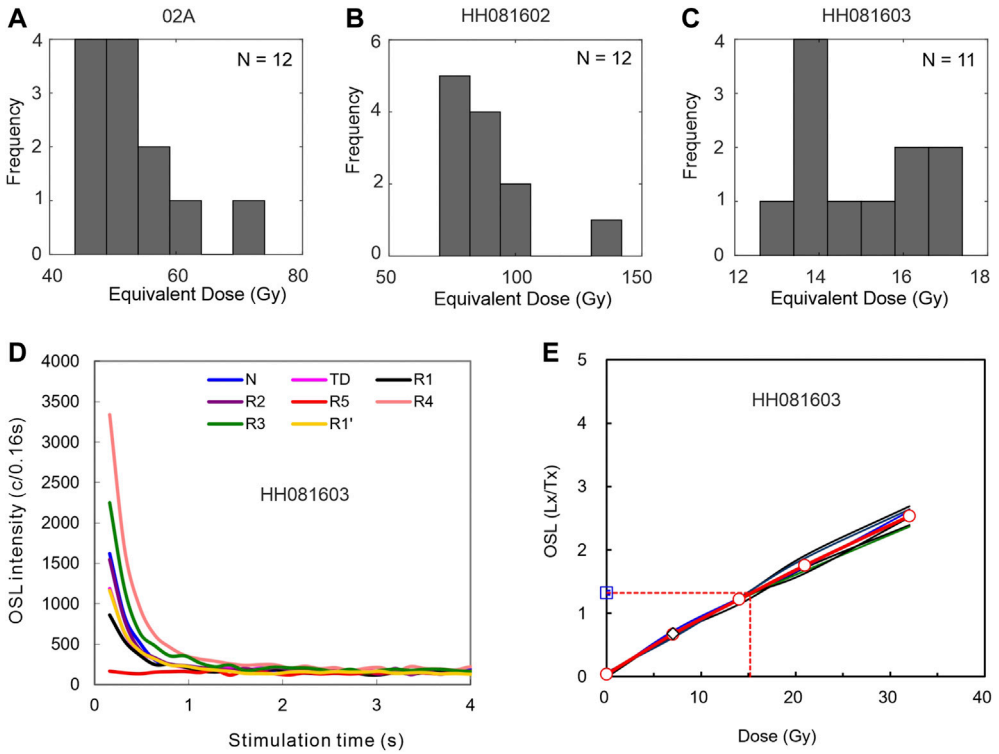

FIGURE 5 | (A–C) Equivalent dose (De) distributions. **(D)** Decay curves for sample HH081603. **(E)** OSL growth curves of individual aliquots, as well as the SGC (the bold red line), for sample HH081603.

TABLE 1 | OSL dating results.

Sample no.	Terrace	Longitude (°E)	Latitude (°N)	Altitude (m)	Equivalent dose (Gy)	Dose rate (mGy/a)	Age (ka)	Material	Location
2A	Q-T1c	100.16	38.30	2519	52.63 ± 1.52	4.15 ± 0.28	12.7 ± 0.9	Sand	Qilian basin
HH081603	Y-T2	100.03	38.66	2013	3.38 ± 0.26	15.5 ± 0.6	4.6 ± 0.4	Sand	Zoulang Nan Shan
HH081602	Y-T4	100.11	38.77	1714	3.68 ± 0.28	88.3 ± 3.7	24.0 ± 2.1	Sand	Zoulang Nan Shan
HH081601	Y-T5	100.11	38.78	1749	3.03 ± 0.23	290.7 ± 11.8	96.0 ± 8.4[a]	Sand	Zoulang Nan Shan
HH0818T5	Y-T5	100.16	38.81	1710	3.51 ± 0.27	303.4 ± 13.9	86.5 ± 7.8[a]	Sand	Zoulang Nan Shan

[a]*Indicates the excluded ages of terrace deposits. The dose rate of HH081601 and HH0818T5 are excessive that beyond the effective range of quartz dating.*

Ren et al. (2019) obtained three OSL samples from the sand lens of terrace Y-T3 (named T2 in the text). One sample from close to the top of the gravels yielded an age of ~10 ka and one sample form near the base of the gravels yielded an age of ~23 ka. The former may represent the abandonment age of terrace Y-T3 and the latter provides an age for the beginning of the Y-T3 deposit. Moreover, the age of the eolian loess atop surface Y-T3 was dated to 9.1 ka (Li et al., 1995), and thus terrace Y-T3 was formed between 9 and 10 ka. The top of the fluvial gravels of Y-T2 is 28 m above the modern riverbed and the abandonment age was suggested to be ~5 ka (Li et al., 1999). The top of the fluvial gravels of Y-T1 is 10 m above the modern riverbed, which can be correlated to the youngest terrace along the mouth of the Red Sand River, a tributary close to the Heihe river mouth (**Figure 3A**). Terrace Y-T1 of the Red Sand River has only a thin (45 cm) loess cover and the basal loess on this terrace has the age of only 1.3 ka (Hetzel et al., 2004). This indicates that the youngest terrace in this region was formed in the latest Holocene.

4.1.2 Zoulan Nan Shan Site

The Zoulan Nan Shan site is from the NQF and extends ~25 km upstream (**Figures 3A**, **6B**). Five transects were surveyed and five samples were dated. Along transect YL01 (**Figure 4A**), T2 stands 16 m above the modern riverbed with a thin layer of floodplain

TABLE 2 | ^{10}Be exposure dating results.

Sample	Sample location	Latitude (°N)	Longitude (°E)	Elevation (m)	Thick-ness cm	Shielding factor[a]	Quartz (g)	^{10}Be[b] (10^5 atoms g^{-1})	^{10}Be[c] (10^5 atoms g^{-1})	Age[d] (ka)	Loess thickness[e] (cm)	Age[f] (ka)
CN-14	Y-T6	38.81	100.17	1802	5	0.994	15.68	17.01 ± 0.29	15.86 ± 0.17	102.8 ± 6.5	45	100.6 ± 3.9

[a]*The shielding factor includes correction for horizon shielding and for the dip of the surface as well as a correction for sample thickness assuming a rock density of 2.65 g cm^{-3}.*
[b]*Measured ^{10}Be concentration of the samples.*
[c]*^{10}Be concentration has been corrected for inheritance using the estimated blank ^{10}Be concentration of 1.15 ± 0.06 × 105 atoms g^{-1}, which was derived from the modern sediments of the Heihe River by Palumbo et al. (2011).*
[d]*Exposure age calculated without correction for the loess cover (1σ) with the CRONUS-Earth ^{10}Be–^{26}Al online calculator (http://hess.ess.washington.edu/, version 2.3), using the time-dependent production rate scaling model of Lal (1991)–Stone (2000).*
[e]*Thickness of aeolian loess deposited on the gravel deposit.*
[f]*Exposure age calculated with a correction for the loess cover (1σ). This assumes a loess deposition since 12 ± 2 ka with an accumulation rate of 21.7 cm/ka (Stokes et al., 2003; Küster et al., 2006) (the uncertainty of the accumulation rate is not included); all ages were calculated assuming zero erosion.*

deposits (the strath was not identified), and the gravels are covered by > 10 m of colluvial sediments. One OSL sample (HH081603) was collected from floodplain deposits and yielded an age of 4.6 ± 0.4 ka, which is consistent with the previous dating of T2 along the mountain front (~5 ka, Li et al., 1999). Along transect YL02 (**Figure 4B**), there are three terraces (Y-T3 to Y-T5) on the valley slope, which are 17, 27, and 62 m above the present-day riverbed, respectively. Along transect YL03 (**Figure 4C**), the gravel layer of Y-T4 is 6-m-thick and covered by ~1 m of floodplain deposits. OSL sample HH081602 was collected from the floodplain deposits and yielded an age of 24.0 ± 2.1 ka, which agrees with the age of the initiation of the Y-T3 deposit (~22 ka, **Figure 4F**). On transect YL04 (**Figure 5D**), three terraces (Y-T3 to Y-T5) are 15, 25, and 68 m above the present-day riverbed, respectively. One sample from a sand interlayer on terrace Y-T5 yielded an age of ~96.0 ± 8.4 ka; however, we discarded this result because of the excessive dose rate (**Table 1**). On transect YL05 (**Figure 5E**), the highest terrace (Y-T6) was 114 m above the modern river and overlain by ~26 m of fluvial gravels, which in turn are covered by 40–50 cm of aeolian loess. One ^{10}Be exposure sample on the T6 surface (CN-14) was collected and yielded an age of 100.6 ± 3.9 ka. Y-T5 stands 97 m above the modern riverbed and the thickness of the fluvial gravels is ~20 m, which are covered by > 10 m of colluvial sediments. One sample from a sand interlayer on this terrace yielded the age of ~86.5 ± 7.8 ka; however, this result was also discarded because of the excessive dose rate (**Table 1**). Y-T4 is widespread and has a thick gravel layer (~15 m). The strath is 40 m above the modern riverbed and the terrace surface is 55 m. Terrace Y-T3 stands 44 m above the modern riverbed and the thickness of the fluvial gravels is 5 m. Along the mountain front, the NQF has dislocated the terraces of the Heihe River (**Figure 3A**). Complete staircase preservation permits the straightforward fitting between the terraces on the hanging wall and the footwall of the NQF.

Combined with the results of this study and the previous studies mentioned above, the fluvial terraces at the mountain front and the Zoulang Nan Shan sites were formed at 100.6 ± 3.9 ka (Y-T6), 24.0 ± 2.1 ka (Y-T4), 9–10 ka (Y-T3), ~5 ka (Y-T2) and 1.3 ka (Y-T1).

4.1.3 Qilian Basin Site

At the Qilian basin site, most of the terraces are incised into Cretaceous sandstone or Ordovician metamorphic rocks. The gravel layers are usually covered by floodplain deposits of sands and capped with varying depths of eolian loess. There are three lower terraces (Q-T1a, Q-T1b and Q-T1c) always co-extensive. Terrace Q-T1a is 3–5 m high above the modern river level and no suitable sample could be obtained for dating. Terrace Q-T1b is 7 m above the present-day river level and capped with 3 m of fluvial gravels (**Figure 4G**). Exposure of the Q-T1b strath is limited because of the aggradation of the T1a deposits. The strath of Q-T1c is 10 m above the river level and capped by 8 m of fluvial gravels (**Figure 4G**). Sample 2A was from fluvial sand, 30 cm above the basal gravel layer of Q-T1c and yielded an age of 12.7 ± 0.9 ka (**Figure 4G**). Utilizing OSL dating, our previous study showed that the terraces in the Qilian basin

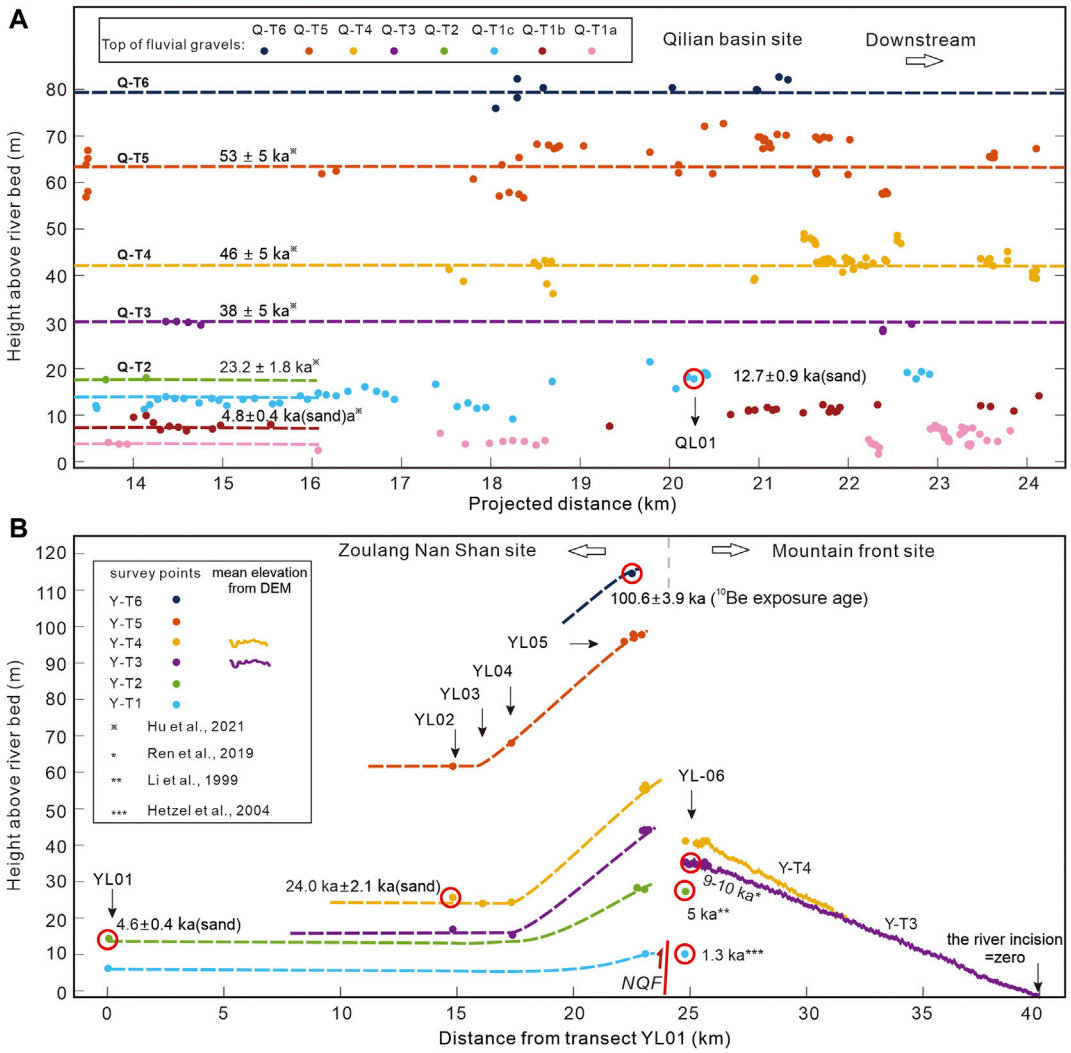

FIGURE 6 | Results of the terrace survey showing the longitudinal profiles (small colored dots) for each terrace level at the Qilian basin site **(A)**, the Zoulang Nan Shan site and the mountain front site **(B)**. The dashed lines are reconstructed pre-incision longitudinal profiles. The oscillations in the Y-T3 and T4 profiles are due to the lower resolution of the regional DEM.

TABLE 3 | River incision rates at the river mouth (transect YL05).

Terrace	Y-T1	Y-T2	Y-T3	Y-T4	Y-T5	Y-T6
Height of terrace (m)	10	28	44	55	97	114
Ages of terrace deposits or loess (ka)	1.3 ± 0.1	5[a]	9–10[b]	24.0 ± 2.1	—	100.6 ± 3.9
River incision rate (mm/yr)	7.7 ± 0.8	5.6 ± 0.7	4.6 ± 0.4	2.3 ± 0.3	—	1.1 ± 0.1

[a]*Age from Li et al. (1999).*
[b]*Ages from Li et al. (1999) and Ren et al. (2019). Incision rates (2σ) were calculated by Monte Carlo simulation (1000-times), with assuming 5% error in height of terrace.*

site were formed at 53 ± 5 ka, 46 ± 5 ka, 38 ± 5 ka, 23.2 ± 1.8 ka and 4.8 ± 0.4 ka, respectively (Hu et al., 2021). Combined with the results of this study, we conclude that the fluvial terraces in this region were formed at 53 ± 5 ka (Q-T5), 46 ± 5 ka (Q-T4), 38 ± 5 ka (Q-T3), 23 ± 2 ka (Q-T2), 12.7 ± 0.9 ka (Q-T1c) and 4.8 ± 0.4 ka (Q-T1b).

4.2 Late Quaternary Rates of River Incision

At the mouth of the Heihe River (transect YL05), the river incision rate is 1.1 ± 0.1 mm/yr for the highest terrace Y-T6 since ~100 ka (**Table 3**). For the lower terraces along transect YL05, the river incision rates since ~24, 10, 5, and 1.3 ka are 2.3 ± 0.3 mm/yr, 4.6 ± 0.4 mm/yr, 5.6 ± 0.7 mm/yr and 7.7 ± 0.8 mm/

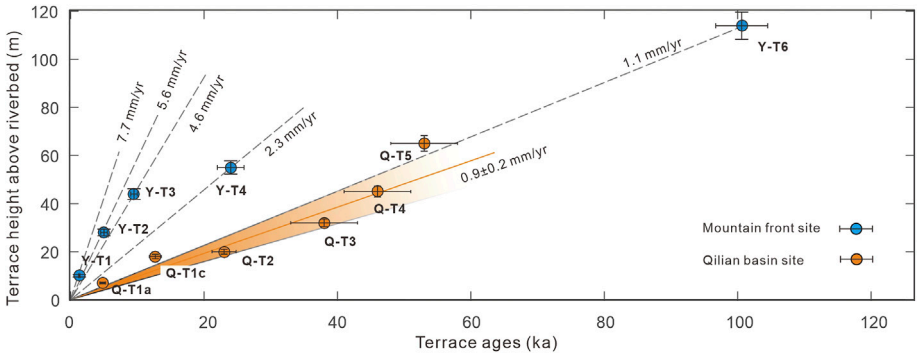

FIGURE 7 | Plot of ages versus the heights of the different terraces. The blue bars indicate the age errors. The rate of 0.9 ± 0.2 mm/yr is derived by linear fitting with 95% confidence intervals.

TABLE 4 | River incision rates at the Qilian basin site.

Terrace	Q-T1b	Q-T1c	Q-T2	Q-T3	Q-T4	Q-T5
Height of terrace (m)	7	18	20	32	45	65
Ages of terrace deposits or loess (ka)	4.8 ± 0.4[a]	12.7± 0.9	23.2 ± 1.8[a]	38 ± 5[a]	46 ± 5[a]	53 ± 5[a]
River incision rate (mm/yr)	1.5 ± 0.2	1.4 ± 0.1	0.9 ± 0.1	0.9 ± 0.1	1.0 ± 0.1	1.3 ± 0.2

[a]*Ages from Hu et al. (2021). Incision rates (2σ) were calculated by Monte Carlo simulation (1000-times), assuming a 5% error for the height of the terrace.*

yr, respectively (**Table 3**). Along transect YL03, the river incision rate is 1.0 ± 0.1 mm/yr since ~24 ka, and along transect YL01, the river incision rate is 3.5 ± 0.2 mm/yr since ~4.6 ka.

Along the Qilian basin reach, the incision rates range from 0.9 mm/yr to 1.5 mm/yr since ~53 ka, and we propose that the regional mean fluvial incision rate is 0.9 ± 0.2 mm/yr (**Figure 7**). The terrace ages define an approximately linear trend when plotted versus the heights of the terrace trend above the riverbed, suggesting that river incision has remained constant from least 53 ka to the present.

In summary, our results reveal the following spatiotemporal pattern of river incision along the Heihe River (**Figure 7**): 1) incision rates along the mountain front increased temporally from 1.1 ± 0.1 mm/yr in the late Pleistocene to 7.7 ± 0.8 mm/yr in the Holocene; 2) incision rates since ~5 ka decreased from 5.6 ± 0.7 mm/yr (YL05) to 3.5 ± 0.2 mm/yr (YL01) and 1.5 ± 0.2 mm/yr (QL01, Qilian basin), indicating that the rates of river incision during the Holocene have decreased upstream; 3) incision rates along the Qilian basin reach were constant during the late Pleistocene (0.9 ± 0.2 mm/yr). The mean heights, abandonment ages, and mean incision rates of the terraces at the mountain front and the Qilian basin are summarized in **Table 3** and **Table 4**.

5 DISCUSSION

5.1 Temporal Variations in River Incision Rates

The incision rates calculated from the fluvial terraces along the Heihe River in this study varied between 0.9 and 7.7 mm/yr since the late Pleistocene. These values are significantly higher than the landscape-scale erosion rates estimated from cosmogenic ^{10}Be concentrations in river sediments. The millennial-scale catchment-averaged denudation rates derived from the trunk are 0.3–0.4 mm/yr (Hu et al., 2015a; Palumbo et al., 2011; **Figure 1**). A possible reason for the lower ^{10}Be-derived erosion rates is the spatially weighted values over the drainage area of the Ganzhou basin (**Figure 1**). The Ganzhou basin is a piggy-back basin that was infilled with thick Quaternary deposits, suggesting that an endorheic drainage system was established here (Li, 1994). Although the Ganzhou basin is now externally drained, the upland maintains relatively low erosion rates (<0.2 mm/yr, Hetzel, 2013; Hu et al., 2015a). Another reason for the different rates estimated using the two different methods may be the lagged response of the hillslopes to a recently accelerated trunk river incision event. Along the northern margin of the Zoulang Nan Shan, the river incision rates are 5–10 mm/yr during the Holocene (Hetzel et al., 2006; Tian et al., 2017; Liu et al., 2019; Yang et al., 2020). However, denudation rates from several catchments draining the Zoulang Nan Shan are < 1 mm/yr (Palumbo et al., 2011; Hu et al., 2015a). This common phenomenon supports our view that, along the northern margin of the Zoulang Nan Shan, the landscape-scale erosion estimated from cosmogenic ^{10}Be concentrations in river sediments lags the trunk river incision rate.

A notable feature of these incision rates is that the rates calculated for the Holocene are substantially higher than those estimated over the late Pleistocene. Finnegan et al. (2014) showed that the estimated fluvial incision rates will be greater, due to the shorter measurement interval, also known as the “Sadler effect” (Sadler, 1981). However, in contrast to what would be expected

for the "Sadler effect", we observe that the incision rates in the Qilian basin are consistent during different measurement intervals. There is no reason why this effect should differentially influence the Heihe River. Consistent with an earlier compilation (Hetzel et al., 2006; Tian et al., 2017; Liu et al., 2019; Yang et al., 2020), the rates calculated over the Holocene are substantially higher than those estimated over the late Pleistocene. The longitudinal geometry of the foreland basin was interpreted to reflect climate change during the latest Pleistocene–early Holocene (Poisson and Avouac, 2004; Lu et al., 2018; Malatesta et al., 2018; Lu et al., 2020; Wang et al., 2022). During the last glacial period (17–24 ka, Osman et al., 2021), large volumes of sediment accumulated in the mountain front area, resulting in alluvial fan development (e.g., Y-T4 and Y-T3). The increasing sediment flux would be expected to cause continuous aggradation and thus the steepening of the fans. Until the warm and wet Holocene, river incision became dominant, leading to alluvial fan abandonment. The lower ratio between the sediment flux and water discharge, due to the increased precipitation, will finally result in the decrease of the river's gradient (Malatesta and Avouac, 2018; Lu et al., 2020). As a result, at the mountain front site, river incision rates for the Holocene increased significantly.

5.2 Spatial Variation of River Incision

As shown by the terrace profiles at the mountain front site, the amount of river incision is still significant and only farther north does it gradually decrease to zero (~40 km, **Figure 6B**). As a result, the spatial pattern of river incision shows a downstream-decreasing trend from the maximum where the river exits the range (**Figure 6B**).

The terrace profiles at the Zoulang Nan Shan site also show a gradual and progressive incision and increased spacing downstream (**Figure 6B**). The terrace profiles exhibit long-wavelength folds across the Qilian Shan: e.g., the western Qilian Shan (Liu et al., 2019; Wang et al., 2020) and the eastern Qilian Shan (Hu et al., 2015b; Zhong et al., 2020). Because of the fold-related increase in vertical uplift, tectonics could have maintained further river entrenchment, which may explain the increased vertical terrace spacing in the Zoulang Nan Shan. The Holocene rock uplift of the fold has been estimated to be < 10 m (with a maximum vertical uplift rate of 1 mm/yr) (Liu et al., 2019; Wang et al., 2020). Taking terrace Y-T3 (9–10 ka) as an example, the maximum vertical uplift of ~10 m is low compared to the maximum incision of ~44 m (transect YL05, **Figure 4E**). Thus, we prefer to conclude that the enhanced incision was caused not only by the differential uplift of the Zoulang Nan Shan, but also by the base level lowering of the foreland river. Furthermore, the vertical slip on the NQF and the enhanced incision would contribute the base level lowering at the mountain front. There is a clear fault scarp on terrace Y-T3, indicating that 2–3 m vertical uplift on the NQF during the Holocene (Ren et al., 2019). This vertical uplift might be ignored. Therefore, it is more likely that climate change was the main cause of the vertical spacing of the Zoulang Nan Shan terrace profiles.

According to the forgoing processes, an incisional wave resulting from climate change propagated upstream towards the range. However, along the Qilian basin reach, all terrace surfaces are approximately parallel to the modern riverbed (**Figure 6A**) and river incision has remained constant from at least ~53 ka to the present. Therefore, the incisional wave resulting from climate change only affected the river over a limited distance and has not propagated upstream towards the Qilian basin. This phenomenon further explains an earlier question in **Section 5.1**: why ^{10}Be-derived erosion from several catchments draining the Zoulang Nan Shan lags the trunk river incision. We speculate that the incision wave has not travel through much further to the upstream and affect landscape there. Thus, the equilibrium between landscape-scale erosion and river incision have not achieved yet. Unfortunately, the stream or the terrace profiles do not provide clear evidence for knickpoint migration. On the other hand, river incision in the Qilian basin is coupled with ongoing uplift driven by the fault activity of the NQF (~1 mm/yr) (Xiong et al., 2017; Cao et al., 2019). We therefore suggest that tectonic uplift driven by fault activity sets the background rate of river incision and that the climatically-induced adjustment of the longitudinal profile is limited to the downstream reach, especially along the range front.

6 CONCLUSION

We report well-preserved fluvial terraces along three reaches of the Heihe River in northeastern Tibet. At the mountain front site, river incision rate was ~1 mm/yr over the past 100 kyr, while it ranged from 2 to 7 mm/yr during the Holocene. In the interior of the mountain range (Qilian basin site), river incision rates were ~1 mm/yr since ~53 ka, suggesting that the upstream incision rate remained stable from the late Pleistocene to the Holocene. We conclude that the long-term rate of incision (since the late Pleistocene) is explained by ongoing uplift driven by fault activity, which sets the background rate of fluvial incision (~1 mm/yr). The fast incision rates during the Holocene are attributed to the progressive lowering of the river gradient induced by the warm and wet Holocene climate. The reconstructed longitudinal profiles show semi-parallel terraces in the Qilian basin, and progressively increasing terrace spacing before exiting the range, followed by decreased terrace spacing in the foreland. The most plausible explanation for this morphology is the increased fluvial discharge during the Holocene which promoted the accelerated piedmont entrenchment of the Heihe River. In turn, the enhanced incision of the Heihe River propagated upstream towards the range, but it only affected the river profile within a limited distance. Finally, the denudation rates on the millennial timescale estimated from previous studies in the region are < 1 mm/yr, suggesting that landscape-scale erosion in this region lags the trunk river incision. These results suggest that climate changes and the hydrologic response over time are important for modulating river incision rates

on various spatial and temporal scales in a tectonically active region.

DATA AVAILABILITY STATEMENT

The original contributions presented in the study are included in the article/Supplementary Material, further inquiries can be directed to the corresponding author.

AUTHOR CONTRIBUTIONS

XC wrote the first draft of the manuscript, conducted the field and lab work, and constructed the figures. XH contributed to conception and design of the study, led the field investigations. BP provided the funding and resources for this research. ZZ analyzed parts of the data. All authors contributed to manuscript revision, read, and approved the submitted version.

FUNDING

This research was financially supported by the National Natural Science Foundation of China (award 41730637, 42101004), the Strategic Priority Research Program (A) of Chinese Academy of Sciences (award XDA2010030806) and the Second Tibetan Plateau Scientific Expedition (award 2019QZKK0205).

ACKNOWLEDGMENTS

We thank Zhenling Wen, Miao Chen, Taian Chen, Xianghe Ji, Bingxue Qin, and Xiaohua Li (Lanzhou University) for their assistances with the field work. The OSL experiments were completed by Yixuan Wang (Qinghai Institute of Salt Lakes, Chinese Academy of Sciences) and Chang Huang, Yulong Ou, Min Cao (China University of Geosciences, Wuhan) and we acknowledge their careful work.

REFERENCES

Anderson, R. S., Repka, J. L., and Dick, G. S. (1996). Xplicit Treatment of Inheritance in Dating Depositional Surfaces Using *In Situ* ^{10}Be and ^{26}Al. *Geol* 24 (1), 47–51. doi:10.1130/0091-7613(1996)024<0047:etoiid>2.3.co;2

Bovet, P. M., Ritts, B. D., Gehrels, G., Abbink, A. O., Darby, B., and Hourigan, J. (2009). Evidence of Miocene Crustal Shortening in the North Qilian Shan from Cenozoic Stratigraphy of the Western Hexi Corridor, Gansu Province, China. *Am. J. Sci.* 309 (4), 290–329. doi:10.2475/00.4009.02

Burbank, D. W., and Anderson, R. S. (2011). *Tectonic Geomorphology*. second ed. Chichester: John Wiley & Sons.

Burbank, D. W., Leland, J., Fielding, E., Anderson, R. S., Brozovic, N., Reid, M. R., et al. (1996). Bedrock Incision, Rock Uplift and Threshold Hillslopes in the Northwestern Himalayas. *Nature* 379 (6565), 505–510. doi:10.1038/379505a0

Cao, X., Hu, X., Pan, B., Zhang, J., Wang, W., Mao, J., et al. (2019). A Fluvial Record of Fault-Propagation Folding along the Northern Qilian Shan Front, NE Tibetan Plateau. *Tectonophysics* 755, 35–46. doi:10.1016/j.tecto.2019.02.009

Cao, X., Hu, X., Pan, B., Zhao, Q., Chen, T. a., Ji, X., et al. (2021). Using Fluvial Terraces as Distributed Deformation Offset Markers: Implications for Deformation Kinematics of the North Qilian Shan Fault. *Geomorphology* 386, 107750. doi:10.1016/j.geomorph.2021.107750

Craddock, W. H., Kirby, E., Harkins, N. W., Zhang, H., Shi, X., and Liu, J. (2010). Rapid Fluvial Incision along the Yellow River during Headward Basin Integration. *Nat. Geosci.* 3 (3), 209–213. doi:10.1038/ngeo777

Daniels, J. M. (2008). Distinguishing Allogenic from Autogenic Causes of Bed Elevation Change in Late Quaternary Alluvial Stratigraphic Records. *Geomorphology* 101 (1-2), 159–171. doi:10.1016/j.geomorph.2008.05.022

Ferrier, K. L., Huppert, K. L., and Perron, J. T. (2013). Climatic Control of Bedrock River Incision. *Nature* 496, 206–209. doi:10.1038/nature11982

Finnegan, N. J., Schumer, R., and Finnegan, S. (2014). A Signature of Transience in Bedrock River Incision Rates over Timescales of 10(4)-10(7) Years. *Nature* 505 (7483), 391–394. doi:10.1038/nature12913

Hetzel, R., Tao, M., Stokes, S., Niedermann, S., Ivy-Ochs, S., Gao, B., et al. (2004). Late Pleistocene/Holocene Slip Rate of the Zhangye Thrust (Qilian Shan, China) and Implications for the Active Growth of the Northeastern Tibetan Plateau. *Tectonics* 23 (6), TC6006. doi:10.1029/2004tc001653

Hetzel, R., Niedermann, S., Tao, M., Kubik, P. W., and Strecker, M. R. (2006). Climatic versus Tectonic Control on River Incision at the Margin of NE Tibet: ^{10}Be Exposure Dating of River Terraces at the Mountain Front of the Qilian Shan. *J. Geophys. Res.* 111 (F3), F03012. doi:10.1029/2005jf000352

Hetzel, R. (2013). Active Faulting, Mountain Growth, and Erosion at the Margins of the Tibetan Plateau Constrained by In Situ-produced Cosmogenic Nuclides. *Tectonophysics* 582 (1), 1–24. doi:10.1016/j.tecto.2012.10.027

Hu, K., Fang, X., Zhao, Z., and Granger, D. (2015a). Erosion Rates of Northern Qilian Mountains Revealed by Cosmogenic 10 Be. *Adv. Earth Sci.* 30 (02), 268–275. doi:10.11867/j.issn.1001-8166.2015.02.0268

Hu, X., Pan, B., Kirby, E., Gao, H., Hu, Z., Cao, B., et al. (2015b). Rates and Kinematics of Active Shortening along the Eastern Qilian Shan, China, Inferred from Deformed Fluvial Terraces. *Tectonics* 34, 2478–2493. doi:10.1002/2015tc003978

Hu, X., Cao, X., Li, T., Mao, J., Zhang, J., He, X., et al. (2021). Late Quaternary Fault Slip Rate within the Qilian Orogen, Insight into the Deformation Kinematics for the NE Tibetan Plateau. *Tectonics* 40 (5), e2020TC006586. doi:10.1029/2020tc006586

Kirby, E., and Whipple, K. X. (2012). Expression of Active Tectonics in Erosional Landscapes. *J. Struct. Geol.* 44, 54–75. doi:10.1016/j.jsg.2012.07.009

Küster, Y., Hetzel, R., Krbetschek, M., and Tao, M. (2006). Holocene Loess Sedimentation along the Qilian Shan (China): Significance for Understanding the Processes and Timing of Loess Deposition. *Quat. Sci. Rev.* 25 (1), 114–125. doi:10.1016/j.quascirev.2005.03.003

Lai, Z.-P., and Wintle, A. G. (2006). Locating the Boundary between the Pleistocene and the Holocene in Chinese Loess Using Luminescence. *Holocene* 16 (6), 893–899. doi:10.1191/0959683606hol980rr

Lai, Z., Wintle, A. G., and Thomas, D. S. (2007). Rates of Dust Deposition between 50 Ka and 20 Ka Revealed by OSL Dating at Yuanbao on the Chinese Loess Plateau. *Palaeogeogr. Palaeoclimatol. Palaeoecol.* 248 (3), 431–439. doi:10.1016/j.palaeo.2006.12.013

Lal, D. (1991). Cosmic Ray Labeling of Erosion Surfaces: *In Situ* Nuclide Production Rates and Erosion Models. *Earth Planet. Sci. Lett.* 104, 424–439. doi:10.1016/0012-821x(91)90220-c

Li, Y., Li, B., and Yang, J. (1995). Late Quaternary Movement on the Heihekou Fault, West Gansu, China (In Chinese). *Acta Sci. Nat. Univ. Pekin.* 31 (03), 351–357.

Li, Y., Yang, J., Tan, L., and Duan, F. (1999). Impact of Tectonics on Alluvial Landforms in the Hexi Corridor, Northwest China. *Geomorphology* 28 (3), 299–308. doi:10.1016/s0169-555x(98)00114-7

Li, Y. L. (1994). *Mechanism and Evolution of Tectonic Landforms in the Middle Hexi Corridor (In Chinese)*. Doctor Doctor. Beijing: Beijing university.

Liu, X.-w., Yuan, D.-y., and Su, Q. (2019). Late Pleistocene Slip Rate on a Blind Thrust in the Western Qilian Shan, NW China. *Geomorphology* 345, 106841. doi:10.1016/j.geomorph.2019.106841

Lu, H., Cheng, L., Wang, Z., Zhang, T., Lü, Y., Zhao, J., et al. (2018). Latest Quaternary Rapid River Incision across an Inactive Fold in the Northern

Chinese Tian Shan Foreland. *Quat. Sci. Rev.* 179, 167–181. doi:10.1016/j.quascirev.2017.10.017

Lu, H., Wu, D., Zhang, H., Ma, Y., Zheng, X., and Li, Y. (2020). Spatial Patterns of Late Quaternary River Incision along the Northern Tian Shan Foreland. *Geomorphology* 357, 107100. doi:10.1016/j.geomorph.2020.107100

Malatesta, L. C., and Avouac, J.-P. (2018). Contrasting River Incision in North and South Tian Shan Piedmonts Due to Variable Glacial Imprint in Mountain Valleys. *Geology* 46 (7), 659–662. doi:10.1130/g40320.1

Malatesta, L. C., Avouac, J.-P., Brown, N. D., Breitenbach, S. F. M., Pan, J., Chevalier, M.-L., et al. (2018). Lag and Mixing during Sediment Transfer across the Tian Shan Piedmont Caused by Climate-Driven Aggradation-Incision Cycles. *Basin Res.* 30 (4), 613–635. doi:10.1111/bre.12267

Murray, A. S., and Wintle, A. G. (2000). Luminescence Dating of Quartz Using an Improved Single-Aliquot Regenerative-Dose Protocol. *Radiat. Meas.* 32 (1), 57–73. doi:10.1016/S1350-4487(99)00253-X

Niedermann, S., and Niedermann, S. (2002). Cosmic-Ray-Produced Noble Gases in Terrestrial Rocks: Dating Tools for Surface Processes. *Rev. Mineralogy Geochem.* 47 (1), 731–784. doi:10.2138/rmg.2002.47.16

Osman, M. B., Tierney, J. E., Zhu, J., Tardif, R., Hakim, G. J., King, J., et al. (2021). Globally Resolved Surface Temperatures since the Last Glacial Maximum. *Nature* 599 (7884), 239–244. doi:10.1038/s41586-021-03984-4

Palumbo, L., Hetzel, R., Tao, M., and Li, X. (2011). Catchment-wide Denudation Rates at the Margin of NE Tibet from In Situ-produced Cosmogenic ^{10}Be. *Terra nova.* 23 (1), 42–48. doi:10.1111/j.1365-3121.2010.00982.x

Pan, B., Burbank, D., Wang, Y., Wu, G., Li, J., and Guan, Q. (2003). A 900 k.Y. Record of Strath Terrace Formation during Glacial-Interglacial Transitions in Northwest China. *Geology* 31 (11), 957–960. doi:10.1130/g19685.1

Poisson, B., and Avouac, J. P. (2004). Holocene Hydrological Changes Inferred from Alluvial Stream Entrenchment in North Tian Shan (Northwestern China). *J. Geol.* 112 (2), 231–249. doi:10.1086/381659

Ren, J., Xu, X., Zhang, S., Ding, R., Liu, H., Liang, O., et al. (2019). Late Quaternary Slip Rates and Holocene Paleoearthquakes of the Eastern Yumu Shan Fault, Northeast Tibet: Implications for Kinematic Mechanism and Seismic Hazard. *J. Asian Earth Sci.* 176, 42–56. doi:10.1016/j.jseaes.2019.02.006

Roberts, H. M., and Duller, G. A. T. (2004). Standardised Growth Curves for Optical Dating of Sediment Using Multiple-Grain Aliquots. *Radiat. Meas.* 38 (2), 241–252. doi:10.1016/j.radmeas.2003.10.001

Sadler, P. M. (1981). Sediment Accumulation Rates and the Completeness of Stratigraphic Sections. *J. Geol.* 89 (5), 569–584. doi:10.1086/628623

Stokes, S., Hetzel, R., Bailey, R., and Mingxin, T. (2003). Combined IRSL-OSL Single Aliquot Regeneration (SAR) Equivalent Dose (D e) Estimates From Source Proximal Chinese Loess. *Quat. Sci. Rev.* 22 (10), 975–983. doi:10.1016/s0277-3791(03)00044-1

Stone, J. O. (2000). Air Pressure and Cosmogenic Isotope Production. *J. Geophys. Res.* 105 (B10), 23753–23759. doi:10.1029/2000jb900181

Tian, Q., Zheng, W., Zhang, D., Zhang, Y., Xu, B., and Huang, L. (2017). Influence of Tectonics and Climate on the Evolution of Fluvial Terraces: A Case Study of the Hongshuiba and Maying Rivers in the Northern Margin of the Qilian Mountains. *Seismol. Geol.* 39 (06), 1283–1296. doi:10.3969/j.issn.0253-4967.2017.06.013

Wang, Y., Oskin, M. E., Zhang, H., Li, Y., Hu, X., and Lei, J. (2020). Deducing Crustal-Scale Reverse-Fault Geometry and Slip Distribution from Folded River Terraces, Qilian Shan, China. *Tectonics* 39 (1), e2019TC005901. doi:10.1029/2019tc005901

Wang, Y., Oskin, M. E., Li, Y., and Zhang, H. (2022). Rapid Holocene Bedrock Canyon Incision of Beida River, North Qilian Shan, China. *Earth Surf. Dynam.* 10 (2), 191–208. doi:10.5194/esurf-10-191-2022

Xiong, J., Li, Y., Zhong, Y., Lu, H., Lei, J., Xin, W., et al. (2017). Latest Pleistocene to Holocene Thrusting Recorded by a Flight of Strath Terraces in the Eastern Qilian Shan, NE Tibetan Plateau. *Tectonics* 36 (12), 2973–2986. doi:10.1002/2017tc004648

Yang, H., Yang, X., Huang, X., Li, A., Huang, W., and Zhang, L. (2018). New Constraints on Slip Rates of the Fodongmiao-Hongyazi Fault in the Northern Qilian Shan, NE Tibet, from the 10 Be Exposure Dating of Offset Terraces. *J. Asian Earth Sci.* 151, 131–147. doi:10.1016/j.jseaes.2017.10.034

Yang, H., Yang, X., Huang, W., Li, A., Hu, Z., Huang, X., et al. (2020). ^{10}Be and OSL Dating of Pleistocene Fluvial Terraces along the Hongshuiba River: Constraints on Tectonic and Climatic Drivers for Fluvial Downcutting across the NE Tibetan Plateau Margin, China. *Geomorphology* 348, 106884. doi:10.1016/j.geomorph.2019.106884

Zheng, D., Clark, M. K., Zhang, P., Zheng, W., and Farley, K. A. (2010). Erosion, Fault Initiation and Topographic Growth of the North Qilian Shan (Northern Tibetan Plateau). *Geosphere* 6 (6), 937–941. doi:10.1130/ges00523.1

Zhong, Y., Xiong, J., Li, Y., Zheng, W., Zhang, P., Lu, H., et al. (2020). Constraining Late Quaternary Crustal Shortening in the Eastern Qilian Shan from Deformed River Terraces. *J. Geophys. Res. Solid Earth* 125 (9), e2020JB020631. doi:10.1029/2020jb020631

Conflict of Interest: The authors declare that the research was conducted in the absence of any commercial or financial relationships that could be construed as a potential conflict of interest.

Publisher's Note: All claims expressed in this article are solely those of the authors and do not necessarily represent those of their affiliated organizations, or those of the publisher, the editors and the reviewers. Any product that may be evaluated in this article, or claim that may be made by its manufacturer, is not guaranteed or endorsed by the publisher.

frontiers | Frontiers in Earth Science

ORIGINAL RESEARCH
published: 15 July 2022
doi: 10.3389/feart.2022.940212

Luminescence Sensitivity of Quartz From Rocks Under *in situ* Chemical Weathering Conditions

Zheng Cao[1], *Yingying Jiang*[2], *Jiandong Xu*[3,4]*, *Juxing Zhao*[5] *and Cheng Zhao*[1]

[1]Key Laboratory for Earth Surface Processes, Department of Geography, Peking University, Beijing, China, [2]Qinghai Institute of Salt Lakes, Chinese Academy of Sciences, Xining, China, [3]State Key Laboratory of Plateau Ecology and Agriculture, Qinghai University, Xining, China, [4]School of Earth Science and Resources, China University of Geosciences, Beijing, China, [5]Fujian Exploration Institute of Coalfield Geology, Fujian, China

In provenance investigation of Quaternary sediments, quartz luminescence sensitivity (QLS) has been employed as a technique. The weathering and influence on the earliest signs of luminescence sensitivity of sedimentary quartz require more consideration. In this study, the QLS properties of eight samples of Permian biotite monzogranite from a borehole in the southern tropics of China are investigated. The degree of chemical weathering does not correspond with the QLS values of samples that have undergone varying degrees of *in situ* weathering. We hypothesize that the variation of the irradiation field during the *in situ* chemical weathering process may affect the QLS, but not considerably within 200 ka. In addition, we discovered that quartz from the same source undergoes varying degrees of *in situ* chemical weathering, but has a constant response to irradiation-bleaching cycles (IBCs). The presence of variances in the thermal activation curves (TACs) of the same rock body indicates that further research is required to apply TAC as a provenance indicator.

Keywords: luminescence sensitivity, provenance analysis, weathering index, granite weathering, quartz

OPEN ACCESS

Edited by:
Yuxin Fan,
Lanzhou University, China

Reviewed by:
Shugang Kang,
Institute of Earth Environment (CAS), China
Ali Abedini,
Urmia University, Iran

***Correspondence:**
Jiandong Xu
2018990059@qhu.edu.cn

Specialty section:
This article was submitted to Quaternary Science, Geomorphology and Paleoenvironment, a section of the journal Frontiers in Earth Science

Received: *10 May 2022*
Accepted: *17 June 2022*
Published: *15 July 2022*

Citation:
Cao Z, Jiang Y, Xu J, Zhao J and Zhao C (2022) Luminescence Sensitivity of Quartz From Rocks Under in situ Chemical Weathering Conditions. Front. Earth Sci. 10:940212. doi: 10.3389/feart.2022.940212

1 INTRODUCTION

Thermoluminescence (TL) and optically stimulated luminescence (OSL) refers to light emission of semiconductors or insulating materials which could store energy in the crystal lattice and emit light under thermally or optically stimulated. TL and OSL have become powerful research tools in the fields of materials (Pires et al., 2011; Kalita et al., 2019; Ike et al., 2021), geosciences (Singhvi et al., 1982; Lai, 2006; Fuchs and Owen, 2008), and environmental and medical science (Higashimura et al., 1963; Yukihara and McKeever, 2008) in the past two decades. A wide range of natural and artificial materials have been used in the testing of TL and OSL. Quartz is the most prevalent mineral on the earth's surface and has good resistance to weathering and so it is widely used in dosimetry and Quaternary geochronology. However, it was found that the luminescence sensitivity of quartz changed obviously during the dating protocol, which caused an inconsistent response of quartz to radiation dose. Although the change in luminescence sensitivity could be calibrated by a series of well-designed dating protocols, the single aliquot regenerative dose protocols (Murray and Wintle, 2000; Murray and Wintle, 2003), the mechanism is still unclear.

Many studies aiming to calibrate this phenomenon in the laboratory have demonstrated that variations in quartz luminescence sensitivity (QLS) are related to irradiation (Zimmerman, 1971; Benny et al., 2000), bleaching (Li and Wintle, 1992; Zhou and Wintle, 1994) and heating (Rendell

et al., 1994; Bøtter-Jensen et al., 1995; Armitage et al., 2000). Extensive research shows the behaviors of quartz under laboratory conditions, but the reasons for these behaviors are still not clear. Meanwhile, studies focused on the effects of sedimentary transport processes and the characterization of source materials on the QLS have been developed. Aiming to discover and understand the relationships between QLS and the petrological background of quartz, studies have been undertaken in the following areas: the age of intrusive granite (Rink, 1994), crystallization temperature (Sawakuchi et al., 2011b), inclusions (Chauhan and Singhvi, 2019), thermal and sedimentary history (Preusser et al., 2006; Pietsch et al., 2008; Zheng et al., 2009; Fitzsimmons, 2011; Sawakuchi et al., 2011a; Lü and Sun, 2017; Sawakuchi et al., 2018; Chang and Zhou, 2019; Nian et al., 2019; Li and Zhou, 2020; Sawakuchi et al., 2020; Bartyik et al., 2021; del Río et al., 2021). These exploratory efforts have enhanced our understanding of QLS and expanded its application scenarios.

Many new discoveries have also emerged while exploring the QLS of diverse types of sediments, such as aeolian, fluvial and coastal sediments. Different deserts of northern China exhibit discrepancies in QLS and a decreasing trend from east to west, with one exception of the Gurbantunggut Desert (Li et al., 2007; Zheng et al., 2009; Lü and Sun, 2017). Vertical variations in QLS measured from loess-paleosol sequences show a good correlation with other proxies, such as median grain size and magnetic susceptibility, which may reflect climate change or sediment transport dynamic changes (Lü et al., 2014; Qiu and Zhou, 2015; Li and Zhou, 2020; Lü et al., 2020). With an increasing distance of fluvial sediment transportation, sensitizing QLS is observed by Pietsch et al. (2008) and Sawakuchi et al. (2011a), but this growing trend does not always persist. Sawakuchi et al. (2018) considered the QLS as a proxy for denudation rates in the Amazon basin rather than a proxy for transportation distance. In addition, studies using the thermal activation curve (TAC) of quartz to distinguish sediment sources have shown that it appears to be feasible (Chang and Zhou, 2019; Nian et al., 2019; Li and Zhou, 2020).

The variation and characterization of QLS in geological processes from protoliths to sediments requires a deeper and more detailed understanding before it can be applied to a broader range of scenarios. As an important part of the source–sink process, the influence of weathering or denudation on the QLS is still unclear. Previous research (Preusser et al., 2006; Pietsch et al., 2008; Fitzsimmons, 2011; Sawakuchi et al., 2011a; Sawakuchi et al., 2018; Nian et al., 2019; Bartyik et al., 2021; Nelson et al., 2022) have explored that the QLS signature will be modified during the transport process, which could impair the reliability of the QLS as a provenance proxy. However, their studies did not decouple the effects of weathering or denudation from those of transport processes. In this study, quartz extracted from the drill of southeastern China enduring intense *in situ* chemical weathering was evaluated to characterize quartz luminescence sensitivity. Additionally, the applicability of thermal activation curve (TAC) and irradiation-bleaching cycle (IBC) analysis in provenance tracing is discussed. This research has implications for understanding QLS changes caused by *in situ* chemical weathering, as well as evidence for determining whether QLS sensitizing process is dominant under natural conditions.

2 GEOLOGICAL SETTING AND SAMPLE

2.1 Geological Setting

The borehole representing chemical weathering conditions is located in the southern part of Sanming city, the subtropical monsoon area of southeastern China, Fujian Province (117.448E, 26.006N). Since the study area is located at the convergence of trade winds and westerlies, the climate is controlled by the couplings of monsoon and subtropical highs. In general, the summer (May—September) climate character of the study area is hot and rainy, while it is warm and relatively dry in winter (December—January). The climate data for the study site are for the period 1981–2010 and are from the China Meteorological Data Service Centre (data.cma.cn). The annual average temperature in the Sanming area is 19.6°C, with extreme high temperatures reaching 41.4°C. The average number of days with maximum temperatures above 30°C over the years is 122.8. Precipitation is plentiful throughout the year, with an average annual precipitation of 1,665.2 mm and a maximum continuous precipitation (day) of 444 mm (15 days) over the years. In addition, the study area was also affected by typhoons in summer. All the above conditions resulted in a relative humidity reaching 78% in study area over the year. In summary, the Sanming area is a typical area of intense chemical weathering.

The study area is located in the western part of the Zhenghe-Dapu fault zone, which belongs to the northern end of the Yongmei sag. After the convergence of the Cathysia and Yangzi blocks as part of the Rodinia supercontinent in the early Neoproterozoic (Li et al., 2002), the study area gradually broke up into rift valleys or troughs during supercontinent rifting, and formed giant thick marine deposits during the late Neoproterozoic to Early Paleozoic (Shu, 2012; Shu et al., 2021). With the strong tectono-thermal events in South China during the Silurian, the sediments were deformed and uplifted by compression. At the same time, magmatic activity was frequent, forming a large number of S-type granites and fewer I-type granites (Shu, 2006). The super-thick dolomite and limestone from the Early Paleozoic until the Early Triassic reflect a slow south-to-north transgression (Zu et al., 2012). The study area received strong north-south extrusion during the Indo-Chinese period leading to crustal thickening, accompanied by large-scale magmatic activity (Zhang et al., 2009). During the Cretaceous period, the study area was characterized by three-stage tectono-thermal events and andesites and rhyolites caused by strong volcanic activities (Li et al., 2014). During the Cenozoic period, continuous subduction of the Pacific plate resulted in regional uplift and denudation of the study area (Bureau of Geology and Mineral Resources of Fujian Province, 1985).

In the study area the basement is covered by effusive rock strata and sedimentary rocks formed from Paleozoic to Cenozoic. Both strata and intrusive rocks have undergone intensive tectonic movements, resulting in unformed and discontinuous strata. The Quaternary strata are remnants of alluvium and floodplain, consisting of clay, sand, gravel and rock fragments, with uneven thickness distribution. The residual slope deposits are widely distributed in mountains, gullies and gentle hills, while the alluvial deposits are mainly distributed in river valleys. Small flat Quaternary terraces, small basins connected by the Shaxi River, and low hills constitute the main geomorphic type in the study region.

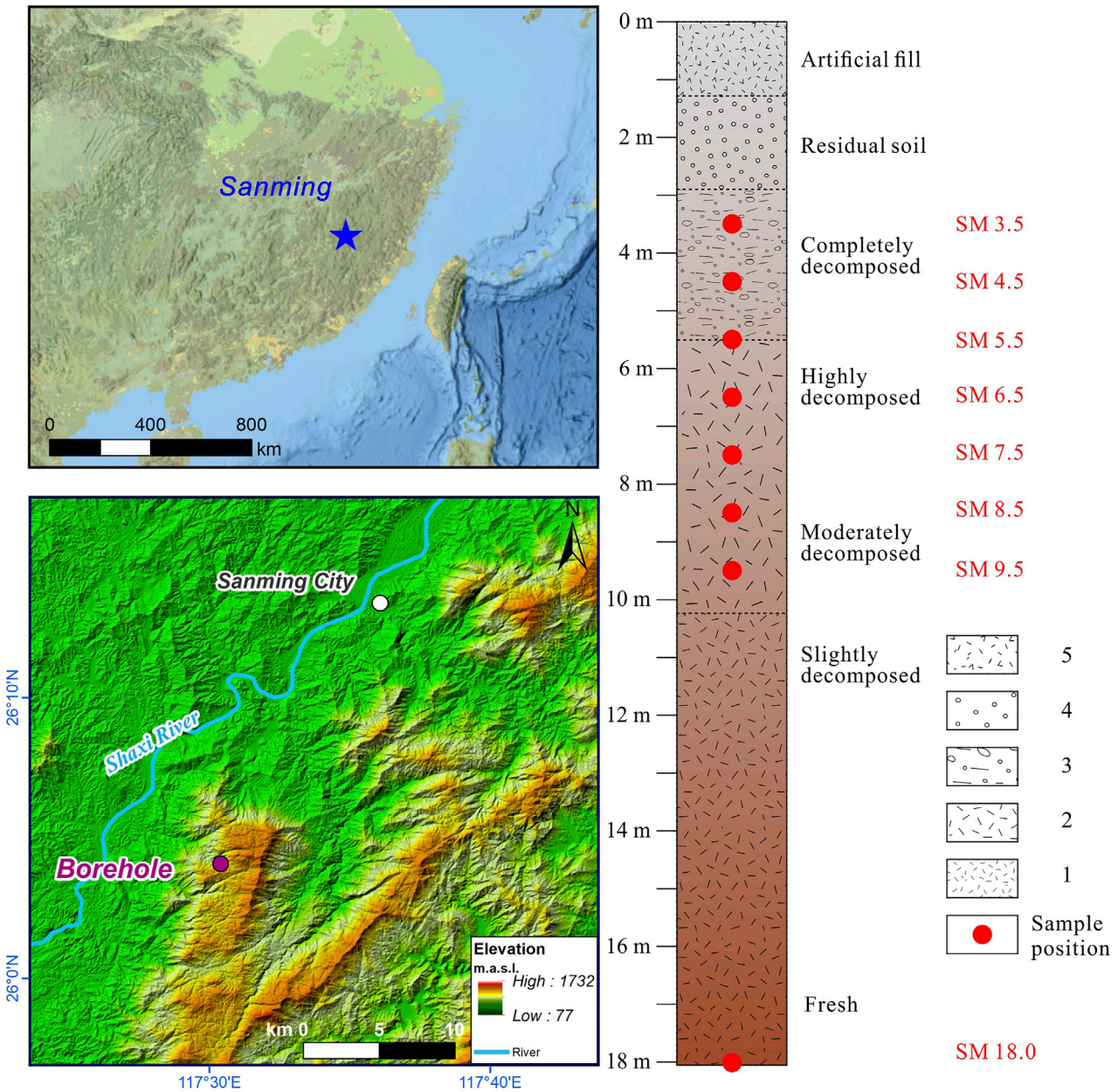

FIGURE 1 | The top left map shows the location of Sanming in China. The topographic map on the lower left shows the exact location of the borehole in Sanming. The DEM raster data were obtained from AW3D30 of JAXA (Takaku et al., 2020). The schematic diagram on the right shows the Sanming borehole. 1–5 in the legend indicate different degrees of weathering.

2.2 Sample

The drill was conducted by the Fujian Exploration Institute of Coalfield Geology, penetrated Quaternary sediments and regolith, finished in the body of Permian greyish medium-grained biotite monzogranite, at a depth of 18.1 m. According to the field work, the drill core was divided into 5 layers: I. human activities disturbed layer (0~1.3 m); II. Quaternary sediments or residual soil layer (1.3~2.9 m); III. completely weathered rock (2.9~5.6 m); IV. highly weathered rock (5.6~10.2 m); V. moderately weathered to fresh rock (10.2~18.1 m). To avoid human interference or sediments from different sources, we sampled 8 weathered rocks from 3.5 to 18.0 m, and the specific positions are shown in the map on the top left of the **Figure 1**.

3 METHODS

3.1 Quartz Sample Preparation

All the granite rocks were crushed and ground after washing with distilled water. The samples for element analysis were ground into

powder (diameters < 40 μm) without any separation. The samples for luminescence analysis were crushed and ground, and mixed grains between 180 and 250 μm were selected by wet sieving. The grains were treated with 10% HCl and 30% H_2O_2 solutions to remove carbonates and organic matter, and then heavy liquids of 2.62 and 2.75 g/cm^3 were used to separate quartz and plagioclase from heavy minerals and potassium feldspar (Aitken, 1998). As quartz and plagioclase have similar densities, 40 min HF etching was used to remove the latter. Using differences in hydrodynamics, micas were also removed from the system, preventing their luminescence from affecting the weak luminescence of the rock (Kortekaas and Murray, 2005). Quartz grains were checked by using the X-Ray Diffraction (XRD) and OSL IR depletion ratio (Duller, 2003) to qualify the purity after etching. The mass of aliquots of adhered quartz grains was weighed with a Mettler Toledo XPR10 microbalance with a precision of 1 μg. The average mass on each aliquot is approximately 4–6 mg. The details of the sample preparation protocol are described in the **Supplementary Materials**.

3.2 Luminescence Analysis

3.2.1 Equipment

All luminescence measurements were conducted on a Lexsyg Smart TL/OSL Reader at Peking University, which was equipped with an IR laser diode (850 ± 3 nm, up to 400 mW/cm^2 at the sample position) and 5 blue LEDs filtered by 3 mm Schott GG455 glass (458 ± 10 nm, up to 100 mW/cm2 at the sample position). A homogeneous irradiation field is provided by a specially designed circular arranged Beta (^{90}Sr-^{90}Y, 1.6 GBq) source (Richter et al., 2012). Bi-alkaline photomultiplier tubes (Hamamatsu H7360-02, 300–650 nm) with quantum efficiencies of approximately 27% at 400 nm are used for receiving signals (Richter et al., 2013).

3.2.2 Procedures of Measurements of Quartz Luminescence Sensitivity, Irradiation-Bleaching Cycles, and Thermal Activation Curves

The luminescence sensitivity of quartz was measured following the procedures (**Table 1**). First, the aliquot was bleached enough long (120–180 s) by blue light at 125°C to reduce the quartz signal to the background level, and 11.25 Gy beta dose was given to the sample after bleaching. Second, the aliquot was heated to 220°C to measure the TL signal responding to the given dose, and the integration from 70 to 120°C of the signal was used to calculate the quartz 110°C TL intensity. Next, infrared stimulation was used to ensure that the signal of feldspar inclusions would not affect the quartz OSL sensitivity. Finally, the quartz OSL was obtained by 115 s blue stimulation at 125°C, and the signal for the initial 2 s minus the background value was summed to represent the OSL intensity. A stimulated temperature of 125°C reduces the probability of retrapping by traps when electrons recombine with holes. According to the definition of luminescence sensitivity, we used mass and given dose to normalize quartz 110°C TL and OSL intensity as sensitivity, respectively. Each sample was represented by five aliquots accurately weighed on a microbalance at the 1 μg level.

The measurements of irradiation-bleaching cycles (IBCs) are the loop of QLS measurements. To reduce the amount of data and test time, only signals at specific loops were recorded. The protocol for measurements for TAC was the same as that for the QLS and is shown in **Table 2**. The differences between them are the step of thermal activation before beta dose is given.

3.3 Weathering Analysis

For the purpose of evaluating chemical weathering indices, X-ray fluorescence (XRF) is a rapid and convenient method for whole-rock analysis. A wavelength dispersive (WD) XRF (Rigaku ZSX Primus II) at the State Key Laboratory of Plateau Ecology and Agriculture was used to analyze major elements in the whole-rock powder in the ppm to 100% range. The crushed and ground samples mentioned in **Section 3.1** were dried in a vacuum drying chamber for 8 h at 110°C to remove moisture. Loss on ignition (LOI) was determined by heating a 2–3 g sample in a muffle oven at 1,050°C for 1 h and weighing immediately after cooling in a desiccator to avoid absorption of air moisture. Samples (3–4 g) were placed into a plastic ring (diameter of 35 mm) without any binder and pressed into a discoidal pallet under 400 bar for 2 min. XRF results were output as the mass percentage of major elements adjusted by LOI and were converted to the molar proportion to calculate the chemical weathering indices.

The mineralogy of the whole-rock powder was determined by X-ray diffraction (XRD) with a Rigaku D/Max 2500PC equipment with radiation from CuKα (λ = 1.5406 Å) at 40 KV and 200 mA. We obtained diffractograms of air-dried mounts for a 2θ range from 3° to 70° at a scanning speed of 8°/min. Panalytical Highscore software and crystallographic information file (CIF) from Crystallography Open Database (Vaitkus et al., 2021) were used to identify minerals and calculate mineral proportions by semi-quantitative methods.

4 RESULTS

4.1 Quartz Luminescence Sensitivity Signatures in Sanming Borehole

The quartz luminescence sensitivity variations in the Sanming borehole, monitored by 110°C TL and OSL, did not exhibit an obvious trend with the change in depth, as shown in **Figure 2** and **Table 5**. The distribution of data for 110°C TL sensitivity was relatively concentrated, falling within the range of 141.7–99.6 counts/(Gy*mg). The OSL sensitivity values were small overall with slight fluctuations and distributed in the range of 22.6–27.9 counts/(Gy*mg). Both the QLS of the 110°C TL and OSL showed fluctuating patterns of variation along depth, but the former showed a gradual increase along depth above 6.5 m. A total of 40 aliquots for all 8 samples are projected in an X-Y coordinate system with OSL sensitivity and 110°C TL sensitivity as axes. As in **Figure 3A**, the data points representing all the 40 aliquots are almost clustered together and do not show clear distinguishability.

Using the R package numOSL (Peng et al., 2013), we analyzed the composition of the luminescence signals of eight samples with different degrees of weathering. CW-OSL is considered to be resolved into three components based on their decay rates (Smith

TABLE 1 | Protocol for measurements of quartz luminescence sensitivity (QLS) and sensitivity response to irradiation-bleaching cycles (IBC).

Step	Procedure	Observe
1	Blue light bleaching 180 s at 125°C, 50 mW/cm^2	110°C TL S_n (n = 0, 1, 2, 5, 10, 15, 25)
2	Beta irradiation, 11.25 Gy	
3	TL (5 K/s from 25 to 220°C, 10 s)	
4	OSL IR Laser for 120 s at 25°C	
5	OSL Blue LED for 115 s at 125°C, 50 mW/cm^2	OSL Sn (n = 0, 1, 2, 5, 10, 15, 25)
6	Go to step 1 for next cycle	

TABLE 2 | Protocol for measurements of thermal activation curves (TAC).

Step	Procedure	Observe
1	Blue light bleaching for 120 s at 25°C, 50 mW/cm^2	110°C TL S_n (n = 0,1,2...)
2	Heat to T °C (Initial T = 200°C) for 60 s, 5K/s	
3	Beta irradiation, ~ 11.2 Gy	
4	TL (5 K/s from 25 to 220°C, 10 s)	
5	OSL Blue LED for 40 s at 125°C, 50 mW/cm^2	OSL S_n (n = 0,1,2...)
6	Go to step 1, T = T + 40°C	

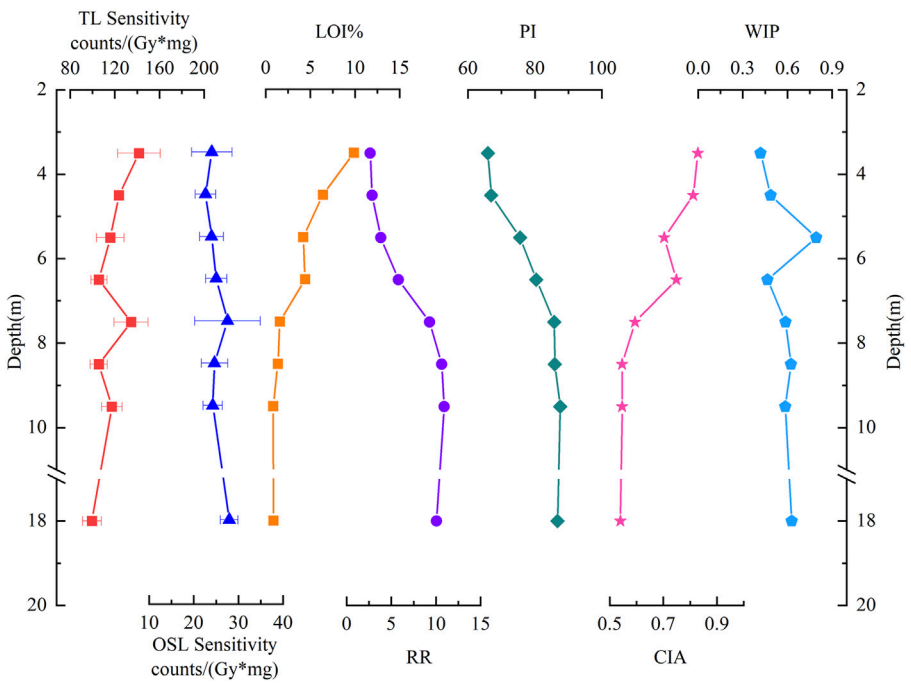

FIGURE 2 | The QLS changes with depth in the Sanming borehole and its relationship to different chemical weathering indices. The calculation of weathering indices is listed in **Table 4**, including Loss on Ignition (LOI), Ruxton Ration (RR), Production Index (PI), Chemical Index of Alteration (CIA), and Weathering Index of Parker (WIP). The error bar denotes the standard deviation of TL and OSL sensitivity. Please note the gap between 10 and 18 m.

and Rhodes, 1994), which are fast, medium and slow component. The decay curves were fitted according to equation given below:

$$I(t) = I_{00} + I_{01}e^{-\lambda_1 t} + I_{02}e^{-\lambda_2 t} + I_{03}e^{-\lambda_3 t}$$

where λ_1, λ_2, λ_3 are the decay rate related to electron detrapping cross-sections, and I_{0k} (k=1,2,3) are initial luminescence signal intensity related to the initial populations of electrons in traps (Bluszcz and Adamiec, 2006; Zhou et al., 2010), and I_{00} is a constant component and is regarded as a background signal.

Figure 4 shows the decay curve raw data and the three components, where the sum of slow component signal and the background signal are shown as a separate item. It can be observed that all samples are dominated by the slow component. After 10 s of stimulation, the samples contain

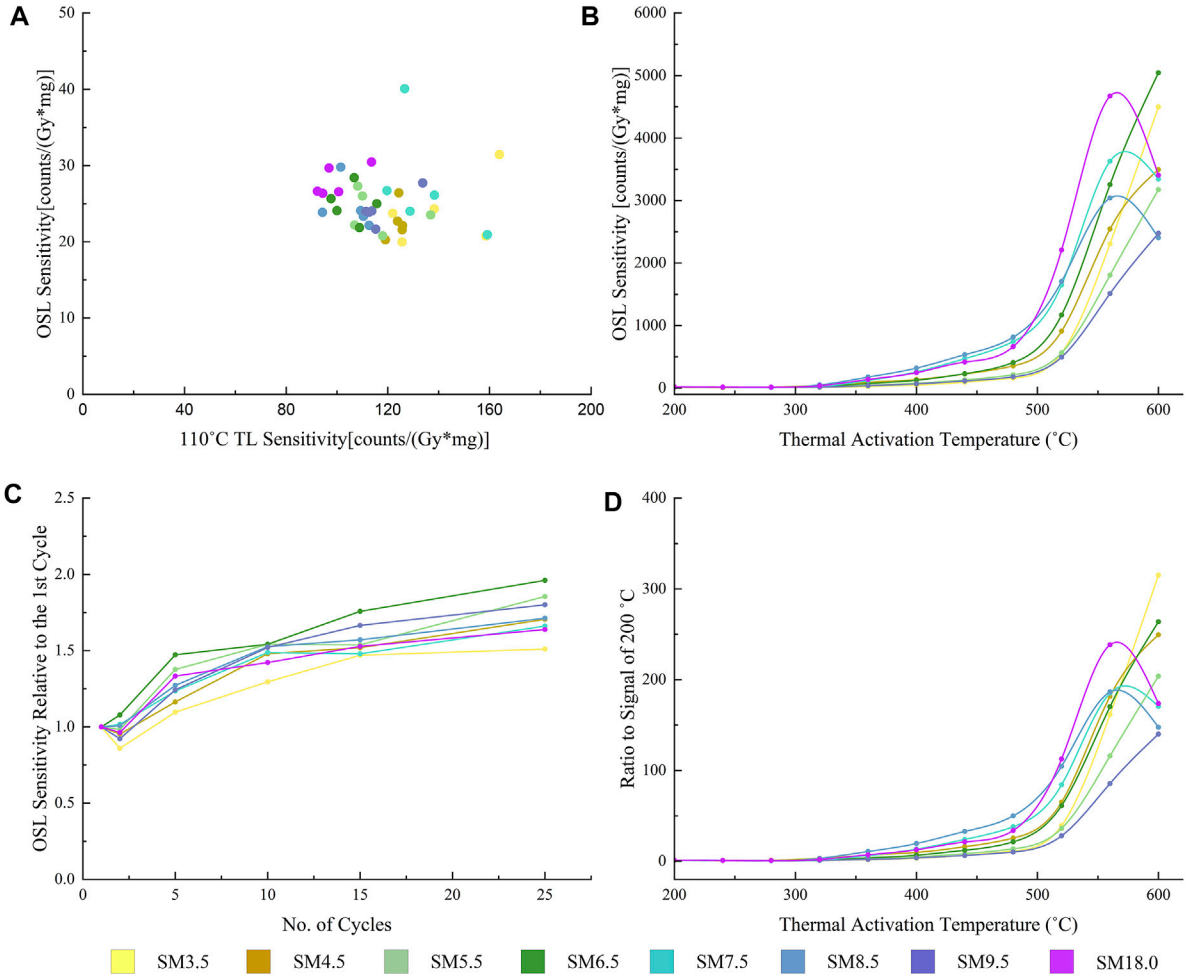

FIGURE 3 | Quartz luminescence sensitivity (QLS), thermal activation curve (TAC) and irradiation-bleaching cycles (IBCs) result in Sanming borehole. **(A)** QLS values of OSL sensitivity and 110°C TL sensitivity. **(B)** The absolute value of OSL sensitivity at different thermal activation temperatures. **(C)** The relative values of OSL sensitivity in IBC (normalized by the absolute value of the respective 1st cycle). **(D)** The relative value of OSL sensitivity at different thermal activation temperatures (normalized by the absolute value of 200°C).

almost no fast and medium components, and the slow components decay at a steady low rate. **Figure 5** shows the relative proportions of the three components as a function of excitation time. We noticed that the top 4 samples of borehole had more fast components than the bottom samples. The percentage of "BG+Slow Component" signal (sum of slow component and background signal) for the top 4 samples reached 95% at 5.0 s and 90% at 1.5 s on average. In contrast, the bottom 4 samples reached this ratio much faster, at 2.6 and 1 s, respectively.

4.2 Chemical Weathering Parameters in Sanming Borehole

Table 3 shows the weight percentages of the major chemical elements measured by XRF and adjusted by the LOI parameter. From the bottom to the top of the borehole, Na_2O, K_2O, SiO_2, and CaO decreased upwards, while Al_2O_3 and iron oxides Fe_2O_3 increased significantly with increasing degree of weathering. MgO, P_2O_5, TiO_2, and MnO did not exhibit any obvious trends with depth. LOI parameters were calculated and are listed in **Table 3**, which also increases with the observed grade of chemical weathering in field. In general, with the decreasing depth of the borehole, soluble and mobile elements were removed, while immobile and nonsoluble elements increased relatively. Although the trend of the concentration of the above elements in the borehole is obvious, there are still some exceptional points, and the reasons for these points will be discussed in **Section 5.1**.

4.3 Mineralogy Evidence of Weathering

The XRD spectra of 8 samples from the Sanming drill hole at different depths were compared and are shown in **Figure 6**. Overall, there is consistency between the 8 spectra, but there is also variation. It can be clearly seen that the strongest peak (2θ = 26.59°) in all samples at different depths is from the quartz

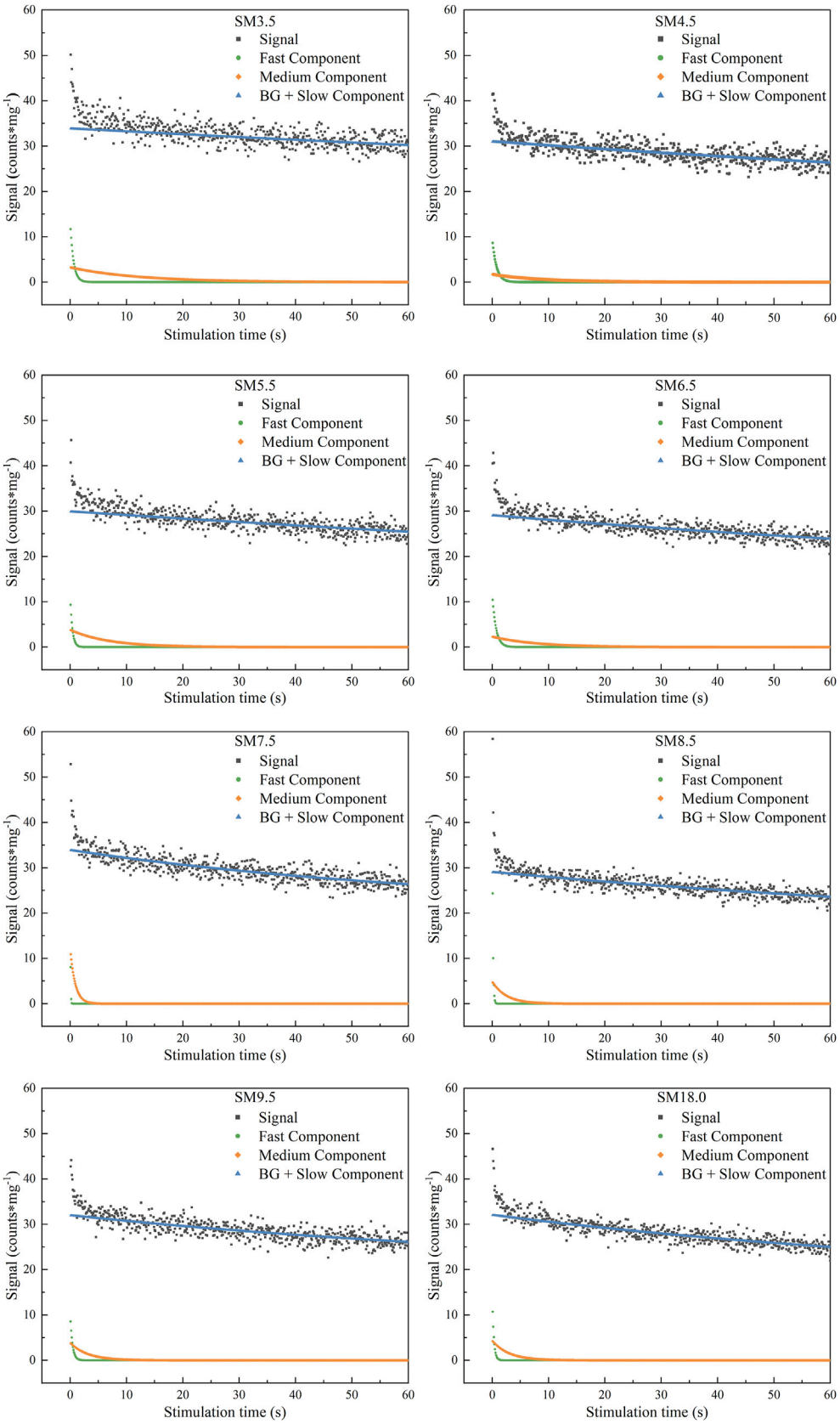

FIGURE 4 | The decay curves of 8 samples and the fast, medium and slow components obtained after curve deconvolution. Since the fast and medium components decayed rapidly to zero and the slow component decayed at a constant rate, only the first 60 s of data were intercepted and plotted.

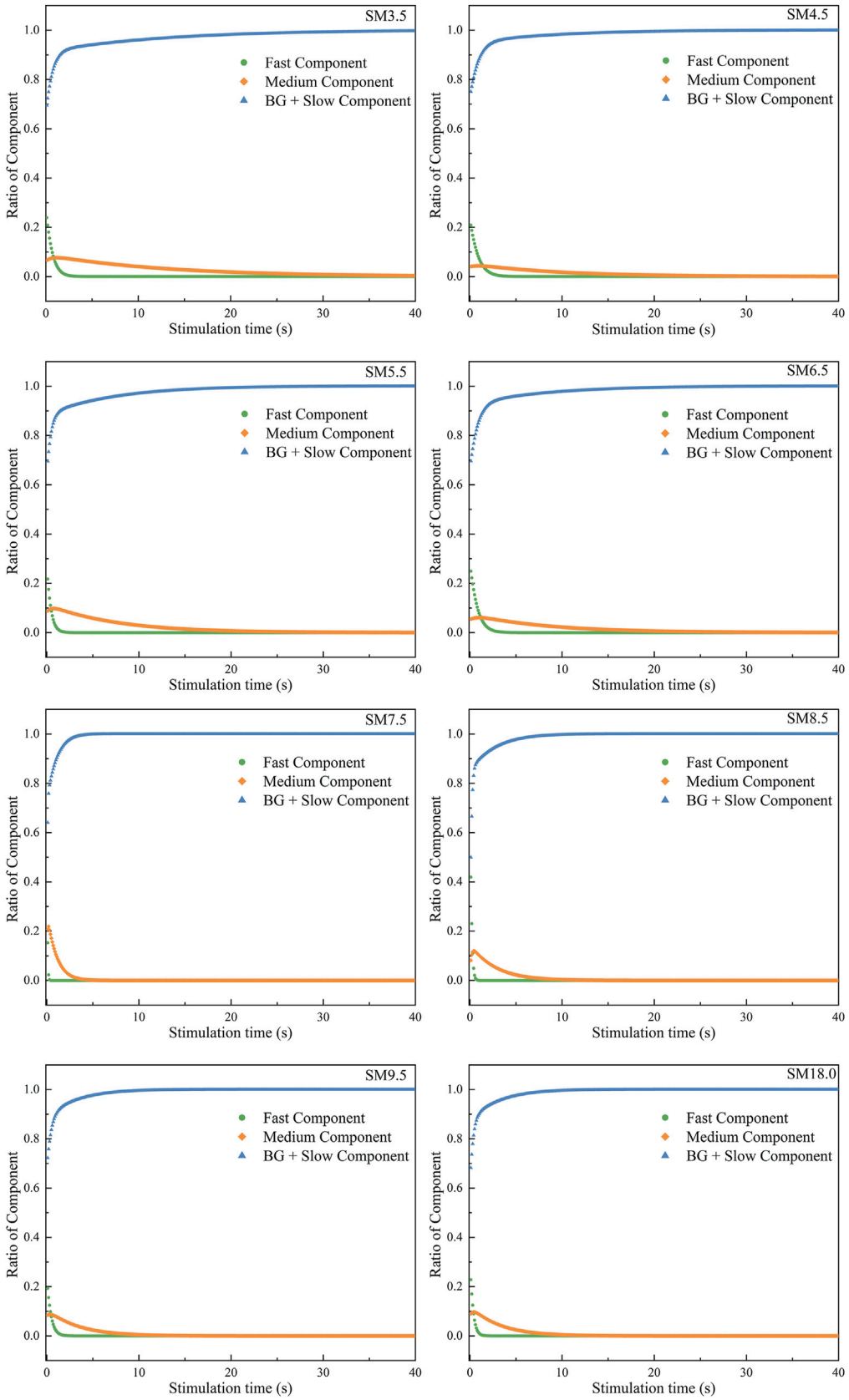

FIGURE 5 | The fast, medium and slow components variations with the stimulation time. For an apparent presentation, the first 40 s of data were intercepted for plotting.

TABLE 3 | Major chemical element weight percentage (%) and LOI of Sanming Borehole.

No.	LOI%	Na_2O	MgO	Al_2O_3	SiO_2	P_2O_5	SO_3	K_2O	CaO*	TiO_2	MnO	FeO(total)	ZnO	NiO	V_2O_5	BaO	PbO	Cr_2O_3	SUM
SM3.5	9.87	0.0000	0.1028	27.9188	43.1170	0.0315	0.0000	4.8157	0.2999	1.7449	0.0971	11.9372	0.0314	0.0123	0.0178	0.0000	0.0000	0.0000	**100.0000**
SM4.5	6.42	0.0000	0.0540	26.8693	45.1917	0.0619	0.0000	5.7116	0.0405	1.7484	0.1131	13.6571	0.0000	0.0000	0.0000	0.1338	0.0000	0.0000	**100.0000**
SM5.5	4.19	0.0351	0.0498	24.0848	54.3018	0.1046	0.0000	9.2729	0.0466	1.1927	0.0932	6.3876	0.0000	0.0000	0.0000	0.2386	0.0000	0.0000	**100.0001**
SM6.5	4.41	0.0331	0.0702	17.9551	61.4402	0.0887	0.0250	5.4159	0.0553	1.3307	0.1943	8.9616	0.0240	0.0000	0.0000	0.0000	0.0000	0.0000	**99.9999**
SM7.5	1.58	0.2917	0.0748	12.5538	68.7137	0.1389	0.0000	6.3863	0.6420	1.2630	0.1882	8.0081	0.0177	0.0000	0.0000	0.1138	0.0000	0.0264	**100.0001**
SM8.5	1.36	0.2066	0.0702	10.8863	68.2633	0.1525	0.0000	6.9077	0.6663	1.3575	0.0000	9.9735	0.0274	0.0000	0.0000	0.1279	0.0000	0.0000	**100.0001**
SM9.5	0.82	0.2412	0.0693	11.0754	71.3314	0.1054	0.0210	6.2855	1.1055	0.9974	0.2639	7.5587	0.0526	0.0000	0.0000	0.0000	0.0174	0.0447	**99.9896**
SM18.0	0.87	0.3341	0.0992	11.7575	69.7376	0.1566	0.0000	6.6223	1.2620	0.9682	0.1609	7.9748	0.0000	0.0000	0.0000	0.0000	0.0000	0.0538	**100.0000**

CaO: silicate bond and Carbonate bond CaO.*

mineral, as it is the most weathering resistant mineral. The plagioclase decreased with increasing weathering and was not even visible in samples above 6.5 m. The peaks of mica also gradually disappeared in the samples above 6.5 m. The characteristic peaks of kaolinite or chlorite ($2\theta = 12.40^{\circ}$) and illite ($2\theta = 19.85^{\circ}$) can be clearly seen in the sample at 3.5 m.

4.4 Irradiation-Bleaching Cycles and Thermal Activation Curves in Sanming Borehole

We assessed the IBC values of 8 samples from the Sanming borehole, and each of them were normalized by the respective first cycle value. As shown in **Figure 3C**, the 8 samples at different depths exhibit relatively the same trend of variation. The normalized IBC values grew gradually with the increase in the number of cycles. After the 1st, 2nd, 5th, 10th, 15th, and 25th cycles, the normalized IBC values of all samples did not show a large dispersion. The normalized IBC values gradually increased from 0.9 to 1.1 at the first cycle to 1.5–2.0 at the last cycle. Additionally, we noticed that some samples (SM5.5) maintained a faster increasing trend after the last cycle, while some samples (SM3.5) remained almost unchanged.

We performed TAC experiments in the interval from 200 to 600°C, with one measurement at each temperature rise of 40°C. The absolute values of the TAC test results are presented in **Figure 3B**., showing the variations of OSL sensitivity under thermal activation temperatures. The absolute values of TAC of the 8 samples remained almost constant for the measurements before 320°C. As the heating continued, the absolute values of the samples had a faster rise and a larger difference. The 8 samples were divided into two parts: one part reached the peak and subsequently dropped back (SM7.5, 8.5, 18), and the other part continued to increase (the other 5 samples). In **Figure 3D**., the absolute value of OSL sensitivity is normalized by the respective value of 200°C and the same pattern is also found in the normalized results.

5 DISCUSSION

5.1 Quartz Luminescence Sensitivity Constrained by Chemical Weathering

In a normal chemical weathering process under humid-warm climate conditions, hydrolysis results in silica movement in a profile, that is, irregular and small, while alkali and alkaline earth metals are greatly depleted (Parker, 1970). The common principle of weathering indices assumes that the major element distribution in parent rock is homogeneous on a certain scale, and the initial weathering degree is equal or the weathering starting line is the same for the samples.

Different weathering indices have been introduced to estimate the degree of weathering for various weathering conditions or weathering matrix. Although more than 30 different weathering indices were introduced, 5 indices applicable to granite, including RR (Ruxton Ratio), PI (Product Index), CIA (Chemical Index of Alteration), WIP (Weathering Index of Parker) and LOI, were

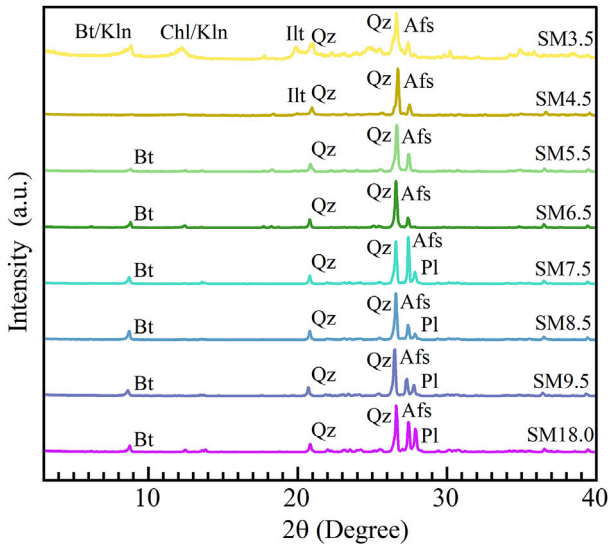

FIGURE 6 | Comparison of XRD spectra of in situ chemical weathering of eight samples from the Sanming drill hole. Bt: Biotite, Chl: Chlorite, Kln: Kaolinite, Ilt: Illite, Qz: Quartz, Afs: Alkali feldspar, Pl: Plagioclase (Warr, 2021).

chosen to evaluate chemical weathering intensity or extent in quantitative rather than qualitative terms in the current experiment. The Ruxton (1968) has been proven to be a good index for acidic or felsic rocks, and it assumes that alumina and other sesquioxides are immobile during weathering. WIP (Parker, 1970) is based on bond strength with oxygen and the proportion of mobile major elements (i.e., Na, K, Mg and Ca). CIA (Nesbitt and Young, 1982) applies the molecular ratio between immobile and mobile major elements, reflecting the conversion of feldspars to clays. LOI assesses weathering by calculating OH^- ions during the weathering process and ignoring a small amount of other volatiles (Sueoka et al., 1985; Gupta and Rao, 2001). **Tables 4**, **5** summarize and express specific calculation formulas and results.

PI and RR decreased as the grade of weathering increased, LOI and CIA increased as the grade of weathering increased, while WIP did not show an expected tendency as shown in **Figure 2**. It demonstrated a gradual decreasing weathering effect from 3.5 to 7.5 m and a nearly constant trend from 7.5 to 18.0 m. The initial results of major elements are compatible with the phenomena observed in the field work. Both WIP and CIA exhibited the same variation trend with an odd point at a depth of 5.5 m, where the potassium content was higher than that at all other points, which caused abnormalities in the indices. In contrast, PI employ a calculation method similar to that of CIA or WIP but does not involve potassium, so it gradually increases with depth until it plateaus without outliers. The LOI increased continuously with increased weathering, representing the value of OH^- in the secondary mineral formation, which is the residual of weathering.

The mineralogical results show that the fresh granite of the Sanming borehole is mainly composed of quartz, plagioclase, alkali feldspar and biotite. With increasing weathering, feldspar and mica chemically decomposed and transformed into hydrous clay minerals, such as kaolinite, illite and chlorite. Our experiments demonstrate from the mobility of chemical elements and the transformation between minerals that chemical weathering of the borehole is present and gradually increases from the bottom to the top.

QLS could be affected by congenital or acquired factors, such as crystallization (Sawakuchi et al., 2011b), inclusions (Chauhan and Singhvi, 2019), irradiation (Zimmerman, 1971; Benny et al., 2000), bleaching (Li and Wintle, 1992; Zhou and Wintle, 1994), or thermal history of quartz grains. The Sanming borehole, penetrated the weathering layer, was drilled on a Carboniferous granitic pluton that crops out on the surface and occupies an area of approximately 80 km^2. Compared to the large pluton, the heterogeneity of minerals in the borehole should be ignored, and quartz grains should be considered to have the same crystallization conditions, thermal history, and similar composition. Moreover, *in situ* weathering conditions do not allow quartz to enter the loop of irradiation-bleaching cycles (IBCs), which have already been proven to lead to an increase in QLS (Pietsch et al., 2008). Thus, the most likely factors affecting QLS are 1) the variation intensity of irradiation due to the changes in the radiation field, 2) the absorbed dose after being shielded by water, and 3) the dissolution of the surface layer of quartz by water. During the weathering process, the migration of radioactive elements would change the radiation field significantly (Jeong et al., 2007). For example, the alpha dose rate (Gy/ka) per ppm for the natural uranium series is 2.78, and the beta dose rate is 0.7982 Gy/ka for natural potassium at a 1% concentration (Adamiec and Aitken, 1998; Guérin et al., 2011). The pores and fractures of granite increase with the intensity of weathering, providing space for water to shield quartz grains against α, β, and γ radiation, which results in quartz gains receiving varying radiation doses during the chemical weathering process. Water not only protects the quartz grains from radiation but also dissolves them. Although the dissolution of quartz at 25°C and at neutral pH is slight (~$10^{-14.5}$ to $10^{-15.1}$ $mol/m^2/s$) (Schulz and White, 1999), it is also possible to affect the morphology of quartz by creating etch pits and fragmentations that may have effects on QLS. Meanwhile, the gradual expansion of pores and fractures provides channels for radon to escape, which decreases the subsequent radioactive decay chain and intensity of the radiation field. Overall, the main factors that may affect the QLS in the Sanming borehole are fluctuations in the radiation field in the historical period, which are caused by dissolution of quartz grains, water shielding and migration of radioactive elements.

It is quite difficult to recover the radiation field controlled by such complex conditions in the historical period. The chemical weathering process may be regarded as a black-box model combining three input variables: radiation field, water shield, and dissolution of quartz surface. Sawakuchi et al. (2018) considered that a longer duration of chemical weathering increases the QLS, which accounts for the high-sensitivity quartz in the cratonic areas of the Central Brazil shield. In our results, the relationship between OSL sensitivity and chemical weathering indices was not significant in the *in situ* chemical weathering scenario, indicating that the OSL

TABLE 4 | Chemical weathering indices used in this study.

Weathering Index	Formula	Ideal Tendency with Degree of Weathering	References
CIA (Chemical Index of Alteration)	$Al_2O_3/(Al_2O_3+ K_2O+ CaO† + Na_2O) \times 100$	Increase	Nesbitt (1979), Nesbitt and Young (1982)
PI (Product index)	$SiO_2/(SiO_2 + TiO_2 + Fe_2O_3 + FeO + Al_2O_3)$	Decrease	Reiche (1943)
RR (Ruxton ratio)	SiO_2/Al_2O_3	Decrease	Ruxton (1968)
WIP (Weathering Index of Parker)	$(CaO†/0.7 + 2Na_2O/0.35 + 2K_2O/0.25 + MgO/0.9) \times 100$	Decrease	Parker (1970)
Loss on Ignition	H_2O (+and-)	Increase	Sueoka et al. (1985)

CaO†: silicate bond CaO.

TABLE 5 | Quartz luminescence sensitivity and chemical weathering indices for samples from Sanming Borehole.

Depth (m)	OSL Sensitivity	Standard deviation	TL Sensitivity	Standard deviation	CIA	PI	RR	WIP	LOI %
	counts/(Gy*mg)		counts/(Gy*mg)						
3.5	24.045	4.534	141.677	18.987	0.829	65.957	2.621	0.419	9.874
4.5	22.618	2.309	123.745	2.750	0.811	66.973	2.854	0.488	6.419
5.5	23.965	2.680	116.015	12.436	0.703	75.635	3.826	0.793	4.192
6.5	25.001	2.386	105.790	7.199	0.749	80.427	5.807	0.466	4.406
7.5	27.573	7.351	134.527	15.309	0.595	85.813	9.289	0.588	1.582
8.5	24.649	2.972	105.629	7.605	0.547	85.918	10.642	0.625	1.361
9.5	24.257	2.176	117.331	9.272	0.546	87.575	10.930	0.586	0.820
18.0	27.940	1.972	99.569	8.431	0.540	86.744	10.066	0.628	0.873

sensitivity was less sensitive to three variables together. TL sensitivity monitored by 110°C exhibits a trend consistent with the intensity of chemical weathering. As the borehole is only 18 m in depth, and we cannot speculate whether the QLS would have remained constant if weathering had proceeded. However, we can conclude that 110°C TL sensitivity is more responsive to chemical weathering under the same conditions. This can also be noticed in previous work (Lü et al., 2014; Lü and Sun, 2017; Li and Zhou, 2020; Lü et al., 2020), where quartz in Paleosol or Pedocomplex has a higher QLS compared to loess, and the luminescence sensitivity of TL is several times higher than that of OSL. The difference, however, is that our QLS values are in the tens to hundreds of percent of the values in the above literature. Yang and Zhou (2019) used the uranium disequilibrium method to estimate that the chemical weathering rate of granite is 0.038 mm/year in the northern part of Guangdong Province, a mountain area with weathering conditions close to Sanming. We assume that samples above 7.5 m were weathered at the rate described above and concluded that the QLS caused by the variate intensity of irradiation will not change significantly in at least 200 ka under such weathering conditions.

5.2 Irradiation-Bleaching Cycles and Thermal Activation Curves

Changes in the luminescence sensitivity of quartz particles during irradiation-bleaching cycles (IBCs) have been extensively studied. Some of the studies have yielded a good linear correlation between the increase in QLS and the increase in the number of IBCs (Preusser et al., 2006; Pietsch et al., 2008; Zheng et al., 2009; Chang and Zhou, 2019; Li and Zhou, 2020; Bartyik et al., 2021). Nevertheless, several studies demonstrated controversial phenomena in which QLS does not increase with the number of IBCs (Fitzsimmons, 2011; Sawakuchi et al., 2018). There is insufficient evidence to suggest that differences in IBC can be explained by differences between weathering alone. However, the QLS of the eight samples tended to increase gradually with the number of IBCs, while maintaining a good consistency. This indicates that although the quartz has undergone different grades of *in-situ* chemical weathering, it maintains a consistent response to IBC, which may facilitate the subsequent use of IBC for source tracing or geomorphic process analysis.

The heating rate and the time held at high temperatures together affect the shape and peak position of the TAC (Aitken, 1985). To facilitate comparison, all the TAC data of the current study were obtained by the same thermal treatment. Aitken (1985) assumed that the TAC reflects the distribution of reservoir traps (R) and luminescence traps (L), both of which were proposed by Zimmerman (1971). He also suggested that R traps close to the valence band have their holes transferred to the L centers at a lower temperature than traps that are not as close. Many studies have taken advantage of this feature and concluded that TAC can distinguish the source of sediments (Zheng et al., 2009; Chang and Zhou, 2019; Nian et al., 2019; Li and Zhou, 2020). In contrast, our study shows that the TAC of quartz differs significantly even from that of the same rock mass, especially in the Sanming borehole (**Figure 3** and **Section 4.3**). Considering the large differences between *in situ* weathering residuals and sediments, we are unable to

conclude the TAC characteristics of quartz from the same rock mass after geomorphic processes such as denudation and transport.

6 CONCLUSION

In this study, eight samples from areas of intense chemical weathering were used to analyze the constraints of chemical weathering processes on QLS. The quartz 110°C TL sensitivity is more sensitive to chemical weathering relative to OSL sensitivity, although this tendency to enhance with chemical weathering is limited in our drilled samples. The samples from the upper part of the borehole that experienced stronger chemical weathering had more fast component than the samples from the bottom, but not significantly. Using the weathering rates of similar areas, we assumed that the QLS does not receive obvious alterations from *in situ* chemical weathering within 200 ka. We have found that quartz from the same source undergoes different degrees of *in situ* chemical weathering, but maintains a consistent response to IBC, which may also be a beneficial tool for geomorphic analysis. The thermal activation curve (TAC) results of the same rock mass show large differences, shaking the reliability of TAC as a provenance indicator. However, considering the differences between sediments and *in situ* weathering residuals, the reliability of TAC as a provenance indicator needs further study.

DATA AVAILABILITY STATEMENT

The original contributions presented in the study are included in the article/**Supplementary Material**, further inquiries can be directed to the corresponding author.

AUTHOR CONTRIBUTIONS

ZC contributed to conception and design of the study. ZC, YJ, and JX performed the statistical analysis. JZ organized the fieldwork. ZC, JX, and CZ organized the experiment. ZC wrote the first draft of the manuscript. All authors contributed to manuscript revision, read, and approved the submitted version.

ACKNOWLEDGMENTS

We are grateful to Professor Liping Zhou for his valuable comments and helpful discussions during this work. We also thank the two reviewers, whose constructive comments made the manuscript a great improvement.

SUPPLEMENTARY MATERIAL

The Supplementary Material for this article can be found online at: https://www.frontiersin.org/articles/10.3389/feart.2022.940212/full#supplementary-material

REFERENCES

Adamiec, G., and Aitken, M. J. (1998). Dose-Rate Conversion Factors: Update. *Anc. TL* 16 (2), 37–50.

Aitken, M. J. (1998). *An Introduction to Optical Dating: The Dating of Quaternary Sediments by the Use of Photon-Stimulated Luminescence*. Oxford: Oxford University Press.

Aitken, M. J. (1985). *Thermoluminescence Dating*. London: Academic Press.

Armitage, S. J., Duller, G. A. T., and Wintle, A. G. (2000). Quartz from Southern Africa: Sensitivity Changes as a Result of Thermal Pretreatment. *Radiat. Meas.* 32 (5-6), 571–577. doi:10.1016/S1350-4487(00)00053-6

Bartyik, T., Magyar, G., Filyó, D., Tóth, O., Blanka-Végi, V., Kiss, T., et al. (2021). Spatial Differences in the Luminescence Sensitivity of Quartz Extracted from Carpathian Basin Fluvial Sediments. *Quat. Geochronol.* 64, 101166. doi:10.1016/j.quageo.2021.101166

Benny, P. G., Sanjeev, N., Gundu Rao, T. K., and Bhatt, B. C. (2000). Gamma Ray Induced Sensitization of 110°C TL Peak in Quartz Separated from Sand. *Radiat. Meas.* 32 (3), 247–252. doi:10.1016/S1350-4487(99)00268-1

Bluszcz, A., and Adamiec, G. (2006). Application of Differential Evolution to Fitting OSL Decay Curves. *Radiat. Meas.* 41 (7), 886–891. doi:10.1016/j.radmeas.2006.05.016

Bøtter-Jensen, L., Agersnap Larsen, N., Mejdahl, V., Poolton, N. R. J., Morris, M. F., and McKeever, S. W. S. (1995). Luminescence Sensitivity Changes in Quartz as a Result of Annealing. *Radiat. Meas.* 24 (4), 535–541. doi:10.1016/1350-4487(95)00006-z

Bureau of Geology and Mineral Resources of Fujian Province (1985). *Regional Geology of Fujian Province*. Beijing: Geological Publishing House.

Chang, Z., and Zhou, L. (2019). Evidence for Provenance Change in Deep Sea Sediments of the Bengal Fan: A 7 Million Year Record from IODP U1444A. *J. Asian Earth Sci.* 186, 104008. doi:10.1016/j.jseaes.2019.104008

Chauhan, N., and Singhvi, A. K. (2019). Changes in the Optically Stimulated Luminescence (OSL) Sensitivity of Single Grains of Quartz During the Measurement of Natural OSL: Implications for the Reliability of Optical Ages. *Quat. Geochronol.* 53, 101004. doi:10.1016/j.quageo.2019.101004

del Río, I., Sawakuchi, A. O., Góes, A. M., Hollanda, M. H. B. M., Furukawa, L. Y., Porat, N., et al. (2021). Luminescence Signals of Quartz and Feldspar as New Methods for Stratigraphic Discrimination and Provenance Analysis of Siliciclastic Successions: The Case of the Parnaíba Basin (Brazil) of West Gondwana. *Basin Res.* 33 (6), 2938–2959. doi:10.1111/bre.12590

Duller, G. A. T. (2003). Distinguishing Quartz and Feldspar in Single Grain Luminescence Measurements. *Radiat. Meas.* 37 (2), 161–165. doi:10.1016/s1350-4487(02)00170-1

Fitzsimmons, K. (2011). An Assessment of the Luminescence Sensitivity of Australian Quartz with Respect to Sediment History. *Geochronometria* 38 (3), 199–208. doi:10.2478/s13386-011-0030-9

Fuchs, M., and Owen, L. A. (2008). Luminescence Dating of Glacial and Associated Sediments: Review, Recommendations and Future Directions. *Boreas* 37 (4), 636–659. doi:10.1111/j.1502-3885.2008.00052.x

Guérin, G., Mercier, N., and Adamiec, G. (2011). Dose-Rate Conversion Factors: Update. *Anc. TL* 29 (1), 5–8.

Gupta, A. S., and Rao, S. K. (2001). Weathering Indices and Their Applicability for Crystalline Rocks. *Bull. Eng. Geol. Environ.* 60 (3), 201–221. doi:10.1007/s100640100113

Higashimura, T., Ichikawa, Y., and Sidei, T. (1963). Dosimetry of Atomic Bomb Radiation in Hiroshima by Thermoluminescence of Roof Tiles. *Science* 139 (3561), 1284–1285. doi:10.1126/science.139.3561.1284.b

Ike, P. O., Folley, D. E., Agwu, K. K., Chithambo, M. L., Chikwembani, S., and Ezema, F. I. (2021). Influence of Dysprosium Doping on the Structural, Thermoluminescence and Optical Properties of Lithium Aluminium Borate. *J. Lumin.* 233, 117932. doi:10.1016/j.jlumin.2021.117932

Jeong, G. Y., Cheong, C.-S., and Choi, J.-H. (2007). The Effect of Weathering on Optically Stimulated Luminescence Dating. *Quat. Geochronol.* 2 (1-4), 117–122. doi:10.1016/j.quageo.2006.05.023

Kalita, J. M., Thomas, S., and Chithambo, M. L. (2019). Thermally and Optically Stimulated Luminescence of Natural Red and Blue Corundum (Al_2O_3). *J. Luminescence* 205, 417–422. doi:10.1016/j.jlumin.2018.09.058

Kortekaas, M., and Murray, A. S. (2005). A Method for the Removal of Mica from Quartz Separates. *Anc. TL* 23 (2), 43–46.

Lai, Z. (2006). Testing the Use of an OSL Standardised Growth Curve (SGC) for Determination on Quartz from the Chinese Loess Plateau. *Radiat. Meas.* 41 (1), 9–16. doi:10.1016/j.radmeas.2005.06.031

Li, J., Zhang, Y., Dong, S., and Johnston, S. T. (2014). Cretaceous Tectonic Evolution of South China: A Preliminary Synthesis. *Earth-Science Rev.* 134, 98–136. doi:10.1016/j.earscirev.2014.03.008

Li, S.-H., Chen, Y.-Y., Li, B., Sun, J., and Yang, L.-R. (2007). OSL Dating of Sediments from Deserts in Northern China. *Quat. Geochronol.* 2 (1-4), 23–28. doi:10.1016/j.quageo.2006.05.034

Li, S.-H., and Wintle, A. G. (1992). Luminescence Sensitivity Change Due to Bleaching of Sediments. *Int. J. Radiat. Appl. Instrum. Part D. Nucl. Tracks Radiat. Meas.* 20 (4), 567–573. doi:10.1016/1359-0189(92)90006-h

Li, Y., and Zhou, L. (2020). Variations of Thermally and Optically Stimulated Luminescence Sensitivity of Loess and Pedocomplex Samples from Southern Tajikistan, Central Asia. *Geochronometria* 48 (1), 242–252. doi:10.1515/geochr-2015-0118

Li, Z.-X., Li, X.-h., Zhou, H., and Kinny, P. D. (2002). Grenvillian Continental Collision in South China: New SHRIMP U-Pb Zircon Results and Implications for the Configuration of Rodinia. *Geology* 30 (2), 163–166. doi:10.1130/0091-7613(2002)030<0163:gccisc>2.0.co;2

Lü, T., Sun, J., Feathers, J. K., and Sun, D. (2020). Spatiotemporal Variations and Implications of Luminescence Sensitivity of Quartz Grains on the Chinese Loess Plateau since the Last Interglaciation. *Quat. Res.* 99, 190–203. doi:10.1017/qua.2020.53

Lü, T., Sun, J., Li, S.-H., Gong, Z., and Xue, L. (2014). Vertical Variations of Luminescence Sensitivity of Quartz Grains from Loess/Paleosol of Luochuan Section in the Central Chinese Loess Plateau Since the Last Interglacial. *Quat. Geochronol.* 22, 107–115. doi:10.1016/j.quageo.2014.04.004

Lü, T., and Sun, J. (2017). Luminescence Sensitivities of Quartz Grains from Eolian Deposits in Northern China and Their Implications for Provenance. *Quat. Res.* 76 (2), 181–189. doi:10.1016/j.yqres.2011.06.015

Murray, A. S., and Wintle, A. G. (2000). Luminescence Dating of Quartz Using an Improved Single-Aliquot Regenerative-Dose Protocol. *Radiat. Meas.* 32 (1), 57–73. doi:10.1016/S1350-4487(99)00253-X

Murray, A. S., and Wintle, A. G. (2003). The Single Aliquot Regenerative Dose Protocol: Potential for Improvements in Reliability. *Radiat. Meas.* 37 (4-5), 377–381. doi:10.1016/S1350-4487(03)00053-2

Nelson, M. S., Eppes, M. C., and Rittenour, T. M. (2022). Quartz Luminescence Sensitivity from Sediment versus Bedrock in Highly Weathered Soils of the Piedmont of North Carolina, South-Eastern USA. *Quat. Geochronol.* 72, 101343. doi:10.1016/j.quageo.2022.101343

Nesbitt, H. W. (1979). Mobility and Fractionation of Rare Earth Elements During Weathering of a Granodiorite. *Nature* 279 (5710), 206–210. doi:10.1038/279206a0

Nesbitt, H. W., and Young, G. M. (1982). Early Proterozoic Climates and Plate Motions Inferred from Major Element Chemistry of Lutites. *Nature* 299 (5885), 715–717. doi:10.1038/299715a0

Nian, X., Zhang, W., Qiu, F., Qin, J., Wang, Z., Sun, Q., et al. (2019). Luminescence Characteristics of Quartz from Holocene Delta Deposits of the Yangtze River and Their Provenance Implications. *Quat. Geochronol.* 49, 131–137. doi:10.1016/j.quageo.2018.04.010

Parker, A. (1970). An Index of Weathering for Silicate Rocks. *Geol. Mag.* 107 (6), 501–504. doi:10.1017/s0016756800058581

Peng, J., Dong, Z., Han, F., Long, H., and Liu, X. (2013). R Package numOSL: Numeric Routines for Optically Stimulated Luminescence Dating. *Anc. TL* 31 (2), 41–48.

Pietsch, T. J., Olley, J. M., and Nanson, G. C. (2008). Fluvial Transport as a Natural Luminescence Sensitiser of Quartz. *Quat. Geochronol.* 3 (4), 365–376. doi:10.1016/j.quageo.2007.12.005

Pires, E. L., Tatumi, S. H., Mittani, J. C. R., Kinoshita, A., Baffa, O., and Caldas, L. V. E. (2011). TL, OSL and ESR Properties of Nanostructured KAlSi3O8:Mn Glass. *Radiat. Meas.* 46, 1492–1495. doi:10.1016/j.radmeas.2011.04.041

Preusser, F., Ramseyer, K., and Schlüchter, C. (2006). Characterisation of Low OSL Intensity Quartz from the New Zealand Alps. *Radiat. Meas.* 41 (7-8), 871–877. doi:10.1016/j.radmeas.2006.04.019

Qiu, F., and Zhou, L. (2015). A New Luminescence Chronology for the Mangshan Loess-Palaeosol Sequence on the Southern Bank of the Yellow River in Henan, Central China. *Quat. Geochronol.* 30, 24–33. doi:10.1016/j.quageo.2015.06.014

Reiche, P. (1943). Graphic Representation of Chemical Weathering. *J. Sediment. Res.* 13 (2), 58–68. doi:10.1306/d4269198-2b26-11d7-8648000102c1865d

Rendell, H. M., Townsend, P. D., Wood, R. A., and Luff, B. J. (1994). Thermal Treatments and Emission-Spectra of TL from Quartz. *Radiat. Meas.* 23 (2-3), 441–449. doi:10.1016/1350-4487(94)90077-9

Richter, D., Pintaske, R., Dornich, K., and Krbetschek, M. (2012). A Novel Beta Source Design for Uniform Irradiation in Dosimetric Applications. *Anc. TL* 30 (2), 57–63.

Richter, D., Richter, A., and Dornich, K. (2013). Lexsyg - A New System for Luminescence Research. *Geochronometria* 40 (4), 220–228. doi:10.2478/s13386-013-0110-0

Rink, W. J. (1994). Billion-Year Age-Dependence of Luminescence in Granitic Quartz. *Radiat. Meas.* 23 (2-3), 419–422. doi:10.1016/1350-4487(94)90074-4

Ruxton, B. P. (1968). Measures of the Degree of Chemical Weathering of Rocks. *J. Geol.* 76 (5), 518–527. doi:10.1086/627357

Sawakuchi, A. O., Blair, M. W., DeWitt, R., Faleiros, F. M., Hyppolito, T., and Guedes, C. C. F. (2011a). Thermal History versus Sedimentary History: OSL Sensitivity of Quartz Grains Extracted from Rocks and Sediments. *Quat. Geochronol.* 6 (2), 261–272. doi:10.1016/j.quageo.2010.11.002

Sawakuchi, A. O., DeWitt, R., and Faleiros, F. M. (2011b). Correlation Between Thermoluminescence Sensitivity and Crystallization Temperatures of Quartz: Potential Application in Geothermometry. *Radiat. Meas.* 46 (1), 51–58. doi:10.1016/j.radmeas.2010.08.005

Sawakuchi, A. O., Jain, M., Mineli, T. D., Nogueira, L., Bertassoli, D. J., Häggi, C., et al. (2018). Luminescence of Quartz and Feldspar Fingerprints Provenance and Correlates with the Source Area Denudation in the Amazon River Basin. *Earth Planet. Sci. Lett.* 492, 152–162. doi:10.1016/j.epsl.2018.04.006

Sawakuchi, A. O., Rodrigues, F. C. G., Mineli, T. D., Mendes, V. R., Melo, D. B., Chiessi, C. M., et al. (2020). Optically Stimulated Luminescence Sensitivity of Quartz for Provenance Analysis. *Methods Protoc.* 3 (1), 6. doi:10.3390/mps3010006

Schulz, M. S., and White, A. F. (1999). Chemical Weathering in a Tropical Watershed, Luquillo Mountains, Puerto Rico III: Quartz Dissolution Rates. *Geochim. Cosmochim. Acta* 63 (3-4), 337–350. doi:10.1016/S0016-7037(99)00056-3

Shu, L. (2012). An Analysis of Principal Features of Tectonic Evolution in South China Block. *Geol. Bull. China* 31 (7), 1035–1053. (Chinese with English Abstract).

Shu, L. (2006). Predevonian Tectonic Evolution of South China: From Cathaysian Block to Caledonian Period Folded Orogenic Belt. *Geol. J. China Univ.* 12 (4), 418–431. (Chinese with English Abstract).

Shu, L., Yao, J., Wang, B., Faure, M., Charvet, J., and Chen, Y. (2021). Neoproterozoic Plate Tectonic Process and Phanerozoic Geodynamic Evolution of the South China Block. *Earth-Sci. Rev.* 216, 103596. doi:10.1016/j.earscirev.2021.103596

Singhvi, A. K., Sharma, Y. P., and Agrawal, D. P. (1982). Thermoluminescence Dating of Sand Dunes in Rajasthan, India. *Nature* 295 (5847), 313–315. doi:10.1038/295313a0

Smith, B. W., and Rhodes, E. J. (1994). Charge Movements in Quartz and Their Relevance to Optical Dating. *Radiat. Meas.* 23 (2-3), 329–333. doi:10.1016/1350-4487(94)90060-4

Sueoka, T., Lee, I., Muramatsu, M., and Imamura, S. (1985). "Geomechanical Properties and Engineering Classification for Decomposed Granite Soils in Kaduna District, Nigeria," in Proceedings of the First International Conference on Geomechanics in Tropical Lateritic and Saprolitic Soils, Brasilia, February 11-14, 1985, 175–186.

Takaku, J., Tadono, T., Doutsu, M., Ohgushi, F., and Kai, H. (2020). Updates of 'Aw3D30' Alos Global Digital Surface Model with Other Open Access Datasets. *Int. Arch. Photogramm. Remote Sens. Spat. Inf. Sci.* XLIII-B4-2020, 183–189. doi:10.5194/isprs-archives-XLIII-B4-2020-183-2020

Vaitkus, A., Merkys, A., and Gražulis, S. (2021). Validation of the Crystallography Open Database Using the Crystallographic Information Framework. *J. Appl. Cryst.* 54 (2), 661–672. doi:10.1107/s1600576720016532

Warr, L. N. (2021). IMA-CNMNC Approved Mineral Symbols. *Mineral. Mag.* 85 (3), 291–320. doi:10.1180/mgm.2021.43

Yang, H., and Zhou, S. (2019). Application of Uranium Disequilibrium in the Study of the Weathering Rate of the Granite in Northern Guangdong. *J. South China Normal Univ. Nat. Sci. Ed.* 51 (5), 84–91. (Chinese with English Abstract). doi:10.6054/j.jscnun.2019088

Yukihara, E. G., and McKeever, S. W. S. (2008). Optically Stimulated Luminescence (OSL) Dosimetry in Medicine. *Phys. Med. Biol.* 53 (20), R351–R379. doi:10.1088/0031-9155/53/20/r01

Zhang, Y., Xu, X., Jia, D., and Shu, L. (2009). Deformation Record of the Change from Indosinian Collision-Related Tectonic System to Yanshanian Subduction-Related Tectonic System in South China During the Early Mesozoic. *Earth Sci. Front.* 16 (1), 234–247. (Chinese with English Abstract).

Zheng, C., Zhou, L., and Qin, J. (2009). Difference in Luminescence Sensitivity of Coarse-Grained Quartz from Deserts of Northern China. *Radiat. Meas.* 44 (5-6), 534–537. doi:10.1016/j.radmeas.2009.02.013

Zhou, L., Fu, D., and Zhang, J. (2010). An Analysis of the Components of the Luminescence Signals of Selected Polymineral and Quartz Samples from Loess in Western China and Southern Tajikistan, and Their Suitability for Optical Dating. *Quat. Geochronol.* 5 (2-3), 149–153. doi:10.1016/j.quageo.2009.05.008

Zhou, L., and Wintle, A. G. (1994). Sensitivity Change of Thermoluminescence Signals After Laboratory Optical Bleaching - Experiments with Loess Fine Grains. *Quat. Sci. Rev.* 13 (5-7), 457–463. doi:10.1016/0277-3791(94)90058-2

Zimmerman, J. (1971). The Radiation-Induced Increase of the 100°C Thermoluminescence Sensitivity of Fired Quartz. *J. Phys. C. Solid State Phys.* 4 (18), 3265–3276. doi:10.1088/0022-3719/4/18/032

Zu, F., Shu, L., and Li, C. (2012). Evolution Features of Depositional and Tectonic Setting from Late Paleozoic to Meso—Cenozoic in the Yong'an Basin. *Geol. Rev.* 58 (01), 126–148. (Chinese with English Abstract). doi:10.16509/j.georeview.2012.01.005

Conflict of Interest: The authors declare that the research was conducted in the absence of any commercial or financial relationships that could be construed as a potential conflict of interest.

Publisher's Note: All claims expressed in this article are solely those of the authors and do not necessarily represent those of their affiliated organizations, or those of the publisher, the editors and the reviewers. Any product that may be evaluated in this article, or claim that may be made by its manufacturer, is not guaranteed or endorsed by the publisher.

frontiers | Frontiers in Earth Science

ORIGINAL RESEARCH
published: 25 July 2022
doi: 10.3389/feart.2022.939766

The Chronology of Early Human Settlement in Three Gorges Region, China—Contribution of Coupled Electron Spin Resonance and Uranium-Series Dating Method

Fei Han[1], Jean-Jacques Bahain[2], Qingfeng Shao[3], Xuefeng Sun[4], Pierre Voinchet[2], Ping Xiao[5], Manchen Huang[1], Mengqi Li[1] and Gongming Yin[6]*

[1]Yunnan Key Laboratory of Earth System Science, Yunnan University, Kunming, China, [2]Histoire Naturelle de l'Homme Préhistorique (HNHP)—UMR 7194, Département Homme et Environnement du MNHN, Paris, France, [3]College of Geography Science, Nanjing Normal University, Nanjing, China, [4]School of Geography and Ocean Science, Nanjing University, Nanjing, China, [5]College of Teacher Education, Yuxi Normal University, Yuxi, China, [6]Institute of Geology, China Earthquake Administration, Beijing, China

OPEN ACCESS

Edited by:
Yuxin Fan,
Lanzhou University, China

Reviewed by:
Hua Tu,
Shantou University, China
Tongyan Lyu,
Chinese Academy of Geological Sciences (CAGS), China

***Correspondence:**
Fei Han
hanfei@ynu.edu.cn

Specialty section:
This article was submitted to Quaternary Science, Geomorphology and Paleoenvironment, a section of the journal Frontiers in Earth Science

Received: 09 May 2022
Accepted: 20 June 2022
Published: 25 July 2022

Citation:
Han F, Bahain J-J, Shao Q, Sun X, Voinchet P, Xiao P, Huang M, Li M and Yin G (2022) The Chronology of Early Human Settlement in Three Gorges Region, China—Contribution of Coupled Electron Spin Resonance and Uranium-Series Dating Method. Front. Earth Sci. 10:939766. doi: 10.3389/feart.2022.939766

The Three Gorges region (TGR) located in the geographic center of China, is a transition zone between mountain and plain areas, and a probable migration corridor for hominins and other mammals between South and North China. Detailed chronological information of paleoanthropological evidence in this area could help us better understand the human evolution in East Asia. The OSL and U-series dating methods are two conventional dating methods generally adopted to date such sites; however, their applications were limited by the dating range—restricted to several hundred of millennia and ambiguous stratigraphic relationship between the archaeological remains and the dating target materials. Cosmogenic nuclide burial dating of quartzite stone artifacts and coupled electron spin resonance and uranium series dating (ESR/U-series) of fossil teeth have the potential to date Early–Middle Pleistocene hominin sites in Asia and were applied increasingly in China in recent years. However, the application of cosmogenic $^{26}Al/^{10}Be$ burial dating is limited in TGR because most sites are dominated by limestone, leading to the scarcity of the quartz component. In this case, the coupled ESR/U-series method plays a more important role in the establishment of the chronology of human settlement. In TGR, by using the coupled ESR/U-series method, we have dated seven important Early and Middle Pleistocene hominin settlement sites, including Longgupo, Jianshi, Yunxian, Meipu, Bailongdong, Changyang, and Yumidong sites. Based on our dating results, we propose that hominins were settled in TGR probably from the early stage of Early Pleistocene (~2.5–2.2 Ma) at the Longgupo site to the late Middle Pleistocene to Late Pleistocene of the Yumidong site (~274–14 ka) and very likely to spread to other parts of East Asia during this time period. In view of the potential of coupled ESR/U-series dating on fossil teeth from the hominin sites in the TGR, future work may consider the micro damage or non-destructive analysis of enamel fragment with the ESR method and laser ablation ICP-MS techniques that will make possible the direct dating of precious human fossils in China.

Keywords: ESR/U-series dating, fossil teeth, hominin, Three Gorges, China

INTRODUCTION

In recent years, numerous new fossil hominin findings in the Three Gorges region (TGR) have reshaped our understanding of the human settlement and evolution in China and East Asia. However, it was difficult to put these discoveries in a precise temporal context due to the lack of suitable dating methods. Published data on these sites were mainly based on fauna assemblage or paleomagnetic method, only a few radiometric dating works were carried out on the materials associated with the human remains, such as charcoals, speleothems, or sediments rather than the fossils itself. Such way of dating is problematic sometimes because of the ambiguous stratigraphic relationship between the associated materials and the target specimen. Meanwhile, some commonly used techniques were limited by their dating range, such as radiocarbon dating (<50 ka), OSL dating (<500 ka), and U-series dating (<700 ka); as a consequence, many questions about human survival and evolution cannot be fully addressed. Cosmogenic nuclides ^{26}Al/^{10}Be burial dating is a technique developed in the last two decades and shows the potential of dating quartz minerals, especially in the sediments of the cave site. However, in the TGR, the geological setting of limestone makes the extraction of enough quartz for ^{26}Al/^{10}Be burial dating rather difficult or even unsuccessful in many cases. Coupled electron spin resonance and uranium-series dating method (ESR/U-series) evolve from the traditional ESR fossil dating and were successfully applied to some significant paleoanthropological sites in recent years (Gran Dolina, Falguères et al., 1999; Kalinga, Ingicco et al., 2018; Jebel Irhoud, Richter et al., 2017; Misliya, Hershkovitz et al., 2018; Broken Hill, Grün et al., 2020). The advantage of this method is not only the wide dating range that almost covers the entire Quaternary period but also its various dating targets, including the animal fossils, which sometimes have preserved the direct evidence of human activities. In this article, we present a detailed introduction of the coupled ESR/U-series dating method on fossil teeth and its application to the Middle and Early Pleistocene hominin sites in the TGR, requirements and limitations of this dating approach are also discussed.

Coupled ESR/U-series Dating on Fossil Teeth

The electron spin resonance (ESR) dating is a trapped charge dating technique similar to luminescence dating, which is based on the accumulation of unpaired electrons or holes in the crystal lattices of minerals caused by the exposure to natural radiation (Grün, 1989; Rink, 1997). The number of traps is functional related to the received radiation dose and is reflected by the measured ESR signal intensity. It depends not only on the dose rate (annual dose) but also on the duration of radiation which corresponds to the ESR age of the dated sample. The total dose the sample received in the past is called equivalent dose (D_E) or paleodose, and it could be expressed as the following function:

$$D_E = \int_0^t D(t)dt. \quad (1)$$

In the case the dose rate is a constant, the aforementioned equation could be simplified as

$$D_E = D(t)T \quad (2)$$

where the ESR age T can be calculated by $D_E/D(t)$ directly, and it is a basic formula used for quartz grains ESR dating.

In the case of fossil teeth dating, the situation is quite more complex. The fossil teeth which are composed of different dental tissues (enamel, dentine, and cementum) will absorb the uranium from the surrounding environment after burial. The radioactive decay from the uranium series isotopes will contribute to the dose rate as internal dose and makes the dose rate vary with time. In order to model the uranium migration process in the fossil tooth and the evolution of the internal dose rate, U-series analysis needs to be combined with the ESR measurement, and the US model was proposed by Grün et al. (1988) by using a U-uptake parameter p to describe the U-uptake history:

$$U(t) = U_m(t/T)^{p+1} \quad (3)$$

where $U(t)$ is the uranium concentration at time t, U_m is the measured U concentration at present-day, and T is the age of the samples.

The age calculation process of the US model is shown in **Figure 1**, and the mathematical basis was described by Shao et al. (2015). When p values equal to −1 and 0, it corresponds to early uptake (EU) and linear (LU) models, respectively, which assumes that uranium is absorbed in the early stage or constantly after the burial of fossil teeth. The EU and LU models were generally adopted in the early years of ESR age calculation and used to bracket the fossil age. However, recent uptake of uranium ($p > 0$) can also occur in the fossil samples as well as U-leaching which was indicated by ^{230}Th/^{234}U ratio higher than unity. In such case of U loss, the US model cannot calculate the fossil age, and the acceleration uptake (AU) model was proposed to stimulate the uranium migration process (Shao et al., 2012). The AU model describes the uranium uptake in the dental tissues as an accelerating process by introducing an initial uptake rate (f) and the acceleration of this initial uptake rate (a). The a/f ratio is then defined as a U-uptake parameter n for computation. This model also necessitates the U-series analysis of the different dental tissues, and it can be used to calculate the age of the sample with a measured ^{230}Th/^{234}U ratio higher than one (system beyond equilibrium) by a negative n value when the US model cannot be applied.

In the present study, both US and AU models were used to obtain the ESR/U-series ages of the fossil samples from hominin sites in the TGR.

Three Gorges Region

The uplift of the Tibetan Plateau is the most distinguished tectonic movement in the Cenozoic, and it promoted to shape present landscape of China with three geomorphologic steps. The highest step is the Tibetan Plateau (average altitude >4,000 m a.s.l.), the Mongolian Plateau–Loess Plateau–Yunnan Plateau forms the second step (average altitude 1,000–2,000 m a.s.l.), and the lowest eastern plain is the third one (average

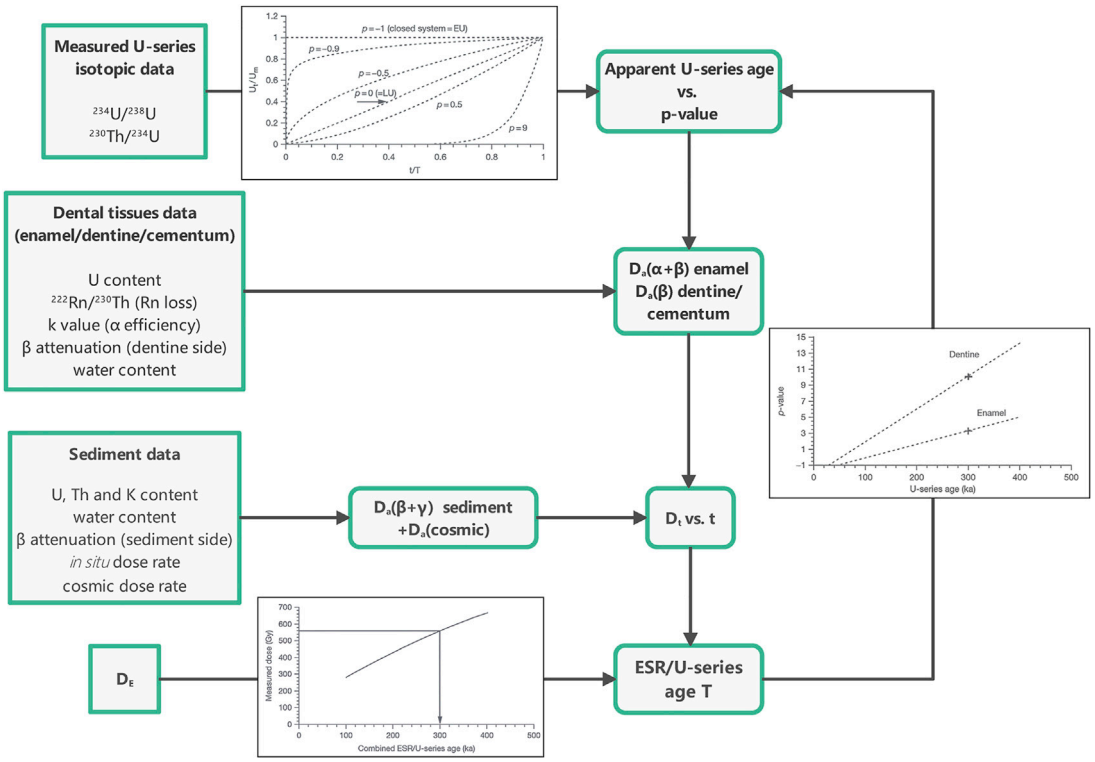

FIGURE 1 | Flowchart of the ESR/U-series age calculation process with the US model (*p*-value) (after Grün et al., 1988).

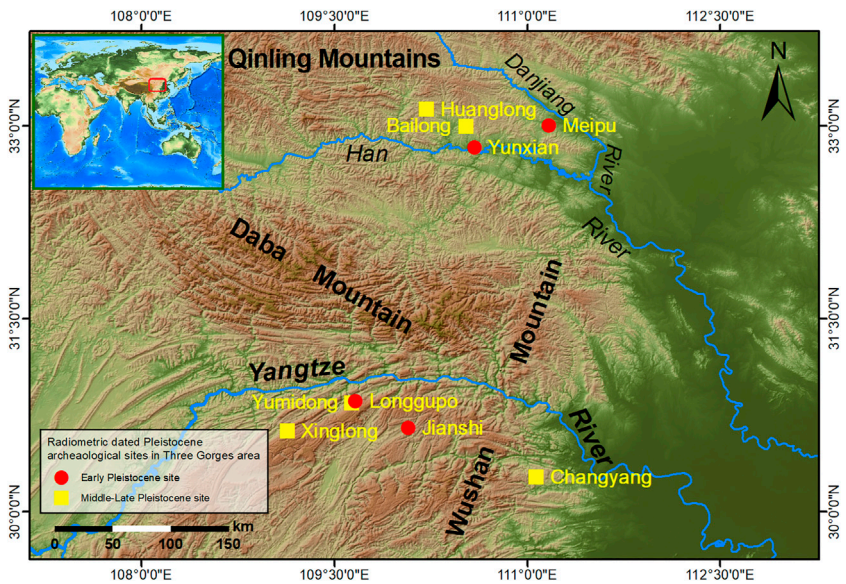

FIGURE 2 | Location map of the hominin settlement sites in the Three Gorges region mentioned in the text.

altitude <500 m a.s.l.). The TGR, composed by Qutang Gorge (~8 km long), Wu Gorge (~46 km long) and Xiling Gorge (~66 km long) from Fengjie County, Chongqing Municipality in the west to Yichang city, Hubei Province in the east, is the transition region between the second and third geomorphologic steps. Numerous hominin sites are distributed along the TGR in a broad sense, which covers the area along the Yangtze River, but also the sites close to the Han River, one of the largest tributaries of the Yangtze River and Danjiang River, a tributary of the Han River in the western Hubei area, both originated and flowing

TABLE 1 | A summary of the hominin sites in Three Gorge area mentioned in the text.

Site name	Location	Latitude(°N)	Longitude(°E)	Elevation(m)	Site type	Fauna	Age[1]	Dating method[2]	Dating material	Reference
Longgupo	Wushan County, Chongqing	30.8631	109.6656	830	cave/ fissure	Late Pliocene-Early Pleistocene	2.0 - 2.5 Ma	Paleomag	sediment	Sun et al., submitted
							~ 2.2 - 2.5 Ma	ESR/U	fossil teeth	Han et al., 2017
Jianshi	Jianshi County, Hubei	30.6541	110.0748	738	cave	Early Pleistocene	> 2.14 Ma (below Layer 6)	Paleomag	sediment	Cheng et al., 2004
							1.52 ± 0.09 Ma (Layer 8) / 1.05 ± 0.05 Ma (Layer 4)	ESR/U	fossil teeth	Han et al., submitted
Yunxian	Yunxian County, Hubei	32.8317	110.5897	219	river terrace	early Middle Pleistocene-late Early Pleistocene	936 ka	Paleomag	sediment	de Lumley and Li, 2008
							1.10 ± 0.16 Ma	ESR/U & ESR	fossil teeth & quartz sand	Bahain et al., 2017; in progress
Meipu	Yunxian County, Hubei	33.0047	111.1708	263	cave	early Middle Pleistocene-late Early Pleistocene	780 - 990 ka (Layer 2)	Paleomag	sediment	Xing et al., 2021
							> 630 ka (bottom of Layer 1)	U-Th	flowstone	
							849 ± 39 ka (Layer 2)	ESR/U	fossil teeth	Han et al., 2022
Bailong Cave	Yunxi County, Hubei	32.9944	110.526	550	cave	Middle Pleistocene/late Early Pleistocene	~0.78 Ma	Paleomag	sediment	Kong et al., 2018
							578 ± 26 ka (Layer 1-3)	ESR/U	fossil teeth	Han et al., 2019, this study
							0.76 ± 0.06 Ma (Layer 4-6)	$^{26}Al/^{10}Be$	quartz sand & gravel	Liu et al., 2015
Changyang	Changyang County, Hubei	30.2701	111.0698	730	cave	early Late Pleistocene-late Middle Pleistocene	193 - 143 ka	U-Th	fossil teeth	Lu et al., 2020
								ESR/U	fossil teeth	Bahain et al., in progress
Xinglong Cave	Fengjie County, Chongqing	30.6275	109.135	1260	cave	Late Middle Pleistocene	129-199 ka	U-Th	flowstone	Peng et al., 2014
Yumidong	Wushan County, Chongqing	30.8457	109.6359	1085	cave	Holocene-late Middle Pleistocene	14 - 41 ka (Layer 2)	^{14}C	charcoal	Shao et al., 2022
							4.8 - 22.6 ka (Layer 2) / 46.7 - 112.7 ka (Layer 3-15)	U-Th	bone	
							35 - 291 ka (Layer 2-15)		speleothem	
							~ 65 - 295 ka (Layer 2-11)	ESR/U	fossil teeth	

[1]*Note: The stratigraphic layer of the dated sample was present in parentheses. No layer information was given if the age range brackets the hominin fossil layer or estimated by paleomagnetism.*
[2]*Paleomag - Paleomagnetism; ESR/U - Coupled ESR/U-series method; $^{26}Al/^{10}Be$ - Cosmogenic burial dating method.*

through the Qinling Mountains (**Figure 2**) (**Table 1**). As the western Hubei and TGR were located in the geographic center of China, it is a crucial passage area of the hominin settlement and migration between South and North China.

The Three Gorges was formed by severe incision along narrow fault zones, in response to the tectonic uplift of massive limestone formations of late Paleozoic and Mesozoic age (Zheng et al., 2013; Zhang et al., 2021). The Yangtze River transects the Huangling anticline at the eastern margin of the Three Gorges (Richardson et al., 2010). The region is dominated by a subtropical humid climate nowadays, which is warm in winter and cool in summer. Sedimentological and geochemical studies of the river terrace deposits in the TGR indicate a warm–wet climate during the Early and Middle Pleistocene period and gradually change to a cold–dry environment since the late Middle Pleistocene probably in relation to the uplift of Qinghai–Tibet Plateau (Gonghe Movement), which enhances the plateau monsoon and weaken and block the Indian monsoon (Xiang et al., 2020).

Evidence of the environmental changes mentioned above is also proven by the occurrence of *Gigantopithecus blacki*, a representative primate once lived in Southeast Asia and South China. A carbon stable isotopic composition analysis of the enamel of *Gigantopithecus blacki* teeth indicates their habit was limited to a forested environment with a general vegetarian diet (Bocherens et al., 2017). Due to the climatic shifts during the Pleistocene, *Gigantopithecus blacki* were forced to migrate from the TGR which had a warm and humid climate during the Early Pleistocene period (e.g., Longgupo and Jianshi sites) to the more southern region, such as Guangxi and Guizhou provinces in China and Southeast Asia, and probably became extinct at the late Middle Pleistocene or early Late Pleistocene period because of the reduction of forest environment and food shortage. Although some mammalian species of North China appeared in the sites of South China, the evidence of the highest altitude of *Gigantopithecus blacki* were found only in the south of the Yangtze River, which indicates the natural barrier of the Yangtze River may already exist at the beginning of the Quaternary period, and it could be partially supported by the recent ESR dating study of the sand lenses in the Yichang Gravel Layer, which indicate the Three Gorges valley incision and the channelization of the Yangtze River began probably before ~1 Ma (Wei et al., 2020).

The fauna assemblage found in Three Gorges hominin sites belong to the main types of the Oriental Realm and was represented by the *Ailuropoda–Stegodon* fauna (*sensu lato*). The early stage of the *Ailuropoda–Stegodon* fauna include the typical *Gigantopithecus*-bearing assemblage, which can be found in two Early Pleistocene sites—Longgupo and Jianshi. The Middle Pleistocene *Ailuropoda–Stegodon* fauna (*sensu stricto*) is commonly found in the karstic deposits of caves and fissures, and the most representative assemblage is the Yanjinggou fauna, which was found by Walter Granger during the 1920s in Sichuan Province (now allocated to Chongqing municipality) (Colbert and Hooijer, 1953). Three karst caves discovered in the later time in Guangxi Province—Daxin, Wuming, and Bama yielded not only *Ailuropoda–Stegodon* fauna but also *Gigantopithecus* remains. The fauna assemblage comparison of our studied Bailongdong site near the Han River with Gongwangling and Yunxian sites indicate an early stage of the Middle Pleistocene. Last, the Late Pleistocene *Ailuropoda–Stegodon* fauna (*sensu lato*) recorded in the TGR contains few archaic forms; meanwhile, it shows the features similar to the Middle Pleistocene *Ailuropoda–Stegodon* fauna and modern Oriental Realm (Wu and Olsen, 1985). The presence of *Hyaena ultima* in Changyang site indicates its relatively early age in comparison with some other typical Late Pleistocene sites in South China (e.g., Maba site in Guangdong Province or Tongzi site in Guizhou Province). As the TGR is a transitional zone between South and North China, the fossiliferous assemblages from some of the sites in this region show a mixed characteristic of both northern and southern faunas. A detailed comparison of the fauna assemblage from the hominin sites in the TGR with two hominin sites nearby—Gongwangling (Early Pleistocene) and Chenjiawo (Middle Pleistocene) in Shaanxi Province is shown in **Supplementary Table S1**.

The stone artifacts found in the early hominin sites in western Hubei and TGR are not as sophisticated as those unearthed in North China for the same period. This phenomenon may contribute partly to the limitation of the raw materials since a large number of the sites are situated in the limestone area, and the characteristics of the lithic made by limestone sometimes are difficult to distinguish from the traces formed by the natural process. The use of bamboo tools may be another reason to explain the relatively lagging lithic techniques in the vast area of South China and Southeast Asia compared with Europe and even North China. A recent experimental study shows that the tools made by bamboo could almost completely replace the basic function of some stone tools to cut the meat (Bar-Yosef et al., 2012). The primitive stone artifacts unearthed from the early sites in the TGR therefore may not reflect the real technology level at that time, since the wide spread of bamboo and other arbores in South China could be good materials for making tools and were used by local people even nowadays. However, the woodworks were not easy to be preserved for a long time in the warm and humid environment, except for some special conservation environment (e.g., Gantangqing site, Yunnan Province) (Gao et al., 2021).

CHRONOLOGICAL STUDY OF THE HOMININ SETTLEMENT SITES IN THE THREE GORGES REGION

Due to the relatively survivable climate and natural environment in South China during almost the entire Pleistocene period, the chronology of the hominin sites in the TGR is difficult to be established only rely on fauna and lithic culture evidences. Meanwhile, most of the sites discovered in this region are associated with cave or fissure environments with limestone parent rock, in which the optimal dating materials for some routine optical dating methods (e.g., OSL dating) are limited. For the Early Pleistocene and early Middle Pleistocene sites, which are beyond the dating range of the U–Th method, cosmogenic $^{26}Al/^{10}Be$ burial dating may works

occasionally if enough quartz minerals can be extracted from the sites. Because of the complexity and interruption of the deposition in some cave sites, the paleomagnetic dating study is only valid if other radiometric dates are available to provide a constraint. In most cases, coupled ESR/U-series dating of fossil teeth is the only feasible chronological method to study the early human settlement in the TGR.

Here, we give a brief introduction of the hominin settlement sites in the TGR that we have dated by the coupled ESR/U-series dating method in recent years (based on the chronological sequence), the limitations and cautions of this method are also addressed in the discussion part in order to call attention to its application in archaeological dating.

Longgupo

Discovered in the 1980s, the Longgupo site ("Longgu" is literally translated as "dragon bone" in Chinese, which are the mammalian fossils used in Chinese medicine, and "po" means hillside) is about 16 km south of the Yangtze River (**Figure 2**). It is located on a limestone hill slope (830 m a.s.l.) filled with Plio–Pleistocene deposits. The Longgupo site was once a cave but carpeted by collapsed breccias during the Pleistocene period (Rasse et al., 2011). It is well known because of the discovery of a mandible fragment with two teeth and an upper incisor, which show affinities with African early *Homo* specimens. The site was previously dated to ~ 1.9 Ma by both paleomagnetism and ESR methods and was thought as the earliest evidence of human occurrence in Asia challenging the "Out-of-Africa" theory (Huang et al., 1995). Although the fossil specimens were questioned by a batch of scholars and considered as ape instead of *Homo* (Schwartz and Tattersall, 1996; Ciochon, 2009; Etler, 2009), the stone artifacts recovered from the stratigraphic layers were identified and confirmed by the specialists (Huang et al., 1995; Boëda and Hou, 2011) and led to speculation of the status of the tool-makers (Dennell, 2009).

From 2003 to 2006, a Sino-Franco joint excavation recovered thousands of stone artifacts from re-divided stratigraphic layers of the south and north walls (Boëda and Hou, 2011). A new chronological study was conducted during the joint excavation by using paleomagnetism and ESR/U-series methods. The coupled ESR/U-series method was applied to 17 fossil teeth from different layers and it was possible to reconstruct the uranium migration history more precisely. The US-ESR age results of Longgupo fossil teeth range from ~2.2–2.5 Ma (Han et al., 2017), which confirms the site as one of the earliest evidences of hominin settlement in East Asia.

Jianshi

The Jianshi hominin site (also called Longgudong site, "dong" means cave in Chinese) is a cave site located in the west of Hubei Province, about 400 km west of Wuhan and 50 km south of Three Gorges (**Figure 2**). The specimens of *Gigantopithecus blacki* and three hominin teeth were discovered in 1970 (Gao, 1975; Li et al., 2017). The cave has two entrances, facing east and west, and the paleomagnetic dating work conducted by two teams gives different results and interpretations (Cheng et al., 2003; Shi, 2006), which made the age of Jianshi debatable. The fauna analysis and comparison with some Early Pleistocene sites of China indicate that Jianshi assemblage corresponds probably to an early stage of Early Pleistocene, younger than the Longgupo site nearby but older than Gongwangling and Yunxian sites (Zheng, 2004).

Our coupled ESR/U-series dating of two mammalian fossil teeth from the lower layer 8 gives a weight mean age of 1,521 ± 92 ka, while another two teeth from the upper layer 4 yield a mean age of 1,052 ± 49 ka (Han et al., submitted). Our ESR/U-series dating results are younger than previous paleomagnetic dating interpretation which proposes that the hominin fossil layer in the Jianshi site was older than the Reunion event (>2.14 Ma) (Cheng et al., 2003), but in agreement with the fauna record which suggests Jianshi is younger than the neighboring Longgupo site dated by the ESR/U-series method and paleomagnetism (Han et al., submitted).

Meipu

The Meipu site is located in Meipu Commune, Yunxian County, Hubei Province (about 90 km northeast of Yunxian Man site) (**Figure 2**). Four human teeth were found in 1975 and during the excavations in the following years, including two incisors, one molar, and one premolar. The human teeth fossils show similarity with Zhoukoudian *Homo erectus* teeth according to Wu and Dong (1980). More than 20 species of mammalian fossils and one stone core were also unearthed with the human fossils. Most of the species found in the Meipu site belong to *Ailuropoda–Stegodon* fauna typical in South China. The identified fossils also include *Gomphotherium* and *Hyaena brevirostris licenti*, which indicates a late Early Pleistocene to early Middle Pleistocene age.

The deposition in the Meipu cave was divided into three layers: the upper flowstone layer (~0.3 m thick), the intermediate yellow sandy clay layer (~0.5–2.5 m thick), and the lower firm yellow deposit with small breccias (~0.6 m) (Xu, 1978). We carried out the coupled ESR/U-series dating study on nine fossil teeth collected from the intermediate layer where hominin remains were unearthed. The fossil dating provided two main age groups at 541 ± 48 ka and 849 ± 39 ka, respectively; the older age group is in agreement with the U-series age (>630 ka) of the flowstone overlying the fossil layer and the paleomagnetic data, which placed the Brunhes–Matuyama boundary in the fossil layer (Xing et al., 2021; Han et al., 2022). The reason for this age difference is probably caused by the U-content discrepancy in the enamel of the dated fossil samples. This study exhibits the limitation of ESR/U-series fossil dating and the importance of using multiple dating approaches when it is possible in order to identify the problematic ages (Han et al., 2022).

Yunxian (Quyuanhekou)

The Yunxian site is located on the fourth terrace of the left bank of the Han River in Hubei Province, China (**Figure 2**). The top of the terrace is about 50 m above the water level, and two deformed hominin skulls were discovered in its fluvial sediments in 1989 in association with a number of stone artifacts, including choppers, chopping tools, and bifaces. Most of them were made by the large gravels from the river beach (Li and Etler, 1992). Abundant

animal fossils were found in the site and showed a mixing of typical species from both North and South China, which may indicate the geographic barrier of the Qinling Mountains was not formed sufficiently to hinder the migration of mammals. The fauna assemblage of the Yunxian site exhibits the similarity with the Lantian Gongwangling site in Shaanxi Province, which represents a typical Early Pleistocene record (Dong, 2016).

Initial paleomagnetic dating of the Yunxian Man site placed the hominin layer at 870–830 ka (Yan, 1993). A subsequent ESR dating study of nine fossil teeth from the fossil layer 3 by assuming the EU model for age calculation gave a mean age of 581 ± 93 ka (Chen et al., 1997), and the authors argued that the ESR ages were underestimated due to the very high U-content in enamel. Magnetostratigraphic study of the geological section of the Yunxian site was resumed in 2000 by a Sino-French archaeological team, and the B/M boundary was observed on the top of the stratigraphic sequence. Based on this study, the archaeological layer of the Yunxian site was placed at 936 ka (de Lumley and Li, 2008). The succeeding chronological studies of the Yunxian Man site conducted an ESR/U-series dating work on two herbivorous teeth from the hominin layer and the quartz sands from the fluvial sediment of the fossil layers and obtained a mean age of 1.10 ± 0.16 Ma, which confirmed the Early Pleistocene age of the Yunxian Man site (Tissoux et al., 2008). Recent studies of the ESR fossil dating show that the single saturation exponential function commonly used for paleodose determination of fossil enamel samples will cause dose overestimation (Duval and Grün, 2016), and the U-series analysis of Yunxian samples also indicate the possibility of uranium leaching in the dental tissues. Therefore, aforementioned ESR/U-series dating results of the Yunxian samples should be considered as the maximum age of the site (Bahain et al., 2017).

Bailong Cave

The Bailong Cave site (called "Bailongdong" in Chinese), discovered in 1976, was located in Yunxi County, Hubei Province (**Figure 2**). Six human teeth were found in the excavation of the 1970s and 1980s, and one more tooth unearthed in 2008. Several mammalian teeth collected from the hominin fossil layer were dated by the coupled ESR/U-series dating method (Han et al., 2019). Both gamma and beta external dose rates were reconstructed from the laboratory analysis of the sediment around the fossil samples. This may sometimes cause the bias of the gamma dose estimation due to the heterogeneous depositional environment of the site. In order to reconstruct the external dose rate of the dated samples more precisely, we therefore revisited the site in 2019 in order to realize *in situ* gamma dose measurement using a portable gamma spectrometer. The sample ages were recalculated with the new measured *in situ* dose rate values.

The recalculated ESR/U-series ages of the fossil samples from the Bailongdong site were generally older than the ones in the previous study from 5.6% to 25.4%. This is due to the *in situ* measured gamma dose rates by portable gamma spectrometer, which were significantly lower than the values measured in the laboratory by HpGe gamma spectrometer between 19.3% and 47.6% (**Supplementary Table S2**). Although the updated ESR/U-series ages of Bailongdong fossil samples became older as a whole, they are still in agreement with the cosmogenic $^{26}Al/^{10}Be$ burial age of the quartz sands and gravels from the sediment beneath (<0.76 ± 0.06 Ma) (Liu et al., 2015), the mid-Middle Pleistocene age of the fauna record (Tong et al., 2019) and the magnetostratigraphic results which dates the hominin-bearing layer to the early Brunhes Chron (Kong et al., 2018). The ESR/U-series dating of the Bailongdong site reemphasized; hence, the importance of the *in situ* measurement of the external gamma dose for the fossil age calculation.

Changyang

The Changyang hominin site, a cave site in Changyang County, Hubei Province, is located about 40 km south of the Yangtze River (**Figure 2**). A maxillary fragment was first discovered in 1956 by a local farmer, and a lower human premolar and abundant mammalian fossils were found in 1957 during the following investigation of the IVPP team. The morphological features of the Changyang hominin fossils were described by Chia (1957) and were considered close to the modern human than Zhoukoudian *Homo erectus*. Changyang was the first Middle Pleistocene hominin site discovered in South China, and an initial dating study by alpha-spectrometer U-series analysis of two fossil teeth gives the ^{230}Th age of 196 ± $^{20}/_{17}$ ka and 194 ± $^{24}/_{20}$ ka, respectively (Yuan et al., 1986). Most recent re-dating work on carbonate crystals and tooth fossils by the ICP-MS U-series technique suggests the age of Changyang site range from 196 to 143 ka, which conforms with the previous results (Lu et al., 2020). As the U–Th analysis of the fossil bone could only obtain the apparent age because of its open system behavior, coupled ESR/U-series dating study of the fossil teeth from the site is currently underway in order to establish a more reliable chronology of the Changyang hominin site.

Yumidong

The Yumidong Cave, about 4 km southwest of the Longgupo site, is located in Miaoyu Town, Wushan County, Chongqing Municipality (**Figure 2**). The site is a horizontal limestone cave with a skylight about 3 m in diameter, at ~20 m distance from the cave entrance. The site was discovered in 2004 and a large number of stone artifacts and mammalian fossils were unearthed during the excavations conducted in 2011–2013 (Wei et al., 2017).

The cave deposits are mainly composed of brown karstic sandy clay and limestone breccia and the stratigraphic sequence was divided into five layers initially by Wei et al. (2017) and further subdivided in detail into 18 layers (Shao et al., 2022). Two fossil teeth and three calcite samples collected from Layer 2, 3 and 4 were dated by the U-series method at the University of Queensland, the tooth sample from Layer 2 gives an age of ~8.4 ka, while another tooth sample and one calcite sample from Layer 3 were dated to ~78.5 ka and ~75.2 ka, respectively. The other two calcite samples from Layer four yield distant U-series ages of 198 ± 51 ka and 398 ± 30 ka, respectively, and put the deposits of the Yumidong site range from ~400 ka to ~ 8 ka (Wei et al., 2017).

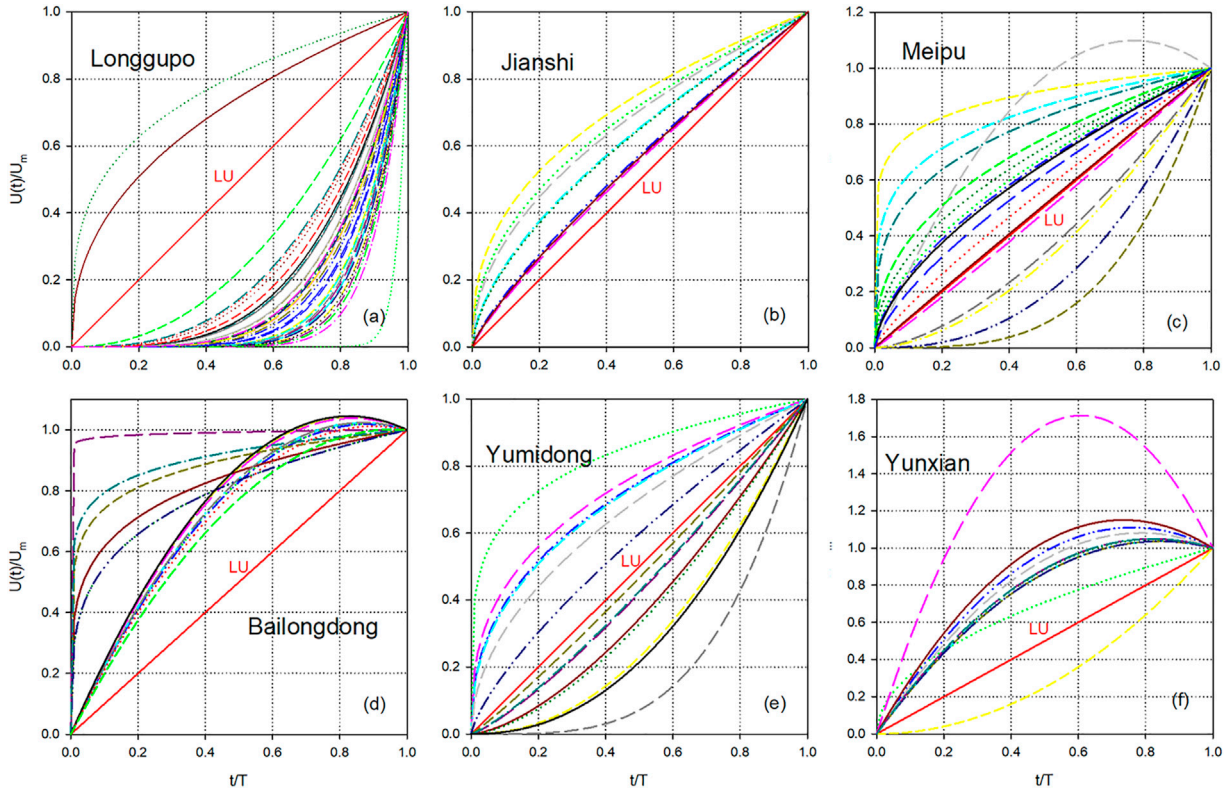

FIGURE 3 | Uranium migration process of the dated fossil samples by the ESR/U-series method from six sites in the Three Gorges region reconstructed by US (*p*-value) or AU model (*n*-value) (the U-uptake history of both enamel and dentine tissues of each sample from the site were present in the same figure with different colors.

To better constrain the chronology of the Yumidong depositional sequence, a multimethod dating study was realized including coupled ESR/U-series analyses on six fossil teeth from L2 to L12, and a Bayesian approach was used to refine the chronostratigraphy of the Yumidong site (Shao et al., 2022). Based on this study, a ~300 ka long history of human occupation in the Yumidong site was established, and it indicates a continuous human settlement in the TGR during cold and warm stages from late Middle Pleistocene to the Late Pleistocene period.

Xinglong Cave

Xinglong Cave, located about 90 km south of the Yangtze River in Fengjie County, Chongqing municipality (**Figure 2**), was discovered in 2001 by a Chinese expedition team (Gao et al., 2004). One human molar was unearthed from the site, and an engraved tusk of *Stegodon orientalis* was found in the same layer. It was considered the intentional engravings and may relate to the earliest art form in East Asia.

The deposition of Xinglong Cave was divided into six layers, and more than 50 species of mammalian fossils and 20 stone artifacts came from layer 2, which bears the human remains. The fauna assemblage suggests a late Middle Pleistocene age of the Xinglong site, and U-series analysis of the enamel and dentine tissues from a molar of *Stegodon orientalis* gave the age of the cultural layer of the Xinglong site between 120 and 150 ka (Gao et al., 2004). The updated U-series ages obtained by MC-ICPMS dating on the flowstone samples collected above and beneath the fossil layer show the weighted mean of 129 ± 5 ka and 199 ± 16 ka, respectively, which could bracket the age of the human remains in Xinglong Cave (Peng et al., 2014). In future, direct dating of the fossil teeth from the human fossil-bearing layer by coupled ESR/U-series method may constrain the age of the Xinglong site more precisely.

RESULTS AND DISCUSSION

The ESR/U-series ages and modeled uranium uptake history of five hominin sites in the TGR (no hominin fossils found in the Yumidong site) are shown in **Table 1**; **Figure 3**. Not like our previously dated Paleolithic open sites in the Nihewan Basin, which has intensive surface erosion and complex hydrodynamic conditions that may cause repeat U uptake and loss in the dental tissues (Han et al., 2015), most of the hominin sites we analyzed in the TGR are cave sites with a geological limestone background except Yunxian Man site which is situated on Han river terrace. However, even preserved in a similar cave deposition environment, the fossil teeth collected in different caves show the distinct variation of the U-migration process. In the Longgupo site, the majority of the analyzed teeth display a very recent U-uptake history ($p > 0$) (**Figure 3A**), which may

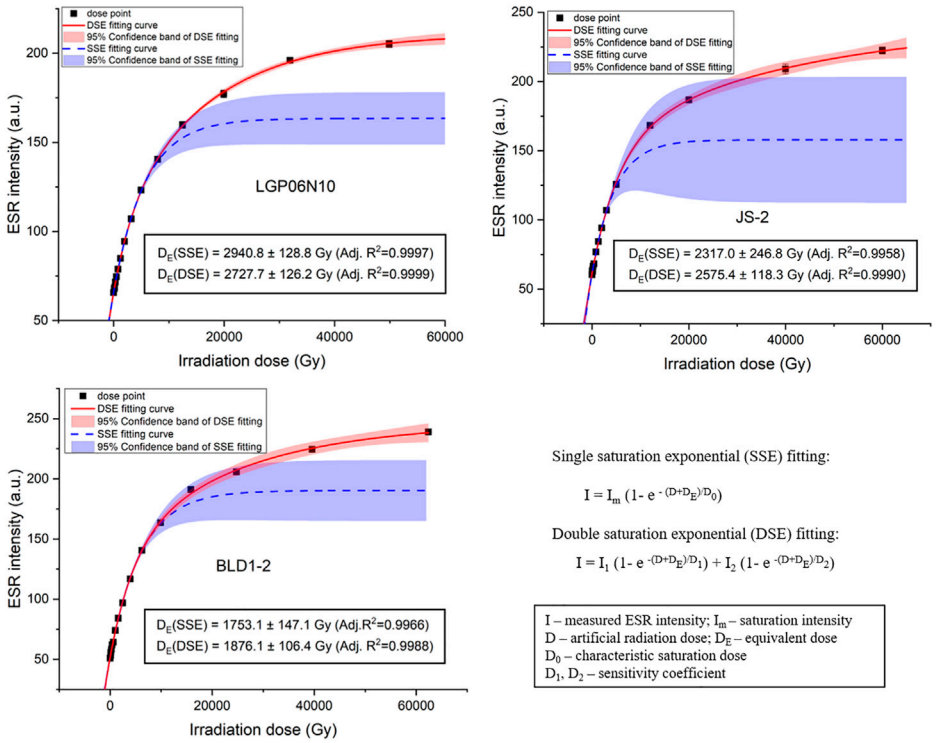

FIGURE 4 | Equivalent dose (D_E) of fossil samples from Three Gorges sites (LGP06N10 from the Longgupo site, JS-2 from Jianshi site, and BLD1-2 from Bailongdong site) determined by single saturation exponential (SSE) function (blue-dashed line and confidence band) with 10 dose points up to 5 kGy and double saturation exponential (DSE) function (red solid line and confidence band) with 15 dose points up to 60 kGy.

indicate a dramatic hydrological change during the Last Pleistocene in relation with the collapse of the cave ceiling, making the Longgupo site look like a fissure site rather than a cave nowadays (Rasse et al., 2011; Han et al., 2012, 2017). The *p*-values of four teeth from the Jianshi cave range between −1 and 0, which indicate a relatively early uptake of uranium in the dental tissues (**Figure 3B**) (Han et al., submitted). The fossil samples from the youngest Yumidong site show different uranium uptake behaviors which both relatively early and recent uptake history were indicated by *p*-values (**Figure 3E**) (Shao et al., 2022). Three fossil samples from the Bailongdong site exhibit early U-uptake history, while the other five experienced U loss based on their U-series data, and the ESR/U-series ages can be obtained only using the AU model (**Figure 3D**) (Han et al., 2019). The Meipu samples have the most variable U-migration history in which early, recent, and approximately linear uptake of uranium were all present, and the dentine tissue of one sample also exists in the U-loss (**Figure 3C**) (Han et al., 2022). Last, the only site with an open environment in this study—the Yunxian site displays an obviously different U-migration history from other sites, in which the uranium leaching process was present in all the fossil samples except one (Bahain et al., in progress) (**Figure 3F**). The coupled ESR/U-series analysis of teeth from the aforementioned sites indicates that there is no certain rule of uranium migration history in the fossil teeth even from the same site. The fossil teeth ESR ages of a majority of hominin sites in China obtained previously by assuming specific U-uptake models, in which the uptake history was postulated (e.g., EU and LU models) should be cited with great caution and need to be re-evaluated in the future.

Which Fitting Function Should be Used for D_E Determination?

In the early study of ESR dating, the single saturation exponential fitting (SSE) function was commonly used for D_E determination. It is based on the assumption of the exponential growth of a single paramagnetic center with the increase of radiation dose. The fossil teeth fragment ESR study in recent years indicates that the ESR signal of enamel tissues is generated by at least two CO_2^- radicals, which has different dose responses with natural and artificial radiation. A double saturation exponential (DSE) function which was first used for the coral samples has been proposed for the D_E determination of fossil enamel, and it has been proven to fit the dose points better than SSE, especially for the old fossil samples (Duval et al., 2009; Han et al., 2011). However, in order to use the DSE function for D_E determination, it needs at least 15 aliquots and irradiated with a high maximum dose (>10 kGy) to ensure the fitting precision, which is difficult to be achieved sometimes by the small fossil teeth and irradiation facilities without a well-established calibration curve in the high dose range. To find the better fitting function for D_E determination, we compared the goodness of fit of two functions quantitatively by analyzing the fossil enamel samples from the Early and Middle Pleistocene sites in the TGR. For the Early Pleistocene sites

of Longgupo and Jianshi, our study shows that the DSE function indeed fits the dose points better than the SSE one in case the requisite of 15 aliquots irradiated up to 50 kGy can be met. For the Middle Pleistocene sites, the D_E are usually less than 2,000 Gy, it could be obtained by irradiating 10 aliquots up to 5 kGy, and the fitting results are in consistent with the DSE ones in the error range (**Figure 4**). According to our study, the conventional SSE fitting function could provide a reliable D_E in case the maximum irradiation dose is no more than 5 kGy, and it has an advantage over DSE function when the sample volumes are limited and could be only divided into less than 15 aliquots.

Reconstruction of the External Dose Rate

The reconstruction of the external dose rate of the fossil teeth which are contributed by the surrounding sediments in their burial environment is crucial for obtaining reliable ESR/U-series age. The reliability of the fossil ages was greatly affected by the external dose rate, particularly in the case that the external dose rate account for a large portion of the total dose rate. However, the accuracy of external dose rate reconstruction was hindered by several cases mentioned as follows: 1) the absence of the provenance information of the fossil samples. This is the worst situation for reconstructing the external dose and making it even impossible. However, it is not an uncommon situation, especially for some hominin sites in China excavated in the early years, in which detailed records of the position of the archaeological remains were lacking. Fortunately, the fossil teeth from the Three Gorges sites we used for coupled ESR/U-series dating were all collected *in situ* or from the formal excavation with definite unearthed position records, which significantly reduces the uncertainty of external dose rate reconstruction; 2) inaccessibility of the fossil section or incapability to provide *in situ* dose rate measurement. This issue may be due to natural or man-made causes such as the rainy season (Han et al., 2019) or road construction, in which the original section did not survive (Han et al., 2016). In most cases, revisiting the site is necessary to fulfill or refine the *in situ* measurement, and only in this way more reliable ESR/U-series ages of the fossil samples could be obtained, like our dating work on Longgupo (see the impact on results in Han et al., 2012, 2017) and Bailongdong sites (Han et al., 2019, this study); and 3) the inhomogeneous deposition environment in the surrounding area of the dated fossil samples. This is the most common case in the archaeological sites in which different kinds of deposits and remains were present in the fossil layer, and make it a typical "lumpy" environment. Some scholars proposed different ways to stimulate the gamma dose rates in such environment (Brennan et al., 1997; Nathan and Grün, 2003) and model the external dose rates variation by the absorption of uranium in the surrounding fossil fragments (Blackwell and Blickstein, 2000; Guibert et al., 2009). However, none of them could completely replace the *in situ* measurement with a portable gamma spectrometer or TL dosimeter, and sometimes measuring the gamma dose rate in variable positions surrounding the dated fossil sample and using the averaged values for the age calculation is the most straightforward way. In the case *in situ* measurement is not possible, the sediment attached on the surface of the fossil may provide the only choice for external dose rate reconstruction, and the distribution of gamma dose rates may be discussed in order to give a reasonable range of the fossil ESR/U-series ages (Duval et al., 2019).

The ESR isochron dating of the fossil teeth may be another solution for the external dose rate reconstruction. It plots the D_E vs. internal dose rate of several subsamples from one single tooth to build the isochron, the intercept is the external dose the fossil sample received from the surrounding sediments, and the slope of the isochron could give the fossil age (Blackwell and Schwarcz, 1993). To build an ideal isochron, it needs the subsamples to experience the same external dose during the burial history and have a discrepancy of uranium content in the enamel tissue; the variation of the internal dose rate of subsamples ensures the precision of isochron construction. Most of the isochron ESR dating studies were realized through the EU and LU models for calculating the internal dose rate of subsamples (Blackwell and Blickstein, 2000; Blackwell et al., 2016).

We have tried to combine the US model with the isochron technique to calculate the isochron age of five fossil samples from the adjacent squares in layer C III′6 of the Longgupo site (Han et al., 2012). It should be noted that the assumption of applying the isochron method on the fossil teeth is that all the subsamples analyzed shared the same external dose rate. However, the external dose rate not only includes the gamma dose rate from the surrounding sediments which is considered identical to the subsamples but also the beta dose rate which is contributed by the beta radiation (attenuation depth ~2 mm) from the sediments attached on the surface of enamel (or cementum if existing). This beta dose rate component may vary from each subsample, which makes their external dose rate not exactly the same. That might explain why the isochron does not works so well in some cases even though the subsamples were collected from the same place and have variable U contents.

Uranium Distribution in the Enamel

During our ESR/U-series dating study on the fossil teeth from the Three Gorges sites, the age results of some of the samples were obviously underestimated (Han et al., 2022), and it could not be attributed to a problematic D_E determination or a bias linked to the external dose rate estimation. We observed that in such cases the U content in the enamel tissues was often much higher than in other samples even about one order, and it could not be explained simply to the contamination of dentine tissues on the enamel surface because the D_E value is generally high and dentine contribute little to the ESR signal and D_E. Bahain et al. (1992) noticed the high U content in the enamel samples of Isernia, Italy, and they supposed that uranium is concentrated in the impure zones of the enamel, which capture the most electrons created by ionization, and this may lead to inverse correlation of the U concentration and alpha efficiency due to the irradiation sensitivity change. Chen et al. (1997) also mentioned the similar situation of high U-content in Yunxian enamel samples and suggested that it may cause the age underestimation by micro-regional saturation of the paramagnetic centers in the enamel. The fossil dating works were carried out again in the years later on the aforementioned two sites by the coupled ESR/U-series method (Shao et al., 2011; Bahain et al., 2017; Bahain et al., 2021, in progress). Although the age underestimation of Isernia was considered to be mainly attributed to the variation of the environmental gamma dose rate related to the recent

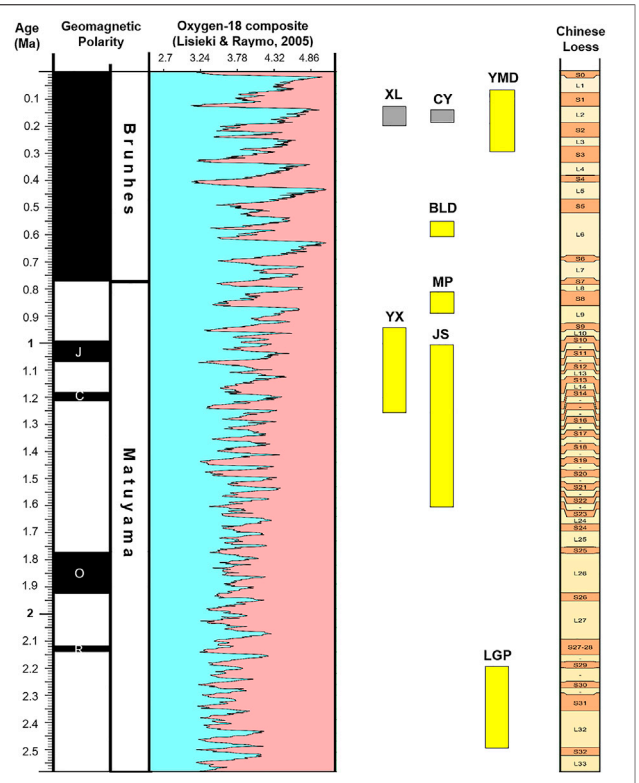

FIGURE 5 | Chronological and paleoenvironmental summary of the hominin sites in the TGR dated by radiometric methods. The age bars with golden color are obtained by the coupled ESR/U-series method, and the gray color was yielded by other radiometric dating methods (the chart was generated by TimeScale Creator GTS 2020).

U-uptake of bones in the archaeological level, the Yunxian fossil samples again show very high uranium concentration in the enamel samples and significantly younger than the paleomagnetic results. This is also the case of Meipu samples we analyzed in the recent study (Han et al., 2022), the distribution of ESR/U-series ages of fossil samples collected from the same fossil layer was divided into two groups, and the younger one with much high enamel U-content was obviously underestimated based on another independent age constraint. In recent years, the laser ablation ICP-MS technique was developed to investigate the spatial distribution of uranium in dental tissues (Grün et al., 2014). However, at present high-resolution U-series data could be obtained only on the flat cross-section of the fossil teeth. Few studies of uranium distribution were carried out on the irregular surface of the enamel, and the non-destructive 3D U-mapping may help to select the optimal part of the enamel with low uranium concentration for the further dating study.

Combined Multiple Dating Techniques Approach

The dating study of hominin sites in the TGR does show the great potential of the ESR dating method. However, the limitation of ESR/U-series dating on fossil teeth was also discussed above in order to call attention to the questionable age results. If the sampling condition permits, applying multiple dating methods to different kinds of dating materials is preferable, and they could complement each other and eliminate the disadvantages and limits due to the assumption or requirement of the methods. The study of the Yumidong site shows clearly the advantages and interests of such multi-methods approach to provide a single unified chronological framework (Shao et al., 2022).

For the Early and Middle Pleistocene sites, cosmogenic $^{26}Al/^{10}Be$ burial dating on the quartz sands and gravels could be combined with coupled ESR/U-series dating on the fossil teeth. It was attempted to date Bailongdong and Meipu sites, but the extraction of quartz minerals in these two cave sites was tough due to the limestone background. U-series dating of the speleothem may constrain the age of the interested archaeological remains if their stratigraphic relationship could be clarified. In Meipu cave, the U-series dating of the flowstone layer overlain helps to identify the problematic ESR/U-series ages of the fossil teeth samples from the fossil layer beneath (Han et al., 2022). Due to the open system behavior of fossil bones, their apparent U-series age should always be considered as the minimum age limit in the case of no U-loss occurred.

Archaeological Perspectives

At the time of writing this article, five archaeological sites with hominin fossils were dated by the coupled ESR/U-series method in the TGR and western Hubei area: Jianshi, Yunxian, Meipu, Bailongdong, and Changyang sites mentioned above. Although the phylogenetic status of the fossil specimen found in Longgupo and Jianshi sites on the hominin evolutionary relationship is still controversial, the morphological features of the hominin fossils from Yunxian, Meipu, Bailongdong, and Changyang sites do represent different stages of human evolution in East Asia, and the most recent study of the Meipu hominin fossil teeth shows their features are intermediate between early *Homo* specimens in Africa and Dmanisi in Georgia, and Middle Pleistocene hominins in East Asia which represent by Zhoukoudian *Homo erectus* (Xing et al., 2021). The two skulls from the Yunxian Man site were seriously deformed by the strata compression, and the reconstructions of the fossils by 3D virtual imaging techniques confirmed the specimens to *Homo erectus* and also indicate the variability of this species (Vialet et al., 2010). More detailed 3D reconstruction work of the Yunxian Man skulls is ongoing in order to specify their evolutionary position. The Bailongdong fossil specimens were also classified as *Homo erectus*, but the more in-depth morphological study was limited because only fossil teeth were found in the site. The Changyang hominin was classified previously as archaic *Homo sapiens* (Wu and Poirier, 1995), and recent studies of the premolar from Changyang specimen show the features aligned with Asian *Homo erectus* and probably indicate a late representative of an East Asian *Homo erectus* lineage (Pan et al., 2019). Due to its late Middle Pleistocene age and other non-*Homo erectus* evidence (Denisovans probably) found in China (e.g. Panxian Dadong, Tongzi and Xujiayao hominin sites), it may support a multi-lineage and discontinuous settlement of hominin in East Asia (Pan et al., 2020).

The lithic industry of the Longgupo site is difficult to compare with other sites in China because of its old age and the majority of

the raw materials of tools were cobbles or blocks of local limestone, which could explain the choice of variable operational processes and high rate of presence of knapping accidents (Boëda and Hou, 2011). In numerous of Middle–Late Pleistocene Paleolithic sites found in the TGR and Han River valley, the raw materials were selected water-rounded cobbles from the river beds, and the operative schemes of lithic production show continuity and stability (Pei et al., 2013), and distinct from those of the West, which suggest the Paleolithic cultures in this region may follow an independent trajectory (Li et al., 2014, 2018).

The distribution statistics of hominin sites in China from Early Pleistocene to Late Pleistocene show that the *Homo* sites during the period of Early Pleistocene were more restricted to central and southern China, and gradually present in the east and northern China since the Middle Pleistocene (Bae et al., 2018). This pattern may be driven by the paleoclimatic variation during the Early and early Middle Pleistocene and the ability to transport portable water. In the last two decades, some new hominin sites were discovered successively in the western Hubei and TGR (e.g., Huanglong Cave, Leiping, Migong, and Caotang sites) (Liu et al., 2006, 2010; Wu et al., 2006; Shen et al., 2013), more detailed excavation and dating works of the sites are still in progress. In a word, we believe that the TGR in central China which found abundant hominin sites from the Early Pleistocene to the Late Pleistocene may not only be the migration corridor of hominins and other mammals between southern and northern China, but probably also a diffusion center for the Middle and Late Pleistocene *Homo* appeared in the north and east of China (**Figure 5**).

CONCLUSION AND PERSPECTIVE

At present, the earliest hominin site in East Asia is the Yuanmou site in Yunnan Province, South China. It was dated to ~ 1.7 Ma by the paleomagnetic method (Zhu et al., 2008), and this age was recently confirmed by cosmogenic $^{26}Al/^{10}Be$ isochron burial dating in a recent study (Luo et al., 2020). In North China, although there is still a debate about the age of the Lantian Man site, which was dated about 1.6 Ma by $^{26}Al/^{10}Be$ burial dating (Tu et al., 2017), some recent discoveries and restudies of the paleolithic sites do show the early evidence of hominin settlement at the early stage of Early Pleistocene (Shangchen, ~ 2.12 Ma, Zhu et al., 2018; Xihoudu, ~2.43 Ma Shen et al., 2020). Although we could not entirely exclude the possibility that a separate migration route may exist along the high latitude area in North China during the Early and Middle Pleistocene, our chronological studies of the hominin sites in the TGR indicate that the hominin activities already existed in this corridor zone between South and North China during the Early Pleistocene period. The Longgupo site, though the fossil species identification is still in debate (Dalton, 2009), the stone artifacts with distinct characters and the updated ESR/U-series age of the site at ~2.2–2.5 Ma make it as old as the earliest evidence in North China. Other hominin sites of the Early Pleistocene age have also been discovered in recent years in South China, some of them were found associated with another giant primate—*Gigantopithecus blacki* in the same living place, and coupled ESR/U-series dating on the mammalian fossil teeth has shown a great potential to apply on these cave sites. The combination of ESR measurement of the enamel fragment and Laser-ablation ICP-MS analysis of the dental tissues highlight the possibility of minimum or non-destructive analysis of the precious human fossils, with accurate and detailed measurement of the external dose rate of the fossil specimen, the ESR dating method will continue to make a significant contribution to our understanding of the history of human evolution in China and East Asia.

DATA AVAILABILITY STATEMENT

The original contributions presented in the study are included in the article/**Supplementary Material**; further inquiries can be directed to the corresponding author.

AUTHOR CONTRIBUTIONS

FH and J-JB conducted the ESR/U-series dating work of the fossil teeth samples from Longgupo, Jianshi, Meipu, Yunxian, and Bailongdong sites, and FH wrote the first draft; QS conducted the ICP-MS U-series analysis and dating work of Yumidong site; XS conducted the dating study of Changyang site; J-JB and PV conducted the *in situ* gamma dose rate measurement; and PX and MH assisted in illustration and text processing. All authors participated in compiling the manuscript.

FUNDING

This work is supported by the National Natural Science Foundation of China (Grant nos. 41772174 and 41877430), the NSFC-CNRS Sino-French cooperation project (Grant no. 41911530235), the Sino-French Cai Yuanpei Program (Project no. 41378UF), and Yunnan Fundamental Research Project (Project no. 202201AT070211).

ACKNOWLEDGMENTS

Our thanks to Luo Yunbin, Lu Chengqiu, and He Cunding for their help with our field work. We thank Darryl Granger (Purdue University) for supporting the chemical separation and AMS measurement of ^{10}Be and ^{26}Al samples. We also thank Huili Yang (IGCEA) for helping the HpGe gamma spectrometer measurement of the sediment.

SUPPLEMENTARY MATERIAL

The Supplementary Material for this article can be found online at: https://www.frontiersin.org/articles/10.3389/feart.2022.939766/full#supplementary-material

REFERENCES

Bae, C. J., Li, F., Cheng, L., Wang, W., and Hong, H. (2018). Hominin Distribution and Density Patterns in Pleistocene China: Climatic Influences. *Palaeogeogr. Palaeoclimatol. Palaeoecol.* 512, 118–131. doi:10.1016/j.palaeo.2018.03.015

Bahain, J.-J., Shao, Q., Han, F., Sun, X., Voinchet, P., Liu, C., et al. (2017). Contribution des méthodes ESR et ESR/U-Th à la datation de quelques gisements pléistocènes de Chine. *L'Anthropologie* 121, 215–233. doi:10.1016/j.anthro.2017.06.001

Bahain, J.-J., Voinchet, P., Vietti, A., Shao, Q., Tombret, O., Pereira, A., et al. (2021). ESR/U-Series and ESR Dating of Several Middle Pleistocene Italian Sites: Comparison with $^{40}Ar/^{39}Ar$ Chronology. *Quat. Geochronol.* 63, 101151. doi:10.1016/j.quageo.2021.101151

Bahain, J.-J., Yokoyama, Y., Falguères, C., and Sarcia, M. N. (1992). ESR Dating of Tooth Enamel: A Comparison with KAr Dating. *Quat. Sci. Rev.* 11, 245–250. doi:10.1016/0277-3791(92)90069-k

Bar-Yosef, O., Eren, M. I., Yuan, J., Cohen, D. J., and Li, Y. (2012). Were Bamboo Tools Made in Prehistoric Southeast Asia? An Experimental View from South China. *Quat. Int.* 269, 9–21. doi:10.1016/j.quaint.2011.03.026

Blackwell, B. A. B., and Blickstein, J. I. B. (2000). Considering Sedimentary U Uptake in External Dose Rate Determinations for ESR and Luminescent Dating. *Quat. Int.* 68-71, 329–343. doi:10.1016/s1040-6182(00)00056-2

Blackwell, B. A. B., Skinner, A. R., Blickstein, J. I. B., Montoya, A. C., Florentin, J. A., Baboumian, S. M., et al. (2016). ESR in the 21st Century: From Buried Valleys and Deserts to the Deep Ocean and Tectonic Uplift. *Earth-Science Rev.* 158, 125–159. doi:10.1016/j.earscirev.2016.01.001

Blackwell, B. A., and Schwarcz, H. P. (1993). ESR Isochron Dating for Teeth: A Brief Demonstration in Solving the External Dose Calculation Problem. *Appl. Radiat. Isotopes* 44, 243–252. doi:10.1016/0969-8043(93)90227-2

Bocherens, H., Schrenk, F., Chaimanee, Y., Kullmer, O., Mörike, D., Pushkina, D., et al. (2017). Flexibility of Diet and Habitat in Pleistocene South Asian Mammals: Implications for the Fate of the Giant Fossil Ape Gigantopithecus. *Quat. Int.* 434, 148–155. doi:10.1016/j.quaint.2015.11.059

Boëda, É., and Hou, Y.-M. (2011). Étude du site de Longgupo Synthèse. *L'Anthropologie* 115, 176–196.

Brennan, B. J., Schwarcz, H. P., and Rink, W. J. (1997). Simulation of the Gamma Radiation Field in Lumpy Environments. *Radiat. Meas.* 27, 299–305. doi:10.1016/s1350-4487(96)00133-3

Chen, T.-M., Yang, Q., Hu, Y.-Q., Bao, W.-B., and Li, T.-Y. (1997). ESR Dating of Tooth Enamel from Yunxian homo Erectus Site, China. *Quat. Sci. Rev.* 16, 455–458. doi:10.1016/s0277-3791(96)00095-9

Cheng, J., Gao, Z., Zheng, S., Zhang, Z., Liu, L., Feng, X., et al. (2003). Study on the Sediments of the Longgu Cave with Gigantopithecus at Gaoping, Western Hubei, China. *Geoscience* 17 (3), 268–274. (In Chinese with English Abstract).

Cheng, J., Gao, Z., Zheng, S., Zhang, Z., Liu, L., Feng, X., et al. (2004). The Gaoping Formation—A New Stratigraphic Unit with the Gigantopithecus Fossils from West Hubei. *J. Stratigr.* 28, 223–229. (In Chinese with English Abstract).

Chia, L. P. (1957). Notes on the Human and Some Other Mammalian Remains from Changyang, Hupei. *Vertebr. Palasiat.* 1, 247–257.

Ciochon, R. L. (2009). The Mystery Ape of Pleistocene Asia. *Nature* 459, 910–911. doi:10.1038/459910a

Colbert, E. H., and Hooijer, D. A. (1953). Pleistocene Mammals from the Limestone Fissures of Szechwan, China. *Bull. Am. Mus. Nat. Hist.* 102, 1–134.

Dalton, R. (2009). Early Man Becomes Early Ape. *Nature* 459, 899. doi:10.1038/459899a

de Lumley, H., and Li, T. (2008). *Le site de l'homme de Yunxian, Quyuanhekou, Quingqu, Yunxian, Province du Hubei*. Paris: CNRS Éditions, 592.

Dennell, R. (2009). *The Palaeolithic Settlement of Asia*. Cambridge: Cambridge University Press.

Dong, W. (2016). Biochronological Framework of Homo Erectus Horizons in China. *Quat. Int.* 400, 47–57. doi:10.1016/j.quaint.2015.09.019

Duval, M., Fang, F., Suraprasit, K., Jaeger, J.-J., Benammi, M., Chaimanee, Y., et al. (2019). Direct ESR Dating of the Pleistocene Vertebrate Assemblage from Khok Sung Locality, Nakhon Ratchasima Province, Northeast Thailand. *Palaeontol. Electron* 22 (3), 69 1–25. doi:10.26879/941

Duval, M., and Grün, R. (2016). Are Published ESR Dose Assessments on Fossil Tooth Enamel Reliable? *Quat. Geochronol.* 31, 19–27. doi:10.1016/j.quageo.2015.09.007

Duval, M., Grün, R., Falguères, C., Bahain, J.-J., and Dolo, J.-M. (2009). ESR Dating of Lower Pleistocene Fossil Teeth: Limits of the Single Saturating Exponential (SSE) Function for the Equivalent Dose Determination. *Radiat. Meas.* 44, 477–482. doi:10.1016/j.radmeas.2009.03.017

Etler, D. A. (2009). Mystery Ape: Other Fossils Suggest that It's No Mystery at All. *Nature* 460, 684. doi:10.1038/460684a

Falguères, C., Bahain, J. J., Bischoff, J. L., Pérez-González, A., Ortega, A. I., Ollé, A., et al. (2013). Combined ESR/U-Series Chronology of Acheulian Hominid-Bearing Layers at Trinchera Galería Site, Atapuerca, Spain. *J. Hum. Evol.* 65, 168–184. doi:10.1016/j.jhevol.2013.05.005

Falguères, C., Bahain, J. J., Yokoyama, Y., Arsuaga, J. L., Bermudez de Castro, J. M., Carbonell, E., et al. (1999). Earliest Humans in Europe: The Age of TD6 Gran Dolina, Atapuerca, Spain. *J. Hum. Evol.* 37, 343–352. doi:10.1006/jhev.1999.0326

Gao, J. (1975). Australopithecine Teeth Associated with Gigantopithecus. *Certebrata Palasiat*. (In Chinese with English Abstract).

Gao, X., Huang, W. B., Xu, Z. Q., Ma, Z. B., and Olsen, W. (2004). 120-150 Ka Human Tooth and Ivory Engravings from Xinglongdong Cave, Three Gorges Region, South China. *Chin. Sci. Bull.* 48, 2466–2472. doi:10.1360/03wd0214

Gao, X., Liu, J.-H., Ruan, Q.-J., Ge, J., Huang, Y., Liu, J., et al. (2021). *300,000-Year-Old Wooden Tools from Gantangqing, Southwest China*. 16 February 2021, PREPRINT (Version 1) Available at Research Square. doi:10.21203/rs.3.rs-226285/v1

Grün, R., Pike, A., McDermott, F., Eggins, S., Mortimer, G., Aubert, M., et al. (2020). Dating the Skull from Broken Hill, Zambia, and its Position in Human Evolution. *Nature* 580, 372–375. doi:10.1038/s41586-020-2165-4

Grün, R., Eggins, S., Kinsley, L., Moseley, H., and Sambridge, M. (2014). Laser Ablation U-Series Analysis of Fossil Bones and Teeth. *Palaeogeogr. Palaeoclimatol. Palaeoecol.* 416, 150–167.

Grün, R. (1989). Electron Spin Resonance (ESR) Dating. *Quat. Int.* 1, 65–109.

Grün, R., Schwarcz, H. P., and Chadam, J. (1988). ESR Dating of Tooth Enamel: Coupled Correction for U-Uptake and U-Series Disequilibrium. *Int. J. Radiat. Appl. Instrum. Part D. Nucl. Tracks Radiat. Meas.* 14, 237–241.

Guibert, P., Lahaye, C., and Bechtel, F. (2009). The Importance of U-Series Disequilibrium of Sediments in Luminescence Dating: A Case Study at the Roc de Marsal Cave (Dordogne, France). *Radiat. Meas.* 44, 223–231. doi:10.1016/j.radmeas.2009.03.024

Han, F., Bahain, J.-J., Boëda, É., Hou, Y., Huang, W., Falguères, C., et al. (2012). Preliminary Results of Combined ESR/U-Series Dating of Fossil Teeth from Longgupo Cave, China. *Quat. Geochronol.* 10, 436–442. doi:10.1016/j.quageo.2012.03.006

Han, F., Bahain, J.-J., Deng, C., Boëda, É., Hou, Y., Wei, G., et al. (2017). The Earliest Evidence of Hominid Settlement in China: Combined Electron Spin Resonance and Uranium Series (ESR/U-Series) Dating of Mammalian Fossil Teeth from Longgupo Cave. *Quat. Int.* 434, 75–83. doi:10.1016/j.quaint.2015.02.025

Han, F., Bahain, J.-J., Liu, C., and Yin, G. (2015). Testing Mathematical Uranium Migration Models in Combined ESR/U-series Dating of Fossil Teeth from Open-Air Sites. *Quat. Geochronol.* 30, 519–523. doi:10.1016/j.quageo.2015.05.009

Han, F., Bahain, J.-J., Voinchet, P., Jin, M., and Yin, G. (2022). Radiometric Dating of Meipu Hominin Site in China by Coupled ESR/U-Series and Cosmogenic $^{26}Al/^{10}Be$ Burial Dating Methods. *Quat. Geochronol.*, 101295. doi:10.1016/j.quageo.2022.101295

Han, F., Bahain, J.-J., Voinchet, P., Shao, Q., and Yin, G. (2022). Dating the Northernmost Evidence of the Coexistence of Hominin and Gigantopithecus from Jianshi Longgudong Cave, China. *J. Hum. Evol.* (Submitted).

Han, F., Bahain, J.-J., Yin, G., and Liu, C. (2012). Combined ESR and U-Series Isochron Dating of Fossil Tooth from Longgupo Cave. *Nucl. Tech.* 35 (12), 923–928. (In Chinese with English Abstract).

Han, F., Shao, Q., Bahain, J.-J., Sun, X., and Yin, G. (2019). Coupled ESR and U-Series Dating of Middle Pleistocene Hominin Site Bailongdong Cave, China. *Quat. Geochronol.* 49, 291–296. doi:10.1016/j.quageo.2018.02.004

Han, F., Sun, C., Bahain, J.-J., Zhao, J., Lin, M., Xing, S., et al. (2016). Coupled ESR and U-Series Dating of Fossil Teeth from Yiyuan Hominin Site, Northern China. *Quat. Int.* 400, 195–201. doi:10.1016/j.quaint.2015.05.052

Han, F., Yin, G., Bahain, J.-J., Garcia, T., Liu, C., Gao, L., et al. (2011). The Influence of Different Fitting Functions on Paleodose Determination in ESR Dating of Tooth Enamel – Taking Longgupo Tooth Fossils as an Example. *Nucl. Tech.* 34 (2), 116–120. (in Chinese with English abstract).

Hershkovitz, I., Weber, G. W., Quam, R., Duval, M., Grün, R., Kinsley, L., et al. (2018). The Earliest Modern Humans Outside Africa. *Science* 359, 456–459. doi:10.1126/science.aap8369

Huang, W., Ciochon, R., Gu, Y., Larick, R., Qiren, F., Schwarcz, H., et al. (1995). Early Homo and Associated Artefacts from Asia. *Nature* 378, 275–278. doi:10.1038/378275a0

Huang, W., and Fang, Q. (1991). *Wushan Hominid Site*. Beijing: Ocean. (In Chinese with English Abstract).

Ingicco, T., van den Bergh, G. D., Jago-on, C., Bahain, J.-J., Chacón, M. G., Amano, N., et al. (2018). Earliest Known Hominin Activity in the Philippines by 709 Thousand Years Ago. *Nature* 557, 233–237. doi:10.1038/s41586-018-0072-8

Kong, Y., Deng, C., Liu, W., Wu, X., Pei, S., Sun, L., et al. (2018). Magnetostratigraphic Dating of the Hominin Occupation of Bailong Cave, Central China. *Sci. Rep.* 8, 9699. doi:10.1038/s41598-018-28065-x

Li, H., Li, C., and Kuman, K. (2017). Longgudong, an Early Pleistocene Site in Jianshi, South China, with Stratigraphic Association of Human Teeth and Lithics. *Sci. China Earth Sci.* 60, 452–462. doi:10.1007/s11430-016-0181-1

Li, T., and Etler, D. A. (1992). New Middle Pleistocene Hominid Crania from Yunxian in China. *Nature* 357, 404–407. doi:10.1038/357404a0

Li, Y., Sun, X., and Bodin, E. (2014). A Macroscopic Technological Perspective on Lithic Production from the Early to Late Pleistocene in the Hanshui River Valley, Central China. *Quat. Int.* 347, 148–162. doi:10.1016/j.quaint.2014.05.044

Li, Y., Zhou, Y., Sun, X., and Li, H. (2018). New Evidence of a Lithic Assemblage Containing *In Situ* Late Pleistocene Bifaces from the Houfang Site in the Hanshui River Valley, Central China. *Comptes Rendus Palevol* 17, 131–142. doi:10.1016/j.crpv.2015.12.005

Lisiecki, L. E., and Raymo, M. E. (2005). Pliocene-Pleistocene Stack of Globally Distributed Benthic Stable Oxygen Isotope Records, Supplement To: Lisiecki, LE; Raymo, ME (2005): A Pliocene-Pleistocene Stack of 57 Globally Distributed Benthic d18O Records. *Paleoceanography* 20, PA1003. doi:10.1029/2004pa001071

Liu, W., Gao, X., Pei, S., Wu, X., and Huang, W. (2006). Research Progress of Paleoanthropology in West Hubei and the Three Gorges Region. *Quat. Sci.* 26 (4), 514–521. (In Chinese with English Abstract).

Liu, W., Wu, X., Pei, S., Wu, X., and Norton, C. J. (2010). Huanglong Cave: A Late Pleistocene Human Fossil Site in Hubei Province, China. *Quat. Int.* 211, 29–41. doi:10.1016/j.quaint.2009.06.017

Liu, X., Shen, G., Tu, H., Lu, C., and Granger, D. E. (2015). Initial $^{26}Al/^{10}Be$ Burial Dating of the Hominin Site Bailong Cave in Hubei Province, Central China. *Quat. Int.* 389, 235–240. doi:10.1016/j.quaint.2014.10.028

Lu, C., Xu, X., and Sun, X. (2020). Re-Dating Changyang Cave in Hubei Province, Southern China. *Quat. Int.* 537, 1–8. doi:10.1016/j.quaint.2020.02.001

Luo, L., Granger, D. E., Tu, H., Lai, Z., Shen, G., Bae, C. J., et al. (2020). The First Radiometric Age by Isochron $^{26}Al/^{10}Be$ Burial Dating for the Early Pleistocene Yuanmou Hominin Site, Southern China. *Quat. Geochronol.* 55, 101022. doi:10.1016/j.quageo.2019.101022

Nathan, R., and Grün, R. (2003). Gamma Dosing and Shielding of a Human Tooth by a Mandible and Skull Cap. *Anc. TL* 21, 79–84.

Pan, L., Dumoncel, J., Mazurier, A., and Zanolli, C. (2020). Hominin Diversity in East Asia During the Middle Pleistocene: A Premolar Endostructural Perspective. *J. Hum. Evol.* 148, 102888. doi:10.1016/j.jhevol.2020.102888

Pan, L., Dumoncel, J., Mazurier, A., and Zanolli, C. (2019). Structural Analysis of Premolar Roots in Middle Pleistocene Hominins from China. *J. Hum. Evol.* 136, 102669. doi:10.1016/j.jhevol.2019.102669

Pei, S., Gao, X., Wu, X., Li, X., and Bae, C. J. (2013). Middle to Late Pleistocene Hominin Occupation in the Three Gorges Region, South China. *Quat. Int.* 295, 237–252. doi:10.1016/j.quaint.2012.04.016

Peng, H., Ma, Z., Huang, W., and Gao, J. (2014). $^{230}Th/U$ Chronology of a Paleolithic Site at Xinglong Cave in the Three-Gorge Region of South China. *Quat. Geochronol.* 24, 1–9. doi:10.1016/j.quageo.2014.07.001

Rasse, M., Huang, W., and Boëda, É. (2011). Le site de Longgupo dans son environnement géologique et géomorphologique. *L'Anthropologie* 115, 23–39. doi:10.1016/j.anthro.2010.11.001

Richardson, N. J., Densmore, A. L., Seward, D., Wipf, M., and Yong, L. (2010). Did Incision of the Three Gorges Begin in the Eocene? *Geology* 38, 551–554. doi:10.1130/g30527.1

Richter, D., Grün, R., Joannes-Boyau, R., Steele, T. E., Amani, F., Rué, M., et al. (2017). The Age of the Hominin Fossils from Jebel Irhoud, Morocco, and the Origins of the Middle Stone Age. *Nature* 546, 293–296. doi:10.1038/nature22335

Rink, W. J. (1997). Electron Spin Resonance (ESR) Dating and ESR Applications in Quaternary Science and Archaeometry. *Radiat. Meas.* 27, 975–1025. doi:10.1016/s1350-4487(97)00219-9

Schwartz, J. H., and Tattersall, I. (1996). Whose Teeth? *Nature* 381, 201–202. doi:10.1038/381201a0

Shao, Q., Bahain, J.-J., Falguères, C., Dolo, J.-M., and Garcia, T. (2012). A New U-Uptake Model for Combined ESR/U-Series Dating of Tooth Enamel. *Quat. Geochronol.* 10, 406–411. doi:10.1016/j.quageo.2012.02.009

Shao, Q., Bahain, J.-J., Falguères, C., Peretto, C., Arzarello, M., Minelli, A., et al. (2011). New ESR/U-Series Data for the Early Middle Pleistocene Site of Isernia la Pineta, Italy. *Radiat. Meas.* 46, 847–852. doi:10.1016/j.radmeas.2011.03.026

Shao, Q., Chadam, J., Grün, R., Falguères, C., Dolo, J.-M., and Bahain, J.-J. (2015). The Mathematical Basis for the US-ESR Dating Method. *Quat. Geochronol.* 30, 1–8. doi:10.1016/j.quageo.2015.07.002

Shao, Q., Philippe, A., He, C., Jin, M., Huang, M., Jiao, Y., et al. (2022). Applying a Bayesian Approach for Refining the Chronostratigraphy of the Yumidong Site in the Three Gorges Region, Central China. *Quat. Geochronol.* 70, 101304. doi:10.1016/j.quageo.2022.101304

Shen, G., Wang, Y., Tu, H., Tong, H., Wu, Z., Kuman, K., et al. (2020). Isochron $^{26}Al/^{10}Be$ Burial Dating of Xihoudu: Evidence for the Earliest Human Settlement in Northern China. *L'Anthropologie* 124, 102790. doi:10.1016/j.anthro.2020.102790

Shen, G., Wu, X., Wang, Q., Tu, H., Feng, Y.-x., and Zhao, J.-x. (2013). Mass Spectrometric U-Series Dating of Huanglong Cave in Hubei Province, Central China: Evidence for Early Presence of Modern Humans in Eastern Asia. *J. Hum. Evol.* 65, 162–167. doi:10.1016/j.jhevol.2013.05.002

Shi, L. F. (2006). Comments on "The Gaoping Formation——A New Stratigraphic Unit with the Gigantopithecus Fossils from West Hubei". *J. Stratigr.* 2. (In Chinese with English Abstract).

Sun, L., Deng, C. L., Liu, C. C., Ge, J. Y., Yang, S. X., Zhang, S., et al. (2022). Reassessing the Age of the Early Pleistocene Longgupo Fauna, Southern China: An Updated Magnetostratigraphic Perspective. *Quat. Int.* (Submitted).

Tissoux, H., Bahain, J. J., de Lumley, H., Li, T., Feng, X., and Li, W. (2008). *Le site de l'homme de Yunxian: Quyuanhekou, Qingqu, Yunxian, Province du Hebei*, 237–252. Essai de datation par les methods de la résonance paramagnétique électronique et du déséquillibre dans les familles de l'uranium combines (RPE/U-Th) de dents d'herbivores et par résonance paramagnétique électronique (RPE)

Tong, H. W., Zhang, B., Wu, X. Z., and Qu, S. M. (2019). Mammalian Fossils from the Middle Pleistocene Human Site of Bailongdong in Yunxi, Hubei. *Acta Anthropol. Sin.* 38 (4), 613–640. (In Chinese with English Abstract).

Tu, H., Shen, G., Granger, D., Yang, X., and Lai, Z. (2017). Isochron $^{26}Al/^{10}Be$ Burial Dating of the Lantian Hominin Site at Gongwangling in Northwestern China. *Quat. Geochronol.* 41, 174–179. doi:10.1016/j.quageo.2017.04.004

Vialet, A., Guipert, G., Jianing, H., Xiaobo, F., Zune, L., Youping, W., et al. (2010). Homo Erectus from the Yunxian and Nankin Chinese Sites: Anthropological Insights Using 3D Virtual Imaging Techniques. *Comptes Rendus Palevol* 9, 331–339. doi:10.1016/j.crpv.2010.07.017

Wei, C., Voinchet, P., Zhang, Y., Bahain, J.-J., Liu, C., Kang, C., et al. (2020). Chronology and Provenance of the Yichang Gravel Layer Deposits in the Jianghan Basin, Middle Yangtze River Valley, China: Implications for the Timing of Channelization of the Three Gorges Valley. *Quat. Int.* 550, 39–54. doi:10.1016/j.quaint.2020.03.020

Wei, G., Huang, W., Boëda, E., Forestier, H., He, C., Chen, S., et al. (2017). Recent Discovery of a Unique Paleolithic Industry from the Yumidong Cave Site in the Three Gorges Region of Yangtze River, Southwest China. *Quat. Int.* 434, 107–120. doi:10.1016/j.quaint.2014.11.048

R. K. Wu and J. W. Olsen (Editors) (1985). *Paleoanthropology and Paleolithic Archaeology in the People's Republic of China*. 1st ed. (Walnut Creek: Routledge). doi:10.4324/9781315423135

Wu, R. K., and Dong, X. R. (1980). The fossil human teeth from Yunxian, Hubei. *Vertebr. Palasiat.* 18, 142–179. (in Chinese with English abstract).

Wu, X., Liu, W., Gao, X., and Yin, G. (2006). Huanglong Cave, a New Late Pleistocene Hominid Site in Hubei Province, China. *Chin. Sci. Bull.* 51, 2493–2499. doi:10.1007/s11434-006-2125-x

Wu, X. Z., and Poirier, F. E. (1995). *Human Evolution in China: A Metric Description of the Fossils and a Review of the Sites*. New York: Oxford University Press.

Xiang, F., Huang, H., Ogg, J. G., Zhu, H., and Kang, D. (2020). Quaternary Sediment Characteristics and Paleoclimate Implications of Deposits in the Three Gorges and Yichang Areas of the Yangtze River. *Geomorphology* 351, 106981. doi:10.1016/j.geomorph.2019.106981

Xing, S., Martinón-Torres, M., Deng, C., Shao, Q., Wang, Y., Luo, Y., et al. (2021). Early Pleistocene Hominin Teeth from Meipu, Southern China. *J. Hum. Evol.* 151, 102924. doi:10.1016/j.jhevol.2020.102924

Xu, C. H. (1978). "The Excavation at Fossil Hominin Site of Yunxian, Hubei," in *Proceedings of Paleoanthropology* (Beijing: Science Press), 175–179. (In Chinese).

Yan, G. L. (1993). A Preliminary Study on Magnetic Stratigraphy of the Geological Section with the Fossil Bed of *Yunxian Homo* of Hubei. *Earth Sci. – J. China Univ. Geosciences* 18 (2), 221–226. (In Chinese with English Abstract).

Yuan, S. X., Chen, T. M., and Gao, S. J. (1986). Uranium Series Chronological Sequence of Some Palaeolithic Sites in South China. *Acta Anthropol. Sin.* 5, 179–190. (In Chinese with English Abstract).

Zhang, Z., Daly, J. S., Li, C. a., Tyrrell, S., Sun, X., Badenszki, E., et al. (2021). Formation of the Three Gorges (Yangtze River) No Earlier Than 10 Ma. *Earth-Science Rev.* 216, 103601. doi:10.1016/j.earscirev.2021.103601

Zheng, H., Clift, P. D., Wang, P., Tada, R., Jia, J., He, M., et al. (2013). Pre-Miocene Birth of the Yangtze River. *Proc. Natl. Acad. Sci. U.S.A.* 110, 7556–7561. doi:10.1073/pnas.1216241110

Zheng, S. H. (2004). Jianshi Hominid Site. In *Series Monograph I 412*. Beijing: Science Press. (In Chinese with English Abstract).

Zhu, R. X., Potts, R., Pan, Y. X., Yao, H. T., Lü, L. Q., Zhao, X., et al. (2008). Early Evidence of the Genus Homo in East Asia. *J. Hum. Evol.* 55, 1075–1085. doi:10.1016/j.jhevol.2008.08.005

Zhu, Z., Dennell, R., Huang, W., Wu, Y., Qiu, S., Yang, S., et al. (2018). Hominin Occupation of the Chinese Loess Plateau Since About 2.1 Million Years Ago. *Nature* 559, 608–612. doi:10.1038/s41586-018-0299-4

Conflict of Interest: The authors declare that the research was conducted in the absence of any commercial or financial relationships that could be construed as a potential conflict of interest.

frontiers | Frontiers in Earth Science

TYPE Original Research
PUBLISHED 04 August 2022
DOI 10.3389/feart.2022.933342

OPEN ACCESS

EDITED BY
Hui Zhao,
Chinese Academy of Sciences (CAS), China

REVIEWED BY
Jun Peng,
Hunan University of Science and Technology, China
Jie Chen,
China Earthquake Administration, China

*CORRESPONDENCE
Anchuan Fan,
anchuan@ustc.edu.cn

SPECIALTY SECTION
This article was submitted to Quaternary Science, Geomorphology and Paleoenvironment, a section of the journal Frontiers in Earth Science

RECEIVED 30 April 2022
ACCEPTED 11 July 2022
PUBLISHED 04 August 2022

CITATION
Wang C-X, Zhang X, Zhang Y, Wu Y, Huang C and Fan A (2022), Luminescence dating of heated quartz extracted from burnt clay and pottery excavated from the Lingjiatan archaeological site, China. *Front. Earth Sci.* 10:933342. doi: 10.3389/feart.2022.933342

Luminescence dating of heated quartz extracted from burnt clay and pottery excavated from the Lingjiatan archaeological site, China

Chun-Xin Wang[1,2], Xiaolei Zhang[3], Yunyi Zhang[1,2], Youjin Wu[1,2], Chang Huang[4] and Anchuan Fan[1,2]*

[1]USTC Archaeometry Laboratory, University of Science and Technology of China, Hefei, China, [2]Department for the History of Science and Scientific Archaeology, University of Science and Technology of China, Hefei, China, [3]Anhui Provincial Institute of Cultural Relics and Archaeology, Hefei, China, [4]Department of Earth Sciences, The University of Hong Kong, Hong Kong, China

This study utilizes OSL-SAR, TL-SAR, and TL-MAAD methods to date heated quartz extracted from burnt clay and pottery samples from the Lingjiatan archaeological site, China. The OSL components of the heated quartz were determined by deconvoluting the CW-OSL curve, and the Fast Ratio value was used to distinguish whether the initial OSL signal was dominated by the fast component. The results show two types of quartz OSL characteristics in the initial signals: Type I is dominated by the fast component (Fast Ratio values > 10), while Type II is dominated by the medium and slow components (Fast Ratio values < 10). Type I samples show bright OSL signals, and a preheat plateau appears from a relatively low temperature. The recuperation is negligible, and reliable equivalent doses can be obtained using the conventional OSL-SAR measurement conditions. In contrast, the OSL signal of Type II samples is relatively dim, and the preheat plateau appears from a much higher temperature than in Type I samples. The recuperation of Type II samples increases significantly at higher preheat temperatures. Significant D_e underestimation of Type II samples was observed at lower preheat temperatures. It is noted that the thermal transfer effect can be attenuated by increasing the OSL stimulation temperature. Therefore, a modified OSL-SAR measurement condition, with higher preheat, cut-heat and stimulation temperatures, was used to date Type II samples. The OSL-SAR ages of most of these two types of samples agree well with the independent ^{14}C ages, demonstrating that OSL-SAR can be used to date heated archaeological materials at high firing temperatures (~900°C). The Lingjiatan archaeological site was determined to be approximately 5.4–5.8 ka BP $_{2022}$.

KEYWORDS

OSL component, age underestimation, heated quartz, luminescence dating, lingjiatan site

1 Introduction

Since the 1960s, Aitken has utilized thermoluminescence (TL) dating to determine the time of the last heating event of heated archaeological materials (Aitken et al., 1964, Aitken et al., 1968). In the past 2 decades, the single aliquot regenerative dose optically stimulated luminescence (OSL-SAR) dating protocol has been proven to be a robust approach in sediment dating (Murray and Wintle, 2000; Wintle and Murray, 2006; Murray et al., 2021). Archaeologists started to apply the OSL-SAR method to date heated archaeological materials, such as pottery, brick, tile, heated lithic (flint or stone), burnt clay, kiln, metallurgical slag, etc. (Gautier, 2001; Bailiff, 2007; Liritzis et al., 2016; Richter et al., 2017; Zander et al., 2019; Sun et al., 2021; Wang et al., 2022). The OSL signal can be deconvolved into components with different decay rates (Huntley et al., 1996; Bailey et al., 1997; Bulur, 2000; Jain et al., 2003), and they have different characteristics, such as thermal stability, bleaching rate, dose saturation, and annealing temperature response (Singarayer and Bailey, 2003; Tsukamoto et al., 2003; Gong et al., 2014, 2015). The OSL-SAR method is considered reliable for quartz if the fast component dominates its initial OSL signal (e.g., within 0.8 s). In the research of geological sediments, if the initial OSL signal contains a significant thermally unstable medium or slow component, the OSL age would be underestimated (Choi et al., 2003a; Tsukamoto et al., 2003; Thomas et al., 2005; Li and Li, 2006; Steffen et al., 2009). However, some previous studies proposed that medium or slow components of the quartz OSL signal in some samples were thermally stable and did not affect the OSL age (Singarayer and Bailey, 2003; Fan et al., 2009).

Multiple studies suggested that the OSL age of heated archaeological quartz was significantly influenced by the component characteristics. For example, Fu et al. (2010) found that the initial OSL signals of burnt clay from the Qujialing archaeological site in China were all dominated by the fast component, and their OSL ages were consistent with the independent ^{14}C ages. When Solongo et al. (2021) dated the OSL ages of two Mongolian bricks, the initial OSL of one red brick was dominated by the fast component, and the age agreed with the historical age, while the medium component of another gray brick was significant, and the dating result was underestimated. Anderson and Feathers (2019) found two types of samples with different decay rates in the OSL dating of pottery from archaeological sites in the Arctic. One type with a fast decay rate results in reasonable ages, while the other type with a slower decay rate is exceptionally overestimated. Recently, Wang et al. (2022) reported that a high annealing temperature (over 600–800°C) would decrease the OSL decay rate of quartz through pure quartz simulation heating experiments.

Until now, the component characteristics of heated archaeological quartz with two different OSL decay rates and their effects on OSL dating results remain unclear. This study focused on burnt clay and pottery shards, which are the most commonly found materials in Chinese archaeological sites. The burnt clay and pottery shards excavated from the Lingjiatan archaeological site were used as an example to investigate the component characteristics of the samples with different OSL decay rates, quantitatively described as Fast Ratio (Durcan and Duller, 2011), and to explore the effects of preheat and stimulation temperatures on recuperation and D_e estimates. OSL-SAR was compared with TL-SAR, TL-MAAD, and ^{14}C dating methods to verify the accuracy of OSL-SAR in dating heated archaeological quartz with different components.

2 Archaeological context and sampling

The Lingjiatan site (31°29′ N, 118°02′ E) (Figure 1) is a large Late Neolithic archaeological site located in the East China Plain on flat terrain with an average elevation of approximately 18 m. The site belongs to Hanshan County, Maanshan City, Anhui Province. It is approximately 20 km from Chaohu Lake to the west, 35 km from the Yangtze River to the east, 5 km from Taihu Mountain to the north, and adjacent to the north bank of the middle section of the Yuxi River to the south (Anhui Provincial Institute of Cultural Relics and Archaeology, 2006). In the site, a large number of precious jades, stone tools and pottery have been unearthed. The discovery of Neolithic burials, altars and sacrificial pits within the site indicates that the Lingjiatan site is an essential part of Chinese civilization. There exists a massive region with densely distributed burnt clay at this site, covering an area of more than 3,000 m^2. Likely to be the remains of large-scale public buildings such as temples or palaces, this large area of burnt clay is an important relic of the Neolithic period in China, but without an absolute age published. Therefore, this study used the luminescence dating method to determine the absolute age of these heated archaeological materials, which will provide solid chronological evidence for further research on the function of the giant prehistoric public building remains at the Lingjiatan site. The samples in this study contain seven burnt clay blocks and three pottery shards, all taken from the burnt clay layer. Burnt charcoal chips and plant remains were extracted from the burnt clay, which provides suitable material for comparing the luminescence and ^{14}C ages.

3 Methodology

3.1 Optically stimulated luminescence and thermoluminescence dating

For burnt clay, the pure fine-grained quartz was extracted using a fine-grained technique. The burnt clay samples were cut by a diamond saw, and approximately 2–3 g of powders

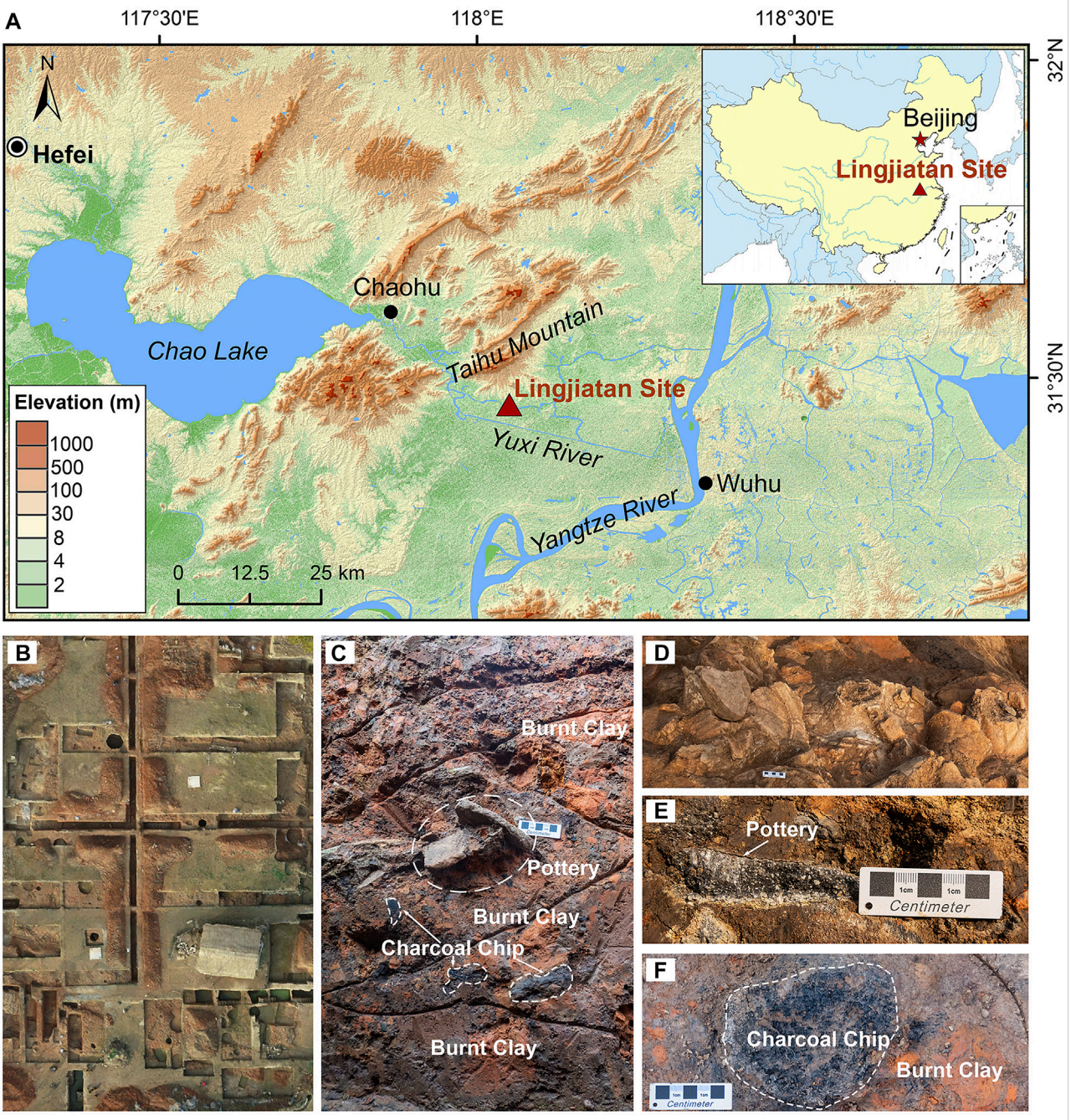

FIGURE 1
(A) The location of the Lingjiatan archaeological site. **(B)** Aerial view of the site excavation. **(C)** The picture shows the red burnt clay profile with the pottery shards collected for dating buried in the burnt clay. The black material mixed in burnt clay is burnt charcoal chips collected for radiocarbon dating. **(D)** The picture shows the pottery heap formed by a large number of pottery. **(E)** Buried pottery shard, similar to **(C)**. **(F)** Large carbonized wooden building Pedestal, surrounded by burnt clay.

were extracted from the unexposed position on the profile using a drill. The 4–11 μm grains were extracted by hydrostatic sedimentation according to Stokes' Law and treated with 10% hydrochloric acid and 10% hydrogen peroxide for 1 h each to remove possible carbonates and organic matter, respectively. The samples were then treated with 15% fluorosilicic acid for 8 h to remove feldspar and clay minerals. Finally, the samples were treated with 10%

TABLE 1 Summary of sample description, radioactive element content, dose rate, OSL, TL and ^{14}C ages.

Sample ID	Type	Sample.description	Grain Size (μm)	Radioactive elements content			Water content (%)	Environment dose rate					Method	Integration.interval (TL)	OD (%)	D_e (Gy)	Age (ka)[c]
				U (ppm)	Th (ppm)	K (%)		α (Gy/ka)	β (Gy/ka)	γ (Gy/ka)	Cosmic (Gy/ka)	Total dose rate (Gy/ka)					
LJTBE02	Type II	burnt clay	4–11	2.1 ± 0.2	12.0 ± 1.2	1.4 ± 0.1	0.6 ± 0.3	0.51 ± 0.04	1.71 ± 0.07	1.14 ± 0.06	0.14 ± 0.01	3.51 ± 0.11	OSL-SAR	—	2.6 ± 4.9	20.0 ± 0.4	**5.7 ± 0.2**
													TL-SAR	290–330°C	28.3 ± 6.8	15.5 ± 1.2	4.4 ± 0.4
													TL-MAAD	280–375°C	—	20.5 ± 1.9	**5.8 ± 0.6**
LJTBE03/04	Type II	burnt clay	4–11	2.3 ± 0.2	14.0 ± 1.4	1.6 ± 0.1	0.0 ± 0.0	0.59 ± 0.05	1.98 ± 0.08	1.32 ± 0.07	0.14 ± 0.01	4.02 ± 0.12	OSL-SAR	—	10.2 ± 3.2	19.7 ± 0.8	**4.9 ± 0.2**
													TL-MAAD	290–350°C	-	18.7 ± 1.3	**4.6 ± 0.4**
LJTBE05	Type II	burnt clay	4–11	2.7 ± 0.3	15.0 ± 1.5	1.7 ± 0.1	0.2 ± 0.1	0.65 ± 0.06	2.14 ± 0.09	1.44 ± 0.08	0.14 ± 0.01	4.37 ± 0.13	OSL-SAR	—	12.9 ± 3.2	17.9 ± 0.6	4.1 ± 0.2
LJTBE06/07	Type II	burnt clay	4–11	2.4 ± 0.2	14.0 ± 1.4	1.6 ± 0.1	0.1 ± 0.0	0.60 ± 0.05	2.04 ± 0.08	1.35 ± 0.07	0.14 ± 0.01	4.12 ± 0.13	OSL-SAR	—	6.8 ± 5.9	23.9 ± 1.0	**5.8 ± 0.3**
LJTBE01	Type I	burnt clay	4–11	2.3 ± 0.2	15.4 ± 1.5	2.1 ± 0.1	9.3 ± 4.7	0.55 ± 0.06	2.15 ± 0.14	1.37 ± 0.10	0.14 ± 0.01	4.21 ± 0.19	OSL-SAR	—	0	25.0 ± 0.4	**6.0 ± 0.3**
													TL-SAR	290–380°C	0	27.6 ± 0.7	6.6 ± 0.3
													TL-MAAD	270–375°C	—	25.7 ± 9.0	**6.1 ± 2.2**
LJTBE08	Type I	burnt clay	4–11	2.3 ± 0.2	15.7 ± 1.6	1.5 ± 0.1	0.8 ± 0.4	0.62 ± 0.06	1.90 ± 0.08	1.36 ± 0.08	0.14 ± 0.01	4.03 ± 0.13	OSL-SAR	—	0	20.9 ± 0.3	**5.2 ± 0.2**
													TL-SAR	290–330°C	3.8 ± 6.5	39.2 ± 1.6	9.7 ± 0.5
													TL-MAAD	290–350°C	—	19.1 ± 2.7	**4.7 ± 0.7**
LJTBE09	Type I	burnt clay	4–11	1.6 ± 0.2	16.0 ± 1.6	1.3 ± 0.1	0.2 ± 0.1	0.57 ± 0.05	1.69 ± 0.07	1.26 ± 0.08	0.14 ± 0.01	3.66 ± 0.12	OSL-SAR	—	1.2 ± 5.8	18.1 ± 0.3	**5.0 ± 0.2**
													TL-SAR	290–330°C	30.1 ± 7.1	11.5 ± 1.0	3.2 ± 0.3
													TL-MAAD	290–375°C	—	17.2 ± 3.0	**4.7 ± 0.8**
LJTPott04	Type I	pottery	150–250	5.0 ± 0.5	13.0 ± 1.3	2.3 ± 0.1	3.5 ± 1.8	0.00 ± 0.00	2.50 ± 0.12	1.34 ± 0.12[a]	0.14 ± 0.01	3.97 ± 0.17	OSL-SAR	—	10.0 ± 8.6	19.6 ± 1.0	**4.9 ± 0.3**
LJTPott05	Type I	pottery	150–250	4.2 ± 0.4	16.0 ± 1.6	2.4 ± 0.1	8.3 ± 4.1	0.00 ± 0.00	2.40 ± 0.15	1.32 ± 0.14[a]	0.14 ± 0.01	3.86 ± 0.21	OSL-SAR	—	18.2 ± 3.2	18.4 ± 0.8	**4.8 ± 0.3**
LJTPott06	Type I	pottery	63–90	3.0 ± 0.3	17.0 ± 1.7		33.1 ± 16.5				0.14 ± 0.01		OSL-SAR	—	0		**5.9 ± 0.6**

(Continued on following page)

10.3389/feart.2022.933342

TABLE 1 (*Continued*) Summary of sample description, radioactive element content, dose rate, OSL, TL and ^{14}C ages.

Sample ID	Type	Sample.description	Grain Size (μm)	Radioactive elements content			Water content (%)	Environment dose rate					Method	Integration.interval (TL)	OD (%)	D_e (Gy)	Age (ka)[c]
				U (ppm)	Th (ppm)	K (%)		α (Gy/ka)	β (Gy/ka)	γ (Gy/ka)	Cosmic (Gy/ka)	Total dose rate (Gy/ka)					
						1.8 ± 0.1		0.00 ± 0.00	1.55 ± 0.24	1.14 ± 0.13[a]		2.83 ± 0.27				16.7 ± 0.2	
													TL-SAR	275–385°C	0	21.0 ± 0.6	7.4 ± 0.7
LJTCarbon-1[d]	—	plant remain	—	—	—	—	—	—	—	—	—	—	—	—	—	—	**5.4–5.7**[b]
LJTCarbon-2[d]	—	charcoal chip	—	—	—	—	—	—	—	—	—	—	—	—	—	—	**5.7–5.8**[b]
AnhuiKGS-1[e]		plant ash	—	—	—	—	—	—	—	—	—	—	—	—	—	—	**5.4–5.8**[b]
AnhuiKGS-2[e]		charcoal chip	—	—	—	—	—	—	—	—	—	—	—	—	—	—	**5.2–5.5**[b]

[a]The gamma dose rate of the pottery shards is calculated by measuring the content of U, Th, and K radioactive elements around the shards. Therefore, the environmental dose rate of the pottery shard is the sum of the alpha and beta dose rates inside the shard and the gamma dose rate of the buried soil around the shard.

[b]The radiocarbon age after the correction has been converted to a calendar year before 2022, namely, BP_{2022}.

[c]The bold font indicates the accepted ages.

[d]The radiocarbon ages measured in this study.

[e]The radiocarbon ages cited from a previous study (Anhui Provincial Institute of Cultural Relics and Archaeology, 2006).

10.3389/feart.2022.933342

hydrochloric acid to remove the fluoride generated by the reaction. If the prepared samples contained any IRSL signals, the last two steps of fluorosilicic acid and hydrochloric acid treatments were repeated until no IRSL signals could be detected. For pottery, a coarse-grain technique was used. The surface-exposed parts (2–3 mm) were first removed using a drill, then gently ground with an iron mortar and then sieved to separate the >63 μm fraction. The chemical treatment was similar to that of the fine grain, the only difference being that the fluorosilicic acid was replaced by 40% hydrofluoric acid with a dissolution time of 40 min. Subsequently, sodium polytungstate solutions of 2.60 and 2.70 g/cm^3 were used to separate the remaining feldspar and heavy minerals. Finally, 63–90 and 150–250 μm coarse-grained quartz grains were extracted through second sieving.

The luminescence dating procedure was carried out on a Risø TL/OSL-DA-20 instrument with a ^{90}Sr/^{90}Y β radioactive source. The stimulation light source was 470 ± 30 nm blue LEDs (Bøtter-Jensen et al., 2003a) with a maximum power of 45 mW/cm^2. An EMI 9235QB photomultiplier tube equipped with a Φ = 45 mm × 7.5 mm U-340 filter was used to detect ultraviolet emission (Bøtter-Jensen et al., 1995).

As shown in Table 1, three protocols were used to obtain D_e. Namely, the single aliquot regenerative dose optically stimulated luminescence dating (OSL-SAR) (Murray and Wintle, 2000; Wintle and Murray, 2006), the single aliquot regenerative dose thermoluminescence dating (TL-SAR) (Bluszcz and Bøtter-Jensen, 1995; Richter and Krbetschek, 2006) and the multiple aliquots additive doses (TL-MAAD) (Aitken, 1985).

For OSL-SAR, the width of a single channel was 0.16 s, and the first 0.8 s and the last 8 s of the OSL signal were used as the integration intervals for the signal and background, respectively. The dose response curves were fitted with exponential or linear functions, and each aliquot was subjected to a series of rejection criteria., i.e., a recycling ratio of 0.9–1.1, Tn is more than three sigma above the background, the relative standard error of Tn is below 10% and the recuperation is within ±5%. The relationship among preheat temperature, stimulation temperature and D_e estimation was investigated, which was used to determine the optimal measurement conditions. A dose recovery test was used to characterize the effectiveness of the method.

During the application of the TL-SAR method, TL signals were recorded from room temperature to a maximum of 450°C. Both the D_e plateau test (relationship between D_e and integration temperature) and the heated plateau test (ratio of the first regenerated dose signal to the natural dose signal, i.e., R1/N) were performed (Richter et al., 2014). The temperature range in which appear both plateaus simultaneo usly was considered as the TL integration interval.

For TL-MAAD, the TL signals of N (natural), N+β and N+2β are used to build the dose response curve (DRC), and each step contains three aliquots. Similar to TL-SAR, the D_e plateau and heating plateau (the ratio of N to N+β) are used to determine the TL integration interval. The D_e before correction (Q) can be obtained by intercepting the DRC with the *y*-axis. In the supra-linearity test, a series of aliquots were hot bleached at 450°C and given small incremental regenerative doses to establish the DRC used to obtain the initial correction value (I). The corrected palaeodose P equals Q + I (Aitken, 1985; Zander et al., 2019). Supplementary Table S1 in the Supplementary Material shows the details.

3.2 Data analysis using R

3.2.1 CW-OSL fitting

The OSL signals can be divided into multiple components (fast, medium, slow components, etc.) by deconvoluting continuous-wave OSL or linearly modulated OSL curves (Huntley et al., 1996; Bailey et al., 1997; Jain et al., 2003). Although simple, CW-OSL contains the same physical information as LM-OSL but demonstrates a higher signal-to-noise ratio (Choi et al., 2006; Huntley, 2006; Jain and Lindvold, 2007; Rawat et al., 2014). This study used CW-OSL nonlinear fitting to monitor the OSL component properties of natural and regenerative dose signals. Assuming that each component in CW-OSL follows an exponential decay, the CW-OSL signal [L(t)] as a function of time (t) can be expressed as Eq. 1. (Bulur, 2000; Bøtter-Jensen et al., 2003b).

$$L(t) = \sum_1^i n_i b_i \, exp\,(-b_i t) = \sum_1^i I_i \, exp\,(-b_i t) \tag{1}$$

where i (i = 1, 2, 3 . . .) represents the ith decaying component, n_i represents the number of initially trapped electrons of the ith component, b_i represents the detrapping probability of the ith component (unit is s^{-1}), and I_i represents the initial OSL intensity of the ith component. Meanwhile, the relationship of the photoionization cross-section of the ith component (σ_i, the unit is cm^2), detrapping probability of the ith component (b_i), stimulating photon flux (I_0, unit is photons/(scm^2)), maximum LED stimulation power (P_{max}, i.e., at 100% LED power percent, unit is mW/cm^2), and LED power percent set in Risø Sequence Editor (η, unit is %) satisfies Eqs 2, 3. [Adapted from Choi et al. (2006)]

$$b_i = \sigma_i I_0 \tag{2}$$

$$\eta P_{max} = E I_0 \tag{3}$$

The stimulation light source was a blue LED (λ = 470 ± 30 nm), the corresponding single-photon energy (E) was 4.23 × 10^{-19} Ws, and P_{max} (45 mW/cm^2) was obtained from Risø according to the instrument serial number. All deconvolution processes used the fit_CWCurve () function (Kreutzer, 2022) in the R package "luminescence".

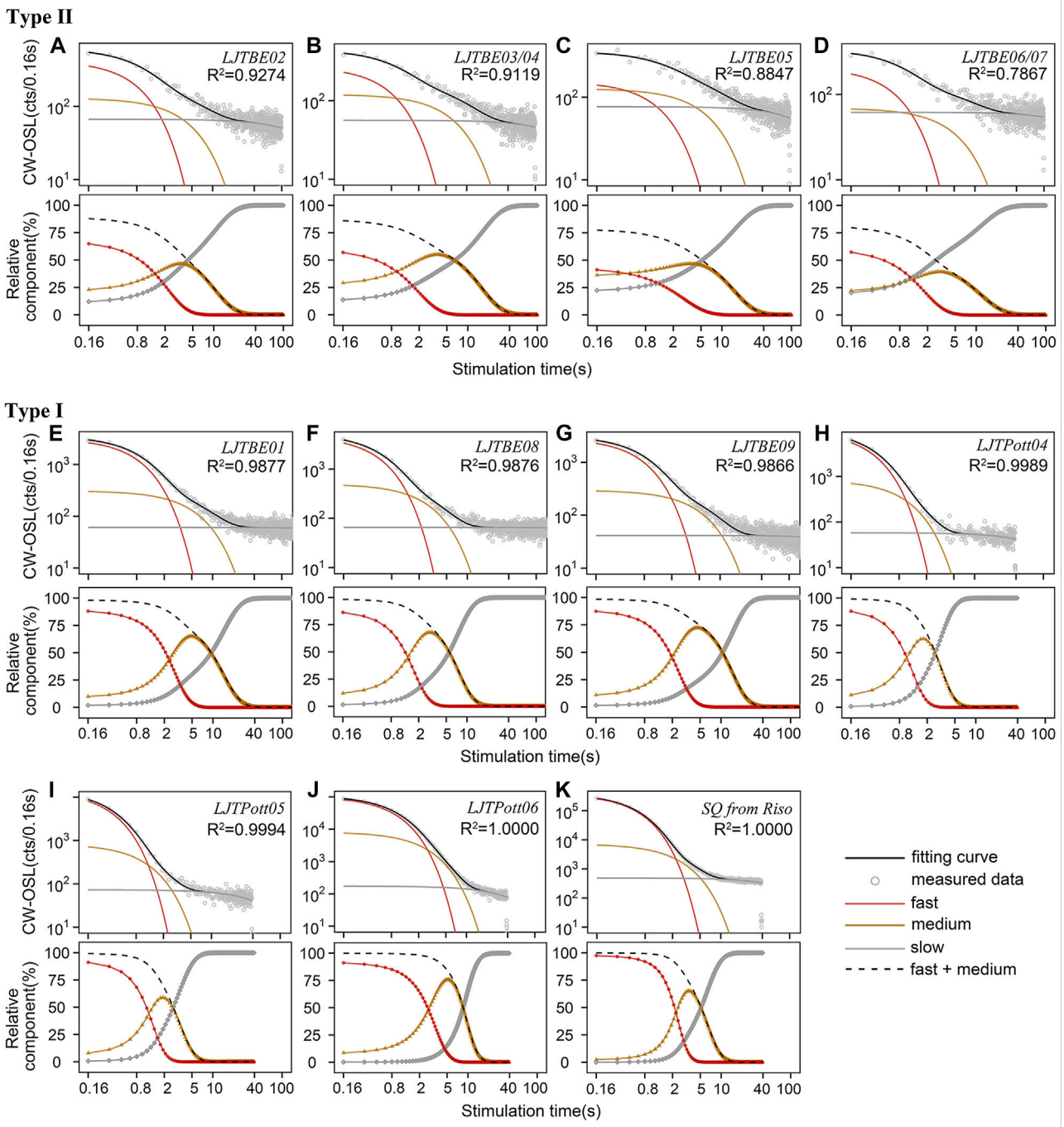

FIGURE 2
The component photon counts and relative percentages of the natural OSL decay curves after deconvolution using CW-OSL fitting. All original curve data are obtained from the pure quartz OSL-SAR dating procedures. **(A–D)** Type II samples. This type of sample is dim, which shows the characteristics of a slow decay rate. In the initial OSL curves (within 0.8 s), a relatively minor proportion of fast components, or even not dominated by fast components, and significant medium and slow components. Four samples belong to type II, their preheat temperature is 260°C, and their excitation temperature is 180°C. **(E–K)** Type I samples. This type of sample is bright, showing a fast decay rate. The fast component dominates the initial OSL signal (within 0.8 s), while the medium and slow components account for a minor proportion. Six samples belong to type I, their preheat temperature is 200°C, and their stimulation temperature is 125°C. **(K)** Is a control sample of the standard radiation source calibration quartz (SQ) provided by Risø.

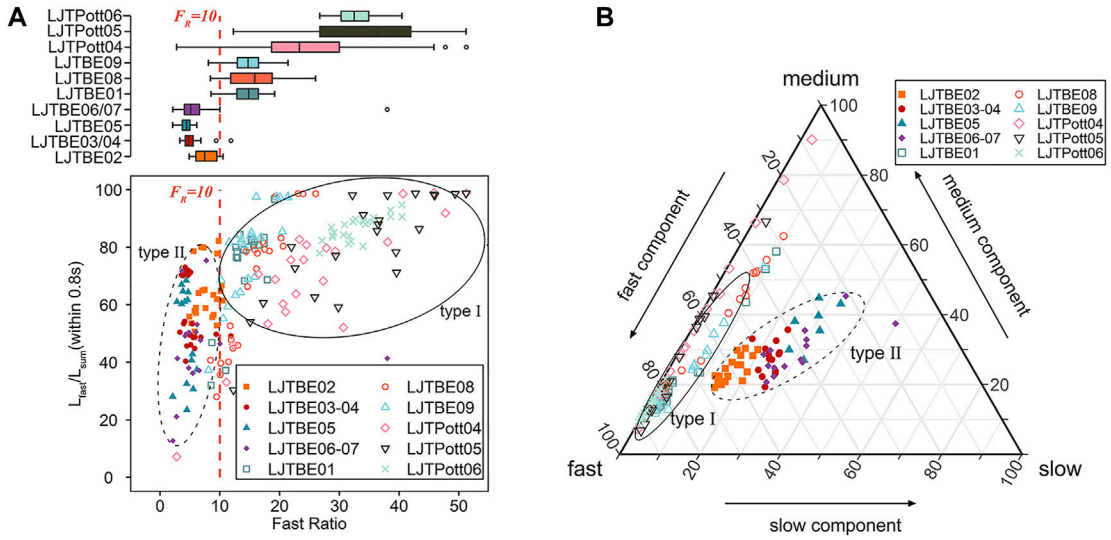

FIGURE 3
(A) The graph shows the Fast Ratio (F_R) versus the proportion of the fast component in the initial signal. The proportion is obtained by calculating the integral of the first 0.8 s of the CW-OSL curve. The samples can be classified into two types based on F_R and L_{fast}/L_{sum}. The F_R values of type I are greater than 10, and the fast component dominates the initial signal. The F_R values of Type II samples are less than 10, and the fast component is not significant in the initial OSL signal. All the data were calculated from the natural OSL decay curves during pure quartz OSL-SAR dating procedures. **(B)** The ternary diagram shows the relative proportions of fast, medium and slow components for the pure quartz natural CW-OSL signals. Similar to the results in **(A)**, these samples can be classified into type I and type II according to the relative contributions of the three components.

3.2.2 Fast ratio

Fast ratio (Durcan and Duller, 2011) can be used to distinguish whether the fast component dominates the initial signal of quartz. The fast ratio value can be described by the following equation:

$$F_R = \frac{L_F - L_M}{L_M - L_{bg}} \tag{4}$$

where L_F or L_M means the representative channel signal whose proportion of fast or medium component intensity is largest, respectively. L_M can also be obtained by the time when the fast component intensity decreases to 1%. Similarly, L_{bg}, namely, the average background signal, can be calculated from the medium component intensity decreasing to 1%–0.1% of its initial value (Durcan and Duller, 2011). Eq. 5 describes the relationship between b_i (which has been discussed in 3.2.1) and t_i, where t_i represents the time when the signal of component i decreases to 1% of its initial value. The relationship between the time when the signal of the *i*th decaying component depletes to 1% of its initial values (t_i) and the corresponding detrapping probability of the *i*th component (b_i) can be calculated as follows:

$$\frac{I_i\, exp(-b_i t_i)}{I_i} = \frac{1}{100} \tag{5}$$

$$\frac{1}{exp(b_i t_i)} = \frac{1}{100} \tag{6}$$

$$100 = exp(b_i t_i) \tag{7}$$

$$\ln(100) = b_i t_i \tag{8}$$

$$t_i = \frac{\ln(100)}{b_i} \tag{9}$$

Using t_i calculated from Eq. 9, we can obtain the corresponding L_F, L_M, and L_{bg} from the OSL curve for the calculation of the fast ratio value by Eq. 4.

3.2.3 D_e estimation, age model and radial plot

The R package "numOSL" (Peng et al., 2013; R Core Team, 2016; Peng and Li, 2017) is used to fit DRC and estimate D_e based on the rejection criteria mentioned above. According to the firing temperature results obtained from the thermal expansion method (see Supplementary Figure S3), the samples in this study were fully hot bleached. Therefore, only the central age model (Galbraith and Roberts, 2012) was used to calculate the D_e. The D_e calculation and plotting radial plot used the calc_CentralDose () function (Burow, 2022) and plot_RadialPlot () function (Dietze and Kreutzer, 2022) in the R package "luminescence", respectively.

3.2.4 Dose rate

The dose rate was calculated using the use_DRAC () function (Durcan et al., 2015; Kreutzer et al., 2022) in the R package 'luminescence'. α, β, and γ dose rate contributions are converted from radioactive elements U, Th, ^{4}K using radionuclide conversion factors reported by Guérin et al. (2011). Attenuation factors caused by water are reported by Aitken and Xie (1990) and Zimmerman (1971), which are 1.49, 1.25, and 1.14 for α, β, and γ dose rate

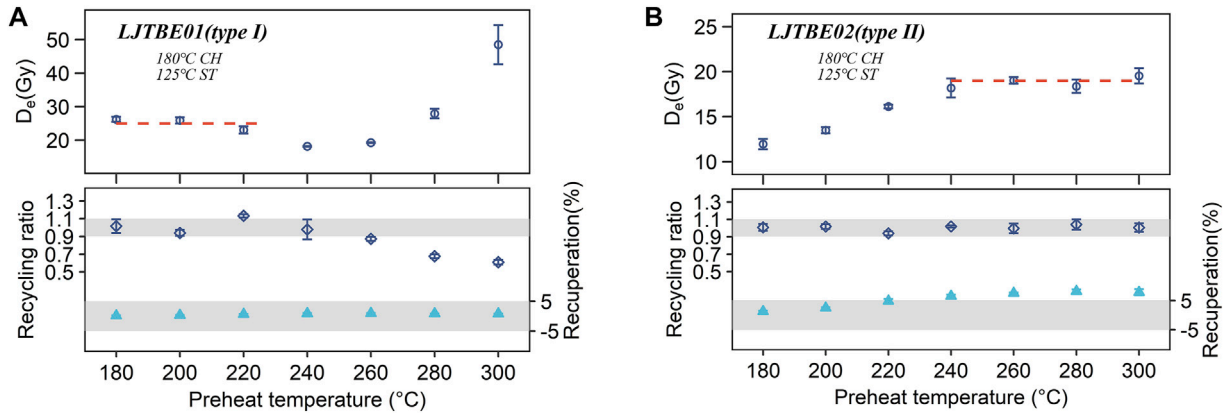

FIGURE 4
(A) The preheat plateau test of representative type I samples (*LJTBE01*) with a plateau region of 180–220°C. The cut-heat was 180°C. The red dashed line represents the average value of different aliquots of D_e in this region of approximately 25.0 Gy. The data for each temperature point are calculated from the mean value of three aliquots. **(B)** The preheat plateau test of typical type II samples (*LJTBE02*) with a plateau region of 240–300°C, and the average value in this region is approximately 18.8 Gy.

contributions, respectively. The water content was based on the measured values, and a relative error of 50% was assumed. To calculate the alpha dose for fine-grained quartz, an alpha efficiency (α-value) of 0.038 ± 0.002 was determined according to Rees-Jones (1995). The attenuation factors of α and β dose rates for different grain sizes are based on Bell (1980) for alpha particles and Guérin et al. (2012) for beta particles. Cosmic was calculated using the formula proposed by Prescott and Hutton (1988, 1994). The relative error for the cosmic dose rate is taken as 10% (Durcan et al., 2015). The contents of U and Th were obtained using ICP-MS, and K was obtained using ICP-OES. The relative errors of radioactive elements U, Th, and ^{4}K were taken as 10%, 10%, and 5%, respectively (Wang et al., 2022).

For the burnt clay, we selected samples of a large size (approximately 15–30 cm) so that the dose rate was mainly from within itself. For pottery, the total dose rate can be divided into the internal dose rate of the pottery itself and the external dose rate generated by the soil around the pottery (after removing approximately 3 mm from the surface, the external dose rate only indicates the γ dose rate). To maximize the accuracy of the dose rate, we also measured the radioactive element content of the sediments attached to the surface of the pottery to calculate the external dose rate.

4 Results

4.1 Fast ratio and relative component contribution

The burnt clay and pottery collected from the Lingjiatan site can be classified into Type I (Figures 2A–D) and Type II (Figures 2E–K) according to the quartz natural dose brightness and relative component proportions. Burnt clay *LJTBE01*, *LJTBE08*, *LJTBE09*, pottery *LJTPott01*, *LJTPott05*, and *LJTPott06* belong to Type I (6 samples), while *LJTBE02*, *LJTBE03/04*, *LJTBE05*, and *LJTBE06/07* belong to Type II (4 samples). To compare the discrepancy in sensitivity between these two types of samples, the OSL sensitivity (counts/Gy/mg) of T_n within 0.8 s was calculated (see Supplementary Table S2). The higher quartz brightness of the Type I sample (average of approximately 502–14,624 counts/Gy/mg of T_n for different samples) indicates a higher sensitivity of the OSL signal. The Type II sample has relatively dimer quartz brightness (average of approximately 81–148 counts/Gy/mg of T_n for different samples), indicating a lower OSL sensitivity. For Type II samples, the relative fast component proportion varies from 34% to 60% between samples, from 25% to 37% for the medium component, and from 16% to 29% for the slow component. For Type I samples, the fast, medium and slow component variations range from 60%–86%, 14%–39%, and 0.4%–5%, respectively. Although Figure 2 shows only the component characteristics of the natural signal, the results of regenerative doses and test doses in the subsequent cycles show consistent results compared with Figure 2 (see Supplementary Table S2 for details).

The Fast Ratio (F_R) and relative component contributions for all samples (only the natural dose is shown, see Supplementary Figure S2 for the other cycles) are shown in Figures 3A,B, respectively. The results indicate that the two types of samples have different F_R values, illustrating the variation of component contribution in the initial OSL signals for different samples. Although Durcan and Duller (2011) used F_R = 20 as a criterion to distinguish whether the initial OSL signal is

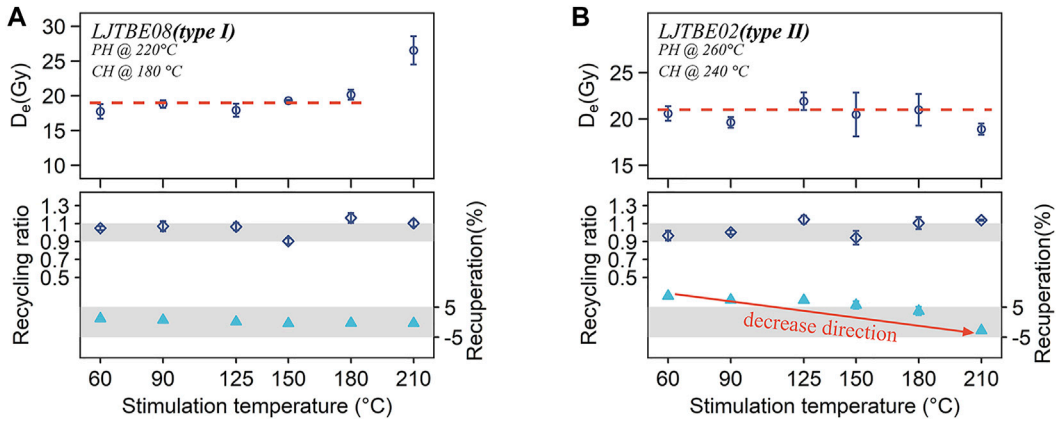

FIGURE 5
(A) D_e varies with stimulation temperature for a representative Type I sample (*LJTBE08*). Preheat and cut-heat temperatures are 220 and 180°C, respectively, with stimulation temperatures varying from 60–210°C. The red dotted line illustrates the range of the plateau. The corresponding recycling ratio and recuperation are also shown. The gray stripes represent the recycling ratio of 0.9–1.1 and ±5% recuperation. **(B)** D_e varies with stimulation temperature for a representative Type II sample (*LJTBE02*). The PH and CH temperatures are 260 and 240°C, respectively. The red arrow represents the trend of decreasing recuperation.

dominated by the fast component, F_R = 10 (Figure 3A) was considered the better criterion for classifying the sample types in this study. For Type I samples, the average F_R values were all higher than 10, and the average F_R values of different samples varied from 10 to 40 (see Supplementary Table S2 for details), indicating that the fast component occupies the relative main part of the initial signal. For Type II samples, the average F_R values were lower than 10, indicating that the medium and slow components were significant in the initial signal.

4.2 Dependence of D_e on preheat temperature

Before optical stimulation in the OSL-SAR method, preheat plays a vital role in clearing shallow trapped electrons (Wintle and Murray, 2006) and transferring part of the charge into the fast component trap, which simulates the charge transfer in a buried environment (Murray et al., 2021). Therefore, the preheat plateau test is necessary before applying routine SAR protocols. Separate preheat plateau tests whose temperatures ranged from 180–300°C with an increment of 20°C were conducted for the above two types of samples. The results showed that these two types of samples had different plateau ranges. For the representative Type I sample *LJTBE01*, the D_e plateau appeared from 180°C, and remained relatively stable in the range of 180–220°C. However, D_es decreased in the preheat temperature region of 220–260°C, which may be caused by the intervention of the shallow trap yielding a TL glow peak at 210–220°C (Figure 7C) (Choi et al., 2003b; Peng et al., 2021). Finally, the D_e would be significantly overestimated above 260°C preheat temperatures (Figure 4A). Between 180 and 260°C, the recycling ratio and recuperation remained between 0.9–1.1 and ±5%, respectively, without significant changes (Figure 4A). However, the recycling ratio beyond this range would be significantly lower, indicating that its OSL sensitivity was not corrected correctly, but the recuperation remained almost constant. The preheat plateau test and TL curves of the other Type I samples showed similar results (Supplementary Figures S5, S6A). For the representative Type II sample *LJTBE02*, the D_e plateau appeared from a relatively high temperature, i.e., 240°C, and a higher plateau region ranging from 240–300°C can be illustrated in Figure 4B. In contrast, the 325°C TL peaks were extremely weak for Type II samples, but 160–170 and 220°C TL peaks were observed (Supplementary Figure S6B). This may be attributed to the red TL emission of heated quartz with high firing temperature rather than the UV TL emission (Haustein et al., 2001; Song et al., 2009; Westaway and Prescott, 2012).

In conclusion, there is a significant difference between TL glow curves of the two types of samples. For example, type II samples exhibited significant 160–170°C TL peaks, while type I samples did not, which may be linked to the more significant medium component of type II samples (Wang et al., 2015; Peng and Wang, 2020). However, how the D_es were influenced by the intervention of shallow electron traps in the heated archaeological quartz and the extent of the influence need to be further studied. As the preheat temperature increased, the recycling ratio remained constant and stayed within 0.9–1.1. In contrast, the recuperation ratio increased significantly and exceeded 5% at 240°C and later, indicating significant thermal transfer phenomena caused by higher preheat temperature

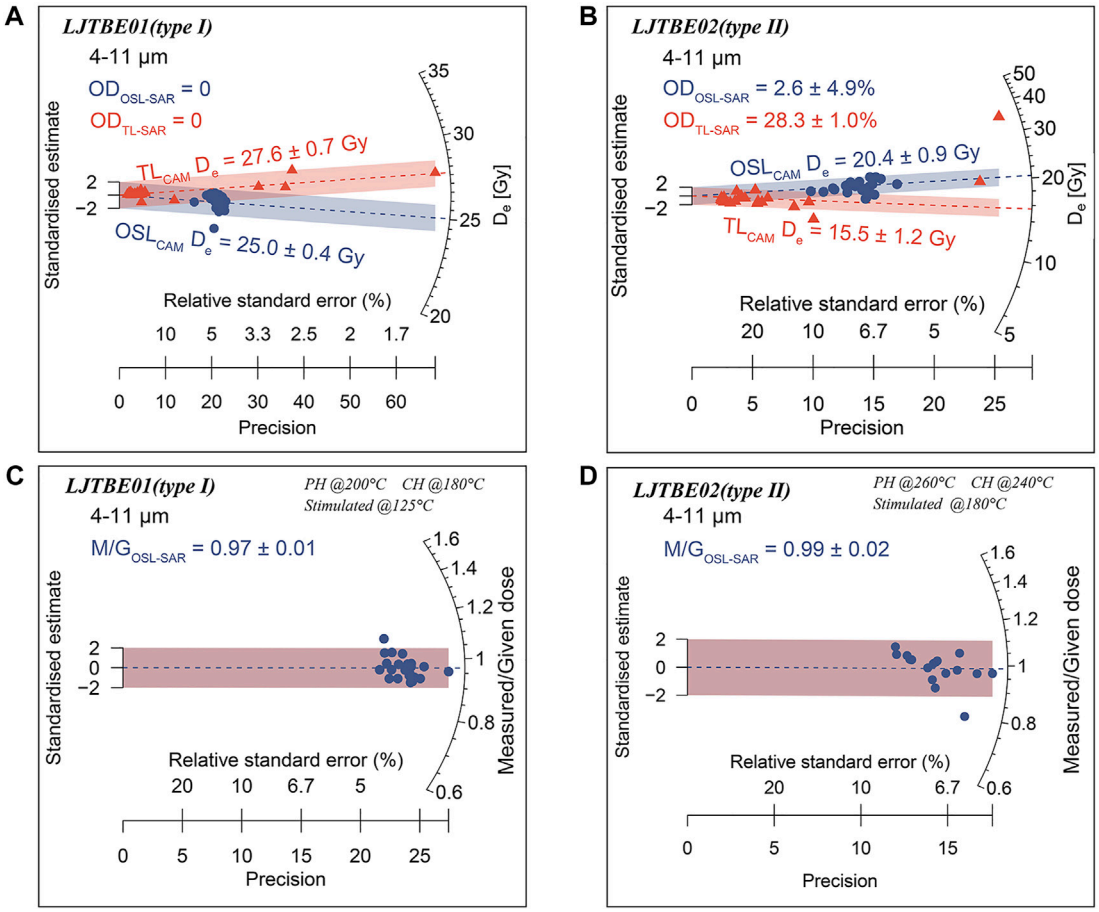

FIGURE 6
(A) Radial plot showing the D_e distribution of a typical Type I sample (*LJTBE01*). The blue circles indicate the D_e values for OSL-SAR dating procedures, and the red triangles indicate those for TL-SAR. **(B)** Similar to **(A)**, this plot shows the radial plot of the representative type II sample (*LJTBE02*). **(C)** The dose recovery test of a typical type I sample (*LJTBE01*), and the M/G indicates the ratio of measured and given doses. **(D)** Like **(C)**, this plot represents the radial plot of a representative type II sample (*LJTBE02*).

(Wintle and Murray, 2006). It can be inferred from the presence of a plateau that this thermal transfer/recuperation effect will not significantly affect D_e (Figures 4A,B). For other samples (not shown in this paper), the preheat plateau results all roughly matched the respective types.

4.3 Dependence of D_e on stimulation temperature

The above preheat plateau test results showed that the recuperation of Type II samples at high preheat temperatures was quite significant. According to the suggestion of Murray and Wintle (2000), increasing the stimulation temperature may reduce recuperation. Therefore, gradient stimulation temperatures (60, 90, 125, 150, 180 and 210°C) were designed for both types of samples to investigate their relationship with D_e and recuperation. D_e values for each temperature step were obtained from three aliquots, and their average values with standard errors were used as the results for each temperature step. In this study, the preheat temperature (PH) and cut-heat temperature (CH) were set as follows: 220°C PH, 180°C CH for type I samples and 260°C, 240°C for Type II samples. Similar to the results of previous studies (Murray and Wintle, 2000; Kijek and Chruścińska, 2015), D_e does not change significantly with increasing stimulation temperature for both types of samples (except for a significant increase of D_e at 210°C stimulation temperature for Type I sample *LJTBE08*), and the recycling ratio remains roughly between 0.9–1.1. However, the recuperation of these two types of samples showed different extents of decrease, as exhibited by a lower extent of decrease for Type I samples (Figure 5A) and a significant extent of decrease for Type II samples (Figure 5B). Specifically, for the Type II sample (*LJTBE02*), the recuperation decreased from approximately 9 to −2%, while for the Type I sample (*LJTBE08*), the recuperation decreased from approximately 3 to −1%.

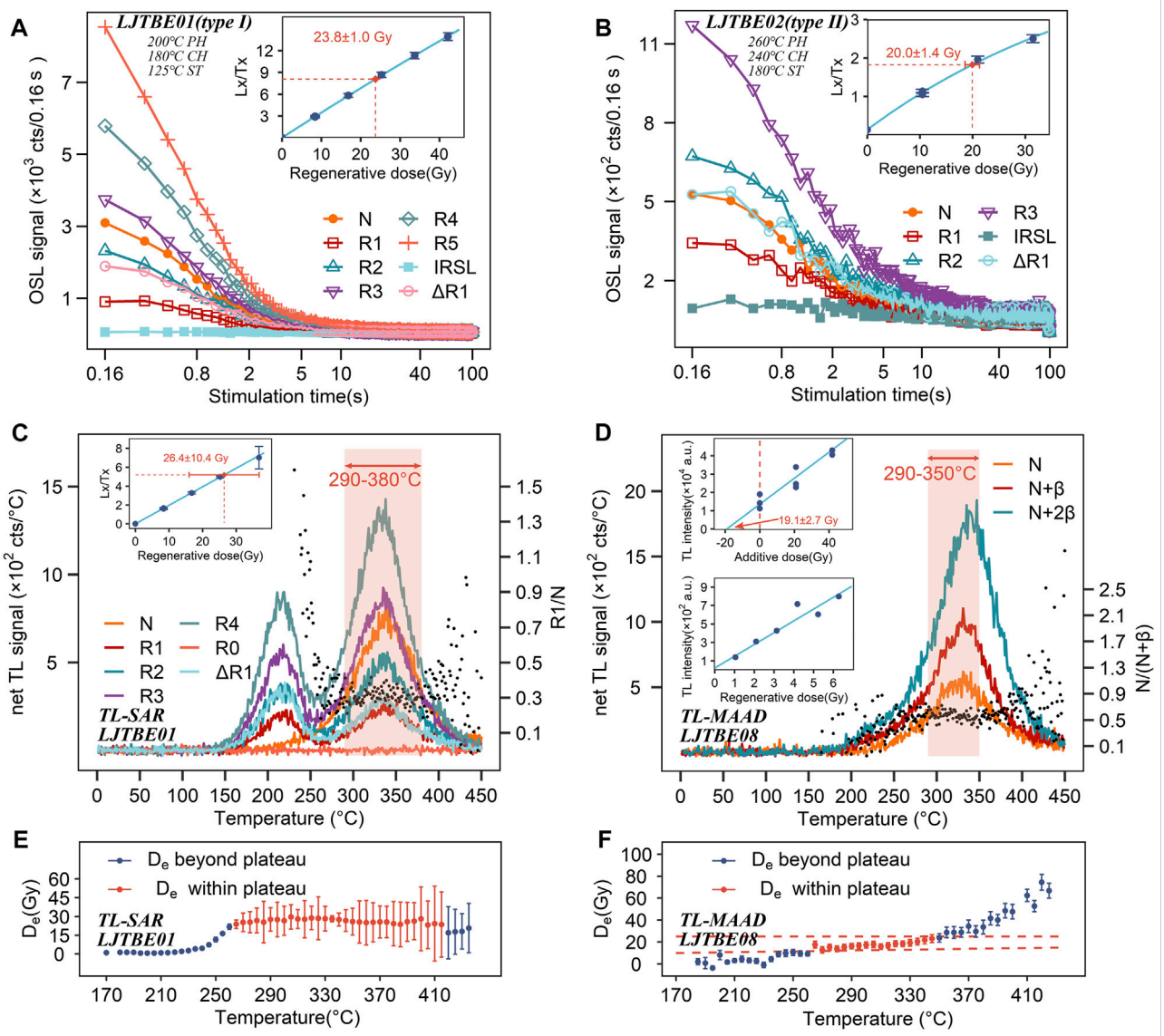

FIGURE 7
(A) The natural (N) and regenerative doses (R1-R5, ΔR1) OSL decay curves and their DRCs for a representative type I sample (*LJTBE01*), where ΔR1 means the repeated dose equal to R1. The IRSL signal is close to the background value, indicating that the sample is not contaminated with feldspar. The preheat (PH) and cut-heat (CH) temperatures for type I samples were 200 and 180°C, respectively, and the stimulation temperature (ST) was 125°C. **(B)** The natural (N) and regenerative doses (R1-R3, ΔR1) OSL decay curves and their DRCs for a representative type II sample (*LJTBE02*). Similarly, the OSL signal of this sample does not contain a feldspar signal. Unlike the type I samples, the PH and CH temperatures for the type II samples were 260 and 240°C, respectively, and the stimulation temperature was 180°C. **(C)** The natural (N) and regenerative (R1-R4, R0, ΔR1) TL curves after background subtraction of a representative sample (*LJTBE01*) for TL-SAR dating procedures, where R0 means the zero dose point and ΔR1 means the repeated dose equals R1. The right axis is the value of R1/N, used to find the heating plateau. The inset shows the corresponding DRC. Combining the results of the heating plateau and D_e plateau, the final TL integration interval of 290–380°C was used to calculate the D_e value. **(D)** The natural (N) and additive doses (N+β, N+2β) TL curves after background subtraction of a typical sample (*LJTBE08*) for TL-MAAD dating procedures. The heating plateau can be inferred from the N/(N+β) marked with black dots. Each dose utilizes three aliquots to obtain the TL signal. The first inset shows the DRC curve, and the second inset indicates the second TL (the first natural TL was bleached by heat) DRC with small doses to check for supra-linearity. The final integration interval is determined to be 290–350°C based on the results of the preheat plateau and the heating plateau. **(E)** D_e plateau of sample *LJTBE01* corresponding to **(C)**. **(F)** D_e plateau of sample *LJTBE08* corresponding to **(D)**.

4.4 Dose recovery test

Murray and Wintle (2000) reported that too low cut-heat temperatures would lead to the failure of the test dose to monitor the sensitivity changes of the traps of interest, and Bailey (2000) used a cut-heat temperature similar to preheat in his study. Therefore, according to the suggestion of Murray and Wintle (2003), the cut-heat in this study was set 20°C lower than the

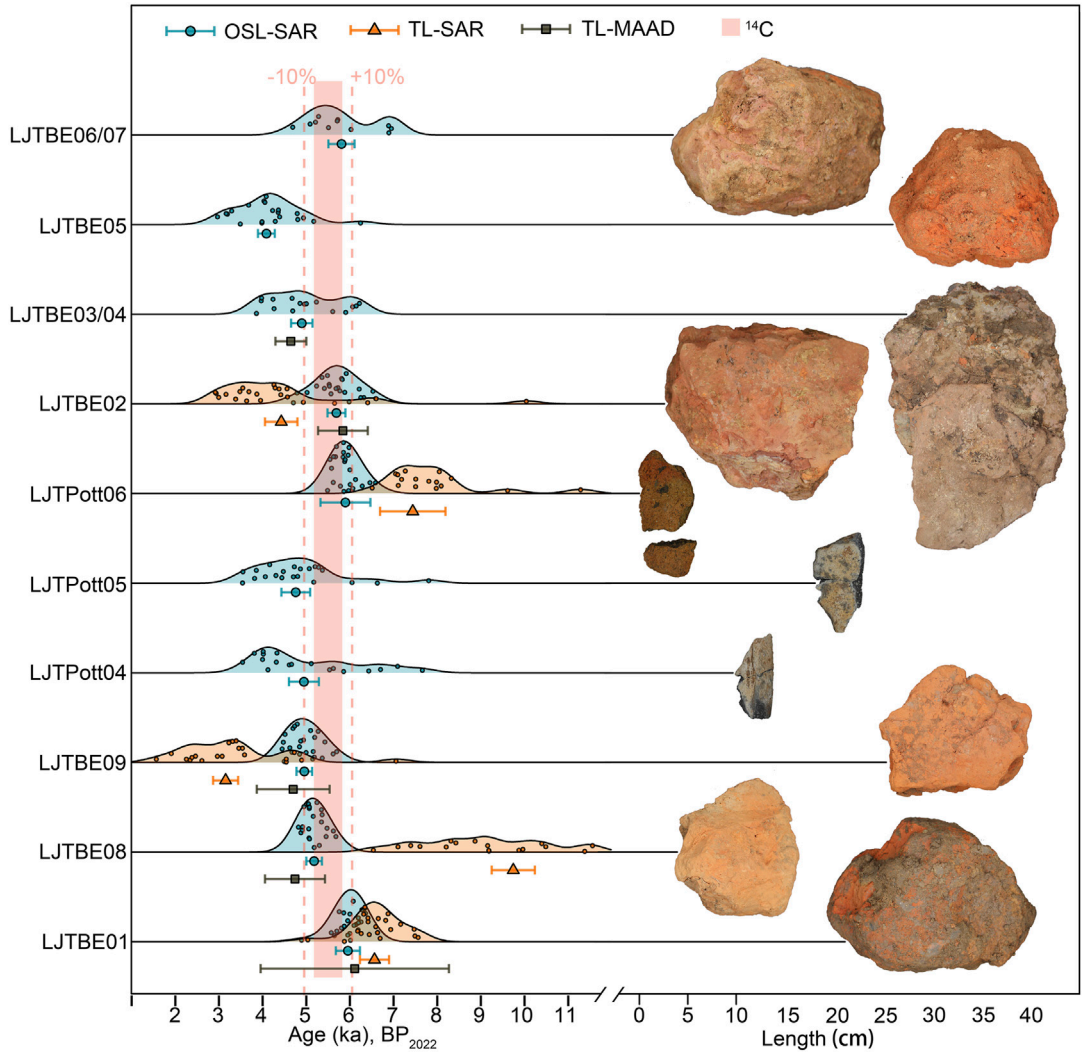

FIGURE 8
Comparison of OSL-SAR, TL-SAR, TL-MAAD and ^{14}C dating methods. The light blue filled color represents the kernel density estimate (KDE) plot of OSL-SAR, and the light brown filled color represents that of TL-SAR. The green solid circles represent the OSL-SAR ages, the red solid triangles represent the TL-SAR ages, the dark blue solid squares represent the TL-MAAD ages, and the pink band represents the range of the two corrected ^{14}C ages. The red dotted lines indicate the range of ±10% mean ^{14}C ages for four samples (two are measured in this study, and the others are cited from previous research).

preheat temperature to improve the result of the dose recovery test. Based on the above results for the preheat plateau and different stimulation temperature tests, the dating conditions of 200°C preheat, 180°C cut-heat, and 125°C stimulation temperature were used for Type I samples, while the dating conditions of 260°C preheat, 240°C cut-heat, and 180°C stimulation temperature were used for Type II. The aliquots used for the dose recovery test were bleached by a solar simulator. Figures 6C,D show the radial plots of the dose recovery test for representative Type I (*LJTBE01*) and Type II (*LJTBE02*) samples, respectively. M/G in the figures refers to the ratio of the measured dose to the given dose, and the ratios of both types of samples are close to 1, indicating the validity of the OSL-SAR method in recovering laboratory irradiation doses.

4.5 Dating results

Figures 7A,B illustrate the uncorrected OSL decay curves in SAR cycles for representative Type I (*LJTBE01*) and Type II (*LJTBE02*) samples. By comparing Figures 7A,B, it is possible to infer that the OSL brightness of the Type II sample is lower. Other type II samples exhibit consistent OSL brightness results. Insets show the DRCs fitted with exponential functions, and the D_e was calculated by

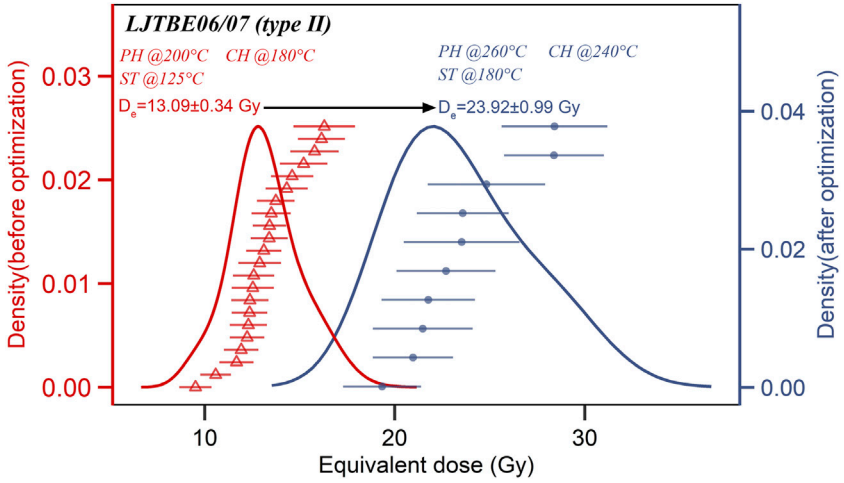

FIGURE 9
OSL-SAR D_e probability density function plots of a representative type II sample (*LJTBE06/07*) at different measurement parameters. The red line represents the underestimated probability density function plot with the measurement parameters of 200°C preheat, 180°C cut-heat and 125°C stimulation temperature. The blue line represents the modified probability density function plot with the measurement parameters of 260°C preheat, 240°C cut-heat and 180°C stimulation temperature. The black arrow represents the direction of modification of the CAM D_e results.

interpolation. The repeated dose points (ΔR1) almost overlap with the first regenerative doses (R1), indicating the effectiveness of the OSL sensitivity correction. Figures 7C,E show the TL grow curve and D_e plateau plot for sample *LJTBE01* in the TL-SAR method. The heating plateau (R1/N) and the D_e plateau (Figure 7E) determine the final TL integration interval of 290–380°C. Figure 7D shows the TL-MAAD method for *LJTBE08*, with the TL integration interval determined to be 290–350°C, according to the heating plateau (N/(N+β)) and the D_e plateau (Figure 7F). For the TL-MAAD method, the TL DRC in low doses may appear supralinear, so it is necessary to establish the second-grow DRC for supra-linearity correction. As shown in the second inset of Figure 7D, the second-grow DRC of sample *LJTBE08* remains linear at low doses, indicating that its supra-linearity is negligible.

Figures 6A,B show the D_e distributions of OSL-SAR and TL-SAR for representative samples of the two types. Although the overdispersion values of OSL-SAR and TL-SAR of *LJTBE01* (Figure 6A) are both close to 0, the relative standard error of OSL-SAR is still smaller than that of TL-SAR, and the other samples behave similarly. Compared with the OSL-SAR method, the D_e obtained by TL-SAR exhibited overestimation (*LJTBE01*, *LJTBE08*, *LJTPott06*) or underestimation (*LJTBE02*, *LJTBE09*), which may be caused by the inappropriate sensitivity correction of the natural TL signal (Lai et al., 2006; Wang et al., 2022). This could also explain why most of the TL-SAR OD values (0%–30.1%) are larger than OSL-SAR (0%–18.2%) (as shown in Figures 6A,B; Table 1).

The corrected ^{14}C ages within the 2σ standard error for the two charcoal chips are 5.5 ± 0.1 ka and 5.7 ± 0.1 ka (BP $_{2022}$, already converted to before 2022). This result agrees well with the ^{14}C ages of grass ash (5.6 ± 0.2 ka BP $_{2022}$) and charcoal chips (5.4 ± 0.2 ka BP $_{2022}$) from the Lingjiatan site determined by previous researchers (Anhui Provincial Institute of Cultural Relics and Archaeology, 2006). The OSL-SAR ages of most Type II samples utilizing the modified measurement parameters (higher preheat and stimulation temperatures) agree well with those of all Type I samples within 10% error of the radiocarbon age, except for a significant underestimation of sample *LJTBE05* for Type II samples with unknown reasons (see Figure 8; Table 1). The slight OSL-SAR age variations of the other samples may come from inaccurate radioactive element measurements or water content estimations. The mean values of TL-MAAD also seem to agree with radiocarbon ages within the ±10% error range, but their relative errors are much larger than those of OSL-SAR, probably from the weighing errors of different aliquots. The TL-SAR ages are rejected in this study due to the inadequate sensitivity corrections discussed above.

5 Discussion

5.1 Relationship between component characteristics and measurement cycles and thermal history

There are differences in the fundamental parameters (σ, photoionization cross-section) of quartz extracted from different archaeological samples, but not varying significantly within the error range between different OSL-SAR cycles (see Supplementary Figure S1 in Supplementary Material). The relative component contributions and the fast

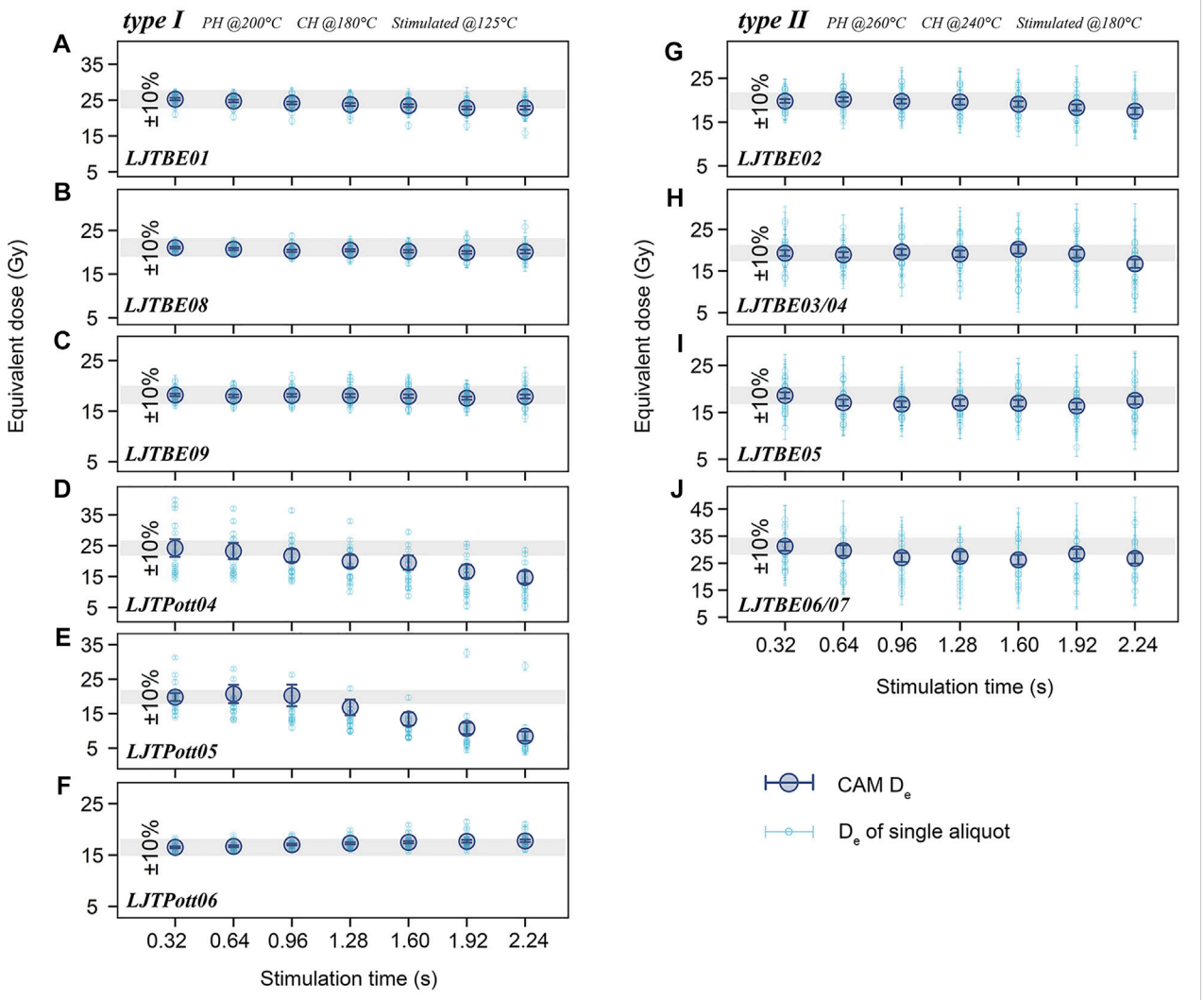

FIGURE 10
(A–F) $D_e(t)$ plot of type I samples. The small light blue hollow circle represents the D_e values and its standard error for one aliquot. The large dark blue filled circle represents the CAM D_e and its error. The integration intervals of stimulation times were 0–0.32 s, 0.32–0.64 s, 0.64–0.96 s, 0.96–1.28 s, 1.28–1.60 s, 1.60–1.92 s, and 1.92–2.24 s, respectively. **(G–J)** Similar $D_e(t)$ plot of type II samples as in **(A–F)**. The gray bands represent the ±10% CAM D_e error for the first (0–0.32 s) integration interval.

ratio values will not change significantly with the OSL-SAR cycle. The results in this study are consistent with those of Nian et al. (2019), who found that 200–600°C annealing did not significantly change the relative component contribution of sedimentary quartz.

According to the results of the firing temperatures determined by the thermal expansion method (see Supplementary Material), the firing temperatures of samples *LJTBE01* and *LJTBE05* (Type I) and sample *LJTBE03/04* (Type II) are approximately 900–950°C. However, the firing temperature of sample *LJTPott06* (Type I) may be lower than 770°C, which indicates that the firing temperature determined by this method cannot completely distinguish these two types in this study. The F_R is larger for the lower firing temperature sample *LJTPott06* (F_R ~31–40), while the F_R is smaller for the higher firing temperature samples *LJTBE01* (F_R ~6–18), *LJTBE03/04* (F_R ~4–9), and *LJTPott05* (F_R ~14–36), indicating that the Fast Ratio value can distinguish between relatively high and low temperature thermal history in 600–1,000°C, based on the simulation annealing experiments of Wang et al. (2022). They reported that annealing temperatures above 600–800°C would significantly reduce the fast ratio values of quartz, contrary to Gong et al. (2015), who heated the quartz gradient to 500°C. These different results indicate that the OSL properties of archaeological heated quartz have changed significantly at

high temperatures (over 600–800°C), leading to this difference from geological quartz.

5.2 D_e underestimation caused by inappropriate preheat temperature

Typically, before conducting OSL measurements, suitable preheating is required to avoid the influences of shallow electrons on D_e determination (Choi et al., 2003b; Peng et al., 2021). As suggested by Wintle and Murray (2006), a higher preheat temperature (e.g., 260°C) is typically used for older samples, while a lower preheat temperature (e.g., 200°C) is typically used for younger samples to avoid thermal transfer effects on D_e estimations (Rhodes, 2000). However, for the relatively young (<6 ka) Late Neolithic archaeological burnt clay and pottery in this study, preheat temperatures that are too low may cause significant D_e underestimation for type II samples. For the representative Type II sample *LJTBE06/07*, the D_e obtained at the 200°C preheat temperature will be underestimated by approximately 83% compared to the 260°C preheat temperature (see Figure 9). Despite higher stimulation temperatures being used for Type II samples, the stimulation temperature will not significantly affect D_e. When faced with samples collected from the same site or from a single stratigraphic section, an archaeologist or geologist usually selects only one or several representative samples for the preheat plateau test. However, for the samples in this study, this dating strategy is likely to result in a significant D_e underestimation of the Type II samples. Therefore, we suggest that when dating heated archaeological samples (especially for those heated by high firing temperatures), different types of samples should be distinguished by calculating the Fast Ratio, and separated preheat plateau tests should be conducted to avoid erroneous D_e estimation.

5.3 Thermal stability monitored by $D_e(t)$ plot

Since significant medium and slow components were observed in the CW-OSL signals of the archaeological samples, the variation of D_e as a function of the stimulation time (Bailey et al., 2003) was plotted to monitor the thermal stability of the component, i.e., $D_e(t)$ plot (Figure 10). A consistent initial OSL signal of the test dose (within 0.8 s) was used for the sensitivity correction for different integration intervals to avoid large errors in the $D_e(t)$ plot resulting from the reduction of the test dose OSL precision. D_e for each integration interval was calculated from the CAM values of multiple aliquots. Except for *LJTPott04* and *LJTPott05*, the CAM D_e did not change with the integration interval within 2.24 s for all the other archaeological samples in this study, indicating that the D_e values of these samples were not affected by the thermally unstable component. However, the D_e values of samples *LJTPott04* and *LJTPott05* started to decrease after 0.96 s. It is inferred that there may exist a thermally unstable medium component because the medium component dominates the signal proportion between 0.9–2.5 s. In other words, when using the conventional 0.8 s initial OSL signals as the integration interval for all samples with appropriate measurement conditions in this study, the D_e will not be significantly affected by the medium and slow components.

6 Conclusion

This study focused on analyzing the OSL component characteristics of heated quartz extracted from burnt clay and pottery shards from the Lingjiatan archaeological site. Different luminescence brightness and component contributions in the initial (within 0.8 s) OSL signals were observed in these archaeological samples. The Fast Ratio value can be used as a classification criterion to identify the OSL characteristics of these samples. Type I samples had relatively larger Fast Ratio values (F_R>10), and the preheat plateau appeared from lower temperatures. For Type II samples with smaller Fast Ratio values (F_R<10), the preheat plateau appeared from higher temperatures. Applying low preheat temperatures (below the plateau region) for Type II samples would lead to a significant D_e underestimation. Therefore, separated preheat plateau test strategies are necessary for these two types of samples. With the increase in the preheat temperature, the thermal transfer of Type II samples increases much more significantly than that of Type I samples. However, the recuperation can be reduced by raising the stimulation temperature for Type II samples without a significant effect on D_e. The ages obtained by the modified OSL-SAR protocol of most Type II samples (3 of 4 samples) and the conventional OSL-SAR protocol of all Type I samples (6 samples) agreed well with TL-MAAD and ^{14}C within the error range. However, the TL-SAR ages showed either overestimation or underestimation, mainly due to the inappropriate sensitivity correction for natural signals. Finally, the age of the Lingjiatan archaeological site was dated back to approximately 5.4–5.8 ka BP $_{2022}$.

Data availability statement

The original contributions presented in the study are included in the article/Supplementary Material, further inquiries can be directed to the corresponding author.

Author contributions

AF organized and conceptualized the research and reviewed and proofread the manuscript. C-XW, AF, YW, and YZ collected the samples. XZ authorized the sampling. C-XW completed the experiments, analyzed the data and wrote the manuscript. YZ provided the firing temperature data. CH reviewed and proofread the manuscript.

Funding

This study was supported by the National Natural Science Foundation of China (Grant No. 41303080), the Youth Innovation Promotion Association CAS (2018499) and the USTC Research Funds of the Double First-Class Initiative (YD2110002027).

Acknowledgments

We thank Mei Huang and Lingling Shi for helping with the experiments and Fanzhen Feng for proofreading the manuscript. We also thank the reviewers for their revisions and enlightening ideas.

Conflict of interest

The authors declare that the research was conducted in the absence of any commercial or financial relationships that could be construed as a potential conflict of interest.

Publisher's note

All claims expressed in this article are solely those of the authors and do not necessarily represent those of their affiliated organizations, or those of the publisher, the editors and the reviewers. Any product that may be evaluated in this article, or claim that may be made by its manufacturer, is not guaranteed or endorsed by the publisher.

Supplementary material

The Supplementary Material for this article can be found online at: https://www.frontiersin.org/articles/10.3389/feart.2022.933342/full#supplementary-material

References

Aitken, M. J. (1985). *Thermoluminescence dating* (London ; Orlando: Academic Press). U.S.

Aitken, M. J., Tite, M. S., and Reid, J. (1964). Thermoluminescent dating of ancient ceramics. *Nature* 202, 1032–1033. doi:10.1038/2021032b0

Aitken, M. J., Zimmerman, D. W., and Fleming, S. J. (1968). Thermoluminescent dating of ancient pottery. *Nature* 219, 442–445. doi:10.1038/219442a0

Aitken, M., and Xie, J. (1990). Moisture correction for annual gamma dose. *Anc. TL* 8, 6–9.

Anderson, S. L., and Feathers, J. K. (2019). Applying luminescence dating of ceramics to the problem of dating Arctic archaeological sites. *J. Archaeol. Sci.* 112, 105030. doi:10.1016/j.jas.2019.105030

Anhui Provincial Institute of Cultural Relics and Archaeology (2006). *One of lingjiatan field archaeological excavation reports*. Beijing: Cultural Relics Publishing House. (in Chinese).

Bailey, R. M., Singarayer, J. S., Ward, S., and Stokes, S. (2003). Identification of partial resetting using De as a function of illumination time. *Radiat. Meas.* 37, 511–518. doi:10.1016/S1350-4487(03)00063-5

Bailey, R. M., Smith, B. W., and Rhodes, E. J. (1997). Partial bleaching and the decay form characteristics of quartz OSL. *Radiat. Meas.* 27, 123–136. doi:10.1016/S1350-4487(96)00157-6

Bailey, R. M. (2000). The slow component of quartz optically stimulated luminescence. *Radiat. Meas.* 32, 233–246. doi:10.1016/S1350-4487(99)00285-1

Bailiff, I. K. (2007). Methodological developments in the luminescence dating of brick from English late-medieval and post-medieval buildings. *Archaeometry* 49, 827–851. doi:10.1111/j.1475-4754.2007.00338.x

Bell, W. T. (1980). Alpha attenuation in quartz grains for thermoluminescence dating. *Anc. TL* 12, 4–8.

Bluszcz, A., and Bøtter-Jensen, L. (1995). Dosimetric properties of natural quartz grains extracted from fired materials. *Radiat. Meas.* 24, 465–468. doi:10.1016/1350-4487(95)00005-Y

Bøtter-Jensen, L., Agersnap Larsen, N., Mejdahl, V., Poolton, N. R. J., Morris, M. F., McKeever, S. W. S., et al. (1995). Luminescence sensitivity changes in quartz as a result of annealing. *Radiat. Meas.* 24, 535–541. doi:10.1016/1350-4487(95)00006-Z

Bøtter-Jensen, L., Andersen, C. E., Duller, G. A. T., and Murray, A. S. (2003a). Developments in radiation, stimulation and observation facilities in luminescence measurements. *Radiat. Meas.* 37, 535–541. doi:10.1016/S1350-4487(03)00020-9

Bøtter-Jensen, L., McKeever, S. W. S., and Wintle, A. G. (2003b). *Optically stimulated luminescence dosimetry*. 1st ed. Amsterdam ; Boston ; London: Elsevier.

Bulur, E. (2000). A simple transformation for converting CW-OSL curves to LM-OSL curves. *Radiat. Meas.* 32, 141–145. doi:10.1016/S1350-4487(99)00247-4

Burow, C. (2022). "calc_CentralDose(): Apply the central age model (CAM) after Galbraith et al. (1999) to a given De distribution. Function version 1.4.1," in *Luminescence: Comprehensive luminescence DatingDataAnalysis. Rpackageversion0.9.19*. Editors S. Kreutzer, C. Burow, M. Dietze, M. C. Fuchs, C. Schmidt, M. Fischer, et al. Available at: https://CRAN.R-project.org/package=Luminescence.

Choi, J. H., Duller, G. A. T., and Wintle, A. G. (2006). Analysis of quartz LM-OSL curves. *Anc. TL.* 24, 12.

Choi, J. H., Murray, A. S., Cheong, C. S., Hong, D. G., and Chang, H. W. (2003a). The resolution of stratigraphic inconsistency in the luminescence ages of marine terrace sediments from Korea. *Quat. Sci. Rev.* 22, 1201–1206. doi:10.1016/S0277-3791(03)00022-2

Choi, J. H., Murray, A. S., Jain, M., Cheong, C. S., and Chang, H. W. (2003b). Luminescence dating of well-sorted marine terrace sediments on the southeastern coast of Korea. *Quat. Sci. Rev.* 22, 407–421. doi:10.1016/S0277-3791(02)00136-1

Dietze, M., and Kreutzer, S. (2022). "plot_RadialPlot(): Function to create a radial plot. Function version 0.5.7," in *Luminescence: Comprehensive luminescence dating data analysis. R package version 0.9.19*. Editors S. Kreutzer, C. Burow, M. Dietze, M. C. Fuchs, C. Schmidt, M. Fischer, et al.Available at: https://CRAN.R-project.org/package=Luminescence.

Durcan, J. A., and Duller, G. A. T. (2011). The fast ratio: A rapid measure for testing the dominance of the fast component in the initial OSL signal from quartz. *Radiat. Meas.* 46, 1065–1072. doi:10.1016/j.radmeas.2011.07.016

Durcan, J. A., King, G. E., and Duller, G. A. T. (2015). Drac: Dose rate and age calculator for trapped charge dating. *Quat. Geochronol.* 28, 54–61. doi:10.1016/j.quageo.2015.03.012

Fan, A., Li, S.-H., and Li, B. (2009). Characteristics of quartz infrared stimulated luminescence (IRSL) at elevated temperatures. *Radiat. Meas.* 44, 434–438. doi:10.1016/j.radmeas.2009.02.019

Fu, X., Zhang, J.-F., Mo, D.-W., Shi, C.-X., Liu, H., Li, Y.-Y., et al. (2010). Luminescence dating of baked Earth and sediments from the Qujialing archaeological site, China. *Quat. Geochronol.* 5, 353–359. doi:10.1016/j.quageo.2009.06.006

Galbraith, R. F., and Roberts, R. G. (2012). Statistical aspects of equivalent dose and error calculation and display in OSL dating: An overview and some recommendations. *Quat. Geochronol.* 11, 1–27. doi:10.1016/j.quageo.2012.04.020

Gautier, A. (2001). Luminescence dating of archaeometallurgical slag: use of the SAR technique for determination of the burial dose. *Quat. Sci. Rev.* 20, 973–980. doi:10.1016/S0277-3791(00)00010-X

Gong, Z., Sun, J., Lü, T., and Tian, Z. (2014). Investigating the optically stimulated luminescence dose saturation behavior for quartz grains from dune sands in China. *Quat. Geochronol.* 22, 137–143. doi:10.1016/j.quageo.2014.01.003

Gong, Z., Sun, J., and Lü, T. (2015). Investigating the components of the optically stimulated luminescence signals of quartz grains from sand dunes in China. *Quat. Geochronol.* 29, 48–57. doi:10.1016/j.quageo.2015.06.004

Guérin, G., Mercier, N., and Adamiec, G. (2011). Dose-rate conversion factors: Update. *Anc. TL* 29, 5.

Guérin, G., Mercier, N., Nathan, R., Adamiec, G., and Lefrais, Y. (2012). On the use of the infinite matrix assumption and associated concepts: A critical review. *Radiat. Meas.* 47, 778–785. doi:10.1016/j.radmeas.2012.04.004

Haustein, M., Krbetschek, M. R., Trautmann, T., Roewer, G., and Stolz, W. (2001). A luminescence study for dating archaeometallurgical slags. *Quat. Sci. Rev.* 5. doi:10.1016/S0277-3791(00)00038-X

Huntley, D. J., Short, M. A., and Dunphy, K. (1996). Deep traps in quartz and their use for optical dating. *Can. J. Phys.* 74, 81–91. doi:10.1139/p96-013

Huntley, D. J. (2006). Thoughts arising from "Choi, Duller and Wintle: Analysis of quartz LM-OSL curves. *Anc. TL* 24, 69–70.

Jain, M., Murray, A. S., and Bøtter-Jensen, L. (2003). Characterisation of blue-light stimulated luminescence components in different quartz samples: implications for dose measurement. *Radiat. Meas.* 37, 441–449. doi:10.1016/S1350-4487(03)00052-0

Jain, M., and Lindvold, L. (2007). Blue light stimulation and linearly modulated optically stimulated luminescence. *Anc. TL* 25.

Kijek, N., and Chruścińska, A. (2015). Equivalent dose of quartz originating from ceramics obtained by OSL SAR method – tests of protocol parameters. *Radiat. Meas.* 81, 128–133. doi:10.1016/j.radmeas.2015.02.003

Kreutzer, S., Dietze, M., and Burow, C. (2022). "use_DRAC(): Use DRAC to calculate dose rate data. Function version 0.14," in *Luminescence: Comprehensive luminescence dating data analysis. R package version 0.9.19*. Editors S. Kreutzer, C. Burow, M. Dietze, M. C. Fuchs, C. Schmidt, M. Fis- cher, et al.Available at: https://CRAN.R-project.org/package=Luminescence.

Kreutzer, S. (2022). "fit_CWCurve(): Nonlinear least squares fit for CW-OSL curves -beta version. Function version 0.5.2," in *Luminescence: Comprehensive luminescence dating data analysis. R package version 0.9.19*. Editors S. Kreutzer, C. Burow, M. Dietze, M. C. Fuchs, C. Schmidt, M. Fischer, et al.Available at: https://CRAN.R-project.org/package=Luminescence.

Lai, Z., Murray, A. S., Bailey, R. M., Huot, S., and Bøtter-Jensen, L. (2006). Quartz red TL SAR equivalent dose overestimation for Chinese loess. *Radiat. Meas.* 41, 114–119. doi:10.1016/j.radmeas.2005.06.006

Li, B., and Li, S.-H. (2006). Comparison of estimates using the fast component and the medium component of quartz OSL. *Radiat. Meas.* 41, 125–136. doi:10.1016/j.radmeas.2005.06.037

Liritzis, I., Jin, Z., Fan, A., Sideris, A., and Drivaliari, A. (2016). Late helladic and later reuse phases of kastrouli settlement (Greece): Preliminary dating results. doi:10.5281/ZENODO.163775

Murray, A., Arnold, L. J., Buylaert, J.-P., Guérin, G., Qin, J., Singhvi, A. K., et al. (2021). Optically stimulated luminescence dating using quartz. *Nat. Rev. Methods Prim.* 1, 72. doi:10.1038/s43586-021-00068-5

Murray, A. S., and Wintle, A. G. (2000). Luminescence dating of quartz using an improved single-aliquot regenerative-dose protocol. *Radiat. Meas.* 32, 57–73. doi:10.1016/S1350-4487(99)00253-X

Murray, A. S., and Wintle, A. G. (2003). The single aliquot regenerative dose protocol: potential for improvements in reliability. *Radiat. Meas.* 37, 377–381. doi:10.1016/S1350-4487(03)00053-2

Nian, X., Zhang, W., Qiu, F., Qin, J., Wang, Z., Sun, Q., et al. (2019). Luminescence characteristics of quartz from Holocene delta deposits of the Yangtze River and their provenance implications. *Quat. Geochronol.* 49, 131–137. doi:10.1016/j.quageo.2018.04.010

Peng, J., Dong, Z., Han, F., Long, H., and Liu, X. (2013). R package numOSL: numeric routines for optically stimulated luminescence dating. *Anc. TL* 31, 8.

Peng, J., and Li, B. (2017). Single-aliquot regenerative-dose (SAR) and standardised growth curve (SGC) equivalent dose determination in a batch model using the R package 'numOSL'. *Anc. TL* 35, 22.

Peng, J., Wang, X., Adamiec, G., Pagonis, V., and Choi, J.-H. (2021). Modelling the dependence of equivalent dose determined from a dose recovery test on preheating temperature: The intervention of shallow electron traps. *Radiat. Meas.* 142, 106566. doi:10.1016/j.radmeas.2021.106566

Peng, J., and Wang, X. (2020). On the production of the medium component in quartz OSL: Experiments and simulations. *Radiat. Meas.* 138, 106448. doi:10.1016/j.radmeas.2020.106448

Prescott, J. R., and Hutton, J. T. (1994). Cosmic ray contributions to dose rates for luminescence and ESR dating: Large depths and long-term time variations. *Radiat. Meas.* 23, 497–500. doi:10.1016/1350-4487(94)90086-8

Prescott, J. R., and Hutton, J. T. (1988). Cosmic ray and gamma ray dosimetry for TL and ESR. *Int. J. Radiat. Appl. Instrum. Part D. Nucl. Tracks Radiat. Meas.* 14, 223–227. doi:10.1016/1359-0189(88)90069-6

R Core Team (2016). R: A language and environment for statistical computing. Vienna Austria. Available at: https://www.r-project.org/.

Rawat, N. S., Dhabekar, B., Kulkarni, M. S., Muthe, K. P., Mishra, D. R., Soni, A., et al. (2014). Optimization of CW-OSL parameters for improved dose detection threshold in Al2O3:C. *Radiat. Meas.* 71, 212–216. doi:10.1016/j.radmeas.2014.02.013

Rees-Jones, J. (1995). Optical dating of young sediments using fine-grained quartz. *Anc. TL* 13, 9–14.

Rhodes, E. J. (2000). Observations of thermal transfer OSL signals in glacigenic quartz. *Radiat. Meas.* 32, 595–602. doi:10.1016/S1350-4487(00)00125-6

Richter, D., Angelucci, D. E., Dias, M. I., Prudêncio, M. I., Gouveia, M. A., Cardoso, G. J., et al. (2014). Heated flint TL-dating for gruta da oliveira (Portugal): dosimetric challenges and comparison of chronometric data. *J. Archaeol. Sci.* 41, 705–715. doi:10.1016/j.jas.2013.09.021

Richter, D., Grün, R., Joannes-Boyau, R., Steele, T. E., Amani, F., Rué, M., et al. (2017). The age of the hominin fossils from jebel irhoud, Morocco, and the origins of the middle stone age. *Nature* 546, 293–296. doi:10.1038/nature22335

Richter, D., and Krbetschek, M. (2006). A new thermoluminescence dating technique for heated flint. *Archaeometry* 48, 695–705. doi:10.1111/j.1475-4754.2006.00281.x

Singarayer, J. S., and Bailey, R. M. (2003). Further investigations of the quartz optically stimulated luminescence components using linear modulation. *Radiat. Meas.* 37, 451–458. doi:10.1016/S1350-4487(03)00062-3

Solongo, S., Tengis, S., Wagner, G. A., and Hüttel, H.-G. (2021). CW-OSL, LM-OSL and TL dating of bricks from karakorum, Mongolia: Insights from TL spectra. *Geochronometria* 48, 402–414. doi:10.2478/geochr-2020-0003

Song, K.-W., Yun, K.-K., and Hong, D.-G. (2009). Radiation response of thermoluminescence glow peaks separated using a glow curve fitting method for red emission from quartz. *Radiat. Meas.* 44, 611–614. doi:10.1016/j.radmeas.2009.03.034

Steffen, D., Preusser, F., and Schlunegger, F. (2009). OSL quartz age underestimation due to unstable signal components. *Quat. Geochronol.* 4, 353–362. doi:10.1016/j.quageo.2009.05.015

Sun, M., Sun, Y., Wei, H., Hou, G., Xianba, J., Xie, L., et al. (2021). Luminescence dating of relics in ancient cities provides absolute dates for understanding human-land relationships in qinghai lake basin, northeastern Tibetan plateau. *Front. Earth Sci.* 9, 701037. doi:10.3389/feart.2021.701037

Thomas, P. J., Jain, M., Juyal, N., and Singhvi, A. K. (2005). Comparison of single-grain and small-aliquot OSL dose estimates in years old river sediments from South India. *Radiat. Meas.* 39, 457–469. doi:10.1016/j.radmeas.2004.07.005

Tsukamoto, S., Rink, W. J., and Watanuki, T. (2003). OSL of tephric loess and volcanic quartz in Japan and an alternative procedure for estimating De from a fast OSL component. *Radiat. Meas.* 37, 459–465. doi:10.1016/S1350-4487(03)00054-4

Wang, C.-X., Ji, X., Wu, Y., Jin, Z., Zhang, Y., Chen, M., et al. (2022). Quartz OSL and TL dating of pottery, burnt clay, and sediment from Beicun archaeological site, China. *Quat. Geochronol.* 70, 101281. doi:10.1016/j.quageo.2022.101281

Wang, X. L., Du, J. H., Adamiec, G., and Wintle, A. G. (2015). The origin of the medium OSL component in West Australian quartz. *J. Lumin.* 159, 147–157. doi:10.1016/j.jlumin.2014.11.003

Westaway, K., and Prescott, J. (2012). Investigating signal evolution: A comparison of red and UV/blue TL, and UV OSL emissions from the same quartz sample. *Radiat. Meas.* 47, 909–915. doi:10.1016/j.radmeas.2012.01.001

Wintle, A. G., and Murray, A. S. (2006). A review of quartz optically stimulated luminescence characteristics and their relevance in single-aliquot regeneration dating protocols. *Radiat. Meas.* 41, 369–391. doi:10.1016/j.radmeas.2005.11.001

Zander, A., Strebler, D., Classen, E., Rethemeyer, J., and Brückner, H. (2019). Roman traces in Germania magna: New thermoluminescence and pIRIR $_{290}$ data from a lime kiln at Bergisch Gladbach, Germany. *Archaeometry* 61, 506–518. doi:10.1111/arcm.12435

Zimmerman, D. W. (1971). Thermoluminescent dating using fine grains from pottery. *Archaeometry* 13, 29–52. doi:10.1111/j.1475-4754.1971.tb00028.x

frontiers | Frontiers in Earth Science

TYPE Original Research
PUBLISHED 05 August 2022
DOI 10.3389/feart.2022.931075

OPEN ACCESS

EDITED BY
Hao Long,
Nanjing Institute of Geography and Limnology (CAS), China

REVIEWED BY
Yan Li,
China University of Geosciences, China
Jiafu Zhang,
Peking University, China

*CORRESPONDENCE
Baolin Pan,
blpan@cnu.edu.cn

SPECIALTY SECTION
This article was submitted to Quaternary Science, Geomorphology and Paleoenvironment, a section of the journal Frontiers in Earth Science

RECEIVED 28 April 2022
ACCEPTED 28 June 2022
PUBLISHED 05 August 2022

CITATION
Liu X, Li X, Zhao Q, Pan B, Wang J and Wei M (2022), Dose dependency of aliquot sizes and age models from modern alluvial fan deposits of Helan Mountain, China.
Front. Earth Sci. 10:931075.
doi: 10.3389/feart.2022.931075

Dose dependency of aliquot sizes and age models from modern alluvial fan deposits of Helan Mountain, China

Xiuying Liu[1], Xiao Li[1], Qiuyue Zhao[2], Baolin Pan[1]*, Junping Wang[1] and Mingjian Wei[1]

[1]College of Resource Environment and Tourism, Capital Normal University, Beijing, China, [2]Key Laboratory of Tourism and Resources Environment in Universities of Shandong, Taishan University, Tai'an, China

Alluvial fan deposits are identified as evidence of regional climatic variations and tectonic events; therefore, it is crucial to establish absolute time series by dating alluvial fan deposits. Limited exposure to light poses a challenge to accurately estimating the buried ages for alluvial deposits with optically stimulated luminescence (OSL). This challenge has been positively developed by controlling the number of grains on each disk to measure and choosing suitable statistical models for the equivalence dose (D_e) distribution to analyze. In this research, three modern alluvial samples and one modern loess-like sample were collected from the Dashuigou alluvial fan of Helan Mountain, China. The D_e distributions of these four samples were studied by the application of small aliquots (1-, 3-, and 5-mm aliquots) of quartz OSL with the average dose model, central age model, unlogged minimum age model (MAM), lowest 5%, internal/external consistency criterion minimum age model (IEU), and finite mixture model. It is concluded that an overestimation of D_e lower than 1 Gy can be obtained using quartz OSL dating of 1-mm aliquots (~50 grains) with MAM and IEU for the alluvial sediments. The lowest 5% method may underestimate the D_e values of the 1-mm aliquots for young samples. This research makes the dose dependency of aliquot sizes and age models more definite and opens up the possibility of dating paleoalluvial deposits to establish a chronological framework to decipher the implications of paleoclimates and tectonics.

KEYWORDS

Aliquot sizes, Age Models, Modern deposits, Alluvial fan, Quartz OSL dating

Introduction

Alluvial fans are depositional landforms that form in areas where steep high-power channels enter a zone of reduced stream power (Goudie, 2004). It is associated with rapid and short-term flood sedimentation, which sometimes results in natural disasters (Fiorillo and Wilson, 2004; Tang et al., 2012). In addition, alluvial fans are closely related to tectonic activities (Yang et al., 1985; Han, 1992; Hou and Han, 1995; Cui et al., 2007) and

climate changes (Ritter et al., 1995; Cui, 1999). To research the historic process of delivering sediment to an alluvial fan (by debris flows or fluvial processes, Goudie, 2004), dating depositional events is particularly important.

Over the last 2 decades, optically stimulated luminescence (OSL) has been increasingly applied for dating alluvial deposits, including debris flow deposits and flash flood deposits (Jain et al., 2004; Rittenour, 2008; Fuchs et al., 2010; Kenworthy et al., 2014; Sewell et al., 2015; Zhao et al., 2015, 2017; Palstra et al., 2021). However, the applicability of OSL dating from alluvial deposits remains uncertain, especially because incomplete resetting is known as one of the major problems (Olley et al., 1998; Fuchs and Lang, 2001; Stokes et al., 2001). Thus, there would be a significant dose overestimation in the determination of the equivalent dose (D_e) of alluvial sediments. To reduce the effects related to incomplete bleaching, there are a number of studies on the factors associated with D_e, including mineral types (Wallinga et al., 2001; Fiebig and Preusser, 2007), grain sizes (Olley et al., 1998; Hu et al., 2010), transport distance (Stokes et al., 2001; Rodnight et al., 2006), measurement procedures (Wintle, 1997; Wallinga, 2002), aliquot sizes (Duller, 2008), and statistical methods (age models) (Galbraith and Roberts, 2012; Medialdea et al., 2014) in OSL measurements and data analyses.

The OSL signal from quartz is reset more quickly than the infrared-stimulated luminescence from feldspar when the minerals are exposed to sunlight (Godfrey-Smith et al., 1988; Yang et al., 2012). In addition, in many cases, coarser grains are generally better bleached than finer fractions (Olley et al., 1998; Hu et al., 2010; Yang et al., 2017). Moreover, D_e could decrease with increasing transport distance due to the longer time to bleach (Alexanderson, 2007; Vandenberghe et al., 2007; Hu et al., 2010; Zhao et al., 2015). Compared with the multiple-aliquot procedures and the initial single aliquot procedures (Duller, 1994, 1995; Wintle and Murray., 1998), the single aliquot regenerative dose (SAR) protocol (Murray and Wintle, 2000, 2003) does not need to be normalized and can correct the sensitivity change. In general, the SAR protocol with coarser quartz grains is a fairly reliable method of OSL dating for alluvial deposits.

For incompletely bleached sediments, the greater the number of grains on each aliquot that are measured at the same time, the less variation in D_e that will be observed because of the impact of averaging (Olley et al., 1999; Wallinga, 2002; Duller, 2008). A better way to reduce the impact of averaging is to lessen the number of grains on each aliquot (Duller, 2008). It now becomes possible to measure the luminescence from a single grain of quartz to distinguish between well-bleached grains (Thomas et al., 2005; Duller, 2008; Wu et al., 2010; Zhao et al., 2015; Zhao et al., 2017). However, the single grain technique requires considerable time, labor, and specific equipment, which restricts its wide application (Tooth et al., 2007; Yang et al., 2017). Many studies have shown that the application of a specific aliquot size can identify well-bleached populations of sediments with different D_e values (Olley et al., 1999; Tooth et al., 2007; Duller, 2008) and obtain accurate burial doses for modern and old sediments (Medialdea et al., 2014). In addition to the impact of the aliquot sizes, studies on statistical methods have shown that some different age models can be used for the analysis of D_e values to obtain the true deposition ages. The application of statistical methods is essential for incomplete bleaching sediments to identify well-bleached populations (Duller, 2006, 2008; Wu et al., 2010; Yang et al., 2017; Zhao et al., 2015, 2017).

The selection of aliquot sizes and statistical methods is crucial for the OSL dating of incompletely bleached sediments. However, there is a lack of systematic research on the dose dependency of aliquot sizes and age models. It is still unclear from which combination of aliquot sizes and age models the D_e values obtained can be consistent with known ages within the limit of error, especially for fast-accumulating sediments. This work aims to study the dependency of aliquot sizes and age models on D_e using poorly bleached modern alluvial sediments. A series of alluvial fans have developed on the eastern piedmont of Helan Mountain, providing a good location and materials for our research. In this study, the equivalent doses were measured using three aliquot sizes (1, 3, and 5 mm) of 90–125 μm quartz grains for modern deposits from the alluvial fan and calculated by applying six different age models. It is worthwhile to test whether there is a suitable combination of "aliquot sizes and age models" to obtain accurate buried ages for the alluvial deposits.

Geological setting and sampling

The Dashuigou (DSG) alluvial fan is located at the eastern piedmont of Helan Mountain (Figure 1A) in northwestern China with longitudes and latitudes of 106°10′–106°13′E and 38°51′–38°53′N. The Helan Mountains, lithologically, are mainly composed of granite, limestone, quartzite, sandstone, slate, and conglomerate. The general elevation is 2000–3,000 m, and the annual precipitation is 200–400 mm in this area, but the precipitation from June to September accounts for 62% of the annual precipitation (Jiang, 2016). The length of the DSG alluvial fan is ~2.5 km, the width is ~4 km (Figure 1B), and the length of the main stream is approximately 17 km. The sediments from the apex to the middle of the fan are gravelly sand, those from the middle to the edge of the fan are fine gravel and sand, and those at the edge of the fan are sand and soil. In the vertical direction, the sediment at the bottom of a fan is mainly composed of clay or silty material, and the grain size gradually increases to gravel. The structure of the alluvial fan is often composed of interbedded sand and gravel, with sandy lenses in gravel layers or gravelly lenses in sand layers.

All samples were collected from the DSG alluvial fan with a steel horizontal tube into a fresh outcrop of the sediments and sealed to avoid exposure and moisture loss. The depths of all the samples (top of the steel tubes) are 5 mm below the surface.

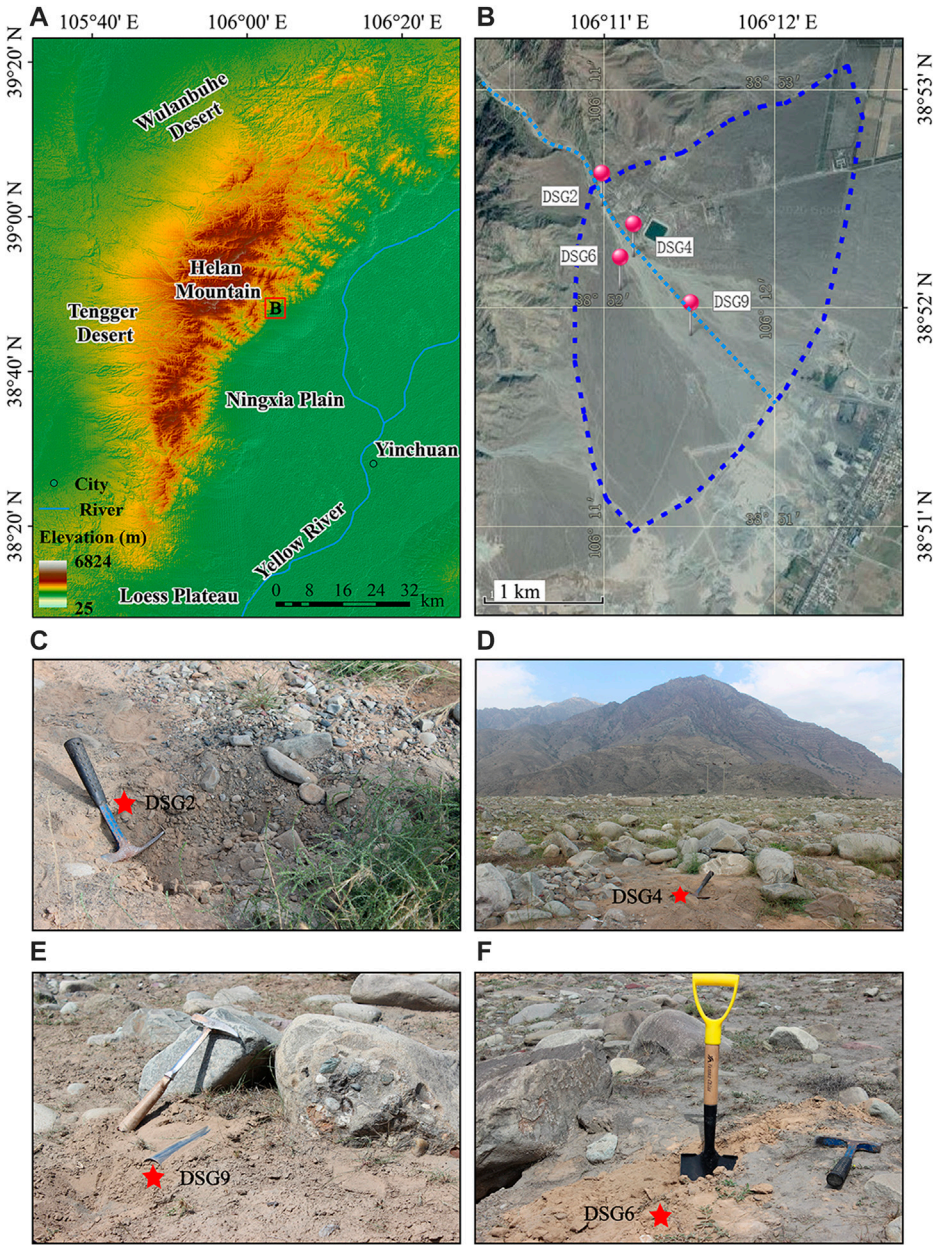

FIGURE 1
Location map of the study site. **(A)** Topographic map of Helan Mountain. **(B)** Satellite map of alluvial fan (sampling points are highlighted in red). **(C–F)** Photos showing the landscape and the sections from which samples were collected: three alluvial deposit samples (DSG2, DSG4, and DSG9) and one loess-like deposit sample (DSG6).

According to news reports, large floods or sparse debris flows have occurred several times in the DSG and its neighboring areas during the last 20 years, and their recurrence period is 5–10 years (Li and Chen, 2006). Therefore, the samples collected from DSG can be regarded as modern sediments (Li et al., 2018). Three alluvial deposit samples (DSG2, DSG4, and DSG9) (Figures 1C–E) and one loess-like deposit sample (DSG6) (Figure 1F) on the alluvial fan surface were collected. DSG2 and DSG4 were taken from the fan head trench gully, and DSG9 was collected from the matrix of the diamicton at the edge of the alluvial fan surface (Figure 1B).

Sample preparation and instrumentation

Sample preparation was performed under subdued red-light conditions. The fraction of 90–125 μm was obtained by

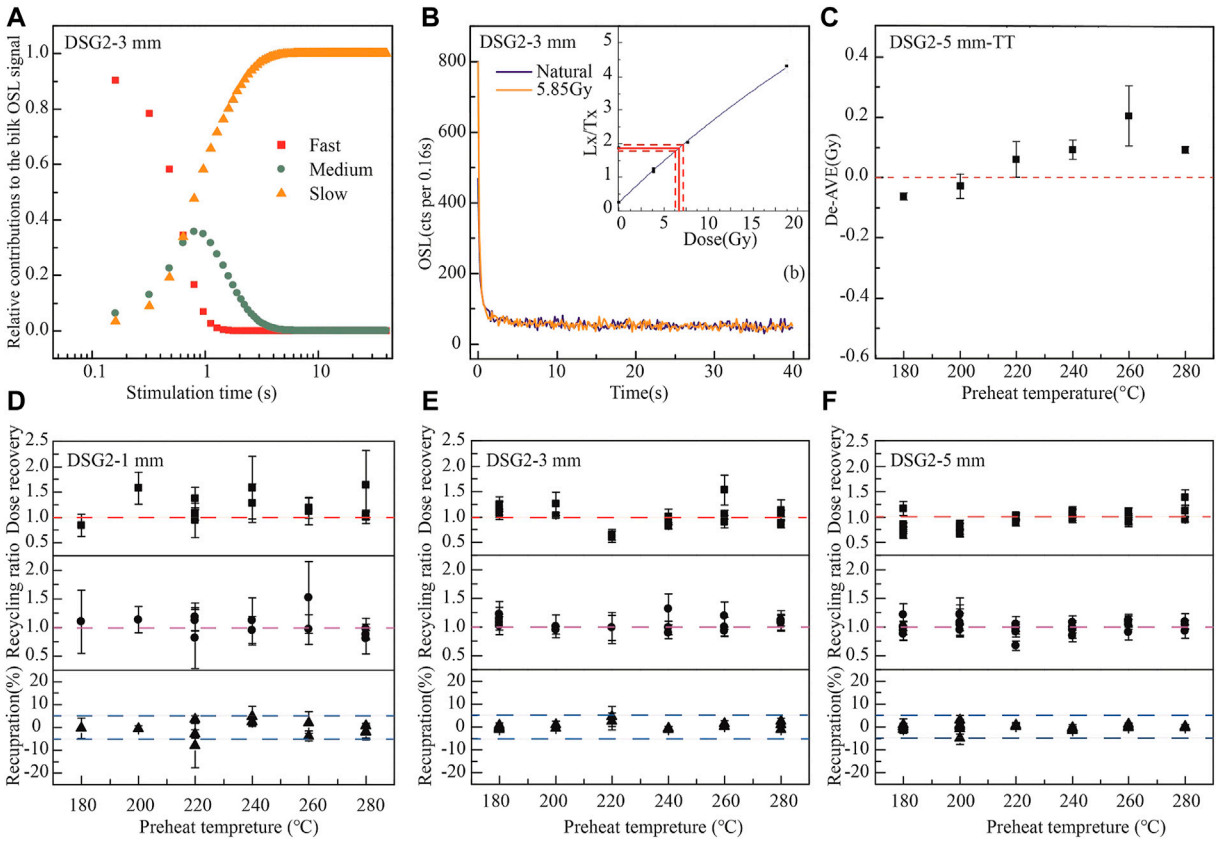

FIGURE 2
(A) Relative contributions from individual components to the bulk optically stimulated luminescence (OSL) signals as a function of the stimulation time for DSG2 with a 3-mm aliquot. **(B)** Decay curve of DSG2 and growth curve (interpolated **B**). **(C)** Thermal transfer (TT) of DSG2 with 5-mm aliquots. **(D–F)** Dose recovery–preheat plateau of DSG2 with different aliquot sizes (1, 3, and 5 mm).

wet sieving from samples and then treated with 10% HCl to remove carbonates and 30% H_2O_2 to remove organic matter. After this, quartz-rich grains were separated by heavy liquid densities of 2.58 and 2.70 g cm^{-3}. This fraction was then etched with 40% HF for 40 min and washed with 10% HCl for 40 min to extract the pure quartz grains. Resieving was needed after chemical treatment to a fraction of 90–125 μm for all samples. The remaining feldspar contamination in quartz grains of all samples was checked using IR measurement (Duller et al., 2003). Quartz grains were glued in a single layer on 9.7 mm stainless steel discs but with different aliquot sizes using silicone oil. To compare the dependency of D_e on aliquot sizes, all the D_e values were measured by 1-, 3 -, and 5-mm aliquots. The number of grains (~50 grains) on the 1-mm aliquot is the average value of six aliquots counted under a microscope, and those of 3 mm (~450 grains) and 5 mm (~1,250 grains) are calculated based on their areas relative to 1-mm aliquots (Duller, 2008).

OSL measurements were carried out on Risø TL/OSL DA-20 readers (Bøtter-Jensen et al., 2010) at Capital Normal University. Optical stimulation used an array of blue (470 nm) LEDs providing a power density of ~40 mW cm^{-2} at the sample position. OSL was measured using blue LED stimulation at 125°C for 40 s. Laboratory irradiation employed a ^{90}Sr/^{90}Y beta source (~0.117 Gy s^{-1}) fitted on the readers at the quartz grain discs. The beta source had good spatial uniformity (<5% standard deviation across the sample area).

Equivalent dose determination

Equivalent dose estimates were measured using the SAR protocol (Murray and Wintle, 2000, 2003; Murray et al., 2021). The relative contributions of individual components as a function of the stimulation time for sample DSG2 show that luminescence signals of quartz are provided by the fast component before 0.48 s (Figure 2A). Therefore, early background subtraction (Cunningham and Wallinga, 2010) was used to analyze the D_e values, which means that the OSL signals were derived from the summation of the first 0.48 s (0.16 s

per channel) of stimulation minus the summation of the following 0.48 s. The decay curve corresponds to the natural dose and to a given dose of ~5.85 Gy, and the growth curve is shown in Figure 2B. Dose estimates were accepted if 1) the relative error on the test dose signal (S_{Tn}) did not exceed 30%, 2) the recycling ratio was equal to unity within two standard deviations, and 3) the recuperation dose was less than 5% of the natural dose (Duller, 2008).

To establish an appropriate thermal treatment, the dependency of D_e on preheat temperatures was investigated using a preheat temperature range of 180°C–280°C with 20°C as the step, which is 20°C higher than a cut heat range of 160°C–260°C (Murray and Wintle, 2003), and ~20% of the expected natural dose was used as the test dose. Thermal transfer (TT) has been considered a limitation to the equivalent dose for young sediments (Rhodes, 2000; Jain et al., 2004). To test the dependency of TT on the preheat temperatures, DSG2 with 5-mm aliquots was used to assess the contribution of TT at different preheat temperatures, and three aliquots were measured at each preheat temperature. Aliquots were bleached twice for 100 s using blue diodes at room temperature (20°C), and the two bleaching steps were separated by a 10,000 s pause (Vandenberghe et al., 2007). Then, the SAR protocol was performed at different preheat temperatures, and three aliquots were measured at each preheat temperature. Although the TT doses (Figure 2C) increase with the preheat temperatures ranging from 180°C to 260°C, they are insignificant when the preheat temperature is not higher than 200°C. To determine the preheat temperature, a dose recovery test was conducted at different preheat temperatures (dose recovery–preheat plateau test). The first three steps of the dose recovery–preheat plateau were the same as those of the TT test. After the second bleaching, the aliquots were given a laboratory dose that was equal to the expected natural dose (for DSG2, the laboratory dose was ~5.85 Gy) before the SAR protocol was performed at different preheat temperatures. Dose recovery–preheat plateau tests for the 1-, 3-, and 5-mm aliquots of DSG2 were carried out, and the results showed that the dose recovery ratios were independent of the preheat temperatures (Figures 2D–F). The dose recovery ratios of the 1-, 3-, and 5-mm aliquots were 1.14 ± 0.28 (n = 18), 1.03 ± 0.13 (n = 18) and 0.94 ± 0.08 (n = 27), respectively. The corresponding recycling ratios were 0.99 ± 0.34, 1.09 ± 0.19 and 1.00 ± 0.13, respectively, and the recuperation dose was less than 5% of the natural dose (−1.51 ± 2.18%, 0.51 ± 0.32% and 0.04 ± 0.27% of the given dose). Combined with the TT results, the preheat temperature of 180°C and a corresponding cut heat temperature of 160°C were adopted in all further D_e measurements.

It is known that statistical analysis of D_e values is essential when calculating D_es and ages. The average dose model (ADM, Guérin et al., 2017) and central age model (CAM, Galbraith et al., 1999) have been commonly used to analyze the D_e distribution for well-bleached sediments with normal distributions of D_e values. The minimum age model (MAM, Galbraith et al., 1999; Arnold et al., 2009) assumes that only a proportion of the D_e values belong to the burial dose distribution and that the other D_e values are part of a normal distribution truncated at the burial dose. This statistical method has been applied to modern earthquake-related sediments to identify the lower D_es, which is related to the true ages (Fattahi et al., 2016; Yang et al., 2017). The internal/external consistency criterion (IEU, Thomsen et al., 2003, 2007) was used to identify the lowest normal dose population, which is presumed to be the population of grains most likely to have been well-bleached at deposition (Zhao et al., 2015, 2017). The lowest 5% (Olley et al., 1998) has been applied to modern debris flow deposits in which the dose distribution includes negative D_e values (Wu et al., 2010). The finite mixture model (FMM, Galbraith and Green, 1990; Galbraith, 2005) has been used to analyze glaciofluvial and debris flow deposits to isolate the dominant well-bleached population (Duller, 2006, 2008).

These six dose statistical analysis methods were applied to estimate the dose distributions of three aliquot sizes in the luminescence package R-project (Burow, 2020a, 2020b, 2020c; Christophe et al., 2020; Smedley, 2020). The ADM and CAM are commonly used to calculate the doses when there is only a single population of grains, which means that the sediments are homogeneous and well-bleached. The MAM assumes that only a part of the measured doses was from well-bleached grains before burial and that the others were from poorly bleached grains. The D_e values appropriate for determining the burial dose of the sediments are defined by the grain population at the lower distribution (Duller, 2008). The FMM is commonly used to estimate the D_e of different components with multipeak distribution. σm in the ADM and σb in the MAM and FMM represent the expected overdispersion (OD) in the data of the well-bleached samples (Cunningham and Wallinga, 2012). The OD of CAM in the dose recovery experiment was applied as the expected OD in the ADM, MAM, and FMM. In the D_e calculation of the ADM, CAM, and FMM, the negative dose estimations were removed. The lowest 5% can be used to calculate the D_es when the dose distribution includes negative D_e values (Bailey and Arnold, 2006). The IEU is usually used to identify the minimum normal dose population that is most likely well-bleached before being buried. The parameter values of a (slope) and b (intercept) in the IEU were found to be 0.13 ± 0.02 and 0.04 ± 0.02 Gy with beta dose recovery (0 and 5.85 Gy) tests, respectively.

Results and discussion

The choice of S_{Tn} is an influencing factor in an acceptable number of aliquots to determine D_e distributions. To test the importance of the S_{Tn} to the D_e values, the CAM, ADM, MAM, and FMM D_es were calculated with the S_{Tn} ranging from 10 to

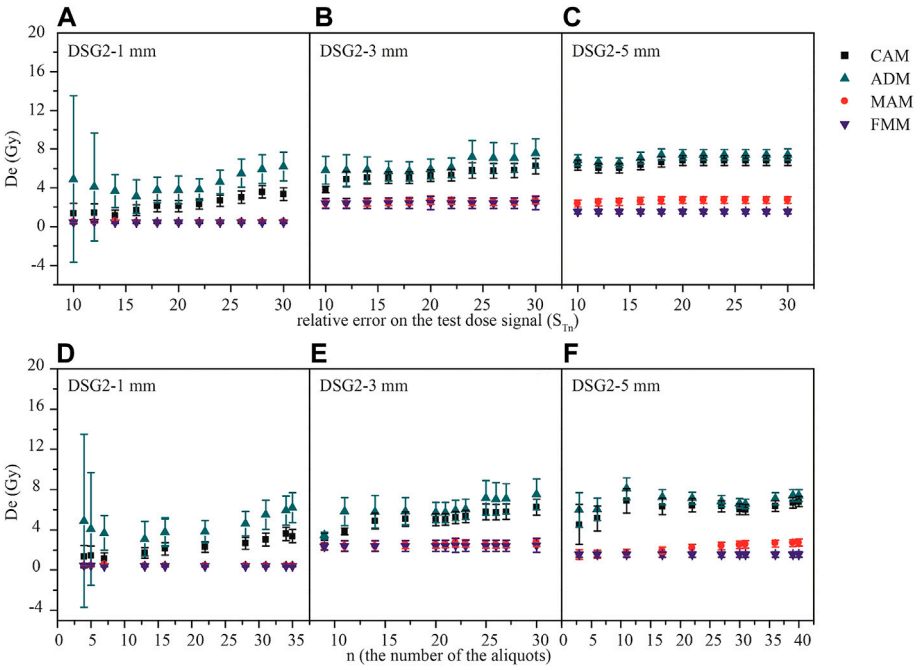

FIGURE 3
(A–C) Effect of rejection criteria of the relative error on the test dose signal (S_{Tn}). **(D–F)** Quantity of the aliquots accepted on the dose of the CAM, ADM, MAM, and FMM with different aliquot sizes.

30%. For the MAM and FMM, the D_e values are independent of the S_{Tn} for all aliquot sizes (Figures 3A–C). Thus, application of the S_{Tn} range from 10 to 30% has no impact on the absolute MAM and FMM doses determined. Similar appearances have been described for CAM by Thomsen et al., 2012, 2016. However, in our study, the precision is increased for the CAM and ADM when the S_{Tn} is higher than 15%, which may be due to the small quantity (fewer than 10) of the aliquots accepted to calculate D_es. Furthermore, the D_e values as a function of the number of aliquots with the different age models are shown in Figures 3D–F. This indicates that the D_e values are stable when the number of aliquots used to calculate D_e is more than 10 in the MAM and FMM, but the precision of equivalent dose estimation improves with the increase in the number of aliquots for the ADM and CAM. However, it has been shown that both the precision and accuracy of dose estimations from heterogeneously bleached samples are improved with the increasing number of aliquots with the MAM (Peng et al., 2020). In this research, such variations in MAM were not observed; therefore, more than 15 aliquots accepted in the dose estimations are enough to determine the D_es.

More than 1,000 aliquots were measured for the D_es of the four samples. A kernel density estimate (KDE, Dietze and Kreutzer, 2020) plot for each sample with 1-, 3-, and 5-mm aliquots was constructed to visualize the dose distribution (Figure 4). KDE plots of the three alluvial samples with different aliquot sizes show wide distributions and obvious multiple peaks and wide ranges of D_e values, whereas that of the loess-like sample DSG6 shows a normal distribution with only one peak in Figure 4. This indicates that the alluvial sediments are poorly bleached and contain complex components. However, the presence of probability peaks of 1-mm aliquots close to 0 Gy indicates success in identifying well-bleached populations. According to the KDE plots, n (components) was set as 6, and the results of the D_e were obtained by the lowest dose component of the FMM.

A summary of equivalent doses and ages with different aliquot sizes and age models of four samples is shown in Table 1. For all samples, the D_es obtained with ADM of 1-, 3-, and 5-mm aliquot sizes are consistent within one standard error. The same results are calculated from all the CAM D_es but from DSG2 with 1 mm. The CAM and ADM D_es from the three alluvial samples (DSG2, DSG4, and DSG9) overestimate ~6 and ~3 Gy at least even when a 1-mm aliquot is applied, respectively (Figures 5, 6). Some studies show that the D_es from debris flows and fluvial deposits with small aliquots are overestimated compared to the expected dose, which may be due to the application of CAM or ADM to calculate D_es (Thomsen et al., 2007; Zhao et al., 2015, 2017). Therefore, for incompletely bleached sediments, the application of CAM and ADM needs to be done carefully. Therefore, the MAM, FMM, IEU, and the lowest 5% are applied to estimate the D_es in the following research.

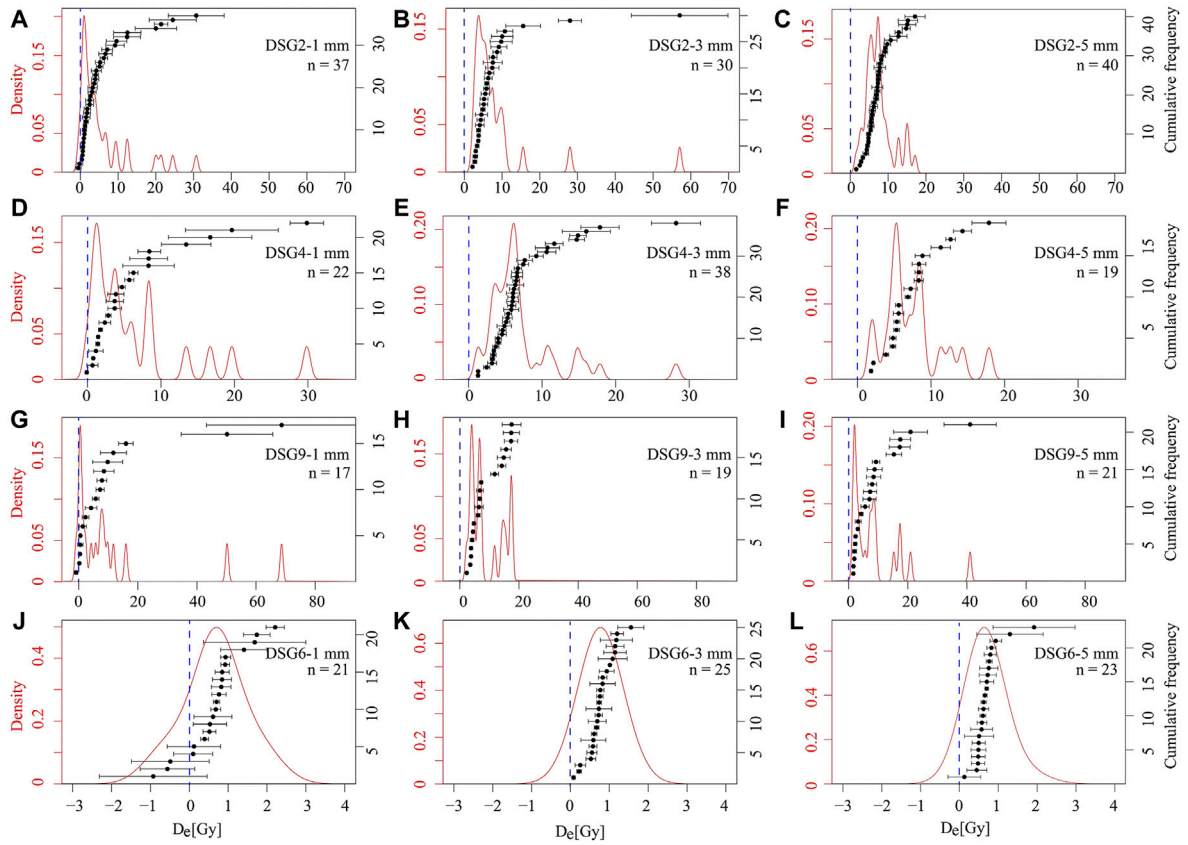

FIGURE 4
Kernel density estimate plots of natural dose distributions from DSG2 with 1-, 3-, 5-mm aliquots **(A–C)**; DSG4 with 1-, 3-, 5-mm aliquots **(D–F)**; DSG9 with 1-, 3-, 5-mm aliquots **(G–I)** and DSG6 with 1-, 3-, 5-mm aliquots **(J–L)**.

TABLE 1 Summary of equivalent doses and ages for different aliquot sizes and age models.

Sample ID	Aliquot size (mm)	n/N	OD (%)	De (Gy)					
				ADM	CAM	MAM	IEU	Lowest 5%	FMM
DSG2	1	37/182	111 ± 14	6.20 ± 1.42	3.37 ± 0.66	0.63 ± 0.09	0.36 ± 0.17	−0.35 ± 0.73	0.42 ± 0.08
	3	30/48	65 ± 9	7.67 ± 1.54	6.25 ± 0.79	2.12 ± 0.48	3.34 ± 0.22	2.48 ± 0.40	3.34 ± 0.27
	5	40/48	45 ± 6	7.47 ± 0.55	6.81 ± 0.52	1.89 ± 0.38	2.64 ± 0.46	2.02 ± 0.18	1.70 ± 0.63
DSG4	1	22/113	94 ± 16	6.86 ± 1.79	4.45 ± 0.97	−0.10 ± 0.53	−0.04 ± 0.31	−0.10 ± 0.18	0.80 ± 0.22
	3	38/48	63 ± 7	7.17 ± 0.79	5.95 ± 0.62	1.28 ± 0.26	1.43 ± 0.28	1.28 ± 0.12	1.28 ± 0.16
	5	19/24	55 ± 9	7.53 ± 0.95	6.52 ± 0.84	1.99 ± 0.41	2.24 ± 0.57	1.84 ± 0.21	2.02 ± 0.24
DSG9	1	17/309	145 ± 29	13.78 ± 6.88	4.84 ± 1.87	0.34 ± 0.17	0.43 ± 0.17	−0.88 ± 0.62	0.48 ± 0.11
	3	19/24	62 ± 10	8.75 ± 1.29	7.30 ± 1.06	2.29 ± 0.54	3.89 ± 0.38	2.29 ± 0.25	2.32 ± 0.45
	5	21/39	90 ± 15	8.66 ± 2.17	5.82 ± 1.18	1.90 ± 0.20	2.03 ± 0.20	1.57 ± 0.32	1.98 ± 0.25
DSG6	1	21/102	40 ± 10	0.96 ± 0.14	0.89 ± 0.11	0.39 ± 0.57	0.67 ± 0.06	−0.93 ± 1.39	0.43 ± 0.26
	3	25/48	38 ± 7	0.78 ± 0.06	0.73 ± 0.07	0.54 ± 0.09	0.18 ± 0.09	0.08 ± 0.04	0.08 ± 0.06
	5	23/39	0 ± 0	0.69 ± 0.03	0.70 ± 0.02	0.66 ± 0.07	–	0.13 ± 0.42	0.69 ± 0.06

ADM is the average dose model proposed by Guérin et al. (2017). CAM is the weighted average including all dose estimates but negative. MAM is the unlogged minimum age model containing nonpositive dose estimates. IEU is the internal/external consistency criterion. "Lowest 5%" is the average of the lowest 5% of the dose estimates. The FMM is obtained by the lowest dose component of the six components in the FMM. The numbers of aliquots accepted (n) and total measured (N) are given. OD is the overdispersion derived from CAM.

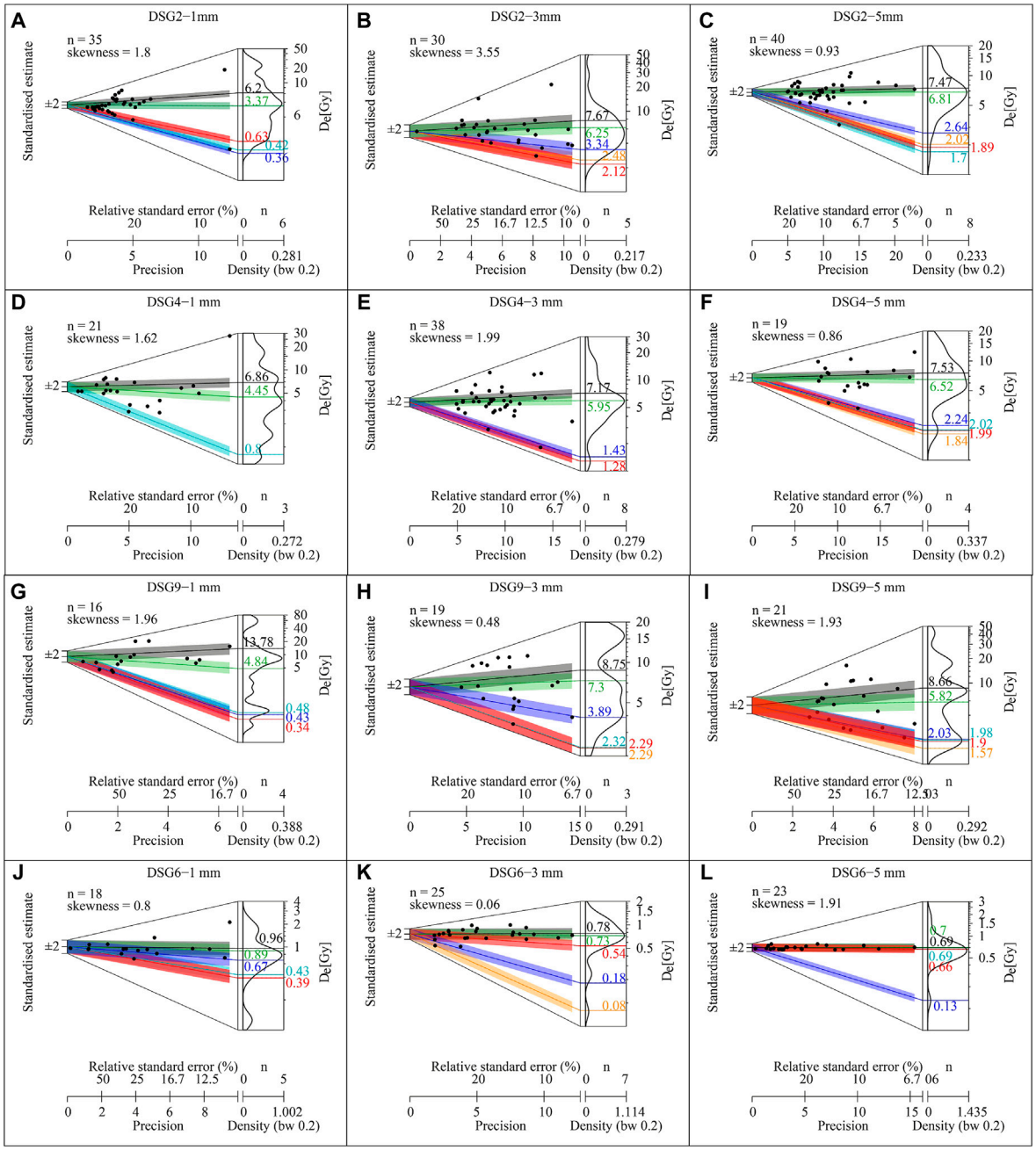

FIGURE 5
Abanico plots of natural dose distributions of DSG2 with 1-, 3-, 5-mm aliquots **(A–C)**; DSG4 with 1-, 3-, 5-mm aliquots **(D–F)**; DSG9 with 1-, 3-, 5-mm aliquots **(G–I)** and DSG6 with 1-, 3-, 5-mm aliquots **(J–L)**.

The MAM, FMM, IEU, and the lowest 5% D_es of 5-mm aliquots from DSG2, DSG4, and DSG9 and 3-mm aliquots from DSG4 are consistent within one standard error. The IEU and FMM D_es of 3-mm aliquots from DSG2 are overestimated compared with the MAM and the lowest 5%. The IEU D_e of 3-mm aliquots from DSG9 is overestimated compared to the MAM, the lowest 5%, and FMM D_es. The results show that D_e values do not change systematically when the aliquot size is larger than 3 mm (Figure 6). This indicates that the 3-mm aliquot is too large to obtain the true dose for the young poorly bleached sediments. Some studies have shown that the D_e of small aliquots (~2 mm or >100 grains) is overestimated compared

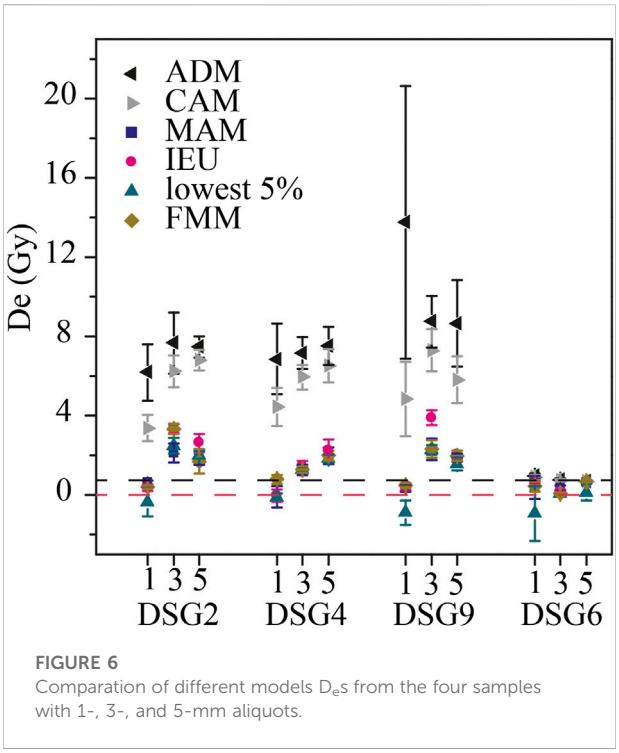

FIGURE 6
Comparation of different models D_es from the four samples with 1-, 3-, and 5-mm aliquots.

with the expected D_e, as the number of grains on the small aliquots is too large to distinguish the well-bleached population, although they used the lowest 5% or MAM (Wu et al., 2010; Colarossi et al., 2020). For the well-bleached sample DSG6, the D_e distributions have no dependency on the aliquot sizes and age models except the lowest 5% D_e of the 1-mm aliquot is negative (Figure 6).

The D_e values of 1 mm from three alluvial samples were quantified by OD values between 94 and 145% (Table 1). The MAM, FMM, IEU, and the lowest 5% D_e values of these three samples range from −0.88 ± 0.62 Gy to 0.80 ± 0.22 Gy of 1-mm aliquots. For the 1-mm aliquots of DSG2 and DSG9, the D_e values calculated by MAM, FMM, and IEU are consistent within one standard error. For DSG4, the MAM, IEU, and lowest 5% D_e values are consistent with ~−0.1 Gy, which is sufficiently close to 0 Gy. This indicates the potential of 1-mm aliquots to obtain the expected deposit doses of the alluvial sediments. The lowest 5% D_e values of DSG2, DSG9, and DSG6 are significantly negative values (−0.35 ± 0.73 Gy, −0.88 ± 0.62 Gy, and −0.93 ± 1.39 Gy). This indicates that the lowest 5% may underestimate the true burial doses. The same underestimations were observed in the young fluvial and paleoflood deposits with the lowest 5% by Bailey and Arnold (2006) and Medialdea et al. (2014). The ratios of the IEU D_es with small aliquots (~30 grains) to the expected dose are consistent with unity within two standard errors for paleoflood deposits (Medialdea et al., 2014). In addition, it is proven by modern earthquake-related deposits of 1-mm aliquots with MAM (Yang et al., 2017).

A dose overestimation of lower than 1 Gy would be allowable for older sediments. A similar suggestion has been made by Medialdea et al. (2014) for fluvial deposits. This indicates that it may be suitable to apply 1-mm (<50 grains) aliquots with MAM or IEU to old alluvial sediment OSL dating. Any heterogeneity in D_e that individual grain may still be masked at the 1-mm aliquot scale analyses, as individual D_e estimates are obtained from 1-mm aliquots containing ~50 grains. Therefore, a single grain needs to be applied with MAM and IEU models to remove this small overestimation for very young sediments.

Conclusion

Three alluvial deposit samples and one loess-like deposit sample were dated in this study by the application of 1-, 3-, and 5-mm aliquots of quartz OSL. Even for the limited dataset from this study, useful information is provided from our results. Based on the results, the rejection criteria for S_{Tn} have no impact on the absolute MAM and FMM doses determined by the range from 10 to 30%. Analyzing D_es with the different statistical models reveals that the MAM and IEU models are more suitable for poorly bleached sediments than the lowest 5% and FMM, and the lowest 5% always underestimates the D_e. Equivalent doses estimated with 1-, 3-, and 5-mm aliquots from modern deposits on the alluvial fan prove the potential of 1-mm aliquots to accurately date incomplete bleaching sediments. OSL dating of 1-mm aliquots (~50 grains) using the MAM and IEU can obtain accurate D_es with an uncertainty of less than 1 Gy for the alluvial deposits. Our study highlights the necessity of combining aliquot sizes and age models to obtain reliable ages of poorly bleached deposits and provides the possibility of accurately dating paleoalluvial deposits.

Data availability statement

The original contributions presented in the study are included in the article/supplementary material; further inquiries can be directed to the corresponding author.

Author contributions

XuL, XaL, QZ, and BP participated in the design of this study, and they all performed the statistical analysis and drafted the manuscript. JW aided with data analysis and manuscript editing. BP and MW carried out the study, collected important background information, and performed the manuscript review. All authors have read and approved the final manuscript. All authors have made substantial contributions to all of the following: 1) the conception and design of the study, acquisition of data, and analysis and interpretation of data; 2) drafting the article or

revising it critically for intellectual content; and 3) final approval of the version to be submitted.

Funding

This research was supported by the Beijing Municipal Education Commission (Grant No. KM201910028007) and the National Natural Science Foundation of China (NSFC, Grant Nos. 41471007, 41301006, 40871017, and 41602353).

Acknowledgments

We are grateful for the critical comments and insightful suggestions from the Editor HL and the reviewers JZ, YL.

Conflict of interest

The authors declare that the research was conducted in the absence of any commercial or financial relationships that could be construed as potential conflicts of interest.

Publisher's note

All claims expressed in this article are solely those of the authors and do not necessarily represent those of their affiliated organizations or those of the publisher, the editors, and the reviewers. Any product that may be evaluated in this article, or claim that may be made by its manufacturer, is not guaranteed or endorsed by the publisher.

References

Alexanderson, H. (2007). Residual OSL signals from modern Greenlandic river sediments. *Geochronometria.* 26, 1–9. doi:10.2478/v10003-007-0001-6

Arnold, L. J., Roberts, R. G., Galbraith, R. F., and Delong, S. B. (2009). A revised burial dose estimation procedure for optical dating of young and modern-age sediments. *Quat. Geochronol.* 4, 306–325. doi:10.1016/j.quageo.2009.02.017

Bailey, R. M., and Arnold, L. J. (2006). Statistical modelling of single grain quartz D_e distributions and an assessment of procedures for estimating burial dose. *Quat. Sci. Rev.* 25, 2475–2502. doi:10.1016/j.quascirev.2005.09.012

Bøtter-Jensen, L., Thomsen, K. J., and Jain, M. (2010). Review of optically stimulated luminescence (OSL) instrumental developments for retrospective dosimetry. *Radiat. Meas.* 45, 253–257. doi:10.1016/j.radmeas.2009.11.030

Burow, C. (2020a). "calc_CentralDose(): apply the central age model (CAM) after galbraith et al. (1999) to a given D_e distribution. function version 1.4.0," in *Luminescence: Comprehensive luminescence dating data analysis.* Editors S. Kreutzer, C. Burow, M. Dietze, M. C. Fuchs, C. Schmidt, M. Fischer, et al. 2020R package version 0.9.10. Available at: https://CRAN.R-project.org/package=Luminescence.

Burow, C. (2020c). "calc_FiniteMixture(): apply the finite mixture model (FMM) after galbraith (2005) to a given D_e distribution. function version 0.4.1," in *Luminescence: Comprehensive luminescence dating data analysis.* Editors S. Kreutzer, C. Burow, M. Dietze, M. C. Fuchs, and C. Schmidt. 2020R package version 0.9.10. Available at: https://CRAN.R-project.org/package=Luminescence.

Burow, C. (2020b). "calc_MinDose(): apply the (un-)logged minimum age model (MAM) after galbraith et al. (1999) to a given D_e distribution. function version 0.4.4," in *Luminescence: Comprehensive luminescence dating data analysis.* Editors S. Kreutzer, C. Burow, M. Dietze, M. C. Fuchs, and C. Schmidt. 2020R package version 0.9.10. Available at: https://CRAN.R-project.org/package=Luminescence.

Christophe, C., Philippe, A., Guérin, G., and Kreutzer, S. (2020). "calc_AverageDose (): Calculate the Average Dose and the dose rate dispersion. Function version 0.1.4," in *Luminescence: Comprehensive luminescence dating data analysis.* Editors S. Kreutzer, C. Burow, M. Dietze, M. C. Fuchs, C. Schmidt, M. Fischer, et al. R package version 0.9.10. Available at: https://CRAN.R-project.org/package=Luminescence.

Colarossi, D., Duller, G. A. T., Roberts, H. M., Tooth, S., and Botha, G. A. (2020). A comparison of multiple luminescence chronometers at Voordrag, South Africa. *Quat. Geochronol.* 60, 101094. doi:10.1016/j.quageo.2020.101094

Cui, W. G., Mu, G. J., Wen, Q., and Yue, J. (2007). Evolution of alluvial fans and reaction to the regional tectonic activity at rage-front of manas river valley. *Res. Soil Water Conservation* 14 (01), 161–163. doi:10.3969/j.issn.1005-3409.2007.01.051

Cui, Z. J. (1999). Debris flow deposit and its signification on hazards prevention and reduction. *Soil Water Conservation Res.* 6 (4), 2–9. (in Chinese).

Cunningham, A. C., and Wallinga, J. (2012). Realizing the potential of fluvial archives using robust OSL chronologies. *Quat. Geochronol.* 12, 98–106. doi:10.1016/j.quageo.2012.05.007

Cunningham, A. C., and Wallinga, J. (2010). Selection of integration time intervals for quartz OSL decay curves. *Quat. Geochronol.* 5 (6), 657–666. doi:10.1016/j.quageo.2010.08.004

Dietze, M., and Kreutzer, S. (2020). "Plot-KDE (): Plot kernel density estimate with statistics. Function version 3.6.0," in *Luminescence: Comprehensive luminescence dating data analysis.* Editors S. Kreutzer, C. Burow, M. Dietze, M. C. Fuchs, C. Schmidt, M. Fischer, et al. 2020R package version 0.9.10. Available at: https://CRAN.R-project.org/package=Luminescence.

Duller, G. A. T., Bøtter-Jensen, L., and Murray, A. S. (2003). Combining infrared- and green-laser stimulation sources in single-grain luminescence measurements of feldspar and quartz. *Radiat. Meas.* 37 (4–5), 543–550. doi:10.1016/S1350-4487(03)00050-7

Duller, G. A. T. (1994). Luminescence dating of poorly bleached sediments from Scotland. *Quat. Sci. Rev.* 13 (5), 521–524. doi:10.1016/0277-3791(94)90070-1

Duller, G. A. T. (1995). Luminescence dating using single aliquots: Methods and applications. *Radiat. Meas.* 24 (3), 217–226. doi:10.1016/1350-4487(95)00150-D

Duller, G. A. T. (2006). Single grain optical dating of glacigenic deposits. *Quat. Geochronol.* 1 (4), 296–304. doi:10.1016/j.quageo.2006.05.018

Duller, G. A. T. (2008). Single-grain optical dating of quaternary sediments: Why aliquot size matters in luminescence dating. *Boreas* 37 (4), 589–612. doi:10.1111/j.1502-3885.2008.00051.x

Fattahi, M., Heidary, M., and Ghasemi, M. (2016). Employing minimum age model (MAM) and finite mixture modeling (FMM) for OSL age determination of two important samples from Ira trench of north tehran fault. *Geochronometria* 43 (1), 38–47. doi:10.1515/geochr-2015-0031

Fiebig, M., and Preusser, F. (2007). Investigating the amount of zeroing in modern sediments of River Danube, Austria. *Quat. Geochronol.* 2 (1), 143–149. doi:10.1016/j.quageo.2006.09.001

Fiorillo, F., and Wilson, R. C. (2004). Rainfall induced debris flows in pyroclastic deposits, campania (southern Italy). *Eng. Geol.* 75 (3-4), 263–289. doi:10.1016/j.enggeo.2004.06.014

Fuchs, M., Fischer, M., and Reverman, R. (2010). Colluvial and alluvial sediment archives temporally resolved by OSL dating: implications for reconstructing soil erosion. *Quat. Geochronol.* 5 (2), 269–273. doi:10.1016/j.quageo.2009.01.006

Fuchs, M., and Lang, A. (2001). OSL dating of coarse-grain fluvial quartz using single-aliquot protocols on sediments from NE Peloponnese, Greece. *Quat. Sci. Rev.* 20, 783–787. doi:10.1016/S0277-3791(00)00040-8

Galbraith, R. F., and Green, P. F. (1990). Estimating the component ages in a finite mixture. *Int. J. Radiat. Appl. Instrum. Part D. Nucl. Tracks Radiat. Meas.* 17 (3), 197–206. doi:10.1016/1359-0189(90)90035-v

Galbraith, R. F., Roberts, R. G., Laslett, G. M., Yoshida, H., and Olley, J. M. (1999). Optical dating of single grains of quartz from jinmium rock shelter, northern Australia. Part I: experimental design and statistical models. *Archaeometry* 41, 339–364. doi:10.1111/j.1475-4754.1999.tb00987.x

Galbraith, R. F., and Roberts, R. G. (2012). Statistical aspects of equivalent dose and error calculation and display in OSL dating: An overview and some recommendations. *Quat. Geochronol.* 11, 1–27. doi:10.1016/j.quageo.2012.04.020

Galbraith, R. F. (2005). *Statistics for fission track analysis*. Boca Raton: Chapman & Hall/CRC. doi:10.1201/9781420034929

Godfrey-Smith, D. I., Huntley, D. J., and Chen, W. H. (1988). Optical dating studies of quartz and feldspar sediment extracts. *Quat. Sci. Rev.* 7 (3), 373–380. doi:10.1016/0277-3791(88)90032-7

Goudie, A. S. (2004). *Encyclopedia of Geomorphology*.

Guérin, G., Christophe, C., Philippe, A., Murray, A. S., Thomsen, K. J., Tribolo, C., et al. (2017). Absorbed dose, equivalent dose, measured dose rates, and implications for OSL age estimates: Introducing the Average Dose Model. *Quat. Geochronol.* 41, 163–173. doi:10.1016/j.quageo.2017.04.002

Han, M. K. (1992). Tectonic Geomorphology. *Adv. Earth Sci.* 007 (005), 61–62. (in Chinese).

Hou, J. J., and Han, M. K. (1995). Geomorphic expression of the activity along north Qinling piedmont fault zone in the late quaternary period. *J. Geogr.* 000 (002), 138. (in Chinese).

Hu, G., Zhang, J. F., Qiu, W. L., and Zhou, L. P. (2010). Residual OSL signals in modern fluvial sediments from the Yellow River (HuangHe) and the implications for dating young sediments. *Quat. Geochronol.* 5 (2), 187–193. doi:10.1016/j.quageo.2009.05.003

Jain, M., Murray, A. S., and Bøtter-Jensen, L. (2004). Optically stimulated luminescence dating: how significantly is incomplete light exposure in fluvial environments? *PubMed* 15 (1–2), 143–157. doi:10.1258/ijsa.2008.008369

Jiang, Z. B. (2016). *Analysis of regional climate change and extreme weather characteristics in helan mountain area*. Lanzhou City, China: Lanzhou University. Master Thesis (in Chinese). doi:10.7666/d.D01300699

Kenworthy, M. K., Rittenour, T. M., Pierce, J. L., Sutfin, N. A., and Sharp, W. D. (2014). Luminescence dating without sand lenses: an application of OSL to coarse-grained alluvial fan deposits of the lost river range, Idaho, USA. *Quat. Geochronol.* 23, 9–25. doi:10.1016/j.quageo.2014.03.004

Li, G. W., and Chen, Y. C. (2006). Analysis on the 060714 rainstorm floodwater east foot of helan mountain in ningxia. *Ningxia Eng. Technol.* 5 (4), 332–334 (in Chinese). doi:10.3969/j.issn.1671-7244.2006.04.004

Li, X. H., Su, Z. S., Na, L., Chen, Y. Y., Chen, Y. H., and Wu, B. G. (2018). Climate characteristics of rainstorm and disaster prevention countermeasures along the eastern Helan Mountain. *Arid. Land Geogr.* 44 (05), 1231–1239. (in Chinese). doi:10.12118/j.issn.10006060.2021.05.04

Medialdea, A., Thomsen, K. J., Murray, A. S., and Benito, G. (2014). Reliability of equivalent-dose determination and age-models in the OSL dating of historical and modern palaeoflood sediments. *Quat. Geochronol.* 22, 11–24. doi:10.1016/j.quageo.2014.01.004

Murray, A. S., Arnold, L. J., Buylaert, J. P., Guérin, G., Qin, J. T., Singhvi, A. K., et al. (2021). Optically stimulated luminescence dating using quartz. *Nat. Rev. Methods Prim.* 1, 72. doi:10.1038/s43586-021-00068-5

Murray, A. S., and Wintle, A. G. (2000). Luminescence dating of quartz using an improved single-aliquot regenerative-dose protocol. *Radiat. Meas.* 32 (1), 57–73. doi:10.1016/S1350-4487(99)00253-X

Murray, A. S., and Wintle, A. G. (2003). The single aliquot regenerative dose protocol: potential for improvements in reliability. *Radiat. Meas.* 37 (4), 377–381. doi:10.1016/S1350-4487(03)00053-2

Olley, J. M., Caitcheon, G. G., and Murray, A. S. (1998). The distribution of apparent dose as determined by optically stimulated luminescence in small aliquots of fluvial quartz: implications for dating young sediments. *Quat. Sci. Rev.* 17 (11), 1033–1040. doi:10.1016/S0277-3791(97)00090-5

Olley, J. M., Caitcheon, G. G., and Roberts, R. G. (1999). The origin of dose distributions in fluvial sediments, and the prospect of dating single grains from fluvial deposits using optically stimulated luminescence. *Radiat. Meas.* 30 (2), 207–217. doi:10.1016/S1350-4487(99)00040-2

Palstra, S. W. L., Wallinga, J., Viveen, W., Schoorl, J. M., Berg, M., Plicht, J., et al. (2021). Cross-comparison of last glacial radiocarbon and OSL ages using periglacial fan deposits. *Quat. Geochronol.* 61, 101128. doi:10.1016/j.quageo.2020.101128

Peng, J., Li, B., and Jacobs, Z. (2020). Modelling heterogeneously bleached single-grain equivalent dose distributions: Implications for the reliability of burial dose determination. *Quat. Geochronol.* 60, 101108. doi:10.1016/j.quageo.2020.101108

Rhodes, E. J. (2000). Observations of thermal transfer OSL signals in glacigenic quartz. *Radiat. Meas.* 32 (5), 595–602. doi:10.1016/S1350-4487(00)00125-6

Rittenour, T. M. (2008). Luminescence dating of fluvial deposits: applications to geomorphic, palaeoseismic and archaeological research. *Boreas* 37 (4), 613–635. doi:10.1111/j.1502-3885.2008.00056.x

Ritter, J. B., Miller, J. R., Enzel, Y., and Wells, S. G. (1995). Reconciling the roles of tectonism and climate in quaternary alluvial fan evolution. *Geol.* 23 (3), 245. doi:10.1130/0091-7613(1995)023<0245:rtrota>2.3.co;2

Rodnight, H., Duller, G. A. T., Wintle, A. G., and Tooth, S. (2006). Assessing the reproducibility and accuracy of optical dating of fluvial deposits. *Quat. Geochronol.* 1 (2), 109–120. doi:10.1016/j.quageo.2006.05.017

Sewell, R. J., Parry, S., Millis, S. W., Wang, N., Rieser, U., DeWitt, R., et al. (2015). Dating of debris flow fan complexes from Lantau Island, Hong Kong, China: the potential relationship between landslide activity and climate change. *Geomorphology* 248, 205–227. doi:10.1016/j.geomorph.2015.07.041

Smedley, R. K. (2020). "calc_IEU(): apply the internal-external-uncertainty (IEU) model after Thomsen et al. (2007) to a given D_e distribution. Function version 0.1.1," in *Luminescence: Comprehensive luminescence dating data analysis*. Editors S. Kreutzer, C. Burow, M. Dietze, M. C. Fuchs, C. Schmidt, M. Fischer, et al. 2020R package version 0.9.10. Available at: https://CRAN.R-project.org/package=Luminescence.

Stokes, S., Bray, H. E., and Blum, M. D. (2001). Optical resetting in large drainage basins: tests of zeroing assumptions using single-aliquot procedures. *Quat. Sci. Rev.* 20 (5), 879–885. doi:10.1016/S0277-3791(00)00045-7

Tang, C., van Asch, T. W. J., Chang, M., Chen, G. Q., Zhao, X. H., and Huang, X. C. (2012). Catastrophic debris flows on 13 August 2010 in the Qingping area, southwestern China: the combined effects of a strong earthquake and subsequent rainstorms. *Geomorphology* 139-140, 559–576. doi:10.1016/j.geomorph.2011.12.021

Thomas, P. J., Jain, M., Juyal, N., and Singhvi, A. K. (2005). Comparison of single-grain and small-aliquot OSL dose estimates in years old river sediments from South India. *Radiat. Meas.* 39 (5), 457–469. doi:10.1016/j.radmeas.2004.07.005

Thomsen, K. J., Jain, M., Bøtter-Jensen, L., Murray, A. S., and Jungner, H. (2003). Variation with depth of dose distributions in single grains of quartz extracted from an irradiated concrete block. *Radiat. Meas.* 37 (4), 315–321. doi:10.1016/S1350-4487(03)00006-4

Thomsen, K. J., Murray, A. S., Boetter-Jensen, L., and Kinahan, J. (2007). Determination of burial dose in incompletely bleached fluvial samples using single grains of quartz. *Radiat. Meas.* 42, 370–379. doi:10.1016/j.radmeas.2007.01.041

Thomsen, K. J., Murray, A. S., Buylaert, J. P., Jain, M., Hansen, J. H., Aubry, T., et al. (2016). Testing single-grain quartz OSL methods using sediment samples with independent age control from the Bordes-Fitte rockshelter (Roches d'Abilly site, Central France). *Quat. Geochronol.* 31, 77–96. doi:10.1016/j.quageo.2015.11.002

Thomsen, K. J., Murray, A. S., and Jain, M. (2012). The dose dependency of the over-dispersion of quartz OSL single grain dose distributions. *Radiat. Meas.* 47 (9), 732–739. doi:10.1016/j.radmeas.2012.02.015

Tooth, S., Rodnight, H., Duller, G. A. T., McCarthy, T. S., Marren, P. M., Brandt, D., et al. (2007). Chronology and controls of avulsion along a mixed bedrock-alluvial river. *Geol. Soc. Am. Bull.* 119 (3–4), 452–461. doi:10.1130/B26032.1

Vandenberghe, D., Derese, C., and Houbrechts, G. (2007). Residual doses in recent alluvial sediments from the ardenne (S Belgium). *Geochronometria.* 28 (1), 1–8. doi:10.2478/v10003-007-0024-z

Wallinga, J., Murray, A. S., Duller, G. A. T., and Törnqvist, T. E. (2001). Testing optically stimulated luminescence dating of sand-sized quartz and feldspar from fluvial deposits. *Earth Planet. Sci. Lett.* 193 (3), 617–630. doi:10.1016/S0012-821X(01)00526-X

Wallinga, J. (2002). Optically stimulated luminescence dating of fluvial deposits: a review. *Boreas* 31 (4), 303–322. doi:10.1111/j.1502-3885.2002.tb01076.x

Wintle, A. G. (1997). Luminescence dating: Laboratory procedures and protocols. *Radiat. Meas.* 27 (5–6), 769–817. doi:10.1016/S1350-4487(97)00220-5

Wintle, A. G., and Murray, A. S. (1998). Towards the development of a preheat procedure for OSL dating of quartz. *Radiat. Meas.* 29 (1), 81–94. doi:10.1016/S1350-4487(97)00228-X

Wu, T., Jaiswal, M. K., Lin, Y. N., Chen, Y., and Chen, Y. (2010). Residual luminescence in modern debris flow deposits from Western taiwan: a single grain approach. *J. Asian Earth Sci.* 38 (6), 274–282. doi:10.1016/j.jseaes.2010.02.002

Yang, H. L., Chen, J., Porat, N., Li, T., Li, W. Q., Xiao, W. P., et al. (2017). Coarse versus fine-grain quartz optical dating of the sediments related to the 1985 Ms 7.1 wuqia earthquake, northeastern margin of the pamir salient, China. *Geochronometria* 44 (1), 299–306. doi:10.1515/geochr-2015-0075

Yang, H. L., Chen, J., Thompson, J. A., and Liu, J. F. (2012). Optical dating of the 12 May 2008, Ms 8.0 Wenchuan earthquake-related sediments: Tests of zeroing assumptions. *Quat. Geochronol.* 10, 273–279. doi:10.1016/j.quageo.2012.02.022

Yang, J. C., Guo, Z. T., and Cao, J. D. (1985). Investigation on the holocene activities of the Helan Mountain piedmont fault by use of geomorphological method. *Seismol. Geol.* 7 (4), 23–31. (in Chinese).

Zhao, Q. Y., Thomsen, K. J., Murray, A. S., Wei, M. J., Pan, B. L., Song, B., et al. (2015). Testing the use of OSL from quartz grains for dating debris flows in miyun, northeast Beijing, China. *Quat. Geochronol.* 30, 320–327. doi:10.1016/j.quageo.2015.03.007

Zhao, Q. Y., Thomsen, K. J., Murray, A. S., Wei, M. J., and Song, B. (2017). Single-grain quartz OSL dating of debris flow deposits from men tou gou, south west Beijing, China. *Quat. Geochronol.* 41, 62–69. doi:10.1016/j.quageo.2017.06.001

frontiers | Frontiers in Earth Science

TYPE Original Research
PUBLISHED 19 August 2022
DOI 10.3389/feart.2022.932834

OPEN ACCESS

EDITED BY
Yuxin Fan,
Lanzhou University, China

REVIEWED BY
Yiwei Chen,
(CAS), China
Xuefeng Sun,
Nanjing University, China

*CORRESPONDENCE
Dongwei NIU,
ndw1986@163.com

SPECIALTY SECTION
This article was submitted to Quaternary Science, Geomorphology, and Paleoenvironment, a section of the journal Frontiers in Earth Science

RECEIVED 30 April 2022
ACCEPTED 21 July 2022
PUBLISHED 19 August 2022

CITATION
GUO Y, XIAN Q, LU C and NIU D (2022), Redating the Zhuwobu Paleolithic site in the Huailai basin, North China, using the MET-pIRIR procedure on K-feldspars. *Front. Earth Sci.* 10:932834. doi: 10.3389/feart.2022.932834

Redating the Zhuwobu Paleolithic site in the Huailai basin, North China, using the MET-pIRIR procedure on K-feldspars

Yujie GUO, Qi XIAN, Chun LU and Dongwei NIU*

Institute of Nihewan Archaeology, College of History and Culture, Hebei Normal University, Shijiazhuang, China

As part of the "generalized Nihewan Basin", the Huailai basin has recently attracted archaeologists' attention. Ten Paleolithic sites were found in this basin in 2014; among these, the Zhuwobu site is the oldest—dated to 504 ± 76 ka using the electron spin resonance (ESR) dating method. This study redated the Zhuwobu site using the multiple elevated temperatures (MET) post infrared (pIR) infrared stimulated luminescence (IRSL) procedure (MET-pIRIR) on both multi-grained single and multiple aliquots of potassium-rich feldspars (K-feldspars). The consistency of the D_e results obtained from the single- and multiple-aliquot procedures mutually supported the reliability of our age results. Our results suggest that the cultural layer at this site was deposited about 280 ± 13 ka (MIS 8) ago, ~220 ka younger than the previous ESR age. Considering the region's tectonic history and the characteristics of the sedimentary facies for the ZWB site, we suggested that the previous ESR age results for the bottom three samples from the sediment profile might be overestimated due to poor bleaching before burial. In contrast, the ESR age of 346 ± 32 ka (MIS 10) for one cultural-layer collected sample might be more reliable due to higher-quality bleaching before burial. Further archaeological, geological, and chronological studies are needed to explore the ancient hominins' survival conditions in the "generalized Nihewan Basin" and possible connections with the renowned Zhoukoudian sites.

KEYWORDS

Huailai basin, MET-pIRIR, K-feldspar, ESR, the "generalized Nihewan Basin"

Introduction

The Nihewan Basin is one of the most critical regions for studying Paleolithic archaeology and early human behaviors of East Asia due to its rich Paleolithic sites (see reviews and references in Yang et al., 2020). The "Nihewan Basin" has different coverage in terms of geographical scope. It usually refers only to the Yangyuan Basin since most Paleolithic sites were initially discovered around the Nihewan village in the eastern

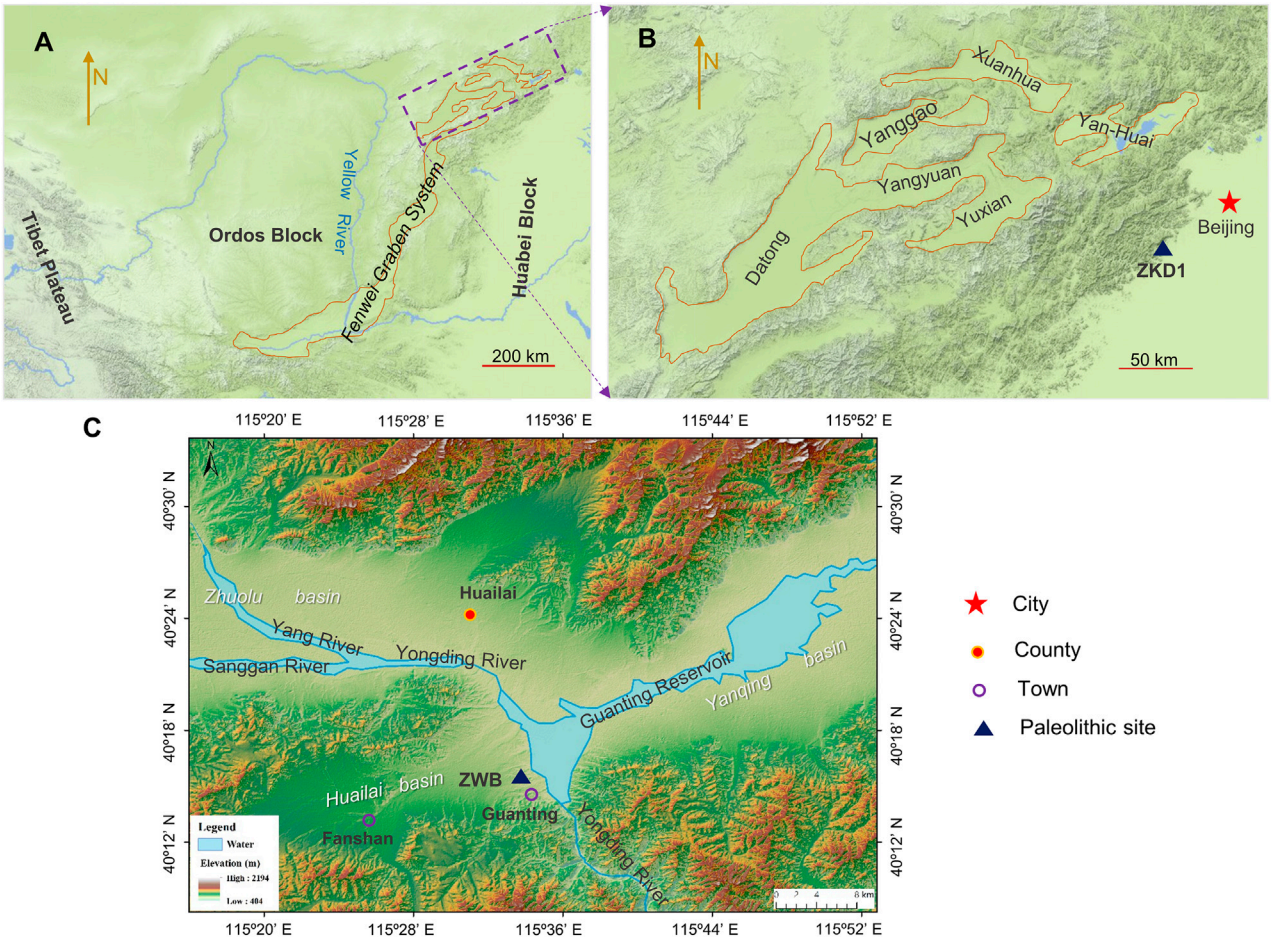

FIGURE 1
Topographic maps showing the locations of the Fenwei Graben System **(A)** and the basins comprising the "generalized Nihewan Basin" B) (courtesy of Tengxun Map). ZKD1 in panel **(B)** represents the Paleolithic site of Zhoukoudian Locality 1. **(C)** Digital elevation model (DEM) of the middle part of the Yan-Huai Basin showing the location of the Zhuwobu (ZWB) paleolithic site.

part of the Yangyuan Basin. As more and more Paleolithic sites are found in the west and south adjacent basins, it sometimes includes the Datong and Yuxian basins. The "generalized Nihewan Basin" includes the adjacent east Yan-Huai Basin, which includes the Xuanhua, Zhuolu, Huailai, and Yanqing basins (Xie et al., 2006). The above basins are part of the Fenwei Graben System, the tectonic boundary between the Ordos Block and the North China Block (Wang et al., 2020) (Figure 1A, B). Paleo-lakes had filled the basins during the Quaternary period. Today, the Sanggan River and its tributaries connect the basins that were once paleo-lakes (e.g., Zhao et al., 2010; Yuan et al., 2011; Guo et al., 2016; Ji and Wang, 2017).

The Huailai basin (also named the Fanshan basin in some literature) is a V-shaped elongated intermountain basin with a length of 100 km from east to west and a width of 20 km from north to south (Figure 1C). The average altitude of the internal basin is ~650 m asl, and the surrounding mountains are over 1000 m asl. The Yongding River (downstream of the Sanggan and Yang Rivers) flows from the north into the south artificial Guanting Reservoir. The internal landscape includes piedmont diluvial-colluvial fans, alluvial-diluvial platforms, and river terraces from the foot of the surrounding mountains to the center of the basin—containing the Quaternary fluvial-lacustrine deposits up to ~200–400 m thick (Wu et al., 1979; Li, 1992). Previous studies in the Huailai basin mainly focused on regional geology, biostratigraphy, and paleoclimatology (e.g., Wu et al., 1979; Li, 1992; Ran et al., 1992; Hu et al., 2000; Zheng et al., 2001; Zhu et al., 2020), while no Paleolithic archaeology studies had been done before 2014. Archaeologists from the Hebei Normal University and the Museum of Huailai County conducted an archaeological field investigation in this basin in 2014, and a total of ten Paleolithic sites were discovered (Niu et al., 2017). Among these, the Zhuwobu (ZWB) site—dated to

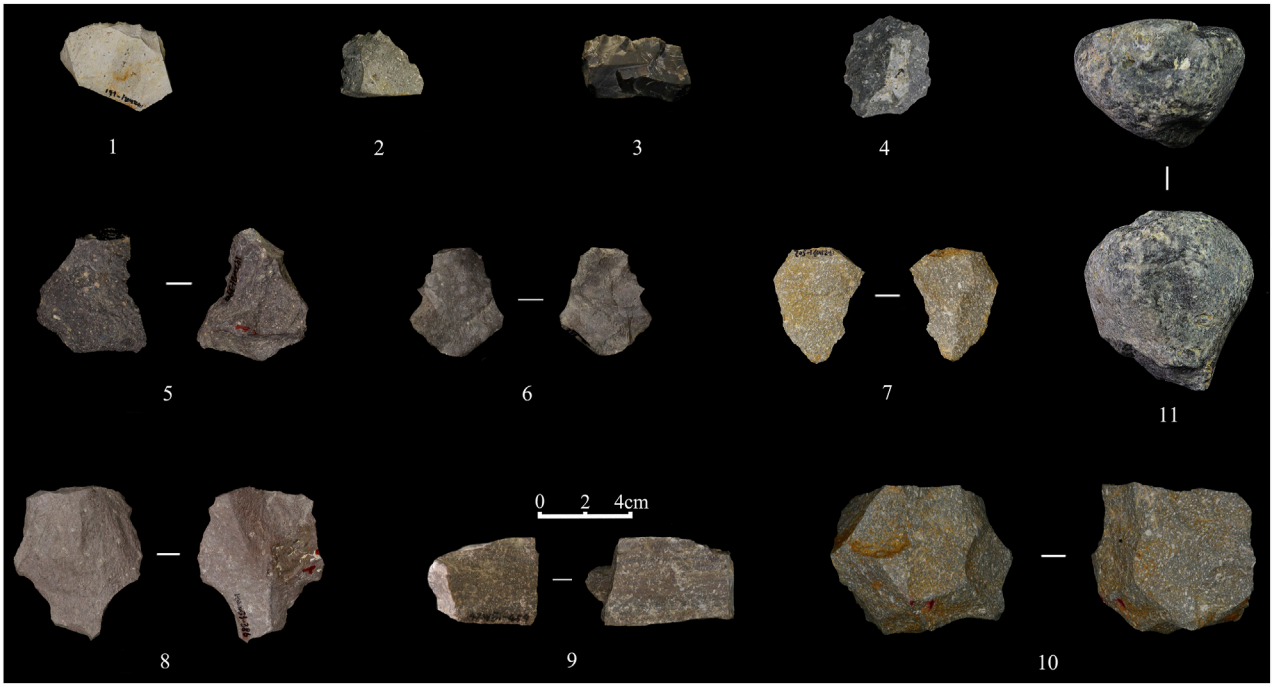

FIGURE 2
Selection of the stone artifacts excavated from ZWB site: (1–4) scrapers; (5–8) complete flakes; (9and10) cores; (11) hammerstone.

504 ± 76 ka using the Electron Spin Resonance (ESR) dating method based on the Ti-Li center of quartz (Li et al., 2018)—is currently the oldest in this basin. This site is essential for us to understand the ancient hominins' survival conditions and interactions with other groups of North China in the Middle Pleistocene. In this study, we redated this site using the regenerative-dose optically stimulated luminescence (Aitken, 1998) dating method to provide a chronological framework reference.

The optically stimulated luminescence (OSL) dating method has become one of the most used numerical dating methods to constrain the timing of sediment deposition worldwide (e.g., Feathers, 2003; Lai, 2010; Rhodes, 2011; Liritzis et al., 2013; Wang, 2014; Hu et al., 2019; Jacobs et al., 2019; Clarkson et al., 2020) since the single-aliquot regenerative-dose (SAR) method was proposed (Murray and Roberts, 1998; Galbraith et al., 1999; Murray and Wintle, 2000, 2003). Quartz and potassium-rich feldspar (K-feldspar) are the two most widely used minerals for luminescence dating. The infrared stimulated luminescence (IRSL) signals from K-feldspars saturate at a much higher radiation dose than the conventional OSL signal from quartz and have the potential to date much older sediments (see reviews in Li et al., 2014a). Luminescence dating on K-feldspars has been successfully applied to the Middle Pleistocene sediments in the Nihewan Basin (e.g., Nian et al., 2013; Guo et al., 2015, 2016, 2020; Rui et al., 2020a; Rui et al., 2020b; Lu et al., 2021; Wang et al., 2021) using either a two-step post infrared (post-IR) IRSL procedure (post-IR IRSL; Thomsen et al., 2008; Buylaert et al., 2009,2012; Thiel et al., 2011) or a multiple elevated temperatures (MET) post-IR IRSL procedure (MET-pIRIR; Li and Li, 2011; Li and Li, 2012). This study redated the Zhuwobu site on K-feldspars using the multi-grained single- and multiple-aliquot regenerative-dose MET-pIRIR procedure to constrain the depositional time for sediments bearing the cultural remains.

Stratigraphy, archaeology, and sampling

The Zhuwopu site (40°15′50″ N, 115°34′12″ E; 498 m asl) is located at the third terrace of the Yongding River in the town of Guanting in Huailai County, Hebei Province (Figure 1C). The site was discovered in 2014, and a total area of 23 m^2 was test excavated by Hebei Normal University and the Huailai Museum during the same year. A total of 262 stone artifacts were discovered (Figure 2). They include cores (11), hammerstones (2), debitage (233, with 51 complete flakes, 7 incomplete flakes, 45 debris, and 130 chunks), stone tools (8), and natural river cobbles (11). The raw materials are dominated by basalt, andesite, siliceous limestone, flint, etc., from the nearby river cobbles. The flaking method is mainly direct hard-hammer percussion. This site's lithics belong to the "flake-tool"

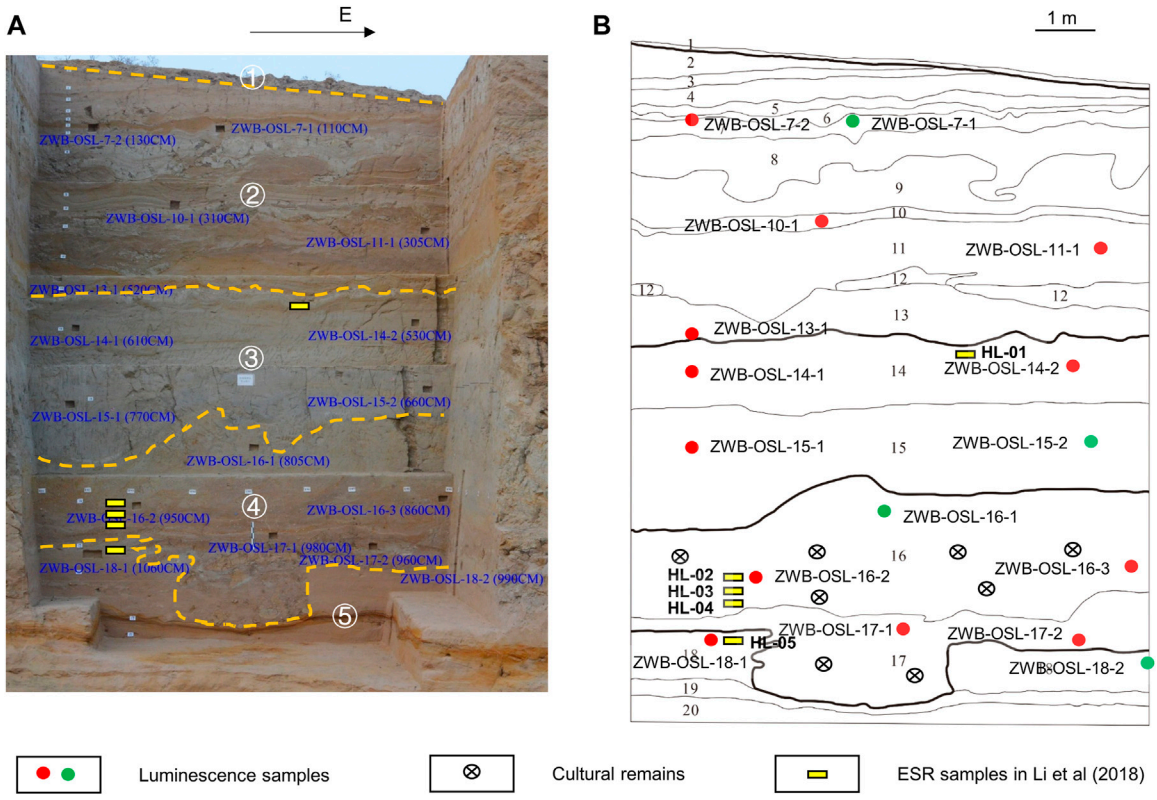

FIGURE 3
Photo **(A)** and graphic sketch **(B)** showing the sedimentary profile and the luminescence and ESR sampling locations of ZWB site. The numbers in circles in panel A) indicate the sedimentary units 1 to 5, and the Arabic numbers in panel B) represent the detailed sedimentary Layers 1 to 20.

technology that existed in North China from the Early to Late Pleistocene (Zhang, 1999; Bar-Yosef and Wang, 2012). A total of 263 animal bone fragments and 21 teeth were recovered, mostly from the remains of steppe ungulates such as antelope, horses, and rhinoceros. The lithic technology details for this site are provided in Niu et al. (2022).

The sedimentary profile of the site's excavated north wall consists of five units comprising 20 layers, which are as follows from top to bottom (Figures 3A, B):

1) Unit 1 (layer 1, ~0.2 m thick): Gray-brown gray soil. The structure is loose, and plant roots are developed.
2) Unit 2 (layers 2–13, ~4.5–5.5 m): Layers of gray-green or gray-black silty clay interbedded with yellow or tawny fine/coarse sands with the internal wave and cross beddings. The layers' upper surfaces were reworked by water flows, resulting in erosional grooves filled with overlying sediments. This unit reflects the interbeds of lakeshore swamp and beach bar sediments, with rapid water level fluctuations.
3) Unit 3 (layers 14–15, ~2.5–3.5 m): Gray-green silty clay with strip lens of gray-yellow fine sands, wave, and horizontal beddings. Fragments of bivalves and calcium carbonate spots are scattered. This unit reflects the lacustrine sediments with relatively weak and stable water flows.
4) Unit 4 (layer 16–17, ~1.8–4.0 m thick): Gray-green, gray-black, and gray-yellow silty clay with the strip lens of gray-yellow fine sands, wave, and horizontal beddings. Fragments of bivalves and calcium carbonate spots are scattered. The erosional basal groove filled with blocks of silty clay indicates a high flood of layer 17. The abundant red-yellow iron oxide and white calcium carbonate spots indicate the development of the seasonal redox and eluviation process. This unit reflects the lakeshore sediments with unstable water flows. Abundant stone artifacts and vertebrate bone fragments were recovered from the lower part of layers 16 and 17.
5) Unit 5 (layers 18–20, >1.5 m): Gray-yellow loose coarse sands, with large-scale cross and horizontal beddings. Layer 19 of red-yellow coarse sand with iron-manganese rusty spot indicates the redox process induced by seasonal groundwater had been developed. This unit reflects the high-energy fluvial sediments.

In all, a sequence of fluvial (unit 5)–lakeshore (unit 4)–lacustrine (unit 3)–lakeshore (unit 2) sediments from the

bottom up indicates a cycle of lake expansion (unit 5 to unit 3), and retreating (unit 3 to unit 2) processes. According to the sedimentary facies and the distribution pattern of the cultural remains, we consider that the remains might have been transported from a distance by a high flood; thus, the numerical age for the sediments of the cultural layer represents the minimum age for the cultural remains.

In this study, 16 block samples (ZWB-OSL-7-1 to -18-2) about 15 × 15 × 15 cm in size were systematically collected from the sedimentary profile for luminescence dating, and 12 of them were measured to save instrumental time. Samples ZWB-OSL-16-2, -16-3, -17-1, and -17-2 were collected from the cultural layer (Figure 3A,B). After the samples were removed from the profile, they were immediately wrapped in aluminum foil and transported for analysis to the Luminescence Dating Laboratory at the Hebei Normal University, China. The previous ESR sampling positions are also shown in Figure 3, and the samples HL-02, -03, and -04 were collected from the cultural layer (Li et al., 2018).

Materials and methods

Sample preparation and dose rate determination

Sample preparation was carried out under subdued red light in the laboratory. The sample blocks' outer layer (~2 cm) was removed and used for dose rate determination. The blocks' remaining internal parts were treated to extract K-feldspar grains using the standard mineral separation techniques (Aitken, 1998). Carbonate and organic matter were removed using HCl (waiting for reactions for 1 day) and H_2O_2 (waiting for 1 week) solutions, respectively. Fractions at the grain-size interval of 90–150 μm were isolated by wet sieving and then dried for density separation. K-feldspar grains were extracted using a heavy liquid with a density of 2.58 g/cm^3. These grains were etched in 10% HF acid for 40 min to remove the grains' alpha-irradiated rinds. The precipitated fluorides generated during HF etching were removed using a 10% HCl solution for at least 2 h. The etched grains were finally dry sieved again to remove the dissolved portions of less than 90 μm. An overall reduction of 10 μm in diameter by HF etching was assumed.

The uranium (U), thorium (Th), and potassium (K) concentrations for each sample were determined using inductively coupled plasma mass spectrometry (ICP-MS) for U and Th and X-ray fluorescence (XRF) for K at Qingdao Sparta Analysis & Test Co., Ltd., China. The internal K and Rb concentrations of the K-feldspar samples were assumed to be 12 ± 1% (Rui et al., 2019) and 400 ± 100 ppm (Huntley and Lamothe, 2001), respectively. The long-term water content was assumed as 15 ± 5% for all samples based on previous studies in this region (Zhao et al., 2010; Nian et al., 2013; Guo et al., 2016; Wang et al., 2021). The total environmental dose rates were calculated using the online DRAC (dose rate and age calculator) v. 1.2 software (Durcan et al., 2015), in which the cosmic-ray contribution to the dose rate was involved. The conversion factors in Adamiec and Aitken (1998) and beta attenuation factors in Mejdahl (1979) were adopted to calculate the dose rates.

TABLE 1 The D_e measurement procedure for the SAR MET-pIRIR measurements (after Li and Li, 2011, 2012).

Step	Treatment	Observed
1	Give regenerative dose, D_i[a]	
2	Preheat at 290°C for 60 s	
3	IRSL measurement at 140°C for 150 s	L_x (140)[b]
4	IRSL measurement at 170°C for 150 s	L_x (170)[b]
5	IRSL measurement at 200°C for 150 s	L_x (200)[b]
6	IRSL measurement at 230°C for 150 s	L_x (230)[b]
7	IRSL measurement at 260°C for 150 s	L_x (260)[b]
8	Give test dose, 240 Gy	
9	Preheat at 290°C for 60 s	
10	IRSL measurement at 140°C for 150 s	T_x (140)[b]
11	IRSL measurement at 170°C for 150 s	T_x (170)[b]
12	IRSL measurement at 200°C for 150 s	T_x (200)[b]
13	IRSL measurement at 230°C for 150 s	T_x (230)[b]
14	IRSL measurement at 260°C for 150 s	T_x (260)[b]
15	IR bleaching at 300°C for 100 s	
16	Return to step 1	

[a] For the first cycle natural signals, i = 0 Gy and D_0 = 0 Gy. The entire sequence is repeated for several regenerative doses, including a zero dose and a repeat dose to monitor the extent of recuperation and the recycling ratio, respectively (Murray and Wintle, 2000, 2003).

[b] The aliquots were held for 20, 30, 30, 30, and 40 s before IR stimulations at each of the temperatures, respectively, to monitor and minimize interference from isothermal decay signals (Fu et al., 2012).

Equivalent dose determination

Aliquots were made by applying a 2 mm diameter coating of silicone spray oil to stainless steel discs (10 mm in diameter) using a tiny brush, followed by a single layer of the K-feldspar grains. D_e measurements were performed on an automated Risø TL/OSL-DA-20 reader (Bøtter-Jensen et al., 2000; Bøtter-Jensen et al., 2003). The optical simulations were conducted using the IR diodes (870 nm) and the laboratory irradiations used a calibrated ^{90}Sr beta source. The luminescent emissions were first filtered by a blue filter pack comprising Schott BG-39 and Corning 7–59 filters and were then detected by an Electron Tubes Ltd. 9235QB15 photomultiplier tube. The instrumental reproducibility error was assumed as 1% for the D_e measurements (Guo et al., 2020). Considering possible bias in the calibration of the laboratory beta source for the D_e measurements (Galbraith and Roberts, 2012), a systematic error of 2% was also added in quadrature to the measurement errors.

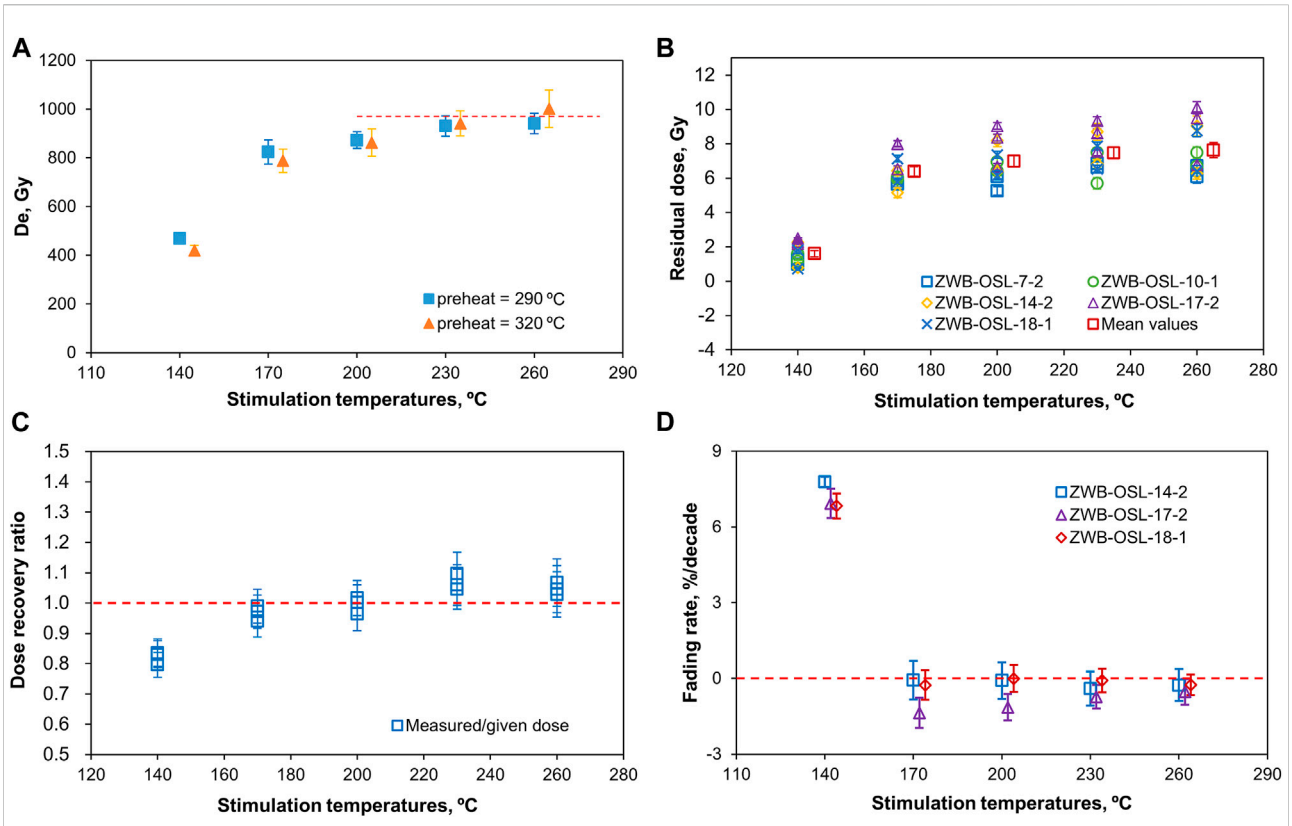

FIGURE 4
(A) The D_e values obtained at preheat temperatures of 290–320°C for sample ZWB-OSL-17-2 measured using the SAR MET-pIRIR procedure on K-feldspars. The data points represent the mean values for two aliquots, and the dashed red line indicates the mean value of ~954 Gy for the D_e values measured at 230°C and 260°C stimulation temperatures. **(B)** The residual doses measured for samples ZWB-OSL-7-2, -10-1, 14-2, -17-2, and -18-1 using the SAR MET-pIRIR procedure, plotted against IR stimulation temperatures. The red squares represent the means of all the aliquots measured at each IR stimulation temperature for the five samples, and each of the other data points represents one aliquot. **(C)** Dose recovery ratios for sample ZWB-OSL-17-2 at different IR stimulation temperatures. Each blue square represents the value for one aliquot. **(D)** Anomalous fading rates for the MET-pIRIR signals of samples ZWB-OSL-14-2, -17-2, and-18-1. The vertical bars in each panel indicate the corresponding standard errors. The symbols are offset laterally for clarity.

A series of SAR MET-pIRIR procedures (50–170°C, 80–200°C, 110–230°C, 140–260°C, and 170–290°C in a step of 30°C) and a two-step post-IR IRSL procedure (200, 290°C), with preheat temperatures 30°C higher than the highest stimulation temperature, were first tested on sample ZWB-OSL-17-2 to find an optimal measurement procedure for ZWB samples. Only the MET-pIRIR$_{140–260\ °C}$ procedure passed the SAR performance tests (see below) and was adapted to measure the D_e for the samples in this study (Table 1). Typical natural IRSL$_{140\ °C}$ and pIRIR$_{170–260\ °C}$ decay curves are shown in Supplementary Figure S1 for one aliquot of sample ZWB-OSL-17-2. The net IRSL signals used for D_e determination were calculated as the sum of the counts in the first 15 s of IRSL decay minus the counts from the final 15 s of stimulation as background. The dose-response curve (DRC) for each aliquot was conducted using the sensitivity-corrected pIRIR signals (L_x/T_x, Table 1) induced from a series of regenerative doses associated with fixed test doses of 240 Gy. The DRCs were fitted using the double exponential function in the Analyst V.4.57 software. The D_e values were determined by interpolating the sensitivity-corrected natural signals (L_n/T_n, Table 1) onto their corresponding DRCs (Murray and Wintle, 2000, 2003).

To check the dependence of D_e on preheat treatment, sample ZWB-OSL-17-2 was test measured with preheat temperatures of 290 and 320 °C. The results are plotted in Figure 4A. It shows that the D_e values increased as the stimulation temperatures increased, achieving a plateau of ~954 Gy for pIRIR$_{230°C}$ and pIRIR$_{260°C}$ at both 290 and 320°C preheating temperatures. It indicates that signals of pIRIR$_{230\ °C}$ and pIRIR$_{260\ °C}$ are "non-faded" (Li and Li, 2011) and independent of preheating treatments. This study adopted the preheat temperature of 290°C to save instrumental time.

Residual dose tests were performed on samples ZWB-OSL-7-2, 10-1, 14-2, 17-2, and 18-1 to check whether the samples from this site were well bleached. Two aliquots of each sample ZWB-OSL-7-2, 10-1, 14-2, and 18-1 were bleached for 10 h, and three aliquots of sample ZWB-OSL-17-2 were bleached for 8 h in the

solar simulator (Hönle: UVACUBE 400). The remaining doses were then measured using the procedure in Table 1, with two regenerative doses of 24 and 72 Gy. The DRCs were linear fitted and did not pass the original point. The results are plotted in Figure 4B. The arithmetic means of the residual doses measured at 140–260°C stimulation temperatures for the five samples are 1.6 ± 0.2, 6.4 ± 0.3, 7.0 ± 0.4, 7.5 ± 0.4, and 7.6 ± 0.5, respectively.

The dose recovery test (Galbraith et al., 1999; Wallinga et al., 2000) was conducted on sample ZWB-OSL-17-2 to check the applicability of the MET-pIRIR procedure for samples from this site. Three aliquots of the sample were bleached for 8 h in the solar simulator, and a dose of 960 Gy was then given to each aliquot as the surrogate "natural" dose. Then the "natural" dose was measured using the procedure in Table 1. The ratios of the measured (subtracting the residual dose) to the given dose are consistent with unity for the $pIRIR_{170-260°C}$ signals (Figure 4C), demonstrating that a known laboratory dose can be accurately recovered for samples from this site using the SAR MET-pIRIR procedure.

A fading test (Huntley and Lamothe, 2001; Auclair et al., 2003; Guo et al., 2015) was conducted on samples ZWB-OSL-14-2, -17-2, and -18-1 to determine the fading rate (g-value, the percentage of signal loss per decade) of the IRSL signals. Four aliquots of each of the three samples that had been used for D_e measurements were first bleached at 300°C using IR light for 150 s to empty any residual/transferred signals in the grains. A fixed-dose of 600 Gy was repeated given to the aliquots following preheating of 290°C, and the $IR_{140°C}$ and $pIRIR_{170-260°C}$ L_x/T_x signals were measured with different delay periods (up to 7 days). The results (Figure 4D) show that the fading rates are consistent with or below zero for the $pIRIR_{170-260°C}$ signals for the three samples. The fading rates below zero might be artifacts of the laboratory measurement procedure, caused by the signal sensitivity which had not been accurately corrected after storage (Buylaert et al., 2012), or the fixed-dose not close to the D_e value, which is not the scope of this study. The D_e plateau and successful dose recovery ratios are enough to validate that the $pIRIR_{230\,°C}$ and $pIRIR_{260°C}$ signals are non-faded, and their calculated ages do not need correction for fading.

To save instrumental time, we applied the standardized growth curve (SGC) method (Li et al., 2015; Guo et al., 2016) to measure the samples' D_e. The SGC was constructed using a series of sensitivity-corrected regenerative-dose induced L_x/T_x signals, which were normalized to the L_x/T_x signals measured at a regenerative dose of 480 Gy from two aliquots of each of the 12 samples. D_e values were then obtained by projecting the natural L_n/T_n signal (normalized to 480 Gy) onto the SGC. The SGC was fitted using the built-in function "fitGrowth" with a double saturation exponential model (model = "dexp") in the "numOSL" package v. 2.6 (Peng et al., 2013; Peng and Li, 2017) in the RStudio software v. 4.0.3 (Figures 5A–E). To check the reliability of the D_e values obtained based on the SGC method, another aliquot from each of the 12 samples was measured using the complete cycles of the SAR procedure. The D_e values obtained from individual DRCs and the SGC are plotted in Figures 5F–J. It can be seen that the D_e values have increasing standard errors as the stimulation temperatures increase due to the normalized L_n/T_n signals approaching the saturated region of the growth curves. The D_e values increasingly deviate from the 1:1 line as the stimulation temperatures increase due to the normalized L_x/T_x signals deviating from the SGCs at higher regenerative doses (Supplementary Figure S2). However, the D_e values deviate no more than 10% from the 1:1 line for each sample, indicating that the SGC method is applicable for the ZWB samples (Li et al., 2015). Thus, another ten aliquots for each sample were measured for only two SAR cycles—one natural and one regenerative-dose (480 Gy) signal associated with their corresponding test dose signals. The final D_e for each sample was obtained by projecting the weighted mean, calculated using the central age model (CAM; Galbraith et al., 1999; Galbraith and Roberts, 2012) of the normalized L_n/T_n values onto the SGC.

It is noted that some SAR D_e values measured at 230 and 260°C in Figures 5F, G are beyond the empirical $2D_0$, corresponding to ~86% of the saturation intensity (Wintle and Murray, 2006) limits of their SGCs. The multi-aliquot regenerative-dose (MAR) pre-dose MET-pIRIR procedure (Li et al., 2013; Guo et al., 2015) was then applied to sample ZWB-OSL-17-2 to inter-check the reliability of the SAR D_e results because the MAR pre-dose procedure has larger D_0 and can date much older sediments than the SAR procedure (see reviews and references in Zhang and Li, 2020). The measurement procedure is listed in Table 2. In this procedure, the sensitivity-corrected L_X/T_1 and the inter-aliquot normalized L_x/T_2 and T_1/T_2 signals can all be used for D_e determination. Aliquots were divided into six groups. One group was used to measure the natural signal. The other five groups were bleached in the solar simulator for 8 h and then given different regenerative doses. The MAR DRCs for the pre-dose MET-pIRIR signals, fitted using a single saturation exponential function, are shown in Figures 6A–C. The MAR DRCs for L_x/T_2 signals at 230 and 260 °C yielded D_0 values of 732 and 721Gy, respectively. Applying the conservative $2D_0$ limit would enable reliable dating to ~1500 Gy, equating to ~430 ka for the ZWB samples. The MAR L_x/T_2 signal measured at 230 and 260 °C yielded D_e values of 1017 ± 49 and 978 ± 44 Gy, respectively, both accounting for about $1.4D_0$ of their corresponded DRCs. The D_e results obtained from the SAR and MAR MET-pIRIR signals at 230 and 260 °C are statistically consistent at 1σ (Figure 6D), mutually supporting the reliability of the D_e results for the ZWB samples obtained in this study.

Results

Based on all the above performance test results, the $pIRIR_{230\,°C}$ and $pIRIR_{260\,°C}$ signals are proved non-faded, independent of preheating treatments, and can recover the

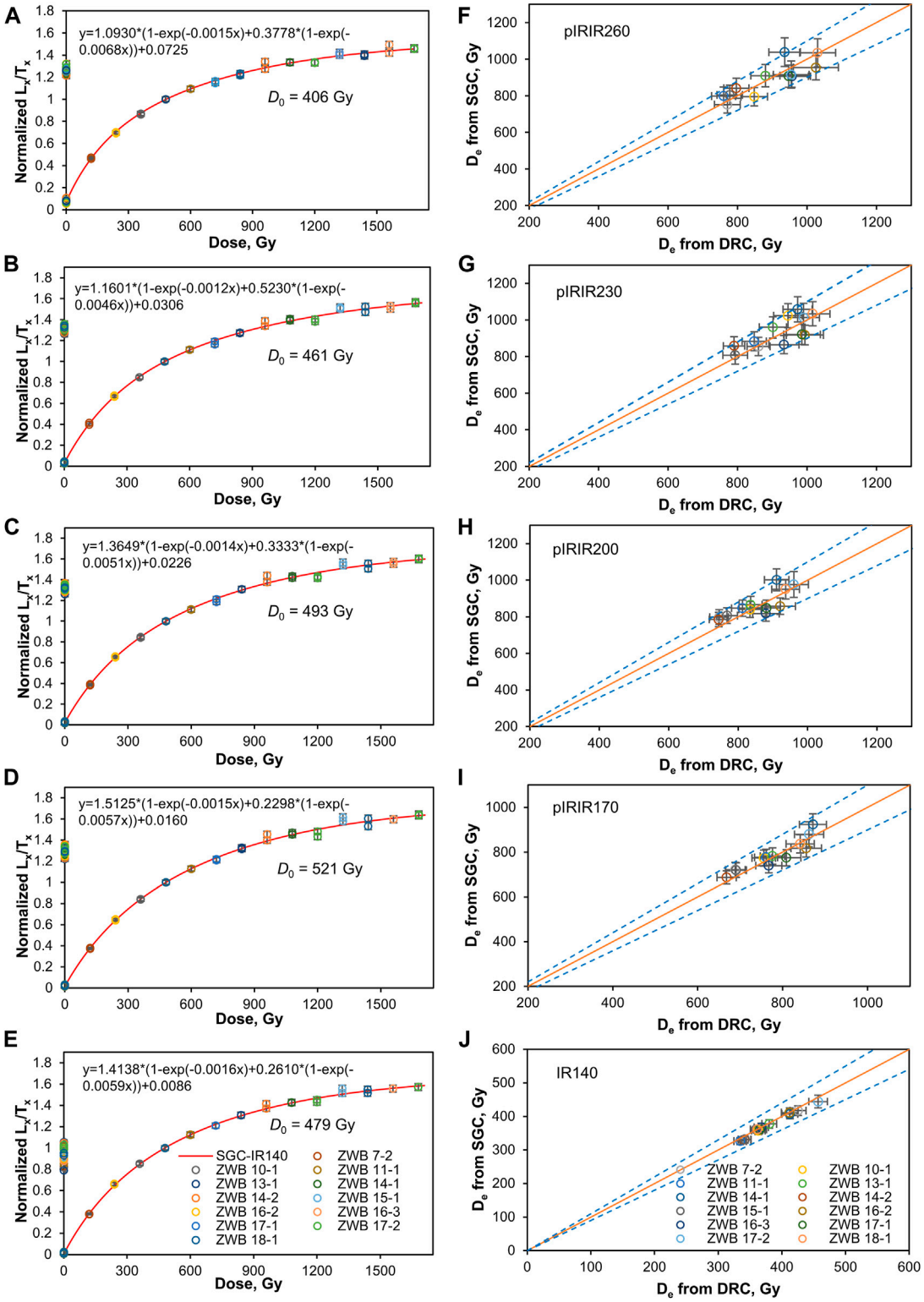

FIGURE 5
(A–E) Standardized growth curves (SGCs) for the L_x/T_x signal (normalized to unity at a dose of 480 Gy) measured at 140–260°C stimulation temperatures using the SAR MET-pIRIR procedure on K-feldspar from samples ZWB-OSL-7-2 to -18-1. The natural signals are shown as the upper set of data points on the *y*-axis. The fitted function and the D_0 values (the characteristic saturation dose, see Figure 6 caption) of the SGCs are shown in each panel. **(F–J)** Equivalent dose (D_e) values obtained from individual dose-response curves (DRC) plotted against those obtained from the SGCs for samples ZWB-OSL-7-2 to -18-1. The solid lines denote the 1:1 relationship, and the dashed lines indicate the 10% deviations. Each data point in each panel indicates the value for one aliquot, and the vertical and horizontal bars indicate the corresponding standard errors.

TABLE 2 The D_e measurement procedure for the MAR pre-dose MET-pIRIR measurements (after Li et al., 2014b).

Step	Treatment	Observed
1	Give regenerative dose, D_i[a]	
2	Preheat at 290°C for 60 s	
3	IRSL measurement at 140 °C for 150 s	$L_{x(140)}$[b]
4	IRSL measurement at 170°C for 150 s	$L_{x(170)}$[b]
5	IRSL measurement at 200°C for 150 s	$L_{x(200)}$[b]
6	IRSL measurement at 230°C for 150 s	$L_{x(230)}$[b]
7	IRSL measurement at 260°C for 150 s	$L_{x(260)}$[b]
8	Give test dose, 240 Gy	
9	Preheat at 290 °C for 60 s	
10	IRSL measurement at 140°C for 150 s	$T_{1(140)}$[b]
11	IRSL measurement at 170°C for 150 s	$T_{1(170)}$[b]
12	IRSL measurement at 200°C for 150 s	$T_{1(200)}$[b]
13	IRSL measurement at 230°C for 150 s	$T_{1(230)}$[b]
14	IRSL measurement at 260°C for 150 s	$T_{1(260)}$[b]
15	Cut heat to 500°C	
16	Give test dose, 480 Gy	
17	Preheat at 290°C for 60 s	
18	IRSL measurement at 140°C for 150 s	$T_{2(140)}$[b]
19	IRSL measurement at 170°C for 150 s	$T_{2(170)}$[b]
21	IRSL measurement at 200°C for 150 s	$T_{2(200)}$[b]
22	IRSL measurement at 230°C for 150 s	$T_{2(230)}$[b]
23	IRSL measurement at 260°C for 150 s	$T_{2(260)}$[b]

[a]For the natural sample, i = 0 Gy and D_0 = 0 Gy. The entire sequence is repeated for several regenerative doses, including a zero dose and a repeat dose.
[b]The aliquots were held for 20, 30, 30, 30, and 40 s before IR, stimulations at each of the temperatures, respectively, to monitor and minimize interference from isothermal decay signals (Fu et al., 2012).

given dose, indicating they are both suitable for dating the ZWB samples. The distributions of the $pIRIR_{230\,°C}$ and $pIRIR_{260\,°C}$ D_e results for each sample are plotted in the radial plots in Figure 7 and Supplementary Figure S3, respectively. The D_e values are distributed around a central value, and their over-dispersion (OD) values, calculated using the CAM, are less than 10% for all samples, indicating they had been well bleached before burial. Since the $pIRIR_{230°C}$ D_e results have relatively lower OD values than the $pIRIR_{260°C}$ D_e results, the CAM D_e values at 230°C were thus used for final age calculations for all the ZWB samples in this study. Since the residual doses are negligible compared to the total D_e (<0.8%), they were not subtracted from the final CAM D_e for each sample. The calculated ages were also not corrected for fading.

The environmental dose rates, CAM D_e values, and the calculated ages at different pIRIR temperatures are summarized in Table 3 and Supplementary Table S1. Here, we only use the ages obtained at 230°C for discussion. The samples' SAR and MAR ages at 230°C are plotted against depth in Figure 8. The samples' ages are broadly consistent with their stratigraphic positions, ranging from ~300 ka to ~240 ka from the bottom up (Figure 8) and covering the time range of the marine isotope stage (MIS) 8 (Lisiecki and Raymo, 2005). The SAR and MAR ages of the samples from the cultural layer (samples ZWB-OSL-16-2, -16-3, -17-1, and -17-2) are consistent at 1 σ (Figure 8) and give a mean value of 280 ± 13 ka, ~220 ka younger than the previous ESR mean age of 504 ± 76 ka (Li et al., 2018).

Discussions

Comparison of the $pIRIR_{230°C}$ and ESR ages in Li et al. (2018)

The ages of the ESR samples HL- 01 to -05 (Figure 3) in Li et al. (2018) are 385 ± 67, 346 ± 32, 501 ± 57, 506 ± 95, and 542 ± 53 ka, respectively. The ESR ages are plotted together with the $pIRIR_{230\,°C}$ ages against depth in Figure 8. The ESR ages are systematically older than the $pIRIR_{230\,°C}$ ages, given that the ESR ages for samples HL-01 and -02 are statistically consistent with their paralleled pIRIR samples at 2 σ. The ESR age for sample HL-02 is rejected by Li et al. (2018) because it is abnormally younger than those of the other two samples of HL-03 and 04 collected from the cultural layer (Figure 8). The discrepancy between the pIRIR and ESR age results could be attributed to the 'underestimation' of the pIRIR age or "overestimation" of the ESR age results.

Similar to luminescence dating, the ESR dating method also aims to date the last exposure of the sediment to sunlight (Yokoyama et al., 1985), and the age is also obtained using the equivalent dose (D_e) dividing the environmental dose rate. The calculations of the environmental dose rates are the same for ESR and luminescence dating methods. The water content was assumed to be 10%, and the cosmic ray contribution was not involved in Li et al.'s study (2018), while the water content is set at 15 ± 5%, and the cosmic ray contribution is involved in this study. However, the assumed water contents are consistent with errors in these two studies, and the cosmic ray contribution is minimal (below 2 m in depth). Therefore, the effect of the environmental dose rates on the age discrepancy between $pIRIR_{230\,°C}$ and ESR methods is negligible.

For the D_e determination, the SAR $pIRIR_{230°C}$ D_e values for the samples in this study (Table 3) account for ~1.9 to 2.1 D_0 of the SGC, reaching the empirical upper limit ($2D_0$) of the reliable D_e estimation suggested by Wintle and Murray (2006). The MAR L_x/T_2 D_e values at 230°C are within the $2D_0$ limit and consistent with the SAR $pIRIR_{230\,°C}$ D_e, indicating that the corresponding SAR SGC was constructed accurately and that much higher D_e values (like $3D_0$) could be estimated (Galbraith and Roberts, 2012; Li et al., 2015; Rui et al., 2020a). Thus, we consider that our $pIRIR_{230\,°C}$ age results are reliable. Based on laboratory experiments, the pIRIR signals in K-feldspars are more light-sensitive and could decrease to a few grays after several hours of bleaching (e.g., Li and Li, 2011; Guo et al., 2016; Wang et al.,

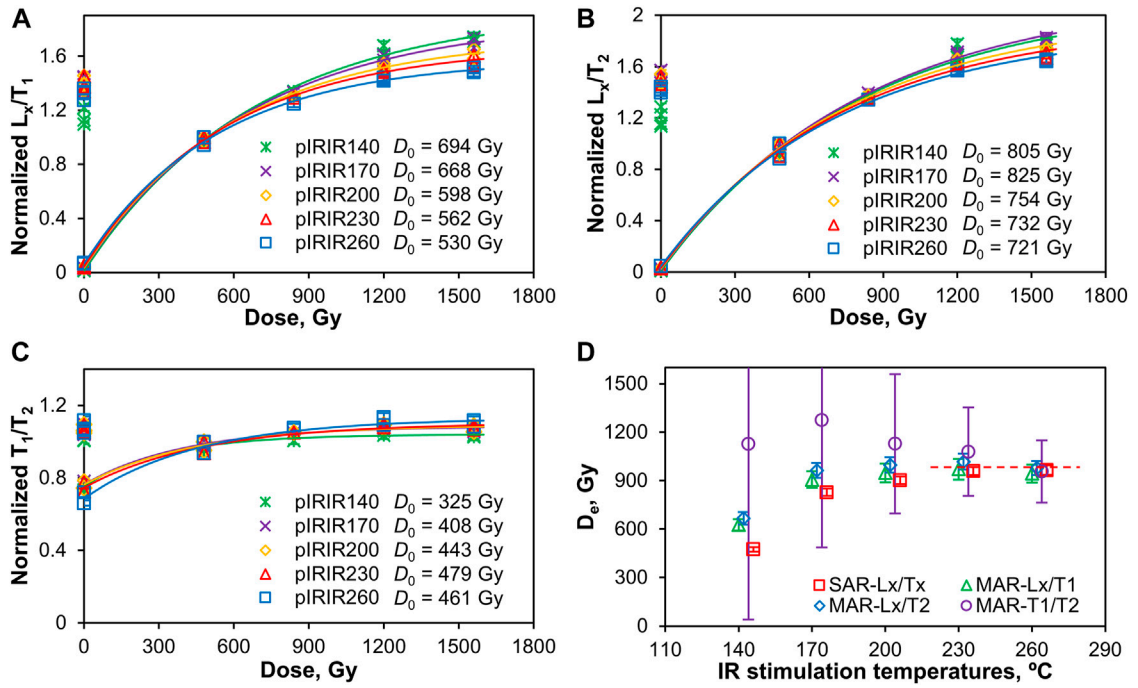

FIGURE 6
(A–C) Dose-response curves (DRC) for the L_x/T_1, L_x/T_2, and T_1/T_2 signals (re-normalized to unity at a dose of 480 Gy) measured at 140–260°C stimulation temperatures using the MAR pMET-pIRIR procedure for sample ZWB-OSL-17-2. The natural signals are shown as the upper set of data points on the *y*-axis. Each data point in panels **(A–C)** represents one aliquot. The curves were fitted using a single saturating exponential function of the form $I = I_0 (1–\exp(–D/D_0)) + y_0$, where I is the normalized IRSL intensity, D is the regenerative dose, D_0 is the characteristic saturation dose (correspond to ~63% of the saturation intensity), and the sum of I_0 and y_0 is the saturation value of the exponential curve. **(D)** D_e values for sample ZWB-OSL-17-2 were measured at 140–260°C using the SAR and MAR pMET-pIRIR procedures. The dashed red line indicates a mean value of ~960 Gy for the D_e values measured at 230°C and 260°C stimulation temperatures from both the SAR and MAR procedures. The data points are offset laterally for clarity. Each data point in panel D) represents the mean values for four aliquots for the MAR procedure, and the CAM values for 12 aliquots for the SAR procedure (Table 3 and Supplementary Table S1). The vertical bars in each panel indicate the corresponding standard errors. It is noted that the natural pIRIR T_n/T_2 signals are close to the saturation levels of their DRCs, resulting in significant errors in the D_e values.

2021), while the ESR signals at the Ti-Li center of the quartz need several tens to over 100 h of bleaching to be reset (e.g., Toyoda et al., 2000; Duval et al., 2017; Ji et al., 2021) using the solar simulator. The low OD values of the SAR De distributions for ZWB samples indicated the pIRIR signals in K-feldspars had been well bleached before burial. In contrast, the bleachability of the signals for the ESR samples was not available except for sample HL-02, which was suggested to have been well bleached before burial by a bleaching test (Li et al., 2018). The sediments of the ZWB profile's cultural layer indicate high-flood deposition (see above description of the sedimentary profile of Units 4 and 5). Thus, the discrepancy between the pIRIR and the ESR age results is possibly caused by overestimating the ESR D_e values, at least for samples HL-03 to -5, due to poor bleaching before burial.

From the geological aspect, the ZWB site is at the boundary of the Huailai and Yanqing basins (Figure 1C). The Huailai basin began falling and accumulating sediments in the Middle Pleistocene, resulting in the Middle-Late Pleistocene alluvial-diluvial sediments up to 200–400 m thick in the basin's center (Wu et al., 1979; Li, 1992). The Yanqing basin had been dominated by falling since Neogene, resulting in the Quaternary fluvial-lacustrine sediments up to 800 m thick in the basin's center (Wu et al., 1979; Li, 1992). The ZWB profile's overall sedimentation rate is ~0.17 m/ka, estimated based on our $pIRIR_{230\ °C}$ chronology (Figure 8), resulting in a thickness of ~110 m deposits for the Middle Pleistocene. A sedimentation rate of ~0.034 m/ka is obtained based on the ESR age results (if rejecting sample HL-02), resulting in a thickness of only ~22 m deposits for the Middle Pleistocene. The thin ~22 m deposits seem too thin to be reasonable because the ZWB profile shows rapid alternations of lakeshore and fluvial deposits (Figure 2), indicating a high sedimentation rate in this area. In addition, Yin and Lu (1996) dated the lacustrine sediments (marked as lacustrine Unit B, correlated to layers 1–17 of ZWB) of the third terrace from sections near ZWB and sections in the middle of the Yanqing basin using the ESR, thermoluminescence (TL), and IRSL methods, resulting in a time range of ~350–160 ka. The lacustrine Unit B's thickness is about 30 m, and a sedimentation

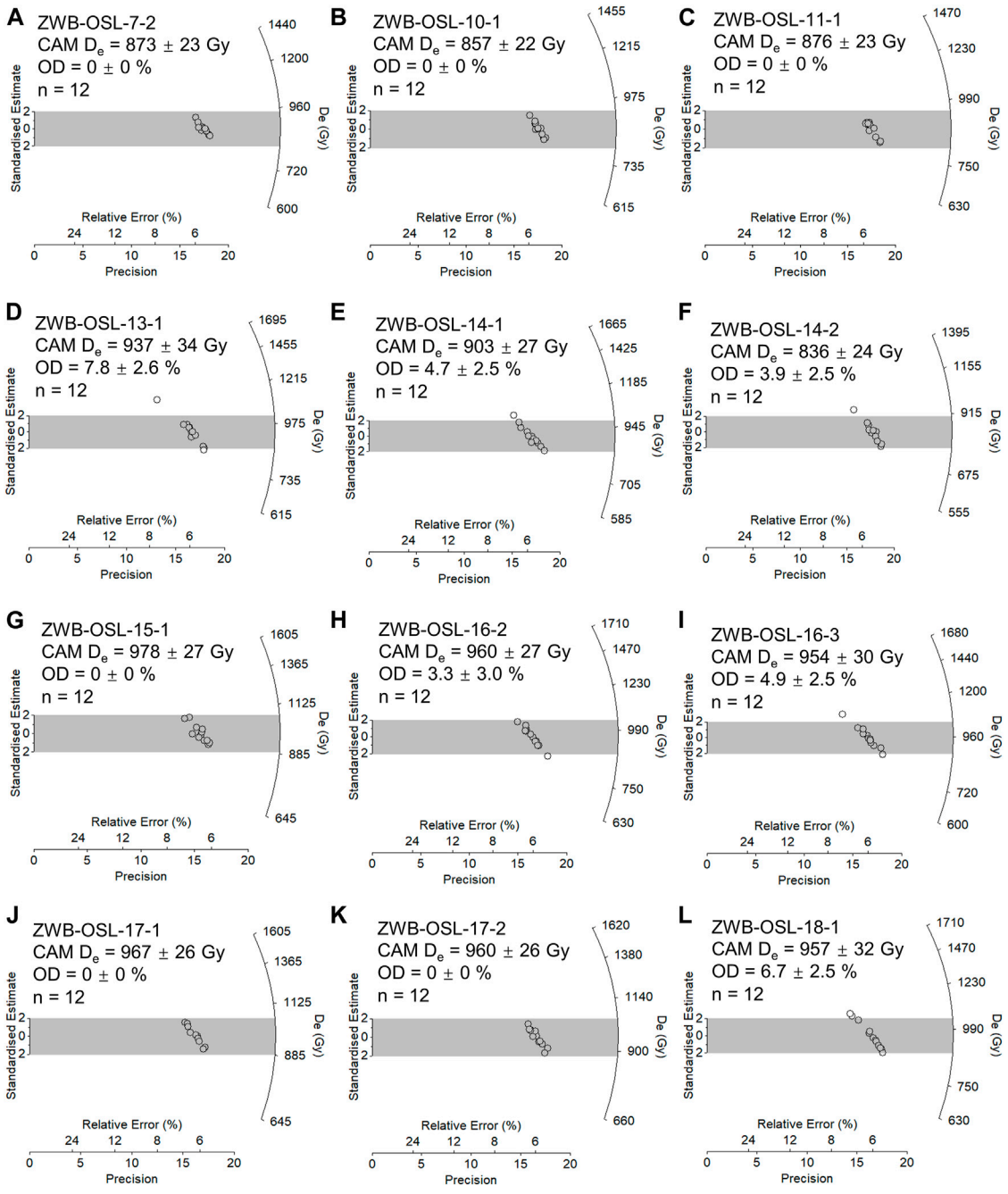

FIGURE 7
(A–L) $pIRIR_{230\ ^{\circ}C}$ D_e distributions of individual aliquots of K-feldspar from samples ZWB-OSL-7-1 to -18-1 were measured, respectively. The gray bands are centered on their central age model (CAM) values. The values of n indicate the number of measured aliquots.

rate of ~0.16 m/ka is thus calculated. The time range (Yin and Lu, 1996) and the computed sedimentation rate are closer to our $pIRIR_{230\ ^{\circ}C}$ age results.

Based on the above discussions, we suggest: 1) our $pIRIR_{230\ ^{\circ}C}$ age results in this study are reliable; 2) the age results for ESR samples HL-03 to -05 might be overestimated due mainly to poor bleaching before burial; 3) the ESR samples HL-01 and -02 might have been better bleached and given statistically consistent age values with the $pIRIR_{230^{\circ}C}$ ages at 2σ. To be conservative, the mean value of 280 ± 13 ka (MIS 8) based on the SAR and MAR $pIRIR_{230^{\circ}C}$ ages for samples ZWB-OSL-16-2, -16-3, -17-1, and -17-2 can be the lower, and the ESR age of 346 ± 32 ka (MIS 10)

TABLE 3 Environmental dose rates, single-aliquot D_e, and ages were measured at 230°C stimulation temperature for K-feldspar samples from ZWB.

Sample	Depth (m)	U (ppm)	Th (ppm)	K (%)	External dose rate (Gy/ka)	Internal dose rate (Gy/ka)[a]	Total dose rate (Gy/ka)	D_e (Gy)	Age (ka)
ZWB-OSL-7-2	1.3	2.50 ± 0.08	8.15 ± 0.24	2.37 ± 0.12	3.237 ± 0.146	0.397 ± 0.104	3.634 ± 0.179	873 ± 23	240 ± 13
ZWB-OSL-10-1	3.1	2.09 ± 0.06	6.05 ± 0.18	2.61 ± 0.13	3.194 ± 0.151	0.397 ± 0.104	3.591 ± 0.184	857 ± 22	239 ± 14
ZWB-OSL-11-1	3.8	1.97 ± 0.06	7.32 ± 0.22	2.44 ± 0.12	3.099 ± 0.144	0.397 ± 0.104	3.496 ± 0.178	876 ± 23	251 ± 14
ZWB-OSL-13-1	5.2	1.55 ± 0.05	3.34 ± 0.10	2.76 ± 0.14	3.014 ± 0.151	0.397 ± 0.104	3.411 ± 0.184	937 ± 34	275 ± 18
ZWB-OSL-14-1	6.1	1.82 ± 0.05	6.50 ± 0.20	2.45 ± 0.12	2.991 ± 0.143	0.397 ± 0.104	3.388 ± 0.177	903 ± 27	266 ± 16
ZWB-OSL-14-2	6.0	2.10 ± 0.06	7.11 ± 0.21	2.32 ± 0.12	2.978 ± 0.139	0.397 ± 0.104	3.376 ± 0.173	836 ± 24	248 ± 15
ZWB-OSL-15-1	7.7	2.41 ± 0.07	11.32 ± 0.34	2.38 ± 0.12	3.324 ± 0.150	0.397 ± 0.104	3.721 ± 0.183	978 ± 27	263 ± 15
ZWB-OSL-16-2	9.5	1.96 ± 0.06	8.00 ± 0.24	2.46 ± 0.12	3.081 ± 0.146	0.397 ± 0.104	3.478 ± 0.179	960 ± 27	276 ± 16
ZWB-OSL-16-3	9.3	1.56 ± 0.05	6.51 ± 0.20	2.64 ± 0.13	3.072 ± 0.15	0.397 ± 0.104	3.469 ± 0.183	954 ± 30	275 ± 17
ZWB-OSL-17-1	10.0	1.63 ± 0.05	7.90 ± 0.24	2.66 ± 0.13	3.179 ± 0.153	0.397 ± 0.104	3.576 ± 0.185	967 ± 26	270 ± 16
ZWB-OSL-17-2	10.3	1.89 ± 0.06	7.58 ± 0.23	2.57 ± 0.13	3.140 ± 0.150	0.397 ± 0.104	3.537 ± 0.183	960 ± 26	271 ± 16
MAR L_x/T_1[b]								971 ± 64	274 ± 23
MAR L_x/T_2[b]								1017 ± 49	288 ± 20
MAR T_1/T_2[b]								1079 ± 275	305 ± 79
ZWB-OSL-18-1	10.6	1.47 ± 0.04	6.33 ± 0.19	2.57 ± 0.13	2.964 ± 0.145	0.397 ± 0.104	3.361 ± 0.179	957 ± 32	285 ± 18

[a]The internal dose rates were estimated by assuming the K content of 12 ± 1% (Rui et al., 2019), and the grain size is 90–150 μm for all the samples.
[b]The final D_e and age values for sample ZWB-17-2 based on the MAR, L_x/T_1, L_x/T_2, and MAR T_1/T_2 signals measured at 230°C stimulation temperature.

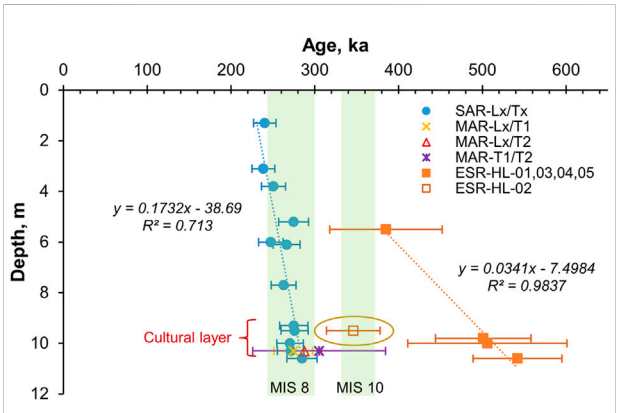

FIGURE 8
Age results obtained based on multi-grained single- and multiple-aliquot K-feldspars in this study for samples ZWB-OSL-7-2 to -18-1, and previous ESR age results for samples HL-01 to -05 presented in Li et al. (2018) plotted against their depth, from top to bottom, respectively. The horizontal bars for each point represent the standard errors. The green bans indicate the Marine Isotope Stage (MIS) boundaries follow Lisiecki and Raymo (2005).

for sample HL-02 can be the upper limit of the cultural layer. However, the contained stone artifact and animal fossil remains should be even older because they were transported to the location by a high flood.

Archaeological implications

The Paleolithic sites in Nihewan Basin have been dated back to ~1.66 Ma (Zhu et al., 2004), and the neighboring (~150 km) Zhoukoudian Locality 1 (ZKD1) dated back to ~0.5 to 0.8 Ma (see reviews and references in Chen and Zhou, 2009). The lithic technologies in both areas belong to the 'small-tool' industry (flake technology), one of the major Paleolithic traditions in North China (Jia et al., 1972; Zhang, 1990, 1999; Liu, 2014; Guo et al., 2017). The close distance and similarities in the lithic technology prompt archaeologists to infer that immigrations or communications might have occurred between the Nihewan and Zhoukou areas as early as the initial Middle Pleistocene (Li and Shi, 2020). As part of the "generalized Nihewan Basin", the Yan-Huai Basin might act

as one of the corridors for the Nihewan people to move east to the Zhoukoudian area or even north to Northeast China. Seeking out early Middle Pleistocene Paleolithic sites in the Yan-Huai Basin is critical for exploring the nature of the initial dispersal of Nihewan people to the Zhoukoudain area. However, considering the Quaternary tectonic activity in this region (Wu et al., 1979), efforts should be paid more to the tectonic uplifting or stable surrounding mountain feet rather than the middle of the Basin, which had been dominated by tectonic falling and sediment accumulation in Quaternary.

Conclusion

This study has dated 12 samples from the Zhuwobu site in the Huailai Basin, using the MET-pIRIR procedure on multi-grained single and multiple aliquots on K-feldspars. The consistency of the D_e results obtained from the MAR and SAR procedure mutually supported the reliability of the age results obtained in this study. The $pIRIR_{230°C}$ ages for the samples are broadly consistent with their stratigraphic positions, ranging from ~300 ka to ~240 ka from the bottom up (Figure 8A), resulting in a mean sedimentation rate of ~0.17 m/ka for the profile. Our results suggest that the cultural layers at this site were deposited 280 ± 13 ka (MIS 8) ago, ~220 ka younger than the previous ESR mean age of 504 ± 76 ka (Li et al., 2018).

Considering the region's tectonic history activity and the characteristics of the sedimentary facies for the ZWB site, we suggest that the ESR ages in Li et al. (2018), at least for samples HL-03 to -05, might be overestimated due to poor bleaching before burial. While the rejected age of 346 ± 32 ka (MIS 10) for sample HL-02—consistent with our $pIRIR_{230°C}$ age results within 2σ—might be more reliable due to being well-bleached before burial. However, the cultural remains should be even older because they were not buried *in situ*. Other dating methods, for example, ESR/U-series on animal fossils, or TT-OSL or Paleomagnetic dating on sediments, are encouraged at this site to cross-check the reliability of the $pIRIR_{230\ °C}$ and the ESR age results. Further archaeological, geological, and chronological studies are needed to explore the ancient hominins' survival conditions in the "generalized Nihewan" region and possible connections with the renowned Zhoukoudian sites.

Data availability statement

The original contributions presented in the study are included in the article/Supplementary Material, further inquiries can be directed to the corresponding author.

Author contributions

YG: conducted the experiments in the laboratory, performed the data analysis, and wrote the manuscript. QX: conducted the experiments in the laboratory. CL: conducted the experiments in the laboratory. DN: organized the project, collected the samples, draw the figures, and reviewed the manuscript.

Funding

This research was supported by the National Natural Science Foundation of China(41902022 and 41702192)and the National Key R&D Program of China(2020YFC1521500).

Acknowledgments

We would like to thank professors Shuwen Pei from the Institute of Vertebrate Paleontology and Paleoanthropology (IVPP), Chenglong Deng from the Institute of Geology and Geophysics, Chinese Academy of Sciences, Fei Xie from the Hebei Provincial Institute of Cultural Relics and Archaeology for their help in the field investigations and sample collections. We thank the editor and the reviewers for their constructive suggestions for this study.

Conflict of interest

The authors declare that the research was conducted in the absence of any commercial or financial relationships that could be construed as a potential conflict of interest.

Publisher's note

Supplementary material

The Supplementary Material for this article can be found online at: https://www.frontiersin.org/articles/10.3389/feart.2022.932834/full#supplementary-material

References

Adamiec, G., and Aitken, M. J. (1998). Dose-rate conversion factors: update. *Anc. TL* 16, 37–46.

Aitken, M. J. (1998). *An introduction to optical dating*. Oxford: Oxford University Press.

Auclair, M., Lamothe, M., and Huot, S. (2003). Measurement of anomalous fading for feldspar IRSL using SAR. *Radiat. Meas.* 37, 487–492. doi:10.1016/s1350-4487(03)00018-0

Bar-Yosef, O., and Wang, Y. P. (2012). Paleolithic archaeology in China. *Annu. Rev. Anthropol.* 41, 319–335. doi:10.1146/annurev-anthro-092611-145832

Bøtter-Jensen, L., Andersen, C. E., Duller, G., and Murray, A. S. (2003). Developments in radiation, stimulation and observation facilities in luminescence measurements. *Radiat. Meas.* 37, 535–541. doi:10.1016/S1350-4487(03)00020-9

Bøtter-Jensen, L., Bulur, E., Duller, G. A. T., and Murray, A. S. (2000). Advances in luminescence instrument systems. *Radiat. Meas.* 32, 523–528. doi:10.1016/s1350-4487(00)00039-1

Buylaert, J. P., Jain, M., Murray, A. S., Thomsen, K. J., Thiel, C., and Sohbati, R. (2012). A robust feldspar luminescence dating method for Middle and Late Pleistocene sediments. *Boreas* 41, 435–451. doi:10.1111/j.1502-3885.2012.00248.x

Buylaert, J. P., Murray, A. S., Thomsen, K. J., and Jain, M. (2009). Testing the potential of an elevated temperature IRSL signal from K-feldspar. *Radiat. Meas.* 44, 560–565. doi:10.1016/j.radmeas.2009.02.007

Chen, T. M., and Zhou, L. P. (2009). Dating of the peking man site: A comparison between existing chronology and the 26Al/10Be burial ages. *Acta Anthropol. Sin.* 28, 285–291. (in Chinese with English abstract). doi:10.16359/j.cnki.cn11-1963/q.2009.03.007

Clarkson, C., Harris, C., Li, B., Neudorf, C. M., Roberts, R. G., Lane, C., et al. (2020). Human occupation of northern India spans the Toba supereruption ~74, 000 years ago. *Nat. Commun.* 11, 961. doi:10.1038/s41467-020-14668-4

Durcan, J. L., King, G. E., and Duller, G. A. T. (2015). DRAC: Dose rate and age calculator for trapped charge dating. *Quat. Geochronol.* 28, 54–61. doi:10.1016/j.quageo.2015.03.012

Duval, M., Arnold, L. J., Guilarte, V., Demuro, M., Santonja, M., and Pérez-González, A. (2017). Electron spin resonance dating of optically bleached quartz grains from the Middle Palaeolithic site of Cuesta de la Bajada (Spain) using the multiple centres approach. *Quat. Geochronol.* 37, 82–96. doi:10.1016/j.quageo.2016.09.006

Feathers, J. K. (2003). Use of luminescence dating in archaeology. *Meas. Sci. Technol.* 14, 1493–1509. doi:10.1088/0957-0233/14/9/302

Fu, X., Li, B., and Li, S. H. (2012). Testing a multi-step post-IR IRSL dating method using polymineral fine grains from Chinese loess. *Quat. Geochronol.* 10, 8–15. doi:10.1016/j.quageo.2011.12.004

Galbraith, R. F., Roberts, R. G., Laslett, G. M., Yoshida, H., and Olley, J. M. (1999). Optical dating of single and multiple grains of quartz from jinmium rock shelter, northern Australia: Part I, experimental design and statistical models. *Archaeometry* 41, 339–364. doi:10.1111/j.1475-4754.1999.tb00987.x

Galbraith, R. F., and Roberts, R. G. (2012). Statistical aspects of equivalent dose and error calculation and display in OSL dating: An overview and some recommendations. *Quat. Geochronol.* 11, 1–27. doi:10.1016/j.quageo.2012.04.020

Guo, Y. J., Li, B., Zhang, J. F., and Roberts, R. G. (2015). Luminescence-based chronologies for Palaeolithic sites in the Nihewan Basin, northern China: First tests using newly developed optical dating procedures for potassium feldspar grains. *J. Archaeol. Sci. Rep.* 3, 31–40. doi:10.1016/j.jasrep.2015.05.017

Guo, Y. J., Li, B., Zhang, J. F., Yuan, B. Y., Xie, F., and Roberts, R. G. (2016). Luminescence ages for three 'Middle Palaeolithic' sites in the Nihewan Basin, northern China, and their archaeological and palaeoenvironmental implications. *Quat. Res.* 85, 456–470. doi:10.1016/j.yqres.2016.03.002

Guo, Y. J., Li, B., Zhang, J. F., Yuan, B. Y., Xie, F., and Roberts, R. G. (2017). New ages for the upper Palaeolithic site of Xibaimaying in the Nihewan Basin, northern China: Implications for small-tool and microblade industries in North-East Asia during marine isotope stages 2 and 3. *J. Quat. Sci.* 32, 540–552. doi:10.1002/jqs.2949

Guo, Y. J., Li, B., and Zhao, H. L. (2020). Comparison of single-aliquot and single-grain MET-pIRIR De results for potassium feldspar samples from the Nihewan Basin, northen China. *Quat. Geochronol.* 56, 101040. doi:10.1016/j.quageo.2019.101040

Hu, H. B., Tian, L. F., and Sun, L. M. (2000). Characteristics and ages of the Pleistocene lithostratigraphy and biostratigraphy in the Huailai-Zhuolu basin, Hebei. *Regional Geol. China* 19, 137–143. (in Chinese with English abstract).

Hu, Y., Marwick, B., Zhang, J. F., Rui, X., Hou, Y. M., Yue, J. P., et al. (2019). Late middle Pleistocene levallois stone-tool technology in southwest China. *Nature* 565, 82–85. doi:10.1038/s41586-018-0710-1

Huntley, D. J., and Lamothe, M. (2001). Ubiquity of anomalous fading in K-feldspars and the measurement and correction for it in optical dating. *Can. J. Earth Sci.* 38, 1093–1106. doi:10.1139/e01-013

Jacobs, Z., Li, B., Shunkov, M. V., Kozlikin, M. B., Bolikhovskaya, N. S., Agadjanian, A. K., et al. (2019). Timing of archaic hominin occupation of Denisova Cave in southern Siberia. *Nature* 565, 594–599. doi:10.1038/s41586-018-0843-2

Ji, H., Liu, C. R., Yin, G. M., Wei, C. Y., and Song, W. J. (2021). ESR dating of the Hougou Paleolithic site in the Nihewan Basin, North china, using both additive and regenerative dose methods. *Quat. Int.* 619, 72–80. doi:10.1016/j.quaint.2021.10.001

Ji, Y. P., and Wang, G. L. (2017). Final disappearing process of the ancient lake during Quaternary in Nihewan. *Acta Geosci. Sin.* 38, 38–42.

Jia, L. P., Gai, P., and You, Y. Z. (1972). Report on the excavation at zhiyu paleolithic site in shanxi Province. *Kaoguxuebao* 1, 39–58. (in Chinese).

Lai, Z. P. (2010). Chronology and the upper dating limit for loess samples from Luochuan section in the Chinese Loess Plateau using quartz OSL SAR protocol. *J. Asian Earth Sci.* 37, 176–185. doi:10.1016/j.jseaes.2009.08.003

Li, B., Jacobs, Z., Roberts, R. G., and Li, S. H. (2013). Extending the age limit of luminescence dating using the dose-dependent sensitivity of MET-pIRIR signals from K-feldspar. *Quat. Geochronol.* 17, 55–67. doi:10.1016/j.quageo.2013.02.003

Li, B., Jacobs, Z., Roberts, R. G., and Li, S. H. (2014a). Review and assessment of the potential of post-IR IRSL dating methods to circumvent the problem of anomalous fading in feldspar luminescence. *Geochronometria* 41, 178–201. doi:10.2478/s13386-013-0160-3

Li, B., and Li, S. H. (2012). Luminescence dating of Chinese loess beyond 130 ka using the non-fading signal from K-feldspar. *Quat. Geochronol.* 10, 24–31. doi:10.1016/j.quageo.2011.12.005

Li, B., and Li, S. H. (2011). Luminescence dating of K-feldspar from sediments: A protocol without anomalous fading correction. *Quat. Geochronol.* 6, 468–479. doi:10.1016/j.quageo.2011.05.001

Li, B., Roberts, R. G., Jacobs, Z., and Li, S. H. (2014b). A single-aliquot luminescence dating procedure for K-feldspar based on the dose-dependent MET-pIRIR signal sensitivity. *Quat. Geochronol.* 20, 51–64. doi:10.1016/j.quageo.2013.11.001

Li, B., Roberts, R. G., Jacobs, Z., Li, S. H., and Guo, Y. J. (2015). Construction of a 'global standardised growth curve' (gSGC) for infrared stimulated luminescence dating of K-feldspar. *Quat. Geochronol.* 27, 119–130. doi:10.1016/j.quageo.2015.02.010

Li, C. A. (1992). Analysis on active tectonics of Quaternary period around Fanshan basin in heibei Province. *Inland Earthq.* 6, 240–245. (in Chinese with English abstract). doi:10.16256/j.issn.1001-8956.1992.03.005

Li, J., and Shi, X. R. (2020). From nihewan to zhoukoudian: The evolution model of paleolithic culture in northern China. *J. Shanxi Univ. (Philosophy Soc. Sci.* 43, 59–67.

Li, W. P., Liu, C. R., Niu, D. W., Wei, C. Y., and Li, J. P. (2018). Electron spin resonance data of the zhuwobao paleolithic site in the Huailai basin of China. *Quat. Sci.* 38, 680–687. (in Chinese with English abstract). doi:10.11928/j.issn.1001-7410.2018.03.12

Liritzis, I., Singhvi, A. K., Feathers, J. K., Wagner, G. A., Kadereit, A., Zacharias, N., et al. (2013). *Luminescence dating in archaeology, anthropology, and geoarchaeology: an overview*. Heidelberg: Springer.

Lisiecki, L. E., and Raymo, M. E. (2005). A Pliocene–Pleistocene stack of 57 globally distributed benthic $\delta^{18}O$ records. *Paleoceanography* 20, PA1003. doi:10.1029/2004pa001071

Liu, Y., and Yang, C. h. (2014). Unveiling the secrets to her heart. *Neuron* 2, 3–5. doi:10.1016/j.neuron.2014.06.019

Lu, Y., Sun, X. F., Zhao, H. L., and Tan, P. Y. (2021). Luminescence dating of youfangbei early late Pleistocene site, Nihewan Basin, north China. *Quat. Res.* 104, 159–169. doi:10.1017/qua.2021.19

Murray, A. S., and Roberts, R. G. (1998). Measurement of the equivalent dose in quartz using a regenerative-dose single-aliquot protocol. *Radiat. Meas.* 29, 503–515. doi:10.1016/s1350-4487(98)00044-4

Murray, A. S., and Wintle, A. G. (2000). Luminescence dating of quartz using an improved single-aliquot regenerative-dose protocol. *Radiat. Meas.* 32, 57–73. doi:10.1016/s1350-4487(99)00253-x

Murray, A. S., and Wintle, A. G. (2003). The single aliquot regenerative dose protocol: Potential for improvements in reliability. *Radiat. Meas.* 37, 377–381. doi:10.1016/s1350-4487(03)00053-2

Nian, X. M., Zhou, L. P., and Yuan, B. Y. (2013). Optically stimulated luminescence dating of terrestrial sediments in the Nihewan Basin and its implication for the evolution of ancient Nihewan Lake. *Quat. Sci.* 33, 403–414. (in Chinese with English abstract). doi:10.3969/j.issn.1001-7410.2013.03.01

Niu, D. W., Wang, X. M., Li, D. Y., and Xie, F. (2022). Report on the test excavation at Zhuwobu paleolithic site in Huailai county, Hebei Province. *Archaelogy* 3, 243–252. (in Chinese).

Niu, D. W., Xue, F., Li, D. Y., Li, Y. H., and Xie, F. (2017). A report on paleolithic survey of 2014 in Huailai basin, Hebei Province. *Acta Anthropol. Sin.* 37, 79–87. (in Chinese with English abstract). doi:10.16359/j.cnki.cn11-1963/q.2017.0071

Peng, J., Dong, Z. B., Han, F. Q., Long, H., and Liu, X. J. (2013). R package numOSL: numeric routines for optically stimulated luminescence dating. *Anc. TL* 31, 41–48.

Peng, J., and Li, Bo. (2017). Single-aliquot regenerative-dose (SAR) and standardised growth curve (SGC) equivalent dose determination in a batch model using the R package 'numOSL. *Anc. TL* 35, 32–53.

Ran, Y. K., Fang, Z. J., Li, Z. Y., Wang, J. B., and Li, R. C. (1992). Paleoseismicity and segmentation along the active fault at the north boundary of huai-zhuolu basin, Hebei Province. *Earthq. Res. China* 8, 74–85. (in Chinese with English abstract).

Rhodes, E. J. (2011). Optically stimulated luminescence dating of sediments over the past 200, 000 years. *Annu. Rev. Earth Planet. Sci.* 39, 461–488. doi:10.1146/annurev-earth-040610-133425

Rui, X., Guo, Y. J., Zhang, J. F., Hu, Y., Mei, H. J., Wang, Y. P., et al. (2019). Luminescence chronology of the palaeolithic–neolithic transition in the yujiagou site at the Nihewan Basin, northern China. *J. Quat. Sci.* 34, 125–137. doi:10.1002/jqs.3086

Rui, X., Li, B., and Guo, Y. J. (2020a). Testing the upper limit of luminescence dating based on standardised growth curves for MET-pIRIR signals of K-feldspar grains from northern China. *Quat. Geochronol.* 57, 101063. doi:10.1016/j.quageo.2020.101063

Rui, X., Li, B., and Guo, Y. J. (2020b). The effect of residual signal on dose measurements using MET-pIRIR signals from K-feldspar. *Quat. Geochronol.* 58, 101065. doi:10.1016/j.quageo.2020.101065

Thiel, C., Buylaert, J. P., Murray, A., Terhorst, B., Hofer, I., Tsukamoto, S., et al. (2011). Luminescence dating of the Stratzing loess profile (Austria)–testing the potential of an elevated temperature post-IR IRSL protocol. *Quat. Int.* 234, 23–31. doi:10.1016/j.quaint.2010.05.018

Thomsen, K. J., Murray, A. S., Jain, M., and Bøtter-Jensen, L. (2008). Laboratory fading rates of various luminescence signals from feldspar-rich sediment extracts. *Radiat. Meas.* 43, 1474–1486. doi:10.1016/j.radmeas.2008.06.002

Toyoda, S., Voinchet, P., Falguères, C., Dolo, J. M., and Laurent, M. (2000). Bleaching of ESR signals by the sunlight: a laboratory experiment for establishing the ESR dating of sediments. *Appl. Radiat. Isotopes* 52, 1357–1362. doi:10.1016/s0969-8043(00)00095-6

Wallinga, J., Murray, A., and Wintle, A. (2000). The single-aliquot regenerative-dose (SAR) protocol applied to coarse-grain feldspar. *Radiat. Meas.* 32, 529–533. doi:10.1016/s1350-4487(00)00091-3

Wang, F. G., Guo, Y. J., Xian, Q., Li, M. Y., Rui, X., and Xie, F. (2021). Luminescence chronology for the Paleolithic site of Xinmiaozhuang Locality 1 (XMZ1) in the Nihewan Basin, northern China, and its paleoenvironmental and archaeological implications. *J. Hum. Evol.* 157, 103033. doi:10.1016/j.jhevol.2021.103033

Wang, F., Xun, S., Peng, J., Huang, Q., Zhao, J., Meng, Z., et al. (2020). A study of the symbiotic relationship between tectonic fissures and faults in the Fenwei Graben System, China. *Environ. Earth Sci.* 79, 212. doi:10.1007/s12665-020-08966-9

Wang, X. (2014). Optically stimulated luminescence dating of sand-dune formed within the little ice age. *J. Asian Earth Sci.* 91, 154–162. doi:10.1016/j.jseaes.2014.05.012

Wintle, A. G., and Murray, A. S. (2006). A review of quartz optically stimulated luminescence characteristics and their relevance in single-aliquot regeneration dating protocols. *Radiat. Meas.* 41, 369–391. doi:10.1016/j.radmeas.2005.11.001

Wu, Z. R., Yuan, B. Y., Sun, J. Z., and Liu, Z. S. (1979). Neotectonics and seismicity of yan-Huai basin in Hebei Province. *Seismol. Geol.* 1, 46–56. (in Chinese with English abstract).

Xie, F., Li, J., and Liu, L. Q. (2006). *Paleolithic archeology in the Nihewan Basin*. Shijiazhuang: Huashan Literature and Arts Press. (in Chinese).

Yang, S. X., Deng, C. L., Zhu, R. X., and Petraglia, M. D. (2020). The paleolithic in the Nihewan Basin, China: Evolutionary history of an early to late Pleistocene record in eastern Asia. *Evol. Anthropol.* 29, 125–142. doi:10.1002/evan.21813

Yin, G. M., and Lu, Y. C. (1996). The Quaternary tectonic events in the Yanqing faulting-down Basin, Beijing. *North China Earthq. Sci.* 14, 19–30. (in Chinese with English abstract)

Yokoyama, Y., Falgueres, C., and Quaegebeur, J. P. (1985). ESR dating of quartz from quaternary sediments: first attempt. *Nucl. Tracks Radiat. Meas.* 10, 921–928. doi:10.1016/0735-245x(85)90109-7

Yuan, B. Y., Xia, Z. K., and Niu, P. S. (2011). *Nihewan rift and early man*. Beijing: Geology Press. (in Chinese).

Zhang, J. J., and Li, S. H. (2020). Review of the post-IR IRSL dating protocols of K-feldspar. *Methods Protoc.* 3, 7. doi:10.3390/mps3010007

Zhang, S. S. (1999). On the important advancements of the Palaeolithic archeology in China since 1949 (in Chinese with English abstract). *Acta Anthr. Sin.* 18, 193–214.

Zhang, S. S. (1990). Regional industrial gradual advance and cultural exchange of Paleolithic in North China (in Chinese with English abstract). *Acta Anthr. Sin.* 9, 322–333.

Zhao, H., Lu, Y., Wang, C., Chen, J., Liu, J., and Mao, H. (2010). ReOSL dating of aeolian and fluvial sediments from Nihewan Basin, northern China and its environmental application. *Quat. Geochronol.* 5, 159–163. doi:10.1016/j.quageo.2009.03.008

Zheng, R. Z., Ji, F. J., and Li, J. P. (2001). Lake development and climatic changes, during the middle and late times of Late Pleistocene in the Yan-Huai Basin. *Seismol. Geol.* 23, 55–62. (in Chinese with English abstract). doi:10.3969/j.issn.0253-4967.2001.01.007

Zhu, R. X., Potts, R., Xie, F., Hoffman, K. A., Deng, C. L., Shi, C. D., et al. (2004). New evidence on the earliest human presence at high northern latitudes in northeast Asia. *Nature* 431, 559–562. doi:10.1038/nature02829

Zhu, Z. Y., Guo, Y., Zhang, X. S., and Jiang, J. J. (2020). Quaternary strata structure characteristics of the drilling hole ZK02 in Huailai region, Hebei Provice. *J. Geol.* 44, 250–257. (in Chinese with English abstract). doi:10.3969/j.issn.1674-3636.2020.03.003

frontiers | Frontiers in Earth Science

TYPE Original Research
PUBLISHED 22 August 2022
DOI 10.3389/feart.2022.967572

OPEN ACCESS

EDITED BY
Hao Long,
Nanjing Institute of Geography and Limnology (CAS), China

REVIEWED BY
Xiaomei Nian,
East China Normal University, China
Xianjiao Ou,
Jiaying University, China

*CORRESPONDENCE
T. Tamura,
toru.tamura@aist.go.jp

SPECIALTY SECTION
This article was submitted to Quaternary Science, Geomorphology and Paleoenvironment, a section of the journal Frontiers in Earth Science

RECEIVED 13 June 2022
ACCEPTED 12 July 2022
PUBLISHED 22 August 2022

CITATION
Tamura T, Okazaki H, Naya T, Nakashima R, Nakazato H, Seike K and Okuno J (2022), Luminescence chronology for identifying depositional sequences in an uplifted coast since the Middle Pleistocene, eastern Japan. *Front. Earth Sci.* 10:967572. doi: 10.3389/feart.2022.967572

Luminescence chronology for identifying depositional sequences in an uplifted coast since the Middle Pleistocene, eastern Japan

T. Tamura[1,2,3]*, H. Okazaki[4], T. Naya[1], R. Nakashima[1], H. Nakazato[5], K. Seike[1] and J. Okuno[6]

[1]Geological Survey of Japan, AIST, Tsukuba, Japan, [2]Graduate School of Frontier Science, The University of Tokyo, Kashiwa, Japan, [3]Institute for Space-Earth Environmental Research, Nagoya University, Nagoya, Japan, [4]Fukada Geological Institute, Tokyo, Japan, [5]Institute for Rural Engineering, NARO, Tsukuba, Japan, [6]National Institute of Polar Research, Tachikawa, Japan

Feldspar post-infrared infrared stimulated luminescence (pIRIR) dating is an advantageous trapped-charge dating method concerning late Quaternary sedimentary records for its direct applicability to clastic sediments and wide time coverage. Its application to depositional sequences in various coastal settings potentially improve our understanding of long-term sea-level changes and regional tectonics that the sequences record. The Kanto coastal plain, eastern Japan is situated in a unique tectonic setting near the triple junction of plate boundaries and characterized by extensive development of the Last Interglacial raised marine terrace in contrast to the longer-term subsidence trend. In this article, we document the application of feldspar pIRIR dating to a 35-m-long sediment core collected from the marine terrace in the northeastern Kanto plain and examine how effective its chronology is for identifying depositional sequences related to the relative sea-level fluctuations since the Middle Pleistocene. The sediment core shows a succession of seven facies units, A to G, in ascending order, representing the shallow marine to shelf (units A to C), fluvial to brackish salt marsh (unit D), beach to shoreface (unit E), fluvial to aeolian (unit F), and loess (unit G) sedimentation. According to pre-tests, pIRIR at 225°C after prior infrared stimulated luminescence at 50°C ($pIRIR_{225}$) was chosen as an optimal signal for dating. $pIRIR_{225}$ is characterized by modest anomalous fading with an average g_{2days}-value of 1.8%/decade. Fading-corrected $pIRIR_{225}$ ages are consistent with the stratigraphy. Units A and B are dated as Marine Oxygen Isotope Stage (MIS) 7 and units C to F as MIS 5. However, uncertainties of individual age estimates do not allow further chronological correlation. Instead, using sea-level changes inferred from characteristic facies transitions as additional constraints, units C to F can be correlated to sub-stages in MIS 5. Unit E represents coastal progradation during the MIS 5c sea-level highstand, which refines the date of the marine terrace around the core site as MIS 5c and revises up the rate of the tectonic uplift accordingly. Our results exemplify a successful application of feldspar pIRIR dating for identifying depositional sequences formed in relations to 100-kyr glacial cycles, in which, with

additional information of the sedimentary facies, higher-frequency sequences may be defined.

KEYWORDS

Last Interglacial period, optically stimulated luminescence, post-infrared infrared stimulated luminescence, sea-level changes, tectonics

Introduction

Feldspar post-infrared infrared stimulated luminescence (pIRIR) dating, since it was introduced (Thomsen et al., 2008; Buylaert et al., 2009), has been applied for constraining the chronology of late Quaternary sedimentary records, leading to important findings in geosciences and archeology (e.g., Stevens et al., 2011, 2018; Li and Li, 2012; Buylaert et al., 2013; Arnold et al., 2014; Nian et al., 2016; Li et al., 2017; Westaway et al., 2017; Rizal et al., 2020; Christ et al., 2021). In addition to the direct applicability to the clastic sediment, feldspar pIRIR dating is advantageous for its broad time coverage from several hundred to hundreds of thousands of years (e.g., Thiel et al., 2011; Reimann and Tsukamoto, 2012; Li et al., 2014). Pleistocene sandy depositional sequences in high-energy coastal settings exemplify cases to which feldspar pIRIR dating is ideally applied but are yet to fully benefit from its development even though their accurate chronology potentially refines our knowledge of long-term coastal environments, sea-level changes, and tectonic displacement that they record (e.g., Murray-Wallace and Woodroffe, 2014).

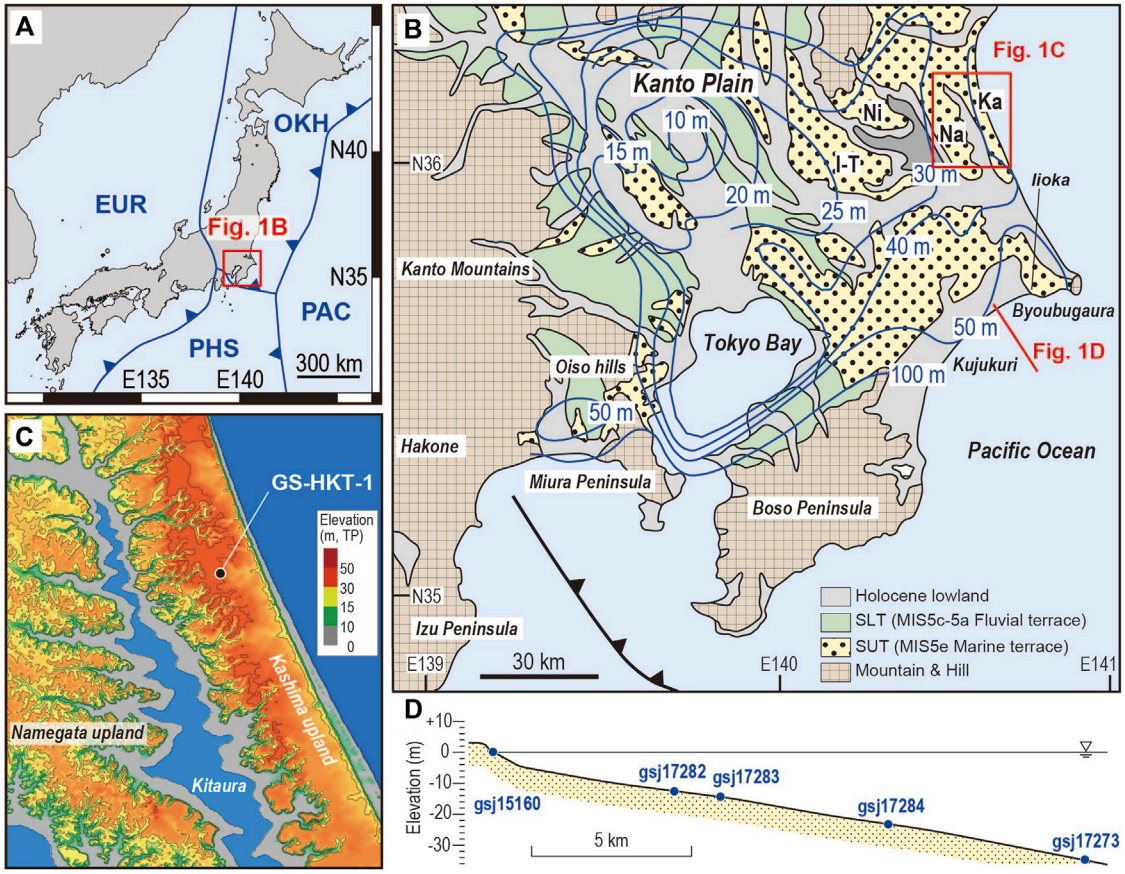

FIGURE 1
(A) Tectonic setting of Japan and the location of the Kanto Plain. **(B)** Landform classification of the Kanto Plain, central Japan. Elevation of the Marine Isotope Stage (MIS) 5e marine terrace (contours shown in blue) is supposed to reflect the tectonic vertical displacement (modified from Kaizuka, 1987). SUT: Shimosa Upper Terrace, SLT: Shimosa Lower Terrace, I–T: Inashiki-Tsukuba upland, Ni: Niihari upland, Na: Namegata upland, Ka: Kashima upland. **(C)** A digital elevation model of the Kashima and Namegata uplands showing the site of core GS-HKT-1 [See location in **(B)**]. The base map is taken from the GSI Map of the Geospatial Information Authority of Japan. **(D)** Cross section across the Kujukuri beach and offshore area [see location in **(B)**]. The positions of five modern sediment samples determined for residual doses are projected onto this single section.

The Kanto plain is a Neogene–Quaternary tectonic basin facing the Pacific coast of central Japan with a 3,000–5,000 m thick accumulation of siliciclastic sediments (e.g., Suzuki, 2002; Takahashi et al., 2005; Suzuki et al., 2011). Since the Middle Pleistocene, the remnant of the basin has been filled with terrigenous and marine deposits under the influence of glacial sea-level cycles to result in depositional sequences referred to as the Shimosa Group (e.g., Tokuhashi and Kondo, 1989; Okazaki et al., 1997). The basin is situated in a unique tectonic setting of the convergent plate margin; it is now covered with the Last Interglacial raised marine terrace that reveals an uplift trend at least over the last 100,000 years in contrast to the longer-term subsidence that resulted in the development of the sedimentary basin (Kaizuka, 1987; Sugai et al., 2013). The depositional sequences in the Kanto plain since the Middle Pleistocene are thus products of the glacial sea-level cycles and tectonic deformation, and with their chronology constrained well, it should improve our understanding of the complicated tectonic history of central Japan and the late Quaternary environmental changes.

Tephrochronology has been constrained well for the Shimosa Group in the southern and western parts of the Kanto plain (Machida and Arai, 2003), close to Quaternary volcanos in the Izu Peninsula and the Hakone and Kanto mountains (Figure 1B). In contrast, tephrochronology in the eastern Kanto plain has been limited owing to fewer tephra layers preserved because of the distance from the source volcanos and high-energy sedimentary environment. Thus, felspar pIRIR potentially refines the chronostratigraphy of the region. Okazaki et al. (2022) determined the pIRIR ages of shallow-marine deposits that comprise the marine terrace at the eastern end of the Kanto plain. The marine terrace was formerly correlated with Marine Oxygen Isotope Stage (MIS) 5e (Sugihara, 1970). These ages, along with a newly identified key tephra, refined the chronology of the terrace as MIS 5c and 5a. Likewise, feldspar pIRIR dating may be further applied to the marine terrace elsewhere and deeper stratigraphy, potentially refining the chronology of the Shimosa Group.

This article presents the application of feldspar pIRIR dating to high-frequency Pleistocene depositional sequences identified in a sediment core from the northeastern Kanto plain. We first test multiple pIRIR signals to select an optimal condition for dating and then discuss the determination of fading rates for correcting the pIRIR ages. The resultant chronology of the sediment core illustrates how effective the corrected pIRIR ages are for defining the depositional sequences formed in relations to glacial sea-level cycles since the Middle Pleistocene.

Study area

The Kanto plain is a coastal plain c. 75 km wide and < +120 m in elevation on the Pacific coast of eastern Japan (Figures 1A,B). It is a relict forearc basin facing the triple junction of plate boundaries that resulted from the subduction of the Pacific and Philippine Sea plates beneath the North American plate to the west and northwest, respectively. Major landforms in the Kanto Plain are Pleistocene uplands and Holocene lowlands. The uplands have two levels: the Shimosa Upper Terrace and the Shimosa Lower Terrace (Sugihara, 1970). The Upper Terrace occurs over the Kanto plain and has been considered the marine terrace formed during the MIS 5e sea-level highstand. The Lower Terrace is generally restricted inland compared to the Upper Terrace and supposed to be the fluvial terrace formed after MIS 5e. The level of the Upper Terrace varies spatially from +10 to +120 m, implying a differing rate of the vertical crustal displacement after MIS 5e (Kaizuka, 1987). Two centers of subsidence to modest uplift are defined in the northwestern part and Tokyo Bay, while a higher-uplift zone occurs along the Pacific coast associated with the northward tilting of the Boso Peninsula (Figure 1B). These variable structures reflect complex tectonics near the triple junction of the plate boundaries (Kaizuka, 1987).

The Quaternary stratigraphy of the Kanto plain is defined by the Lower to Middle Pleistocene Kazusa and Middle to Upper Pleistocene Shimosa groups. The Shimosa Group consists of depositional sequences of fluvial, coastal, and shallow-marine

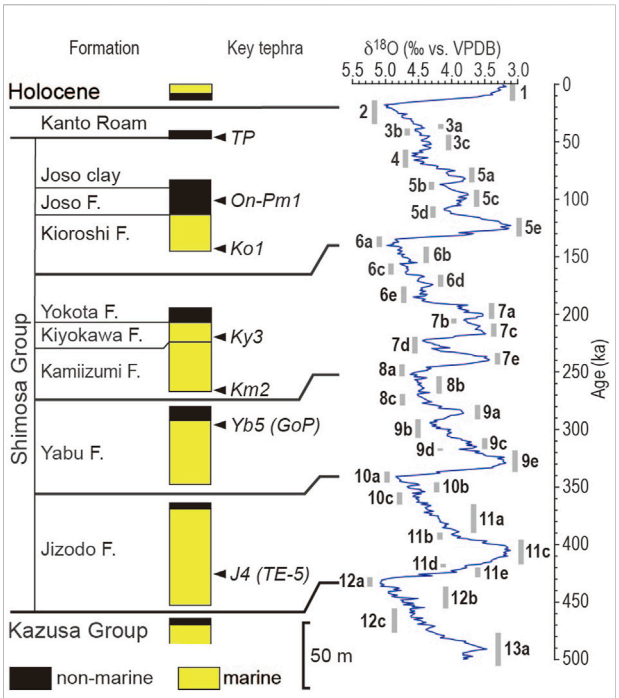

FIGURE 2
Chronostratigraphic chart of the Middle–Upper Pleistocene Shimosa Group and the correlation with the LR04 stack of marine benthic foraminiferal d^{18}O data (Lisiecki and Raymo, 2005) and the marine isotope substages (Railsback et al., 2015) according to Nakazato and Sato. (2001).

sediments. Key tephra layers intercalated in the Shimosa Group provide a well-established tephrochronology in the eastern and southern parts of the Kanto plain, allowing the depositional sequences to be correlated with glacial cycles after MIS 12 (Figure 2; Nakazato and Sato, 2001). The deposits that comprise the marine terrace are referred to as the Kioroshi Formation and have been a subject of detailed sedimentological investigation that allow three-dimensional reconstruction of the sedimentary system (Okazaki and Masuda, 1992; Murakoshi and Masuda, 1992; Ito and O'hara, 1994; Nakazawa et al., 2017). In the eastern Kanto plain, the Kioroshi Formation is characterized by prograded beach–shoreface facies and in places underlying incised-valley facies, being correlated with the sea-level highstand and rise during MIS 5e. In contrast, the central and western parts of the Kioroshi Formation are supposed to represent a large embayment, referred to as Paleo–Tokyo Bay, enclosed by the barrier. This conventional view of the chronology is to be refined at the eastern margin of the Kanto plain, where it is reconstructed as coastal progradation in relations to sea-level oscillations in the later phase of the Last Interglacial period (MIS 5c to 5a) based on a newly identified key tephra, On-Pm1, and a series of pIRIR ages (Okazaki et al., 2022). Moreover, much less has been clarified for sedimentary systems prior to MIS 5e that resulted in the Yokota, Kiyokawa, Kamiizumi, Yabu, and Jizodo formations in descending order (Figure 2). Unconformities that bound these formations are related to the sea-level lowstands in glacial periods, while the relevance of these deposits with the high-frequency sea-level oscillations is yet to be clarified.

The marine terrace in the northeastern Kanto plain is dissected by valleys filled with Holocene sediments and lake waters, being fragmented into several pieces: the Inashiki–Tsukuba, Niihari, Namegata, and Kashima uplands from west to east (Figures 1B,C). The Kioroshi Formation in the Namegata and Kashima uplands represents a prograded barrier system on an open coast, while an embayment is supposed to have been present inland to the barrier (Murakoshi and Masuda, 1992; Nishida and Ito, 2009). The present coast is associated with negligible coastal progradation during the Holocene. Instead, the modern to Holocene analogy of the prograded barrier system is identified in the Kujukuri coast in the southeastern Kanto plain (Figure 1D; Tamura et al., 2008a, 2021).

Methods

Sediment core description and sampling

A sediment core, GS-HKT-1, was obtained on the Kashima upland by using a rotary drilling method with triple tubes. The core site is located 1.8 km inland from the present shoreline and 40.7 m high above the present sea level (Figure 1C). The recovery length and ratio of the core were 35 m and >95%, respectively. The core was halved vertically under controlled red light, and then one side of the halved core was immediately sampled and packed in aluminum bags to prevent further exposure to the light for luminescence dating. Another side of the core was photographed, described, and then used to obtain radiographs with Hitachi X-ray CT-scan Supria Grande. Molluskan shells found in the core were identified and referenced for habitat and ecology according to Okutani (2000). Selected muddy intervals were sampled for diatom analysis. For diatom analysis, smear slides were prepared following the method described in Naya (2019). Smear slides were mounted in an ultraviolet curing resin (NOA 61: Norland Products Inc., refractive index = 1.56). Diatom valves were counted under a light microscope at 1,000x magnification until the total number of valves reached 100.

Sample preparation for luminescence measurements

Luminescence dating was carried out at the Geological Survey of Japan. A total of 16 samples for luminescence dating were prepared under controlled red light to avoid affecting the luminescence signals (Table 1). Sediments within 10 mm from the surface of the halved core were removed and used for measurements of water content and dosimetry. The remaining samples were processed for luminescence measurements. The samples were treated with hydrochloric acid and hydrogen peroxide to remove carbonate and organic matter, respectively. The sand samples were dried and sieved to extract coarse grains 180–250 μm in diameter and then separated using sodium polytungstate liquids of densities 2.58 and 2.53 g/cm^3. The 2.53–2.58 g/cm^3 fraction was taken as K-feldspar coarse grains. A mud sample was processed with a settling cylinder to extract polymineral fine grains of 4–11 μm diameter. Extracted coarse and fine grains were mounted on stainless steel discs to form large (6 mm in diameter) aliquots for luminescence measurements. Modern sand samples collected from the beach and offshore areas of the Kujukuri coast (reported by Tamura et al., 2021; Figure 1D and Table 2) were also measured to estimate the residual doses retained.

Luminescence measurements

Luminescence measurements were performed with a TL-DA-20 Risø TL/OSL reader equipped with infrared (IR) LEDs with the wavelength centered at 850 nm for stimulation and a ^{90}Sr/^{90}Y beta source for laboratory irradiation. Infrared stimulated luminescence (IRSL) from K-feldspar coarse grains and polymineral fine grains through a combination of Schott BG3, BG39, and GG400 filters was measured with a photomultiplier tube.

10.3389/feart.2022.967572

TABLE 1 Details of samples for luminescence dating and estimation of the dose rate.

Sample ID	Lab code	Facies	Depth (m)	Elevation (m)	Water content (%)	U (ppm)	Th (ppm)	K (%)	Rb (ppm)	Cosmic dose rate (Gy/ka)	Total dose rate (Gy/ka)
HKT-1–1	gsj17097	Aeolian/ Fluvial	3.5	37.2	17	0.36	1.77	1.17	41.5	0.13 ± 0.01	2.01 ± 0.14
HKT-1–2	gsj17101	Aeolian/ Fluvial	4.7	36.0	20	0.43	1.9	1.24	46.2	0.11 ± 0.01	2.04 ± 0.14
HKT-1–3	gsj17111	Aeolian/ Fluvial	9.2	31.6	19	0.43	1.94	1.2	44.8	0.07 ± 0.01	1.98 ± 0.14
HKT-1–16	gsj17115	Foreshore	10.6	30.1	21	0.6	2.44	1.24	46.9	0.06 ± 0.01	2.05 ± 0.14
HKT-1–4	gsj17117	Foreshore	11.2	29.5	20	0.59	2.98	1.35	49.5	0.06 ± 0.01	2.18 ± 0.14
HKT-1–5	gsj17123	Upper shoreface	13.5	27.2	26	0.56	2.48	1.61	58.7	0.05 ± 0.01	2.25 ± 0.14
HKT-1–17	gsj17127	Upper shoreface	15.7	25.1	34	0.8	3.06	1.58	80.5	0.04 ± 0.00	2.20 ± 0.14
HKT-1–6	gsj17134	Lower shoreface	19.2	21.5	32	0.83	3.75	1.39	56.1	0.03 ± 0.00	2.12 ± 0.14
HKT-1–7	gsj17139	Marsh to estuary	21.7	19.0	75	6.14	5.69	0.942	53.9	0.03 ± 0.00	2.64 ± 0.13
HKT-1–20	gsj17140	Marsh to estuary	22.2	18.6	44	2.54	3.26	1.16	44.9	0.03 ± 0.00	2.13 ± 0.14
HKT-1–21	gsj17142	Marsh to estuary	23.3	17.5	30	0.68	3.11	1.33	48.3	0.03 ± 0.00	2.04 ± 0.14
HKT-1–8	gsj17143	Shoreface/ Lag	23.6	17.1	31	0.81	4.43	1.32	50.6	0.03 ± 0.00	2.13 ± 0.14
HKT-1–9	gsj17146	Shoreface/ Shelf	25.2	15.6	42	1.06	3.88	1.59	60.5	0.02 ± 0.00	2.19 ± 0.14
HKT-1–10	gsj17150	Shoreface/ Shelf	27.8	13.0	22	0.92	3.41	1.09	39.1	0.02 ± 0.00	2.01 ± 0.14
HKT-1–11	gsj17153	Shoreface/ Shelf	29.1	11.6	25	0.87	3.46	1.11	39.4	0.02 ± 0.00	1.98 ± 0.14
HKT-1–12	gsj17163	Shoreface/ Shelf	34.3	6.4	26	0.74	2.91	1.09	39.9	0.01 ± 0.00	1.89 ± 0.13

TABLE 2 Details of the modern samples collected in the Kujukuri beach and offshore areas. Equivalent doses (D_e) determined are considered as residual doses.

Site	Lab code	Latitude	Longitude	Water depth (m)	D_e from $pIRIR_{225}$ (Gy)	De from $pIRIR_{290}$ (Gy)
Katakai	gsj15160	N35°32′28.2″	E140°27′55.8"	0	4.05 ± 0.36	11.93 ± 1.66
BS9	gsj17282	N35°37′42.1″	E140°37′13.9"	13	10.25 ± 0.62	27.28 ± 1.08
BS10	gsj17283	N35°37′42.3″	E140°40′16.6″	14	10.98 ± 0.25	29.09 ± 1.44
BS23	gsj17284	N35°35′11.9″	E140°41′48.5"	23	11.34 ± 0.34	29.27 ± 1.47
BS34	gsj17273	N35°32′40.0″	E140°45′39.4″	34	7.53 ± 0.62	23.92 ± 1.60

The modified single aliquot-regenerative (SAR) protocol of pIRIR measured at various temperatures after a prior IRSL at 50°C was applied to K-feldspar coarse grains and polymineral fine grains (Table 3; Thomsen et al., 2008; Buylaert et al., 2009; Reimann and Tsukamoto, 2012). To select an optimal signal for dating, we examined four pIRIR signals, measured at 200, 225, 260, and 290°C, referred to here as $pIRIR_{200}$, $pIRIR_{225}$, $pIRIR_{260}$, and $pIRIR_{290}$, respectively. The pIRIR signals were sampled every 0.1 s for 200 s, and the net signal was derived from the integral of the first 2.0 s of the signal after subtracting the background estimated from the last 20 s of the signal. Preheat was given for 60 s with temperatures at 30°C higher than the measurement temperatures of pIRIR.

TABLE 3 Summary of the pIRIR single-aliquot regenerative dose protocol used in this study.

Step	$pIRIR_{200}$ and $pIRIR_{225}$	Signal		$pIRIR_{260}$ and $pIRIR_{290}$	Signal
1	Preheat at 200 or 255°C for 60 s	—	—	Preheat at 290 or 320°C for 60 s	—
2	IR stimulation at 50°C for 200 s	—	—	IR stimulation at 50°C for 200 s	—
3	IR stimulation at 200 or 225°C for 200 s	Lx	—	IR stimulation at 260 or 290°C for 200 s	Lx
4	Test dose	—	—	Test dose	—
5	Preheat at 200 or 255°C for 60 s	—	—	Preheat at 290 or 320°C for 60 s	—
6	IR stimulation at 50°C for 200 s	—	—	IR stimulation at 50°C for 200 s	—
7	IR stimulation at 200 or 225°C for 200 s	Tx	—	IR stimulation at 260 or 290°C for 200 s	Tx
8	Dose and return to step 1	—	—	IR stimulation at 295 or 325°C for 200 s*	—
9	—	—	—	Dose and return to step 1	—

To select an optimal protocol for dating, bleaching experiments and dose recovery tests were practiced with different signals for the selected samples. Six aliquots for each protocol were exposed to artificial sunlight for 4 h in a UVACUBE 400 chamber (Hönle) with a SOL 500 lamp module. After bleaching, three aliquots were dosed by an expected equivalent dose of 200–300 Gy and then used for a dose recovery test; the remaining aliquots were used to estimate the residual dose. Dose recovery was assessed after subtracting the residual dose from the recovered dose. The preliminary ages of sample gsj17123 using different signals were also determined following the procedure described below, except that three replicates of aliquot were integrated for each condition.

With the optimal pIRIR signal, the mean value of the equivalent dose was determined from the measurements of six replicates of medium aliquots (6 mm in diameter) without subtracting the residual dose. In the SAR protocol, four or five regeneration points and a replicate of the second point were measured and data with recycling ratios outside 1.0 ± 0.1 were rejected. Fading tests were also performed on aliquots after equivalent dose measurement to determine the fading rates after Auclair et al. (2003). The results of the fading tests were integrated for all aliquots of both the individual sample and all samples, obtaining the individual and average fading rates, expressed as the g_{2days}-value or dimensionless density of recombination centers, ρ'.

Dose-rate and age determination

The environmental dose rate was determined using the DRAC program of Durcan et al. (2015) based on contributions of both natural radionuclides in sediments and cosmic rays. The concentrations of K were measured by inductively coupled plasma optical emission spectrometry and those of U, Th, and Rb by inductively coupled plasma mass spectrometry; these results were converted to dose rates by applying the conversion factors of Adamiec and Aitken (1998). The attenuation factors used for beta and alpha rays were based on Mejdahl (1979) and Bell (1980), respectively. We used a-values of 0.110 ± 0.005 and 0.15 ± 0.05 for polymineral fine grains and K-feldspar coarse grains, respectively (Balescu and Lamothe, 1994; Kreutzer et al., 2014). The water content was also considered for the dose rate determination based on the measured value with uncertainties of 5%. Cosmic dose rates were calculated according to Prescott and Hutton (1994). D_e values were then divided by the environmental dose rate to obtain uncorrected ages. For uncorrected ages, fading correction was carried out with the individual and average ρ' according to Huntley and Lian (2006) and Kars et al. (2008) and using the R Luminescence package (Kreutzer et al., 2012; Fuchs et al., 2015). All ages are expressed relative to AD 2020.

Results

Sedimentary facies

Seven sedimentary facies units A to G, in ascending order, are defined in core GS-HKT-1 (Figure 3, Supplementary Figures S1, S2). Unit A occurs at depths of 28.5–35.0 m and is very fine to fine sand with a horizontal to low-angle cross lamination. The low-angle cross lamination in places defines minor truncation surfaces. The unit contains pebble-sized mud clasts at its basal part and generally lacks mollusk shells and bioturbation except for escape structures at depths of 28.20–28.90 m. A pebble-to-granule layer 3 cm thick occurs on an erosion surface at 30.65 m, dividing the unit into two subunits A-1 and A-2; these subunits have similar features.

Unit B gradually overlies unit A and is identified at depths of 25.85–28.50 m. This unit is very fine to fine sand containing abundant mollusk shells and granules. Horizontal to low-angle cross lamination with truncation surfaces is recognized in radiographs. The upper part in contrast is heavily bioturbated

10.3389/feart.2022.967572

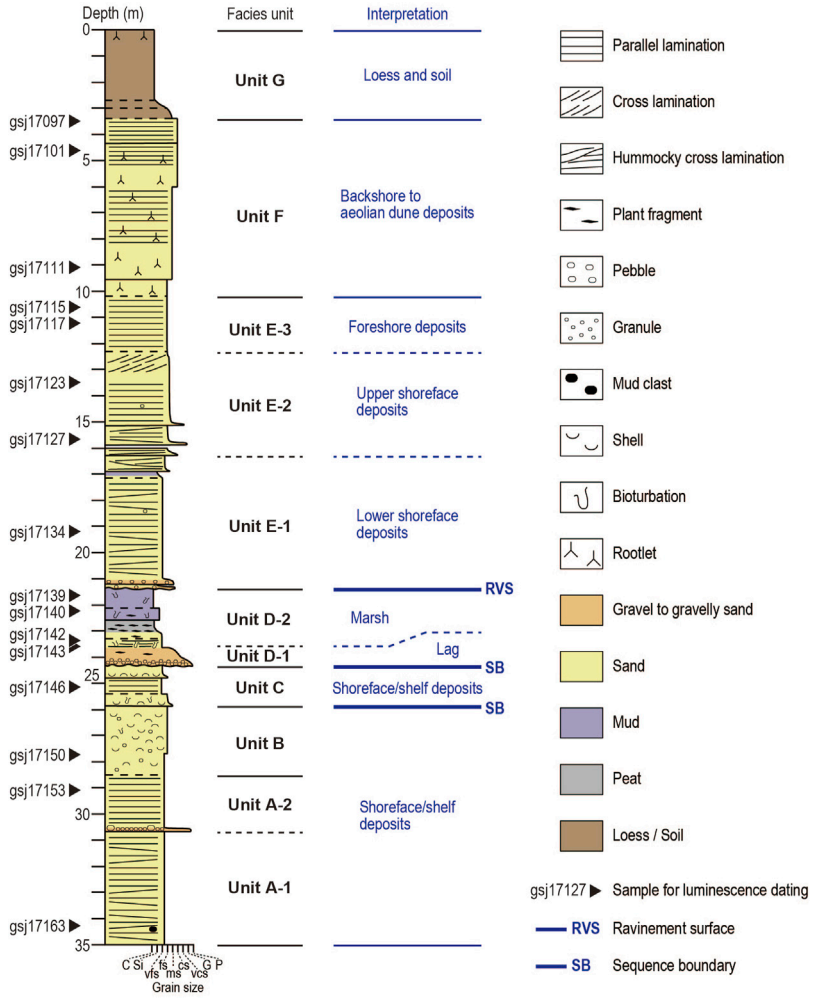

FIGURE 3
Columnar sections of core GS-HKT-1 with definition and interpretation of units A to G, in ascending order and bounding surfaces. Sixteen sediment samples were collected for luminescence dating.

and contains condensed shell beds. Mollusk shells identified in unit B include *Mactra chinensis*, *Mercenaria stimpsoni*, *Nitidotellina minuta*, *Solen strictus*, *Cyclocardia ferruginea*, *Limopsis tokaiensis*, *Acila insignis*, *Siphonalia fusoides*, *Jupiteria* (Saccella) *confusa*, and *Fulvia mutica*. These species live on the sandy seafloor of shallow marines to shelf (Supplementary Table S1; Okutani, 2000). The trace fossil *Bichordites* is identified at depths of 28.00–28.20 m.

Unit C is medium to very fine sand with mollusk shells, defining the core interval from 24.32 to 25.85 m deep. The unit erosionally overlies unit B and consists of two normally graded layers. These layers are characterized by a basal erosion surface and shell-rich layer, normal grading from very fine to medium sand to fine to very fine sand, and well-defined horizontal to low-angle cross lamination with truncation surfaces in the upper part. Mollusk shells identified are species that inhabit the sandy seafloor of shallow marines to shelf, including *Antalis weinkauffi*, *Cyclocardia ferruginea*, *Glycymeris yessoensis*, and *Spisula sachalinensis*. Trace fossils *Bichordites* and *Ophiomorpha* occur at depths of 25.6–25.7 and 25.3 m, respectively.

Unit D occurs at the interval 21.35–24.32 m deep. The unit comprises variable layers that commonly contain plant fragments, and further divided into subunits D-1 and D-2. The subunit D-1, constituting the lower part of unit D, is a gravelly sand 60 cm thick that erosionally overlies unit C. This layer is normally graded from massive coarse sand with granules and pebbles to medium sand with high-angle cross lamination. The graded layer is then conformably overlain by a succession of disturbed centimeter-scale alternations of very fine sand and mud 35 cm thick, massive very fine sand 30 cm thick, and dark-gray peaty mud 40 cm thick, in ascending order. These layers contain plant roots and rootlets. The rest of unit D is subunit D-2.

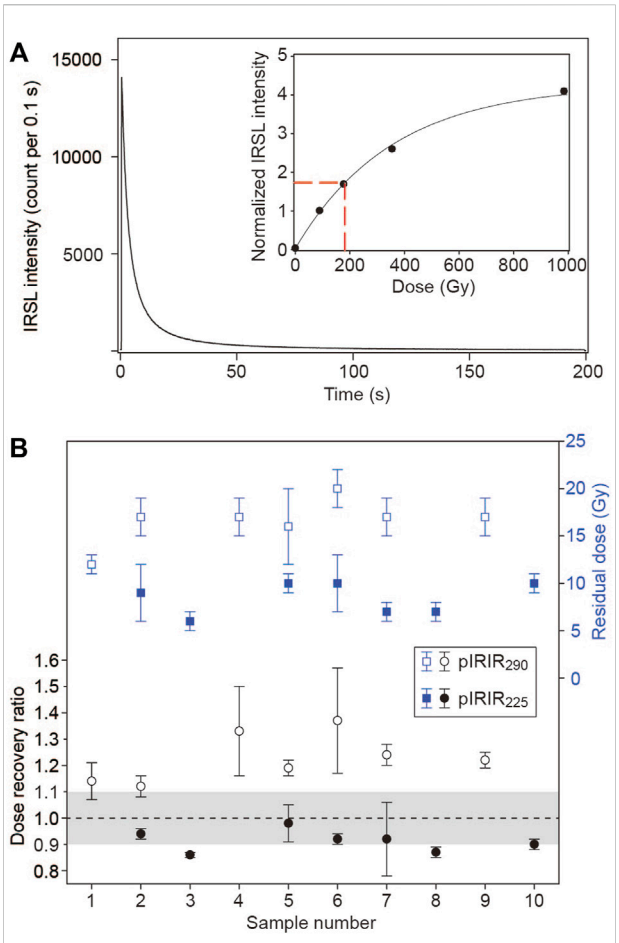

FIGURE 4
(A) Natural decay curve and a dose-response curve (inset) of $pIRIR_{225}$ of K-feldspar coarse grains in sample gsj17123. **(B)** Results of the dose-recovery test and observed residual dose for $pIRIR_{225}$ and $pIRIR_{290}$ in selected samples. 1: gsj17097, 2: gsj17101, 3: gsj17111, 4: gsj17115, 5: gsj17123, 6: gsj17134, 7: gsj17139, 8: gsj17142, 9: gsj17143, 10: gsj17153.

Subunit D-2 is a gray muddy layer 125 cm thick that is graded from sandy silt to clay, erosionally overlying the dark-gray peaty mud of subunit D-1. The lower part of the gray muddy layer is heavily bioturbated, and some burrows are identified as *Ophiomorpha*. In contrast, the upper part is characterized by less dense but larger sandy burrows of *Spongeliomorpha* that appear to have infiltrated from the overlying layer, representing *Glossifungites* Ichnofacies. Diatom valves are found in the peaty mud and gray muddy layer. The peaty mud contains freshwater species, such as *Aulacoseira* spp., *Eunotia* spp., and *Staurosira* spp. The gray muddy layer in contrast is dominated by brackish to marine species such as *Paralia sulcata* and *Pseudopodosira kosugii*, with a larger fraction of freshwater species such as *Staurosira* spp. in the upper part.

Unit E is identified at depths of 21.35–10.20 m. The unit erosionally overlies unit D and defines an upward-coarsening sandy interval. It is divided into subunits E-1, E-2, and E-3, in ascending order. Subunit E-1 constitutes the interval from depths of 16.29–21.35 m. The basal part of the subunit E-1 comprises two poorly sorted layers of very fine sand to granules with angular basal erosion surfaces. These two layers are 5 and 10 cm thick, respectively, bounded by a massive mud layer 5 cm thick. The basal layers are gradually overlain by the rest of subunit E-1 that coarsens upward from very fine sand to very fine-to-fine sand and shows a well-defined horizontal to low-angle cross lamination with a few burrows. The trace fossil *Ophiomorpha* is identified at a depth of 20.50 m. Similar to units A and B, the low-angle cross lamination defines minor truncation surfaces in places. Subunit E-2 is fine to medium sand identified at depths of 12.30–16.29 m, abruptly overlying subunit E-1. The subunit comprises layers characterized by low- to high-angle cross lamination, basal erosion surface, and lags of granules to very coarse sand. Generally, bioturbation is not evident and lamination is well-defined. Subunit E-3 is fine to medium sand with well-defined horizontal lamination, occurring at depths of 10.20–12.30 m.

Unit F is fine to very coarse sand identified at depths of 3.40–10.20 m and gradually overlies unit E-3. This unit generally exhibits rootlets while it varies from massive, through bioturbated, to horizontally laminated with concentrations of heavy minerals. Unit G spans from the ground surface to a depth of 3.40 m. The unit is brownish, massive sandy silt to clay with the lower part 70 cm thick, which defines a transitional interval with an upward decrease in sand content. Rootlets are observed just below the ground surface.

Seven facies units identified in core GS-HKT-1 reveal changes of sedimentary environments; the core site experienced sedimentation in shelf to coastal environments, interrupted with an episode of fluvial to marsh environments, and then was capped with aeolian sedimentation. All of the mollusk shells identified in units B and C are indicative of sandy seafloor environments from the shoreface to shelf. These units, as well as unit A and subunit E-1, show low-angle cross stratification that represents hummocky or swaly cross-stratification of storm deposits (Harms et al., 1975; Leckie and Walker, 1982). According to these features, units A to C and subunit E-1 are interpreted to have been formed by storm processes in the sandy shoreface to shelf. Similar deposits have also been reported from the modern and Holocene shoreface and the shelf off the Kujukuri coast (Figure 1B; Tamura et al., 2007; Nishida et al., 2020). Unit E shows a vertical sandy succession of hummocky or swaly cross-stratification (subunit E-1), high-angle cross lamination (subunit E-2), and a well-defined horizontal lamination (subunit E-3), in ascending order, along with a coarsening upward trend. The high-angle cross stratification and horizontal lamination are interpreted as results of the dune migration in the upper shoreface and beachface sedimentation in the foreshore, respectively. Thus, unit E represents a shoaling

10.3389/feart.2022.967572

TABLE 4 Results of the dose-recovery test and preliminary dating of sample gsj17123 with different pIRIR signals. DRR = dose-recovery ratio, D_e = equivalent dose, ρ′ = dimensionless density of recombination centers.

Signal	DRR	Total dose rate (Gy/ka)	De (Gy)	Uncorrected age (ka)	g2days-value (%/decade)	ρ′	Corrected age (ka)
$pIRIR_{200}$	0.93 ± 0.05	2.25 ± 0.14	179 ± 7	80 ± 6	1.1 ± 0.8	6.9E-07 ± 5.4E-07	93 ± 7
$pIRIR_{225}$	0.98 ± 0.07	2.25 ± 0.14	202 ± 3	90 ± 6	1.0 ± 0.4	6.8E-07 ± 2.7E-07	106 ± 8
$pIRIR_{260}$	1.02 ± 0.07	2.25 ± 0.14	202 ± 5	90 ± 6	0.4 ± 0.2	2.9E-07 ± 1.4E-07	96 ± 8
$pIRIR_{290}$	1.19 ± 0.03	2.25 ± 0.14	229 ± 38	102 ± 18	0.9 ± 0.8	6.4E-07 ± 5.7E-07	117 ± 9

upward succession from the lower shoreface to beach environments (e.g., Clifton, 2006; Isla et al., 2020). Unit D, in contrast to units A to C and E, shows evidence for deposition in freshwater and brackish water environments, most notably from diatoms. Subunit D-1 is interpreted as fluvial lag deposits as it contains plant fragments and rootlets and the coarsest gravels in core GS-HKT-1 with no marine evidence, clearly eroding into the underlying marine deposits of unit C. Freshwater diatoms identified in the basal part of subunit D-2 indicates a marsh environment, and the upward increase of brackish water diatom toward the gray muddy layer is inferred to reflect an increasing influence of saltwater in the marsh environment. Unit F is interpreted to have been deposited in terrigenous environments with aeolian processes as it contains rootlets with no evidence for marine sedimentation. Unit G corresponds to the Younger Kanto Loam, a mixture of loess and volcanic dust and its uppermost part grades to the soil.

Luminescence properties, dose rate, and uncorrected age

Bright pIRIR signals are observed from K-feldspar coarse grains and polymineral fine grains, and the dose-response curves are well-defined (Figure 4A). Dose recovery tests of four pIRIR signals with different temperatures of measurement and preheat for sample gsj17123 yielded variable results (Table 4). The $pIRIR_{290}$ is characterized by a dose recovery ratio markedly higher than 1.1, while the other three signals yielded acceptable ratios within 1.0 ± 0.1 with that of $pIRIR_{200}$ slightly lower. This observation is also confirmed for other selected samples by testing their dose recover ratios of $pIRIR_{225}$ and $pIRIR_{290}$ (Figure 4B). Preliminary dating of sample gsj17123 results in similar uncorrected and corrected ages from $pIRIR_{225}$ and $pIRIR_{260}$. Ages from $pIRIR_{200}$ and $pIRIR_{290}$ are younger and older than those of $pIRIR_{225}$ and $pIRIR_{290}$, respectively, possibly reflecting the trend of the dose recovery ratio. Measurements of the modern sand in the Kujukuri coast indicate that a higher residual dose is retained for $pIRIR_{290}$ than $pIRIR_{225}$ (Table 2), suggesting that the older age of $pIRIR_{290}$ partly owes to the residual dose. The higher residual dose of $pIRIR_{290}$ is also identified in measurements of the selected samples after the 4-h bleaching experiment. These results indicate that $pIRIR_{225}$ and $pIRIR_{260}$ are more suitable for dating than $pIRIR_{200}$ and $pIRIR_{290}$. For its broader application, $pIRIR_{225}$ is used here for further dating.

Natural $pIRIR_{225}$ signals of all the samples are well below the saturation level, and the modified SAR protocol reasonably yields the D_e values. The mean D_e value determined for an individual sample generally decreases upward in the core consistently with the stratigraphy (Table 5). The dose rate

TABLE 5 $pIRIR_{225}$ age estimates. n = the number of aliquots used for age estimation, D_e = equivalent dose, ρ′ = dimensionless density of the recombination centers.

Sample ID	Lab code	Facies	Depth (m)	Elevation (m)	Total dose rate (Gy/ka)	n	De (Gy)	Uncorrected age (ka)	g_{2days}-value (%/decade)	ρ′	Corrected age (ka)
HKT-1–1	gsj17097	Aeolian/Fluvial	3.5	37.2	2.01 ± 0.14	5	149 ± 3	74 ± 5	3.5 ± 0.5	2.37E-06 ± 3.79E-07	104 ± 9
HKT-1–2	gsj17101	Aeolian/Fluvial	4.7	36.0	2.04 ± 0.14	6	170 ± 4	83 ± 6	1.8 ± 0.5	1.21E-06 ± 3.32E-07	117 ± 11
HKT-1–3	gsj17111	Aeolian/Fluvial	9.2	31.6	1.98 ± 0.14	6	180 ± 3	91 ± 6	1.9 ± 0.5	1.30E-06 ± 3.39E-07	127 ± 11
HKT-1–16	gsj17115	Foreshore	10.6	30.1	2.05 ± 0.14	6	169 ± 3	83 ± 6	-0.2 ± 0.5	-1.18E-07 ± 3.34E-07	117 ± 10
HKT-1–4	gsj17117	Foreshore	11.2	29.5	2.18 ± 0.14	6	172 ± 7	79 ± 6	1.9 ± 0.5	1.28E-06 ± 3.34E-07	110 ± 13
HKT-1–5	gsj17123	Upper shoreface	13.5	27.2	2.25 ± 0.14	6	178 ± 6	79 ± 6	1.9 ± 0.5	1.30E-06 ± 3.45E-07	111 ± 14
HKT-1–17	gsj17127	Upper shoreface	15.7	25.1	2.20 ± 0.14	5	189 ± 6	86 ± 6	1.9 ± 0.5	1.30E-06 ± 3.32E-07	117 ± 11
HKT-1–6	gsj17134	Lower shoreface	19.2	21.5	2.12 ± 0.14	6	165 ± 3	78 ± 5	1.5 ± 0.5	1.04E-06 ± 3.36E-07	106 ± 8
HKT-1–7	gsj17139	Marsh to estuary	21.7	19.0	2.64 ± 0.13	6	192 ± 3	73 ± 4	2.2 ± 0.5	1.52E-06 ± 3.62E-07	101 ± 6
HKT-1–20	gsj17140	Marsh to estuary	22.2	18.6	2.13 ± 0.14	6	194 ± 3	91 ± 6	1.7 ± 0.5	1.14E-06 ± 3.55E-07	129 ± 10
HKT-1–21	gsj17142	Marsh to estuary	23.3	17.5	2.04 ± 0.14	6	190 ± 3	93 ± 6	1.9 ± 0.5	1.27E-06 ± 3.40E-07	130 ± 10
HKT-1–8	gsj17143	Lag	23.6	17.1	2.13 ± 0.14	6	182 ± 3	86 ± 6	1.6 ± 0.5	1.05E-06 ± 3.32E-07	120 ± 9
HKT-1–9	gsj17146	Shoreface/Shelf	25.2	15.6	2.19 ± 0.14	6	211 ± 3	96 ± 6	2.0 ± 0.5	1.38E-06 ± 3.35E-07	136 ± 10
HKT-1–10	gsj17150	Shoreface/Shelf	27.8	13.0	2.01 ± 0.14	6	328 ± 5	163 ± 11	1.8 ± 0.5	1.23E-06 ± 3.68E-07	242 ± 19
HKT-1–11	gsj17153	Shoreface/Shelf	29.1	11.6	1.98 ± 0.14	6	310 ± 13	156 ± 13	2.1 ± 0.5	1.44E-06 ± 3.35E-07	230 ± 32
HKT-1–12	gsj17163	Shoreface/Shelf	34.3	6.4	1.89 ± 0.13	6	288 ± 7	152 ± 11	2.3 ± 0.4	1.51E-06 ± 3.35E-07	220 ± 21
—	—	—	—	—	—	—	—	(Average)	1.8 ± 0.1	1.3E-06 ± 8.6E-08	—

10.3389/feart.2022.967572

10.3389/feart.2022.967572

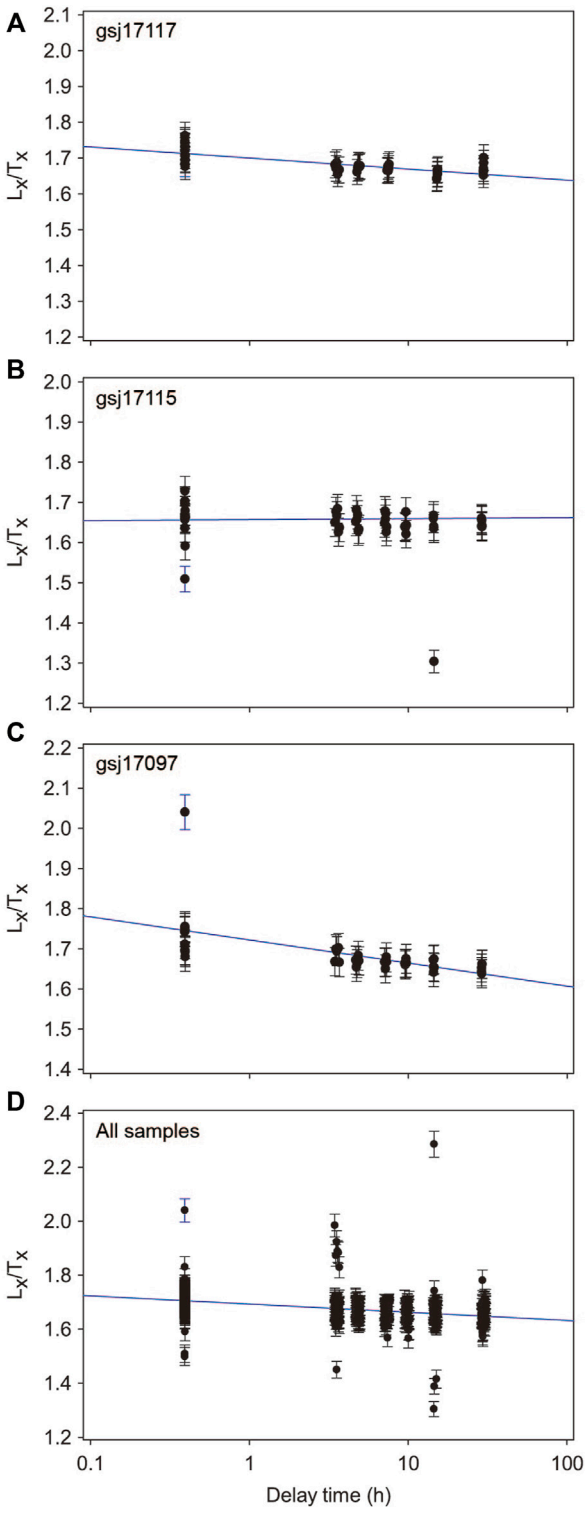

FIGURE 5
Fading test results of $pIRIR_{225}$ integrating all aliquots of **(A)** samples gsj17117, **(B)** gsj17115, and **(C)** 17,097, and **(D)** all of the 16 samples measured here. The result on gsj17117 exemplifies a fading rate close to the average of all samples, while the fading rates of samples gsj17115 and 17,097 are the lowest and highest values of the 16 samples, respectively.

is consistent in coarse-grain samples, ranging from 1.89 to 2.25 Gy/ka, with a slightly higher value of 2.64 Gy/ka for fine grain sample gsj17139. As a result, uncorrected ages are consistent with the stratigraphy. In units E and F, uncorrected ages range between 74 and 91 ka with a few slight reversals, defining no discernible trend. Four uncorrected ages in unit D are slightly older than those in units E and F on average, and an uncorrected age in unit C is slightly further older. A large gap is identified between units B and C; three uncorrected ages in units A and B are 152–163 ka, considerably older than those in the overlying units.

Fading rate and corrected age

Modest anomalous fading is observed in the fading test (Figure 5). In 14 samples, except for samples gsj17097 and 17115, a decrease of luminescence intensity with the time since irradiation, or delay time, is identified and fitted well to define the g_{2days}-value and ρ' (Figure 5A). The g_{2days}-values calculated for these samples are characterized by a narrow range, 1.5–2.2, and centered on 1.8 ± 0.1, a value determined by fitting the results from the aliquots of 16 samples (Figure 5D, Figure 6A); ρ′ shows similar variations to the g_{2days}-value (Figure 6B). Furthermore, there is no vertical trend of the fading rate represented by the g_{2days}-value and ρ' (Table 5). Measurements of samples gsj17097 and 17115 yielded outlier fading rates, reflecting the regression distorted by a few exceptional L_x/T_x values (Figures 5B,C). The fitting of all aliquots, although containing such exceptional values (Figure 5D), is averaged to result in a similar fading rate to that of samples with no exceptional plots (Figure 5A). Although the origin of the exceptional L_x/T_x values is unclear, the fitting of all the aliquots is considered to minimize their effect.

Two series of corrected ages are obtained assuming the fading rate determined for an individual sample or the average fading rate for all samples (Table 5; Figures 6C,7). In general, both series show negligible offsets from each other except for samples gsj17097 and 17115, characterized by outlier fading rates. The corrected age of gsj17097 with the individual rate is remarkably older than the other, leading to a remarkable age reversal. No fading correction is possible for gsj17115 with its negative fading rate, and the uncorrected age defines an age reversal with the three corrected ages in the upper part of the core. The corrected ages with the average fading rate in contrast define a sequence consistent with the stratigraphy when taking into account the errors and thus are considered the final age estimate here.

The final corrected ages indicate an approximate depositional timing of the sediment succession. Five corrected ages from unit E range from 106 to 117 ka with the youngest estimate identified for sample gsj17134, the lowest in the unit. Three corrected ages in unit F are 104–127 ka and younger upward. Sample gsj17111 is dated older than the ages in unit E below and thus appears to be

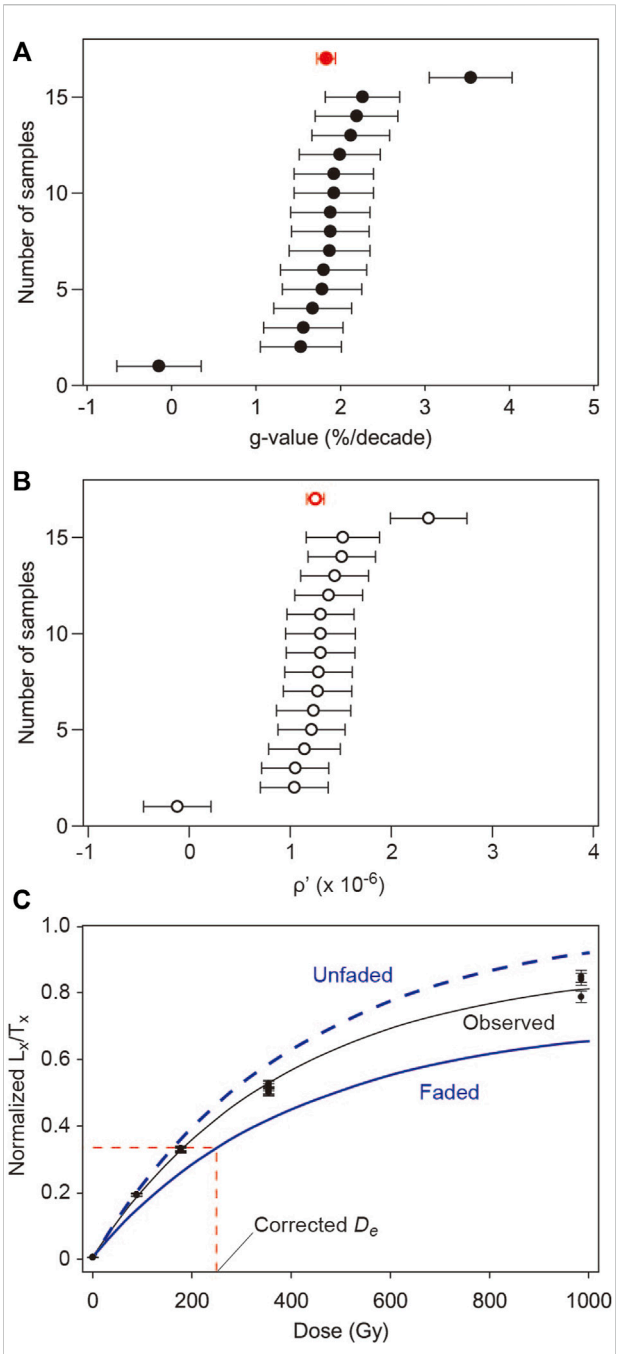

FIGURE 6
(A) Cumulative distribution of the g_{2days}-value determined for an individual sample. A red point shows the average value for all the samples. **(B)** Cumulative distribution of the ρ', dimensionless density of recombination centers. A red point shows the average value for all samples. **(C)** An example of fading correction with measured, unfaded, and faded dose-response curves for the $pIRIR_{225}$ signal from sample gsj17123.

slightly overestimated. The corrected ages in units E and F indicate that these units were deposited sometime from MIS 5e to 5c. The four corrected ages in unit D are consistent with the stratigraphy; the only fine grain sample gsj17139 is dated to MIS 5c to 5d, while the remaining three coarse-grain samples are dated to MIS 5d to 6a. A corrected age in unit C is dated to the begining of MIS5e to 6a. A large hiatus is defined by the corrected ages between units B and C, approximately corresponding to the duration of MIS 6. Three ages in units A and B are associated with larger errors and roughly correlated with MIS 8a to 7a.

Discussion

Identification of depositional sequences

The corrected $pIRIR_{225}$ ages are associated with uncertainties that do not allow a detailed correlation with the marine isotope sub-stages. However, the series of ages are integrated with information of sea-level changes revealed by the facies succession as additional constraints for supporting further chronological interpretation. Three key features of sedimentary facies in core GS-HKT-1 indicative of the sea-level changes include the facies shift from units C to D, internal facies changes in unit D, and the facies shift from units D to E. The transition from units C to D reveals a change from a shallow marine to fluvial environments, which is caused by a relative sea-level fall. The erosional base of unit D is considered an unconformity formed by fluvial erosion. The vertical succession of unit D then represents a shift from a fluvial environment to brackish salt marsh, inferred from units D-1 and D-2, respectively. This shift is caused by transgression owing to a relative sea-level rise. Unit D is likely a fill of an incised-valley dissected onto the unconformity. The deposition of unit D-2 is followed by further transgression and wave erosion in an open marine environment that resulted in the ravinement surface (Nummedal and Swift, 1987), corresponding to the basal erosion surface of unit E. Such facies succession is ubiquitously identified in post-glacial deposits along the Pacific coast of eastern Japan (e.g., Tamura et al., 2003; Tamura and Masuda, 2005). Unit E is a shoaling-upward succession representing coastal progradation during the sea-level highstand with possible minor sea-level fluctuations. These key features of sedimentary facies above unit B indicate sea-level fluctuations characterized by a succession of a fall, rise, and highstand.

The inferred sea-level oscillation allows the correlations of units C to F with the sub-stages in MIS 5 (Figure 8; Waelbroeck et al., 2002). The basal erosion surface of unit C represents a large hiatus spanning MIS 6 and is considered the ravinement surface finally formed by wave erosion in relation to the sea-level rise and transgression from MIS 6a to 5e. Unit C, with a $pIRIR_{225}$ age with errors ranging from 6a to 5e, is thus considered to have been deposited in MIS 5e. The deposition of unit D then occurred between MIS 5e and 5c. Its basal unconformity was thus formed by the sea-level fall from MIS 5e to 5d. The subsequent sea-level

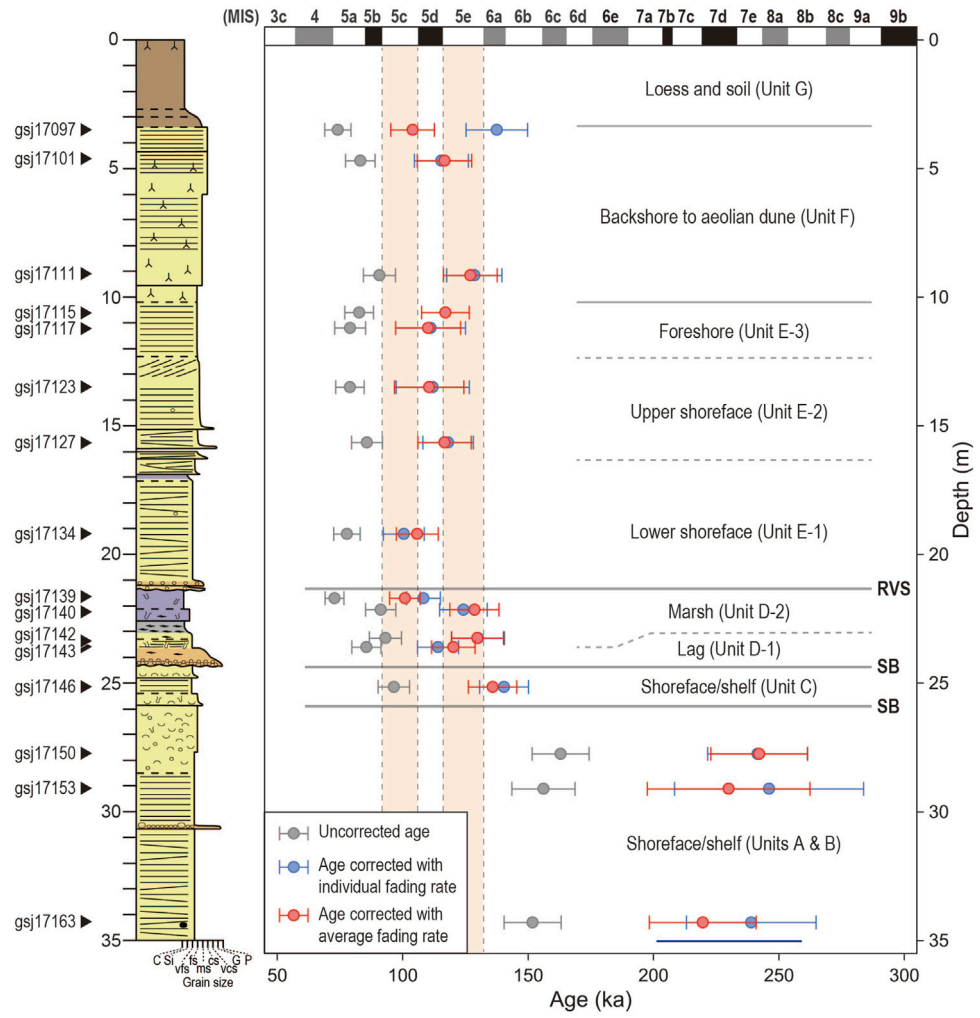

FIGURE 7
Plots of uncorrected and corrected pIRIR$_{225}$ ages of 16 samples in core GS-HKT-1 against core depth. The invervals of MIS 5c and 5e are shaded. The color legend of the core is shown in Figure 2.

lowstand and rise from MIS 5d to 5c resulted in unit D and the overlying ravinement surface. This constrains unit E, with MIS 5e to 5c pIRIR$_{225}$ ages, to represent coastal progradation during the MIS 5c sea-level highstand, followed by aeolian sedimentation of unit F. The marine terrace in the Kashima upland (Figure 1C) is thus correlated with MIS 5c similarly to Ooi et al. (2013), who considered the presence of the MIS 5c marine terrace in the seaward part of the Kashima upland according to tephras.

A diagram is presented in Figure 8 for plotting the corrected and residual-subtracted pIRIR$_{225}$ ages of individual samples against the sample elevation. As most samples were collected from deposits of underwater environments, the overestimation of pIRIR$_{225}$ ages owing to the residual dose is expected. Here, for all samples, the residual dose is assumed as the average determined for pIRIR$_{225}$ signal from the modern samples in the Kujukuri coast (8.83 ± 3.06 Gy; Table 2). The residual dose is divided by an average dose rate of 16 samples in core GS-HKT-1 (2.11 ± 0.17 Gy/ka; Table 1) to obtain possible age overestimation, 4,200 ± 150 years. The possible overestimation is then subtracted from the corrected pIRIR$_{225}$ ages. Even with the residual dose considered, individual ages appear slightly older than MIS that they are correlated with. Potential factors to cause such inaccuracy may include higher residual doses than assumed here and/or uncertainties in the dose rate, especially owing to temporal fluctuations of water content. These factors are not predictable, limiting further accuracy of the age estimate. Nevertheless, the application of pIRIR$_{225}$ dating to core GS-HKT-1 exemplifies how the information of sedimentary facies is used as an additional constraint for providing an accurate

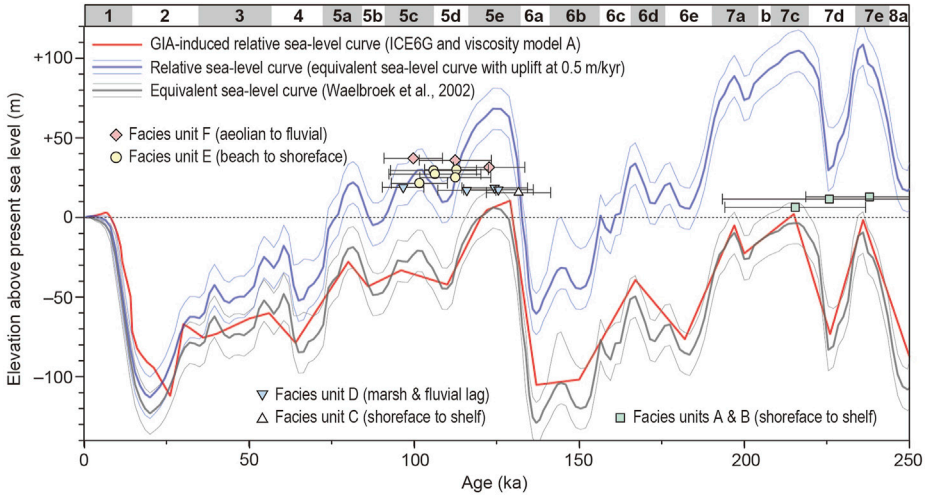

FIGURE 8
Sea-level curves compared with the plots of $pIRIR_{225}$ ages and elevations of samples in core GS-HKT-1. An expected age overestimate due to the residual dose, estimated as 4.2 ± 1.5 kyr, was subtracted from the $pIRIR_{225}$ ages (corrected with the average fading rate). The blue line represents a relative sea-level curve with an uplift rate of 0.5 m/kyr, which assumes the upper boundary of Unit E (or subunit E-3, foreshore facies) represents the sea-level highstand of the MIS 5c. GIA (Glacial Isostatic Adjustment)-induced relative sea-level curve was calculated based on the deglaciation model ICE6G_C (Argus et al., 2014). In order to have one cycle ice history only in ICE6G_C, the pre-history of equivalent sea-level changes before 122 ka was adopted from Waelbroeck et al., 2002. The viscosity model (model A) adopted here assumes that the elastic thickness is 50 km and the upper and lower mantle viscosities are 2×10^{20}, 2×10^{22} Pa s, respectively (Okuno et al., 2014).

chronology to identify high-frequency Pleistocene depositional sequences.

Tectonic uplift and relative sea-level changes

The revised chronology of the marine terrace in the eastern Kanto plain, as proposed in the Kashima upland here and the Iioka upland by Okazaki et al. (2022), refines the rate of the tectonic uplift. While units A, B, C, D-2, and E were deposited around or below the sea level, their age-elevation plots are far above the eustatic sea-level curve (Waelbroeck et al., 2002). This was resulted from the regional uplift owing both to the hydro-isostacy and tectonics. As the Kanto plain is in a far field, its GIA (Glacial Isostatic Adjustment)-induced relative sea level is not significantly offset from an eustatic sea level (Figure 8; Okuno et al., 2014). Thus, the regional uplift is dominated by the tectonic component. The elevation range of unit E-3, +28.4–30.5 m, is approximately indicative of the relative sea level during the MIS 5c highstand (Tamura, 2012), although the level of the corresponding shoreline angle may be somewhat higher. Assuming that the MIS 5c sea-level highstand occurred at 100 ka and was lower than that in MIS 5e (8 ± 5 m; Okuno et al., 2014) by 25 m (De Gelder et al., 2020), an uplift has occurred at the core site by 46.5 ± 5.1 m over the last 100 kyr, which gives the average uplift rate 0.46 ± 0.05 m/kyr, considerably higher than the rate inferred from the marine terrace correlation with MIS 5e, 0.17 ± 0.04 m/kyr, when an uplift is assumed to have occurred by 21.5 ± 5.1 m during 125 kyr. Similar refinement in the Iioka upland yields a rate of 0.70 ± 0.06 m/kyr (Okazaki et al., 2022), indicating spatial variations. Further refinement elsewhere in the Kanto plain should clarify the crustal displacement with higher accuracies and improve the understanding of the regional tectonics (Figure 1B; Kaizuka, 1987).

Extrapolation of the tectonic uplift rate, c. 0.5 m/kyr, to MIS 8a characterizes the relative sea-level curve and estimates the paleo-water depths of facies units (Figure 8). Age-elevation plots of units D and E occur around the contemporary relative sea level, consistent with their sedimentary environments. Unit C is considered to have been deposited at water depths of a few meters to 50 m. The paleo-water depths of units A and B are estimated to be up to 100 m. In the modern shelf off the Kujukuri coast, very fine to fine sand > 1 m thick was deposited after the mid Holocene at water depths up to 124 m (Nishida et al., 2020), much below the storm–wave base (c. 50–60 m; Tamura et al., 2008b). The sand deposition is interpreted to have been caused by the ocean current (Nishida et al., 2020). Units A and B in contrast show clear features of storm-wave deposition, such as hummocky and swaly cross stratifications, and thus were likely formed above the storm–wave base. The shallow-water deposition of units A and B could have been enabled by the significant sea-level fall around MIS 7d. The gravel layer that

separates units A-1 and A-2 possibly records an erosional episode enhanced by the sea-level fall. Otherwise, the relative sea-level curve constructed with the extrapolation of the tectonic uplift may not be valid. The extrapolation requires a temporally consistent tectonic displacement after MIS 7, which is not evident given the unique setting of the Kanto plain with the history of the long-term subsidence in contrast to the ongoing uplift.

Conclusions

We examine the effectiveness of feldspar $pIRIR_{225}$ dating for identifying terrigenous, coastal, and shallow-marine depositional sequences since the Middle Pleistocene, observed in a 35-m-long sediment core from the Last Interglacial-raised marine terrace in the northeastern Kanto plain, a unique Quaternary forearc basin near the triple junction of the plate boundaries. Sixteen fading-corrected $pIRIR_{225}$ ages define a large hiatus spanning MIS 6 and are useful for separating the intervals of MIS 5 and MIS 7. Their uncertainties, however, do not allow further detailed correlation. The sediment facies succession in the core shows some key features representing shifts from shallow-marine to fluvial environments and from fluvial to brackish salt marsh and coastal progradation. Sea-level oscillations inferred from these features can be used for constraining the chronology of the higher-frequency sequences in the MIS 5 interval. Our results exemplify an effective combination of luminescence dating with stratigraphic information for detailed chronological interpretation. The luminescence chronology of the sediment core also refines the date of the marine terrace and revises up the rate of local tectonic uplift. Further application of feldspar pIRIR dating to the Kanto plain likely improves our understanding of the unique tectonic history.

Data availability statement

The original contributions presented in the study are included in the article/Supplementary Material; further inquiries can be directed to the corresponding author.

Author contributions

TT designed the study. TT, HO, HN, and KS analyzed the sediment cores. RN identified species of mollusk shells. TN identified species of diatoms. KS identified trace fossils. TT carried out the luminescence dating and wrote the manuscript. HO, TN, RN, HN, KS, and JO contributed to the discussion and commented on the manuscript. All authors reviewed and approved the final version of the manuscript.

Funding

This study was funded by Grant-in-Aid for Scientific Research (B) (No. 18H01294) from the Japan Society for the Promotion of Science to Toru Tamura and an internal grant from the Geological Survey of Japan, AIST.

Acknowledgments

We express our gratitude to Kana Takamori for her fundamental laboratory assistance. Kumi Yokoi is also thanked for obtaining radiographs. The manuscript was significantly improved by reviewers Xiaomei Nian and Xianjiao Ou, and journal editor Hao Long.

Conflict of interest

The authors declare that the research was conducted in the absence of any commercial or financial relationships that could be construed as a potential conflict of interest.

Publisher's note

Supplementary material

The Supplementary Material for this article can be found online at: https://www.frontiersin.org/articles/10.3389/feart.2022.967572/full#supplementary-material

References

Adamiec, G., and Aitken, M. (1998). Dose-rate conversion factors: Update. *Anc. TL* 16, 37–50.

Argus, D. F., Peltier, W. R., Drummond, R., and Moore, A. W. (2014). The Antarctica component of postglacial rebound model ICE-6G_C (VM5a) based on GPS positioning, exposure age dating of ice thicknesses, and relative sea level histories. *Geophys. J. Int.* 198, 537–563. doi:10.1093/gji/ggu140

Arnold, L. J., Demuro, M., Pares, J. M., Arsuaga, J. L., Aranburu, A., de Castro, J. M. B., et al. (2014). Luminescence dating and palaeomagnetic age constraint on

hominins from Sima de los Huesos, Atapuerca, Spain. *J. Hum. Evol.* 67, 85–107. doi:10.1016/j.jhevol.2013.12.001

Auclair, M., Lamothe, M., and Huot, S. (2003)). Measurement of anomalous fading for feldspar IRSL using SAR. *Radiat. Meas.* 37, 487–492. doi:10.1016/S1350-4487(03)00018-0

Balescu, S., and Lamothe, M. (1994). Comparison of TL and IRSL age estimates of feldspar coarse grains from waterlain sediments. *Quat. Sci. Rev.* 13, 437–444. doi:10.1016/0277-3791(94)90056-6

Bell, W. T. (1980). Alpha dse attenuation in quartz grains for thermoluminescence dating. *Anc. TL* 12, 4–8.

Buylaert, J. P., Murray, A. S., Thomsen, K. J., and Jain, M. (2009). Testing the potential of an elevated temperature IRSL signal from K-feldspar. *Radiat. Meas.* 44, 560–565. doi:10.1016/j.radmeas.2009.02.00710.1016/j.radmeas.2009.02.007

Buylaert, J. P., Murray, A. S., Gebhardt, A. C., Sohbati, R., Ohlendorf, C., Thiel, C., et al.The PASADO Science Team (2013). Luminescence dating of the PASADO core 5022-1D from Laguna Potrok Aike (Argentina) using IRSL signals from feldspar. *Quat. Sci. Rev.* 71, 70–80. doi:10.1016/j.quascirev.2013.03.018

Christ, A. J., Bierman, P. R., Schaefer, J. M., Dahl-Jensen, D., Steffensen, J. P., Corbett, L. B., et al. (2021). A multimillion-year-old record of Greenland vegetation and glacial history preserved in sediment beneath 1.4 km of ice at Camp Century. *Proc. Natl. Acad. Sci. U. S. A.* 118, e2021442118. doi:10.1073/pnas.2021442118

Clifton, H. E. (2006). "A reexamination of facies models for clastic shorelines," in *Facies models revisited*. Editors H. W. Posamentier and R. G. Walker (Oklahoma, United States: SEPM Spec. Publ.), 84, 293–337.

De Gelder, G., Jara-Mu~noz, J., Melnick, D., Fern andez-Blanco, D., Rouby, H., Pedoja, K., et al. (2020). How do sea-level curves influence modeled marine terrace sequences? *Quat. Sci. Rev.* 229, 106132. doi:10.1016/j.quascirev.2019.106132

Durcan, J. A., King, G. E., and Duller, G. A. T. (2015). Drac: Dose rate and age calculator for trapped charge dating. *Quat. Geochronol.* 28, 54–61. doi:10.1016/j.quageo.2015.03.012

Fuchs, M. C., Kreutzer, S., Burow, C., Dietze, M., Fischer, M., Schmidt, C., et al. (2015). Data processing in luminescence dating analysis: An exemplary workflow using the R package 'luminescence. *Quat. Int.* 362, 8–13. doi:10.1016/j.quaint.2014.06.034

Harms, J. C., Southard, J. B., Spearing, D. R., and Walker, R. G. (1975). Depositional environments as interpreted from primary sedimentary structures and stratification sequences. *SEPM Short. Course* 2, 161.

Huntley, D. J., and Lian, O. B. (2006). Some observations on tunnelling of trapped electrons in feldspars and their implications for optical dating. *Quat. Sci. Rev.* 25, 2503–2512. doi:10.1016/j.quascirev.2005.05.011

Isla, M. F., Schwarz, E., and Veiga, G. D. (2020). Record of a nonbarred clastic shoreline. *Geology* 48, 338–342. doi:10.1130/g46800.1

Ito, M., and O'hara, S. (1994). Diachronous evolution of systems tracts in a depositional sequence from the middle Pleistocene palaeo-Tokyo Bay, Japan. *Sedimentology* 41, 677–697. doi:10.1111/j.1365-3091.1994.tb01417.x

Kaizuka, S. (1987). Quaternary crustal movements in Kanto, Japan. *J. Geogr.* 96, 223–240. doi:10.5026/jgeography.96.4_223

Kars, R. H., Wallinga, J., and Cohen, K. M. (2008). A new approach towards anomalous fading correction for feldspar IRSL dating—Tests on samples in field saturation. *Radiat. Meas.* 43, 786–790. doi:10.1016/j.radmeas.2008.01.021

Kreutzer, S., Schmidt, C., DeWitt, R., and Fuchs, M. (2014). The a-value of polymineral fine grain samples measured with the post-IR IRSL protocol. *Radiat. Meas.* 69, 18–29. doi:10.1016/j.radmeas.2014.04.027

Kreutzer, S., Schmidt, C., Fuchs, M. C., Dietze, M., Fischer, M., and Fuchs, M. (2012). Introducing an R package for luminescence dating analysis. *Anc. TL* 30, 1–8.

Leckie, D. A., and Walker, R. G. (1982). Storm-and tide-dominated shorelines in cretaceous moosebar-lower gates interval—Outcrop equivalents of deep basin gas trap in Western Canada. *AAPG Bull.* 66, 138–157.

Li, B., Jacobs, Z., Roberts, R. G., and Li, S. H. (2014). Review and assessment of the potential of post-IR IRSL dating methods to circumvent the problem of anomalous fading in feldspar luminescence. *Geochronometria* 41, 178–201. doi:10.2478/s13386-013-0160-3

Li, B., and Li, S. H. (2012). Luminescence dating of Chinese loess beyond 130 ka using the non-fading signal from K-feldspar. *Quat. Geochronol.* 10, 24–31. doi:10.1016/j.quageo.2011.12.005

Li, Z. Y., Wu, X. J., Zhou, L. P., Liu, W., Gao, X., Nian, X. M., et al. (2017). Late Pleistocene archaic human crania from Xuchang, China. *Science* 355, 969–972. doi:10.1126/science.aal2482

Lisiecki, L. E., and Raymo, M. E. (2005). A Pliocene-Pleistocene stack of 57 globally distributed benthic $\delta^{18}O$ records. *Paleoceanography* 20, PA1003. doi:10.1029/2004PA001071

Machida, H., and Arai, F. (2003). *Atlas of tephra in and around Japan*. Tokyo: University of Tokyo Press, 336.

Mejdahl, V. (1979). Thermoluminescence dating: Beta-dose attenuation in quartz grains. *Archaeometry* 21, 61–72. doi:10.1111/j.1475-4754.1979.tb00241.x

Murakoshi, N., and Masuda, F. (1992). Estuarine, barrier-island to strand-plain sequence and related ravinement surface developed during the last interglacial in the Paleo-Tokyo Bay, Japan. *Sediment. Geol.* 80, 167–184. doi:10.1016/0037-0738(92)90039-t

Murray, A. S., Schmidt, E. D., Stevens, T., Buylaert, J. P., Marković, S. B., Tsukamoto, S., et al. (2014). Dating middle pleistocene loess from stari slankamen (vojvodina, Serbia)—Limitations imposed by the saturation behaviour of an elevated temperature IRSL signal. *Catena* 117, 34–42. doi:10.1016/j.catena.2013.06.029

Murray-Wallace, C. V., and Woodroffe, C. D. (2014). *Quaternary sea level changes: A global perspective*. Cambridge: Cambridge University Press, 484.

Nakazawa, T., Sakata, K., Hongo, M., and Nakazato, H. (2017). Transition from incised valley to barrier island systems during MIS 5e in the northern Chiba area, Kanto Plain, central Japan. *Quat. Int.* 456, 85–101. doi:10.1016/j.quaint.2017.06.031

Nakazato, H., and Sato, H. (2001). sea level changes and tectonics inferred from the quaternary deposits and landforms of Boso Peninsula, central Japan. Chronology of the Shimosa Group and movement of the Kashima uplift zone, central Japan. *Daiyonki-kenkyu.* 40, 251–257. doi:10.4116/jaqua.40.251

Naya, T. (2019). Stratigraphic distribution and biostratigraphic utility of the fossil diatom *Lancineis rectilatus* in the central Kanto Plain, central Japan. *Quat. Int.* 519, 131–143. doi:10.1016/j.quaint.2018.11.002

Nian, X., Li, F., Chen, F., Zhang, W., Zhao, Y., Zhou, J., et al. (2016). Optically stimulated luminescence ages for human occupation during the penultimate glaciation in the Western Loess Plateau of China. *J. Quat. Sci.* 31, e2917. doi:10.1002/jqs.2917

Nishida, N., Ajioka, T., Ikehara, K., Nakashima, R., Katayama, H., Sato, T., et al. (2020). Postglacial stratigraphic evolution of a current-influenced sandy shelf: Offshore Kujukuri strandplain, central Japan. *Sedimentology* 67, 559–575. doi:10.1111/sed.12654

Nishida, N., and Ito, M. (2009). Fluid mud: Distinctive features and implications for genetic stratigraphy. *Jour. Geol. Soc. Jpn.* 115, 149–167. doi:10.5575/geosoc.115.149

Nummedal, D., and Swift, D. J. P. (1987). "Transgressive stratigraphy at sequence-bounding unconformities: Some principles derived from Holocene and cretaceous examples,". Editors D. Nummedal, O. H. Pilkey, and J. D. Howard (Oklahoma, United States: SEPM Spec. Publ.), 41, 241–260.*Sea-level Fluctuation Coast. Evol.*

Okazaki, H., and Masuda, F. (1992). Depositional systems of the late pleistocene sediments in paleo-Tokyo bay area. Ko tokyowan chiiki no taiseki system. *J. Geol. Soc. Jpn.* 98, 235–258.

Okazaki, H., Nara, M., Nakazato, H., Furusawa, A., Ito, K., Tamura, T., et al. (2022). Coastal progradation associated with sea-level oscillations in the later phase of the Last Interglacial period, central Japan. *Quat. Sci. Rev.* 285, 107507. doi:10.1016/j.quascirev.2022.107507

Okazaki, H., Sato, H., and Nakazato, H. (1997). Two types of depositional sequences developed in paleo-tokyo bay, exampled from the Kamiizumi, Kiyokawa and Yokota formations, pleistocene Shimosa Group, Japan. *Jour. Geol. Soc. Jpn.* 103, 1125–1143. doi:10.5575/geosoc.103.1125

Okuno, J., Nakada, M., Ishii, M., and Miura, H. (2014). Vertical tectonic crustal movements along the Japanese coastlines inferred from late Quaternary and recent relative sea-level changes. *Quat. Sci. Rev.* 91, 42–61. doi:10.1016/j.quascirev.2014.03.010

Okutani, T. (2000). *Marine mollusks in Japan*. Tokyo: Tokai University Press, 1173.

Ooi, S., Sairenji, N., Yokoyama, Y., and Ando, H. (2013). Re-examination of terrace surface division of the Hitachi terraces, Ibaraki Prefecture. *Bull. Ibaraki Nat. Mus.* 16, 51–56.

Prescott, J. R., and Hutton, J. T. (1994). Cosmic ray contributions to dose rates for luminescence and ESR dating: Large depths and long-term time variations. *Radiat. Meas.* 23, 497–500. doi:10.1016/1350-4487(94)90086-8

Railsback, L. B., Gibbard, P. L., Head, M. J., Voarintsoa, N. R. G., and Toucanne, S. (2015). An optimized scheme of lettered marine isotope substages for the last 1.0 million years, and the climatostratigraphic nature of isotope stages and substages. *Quat. Sci. Rev.* 111, 94–106. doi:10.1016/j.quascirev.2015.01.012

Reimann, T., and Tsukamoto, S. (2012). Dating the recent past (< 500 years) by post-IR IRSL feldspar–examples from the north sea and baltic sea coast. *Quat. Geochronol.* 10, 180–187. doi:10.1016/j.quageo.2012.04.011

Rizal, Y., Westaway, K. E., Zaim, Y., van den Bergh, G. D., Bettis, E. A., Morwood, M. J., et al. (2020). Last appearance of Homo erectus at Ngandong, Java, 117, 000–108, 000 years ago. *Nature* 577, 381–385. doi:10.1038/s41586-019-1863-2

Sohbati, R., Murray, A. S., Buylaert, J. P., Ortuño, M., Cunha, P. P., Masana, E., et al. (2012). Luminescence dating of P leistocene alluvial sediments affected by the A lhama de M urcia fault (eastern B etics, S pain)–a comparison between OSL, IRSL and post-IR IRSL ages. *Boreas* 41, 250–262. doi:10.1111/j.1502-3885.2011.00230.x

Stevens, T., Buylaert, J. P., Thiel, C., Újvári, G., Yi, S., Murray, A. S., et al. (2018). Ice-volume-forced erosion of the Chinese Loess Plateau global Quaternary stratotype site. *Nat. Commun.* 9, 983. doi:10.1038/s41467-018-03329-2

Stevens, T., Marković, S. B., Zech, M., Hambach, U., and Sümegi, P. (2011). Dust deposition and climate in the Carpathian Basin over an independently dated last glacial–interglacial cycle. *Quat. Sci. Rev.* 30, 662–681. doi:10.1016/j.quascirev.2010.12.011

Sugai, T., Matsushima, H., and Mizuno, K. (2013). Last 400 ka landform evolution of the Kanto Plain: Under the influence of concurrent glacio-eustatic sea level changes and tectonic activity. *J. Geogr.* 122, 921–948. doi:10.5026/jgeography.122.921

Sugihara, S. (1970). Geomorphological developments gp the western shimôsa upland in chiba prefecture, Japan. *Geogr. Rev. Jpn.* 43, 703–718. doi:10.4157/grj.43.703

Suzuki, H., and Tango, T. (2002). A multicenter, randomized, controlled clinical trial of interferon alfacon-1 in comparison with lymphoblastoid interferon-alpha in patients with high-titer chronic hepatitis C virus infection. *Hepatol. Res.* 63, 1–12. doi:10.1016/s1386-6346(01)00139-5

Suzuki, T., Obara, M., Aoki, T., Murata, M., Kawashima, S., Kawai, M., et al. (2011). Identification of lower pleistocene tephras under Tokyo and reconstruction of quaternary crustal movements, Kanto tectonic basin, central Japan. *Quat. Int.* 246, 247–259. doi:10.1016/j.quaint.2011.06.043

Takahashi, M., Hayashi, H., Kasahara, K., Ikawa, T., Kawanaka, T., and Suda, S. (2005). Miocene subsurface half-grabens in the Kanto plain, central Japan. *Rep. Nat. Res. Inst. Ear. Sci. Disast. Prev.* 67, 65–74.

Tamura, T. (2012). Beach ridges and prograded beach deposits as palaeoenvironment records. *Earth. Sci. Rev.* 114, 279–297. doi:10.1016/j.earscirev.2012.06.004

Tamura, T., Komatsubara, J., Sugisaki, S., and Nishida, N. (2021). Residual dose of K-feldspar post-IR IRSL of beach-shoreface sands at Kujukuri, eastern Japan. *Geochronometria* 48, 364–378. doi:10.2478/geochr-2020-0036

Tamura, T., and Masuda, F. (2005). Bed thickness characteristics of inner-shelf storm deposits associated with a transgressive to regressive Holocene wave-dominated shelf, Sendai coastal plain, Japan. *Sedimentology* 52, 1375–1395. doi:10.1111/j.1365-3091.2005.00745.x

Tamura, T., Masuda, F., Sakai, T., and Fujiwara, O. (2003). Temporal development of prograding beach–shoreface deposits: The Holocene of Kujukuri coastal plain, eastern Japan. *Mar. Geol.* 198, 191–207. doi:10.1016/s0025-3227(03)00123-3

Tamura, T., Murakami, F., Nanayama, F., Watanabe, K., and Saito, Y. (2008a). Groundpenetrating radar profiles of Holocene raised-beach deposits in the Kujukuri strand plain, Pacific coast of eastern Japan. *Mar. Geol.* 248, 11–27. doi:10.1016/j.margeo.2007.10.002

Tamura, T., Nanayama, F., Saito, Y., Murakami, F., Nakashima, R., Watanabe, K., et al. (2007). Intra-shoreface erosion in response to rapid Sea-level fall: Depositional record of a tectonically uplifted strand plain, pacific coast of Japan. *Sedimentology* 54, 1149–1162. doi:10.1111/j.1365-3091.2007.00876.x

Tamura, T., Saito, Y., and Masuda, F. (2008b). "Variations in depositional architecture of Holocene to modern prograding shorefaces along the Pacific coast of eastern Japan," in *Recent advances in models of siliciclastic shallow-marine stratigraphy*. Editors G. J. Hampson, R. J. Steel, P. Burgess, and R. W. Dalrymple (Oklahoma, United States: SEPM Spec. Publ), 90, 189–203.

Thiel, C., Buylaert, J. P., Murray, A., Terhorst, B., Hofer, I., Tsukamoto, S., et al. (2011). Luminescence dating of the Stratzing loess profile (Austria)–Testing the potential of an elevated temperature post-IR IRSL protocol. *Quat. Int.* 234, 23–31. doi:10.1016/j.quaint.2010.05.018

Thomsen, K. J., Murray, A. S., Jain, M., and Bøtter-Jensen, L. (2008). Laborato-ry fading rates of various luminescence signals from feldspar-rich sediment extracts. *Radiat. Meas.* 43, 1474–1486. doi:10.1016/j.radmeas.2008.06.002

Tokuhashi, S., and Kondo, Y. (1989). Sedimentary cycles and environments in the middle-late pleistocene Shimosa Group, Boso Peninsula, central Japan. *Jour. Geol. Soc. Jpn.* 95, 933–951. doi:10.5575/geosoc.95.933

Waelbroeck, C., Labeyrie, L., Michel, E., Duplessy, J. C., Mcmanus, J. F., Lambeck, K., et al. (2002). Sea-level and deep water temperature changes derived from benthic foraminifera isotopic records. *Quat. Sci. Rev.* 21, 295–305. doi:10.1016/s0277-3791(01)00101-9

Westaway, K. E., Louys, J., Awe, R., Morwood, M. J., Price, G. J., Zhao, J. X., et al. (2017). An early modern human presence in Sumatra 73, 000–63, 000 years ago. *Nature* 548, 322–325. doi:10.1038/nature23452

frontiers | Frontiers in Earth Science

TYPE Original Research
PUBLISHED 06 September 2022
DOI 10.3389/feart.2022.939638

OPEN ACCESS

EDITED BY
Hui Zhao,
Chinese Academy of Sciences (CAS), China

REVIEWED BY
Jianhui Jin,
Fujian Normal University, China
Linhai Yang,
Shaanxi Normal University, China

*CORRESPONDENCE
Shengli Yang,
shlyang@lzu.edu.cn

SPECIALTY SECTION
This article was submitted to Quaternary Science, Geomorphology and Paleoenvironment, a section of the journal Frontiers in Earth Science

RECEIVED 09 May 2022
ACCEPTED 11 August 2022
PUBLISHED 06 September 2022

CITATION
Liu L, Yang S, Liu X, Li P, Wang H and Zhou J (2022), Variation of luminescence sensitivity of quartz grains from loess in eastern Tibetan Plateau and its provenance significance. *Front. Earth Sci.* 10:939638. doi: 10.3389/feart.2022.939638

Variation of luminescence sensitivity of quartz grains from loess in eastern Tibetan Plateau and its provenance significance

Li Liu, Shengli Yang*, Xiaojing Liu, Pushuang Li, Haiyan Wang and Jiantao Zhou

Key Laboratory of Western China's Environmental Systems (Ministry of Education), College of Earth and Environmental Sciences, Lanzhou University, Lanzhou, China

The loess deposits widely distributed in the eastern Tibetan Plateau (ETP) are important archives for reconstructing the paleoenvironmental changes and dust transportation history of the Tibetan Plateau. A lack of sufficient investigations on the source of the ETP loess has limited our understanding of dust transportation and paleoenvironmental implications. Quartz luminescence sensitivity holds great potential for tracing eolian dust sources. Numerous quartz luminescence sensitivity investigations have provided new insights into the dust sources and transportation of the Chinese loess. However, studies on luminescence sensitivity and its significance for the ETP loess provenance are scarce. In this work, we selected quartz grains in loess from different sites of the ETP to investigate the variation of luminescence sensitivity by testing the 110°C thermoluminescence (TL) peak and optically stimulated luminescence (OSL) sensitivities of quartz grains and discussed the provenance implications for the ETP loess based on quartz luminescence sensitivities. Our results show the quartz luminescence sensitivities of loess at different locations were significantly different in the ETP. The luminescence sensitivity values of the Machang (MC), Xiaojin (XJ), and Wenchuan (WCH) sections were much higher than those of the Xinshi (XS) and Zhouqu (ZQ) sections. The sensitivity values of the 110°C TL peaks and OSL in the paleosol and loess layers show distinct differences. The quartz luminescence sensitivities of the ETP loess are mainly influenced by the dust sources. Our results show that the luminescence sensitivities of quartz grains have great potential for identifying the loess sources in the ETP.

KEYWORDS

quartz, luminescence sensitivity, loess, eastern Tibetan Plateau, provenance

1 Introduction

The loess-paleosol sequence contains abundant information about past environmental changes and is of great significance for past climatic and environmental reconstruction (Liu, 1985; An et al., 1991). Eolian loess is widely distributed in the eastern Tibetan Plateau (ETP), which is one of the most direct and sensitive sedimentary records for studying past environmental changes on the Tibetan Plateau (TP), and has received increasing attention in recent years (Fang et al., 1996; Pan and Wang, 1999; Chen et al., 2022; Yang et al., 2022). The high–altitude loess varies significantly in terms of the origin of the material, transport processes, and depositional environments, and systematic studies of their material sources and transport mechanisms can contribute to an in-depth understanding of the mechanisms and effects of plateau dust cycle processes, atmospheric circulation patterns, and regional environmental changes (Fang et al., 1996; Jiang et al., 1997; Wang et al., 2005; Yang et al., 2021b). However, the loess sources and transportation processes of the ETP have not been fully studied compared to the loess in the Chinese Loess Plateau (CLP) (e.g., Li et al., 2015; Sun et al., 2007; Zhang et al., 2021). Some studies have suggested that the deserts of northwestern China are the potential dust source areas for ETP loess (Tafel, 1914; Ma, 1944; Liu, 1983), and the dust from the Tarim and Qaidam Basins can contribute to the northern TP (Huang et al., 2007; Xu et al., 2015). Whereas, other studies have proposed that the ETP loess is mainly sourced from the inner TP, and local sediments and glacial activities have a great influence on the ETP loess (Fang, 1994; Chen et al., 1997; Wang and Pan, 1997; Yang et al., 2021b; Ling et al., 2022). Thus, the large uncertainty in the source of the Tibetan loess has hindered further understanding of the dust transport dynamics and paleoenvironmental reconstruction in the Tibetan Plateau (Fang, 1994; Sun et al., 2007; Dong et al., 2017).

Luminescence holds unique potential as a sediment tracer and provenance tool (Sawakuchi et al., 2018; Gray et al., 2019). A common approach in source tracing using luminescence is to examine the luminescence sensitivity of quartz grains to source lithology and transport history (Sawakuchi et al., 2012; Zular et al., 2015; Sawakuchi et al., 2018). The luminescence sensitivity is defined as the luminescence intensity per unit dose per unit mass (Gy^{-1} kg^{-1}) (Wintle and Murray, 1999). In nature, there are noticeable differences in the luminescence sensitivity of quartz grains from various depositional environments, and these differences may contain important information about the source area and transport processes. The luminescence sensitivity of quartz grains from different deserts in northern China has significant regional differences (Li et al., 2007; Zheng et al., 2009; Lü and Sun, 2011), implying different source areas of the eolian deposits (Lü and Sun, 2011). Lai and Wintle (2006) suggested that the optically stimulated luminescence (OSL) sensitivity of quartz grains in paleosols was greater than that of the loess layer during the Pleistocene and Holocene transitions at the Luochuan section, which can be ascribed to different provenances. Further investigation suggested that the variation of quartz origins during the glacial-interglacial cycle has a major influence on the luminescence sensitivity (Lü et al., 2014).

The cited studies show the great potential for tracing loess sources by using luminescence sensitivity. However, studies of the ETP loess luminescence sensitivity are lacking. Therefore, we first conduct a detailed investigation of the quartz luminescence sensitivity to examine the temporal and spatial variations of the ETP loess, discuss the factors affecting the change in luminescence sensitivity of quartz grains, and, finally, explore the dust source implications in the ETP based on the luminescence sensitivity of quartz. Our results contribute new insights into the dust source of the ETP loess.

2 Material and methods

2.1 Sampling

The ETP is the transition zone from the Tibetan Plateau to the Sichuan Basin and the CLP, located at roughly 97–103°E and 25–37°N, with an average elevation between 2,500 m and 4,000 m above sea level (Figure 1). The aeolian loess of the ETP is mainly deposited in piedmonts, faulted basins, and river terraces, with varying thicknesses from several to tens of meters (Fang et al., 1996). The climate system is mainly influenced by the Westerlies, the Indian monsoon, and the Tibetan Plateau monsoon (Pan and Wang, 1999; Fang et al., 2004), with distinct dry and wet season differences.

A total of 20 luminescence sensitivity samples were collected from five typical loess-paleosol sequences in the ETP (Figure 1), including the Xinshi (XS) (Yang et al., 2022), Machang (MC), Xiaojin (XJ), Wenchuan (WCH) (Liu et al., 2021), and Zhouqu (ZQ) profiles (Yang et al., 2020). The lithologies, magnetic susceptibility (χ_{lf}) curves, and OSL dating data for all profiles studied are shown in Figure 2. The XS section (31.62°N, 99.98°E, 3,400 m) is located in the western part of the ETP, near Ganzi County. It is situated on the third terrace of the Yalong River (Yang et al., 2022). Field investigations, magnetic susceptibility (χ_{lf}) curves, and luminescence dating results show that the sequence has been deposited since the Last Interglacial, including three paleosols S1, L1S1, and S0 (Yang et al., 2021a). The MC and XJ sections are in the center of the ETP. The MC section (31.50°N, 102.08°E, 2,480 m) is situated on the sixth terrace on the east bank of the Dadu River, near Jinchuan County. In this study, the upper 5 m is selected for the luminescence sensitivity study. Based on the OSL ages, magnetic susceptibilities (χ_{lf}), and the field investigations, this section can be divided into S1, L1, and S0. The XJ section (30.99°N, 102.39°E, 3,191 m) is located on a high terrace of the Dadu River, near Xiaojin County, with a thickness of 6.6 m. According to the field observations, this profile has similar characteristics to the MC profile and can be divided into three units: S1, L1, and S0. The WCH section (31.45°N,

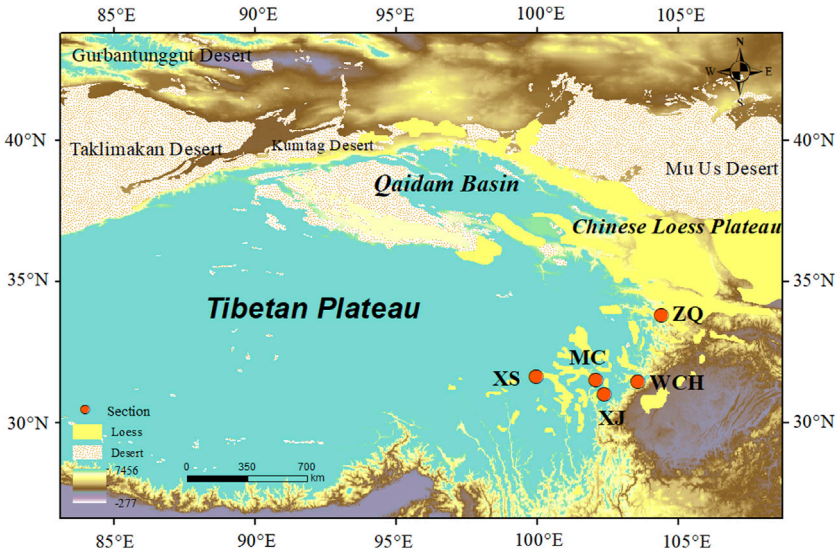

FIGURE 1
Loess distribution and the locations of the study site and sampling profiles (XS, Xinshi; MC, Machang; WCH, Wenchuan; XJ, Xiaojin; ZQ, Zhouqu). (Loess distribution after Liu, 1985; Yang et al., 2010; Muhs, 2013).

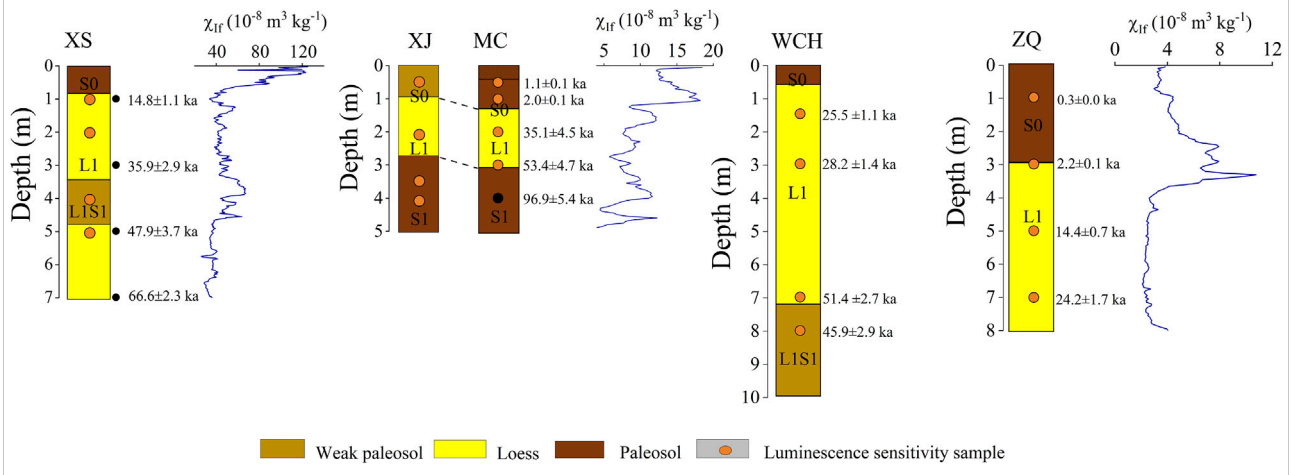

FIGURE 2
Lithology, optically stimulated luminescence (OSL) dating, and magnetic susceptibility (χ_{lf}) of the sampling profiles (L1, Malan loess; S, paleosol). The OSL dating results of the XS, MC, WCH and ZQ sections are taken from Yang et al. (2021a), Li (2021), Liu et al. (2021), and Yang et al. (2020), respectively. (XS, Xinshi, MC, Machang; WCH, Wenchuan; XJ, Xiaojin; ZQ, Zhouqu). The orange dots indicate the samples used in this study for the luminescence sensitivity study, and the black dots indicate the results for all OSL ages but not used in the luminescence sensitivity study.

103.57°E, 1,630 m) and ZQ section (33.78° N, 104.40° E, 2,047 m) is located in the east and northeast of the ETP, respectively. Previous reports showed that WCH and ZQ sections have accumulated since approximately 60 ka (Yang et al., 2020; Liu et al., 2021). The stratigraphic units of WCH and ZQ sections can be identified by field investigations, OSL dating, and environmental proxies (Yang et al., 2020; Liu et al., 2021).

2.2 Sample pretreatment

The luminescence sensitivity of quartz varies significantly with the grain size (Lü and Sun, 2011). For the same mass of quartz with different grain sizes, the finer grains will have a larger total surface area with greater luminescence sensitivities (Lü and Sun, 2011). To avoid the difference in luminescence sensitivities

TABLE 1 Experimental sequences for luminescence sensitivity measurements.

Step	Treatment	Observation
1	Stimulation for the 40s	Optically bleaching the natural OSL signals
2	Given dose	
3	Heat to 260°C	TL measurement and removing the shallow traps
4	Stimulation for the 40s	OSL signals measurement
5	Go to step 2	

of quartz caused by different grain sizes, we selected 38–63 μm quartz grains for the luminescence sensitivity experiment.

The quartz purifications were performed under a subdued red lighting condition at a wavelength of ~655 ± 30 nm. The outer 3–5 cm ends of the tube samples were first removed, and the remaining middle part was wet-sieved to obtain the 38–63 μm grain size fraction. Then the organic matter and carbonates were removed with 30% hydrogen peroxide (H_2O_2) and 10% dilute hydrochloric acid (HCl), followed by soaking in 35% fluorosilicic acid (H_2SiF_6) for approximately 2 weeks to remove the feldspar, then adding 1 mol/L HCl to remove the fluoride precipitate, until finally the purified quartz sample was obtained. The quartz purity is then tested by using the infrared stimulation (IRSL)/OSL ratio (Lai and Murray, 2006).

2.3 Luminescence sensitivities experiment

All the samples were analyzed for luminescence sensitivities at the Luminescence Dating Laboratory at the Key Laboratory of Western China's Environmental Systems (Ministry of Education), Lanzhou University, using an automated Risø thermoluminescence (TL)/OSL DA-20 reader installed with a $^{90}Sr/^{90}Y$ β-radiation source. Blue LEDs (470 nm, ~80 mW/cm^2) on the TL/OSL reader stimulated the quartz OSL signal, which is detected using a photomultiplier tube and a corresponding 7.5 mm Hoya U-340 filter. To avoid the effect of differences in photomultiplier tubes between instruments on the luminescence sensitivity results, all samples were measured in the same instrument. In the quartz luminescence sensitivity experiment, the quartz grains adhered to an approximately 1-cm-diameter stainless steel disc with silicone oil, and all aliquots were weighed with a high-precision (readability of 0.1 mg) analytical electronic balance before and after the grains were placed on the disc for weighted normalization of the luminescence sensitivity signals.

The luminescence sensitivity experimental procedure is shown in Table 1. Ten aliquots of each sample were measured. The aliquots were first bleached at 125°C for 40 s to remove the natural OSL signals, then known laboratory beta irradiation doses (0 Gy, 2.58 Gy, 5.16 Gy, 10.32 Gy) were sequentially applied. Finally, the quartz grains are preheated at 260°C to test the TL signal and stimulated at 125°C for 40 s to obtain the OSL signal.

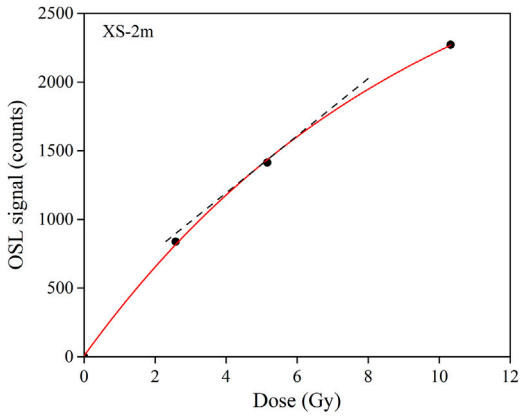

FIGURE 3
Response of regenerative doses (0 Gy, 2.58 Gy, 5.16 Gy, and 10.32 Gy) to the optically stimulated luminescence (OSL) signal for sample XS-2m. All dose-response curves were fitted with an exponential function, and the slope of the tangent line corresponding to the regenerative dose at 5.16 Gy on the growth curve was taken as the corresponding OSL sensitivity.

Data analysis: The dose-response curves were established with the four regenerative doses and the corresponding luminescence signal. The purpose of the regenerative dose of 0 Gy was to check the recuperation. The OSL signal integration of the first 0.32 s in the quartz decay curve minus the last 8 s of background for calculations employing a net OSL signal. The 110°C TL peak areas are derived from integration performed between 100 and 120°C with the dark count deducted. The luminescence sensitivity was calculated according to the method of Lü et al. (2014), and all OSL/TL signals were normalized by the weight of quartz gains and the irradiation dose (Figure 3). In our study, all dose-response curves were fitted with an exponential function, and the slope of the tangent line corresponding to the regenerative dose at 5.16 Gy on the growth curve was taken as the corresponding TL or optically stimulated luminescence (OSL) sensitivity.

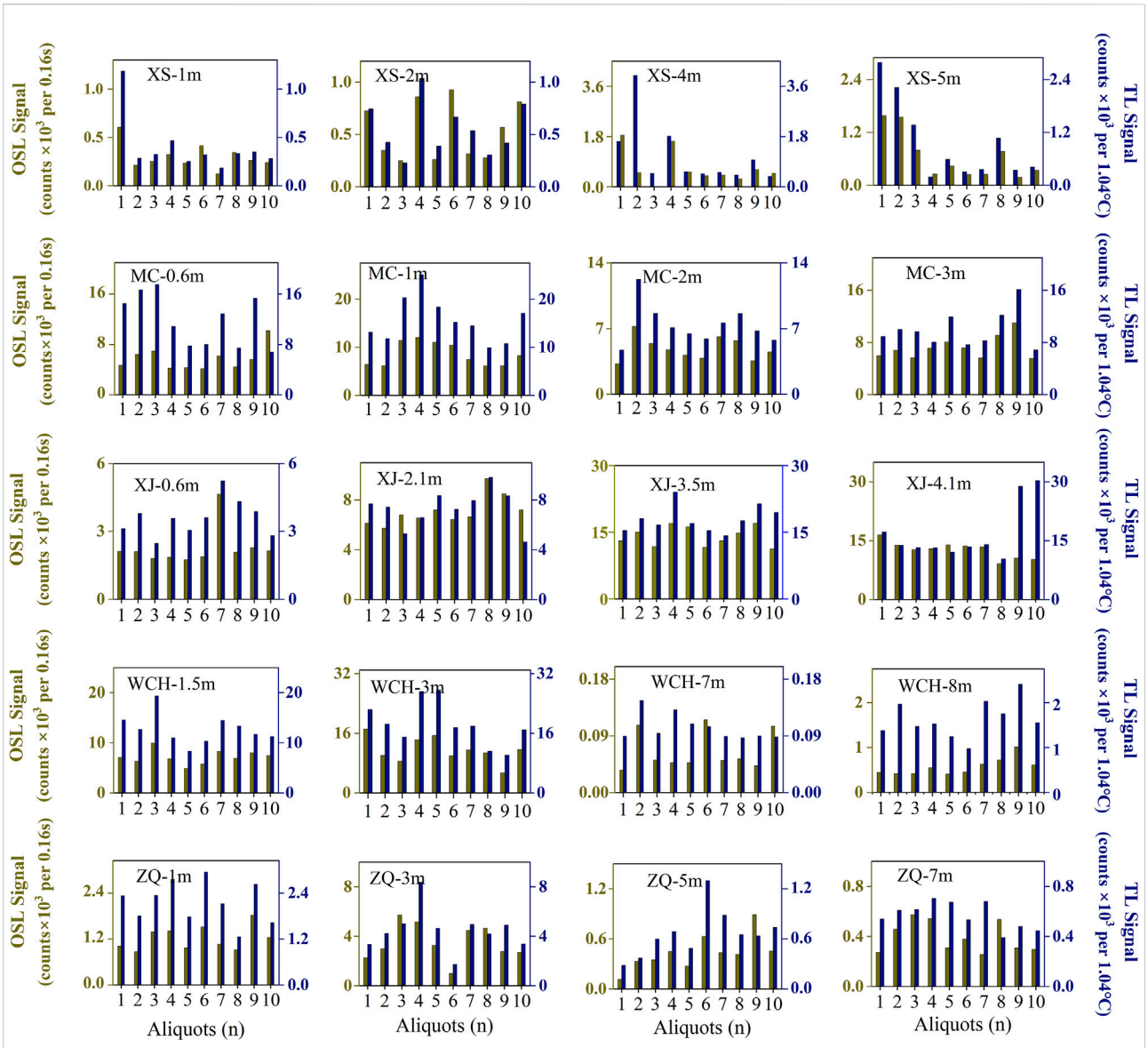

FIGURE 4
Histogram of optically stimulated luminescence (OSL) and 110°C thermoluminescence (TL) signal characteristics of all samples from the XS, MC, XJ, WCH, and ZQ sections. (XS, Xinshi; MC, Machang; WCH, Wenchuan; XJ, Xiaojin; ZQ, Zhouqu).

3 Results

3.1 Characteristics of quartz OSL and TL signals of the eastern Tibetan Plateau loess

Figure 4 illustrates that the OSL signal and 110°C TL peak signal intensity of different aliquots of the same sample vary significantly, showing a discrete distribution of the total data for each sample. The difference in signal intensity is even greater between samples. The OSL signal intensity of XS-1m in the XS profile is the weakest, with OSL signal distribution ranging between 500 counts and 1,000 counts; while the OSL signal intensity of XS-4m is obviously the highest (1,000–16000 counts). The internal difference of OSL signal intensity of XS-4m is the largest in comparison with other samples. The highest OSL intensity occurs in WCH-0.6m and WCH-3m, with the OSL signal varying between 3×10^4 and 8×10^4 counts. The OSL signal in WCH-7m is relatively weak, with overall values of <800 counts. The intensity of the OSL signal in the ZQ profile is lower than that in other profiles, ranging from 100 counts to 6,000 counts, and a lower quartz 110°C TL peak is presented compared to the other sections. The intensity of the 110°C TL peak also varies largely between aliquots of the same

sample and for different samples. The 110°C TL peaks in the ZQ and XS profiles have the weakest intensities among all samples. This discrepancy can be ascribed to the number of quartz grains contributing to the luminescence signal in each measurement aliquot and the different sizes of the luminescence sensitivities of the quartz grains (Pietsch et al., 2008).

3.2 Spatial and temporal characteristics of luminescence sensitivity

The quartz grains from the ETP loess-paleosol sequence show a good characteristic of luminescence signals and strong luminescence sensitivity. Spatial variations of the quartz luminescence sensitivity for all L1 samples are plotted in Figure 7, which shows the significant spatial differences in the luminescence sensitivity for loess at different locations in the ETP. The highest OSL and TL sensitivity occurs in the XJ and WCH loess, especially the WCH loess (falling into a distant region at the upper right in Figure 7), with TL sensitivity values above 8×10^3 counts/Gy/mg, and OSL sensitivity values above 6×10^3 counts/Gy/mg, followed by those of the XJ and MC loess, while the quartz grains of loess from XS and ZQ has the relatively weakest luminescence sensitivity. The OSL and TL sensitivity values of the XS loess are concentrated around 600 counts/Gy/mg and 530 counts/Gy/mg, respectively. And the OSL and TL sensitivity values of ZQ are distributed around 80 counts/Gy/mg and 200 counts/Gy/mg, respectively. Moreover, some overlap can be seen between the sensitivity values of XS samples and those of the MC and XJ sections (Figure 7).

Our results show a distinctive difference in the TL and OSL sensitivities of quartz from paleosol and loess layers at different sites in the ETP (Figure 5). The temporal variations of luminescence sensitivities in the XJ and WCH profiles are obviously higher than those of the other profiles. The higher sensitivity values in the XS and MC sections occurred in the S0 and L1S1 paleosol layers, and the Malan loess (L1) displays a lower luminescence sensitivity; whereas, the Malan loess of the XJ and WCH sections has significantly higher values than the paleosol layer. In addition, the differences between the loess and the Holocene soils (S0) are large compared with the sensitivity values of the weak paleosol (L1S1) in the ETP. The luminescence sensitivity values of the Holocene soil are slightly higher than that of the L1 in the MC and ZQ sections.

4 Discussion

4.1 Comparison of luminescence sensitivity with CLP loess

The OSL sensitivity comparison between the CLP and ETP loess is shown in Figure 6. In our study, the lowest OSL sensitivity of the L1 loess (approximately 215 counts/Gy/mg) appears in the ZQ section. The OSL sensitivity values of the XS, MC, and XJ sections are approximately 600 counts/Gy/mg, 1,060 counts/Gy/mg, and 7,000 counts/Gy/mg in the L1 loess accumulation period. The highest sensitivity value of approximately 9,310 counts/Gy/mg appears in the WCH profile in the L1 layer on the ETP. The Shimao section from the northern CLP has an OSL sensitivity for quartz grains (38–63 μm) of less than 100 counts/Gy/mg during the L1 loess accumulation period (Lü et al., 2021), while the OSL sensitivities of the L1 loess layer at Jingyuan (the particle size fraction used is 45–63 μm) and Luochuan (25–64 μm) are approximately 950 counts/Gy/mg and 1,230 counts/Gy/mg, respectively (Zhang, 2018). An OSL sensitivity value of approximately 333 counts/Gy/mg (38–64 μm) for the L1 was measured in the Xifeng profile (Li and Yang, 2022). In summary, the OSL sensitivity values of medium fraction quartz grains (38–63 μm) of TP loess were generally higher than those of quartz grains of the L1 layers of the CLP. The maximum OSL sensitivity of the ETP loess is 90 times the sensitivity values observed in the CLP, which implies that the dust sources may be different between the ETP and the CLP.

4.2 Factors affecting spatiotemporal luminescence sensitivity changes

The quartz luminescence sensitivity of sediment grains from different depositional environments is mainly influenced by the parent rock and transportation process (i.e., irradiation/bleaching cycles) (Pietsch et al., 2008; Fitzsimmons, 2011; Sawakuchi et al., 2018). Other factors such as heating histories, regional climate change, and soil-forming process potentially may also contribute to quartz luminescence sensitivity (Juyal et al., 2009; Rengers et al., 2017; Sawakuchi et al., 2018). In addition, variations in quartz grain size have significant effects on luminescence sensitivity. In general, the sensitivity values increase with smaller grain sizes (Li and Zhou, 2021; Li and Yang, 2022).

4.2.1 The effect of material source on luminescence sensitivity changes

Quartz grains are stable and weather resistant, so they retain significant information about their source rocks. Thus, they have the potential to identify the dust source regions (Sun and An, 2000; Rink et al., 2001; Qiao and Yang, 2006). In this study, the loess samples we selected are relatively young and have undergone relatively weak weathering processes. Generally, only silty to fine grains (<63 μm) can be transported long distances by wind suspension; sands or gravels can only be transported by saltation or creep (Pye, 1995). And the silt fraction greater than ~40 μm is unaffected by the pedogenesis process (Wang et al., 2002). Therefore, the 38–63 μm quartz grains from the Malan loess samples were investigated because

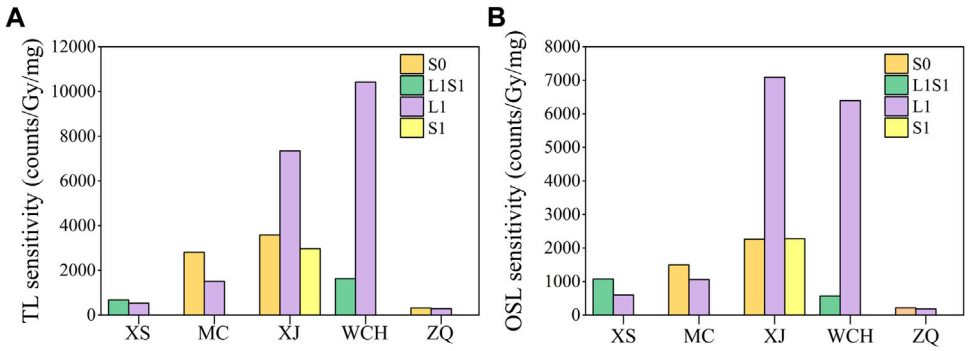

FIGURE 5
Variation of 110°C thermoluminescence (TL) peak **(A)** and optically stimulated luminescence (OSL) sensitivity **(B)** of quartz grains from loess-paleosol layers at different sites (locations shown in Figure 1). (XS, Xinshi; MC, Machang; WCH, Wenchuan,; XJ, Xiaojin; ZQ, Zhouqu).

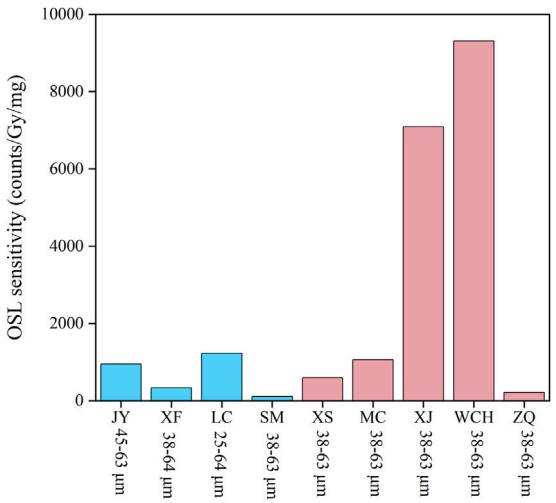

FIGURE 6
Comparison of optically stimulated luminescence (OSL) sensitivity observed for the L1 layer in the Chinese Loess Plateau and eastern Tibetan Plateau (JY, Jingyuan (Zhang, 2018), XF, Xifeng (Li and Yang, 2022); LC, Luochuan (Zhang, 2018), SM, Shimao (Lü et al., 2021); XS, Xinshi; MC, Machang; XJ, Xiaojing, WCH, Wenchuan, and ZQ, Zhouqu).

they are the main dust component of long-distance wind transmission, unaffected by pedogenesis, and carry information about the dust source (Fang, 1994; Yang et al., 2021b).

Our results show that the quartz luminescence sensitivities of loess samples from different locations in the ETP vary noticeably (Figure 7), suggesting that the quartz luminescence sensitivity may be used as a tool to track dust provenance. The dust in the ETP came from various deposits within the TP interior, including glacial–periglacial, alluvial/fluvial, lacustrine, aeolian, and slope deposits (Fang, 1994; Qiao et al., 2006; Ou et al., 2012; Yang et al., 2021b). The XS loess from the Ganzi Basin has a lower luminescence sensitivity, mainly because the XS loess is more affected by glacial–periglacial sediment content compared with other profiles (Fang, 1994), resulting in more quartz grains with relatively weak luminescence sensitivity. A certain overlap with the luminescence sensitivities of the XS, MC, and XJ loess samples occurs, which indicates that the source areas of these loess sections may be mixed. However, the luminescence sensitivity values of the MC and XJ loess sequences are significantly higher than those of the XS loess, which may indicate different dust sources in these sections compared to the XS profile. The highest luminescence sensitivity of the WCH loess, without overlap with other regions, shows a different source region with less contribution of dust materials produced by glacial activity. The luminescence sensitivity of the ZQ section is obviously different from that of other loess profiles on the Tibetan Plateau, but it is close to the luminescence sensitivity values of the CLP profiles (Zhang, 2018; Lü et al., 2021; Li and Yang, 2022). This may indicate that the ZQ loess has a similar dust source to the CLP loess. And, Fang et al. (1999) suggested that the loess of the West Qinling Mountains may mainly come from the neighboring northeastern Tibetan Plateau, so the “dim” source from North Tibetan Plateau may contribute to the lower luminescence sensitivities of the ZQ loess.

Significant temporal variations of luminescence sensitivity of quartz grains from loess-paleosol sequences have also occurred in the ETP. The higher sensitivity values in the XS, MC and ZQ sections occurred in the paleosol layers, and the glacial loess exhibits lower luminescence sensitivity; whereas, the Malan loess layers at XJ and WCH have significantly higher luminescence values than the paleosol layers (Figure 5), which can be mainly attributed to changes in the dust source area. Loess–paleosol sequences in the CLP have shown high luminescence sensitivity

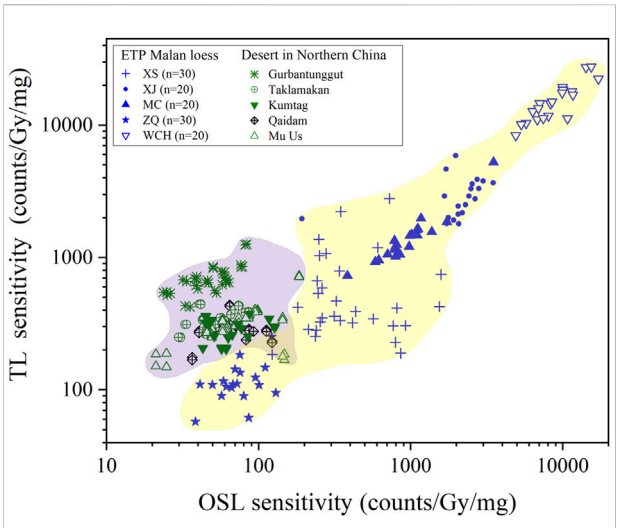

FIGURE 7
The 110°C thermoluminescence (TL) peak versus optically stimulated luminescence (OSL) sensitivity of quartz grains from the Malan loess (L1) in the eastern Tibetan Plateau and for the modern deserts in northwestern China (Lü and Sun, 2011). (XS, Xinshi; MC, Machang; WCH, Wenchuan; XJ, Xiaojin; ZQ, Zhouqu).

in paleosols and low luminescence sensitivity in loess layers, which is considered to be closely related to the sources of the quartz grains (Lai and Wintle, 2006; Lü et al., 2014; Lü et al., 2021).

4.2.2 Other factors affecting the luminescence sensitivity changes

Except for the material sources, other factors such as preburial transport history, heating history, and climate change also are suggested to have important influences on the quartz luminescence sensitivity changes.

The prior transport history, including the natural radiation/bleaching cycles from the source to the sink area, must also be considered as one of the factors affecting the luminescence sensitivity of quartz particles (Moska and Murray, 2006; Pietsch et al., 2008). In general, the more repeated irradiation–burial–exposure cycles, the higher the luminescence sensitivity of quartz grains (Pietsch et al., 2008). However, Liu et al. (2018) found that the luminescence sensitivities of quartz grains from Yellow River sediments were almost the same as those of quartz in the CLP, which indicates the limited impact of the transport–deposition process on luminescence sensitivity. The relationship between the total dose rate of quartz grains and the luminescence sensitivity is shown in Supplementary Figure S1 to investigate the effect of the natural irradiation process on luminescence sensitivity. The results showed a consistent trend between OSL and TL sensitivity, but no consistent change trend between the dose rate and luminescence sensitivity. The trends of OSL and TL sensitivity and total dose rate for the XS section were opposite to that of the luminescence sensitivity (Supplementary Figure S1A). Similar inconsistent variation patterns between luminescence sensitivity and dose rate also occur in the MC, XJ, WCH, and ZQ profiles. This pattern of irregular variations of the luminescence sensitivity and the total dose rate may suggest that luminescence sensitivity is less influenced by irradiation (Lü et al., 2021). In addition, dose rate does not show significant differences with depth in the ETP loess or the CLP loess (e.g., Yang et al., 2020; Lü et al., 2021; Li and Yang, 2022), therefore, we infer that irradiation is not the main factor influencing the quartz luminescence sensitivity of the ETP loess.

Wildfire heating also is suggested as a factor to change the luminescence sensitivity of quartz grains (Rengers et al., 2017). A significant increase in sensitivity values in the S1 layer of the Luochuan section is speculated to be related to wildfire events (Zhang, 2018; Zhang et al., 2022). Climate change can cause changes in the frequency and intensity of fires (Bowman et al., 2009). Microcharcoal preserved in soils is an ideal index and plays an irreplaceable role in understanding past fire histories (Patterson et al., 1987). The microcharcoal records of the XS section show that the large microcharcoal (>100 μm) contents are slightly lower in the L1S1 than in the loess layer (L1), indicating that local natural fire events are not important in the L1S1 stage (Tang et al., 2022). However, the higher sensitivity values in the XS section occurred in the L1S1 paleosol layer, and the lower sensitivity values occurred in the last glacial loess (L1). Therefore, we infer that wildfire heating was not the main factor in the increase of sensitivity values for the XS loess.

In our study, the differences in quartz luminescence sensitivities of the ETP loess and the CLP loess can be mainly attributed to different dust sources. The relatively high luminescence sensitivity of the XJ and WCH profiles can be ascribed to the brighter quartz grains from the source region, while the relatively low sensitivity values of the XS and ZQ loess profiles may be related to a different source area with more “dim” quartz grains that originated in glacial deposits. However, the transport process may have a relatively minor effect on the luminescence sensitivity of quartz grains (Liu et al., 2018). Recent studies on the loess-paleosol sequence in the CLP, such as at Xifeng (Li and Yang, 2022), Luochuan (Lü et al., 2014), and Shimao (Lü et al., 2021), showed that the OSL and TL sensitivities are consistent with glacial-interglacial variations. The similar variations between the quartz OSL/TL sensitivities and the climatic records (such as magnetic susceptibility and grain sizes) may imply luminescence sensitivity has a close relationship to climate changes (Lü et al., 2014; Lü et al., 2021; Li and Yang, 2022), but the causes and mechanisms of these similarities need further investigations.

4.3 Provenance implications for the eastern Tibetan Plateau loess based on quartz luminescence sensitivities

Numerous investigations have shown that the quartz luminescence sensitivity holds great potential for tracing eolian dust sources (Lü and Sun, 2011; Sawakuchi et al., 2018; Lü et al., 2021). From the analysis in Section 4.2, the difference in the luminescence sensitivities of ETP loess samples is thought to be a response to variations in the material sources. Figure 7 shows the significant spatial differences in the luminescence sensitivities for loess at different locations in the ETP. The quartz grains of XJ and WCH profiles exhibit the highest OSL and TL sensitivities, especially the XJ loess, followed by that of the MC loess, while the quartz grains from XS and ZQ have the relatively weakest luminescence sensitivity. In addition to the obvious spatial differences in luminescence sensitivities, there are also obvious vertical variations in the loess-paleosol profile, which are manifested as large differences in the sensitivity values between the loess and paleosol layers in different regions of the ETP (Figure 5). We infer that the spatial and temporal variations in quartz luminescence sensitivity may indicate internal differences in sources of the ETP loess.

The broad deserts in northwest China and the adjacent regions have been regarded as important sources of Chinese loess (Liu and Ding, 1998; Engelbrecht and Derbyshire, 2010), which may also potentially contribute to the ETP loess. However, our results show significant discrepancies in quartz luminescence sensitivities between the ETP loess and the deserts in northern China (including the Gurbantunggut, Taklimakan, Kumtag, Qaidam, and Mu Us) (Figure 7). The OSL sensitivities of quartz grains (90–125 μm fraction) in these deserts of northern China range from 40 counts/Gy/mg to 140 counts/Gy/mg, and the TL sensitivities range from 150 counts/Gy/mg to 1,260 counts/Gy/mg (Lü and Sun, 2011). The sensitivity values of the northern China deserts are close to those of the ZQ loess near the CLP, while they are significantly lower than those of the other Malan loess samples in the ETP (Figure 7). The significant differences in the luminescence sensitivity values may suggest that the northwestern deserts in China were not the main dust source of the ETP loess. It should be noted that due to limited data, we cannot compare the luminescence sensitivity with the same grain size for these two regions, which may introduce some uncertainties. Previous studies have shown that the ETP loess is mainly from the interior of the TP; the northwestern arid zone of the TP is not its main source (Fang, 1994; Yang et al., 2010; Yang et al., 2021b). Our results also show that the ETP loess was mainly sourced from the interior of the Tibetan Plateau, indicating the Tibetan Plateau is an important dust source area. The abundant dust materials derived from the vast west and central Tibetan Plateau can be transported by the westerlies and the plateau winter monsoon, and finally deposited in the ETP (Fang et al., 2004; Yang et al., 2021b). Due to the vast area of the Tibetan Plateau, with significant differences in topography and environment, more research is needed to precisely identify the dust source region of the ETP loess.

5 Conclusion

Based on the analysis and comparison of the luminescence sensitivities of sedimentary quartz from loess at different sites in the eastern Tibetan Plateau, the main conclusions are drawn as follows: The 110°C TL peaks and OSL sensitivities of quartz from different regions of the ETP loess vary widely, especially in the XJ, MC, and WCH samples, which are significantly higher than those of ZQ and XS. The luminescence sensitivity values of quartz are obviously different in loess and paleosol from different areas of the eastern Tibetan Plateau. The luminescence sensitivity of quartz in the ETP loess mainly reflects the variation of dust sources, and the luminescence sensitivity has the potential as an important tool for dust source tracing.

Data availability statement

The raw data supporting the conclusions of this article will be made available by the authors, without undue reservation.

Author contributions

SY and LL designed the study. SY, LL, and HW, carried out fieldwork and collected samples. XJ, LL, and HW performed laboratory analysis. XL, JZ, and PL performed data interpretations. S.Y. and LL wrote the manuscript. All authors discussed interpretations and commented on the manuscript.

Funding

This work was co-supported by the Second Tibetan Plateau Scientific Expedition and Research Program (2019QZKK0602), the National Natural Science Foundation of China (41877447 and 41472147), and the Strategic Priority Research Program of the Chinese Academy of Sciences (XDA20090000).

Acknowledgments

We are grateful for the helpful comments of the reviewers. We also thank Ting Cheng, Shuai Li, Minhao Liang, Dongxue Li, Yuanlong Luo, and Zixuan Chen for their assistance in field and laboratory work.

Conflict of interest

The authors declare that the research was conducted in the absence of any commercial or financial relationships that could be construed as a potential conflict of interest.

Publisher's note

All claims expressed in this article are solely those of the authors and do not necessarily represent those of their affiliated organizations, or those of the publisher, the editors, and the reviewers. Any product that may be evaluated in this article, or claim that may be made by its manufacturer, is not guaranteed or endorsed by the publisher.

Supplementary material

The Supplementary Material for this article can be found online at: https://www.frontiersin.org/articles/10.3389/feart.2022.939638/full#supplementary-material

References

An, Z., Kukla, G., Porter, S. C., and Xiao, J. (1991). Late quaternary dust flow on the Chinese Loess Plateau. *Catena* 18, 125–132. doi:10.1016/0341-8162(91)90012-m

Bailey, R. M., Smith, B. W., and Rhodes, E. J. (1997). Partial bleaching and the decay form characteristics of quartz OSL. *Radiat. Meas.* 27, 123–136. doi:10.1016/s1350-4487(96)00157-6

Bowman, D. M. J. S., Balch, J. K., Artaxo, P., Bond, W. J., Carlson, J. M., Cochrane, M. A., et al. (2009). Fire in the Earth system. *Sci. Am. Assoc. Adv. Sci.* 324 (5926), 481–484. doi:10.1126/science.1163886

Cao, Y., and Han, J. (2009). Wildfire activity and ecological environment change during Holocene in the Yuncheng Basin. *J. Arid Land Resour. Environ.* 23 (2), 125

Chen, G., Sun, S., Fang, X., and Kang, S. (1997). Heavy minerals and provenance of the Malan loess on the Qinghai-Xizang (Tibet) Plateau and its adjacent area. *Acta Sedimentol. Sin.* 15 (4), 134

Chen, Z., Yang, S., Luo, Y., Chen, H., Liu, L., Liu, X., et al. (2022). HIRM variation in the Ganzi loess of the eastern Tibetan Plateau since the last interglacial period and its paleotemperature implications for the source region. *Gondwana Res.* 101, 233–242. doi:10.1016/j.gr.2021.08.008

Dong, Z., Hu, G., Qian, G., Lu, J., Zhang, Z., Luo, W., et al. (2017). High-altitude aeolian research on the Tibetan plateau. *Rev. Geophys.* 55, 864–901. doi:10.1002/2017rg000585

Engelbrecht, J. P., and Derbyshire, E. (2010). Airborne mineral dust. *Elements* 6 (4), 241–246. doi:10.2113/gselements.6.4.241

Fang, X., Cheng, F., Shi, Y., and Li, J. (1996). Garze loess and the evolution of the cryosphere on the Tibetan Plateau. *Chin. Sci. Bull.* 41, 336

Fang, X., Han, Y., Ma, J., Song, L., Yang, S., and Zhang, X. (2004). Dust storms and loess accumulation on the Tibetan plateau: A case study of dust event on 4 march 2003 in lhasa. *Chin. Sci. Bull.* 49, 953–960. doi:10.1360/03wd0180

Fang, X., Li, J., and Voo, R. V. d. (1999). Age and provenance of loess in West Qinling. *Chin. Sci. Bull.* 44, 2188–2192. doi:10.1007/bf03182706

Fang, X. (1994). The origin and provenance of Malan loess along the eastern margin of Qinghai-Xizang (Tibetan) Plateau and its adjacent area. *Sci. China (serise B)* 24, 539

Fitzsimmons, K. E. (2011). An assessment of the luminescence sensitivity of Australian quartz with respect to sediment history. *Geochronometria* 38 (3), 199–208. doi:10.2478/s13386-011-0030-9

Gong, Z., Sun, J., and Lü, T. (2015). Investigating the components of the optically stimulated luminescence signals of quartz grains from sand dunes in China. *Quat. Geochronol.* 29, 48–57. doi:10.1016/j.quageo.2015.06.004

Gray, H. J., Jain, M., Sawakuchi, A. O., Mahan, S. A., and Tucker, G. E. (2019). Luminescence as a sediment tracer and provenance tool. *Rev. Geophys.* 57 (3), 987–1017. doi:10.1029/2019rg000646

Huang, J., Minnis, P., Yi, Y., Tang, Q., Wang, X., Hu, Y., et al. (2007). Summer dust aerosols detected from CALIPSO over the Tibetan Plateau. *Geophys. Res. Lett.* 34 (18), L18805. doi:10.1029/2007gl029938

Jeong, G., and Choi, J. H. (2012). Variations in quartz OSL components with lithology, weathering and transportation. *Quat. Geochronol.* 10, 320–326. doi:10.1016/j.quageo.2012.02.023

Jiang, F., Wu, X., Xiao, H., Zhao, Z., Tian, G., and Liu, K. (1997). The Ganzi loess stratigraphy in the west Sichuan plateau. *Acta Geol. Sin.* 18 (4), 414–420.

Juyal, N., Pant, R. K., Basavaiah, N., Bhushan, R., Jain, M., Saini, N. K., et al. (2009). Reconstruction of last glacial to early Holocene monsoon variability from relict lake sediments of the higher central himalaya, uttrakhand, India. *J. Asian earth Sci.* 34 (3), 437–449. doi:10.1016/j.jseaes.2008.07.007

Lai, Z., and Murray, A. S. (2006). Red TL of quartz extracted from Chinese loess: Bleachability and saturation dose. *Radiat. Meas.* 41, 836–840. doi:10.1016/j.radmeas.2006.04.017

Lai, Z., and Wintle, A. G. (2006). Locating the boundary between the Pleistocene and the Holocene in Chinese loess using luminescence. *Holocene (Sevenoaks)* 16, 893–899. doi:10.1191/0959683606hol980rr

Li, D. (2021). *A comparative study on luminescence dating methods of loess in the eastern margin of Tibetan Plateau*. Lanzhou, China: Lanzhou University.

Li, G., Wen, L., Xia, D., Duan, Y., Rao, Z., Madsen, D. B., et al. (2015). Quartz OSL and K-feldspar pIRIR dating of a loess/paleosol sequence from arid central Asia, Tianshan Mountains, NW China. *Quat. Geochronol.* 28, 40–53. doi:10.1016/j.quageo.2015.03.011

Li, J., and Yang, L. (2022). Variations in the sensitivity of the optically stimulated luminescence from quartz in the Xifeng section: A spatiotemporal comparison across the Chinese Loess Plateau since the last interglaciation. *Quat. Geochronol.* 72, 101353. doi:10.1016/j.quageo.2022.101353

Li, S., Chen, Y., Li, B., Sun, J., and Yang, L. (2007). OSL dating of sediments from deserts in northern China. *Quat. Geochronol.* 2, 23–28. doi:10.1016/j.quageo.2006.05.034

Li, S. (2002). Luminescence sensitivity changes of quartz by bleaching, annealing and UV exposure. *Radiat. Eff. defects solids* 157, 357–364. doi:10.1080/10420150212998

Li, Y., and Zhou, L. (2021). Variations of thermally and optically stimulated luminescence sensitivity of loess and pedocomplex samples from southern Tajikistan, central asia. *Geochronometria* 48 (1), 242. doi:10.1515/geochr-2015-0118

Ling, Z., Yang, S., Xia, D., Wang, X., and Chen, F. (2022). Source of the aeolian sediments in the Yarlung Tsangpo valley and its potential dust contribution to adjacent oceans. *Earth Surf. Process. Landf.* 47 (7), 1860–1871. doi:10.1002/esp.5351

Liu, J., Jiang, F., Chen, J., Sun, Q., Chen, J., and Chen, Z. (2018). Luminescence properties of quartz in the sediments from TypicalChinese rivers and their implications for provenance. *Geol. J. China Univ.* 24, 88

Liu, L., Yang, S., Cheng, T., Liu, X., Luo, Y., Liu, N., et al. (2021). Chronology and dust mass accumulation history of the Wenchuan loess on eastern Tibetan Plateau since the last glacial. *Aeolian Res.* 53, 100748–100810. doi:10.1016/j.aeolia.2021.100748

Liu, T., and Ding, Z. (1998). Chinese loess and the palemonsoon. *Annu. Rev. Earth Planet. Sci.* 26, 111–145. doi:10.1146/annurev.earth.26.1.111

Liu, T. (1985). *Loess and the environment*. Beijing: China Ocean Press.

Liu, X. (1983). *The quarternary in Sichuan Basin sichuan*. Chengdu: Sichuan Sci.& Tech. Pulishers, 88

Lü, T., Sun, J., Feathers, J. K., and Sun, D. (2021). Spatiotemporal variations and implications of luminescence sensitivity of quartz grains on the Chinese Loess Plateau since the last interglaciation. *Quat. Res.* 99, 190–203. doi:10.1017/qua.2020.53

Lü, T., Sun, J., Li, S., Gong, Z., and Xue, L. (2014). Vertical variations of luminescence sensitivity of quartz grains from loess/paleosol of Luochuan section in the central Chinese Loess Plateau since the last interglacial. *Quat. Geochronol.* 22, 107–115. doi:10.1016/j.quageo.2014.04.004

Lü, T., and Sun, J. (2011). Luminescence sensitivities of quartz grains from eolian deposits in northern China and their implications for provenance. *Quat. Res.* 76, 181–189. doi:10.1016/j.yqres.2011.06.015

Ma, R. (1944). Formation of Chinese loess. *Geol. Rev.* 9, 207

Moska, P., and Murray, A. S. (2006). Stability of the quartz fast-component in insensitive samples. *Radiat. Meas.* 41 (7), 878–885. doi:10.1016/j.radmeas.2006.06.005

Muhs, D. R. (2013). The geologic records of dust in the Quaternary. *Aeolian Res.* 9, 3–48. doi:10.1016/j.aeolia.2012.08.001

Ou, X., Zeng, S., Zhou, S., and Lai, Z. (2012). A review on research of loess and environmental change in west Sichuan Plateau of the eastern Qinghai-Tibetan Plateau. *J. Earth Environ.* 3, 692

Pan, B., and Wang, J. (1999). Loess record of Qinghai-Xizang Plateau monsoon variations in the eastern part of the plateau since the last interglacial. *Quat. Sci.*, 330

Patterson, W. A., Edwards, K. J., and Maguire, D. J. (1987). Microscopic charcoal as a fossil indicator of fire. *Quat. Sci. Rev.* 6 (1), 3–23. doi:10.1016/0277-3791(87)90012-6

Pietsch, T. J., Olley, J. M., and Nanson, G. C. (2008). Fluvial transport as a natural luminescence sensitiser of quartz. *Quat. Geochronol.* 3, 365–376. doi:10.1016/j.quageo.2007.12.005

Pye, K. (1995). The nature, origin and accumulation of loess. *Quat. Sci. Rev.* 14 (7-8), 653–667. doi:10.1016/0277-3791(95)00047-x

Qiao, S., and Yang, Z. (2006). Advances in a study on quartz as a tracer for material source. *Adv. Mar. Sci.* 24, 266–274.

Qiao, Y., Zhao, Z., Wang, Y., Wang, S., Fu, J., Li, C., et al. (2006). Magneto stratigraphy and its palepclimatic significance of a loess-soli sequence from Ganzi area, West Sichuan Platrean. *Quat. Sci.* 26, 250–256.

Rengers, F. K., Pagonis, V., and Mahan, S. A. (2017). Can thermoluminescence be used to determine soil heating from a wildfire? *Radiat. Meas.* 107, 119–127. doi:10.1016/j.radmeas.2017.09.002

Rink, W. J., Schwarcz, H. P., Lee, H. K., Rees-Jones, J., Rabinovich, R., and Hovers, E. (2001). Electron spin resonance (ESR) and thermal ionization mass spectrometric (TIMS) 230Th/234U dating of teeth in Middle Paleolithic layers at Amud Cave, Israel. *Geoarchaeology* 16, 701–717. doi:10.1002/gea.1017

Sawakuchi, A. O., Guedes, C. C. F., DeWitt, R., Giannini, P. C. F., Blair, M. W., Nascimento, D. R., et al. (2012). Quartz OSL sensitivity as a proxy for storm activity on the southern Brazilian coast during the Late Holocene. *Quat. Geochronol.* 13, 92–102. doi:10.1016/j.quageo.2012.07.002

Sawakuchi, A. O., Jain, M., Mineli, T. D., Nogueira, L., Bertassoli, D. J., Häggi, C., et al. (2018). Luminescence of quartz and feldspar fingerprints provenance and correlates with the source area denudation in the Amazon River basin. *Earth Planet. Sci. Lett.* 492, 152–162. doi:10.1016/j.epsl.2018.04.006

Sun, J., Li, S., Muhs, D. R., and Li, B. (2007). Loess sedimentation in tibet: Provenance, processes, and link with quaternary glaciations. *Quat. Sci. Rev.* 26 (17), 2265–2280. doi:10.1016/j.quascirev.2007.05.003

Sun, Y., and An, Z. (2000). Sedimentary interpretation of surface textures of quartz grains from the eolian deposits. *Acta Sedimentol. Sin.* 18, 506

Tafel, A. (1914). *My trip to Tibet. A study trip through northwest China and Inner Mongolia to eastern Tibet Stuttgart*. Leipzig, Berlin, 698p.

Tang, G., Yang, S., Miao, Y., Luo, Y., Chen, Z., Liu, L., et al. (2022). Grain size characteristics of microfossil charcoal and the environmental implications in loess deposits from Ganzi, Western Sichuan Plateau. *J. Lanzhou Univ. Nat. Sci.* 58 (3), 289. doi:10.13885/j.issn.0455-2059.2022.03.002

Wang, H., Chen, F., and Zhang, J. (2002). Environmental significance of grain size of loess-paleosol sequence in Western part of Chinese Loess Plateau. *J. Desert Res.* 22, 21.

Wang, J., and Pan, B. (1997). Loess deposits in eastern part of qinghai-xizang plateau: Its characteristics and environment. *J. Desert Res.* 17 (4), 395.

Wang, S., Jiang, F., Tian, G., Fu, J., Liu, K., and Zhao, Z. (2005). The jinchuan loess stratigraghy in Western Sichuan Plateau. *Acta Geol. Sin.* 26 (4), 355. doi:10.3321/j.issn:1006-3021.2005.04.011

Wen, X., Tang, Y., Huang, C., and Gongbo, S. (2014). Multi-material source of loess deposits from the Jiuzhaigou natonal nature reserve on the Eastern margin of the Tibetan Pleteau. *Mt. Res.* 32 (5), 603

Wen, X., Wu, Y., Huang, C., Luo, M., and Chen, K. (2019). *Grain size & elements composition characteristics and their implications for the late Pleistocene loess in the upper reaches of the Minjiang River,China*. Mountain Research

Wintle, A. G., and Murray, A. S. (1999). Luminescence sensitivity changes in quartz. *Radiat. Meas.* 30, 107–118. doi:10.1016/s1350-4487(98)00096-1

Xu, C., Ma, Y. M., You, C., and Zhu, Z. K. (2015). The regional distribution characteristics of aerosol optical depth over the Tibetan Plateau. *Atmos. Chem. Phys.* 15 (20), 12065–12078. doi:10.5194/acp-15-12065-2015

Yang, S., Chen, Z., Chen, H., Luo, Y., Liu, L., Liu, X., et al. (2022). Magnetic properties of the Ganzi loess and their implications for precipitation history in the eastern Tibetan plateau since the last interglacial. *Paleoceanogr. Paleoclimatol.* 37, 1–17. doi:10.1029/2021pa004322

Yang, S., Fang, X., Shi, Z., Lehmkuhl, F., Song, C., Han, Y., et al. (2010). Timing and provenance of loess in the Sichuan Basin, southwestern China. *Palaeogeogr. Palaeoclimatol. Palaeoecol.* 292 (1), 144–154. doi:10.1016/j.palaeo.2010.03.039

Yang, S., Liu, L., Chen, H., Tang, G., Luo, Y., Liu, N., et al. (2021a). Variability and environmental significance of organic carbon isotopes in Ganzi loess since the last interglacial on the eastern Tibetan Plateau. *Catena* 196, 104866. doi:10.1016/j.catena.2020.104866

Yang, S., Liu, N., Li, D., Cheng, T., Liu, W., Li, S., et al. (2020). Quartz OSL chronology of the loess deposits in the Western Qinling Mountains, China, and their palaeoenvironmental implications since the Last Glacial period. *Boreas* 50, 294–307. doi:10.1111/bor.12473

Yang, S., Luo, Y., Li, Q., Liu, W., Chen, Z., Liu, L., et al. (2021b). Comparisons of topsoil geochemical elements from Northwest China and eastern Tibetan Plateau identify the plateau interior as Tibetan dust source. *Sci. Total Environ.* 798, 149240. doi:10.1016/j.scitotenv.2021.149240

Zhang, H., Nie, J., Liu, X., Pullen, A., Li, G., Peng, W., et al. (2021). Spatially variable provenance of the Chinese Loess Plateau. *Geol. (Boulder)* 49 (10), 1155–1159. doi:10.1130/g48867.1

Zhang, J. (2018). *Applications of optically stimulated luminescence dating in the Chinese Loess Plateau*. PhD thesis.

Zhang, J., Li, S., Sun, J., Lü, T., Zhou, X., and Hao, Q. (2022). Quartz luminescence sensitivity variation in the Chinese loess deposits: The potential role of wildfires. *J. Quat. Sci.*, 1–12. doi:10.1002/jqs.3462

Zheng, C., Zhou, L., and Qin, J. (2009). Difference in luminescence sensitivity of coarse-grained quartz from deserts of northern China. *Radiat. Meas.* 44, 534–537. doi:10.1016/j.radmeas.2009.02.013

Zular, A., Sawakuchi, A. O., Guedes, C. C. F., and Giannini, P. C. F. (2015). Attaining provenance proxies from OSL and TL sensitivities: Coupling with grain size and heavy minerals data from southern Brazilian coastal sediments. *Radiat. Meas.* 81, 39–45. doi:10.1016/j.radmeas.2015.04.010

frontiers | Frontiers in Earth Science

TYPE Policy Brief
PUBLISHED 12 September 2022
DOI 10.3389/feart.2022.939964

OPEN ACCESS

EDITED BY
Hema Achyuthan,
Anna University, Chennai, India

REVIEWED BY
Yan Li,
China University of Geosciences, China
Xiaomei Nian,
East China Normal University, China

*CORRESPONDENCE
Xue Rui,
xr145@jlu.edu.cn

SPECIALTY SECTION
This article was submitted to Quaternary Science, Geomorphology and Paleoenvironment,
a section of the journal
Frontiers in Earth Science

RECEIVED 09 May 2022
ACCEPTED 15 August 2022
PUBLISHED 12 September 2022

CITATION
Rui X, Li B and Cohen TJ (2022), Testing the use of continental standardized growth curves (SGCs) for D_e estimation on coarse quartz grains from Lake Woods, Northern Australia.
Front. Earth Sci. 10:939964.
doi: 10.3389/feart.2022.939964

Testing the use of continental standardized growth curves (SGCs) for D_e estimation on coarse quartz grains from Lake Woods, Northern Australia

Xue Rui[1,2]*, Bo Li[2,3] and Tim J. Cohen[3,4]

[1]College of Earth Sciences, Jilin University, Changchun, China, [2]Centre for Archaeological Science, School of Earth, Atmospheric and Life Sciences, University of Wollongong, Wollongong, NSW, Australia, [3]ARC Centre of Excellence for Australian Biodiversity and Heritage, University of Wollongong, Wollongong, NSW, Australia, [4]GeoQuest Research Centre, School of Earth, Atmospheric and Life Sciences, University of Wollongong, Wollongong, NSW, Australia

Using continental SGCs built by Fu et al. (2020) can save significant machine time for constructing SGCs when compared to traditional SGC methods, which need significantly more time for building sample-specific or regional SGCs. In this study, the reliability of continental SGCs is tested using coarse quartz grains (180–212 μm) from Lake Woods in Northern Australia. D_e values obtained by continental SGCs are consistent with D_e values obtained by regional SGCs and by the SAR procedures.

KEYWORDS

quartz, lake woods, regional application, luminescence dating, continental standardized growth curves

1 Introduction

Optically stimulated luminescence (OSL) emissions from quartz grains have been widely used for dating sediments in the Quaternary period since the development of the single-aliquot regenerative-dose (SAR) protocol (e.g., Galbraith et al., 1999; Murray and Wintle, 2000; Wintle and Murray, 2006). In the SAR protocol, a dose-response curve (DRC) is constructed for each aliquot using a series of regenerative doses and their corresponding luminescence signals, and the equivalent dose (D_e) is obtained by projecting the natural luminescence signal onto the DRC. However, when there are many samples or the ages of samples are too high, large regenerative doses and long irradiation times are necessary for building a DRC, and the time required for the measurements can be a major impediment of the SAR protocol applications.

To reduce the amount of machine time required, Roberts and Duller (2004) proposed that T_x not only corrects within-aliquot sensitivity changes but can also act as a between-aliquot normalization step. This assumption offers a potential means of creating a standardized growth curve (SGC), from which the D_e can be estimated by projecting the sensitivity-corrected natural OSL signal re-scaled by the corresponding test dose

(i.e., L_n/T_n*D_t) onto the SGC, established using a number of re-scaled DRCs obtained from an SAR protocol. This SGC method has been applied to single aliquots of quartz from different regions (e.g., Burbidge et al., 2006; Lai, 2006; Lai et al., 2007; Stevens et al., 2007; Telfer et al., 2008; Long et al., 2010; Yang et al., 2011; Chen et al., 2013; Wang et al., 2022).

To further reduce the inter-aliquot variation of DRCs for quartz OSL from same or different samples, Li et al. (2015) suggested a new method for establishing SGCs by dividing the L_x/T_x data by one of the regenerative dose signals (L_{r1}/T_{r1}). This improved method was called regenerative-dose normalization (re-normalization). By applying this method for a range of quartz samples from different regions of Asia, Africa, Europe, and North America, they constructed a common re-normalized DRC (global standardized growth curve, gSGC) for single aliquots of quartz. With numerical simulation, Peng et al. (2016) showed that the gSGC method is intrinsically more precise than the conventional SGC method.

With the development of the re-normalization method, a similar but improved normalized method was proposed by Li et al. (2016), i.e., the least-squares normalization (LS-normalization). This uses an iterative scaling and fitting procedure that takes all of the L_x/T_x ratios into consideration when constructing the SGC. In addition, Fu et al. (2020) have observed that the DRCs for quartz OSL signals of single grains diverge significantly over ~50 Gy, and a set of continental standardized growth curves (cSGCs) were established for single grains of Australian quartz. With cSGC, a D_e can be determined by measuring the natural signal (L_n), two regenerative-dose signals (L_1 and L_2), and the corresponding test-dose signals (T_n, T_1, and T_2). Significant machine time can be saved for constructing SGCs when compared to traditional SGC methods, which need significantly more time for building sample-specific or regional SGCs (rSGCs). In this study, the reliability of cSGC is tested using coarse quartz grains from Lake Woods in Northern Australia, and the cSGC D_es are compared with the D_e results obtained by the full SAR procedure and also with the results obtained by rSGC.

2 Samples, facilities, and measurement

Lake Woods is an ephemeral freshwater lake in the Northern Territory of Australia (Supplementary Figure S1). One beach sample and four lacustrine samples from three pits of Lake Woods were used to establish rSGC. The deposit type, grain size, and D_e ranges for each sample are summarized in Supplementary Table S1. Each sample was collected from cleaned profile walls using stainless steel tubes. After the tubes were removed, they were immediately wrapped in light-proof plastic and transported to the Luminescence Dating Laboratory at the University of Wollongong for analysis. Quartz grains 180–212 μm in diameter were isolated for OSL dating and purified using the standard procedure (e.g., Wintle, 1997). The measurement was performed on a Risø TL/OSL-DA-20 reader equipped with $^{90}Sr/^{90}Y$ beta sources and green (532 nm) laser for single-grain stimulation. OSL signals were detected by an Electron Tubes 9235B photo-multiplier tube fitted with Hoya U-340 filters.

All single-grain quartz measurements were made using the SAR procedure, and experimental conditions are listed in Supplementary Table S2. The grains were stimulated by a green laser for 1.8 s at 125°C, and the net OSL signal was calculated using the first 0.18 s integral of the initial OSL signal minus a background estimated from the last 0.18 s. The value of the SAR D_e was estimated by interpolating the sensitivity-corrected signals (L_n/T_n) onto the corresponding DRC. Grains were rejected if the resulting OSL data failed to satisfy a series of well-established criteria similar to those proposed by Jacobs et al. (2006), namely, if 1) the initial T_n signal was less than 3σ above its corresponding background or its relative standard error is >25%; 2) the recycling ratio or OSL IR depletion ratio differed from unity by more than 2σ; 3) the recuperation ratio (i.e., the ratio of the L_x/T_x value for the 0 Gy and maximum regenerative dose) is >5%; 4) the figure-of-merit (FOM) value is >10% (Peng and Li, 2017); 5) the reduced chi-square (RCS) value for the DRC is >5 (Peng and Li, 2017); 6) the L_n/T_n ratio is statistically consistent with, or higher than, the saturation level of the corresponding DRC; 7) the D_e value is obtained by extrapolation of the fitted DRC, rather than interpolation among the regenerative-dose signals; and 8) the relative standard error (RSE) of D_e exceeds 50%. It should be noted that full criteria (i.e., all eight criteria) would only be applied for SAR D_e estimation (see below).

3 Results

3.1 Regional SGC determination

A total of 45 aliquots (4,500 grains) from five samples were measured by the SAR procedure, and we rejected grains with poor DRCs based on criteria 1)–5) before building rSGCs (Li et al., 2016; Fu et al., 2020). Within SGC determination, 1) we fitted the measured L_x/T_x data for individual grains using a general-order kinetic (GOK) function, i.e., $(x) = a[1 - (1 + bcx)^{(-\frac{1}{c})}] + d$, where x represents the radiation dose and a, b, c, and d are constants (Guralnik et al., 2015; Li et al., 2016). We chose this function here because it has proved to be flexible and robust for fitting DRCs with different shapes (see Peng and Li, 2017),and then, the 'signal growth ratio' (SGR), defined as the ratio between the L_x/T_x values at 200 and 50 Gy based on the best-fit DRCs for individual grains, is calculated. 2) The SGRs of all investigated grains were divided into k groups using the finite mixture model (FMM) (Roberts et al., 2000), with a zero overdispersion value

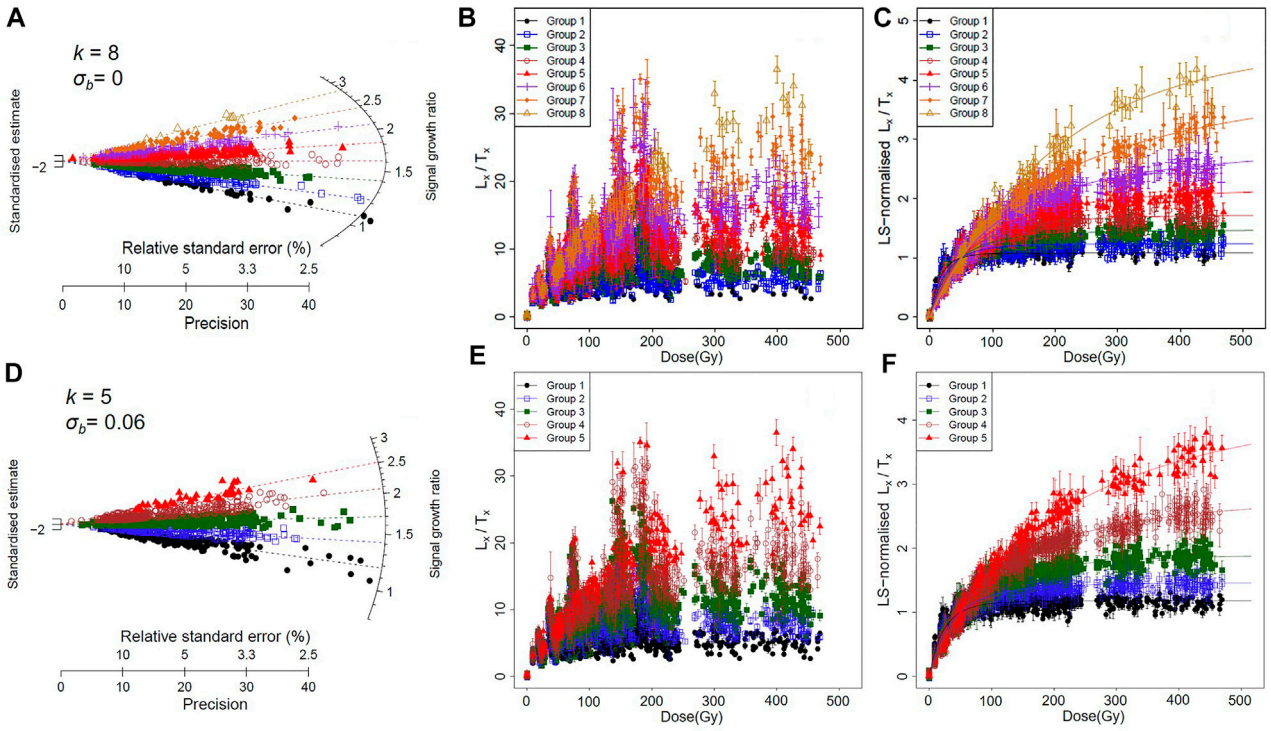

FIGURE 1
(A) Distribution of signal growth ratios for all accepted quartz grains (n = 1,438) from five Lake Woods samples. Different symbols denote the eight groups identified using the finite mixture model and a σ_b value of 0 for each group. **(B)** Single-grain L_x/T_x ratios for the eight groups, plotted as a function of laboratory dose. **(C)** LS-normalized L_x/T_x ratios for the eight groups, based on the data shown in **(B)**. **(D)** Same data in **(A)** but divided into five groups by the FMM (σ_b = 0.06). **(E)** Single-grain L_x/T_x ratios for the five groups in **(D)**. **(F)** LS-normalized L_x/T_x ratios for the five groups, based on the data shown in **(E)**.

(σ_b = 0) for each group (i.e., assuming that the sources of error associated with the signal intensity have been adequately taken into account, see details in Hu et al., 2019). To determine the optimal number of rSGC groups, k was increased from 2 to 10. The optimal number of groups was then estimated as the one associated with the lowest Bayesian information criterion (BIC). 3) The LS-normalization procedure was applied separately to each group to determine their group-specific SGCs.

The SGRs for all the investigated grains are shown in Figure 1A. A large range of SGRs from ~1 to ~3 was observed, indicating that grains have a wide range of saturation doses. For example, the grains with SGRs close to 1.08 (marked by black circle in Figure 1A) correspond to early saturated grains (i.e., there was a negligible increase in the OSL signal beyond 50 Gy). In contrast, grains with L_x/T_x ratios close to 2.85 (marked by yellow triangle in Figure 1A) have a large saturation dose level (keep growing even after 400 Gy). Figure 1C displays the LS-normalized L_x/T_x ratios and common SGCs for all eight groups as a function of the dose. To test the validity of the groupings and establishment of the SGCs, we calculated the ratio between the individual LS-normalized L_x/T_x values and their expected values (based on the best-fit curve) for all the regenerative doses greater than zero. The ratios are plotted in radial plots in Supplementary Figure S2. Around 89–95% of the measured-to-SGC ratios for each group are consistent with unity at 2σ. We propose, therefore, that the DRCs of the Lake Woods quartz grains mentioned here can be represented by eight common SGCs; the best-fit GOK parameters for each SGC are summarized in Supplementary Table S3. Comparing with cSGC (k =6, Supplementary Table S3), our rSGCs have more group numbers and thus have different GOK parameters. When building cSGCs, Fu et al., (2020) assumed all groups have the same σ_b value (0.06). As a 6% overdispersion accounts for the between-grain differences in the DRCs, it may lead to a smaller group number for cSGCs. For a better comparison with the cSGCs, we repeated the building of the rSGC steps but with a fixed σ_b value (σ_b = 0.06), and the calculated optimal k is 5 (Figures 1D–F). As samples for rSGCs were from the same region (i.e., Lake Woods), the fewer groups (with σ_b value of 0.06) than cSGC may contribute to relatively similar OSL properties (e.g., inherent brightness or the shape of the OSL decay curve) of the individual quartz grains. About 90–93% of the measured-to-SGC ratios for each group from five group SGCs (σ_b = 0.06) are consistent with unity at 2σ

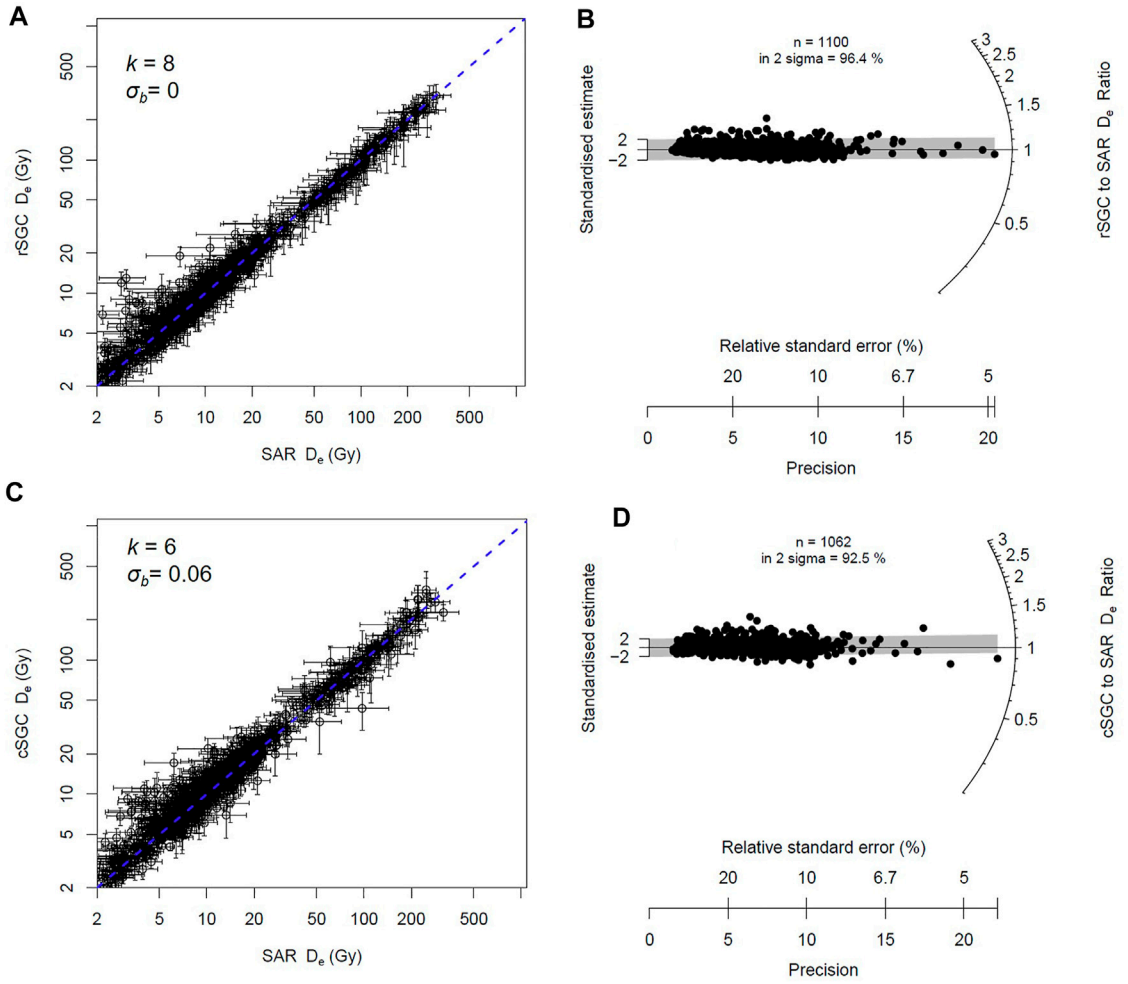

FIGURE 2
(A) Comparison of the SAR and rSGC D_e values (σ_b = 0). The dashed line represents the 1:1 ratio. The ratios of the rSGC and SAR D_e are radially plotted in **(B)**. **(C)** Comparison of the SAR and cSGC D_e values, and the corresponding ratios are radially plotted in **(D)**.

(Supplementary Figure S3). The validation of these two sets of rSGCs is tested in Section 3.2.

3.2 Regional SGC verification

To validate D_e estimates generated by rSGCs, a practical test must demonstrate that the rSGC method can adequately generate the same results as a full SAR protocol. During building of the rSGCs, each grain was assigned to one of the eight groups (σ_b = 0) or to one of the five groups (σ_b = 0.06) (step 2), and the natural signal has been normalized when applying the LS-normalization procedure to each group to determine their group-specific SGCs (step 3). Thus, the normalized natural signal can directly project onto the corresponding SGC to estimate the D_e value for that grain. The obtained SGC D_e values for all non-rejected grains are compared to the SAR D_e values obtained from individual DRCs (Figure 2A and Supplementary Figure S4A). For the SGCs, D_e values were obtained by eight group SGCs (σ_b = 0), and the two sets of D_e values are in good agreement, with 96.4% of the ratios (rSGC D_e/SAR D_e) consistent with unity at 2σ (Figure 2B). Similarly, the ratios are with 94.4% consistency with unity at 2σ for rSGC D_e values obtained by five group SGCs (σ_b = 0.06) (Supplementary Figure S4B).

It should be noted that the comparisons between the SAR and rSGC D_e values shown in Figure 2A and Supplementary Figure S4A are only available for those grains that produce reliable results using both approaches. As shapes for DRCs and for rSGCs are different, the number of grains that pass criteria 6)–8) is also different (Supplementary Table S4). To further test the reliability of the rSGCs, we compared the D_e distributions of three representative Lake Woods samples

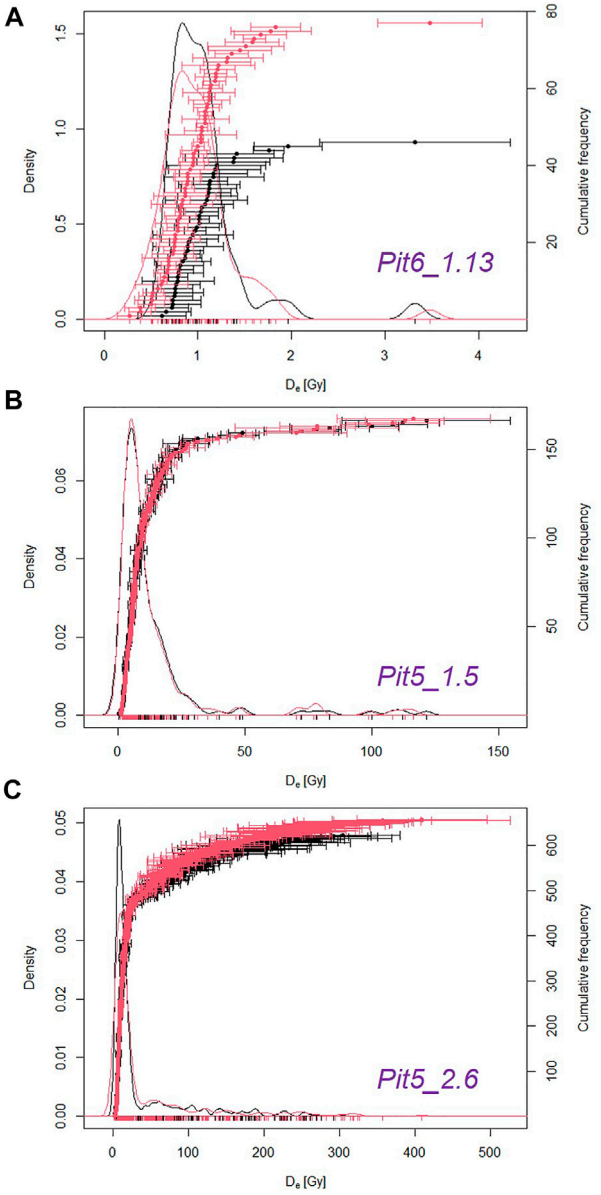

FIGURE 3
Comparison of the D_e values derived using SAR DRCs (black color) and those derived using rSGCs (σ_b =0, red color). **(A)** Sample Pit 6_1.13; **(B)** Sample Pit5_1.15; **(C)** Sample Pit5_2.6.

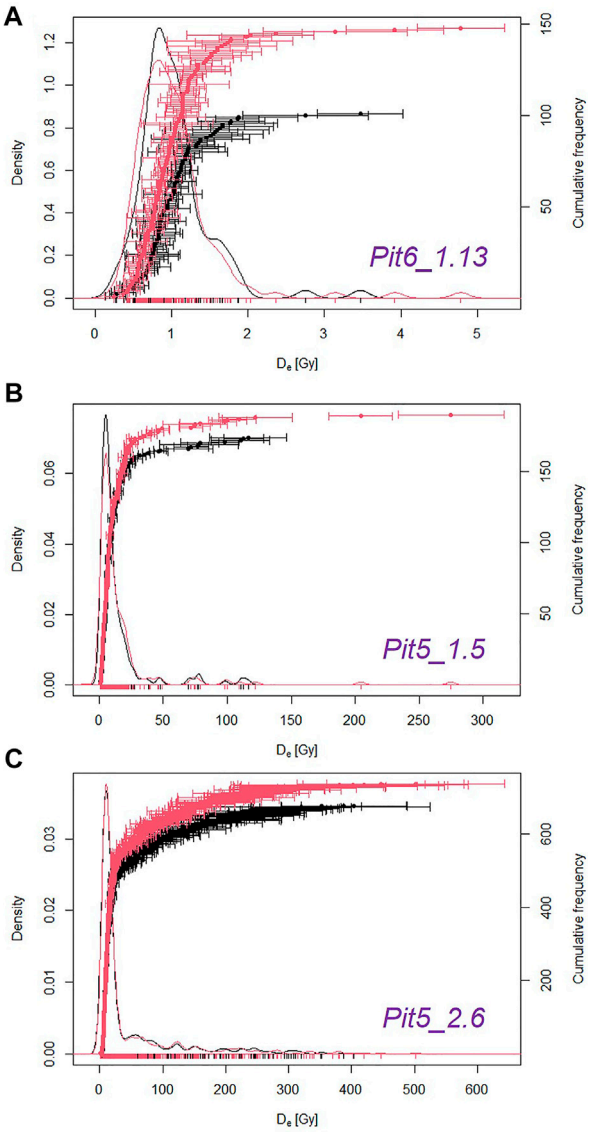

FIGURE 4
Comparison of the D_e values derived using rSGCs (σ_b =0, black color) and those derived using cSGCs (red color). **(A)** Sample Pit 6_1.13; **(B)** Sample Pit5_1.15; **(C)** Sample Pit5_2.6.

(Pit5_1.5, Pit5_2.6, and Pit6_1.13) in Figure 3 and Supplementary Figure S5. For a well-bleached beach sample (Pit6_1.13), the SAR and rSGC D_e (σ_b = 0) distributions have overdispersion values of 20.0 ± 4.8 and 29.8 ± 2.9%, respectively, with most individual D_e values spread randomly about a weighted mean D_e of ~0.98 Gy (Figure 3A). As the CAM D_es are consistent at 2σ (Table 1), we suggest that this increased spread for rSGC D_es does not affect the weighted mean D_e to a significant extent, and similar observations were previously stated by Fu et al. (2020). For lacustrine samples (Pit5_1.5 and Pit5_2.6), both of them showed broad and continuous distribution of D_e values (Figures 3B,C); the corresponding OD values are 94.9 and 106.0% for SAR D_es and 93.3 and 113.1% for rSGC D_es (σ_b = 0). The large spread in D_e may be due to heterogeneous bleaching prior to deposition and/or reworking by bioturbation. In addition to CAM D_e, the Minimum Age Model (MAM) was also applied to these samples to partly identify well-bleached grains. Except the CAM D_e value for Pit5_2.6, the weighted mean D_e values by different

TABLE 1 Weighted mean D_e values for SAR, rSGC, and cSGC. A σ_b value of 0.3 was applied for MAM D_e estimation.

Sample	No. of grains	OD	Approach	Age model 1	D_e (Gy)	Age model 2	D_e (Gy)
Pit6_1.13	53	20.0 ± 4.8	SAR	CAM	0.98 ± 0.04		
	101	29.8 ± 2.9	rSGC (σ_b = 0)	CAM	0.95 ± 0.03		
	101	29.3 ± 2.8	rSGC (σ_b = 0.06)	CAM	0.96 ± 0.03		
	148	36.2 ± 2.6	cSGC	CAM	0.93 ± 0.03		
Pit5_1.5	168	94.9 ± 5.4	SAR	CAM	7.68 ± 0.57	MAM	2.31 ± 0.25
	174	93.3 ± 5.1	rSGC (σ_b = 0)	CAM	7.87 ± 0.56	MAM	2.30 ± 0.22
	176	100.1 ± 5.5	rSGC (σ_b = 0.06)	CAM	8.18 ± 0.63	MAM	2.21 ± 0.22
	190	101.0 ± 5.3	cSGC	CAM	8.40 ± 0.62	MAM	2.14 ± 0.21
Pi5_2.6	626	106.0 ± 3.1	SAR	CAM	17.19 ± 0.74	MAM	7.92 ± 0.30
	678	113.1 ± 3.1	rSGC (σ_b = 0)	CAM	19.00 ± 0.84	MAM	7.67 ± 0.30
	685	114.1 ± 3.2	rSGC (σ_b = 0.06)	CAM	19.53 ± 0.86	MAM	7.75 ± 0.30
	738	113.5 ± 3.0	cSGC	CAM	19.50 ± 0.82	MAM	7.57 ± 0.36

measurement methods (i.e., SAR and rSGC) for these samples are consistent at 2σ (Table 1). Sample Pit5_2.6 includes grains with large D_e values, and around 124 grains (account for 20% of accepted grains) were rejected for criteria 6) and 7) (Supplementary Table S4), which lead to truncation of the full D_e distribution. As the shape for DRCs is different from that of rSGCs, few grains (i.e., 66 grains, account for 10% of accepted grains) were rejected because of extrapolation or saturation. With reduced impact by truncation, the obtained CAM D_e increased from 17.2 ± 0.7 Gy (by SAR data) to 19.0 ± 0.8 Gy (by rSGC data) (Table 1). Regardless of the saturated grains, the general consistency between SAR and rSGC D_es (σ_b = 0) supports that rSGCs perform well for Lake Woods samples. In addition, the OD and the D_e estimates by the CAM and MAM obtained by eight group SGCs are in agreement with those for D_es obtained by five group SGCs (Table 1), and we suggest both rSGC sets are reliable for D_e estimation in Lake Woods.

3.3 Continental SGC verification

In an ideal situation (i.e., the cSGC is reliable for samples from Lake Woods), only three SAR cycles are necessary for cSGC D_e estimation, which involves one cycle for the natural signal and two for regenerative doses, and rejection criteria 1), 4), 6), 7), and 8) can be applied to them. Thus, for each grain, we selected the natural signal, the signal for the second lowest regenerative dose (the lowest being 0 Gy), which lies in the linear portion of the DRC, and the signal for the largest or second largest regenerative dose (which lies beyond the linear region) for cSGC D_e calculation. Using this approach, more grains are accepted than that for SAR or rSGC analysis (Supplementary Table S4). The two selected regenerative doses were referred as D_{r1} and D_{r2}, respectively. The ratio between the L_x/T_x values of D_{r1} and D_{r2} for each accepted grain is calculated, and the obtained ratio is compared with the corresponding ratio for each of the six cSGCs; the latter ratios were calculated by dividing the SGC values at D_{r2} by those at D_{r1}. As the L_x/T_x ratio can quantify the saturation characteristics (e.g., shape of DRC or SGC) of different grains or different group SGCs (Li et al., 2016), this comparison can help us select the specific SGC with similar saturation characteristics to the studied grain. Based on this step, each grain was assigned to one of the six groups from Fu et al., (2020). To normalize the natural signal, the L_{r1}/T_{r1} and L_{r2}/T_{r2} for each grain are multiplied by a scaling factor, such that the sum of squared residuals is minimized. With the scaling factor, the normalized L_n/T_n value can be projected onto the relevant cSGCs to get cSGC D_e, and the obtained cSGC D_e show excellent statistical consistency with the SAR D_e (Figure 2C) and with the rSGC D_e estimates (Supplementary Figure S6A). Around 92.5% of the cSGC-to-SAR D_e ratios (Figure 2D) and 93.9% of the cSGC-to-rSGC D_e ratios (Supplementary Figure S6B) are within 2σ, which validate the use of cSGCs for rapid and robust D_e estimation for quartz grains from Lake Woods.

D_e distributions for the three representative samples (discussed in Section 3.2) are visualized using probability density plots in Figure 4, and the patterns of D_e distributions are generally consistent between the cSGC and rSGC datasets. The OD and the D_e estimates by the CAM and MAM for D_es obtained by cSGC are in agreement with those for D_es obtained by rSGC (Table 1), which further prove the reliability of cSGCs.

4 Conclusion

The application of the cSGC (following Fu et al., 2020) has been successfully verified for coarse-grained quartz samples from Lake Woods. For samples without saturated grains, the D_e values obtained by the cSGC are consistent with the D_e values obtained by the rSGCs and by the SAR procedures. With the verification of the cSGCs, at least 50% of instrument time can be saved comparing the traditional SAR procedure (three SAR cycles for cSGC D_e vs. around seven cycles for SAR D_e measurement), and large instrument time for building rSGC can also be saved (~440 h in this study).

Author contributions

TC conducted the field investigation and collected all samples. XR and TC carried out all the laboratory work. XR, BL, and TC conducted the data analysis and manuscript writing.

Funding

This study was supported by an Australian Research Council (ARC) Future Fellowship to Bo Li (FT140100384), a Foundation for Outstanding Young Teachers in Jilin University to Xue Rui (Grant No. 419080520486), and the ARC Centres of Excellence scheme (Project Number CE170100015) and the ARC Future Fellowship scheme (FT180100524) to Tim Cohen.

Acknowledgments

We thank Richard G. Roberts, Zenobia Jacobs, Yasaman Jafar, and Terry Lachlan for essential support in the luminescence dating laboratory. The open-access publication fee will be provided by Jilin University.

Conflict of interest

The authors declare that the research was conducted in the absence of any commercial or financial relationships that could be construed as a potential conflict of interest.

Publisher's note

All claims expressed in this article are solely those of the authors and do not necessarily represent those of their affiliated organizations, or those of the publisher, the editors, and the reviewers. Any product that may be evaluated in this article, or claim that may be made by its manufacturer, is not guaranteed or endorsed by the publisher.

Supplementary material

The Supplementary Material for this article can be found online at: https://www.frontiersin.org/articles/10.3389/feart.2022.939964/full#supplementary-material

References

Burbidge, C., Duller, G., and Roberts, H. (2006). D_e determination for young samples using the standardised OSL response of coarse-grain quartz. *Radiat. Meas.* 41, 278–288. doi:10.1016/j.radmeas.2005.06.038

Chen, G. Q., Yi, L., Xu, X. Y., Yu, H. J., Cao, J. R., Su, Q., et al. (2013). Testing the standardized growth curve (SGC) to OSL dating coastal sediments from the south Bohai Sea, China. *Geochronometria* 40, 101–112. doi:10.2478/s13386-013-0103-z

Fu, X., Li, B., Jacobs, Z., Jankowski, N. R., Cohen, T. J., and Roberts, R. G. (2020). Establishing standardised growth curves (SGCs) for OSL signals from individual grains of quartz: A continental-scale case study. *Quat. Geochronol.* 60, 101107. doi:10.1016/j.quageo.2020.101107

Galbraith, R. F., Roberts, R. G., Laslett, G. M., Yoshida, H., and Olley, J. M. (1999). Optical dating of single and multiple grains of quartz from jinmium rock shelter, northern Australia: Part I, experimental design and statistical models. *Archaeometry* 41, 339–364. doi:10.1111/j.1475-4754.1999.tb00987.x

Guralnik, B., Li, B., Jain, M., Chen, R., Paris, R. B., Murray, A. S., et al. (2015). Radiation-induced growth and isothermal decay of infrared-stimulated luminescence from feldspar. *Radiat. Meas.* 81, 224–231. doi:10.1016/j.radmeas.2015.02.011

Hu, Y., Li, B., and Jacob, Z. (2019). Single-grain quartz OSL characteristics: Testing for correlations within and between sites in Asia, Europe and Africa. *Methods Protoc.* 3 (1), 2. doi:10.3390/mps3010002

Jacobs, Z., Duller, G. A. T., and Wintle, A. G. (2006). Interpretation of single grain distributions and calculation of. *Radiat. Meas.* 41, 264–277. doi:10.1016/j.radmeas.2005.07.027

Lai, Z.-P., Brückner, H., Zöller, L., and Fülling, A. (2007). Existence of a common growth curve for silt-sized quartz OSL of loess from different continents. *Radiat. Meas.* 42, 1432–1440. doi:10.1016/j.radmeas.2007.08.006

Lai, Z. (2006). Testing the use of an OSL standardised growth curve (SGC) for determination on quartz from the Chinese Loess Plateau. *Radiat. Meas.* 41, 9–16. doi:10.1016/j.radmeas.2005.06.031

Li, B., Jacobs, Z., and Roberts, R. G. (2016). Investigation of the applicability of standardised growth curves for OSL dating of quartz from Haua Fteah cave, Libya. *Quat. Geochronol.* 35, 1–15. doi:10.1016/j.quageo.2016.05.001

Li, B., Roberts, R. G., Jacobs, Z., and Li, S.-H. (2015). Potential of establishing a 'global standardised growth curve' (gSGC) for optical dating of quartz from sediments. *Quat. Geochronol.* 27, 94–104. doi:10.1016/j.quageo.2015.02.011

Long, H., Lai, Z., Fan, Q., Sun, Y., and Liu, X. (2010). Applicability of a quartz OSL standardised growth curve for De determination up to 400 Gy for lacustrine sediments from the Qaidam Basin of the Qinghai-Tibetan Plateau. *Quat. Geochronol.* 5, 212–217. doi:10.1016/j.quageo.2009.05.005

Murray, A. S., and Wintle, A. G. (2000). Luminescence dating of quartz using an improved single-aliquot regenerative-dose protocol. *Radiat. Meas.* 32, 57–73. doi:10.1016/s1350-4487(99)00253-x

Peng, J., and Li, B. (2017). Single-aliquot regenerative-dose (SAR) and standardised growth curve (SGC) equivalent dose determination in a batch model using the R package 'numOSL. *Anc. TL* 35, 32–53. http://ancienttl.org/ATL_35-2_2017/ATL_35-2_Peng_p32-53.pdf.

Peng, J., Pagonis, V., and Li, B. (2016). On the intrinsic accuracy and precision of the standardised growth curve (SGC) and global-SGC (gSGC) methods for

equivalent dose determination: A simulation study. *Radiat. Meas.* 94, 53–64. doi:10.1016/j.radmeas.2016.09.006

Roberts, H., and Duller, G. A. (2004). Standardised growth curves for optical dating of sediment using multiple-grain aliquots. *Radiat. Meas.* 38, 241–252. doi:10.1016/j.radmeas.2003.10.001

Roberts, R. G., Galbraith, R., Yoshida, H., Laslett, G., and Olley, J. M. (2000). Distinguishing dose populations in sediment mixtures: A test of single-grain optical dating procedures using mixtures of laboratory-dosed quartz. *Radiat. Meas.* 32, 459–465. doi:10.1016/s1350-4487(00)00104-9

Stevens, T., Armitage, S. J., Lu, H., and Thomas, D. S. (2007). Examining the potential of high sampling resolution OSL dating of Chinese loess. *Quat. Geochronol.* 2, 15–22. doi:10.1016/j.quageo.2006.03.004

Telfer, M., Bateman, M., Carr, A., and Chase, B. (2008). Testing the applicability of a standardized growth curve (SGC) for quartz OSL dating: Kalahari dunes, South African coastal dunes and Florida dune cordons. *Quat. Geochronol.* 3, 137–142. doi:10.1016/j.quageo.2007.08.001

Wang, X., Qiu, F., Nian, X., Liu, R., and Zhang, W. (2022). Testing the applicability of standardised growth curves (SGCs) for OSL signals of quartz grains from the Yangtze Delta, China. *Quat. Geochronol.* 72, 101348. doi:10.1016/j.quageo.2022.101348

Wintle, A. G. (1997). Luminescence dating: Laboratory procedures and protocols. *Radiat. Meas.* 27, 769–817. doi:10.1016/s1350-4487(97)00220-5

Wintle, A. G., and Murray, A. S. (2006). A review of quartz optically stimulated luminescence characteristics and their relevance in single-aliquot regeneration dating protocols. *Radiat. Meas.* 41, 369–391. doi:10.1016/j.radmeas.2005.11.001

Yang, L., Lai, Z., Long, H., and Zhang, J. (2011). Construction of a quartz OSL standardised growth curve (SGC) for aeolian samples from the Horqin dunefield in northeastern China. *Geochronometria* 38, 391–396. doi:10.2478/s13386-011-0045-2

frontiers | Frontiers in Earth Science

TYPE Original Research
PUBLISHED 06 January 2023
DOI 10.3389/feart.2022.933131

OPEN ACCESS

EDITED BY
Hui Zhao,
Chinese Academy of Sciences (CAS), China

REVIEWED BY
Xiangjun Liu,
Jiaying University, China
Yuxin Fan,
Lanzhou University, China

*CORRESPONDENCE
Jingran Zhang,
jingranzhang@daad-alumni.de

†PRESENT ADDRESS
Benny Guralnik,
CAPRES–a KLA Company, Kongens Lyngby, Denmark

SPECIALTY SECTION
This article was submitted to Quaternary Science, Geomorphology and Paleoenvironment, a section of the journal Frontiers in Earth Science

RECEIVED 30 April 2022
ACCEPTED 22 August 2022
PUBLISHED 06 January 2023

CITATION
Zhang J, Guralnik B, Tsukamoto S, Ankjærgaard C and Reimann T (2023), The bleaching limits of IRSL signals at various stimulation temperatures and their potential inference of the pre-burial light exposure duration. *Front. Earth Sci.* 10:933131. doi: 10.3389/feart.2022.933131

The bleaching limits of IRSL signals at various stimulation temperatures and their potential inference of the pre-burial light exposure duration

Jingran Zhang[1]*, Benny Guralnik[2†], Sumiko Tsukamoto[3], Christina Ankjærgaard[4] and Tony Reimann[5]

[1]School of Geography, Nanjing Normal University, Key Laboratory of Virtual Geographic Environment, Ministry of Education of China, Jiangsu Open Laboratory of Major Scientific Instrument and Equipment, Nanjing, China, [2]Technical University of Denmark, Kongens Lyngby, Denmark, [3]Leibniz Institute for Applied Geophysics, Hannover, Germany, [4]Department of Health Technology, Technical University of Denmark, Roskilde, Denmark, [5]Institute of Geography, University of Cologne, Cologne, Germany

Infrared Stimulated Luminescence (IRSL) techniques are being increasingly used for dating sedimentary feldspars in the middle to late Quaternary. By employing several subsequent stimulations at increasing temperatures, a series of post-IR IRSL (pIRIR) signals with different characteristics (stability and bleachability) can be obtained for an individual sample. It has been experimentally demonstrated that higher-temperature pIRIR signals are more stable, but they tend to exhibit larger residual doses up to few tens of Gy, potentially causing severe age overestimation in young samples. In this study we conducted comprehensive bleaching experiments of IRSL and pIRIR signals using a loess sample from China, and demonstrated that non-bleachable components in the IR (and possibly pIRIR) signals do exist. The level of such non-bleachable signal shows clearly positive correlation with preheat/stimulation temperature, which further supports the notion that lower temperature pIRIR are advantageous to date young samples and sediments especially from difficult-to-bleach environments. These results display a potential in constrain the pre-burial light exposure history of sediment utilizing multiple feldspar post-IR IRSL (pIRIR) signals. For the studied loess sample, we infer that prior to its last burial, the sample has received an equivalent of >264 h exposure to the SOL2 simulator (more than 2,000 h of natural daylight).

KEYWORDS

post-IR IRSL, bleaching experiment, non-bleachable signal, residual dose, pre-burial exposure

Introduction

Luminescence dating is a widely established Quaternary dating method, which is typically used to quantify the amount of time elapsed since a sediment has been last exposed to sunlight (Rhodes, 2011). The method is based on interpolating the natural luminescence intensity onto a regenerated dose response in the laboratory, producing an equivalent dose (D_e) which is the dose the sample has received in nature. The post-IR IRSL (pIRIR) technique, including the two-step pIRIR (Thomsen et al., 2008; Thiel et al., 2011) and multi-elevated-temperature (MET) pIRIR (Li and Li, 2011; Fu and Li, 2013), has been developed based upon the conventional IRSL for dating various sedimentary feldspars. The stability and bleachability are two crucial properties of any luminescence signal to be used for reliable dating, and in the case of feldspar IRSL or pIRIR seem to be interrelated (Jain et al., 2012). The fading rate of pIRIR signals generally decreases with higher stimulation temperature (e.g., Thomsen et al., 2008; Thiel et al., 2011; Li and Li, 2011; Buylaert et al., 2012), however the more stable signals are also progressively difficult to bleach (e.g., Li and Li, 2011; Kars et al., 2014a; Colarossi et al., 2015). As a result, pIRIR signals may be unaffected by anomalous fading but raise concerns about potential age overestimation caused by the unbleachable component (residual), especially for young samples.

So far, the origin and underlying mechanism of this residual signal is still poorly understood. The bleachability and the subsequent residual dose of pIRIR signals has drawn intensive discussions about its effect on a reliable dose determination and whether it should be subtracted. In some cases, modern analogues or artificially bleached samples have also been employed to check the bleachability and any residual dose subtraction (e.g., Buylaert et al., 2011; Li and Li, 2011; Reimann et al., 2011; Fu et al., 2012). Buylaert et al. (2012) proposed a sample-independent characteristic residual of ~4 ± 2 Gy for the pIRIR signal measured at 290°C ($pIRIR_{290}$), as obtained from a finite intercept extrapolated from a group of samples with different burial doses. A commonly agreed opinion is that residual doses might be negligible for older samples but could cause severe age overestimation for young samples. Interestingly, Sohbati et al. (2012) and Zhang et al. (2015a) reported no significant unbleachable residual dose (<10 Gy) in both IR_{50} and $pIRIR_{225}$ signals (after 4 h of SOL2 bleaching), although a positive correlation between the residual doses and the natural doses was noticed. Consequently, no residual correction has been applied for their ages. Conversely, Buylaert et al. (2013) observed no significant trend of residual doses (due to 4 h SOL2) against their corresponding natural doses, and adopted a mean residual dose of 12.6 ± 0.7 Gy to be subtracted from all natural D_es. This difficult-to-bleach component of the pIRIR signal has been considered arising from thermal transfer (Buylaert et al., 2012, 2013). Kars et al. (2014a) carried out comprehensive bleaching experiments for feldspar by exposing samples in the solar simulator with a series of exposure time from 1 h to 11 days. They demonstrated that pIRIR signals measured at higher temperatures are increasingly harder to bleach but none of their bleaching curves reach a plateau within 11 days of solar simulator exposure. Later on, Colarossi et al. (2015) argued that there may be no unbleachable component of pIRIR signal based on the fact that both IR_{50} and pIRIR signals derived from $pIRIR_{225}$ and $pIRIR_{290}$ protocols display a monotonic decrease and do not reach a stable unbleachable limit within 14 days of solar simulator exposure, similar to that of Kars et al. (2014a). However, it is noteworthy that there is still a considerable amount of signal remaining even after 14 days exposure to the solar simulator especially for higher stimulation temperature (e.g., $pIRIR_{290}$) in both studies. Furthermore, Kars et al. (2014a) demonstrated a tendency that the pIRIR signal of young samples bleached much slower than that of the older samples. Yi et al. (2016, 2018) carried out prolonged bleaching experiments (>80 days in solar simulator) for $pIRIR_{290}$ of loess samples from northeastern and southeastern China. The $pIRIR_{290}$ residual signals reached a plateau after ~300 h exposure in both studies, and a constant residual corresponding to a dose of 4–6 Gy were observed. More recently, Cheng et al. (2022) investigated the bleachability of the single grain K-feldspar pIRIR signals and observed significant variations in residual doses (ranging from ~1 Gy to up to ~37 Gy after 40 h sunlight bleaching) among different grains from the same sample, that could cause additional scatter in D_e values.

Due to their differential bleaching rates, the comparison of feldspar IRSL and pIRIR ages with quartz OSL ages can be used to identify well bleached quartz (Murray et al., 2012), and even qualitatively determine the degree of bleaching (Reimann et al., 2015) helping to infer the transport history of various sediments. The development of rock surface exposure dating has allowed to quantify the amount of time that a rock surface has been exposed to sunlight, via utilizing the spatiotemporal evolution of the luminescence bleaching front within a solid (Sohbati, 2013). However, the exposure time of sediments to sunlight prior to their deposition is a relatively unexplored area (Reimann et al., 2015) where assumptions and speculations often dominate. The length of a sediment's exposure to sunlight prior to its deposition is important especially in young samples, where incomplete signal bleaching has the greatest effect on the age of the sediment (resulting in age overestimation). Very often, "modern analogues" (e.g., sediment from a nearby active channel) are used to quantify the expected "residual dose" in the sample of interest (e.g., Buylaert et al., 2009; Reimann et al., 2012; Li et al., 2014); however, such an estimation is valid only if both the modern sediment and the sample of interest experienced the same depositional environments, which is often questionable. Another existing approach is to administer a laboratory bleach for an arbitrary amount of time, and assume that it resets the signal to the level that it experienced in nature (reviewed in Li et al., 2014). Nevertheless, the degree of sediment bleaching prior

TABLE 1 Modified SAR protocol for pIRIR measurements.

Step	Measurement	Observation	Remark
1	Give dose, D_i (i=0, 1, 2, 3. . .)		
2	Preheat for 60 s @ 180–340°C with 20°C interval		
3	IR stimulation, 120 s at 50°C	L_x	IR_{50}
4	IR stimulation for 240 s @ 30°C below preheat in Step 2	L_x	pIRIR
5	Given dose, D_T (~1.72 Gy)		
6	Preheat for 60 s, @180–340°C with 20°C interval		
7	IR stimulation, 120 s @ 50°C	T_x	IR_{50}
8	IR stimulation, 240 s @ 30°C below preheat in Step 2	T_x	pIRIR
9	Return to step 1		

to deposition often remains unknown, and requires further investigation to prevent biased chronologies.

In this study, we measure multiple feldspar IR_{50} and pIRIR signals, and quantify their bleaching rates in the laboratory using SOL2. Through knowledge of an independent age of the same sample, we estimate pIRIR residual doses, and interpolate them onto a laboratory bleaching curve to obtain what we define as the equivalent bleaching time, B_e. This measure then allows us to infer the pre-burial light exposure duration.

Materials and methods

One young loess sample (LUM-2941) from China was chosen to explore the bleaching limit of its IRSL signals (both IR_{50} and pIRIR) at various thermal treatment conditions. It was collected from the northern piedmont of the Qilian Mountain, northwestern China (Zhang et al., 2015a; 2015b), and has been dated using both quartz and polymineral fine grains. The quartz OSL dating yielded an age of 6.3 ± 0.4 ka (Zhang et al., 2015b). The corresponding feldspar fading-corrected ages ranged between 5.8 ± 0.1 ka for $pIRIR_{150}$ and 7.2 ± 0.1 ka for $pIRIR_{310}$ (Zhang et al., 2015a). The dose rates for quartz and feldspar age calculation are 4.31 ± 0.25 Gy/ka and 4.89 ± 0.26 Gy/ka, respectively.

In this study, 14 groups of subsamples (27 aliquots in each group) were bleached in a Hönle SOL2 solar simulator using the full spectrum light, with exposure time ranging between 1 min and 20 days. An extra group of subsamples was prepared without SOL2 bleaching to obtain the natural signal as a reference. All measurements were carried out with an automated Risø DA-15 TL/OSL reader equipped with $^{90}Sr/^{90}Y$ beta source. The feldspar signal of the samples was stimulated with an array of infrared light diodes emitting at 870 nm, and the luminescence was detected through a filter combination of Schott BG39 and Corning 7–59 in the blue-violet region. Modified single-aliquot regenerative dose (SAR) protocols described in Zhang et al. (2015a) were applied; the preheat temperatures varied between 180 and 340°C with 20°C interval and the second stimulation temperature was always 30°C lower than the preheat temperature (Table 1). The test dose was 1.72 Gy. Each data point is the average result of 3 aliquots.

Since the IRSL of feldspar is based on the localized recombination of electrons to nearest neighbour holes, it is expected that the IR_{50} and pIRIR bleaching curves follow power law decay (e.g., Jain et al., 2012). Therefore all bleaching curves were fitted with

$$I = At^{-b} + c \quad (1)$$

where I is normalized luminescence intensity after bleaching, A is a constant, t is the time, b is bleaching rate, and c is residual signal intensity.

Taking the independent age constraint of quartz OSL (6.3 ± 0.4 ka) as the true depositional age, the expected D_e of 30.8 ± 2.6 Gy was obtained for the sample. The fading corrected D_es of the sample were calculated based on the fading corrected feldspar ages (Zhang et al., 2015a) using the R 'Luminescence'-package (Dietze et al., 2013) according to the method of Huntley and Lamothe (2001). The difference between the fading-corrected D_es and the expected D_e (Table 2) was termed "predicted residual dose", and evaluated against the optical bleaching data using a reduced chi-square statistic (Bevington and Robinson, 2003).

Bleaching characteristics of feldspar IRSL signals

The luminescence intensity (L_n/T_n) of the IR_{50} (Figure 1A) and the pIRIR signals (Figure 1B) from all bleached subsamples was normalized to that of the natural subsamples (without bleaching) and plotted against SOL2 exposure time on a log-log scale. It is noteworthy that there is a kink exhibited for all bleaching curves at 1 hour exposure time, especially for pIRIR signals. It is because a new lamp in the solar simulator was used for the first five data points, referring to 1, 3, 5 min 10 and 20 min

TABLE 2 The measured IR_{50} and pIRIR D_es, g-values and the "predicted residual dose" (fading-corrected D_e minus expected D_e) at various temperatures. The measured D_es were previously presented in Zhang et al. (2015a). The expected D_e of 30.8 ± 2.5 Gy is calculated from the quartz OSL age of 6.3 ± 0.4 ka (Zhang et al., 2015b).

Preheat temperature (°C)	Measured D_e (Gy)		g-value (%/decade)		Fading-corrected D_e (Gy)		Predicted residual dose (Gy)	
	IR_{50}	pIRIR	IR_{50}	pIRIR	IR_{50}	pIRIR	IR_{50}	pIRIR
180	21.9 ± 0.2	25.7 ± 0.2	2.84 ± 0.12	1.14 ± 0.22	28.5 ± 3.4	28.2 ± 1.6	-2.3 ± 4.3	-2.6 ± 3.0
200	23.3 ± 0.1	26.8 ± 0.1	2.90 ± 0.15	1.15 ± 0.03	30.3 ± 2.2	29.5 ± 1.6	-0.6 ± 3.4	-1.4 ± 3.0
220	25.0 ± 0.2	28.9 ± 0.2	2.56 ± 0.09	1.34 ± 0.40	31.7 ± 2.6	32.5 ± 2.1	0.9 ± 3.7	1.6 ± 3.3
240	26.6 ± 0.3	30.9 ± 0.2	2.45 ± 0.20	1.17 ± 0.25	33.3 ± 4.2	34.3 ± 2.0	2.4 ± 4.9	3.5 ± 3.2
260	27.8 ± 0.6	31.6 ± 0.8	2.06 ± 0.21	0.98 ± 0.15	33.5 ± 2.0	34.3 ± 2.1	2.7 ± 3.3	3.5 ± 3.3
280	25.9 ± 0.3	30.6 ± 0.1	1.69 ± 0.35	0.86 ± 0.34	30.1 ± 2.0	32.9 ± 1.9	-0.8 ± 3.2	2.1 ± 3.2
300	24.2 ± 0.2	31.7 ± 0.4	1.33 ± 0.15	0.75 ± 0.15	27.2 ± 1.5	33.7 ± 1.9	-3.7 ± 3.0	2.8 ± 3.2
320	23.9 ± 0.9	33.5 ± 0.3	1.07 ± 0.21	0.52 ± 0.34	26.3 ± 1.7	34.9 ± 2.1	-4.6 ± 3.1	4.0 ± 3.3
340	22.4 ± 0.8	35.5 ± 0.6	0.40 ± 1.02	-0.29 ± 0.73	23.1 ± 2.4	35.5 ± 0.6	-7.8 ± 3.5	4.6 ± 2.6

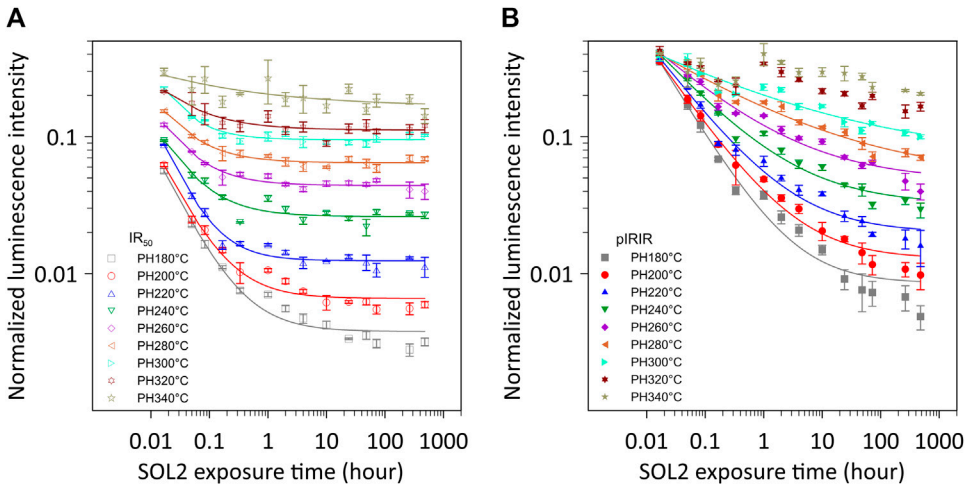

FIGURE 1
Normalized IR_{50} **(A)** and pIRIR **(B)** luminescence intensity under various preheat (stimulation) temperatures, plotted against SOL2 bleaching time. The pIRIR stimulation temperature is always 30°C below the preheat temperature. The bleaching curves were fitted with the Eq. 1.

exposure time, as they were not included in the initial design of the experiment. Nevertheless, the general trend of these bleaching curves is not affected. As expected, the pIRIR signals bleach noticeably slower than their corresponding IR_{50} signals, which is in line with previous studies. As shown in Figure 1, after 1 min (0.017 h) bleaching, the remaining IR_{50} signals accounted for 6% of its natural signal intensity for the lowest temperature to up to 30% for the highest temperature, while all pIRIR signals are reduced to ~35–40%, with a similar trend like the IR_{50} signals. The majority of the IR_{50} bleaching data shows a noticeably nonlinear trend on a log-log scale, asymptoting to a bleaching plateau after ~10 h exposure with seemingly unbleachable signals of up to 14% of their initial intensity (e.g. preheat at 340°C). Conversely, the pIRIR bleaching data do not appear to reach a steady-state level after 480 h exposure in SOL2 solar simulator. These findings are in line with Kars et al. (2014a) and Colarossi et al. (2015).

The bleaching curves were fitted to Eq. 1 given above. The fitted decay rate (b) and relative residual intensity (c) normalized to the natural signal are plotted in Figure 2. It was difficult to accurately fit the decay rate for the IR_{50} signals, because the majority of the signals were bleached before 1 min (0.017 h)

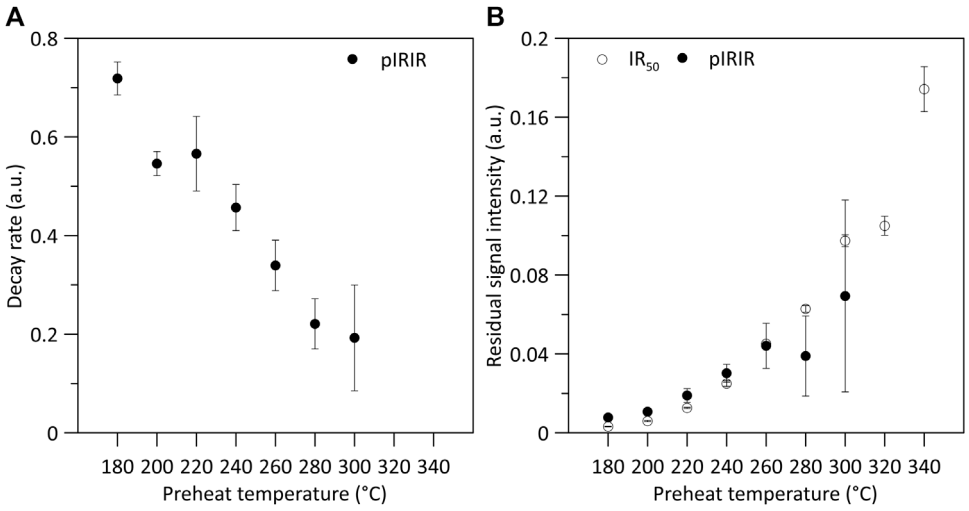

FIGURE 2
(A) The fitted decay rate of pIRIR signals, and **(B)** relative residual intensity normalized to the natural signal for both IR_{50} and pIRIR signals.

SOL2 exposure. The decay rate for the pIRIR signals shows a clear decreasing trend with increasing preheat (and stimulation) temperature (Figure 2A). The pIRIR bleaching curve for the two highest preheat temperatures could not be fitted to due to the scatter of the data. Nevertheless, Figure 2B indicates that the relative residual signal level, which increases with preheat temperature, is consistent between the IR_{50} and pIRIR signals for a same preheat temperature.

The preheat temperature dependence of the feldspar bleaching rate is in accordance with other studies (e.g., Li and Li, 2011; Lowick et al., 2012; Kars et al., 2014a; Colarossi et al., 2015; Reimann et al., 2015), and may be a result of increased distance between traps and recombination centres (e.g., Kars et al., 2014a). For both IR_{50} and pIRIR, more signal remains as the preheat temperature is raised (Figures 1A,B). The bleaching curve of IR_{50} after a 340°C preheat shows almost no clear decrease regardless of the exposure time. This may infer that the light-sensitive charges remaining after the SOL2 exposure have been further thermally removed during the high preheat and most of the detected signals might be originated from the thermal transfer of charge from light-insensitive traps to the IR-sensitive trap (Buylaert et al., 2011). The higher the temperature, the more charges could be thermally transferred. However, this does not explain the plateau at lower preheat temperatures (e.g.<200°C), at which thermal transfer should be minimal. An alternative explanation for the bleaching plateau may involve a competition between optical bleaching of the IR sensitive traps by SOL2, and repopulation of the same traps due to the UV component of the bleaching light (Ollerhead and Huntley, 2011). The equilibrium between optical de-trapping and UV trap refilling could be expected after prolonged exposure, resulting in constant trap concentrations and hence bleaching curve plateaus. However, this hypothesis can also be questioned, as it cannot explain the presence of a plateau in one young coastal sample (W-Zi2; 0.84 ka) from Kars et al. (2014a), which was optically bleached with the UV part of the spectrum filtered out.

Based on the above observations, we confirm the presence of a non-bleachable component in the IRSL signal, and the high likelihood of the same phenomenon occurring in the pIRIR signal, and their strong correlation with preheat (stimulation) temperature. In order to minimize the effect of the residual signal on age determination, our results provide additional experimental evidence, and further support the notion that young samples should preferably be dated using lower preheat and stimulation temperatures in the pIRIR measurement protocol (Madsen et al., 2011; Reimann et al., 2011; Reimann and Tsukamoto, 2012; Zhang et al., 2015a; Reimann et al., 2015) or using the pulsed IR_{50} signal (Tsukamoto et al., 2017).

Inference of the pre-burial light exposure duration utilizing multiple feldspar pIRIR signals

The raw (i.e. fading uncorrected) measured D_e values of the IR_{50} and pIRIR signals of sample LUM-2941 (Zhang et al., 2015a) are shown as triangles in Figure 3. Alongside these direct measurements, the corresponding fading corrected D_e values are shown as squares. Up to 260°C, both IR_{50} and pIRIR datasets are generally in agreement, showing an increase in D_e values as a function of preheat temperature; above 260°C, the pIRIR D_es continue to increase, while the IR_{50} D_es reverse the

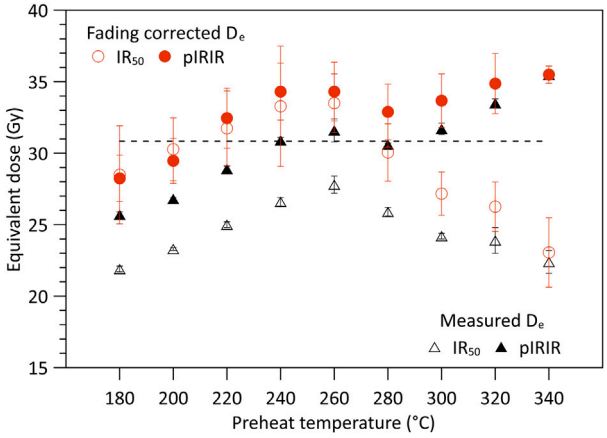

FIGURE 3
D_e values measured in the laboratory (triangles) and fading corrected D_es according to Zhang et al. (2015a). The dashed line denotes the expected D_e calculated based on the quartz OSL age. The $pIRIR_{310}$ D_e (preheat at 340°C) was not corrected as negative g-value was measured. The difference between the expected D_e and the fading corrected D_es is termed "predicted residual dose", and is further shown in Figure 4.

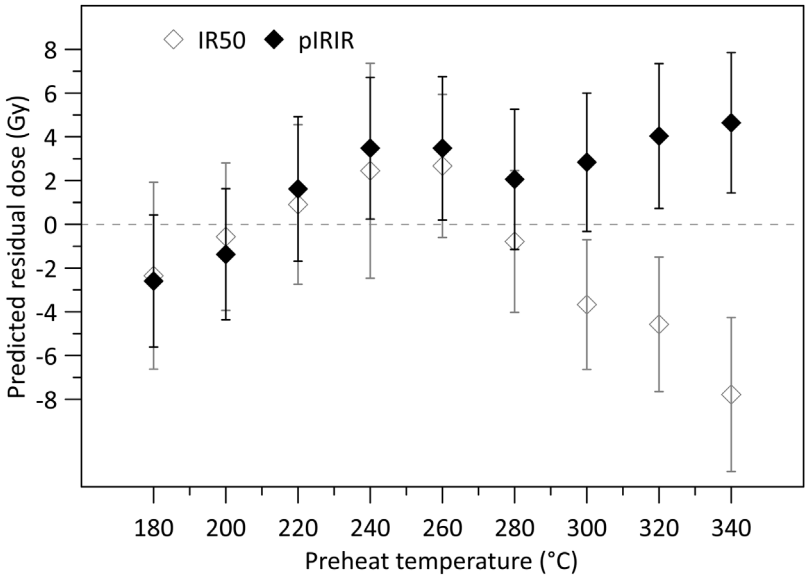

FIGURE 4
Predicted residual doses of the sample, corresponding to the differences between the fading-corrected D_es and the expected D_e (30.8 ± 2.6Gy). The detailed data were presented in Table 2.

trend and decrease, resulting in a peak D_e at a preheat of 260°C. The peak shape discloses an expectable artefact at preheat temperatures >260°C, which has been demonstrated by the failed dose recovery test of this sample (Figure 4A in Zhang et al. (2015a)) at the preheat temperatures >260°C. This behaviour of the IR_{50} signals may be explained by trapping sensitivity change (Kars et al., 2014b). In the complete absence of residual doses, the fading corrected D_es should have been the same as the expected D_e, given that the fading rate measurements and the applied model are both adequate. However, the fading corrected D_es of both IR_{50} and pIRIR signals deviated from the expected value, and displayed a similar trend as the measured ones. As expected, the predicted residual dose increased with preheat temperature, up to 4.6 Gy (Figure 4). This

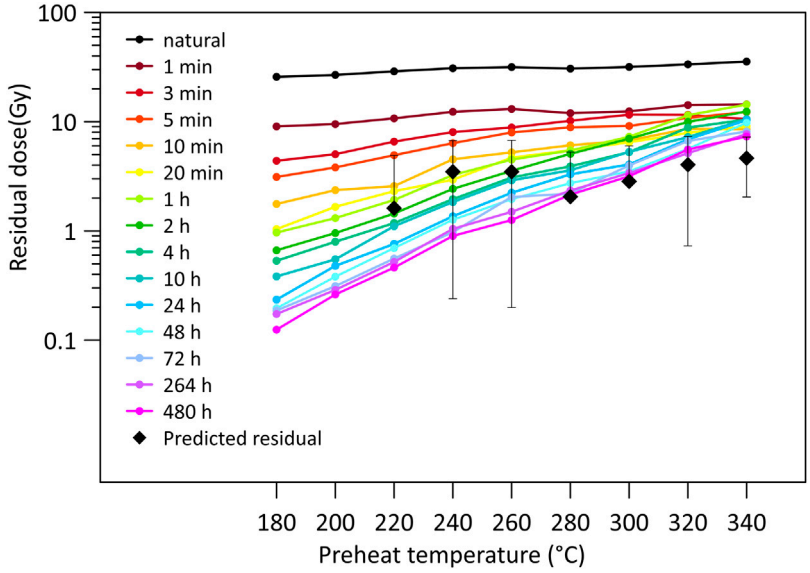

FIGURE 5
Predicted residual doses (solid diamonds; cf. Figure 4) superimposed onto the calculated residual doses from the laboratory bleaching experiments. The calculated residual doses refer to the remaining doses after different exposure times in SOL2. The uncertainties of the predicted residual doses were larger than the values themselves at preheat of 220, 280 and 300°C, so that the error bars on the negative direction cannot display on the log scale.

is in line with our observations in Figure 1, that the bleachability of feldspar pIRIR signals deteriorates towards higher measurement temperatures; consequently, higher residual doses for higher preheats may be expected, regardless of whether the sample is well or poorly bleached. It is noteworthy that for both IR_{50} and pIRIR signals, negative predicted residual doses were generated, which is unrealistic. One possible cause for negative residual doses is the uncertainty on the quartz OSL age (6.3 ± 0.4 ka); if the youngest age of 5.9 ka would be adopted, the negative values of the predicted residual doses would disappear. Another contributing factor is the well-documented trapping sensitivity change of the IR_{50} signal at preheat temperatures >260°C (Kars et al., 2014b), which makes the IR_{50} data not comparable across the different temperature. In the remainder of the paper, we therefore focus only on the pIRIR signal, which is also of primary interest for dating applications.

Since the dose response of the young sample is in its initial linear range, one can multiply the L_n/T_n depletion ratio of the bleaching experiments by the corresponding D_e of that pIRIR signal to obtain the remaining doses after different exposure times in SOL2. These are termed as "calculated residual dose", and are plotted against the corresponding preheat temperature in Figure 5. Predicted residual doses (solid black diamond; cf. Figure 4) were superimposed onto the calculated residual doses for comparison. Figure 5 shows that the light exposure that this sample experienced prior to burial is probably longer than an equivalent of 4 h exposure in solar simulator that usually applied in residual test.

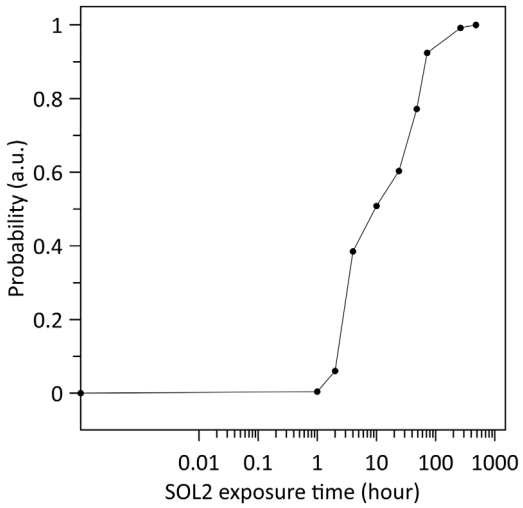

FIGURE 6
Probability of bleaching time prior to sedimentation, obtained by evaluating the goodness-of-fit of the predicted dose residuals against those from known bleaching times in Figure 5, using the reduced chi-square statistic.

To estimate the probability of the bleaching time in nature prior to burial (Figure 6), we evaluated the goodness-of-fit of the predicted residual doses (black diamond in Figure 5) against observed residuals due to known bleaching times in the laboratory (coloured curves in Figure 5), using the reduced chi-square statistic. This enables us to translate the residual dose from the multiple luminescence signals into a B_e value that the sample has likely experienced before its last depositional event. We treated the standardized difference between the observed and predicted residual doses at each of the nine temperatures as a random variable following a standard normal distribution. In this case the sum of squares of these differences will be itself a random variable following a Chi-square distribution with nine degrees of freedom. The bleaching degree is calculated as the integrated area under the upper tail of the probability density curve of the Chi-square distribution, that is, the larger the Chi-square random variable (i.e., the larger the sum of squares of the differences), the smaller the integrated area within the upper tail of the distribution and therefore the lower the degree of bleaching. When all 14 data points of various bleaching time were included, the probability (i.e., the degree of bleaching) showed an early peak at a bleaching time of 20 min (Supplementary Figure S1). We argued that the appearance of this peak is unrealistic for the following reason. As mentioned above, the bleaching results of the first five data points (i.e., with exposure times of 1, 3, 5, 10, and 20 min) were measured using a new lamp, that is, different from the remaining data points (i.e., the exposure times of 1, 2, 4, . . ., 480 h). As a consequence, a merger of the two sets of data will yield unexpected results. Accordingly, we excluded these five data point from Figure 6. We demonstrated that, for sample LUM-2941 collected from the northern piedmont of Qilian Mountains, when the laboratory exposure time exceeds 264 h, the corresponding bleaching degree is >95%. Since the intensity of SOL2 solar simulator is up to 9 times greater than daylight (Dr Honle Sol Sun simulation systems from Uvalight Technology Ltd, 1988), it means that this sample may experience more than two thousand hours daylight exposure prior to last burial in nature. This result implies that the use of standard residual subtraction (measured typically after 2–4 h bleach in SOL2; see Li et al., 2014) could lead to marked overestimation of the actual residual dose (264 h as in this study), leading to age underestimation which should be avoided.

According to the grain size analysis and process-related end-member (EM) modelling, Nottebaum et al. (2015) demonstrated that the dominant grain size fraction of the loess sample (LUM-2941) is coarse to fine silt fraction, which was classified as EM2 and EM3 population. The origin of EM2 and EM3 has been identified to be suspension during dust storm events from sandy and/or Gobi deserts surfaces located to the north of the Qilian Mountains, and constant long distance transport by westerlies, respectively. Both provenances are distant (>10^2 km) from the sampling locality. Regarding the possible travelling time during dust storms and trapping time before burial for such material, our reconstruction result, more than two thousand hours daylight exposure, is a plausible value, even though there is currently no other measure to validate or disprove it. Meanwhile, we are aware that our reconstruction is highly dependent on the availability of reliable age control, correct dose rate determination and accurate g-value measurements. Furthermore, the real sedimentological (transportation) process is rather complex, even for subaerial aeolian sedimentation. Such reconstruction of the B_e value simplifies the nature process, during which the daylight exposure is dominant. And it is noteworthy that such interpretation is only an attempt and the value of B_e is subject to slight difference in the way of calculation. At this stage of practice, the erosion-deposition cycles that the sediment may have experienced prior to the last exposure event have not been taken into consideration. Provided a sample had initially larger dose than the sample in this study (~30 Gy), longer bleaching time would be required to bleach the signals down to the same level.

The bleaching experiments presented in this paper were significantly time-consuming, because a range of pIRIR signals was explored and exploited for the interpolation of predicted residuals onto the laboratory bleaching curves. The advantage of using multiple pIRIR signals to obtain the natural bleaching time is in the intersection of multiple signals with different bleaching characteristics, eventually providing greater confidence in the final result. For future applications, one might consider using fewer (or even a single) pIRIR signal at the expense of less certain knowledge of the bleaching history. Furthermore, the more recent study by Cheng et al. (2022) has demonstrated that the individual grains from the same sample are subject to significant variation in the bleachability, which may result in different residual doses for different grains. The exploration on single grain scale might provide further insight into the pre-burial light exposure history of sediment.

Conclusion

Our results demonstrate that there are non-bleachable components in the IR (and possibly pIRIR) signals, and that the level of this unbleachable signal positively correlates with the preheat/stimulation temperature. It's noteworthy that the relative residual signal level is consistent between the IR_{50} and pIRIR signals for a same preheat temperature. It provides further support that lower temperature pIRIR are advantageous in reducing the contribution of residual signals (possibly induced by thermal transfer), especially when dating young samples and sediments from difficult-to-bleach environments. Taking advantage of results from our extensive bleaching experiments, we explore the pre-deposition bleaching (or transportation) history of the target sediments, based on

observation that feldspar pIRIR signals obtained at different temperatures have different bleaching characteristics. Despite the challenges, limitations, and uncertainties in this approach, we were able to quantify the possible pre-depositional sunlight bleaching time for a loess sample under investigation. That pre-depositional time amounted to an equivalent of at least 264 h exposure in the solar simulator. Our attempt provides further proof-of-concept for the utilization of luminescence dating for photochronometry (Guralnik and Sohbati, 2019), which should particularly benefit the research of sedimentological processes and provenance.

Data availability statement

The original contributions presented in the study are included in the article/Supplementary Material, further inquiries can be directed to the corresponding author.

Author contributions

JZ, ST, and BG contributed to conception and design of the study. JZ organized the database. BG performed the statistical analysis. JZ wrote the first draft of the manuscript. BG and CA rewrote part of the manuscript. All authors contributed to manuscript revision, read, and approved the submitted version.

Funding

JZ was financially supported by the NSFC (Grant No. 41701002) and the STEP (Grant No. 2019QZKK0205).

Acknowledgments

We thank all HAZARD participants for fruitful discussions on feldspar luminescence, and for feedback on work in progress. We are grateful to Li Yan and Peng Jun for their helpful comments and discussions in fading correction models and Chi square test. We appreciate very much the constructive comments from two reviewers.

Conflict of interest

The authors declare that the research was conducted in the absence of any commercial or financial relationships that could be construed as a potential conflict of interest.

Publisher's note

All claims expressed in this article are solely those of the authors and do not necessarily represent those of their affiliated organizations, or those of the publisher, the editors and the reviewers. Any product that may be evaluated in this article, or claim that may be made by its manufacturer, is not guaranteed or endorsed by the publisher.

Supplementary material

The Supplementary Material for this article can be found online at: https://www.frontiersin.org/articles/10.3389/feart.2022.933131/full#supplementary-material

References

Bevington, P. R., and Robinson, D. K. (2013). *Data reduction and error analysis for the physical sciences*. third ed. New York: McGraw-Hill.

Buylaert, J.-P., Jain, M., Murray, A. S., Thomsen, K. J., Thiel, C., and Sohbati, R. (2012). A robust feldspar luminescence dating method for Middle and Late Pleistocene sediments. *Boreas* 41, 435–451. doi:10.1111/j.1502-3885.2012.00248.x

Buylaert, J.-P., Murray, A. S., Gebhardt, A. C., Sohbati, R., Ohlendorf, C., Thiel, C., et al. (2013). Luminescence dating of the PASADO core 5022-1D from Laguna Potrok Aike (Argentina) using IRSL signals from feldspar. *Quat. Sci. Rev.* 71, 70–80. doi:10.1016/j.quascirev.2013.03.018

Buylaert, J. P., Murray, A. S., Thomsen, K. J., and Jain, M. (2009). Testing the potential of an elevated temperature IRSL signal from K-feldspar. *Radiat. Meas.* 44, 560–565. doi:10.1016/j.radmeas.2009.02.007

Buylaert, J. P., Thiel, C., Murray, A. S., Vandenberghe, D., Yi, S. W., and Lu, H. Y. (2011). IRSL and post IR-IRSL residual doses recorded in modern dust samples from the Chinese loess plateau. *Geochronometria* 38, 432–440. doi:10.2478/s13386-011-0047-0

Cheng, T., Zhang, D. J., Zhao, H., Yang, S. L., and Li, B. (2022). Bleachability of pIRIR signal from single-grain K-feldspar. *Quat. Geochronol.* 71, 101321. doi:10.1016/j.quageo.2022.101321

Colarossi, D., Duller, G. A. T., Roberts, H. M., Tooth, S., and Lyons, R. (2015). Comparison of paired quartz OSL and feldspar post-IR IRSL dose distributions in poorly bleached fluvial sediments from South Africa. *Quat. Geochronol.* 30, 233–238. doi:10.1016/j.quageo.2015.02.015

Dietze, M., Kreutzer, S., Fuchs, M. C., Burow, C., Fischer, M., and Schmidt, C. (2013). A practical guide to the R package luminescence. *Anc. TL* 31, 11–18.

Dr Honle Sol Sun simulation systems from Uvalight Technology Ltd (1988). *Pigment and resin Technology* (Bingley, United Kingdom: MCB UP Ltd), 17, 6. doi:10.1108/eb042547

Fu, X., Li, B., and Li, S. H. (2012). Testing a multi-step post-IR IRSL dating method using polymineral fine grains from Chinese loess. *Quat. Geochronol.* 10, 8–15. doi:10.1016/j.quageo.2011.12.004

Fu, X., and Li, S. H. (2013). A modified multi-elevated-temperature post-IR IRSL protocol for dating Holocene sediments using K-feldspar. *Quat. Geochronol.* 17, 44–54. doi:10.1016/j.quageo.2013.02.004

Guralnik, B., and Sohbati, R. (2019). "Fundamentals of photo- and thermochronometry," in *Advances in thermoluminescence and optically stimulated luminescence: Theory, experiments and applications*. Editors R. Chen and V. Pagonis (Singapore: World Scientific).

Huntley, D. J., and Lamothe, M. (2001). Ubiquity of anomalous fading in K-feldspars and the measurement and correction for it in optical dating. *Can. J. Earth Sci.* 38, 1093–1106. doi:10.1139/e01-013

Jain, M., Guralnik, B., and Andersen, M. T. (2012). Stimulated luminescence emission from localized recombination in randomly distributed defects. *J. Phys. Condens. Matter* 24, 385402–402. doi:10.1088/0953-8984/24/38/385402

Kars, R. H., Reimann, T., Ankjærgaard, C., and Wallinga, J. (2014a). Bleaching of the post-IR IRSL signal: New insights for feldspar luminescence dating. *Boreas* 43, 780–791. doi:10.1111/bor.12082

Kars, R. H., Reimann, T., and Wallinga, J. (2014b). Are feldspar SAR protocols appropriate for post-IR IRSL dating? *Quat. Geochronol.* 22, 126–136. doi:10.1016/j.quageo.2014.04.001

Li, B., Jacobs, Z., Roberts, R. G., and Li, S.-H. (2014). Review and assessment of the potential of post-IR IRSL dating methods to circumvent the problem of anomalous fading in feldspar luminescence. *Geochronometria* 41, 178–201. doi:10.2478/s13386-013-0160-3

Li, B., and Li, S. H. (2011). Luminescence dating of K-feldspar from sediments: A protocol without anomalous fading correction. *Quat. Geochronol.* 6, 468–479. doi:10.1016/j.quageo.2011.05.001

Lowick, S. E., Trauerstein, M., and Preusser, F. (2012). Testing the application of post IR- IRSL dating to fine grain waterlain sediments. *Quat. Geochronol.* 8, 33–40. doi:10.1016/j.quageo.2011.12.003

Madsen, A. T., Buylaert, J. P., and Murray, A. S. (2011). Luminescence dating of young coastal deposits from New Zealand using feldspar. *Geochronometria* 38, 379–390. doi:10.2478/s13386-011-0042-5

Murray, A. S., Thomsen, K. J., Masuda, N., Buylaert, J. P., and Jain, M. (2012). Identifying well-bleached quartz using the different bleaching rates of quartz and feldspar luminescence signals. *Radiat. Meas.* 47, 688–695. doi:10.1016/j.radmeas.2012.05.006

Nottebaum, V., Stauch, G., Kai, H., Zhang, J. R., and Lehmkuhl, F. (2015). Unmixed loess grain size populations along the northern Qilian Shan (China): Relationships between geomorphologic, sedimentologic and climatic controls. *Quat. Int.* 372, 151–166. doi:10.1016/j.quaint.2014.12.071

Ollerhead, J., and Huntley, D. J. (2011). Optical dating of young feldspars: The zeroing questions. *Anc. TL* 29, 59–63.

Reimann, T., Notenboom, P. D., De Schipper, M. A., and Wallinga, J. (2015). Testing for sufficient signal resetting during sediment transport using a polymineral multiple-signal luminescence approach. *Quat. Geochronol.* 25, 26–36. doi:10.1016/j.quageo.2014.09.002

Reimann, T., Thomsen, K. J., Jain, M., Murray, A. S., and Frechen, M. (2012). Single-grain dating of young sediments using the pIRIR signal from feldspar. *Quat. Geochronol.* 11, 28–41. doi:10.1016/j.quageo.2012.04.016

Reimann, T., and Tsukamoto, S. (2012). Dating the recent past (<500 years) by post-IR IRSL feldspar- examples from the North Sea and Baltic Sea coast. *Quat. Geochronol.* 10, 180–187. doi:10.1016/j.quageo.2012.04.011

Reimann, T., Tsukamoto, S., Naumann, M., and Frechen, M. (2011). The potential of using K-rich feldspars for optical dating of young coastal sediments – a test case from Darss-Zingst peninsula (southern Baltic Sea coast). *Quat. Geochronol.* 6, 207–222. doi:10.1016/j.quageo.2010.10.001

Rhodes, E. J. (2011). Optically stimulated luminescence dating of sediments over the past 200, 000 years. *Annu. Rev. Earth Planet. Sci.* 39, 461–488. doi:10.1146/annurev-earth-040610-133425

Sohbati, R. (2013). "Luminescence, rock surfaces," in *Encyclopedia of scientific dating methods*. Editors W. J. Rink and J. Thompson (Berlin, Germany: Springer), 7.

Sohbati, R., Murray, A. S., Buylaert, J. P., Ortuño, M., Cunha, P. P., and Masana, E. (2012). Luminescence dating of Pleistocene alluvial sediments affected by the Alhama de Murcia fault (eastern Betics, Spain) - a comparison between OSL, IRSL and post-IR IRSL ages. *Boreas* 41, 250–262. doi:10.1111/j.1502-3885.2011.00230.x

Thiel, C., Buylaert, J. P., Murray, A., Terhorst, B., Hofer, I., Tsukamoto, S., et al. (2011). Luminescence dating of the Stratzing loess profile (Austria)-Testing the potential of an elevated temperature post-IR IRSL protocol. *Quat. Int.* 234, 23–31. doi:10.1016/j.quaint.2010.05.018

Thomsen, K. J., Murray, A. S., Jain, M., and Bøtter-Jensen, L. (2008). Laboratory fading rates of various luminescence signals from feldspar-rich sediment extracts. *Radiat. Meas.* 43, 1474–1486. doi:10.1016/j.radmeas.2008.06.002

Tsukamoto, S., Kondo, R., Lauer, T., and Jain, M. (2017). Pulsed IRSL: A stable and fast bleaching luminescence signal from feldspar for dating Quaternary sediments. *Quat. Geochronol.* 41, 26–36. doi:10.1016/j.quageo.2017.05.004

Yi, S. W., Buylaert, J. P., Murray, A. S., Lu, H. Y., Thiel, C., and Zeng, L. (2016). A detailed post-IR IRSL dating study of the Niuyangzigou loess site in northeastern China. *Boreas* 45, 644–657. doi:10.1111/bor.12185

Yi, S. W., Li, X. S., Han, Z. Y., Lu, H. Y., Liu, J. F., and Wu, J. (2018). High resolution luminescence chronology for Xiashu Loess deposits of Southeastern China. *J. Asian Earth Sci.* 155, 188–197. doi:10.1016/j.jseaes.2017.11.027

Zhang, J. R., Nottebaum, V., Tsukamoto, S., Lehmkuhl, F., and Frechen, M. (2015b). Late Pleistocene and Holocene loess sedimentation in central and Western Qilian Shan (China) revealed by OSL dating. *Quat. Int.* 372, 120–129. doi:10.1016/j.quaint.2014.12.054

Zhang, J. R., Tsukamoto, S., Nottebaum, V., Lehmhuhl, F., and Frechen, M. (2015a). D_e plateau and its implications for post-IR IRSL dating of polymineral fine grains. *Quat. Geochronol.* 30, 147–153. doi:10.1016/j.quageo.2015.02.003

frontiers | Frontiers in Earth Science

TYPE Original Research
PUBLISHED 10 January 2023
DOI 10.3389/feart.2022.939852

OPEN ACCESS

EDITED BY
Yuxin Fan,
Lanzhou University, China

REVIEWED BY
Yujie Guo,
Hebei Normal University, China
Xiangjun Liu,
Jiaying University, China

*CORRESPONDENCE
Yan Li,
yan.li@cugb.edu.cn,
geo-liyan@foxmail.com

SPECIALTY SECTION
This article was submitted to Quaternary Science, Geomorphology and Paleoenvironment, a section of the journal Frontiers in Earth Science

RECEIVED 09 May 2022
ACCEPTED 30 August 2022
PUBLISHED 10 January 2023

CITATION
Li Y, Tsukamoto S, Klinge M, Sauer D and Frechen M (2023), K-feldspar pIRIR$_{150}$ dating of the Late Pleistocene sediments in the NW Khangai Mountains (Mongolia) using a standardized dose-response curve approach.
Front. Earth Sci. 10:939852.
doi: 10.3389/feart.2022.939852

K-feldspar pIRIR$_{150}$ dating of the Late Pleistocene sediments in the NW Khangai Mountains (Mongolia) using a standardized dose-response curve approach

Yan Li[1,2,3]*, Sumiko Tsukamoto[2], Michael Klinge[4], Daniela Sauer[4] and Manfred Frechen[2]

[1]School of Ocean Sciences, China University of Geosciences, Beijing, China, [2]Leibniz Institute for Applied Geophysics, Hannover, Germany, [3]Institute of Geography, University of Göttingen, Göttingen, Germany, [4]Marine and Polar Research Center, China University of Geosciences, Beijing, China

K-feldspar luminescence dating has been widely applied to constrain the timing of Quaternary sedimentation in different environments. However, the measurements are time-consuming. Meanwhile, anomalous fading and partial bleaching are the two potential problems inducing dating uncertainty. In this study, sand-size K-feldspar grains extracted from 32 luminescence samples from the northern slope of the Khangai Mountains, Mongolia, were dated using the post-infrared (IR) infrared stimulated luminescence protocol (pIRIR$_{150}$. subscript shows the second stimulation temperature). The standardized dose-response curves (sDRCs) for luminescence dating, which could improve the measurement efficiency, were constructed. The K-feldspar luminescence chronology has been established after careful investigations of fading correction and bleaching degree of the signals. The sDRCs and individual DRC yield consistent ages, indicating that sDRCs are applicable for luminescence dating with an improvement in measurement efficiency. The fading corrected ages using the two fading correction models are generally in agreement. Based on age comparisons between the radiocarbon dates, the fading corrected pIRIR$_{150}$ and IR$_{50}$ ages, the pIRIR$_{150}$ signal was not fully bleached for several samples. In contrast, some IR$_{50}$ ages were overestimated due to fading over-correction. The investigated profiles have documented the sedimentary information since the last deglaciation.

KEYWORDS

K-feldspar luminescence dating, standardized dose-response curve (sDRC), fading correction, Mongolia, Late Pleistocene

1 Introduction

Quartz and potassium-rich (K-) feldspar luminescence dating methods have been widely applied to establish precise chronologies of Middle-Late Quaternary sediments (Wallinga, 2002; Fuchs and Owen, 2008; Roberts, 2008; Thrasher et al., 2009; Lamothe, 2016). According to the single aliquot regenerative-dose (SAR) protocol (Wintle and Murray, 2000), the K-feldspar infrared stimulated luminescence (IRSL) dating protocol (Wallinga et al., 2000) could be used to date the sediments since the Middle Pleistocene due to the larger dating range compared to that of the standard quartz luminescence signal. For more effective equivalent dose (D_e) estimation, several approaches to constructing the standardized dose-response curve (sDRC) or standardized growth curve (SGC) have been proposed by Roberts and Duller (2004), which has been evaluated for luminescence dating of different types of sediments (Lai, 2006; Telfer et al., 2008; Long et al., 2010). More recently, the sDRCs for quartz OSL and K-feldspar IRSL signals based on the re-normalization and least-squares normalization methods have been constructed in a global field of vision (Li et al., 2015a, 2015b; Li B. et al., 2018). Accordingly, the characteristics of the sDRCs for the OSL signal from quartz fraction and the IRSL signal from various coarse- and fine-grained fractions were explored (Zhang and Li, 2019; Fu et al., 2020).

The accuracy of the K-feldspar IRSL luminescence ages could be potentially influenced by two major issues. First, anomalous fading, as the undesirable loss of the IRSL signal, could result in age underestimation. Athermally more stable signals, such as the post-IR IRSL (pIRIR) (Thomsen et al., 2008; Buylaert et al., 2009; Li and Li, 2011), pulsed IRSL (Tsukamoto et al., 2017), IR photoluminescence (IR-PL) (Prasad et al., 2017), and post-isothermal IRSL (Lamothe et al., 2020), have shown less-to-negligible fading. The outcome of the previous studies has shown that the $pIRIR_{290}$ and MET-$pIRIR_{250}$ (subscript means the stimulation temperature) signals do not fade (Li and Li, 2011; Thiel et al., 2011), which have been widely applied for constraining the timing of sedimentation of various Quaternary archives (Buylaert et al., 2013; Yi et al., 2015; Guo et al., 2016). However, a higher stimulation temperature of the pIRIR signal induces a larger residual dose than that of the signal stimulated at a lower temperature, resulting from the slower bleaching process (Colarossi et al., 2015; Tsukamoto et al., 2017). This is the second problem that influences the accuracy of the luminescence ages, especially for the young sediments, as the level of the residual dose is significant compared to the equivalent dose. Therefore, applying the low-temperature stimulated IRSL signal (fast-to-bleach), such as the $pIRIR_{150}$ (Madsen et al., 2011; Reimann et al., 2011; Long et al., 2014), $pIRIR_{225}$ (Buylaert et al., 2009), and MET-$pIRIR_{170}$ (Fu and Li, 2013) signals, with proper fading correction is reasonable to date the young sediments. Although anomalous fading is not negligible, it can be corrected using the proper models (Huntley and Lamothe, 2001; Lamothe et al., 2003; Wallinga et al., 2007; Kars et al., 2008). Among them, the models proposed by Huntley and Lamothe (2001) are applicable to correct anomalous fading for ages not older than *ca.* 20–50 ka, corresponding to the linear region of the dose growth. The "dose-rate correction" model suggested by Lamothe et al. (2003) could yield reliable corrected ages correlating to both the linear and nonlinear parts of DRC (Lamothe et al., 2003; Li et al., 2018a). Compared to the model of Huntley and Lamothe (2001), the fading correction following Lamothe et al. (2003) is advantageous because it could be applied for the full DRC. It is also beneficial to use the Lamothe et al. (2003) model as no iteration is needed. This model has been used to correct ages associated with the nonlinear dose region in several studies (Mercier et al., 2019; Nalin et al., 2020), but it has rarely been applied to relatively young ages.

Khangai Mountain is located in central Mongolia. Sediments in the Khangai-Gobi-Altai (western Mongolia) since the last glaciation have been widely studied (Peck et al., 2002; Feng et al., 2005, 2007; Schwanghart et al., 2009; Klinge et al., 2017; Lehmkuhl et al., 2018). The north slope of the Khangai Mountain, covered by forest steppe, is regarded within the center of the Siberian-Mongolian High (Böhner, 2006). Investigating the Quaternary archives in this area helps better understand the evolution of the East Asian winter monsoon in the Late Quaternary. A robust chronology is fundamental for explorations of geomorphological processes, glaciation, and palaeoclimatological evolution. Timing of sedimentation in west Mongolia since the Late Pleistocene has been mainly constrained using radiocarbon, quartz, and K-feldspar luminescence dating approaches (see references in Klinge and Sauer, 2019). The geomorphological evolution along the north slope of Khangai Mountain, Mongolia, since the Late Pleistocene has been well studied by Klinge et al. (2022). However, the applicability of the sDRCs and the reliability of the K-feldspar luminescence ages were poorly investigated. In this study, the coarse-grained K-feldspar fraction from 32 luminescence samples of soil, aeolian, alluvial, and colluvial origins was dated using the $pIRIR_{150}$ protocol. Preliminary $pIRIR_{150}$ ages based on the individual DRC have been presented by Klinge et al. (2022). sDRC was constructed based on the re-normalization method suggested by Li et al. (2015a). The fading correction for the $pIRIR_{150}$ and IR_{50} luminescence ages was conducted using the fading correction models proposed by Huntley and Lamothe (2001) and Lamothe et al. (2003). The aim of this study is threefold. First, we aim to construct the sDRCs for the K-feldspar IRSL signals using the re-normalization method of Li et al. (2015a) and the test dose-standardization method of Roberts and Duller (2004). The reliability of the sDRCs was assessed by comparing the ages determined using sDRC and the individual DRCs. Second, the apparent ages are corrected for anomalous fading to evaluate the applicability of the fading corrected models. Finally, the radiocarbon dates, the fading

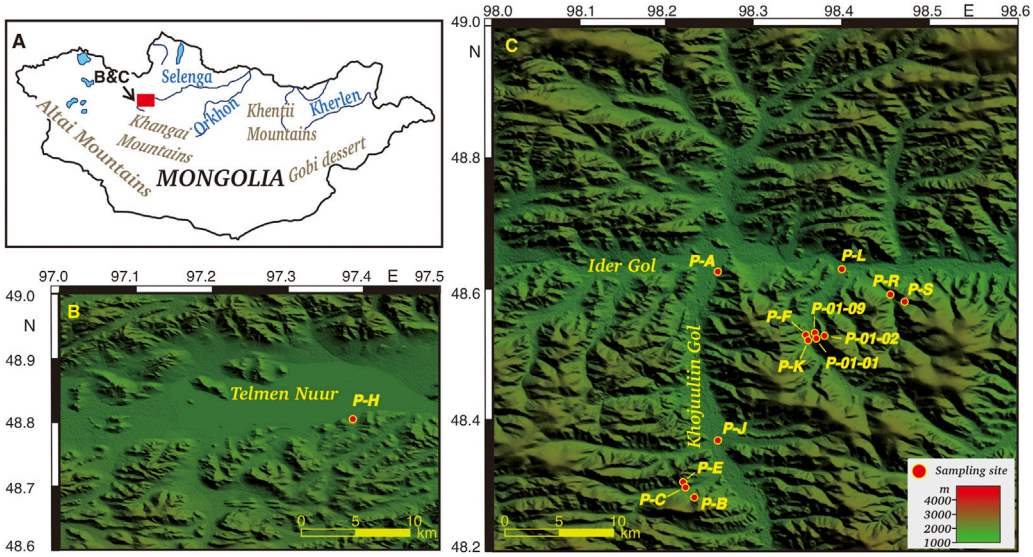

FIGURE 1
Study area and sampling sites. The red block in **(A)** shows the study area, including Telmen Nuur **(B)** and Tosontsengel **(C)**. The Source of the digital elevation model is http://www.cgiar-csi.org.

corrected IR_{50}, and $pIRIR_{150}$ ages are compared to investigate the degree of signal bleaching and determine the timing of sedimentation in the NW Khangai Mountain area since the Late Pleistocene.

2 Sample preparation

In this study, 32 luminescence samples were collected from 14 selected sites in the area of Telmen Nuur (lake) and Tosontsengel to investigate the reliability of the sDRC and luminescence ages and establish the chronological framework of the sediments of different types (Figure 1, Table 1). The sediments are characterized as aeolian, soil, alluvial, and colluvial types. Detailed information on the study area can be found in Klinge et al. (2022) and Supplementary Table S1.

The luminescence samples were taken using cylinders from the freshly prepared profiles. The cylinders were fully filled with the sediments and sealed to avoid material mixture and light exposure. Sample preparation was carried out under subdued red light in the luminescence laboratory of the Leibniz Institute for Applied Geophysics in Hannover, Germany. The outer 2 cm of sediments were discarded for luminescence dating due to potential light exposure. The inner part was dry-sieved, and the dominant fraction at the grain-size interval of either 100–150 or 150–200 μm was collected (Table 1). The selected fraction was then treated with diluted hydrochloric acid (HCl) for 2 hours, sodium oxalate ($Na_2C_2O_4$) for 1 day, and hydrogen peroxide (H_2O_2) for 2 hours to remove carbonate, mineral aggregates, and organic matter, respectively. Heavy liquid separation was conducted after chemical treatment to extract the quartz and K-feldspar grains, corresponding to the heavy liquid density of 2.62–2.70 and <2.58 g/cm^3, respectively. Etching was specially conducted on the quartz grains using 40% hydrofluoric acid (HF) for 1 hour to remove the remaining feldspar grains and etch quartz grains to eliminate the effect of the alpha-irradiated outer layer.

3 Luminescence instrumentation, protocol, and measurements

Luminescence measurements were conducted on automated Risø TL/OSL readers (DA-15/20), equipped with $^{90}Y/^{90}Sr$ beta sources. The mean dose rate of the beta sources ($\dot{D}_{lab}$) was 0.105 ± 0.010 Gy/s. The extracted quartz grains for several samples were first measured using the standard single-aliquot regenerative (SAR) protocol. The results showed that the quartz grains were severely contaminated by feldspar, indicated by the largely underestimated IR/OSL depletion ratio. The K-feldspar pIRIR dating approach was thus used for D_e measurement and age determination. The K-feldspar grains were mounted on stainless-steel aliquots with a diameter of 2.5 mm. During infrared stimulation (870 ± 40 nm), the K-feldspar luminescence signals in the UV-blue wavelengths (320–480 nm) were detected through a combined blue filter pack (Schott BG-39 and Corning 7-59). The aliquots were preheated at 180°C for 60 s, stimulated at 50°C for 100 s

TABLE 1 Sample information and dose rate determination.

Profile	Latitude (°N)	Longitude (°E)	Elevation (m)	Sample ID	Sediment type	Grain size (μm)	Depth (m)	^{238}U (Bq/kg)	^{226}Ra (Bq/kg)	^{210}Pb (Bq/kg)	^{232}Th (Bq/kg)	^{40}K (Bq/kg)	Moisture (%)	Dose rate (Gy/ka)
P-01–01	48.645	98.369	1,915	LUM3769	Soil	100–150	0.48–0.53	21.95 ± 2.11	19.01 ± 0.22	18.08 ± 2.58	28.46 ± 0.29	723.26 ± 3.00	7.5 ± 3.0	3.95 ± 0.15
				LUM3770	Soil	100–150	1.35–1.40	17.34 ± 1.74	16.62 ± 0.21	11.75 ± 1.88	24.54 ± 0.25	669.33 ± 2.63	7.5 ± 3.0	3.66 ± 0.15
P-01–02	48.645	98.378	1,907	LUM3751	Soil	100–150	0.12–0.17	21.51 ± 2.06	21.81 ± 0.78	17.61 ± 1.93	29.50 ± 1.00	728.22 ± 8.78	7.5 ± 3.0	4.05 ± 0.16
				LUM3752	Soil	100–150	0.92–0.97	17.45 ± 1.95	20.39 ± 0.52	15.90 ± 1.62	31.93 ± 1.07	755.53 ± 7.47	7.5 ± 3.0	4.09 ± 0.16
P-01–09	48.646	98.368	1,901	LUM3917	Soil	150–200	0.7–0.75	16.45 ± 1.87	18.07 ± 0.68	15.62 ± 1.91	32.11 ± 0.89	703.56 ± 6.78	7.5 ± 3.0	3.82 ± 0.15
				LUM3919	Soil	150–200	1.95–2.00	15.62 ± 0.97	17.96 ± 0.13	18.80 ± 1.14	25.15 ± 0.14	767.98 ± 1.55	7.5 ± 3.0	3.89 ± 0.15
P-S	48.685	98.469	1,894	LUM3933	Colluvial loam	150–200	0.55–0.60	21.49 ± 2.75	19.92 ± 1.13	20.57 ± 2.96	27.77 ± 1.35	675.49 ± 12.13	5.0 ± 2.5	3.69 ± 0.16
P-C	48.471	98.221	1,913	LUM3758	Soil	100–150	0.15–0.20	23.82 ± 2.53	22.51 ± 0.84	27.67 ± 2.35	31.98 ± 1.14	710.22 ± 8.79	5.0 ± 2.5	4.15 ± 0.16
				LUM3760	Soil	100–150	0.70–0.75	22.58 ± 2.49	19.17 ± 0.79	17.87 ± 2.30	28.72 ± 1.22	760.07 ± 9.34	5.0 ± 2.5	4.14 ± 0.17
				LUM3761	Soil	150–200	1.28–1.33	15.03 ± 2.15	20.28 ± 0.79	15.97 ± 1.97	31.09 ± 0.96	756.75 ± 9.07	5.0 ± 2.5	4.08 ± 0.16
P-E	48.474	98.219	1,830	LUM3764	Soil	150–200	0.77–0.82	19.53 ± 1.85	16.86 ± 0.20	15.81 ± 2.14	34.19 ± 0.266	912.56 ± 2.86	5.0 ± 2.5	4.54 ± 0.16
				LUM3765	Soil	150–200	1.80–1.85	17.28 ± 1.51	16.22 ± 0.21	13.97 ± 1.88	22.53 ± 0.24	763.43 ± 2.69	5.0 ± 2.5	3.89 ± 0.15
				LUM3766	Soil	150–200	2.18–2.23	13.58 ± 1.56	11.94 ± 0.18	14.98 ± 1.95	16.02 ± 0.22	796.21 ± 2.69	5.0 ± 2.5	3.81 ± 0.15
				LUM3767	Soil	150–200	2.50–2.55	14.49 ± 1.49	11.79 ± 0.18	12.24 ± 1.66	16.09 ± 0.22	800.51 ± 2.56	5.0 ± 2.5	3.80 ± 0.15
				LUM3768	Soil	150–200	2.90–2.95	12.91 ± 1.74	12.10 ± 0.17	15.03 ± 2.10	18.17 ± 0.24	798.83 ± 2.95	5.0 ± 2.5	3.83 ± 0.15
P-R	48.693	98.455	1,785	LUM3931	Sandy soil	150–200	0.84–0.89	11.06 ± 1.03	18.15 ± 0.16	13.99 ± 1.26	23.86 ± 0.16	651.64 ± 1.76	5.0 ± 2.5	3.63 ± 0.14
				LUM3932	Sandy soil	150–200	1.73–1.78	12.17 ± 1.04	18.71 ± 0.16	14.18 ± 1.29	24.79 ± 0.17	647.91 ± 1.81	5.0 ± 2.5	3.61 ± 0.14
P-K	48.644	98.361	1,824	LUM3921	Alluvial soil	150–200	0.35–0.40	22.55 ± 1.84	22.73 ± 0.70	23.22 ± 1.92	30.63 ± 0.91	681.43 ± 7.11	7.5 ± 3.0	3.85 ± 0.15
				LUM3922	Alluvial soil	150–200	0.85–0.90	15.53 ± 2.29	19.79 ± 0.78	19.60 ± 2.12	24.90 ± 0.88	725.06 ± 8.65	7.5 ± 3.0	3.82 ± 0.16
P-J	48.528	98.259	1,821	LUM3912	Sandy dune	150–200	1.15–1.20	9.12 ± 1.58	9.59 ± 0.19	8.12 ± 2.03	15.23 ± 0.23	831.47 ± 3.04	5.0 ± 2.5	3.88 ± 0.16
				LUM3913	Sandy dune	150–200	2.10–2.15	7.16 ± 1.57	10.06 ± 0.20	9.51 ± 2.05	15.17 ± 0.25	834.54 ± 3.05	5.0 ± 2.5	3.87 ± 0.16
				LUM3914	Sandy dune	150–200	2.45–2.50	6.50 ± 1.15	8.64 ± 0.17	7.76 ± 1.51	13.69 ± 0.21	855.70 ± 2.64	5.0 ± 2.5	3.87 ± 0.16
				LUM3915	Sandy dune	150–200	3.75–3.00	9.90 ± 1.58	11.44 ± 0.57	11.04 ± 1.49	17.21 ± 0.76	850.48 ± 7.68	5.0 ± 2.5	3.93 ± 0.16
P-L	48.723	98.399	1,690	LUM3923	Sandy soil	150–200	0.27–0.32	22.89 ± 1.82	20.18 ± 0.23	18.22 ± 2.19	26.88 ± 0.28	671.32 ± 2.60	5.0 ± 2.5	3.77 ± 0.15
				LUM3924	Sandy soil	150–200	1.22–1.27	19.79 ± 1.60	15.44 ± 0.20	17.66 ± 1.86	18.30 ± 0.23	738.41 ± 2.63	5.0 ± 2.5	3.74 ± 0.15
P-A	48.720	98.258	1,715	LUM3754	Soil	100–150	0.70–0.75	57.23 ± 3.07	30.47 ± 0.98	27.49 ± 2.48	41.90 ± 1.17	740.61 ± 9.12	20.0 ± 5.0	3.95 ± 0.16
				LUM3755	Soil	150–200	1.17–1.22	17.65 ± 1.46	15.10 ± 0.36	16.70 ± 1.29	23.22 ± 0.71	815.35 ± 5.67	20.0 ± 5.0	3.60 ± 0.16
P-H	48.805	97.389	1,806	LUM3775	Sandy soil	150–200	0.85–0.90	9.54 ± 1.38	11.16 ± 0.20	10.40 ± 2.15	13.36 ± 0.21	813.36 ± 2.86	5.0 ± 2.5	3.84 ± 0.15
P-B	48.462	98.230	2,015	LUM3756	Soil	100–150	0.18–0.23	26.76 ± 1.63	22.05 ± 0.44	21.49 ± 1.47	34.53 ± 0.61	683.71 ± 5.33	7.5 ± 3.0	3.98 ± 0.16
				LUM3757	Soil	100–150	0.75–0.80	25.27 ± 1.61	24.27 ± 0.52	21.58 ± 1.55	38.49 ± 0.65	748.54 ± 5.51	7.5 ± 3.0	4.23 ± 0.16
P-F	48.645	98.361	1,825	LUM3771	Alluvial soil	100–150	0.47–0.52	29.05 ± 1.93	27.08 ± 0.24	28.20 ± 2.31	36.92 ± 0.26	603.04 ± 2.33	7.5 ± 3.0	3.87 ± 0.15
				LUM3772	Alluvial soil	100–150	1.26–1.31	35.49 ± 2.15	27.26 ± 0.26	25.52 ± 2.25	34.87 ± 0.27	661.78 ± 2.69	7.5 ± 3.0	3.99 ± 0.15

10.3389/feart.2022.939852

TABLE 2 The protocol of K-feldspar pIRIR$_{150}$ dating.

Step	Treatment	Observed
1	N, beta dose[a]	
2	Preheat for 60 s at 180°C	
3	IR stimulation for 100 s at 50°C	
4	IR stimulation for 200 s at 150 °C	L_n, L_x[b]
5	Beta dose (Test dose)[c]	
6	Preheat for 60 s at 180°C	
7	IR stimulation for 100 s at 50°C	
8	IR stimulation for 200 s at 150°C	T_n, T_x[b]
9	Return to 1	

[a]One regenerative dose of 10.5 Gy (re-normalization dose) was given to all the aliquots for all the samples during D_e measurement.
[b]The test dose was set to ~30%–50% of the equivalent dose for each sample.
[c]The natural and regenerative luminescence intensities in the text are shown as I_n (L_n/T_n) and I_x (L_x/T_x).

(IR$_{50}$), and stimulated at 150°C for 200 s (pIRIR$_{150}$), respectively (Table 2).

For each sample, 24 aliquots were measured using the pIRIR$_{150}$ protocol. The initial 5 s of the signal was subtracted by the last 15 s to calculate the luminescence intensity (I). The DRCs for individual samples were constructed using the regenerative doses and the corresponding luminescence intensities (I_x). The aliquots which yielded unsatisfactory recycling ratios (either <0.9 or >1.1) were excluded for further D_e determination and DRC construction. Specifically, a regenerative dose of 10.5 Gy was given to all the aliquots as a re-normalization dose for sDRC construction (Table 2).

To evaluate the behavior of dose recovery and the level of the residual signal, the dose recovery test and residual dose measurement were conducted for each sample. Six aliquots of each sample were first bleached in a Hönle SOL2 solar simulator for 4 h. Three of them were measured to determine the residual dose after the 4 h bleaching. The other three bleached aliquots were firstly given a dose close to the D_e value and then measured using the pIRIR$_{150}$ protocol. The obtained D_e was subtracted by the residual dose and then divided by the given dose to calculate the dose recovery ratio. Fading experiments were carried out for all samples to assess anomalous fading for the IR$_{50}$ and pIRIR$_{150}$ signals. The I_x values of three or four aliquots for each sample were repeatedly measured after being given a fixed dose close to the D_e value and stored for various delay times (t_d). The fading rates (g, %/decade) were determined by fitting the I_x - t_d with the logarithm function. The g values were used for fading

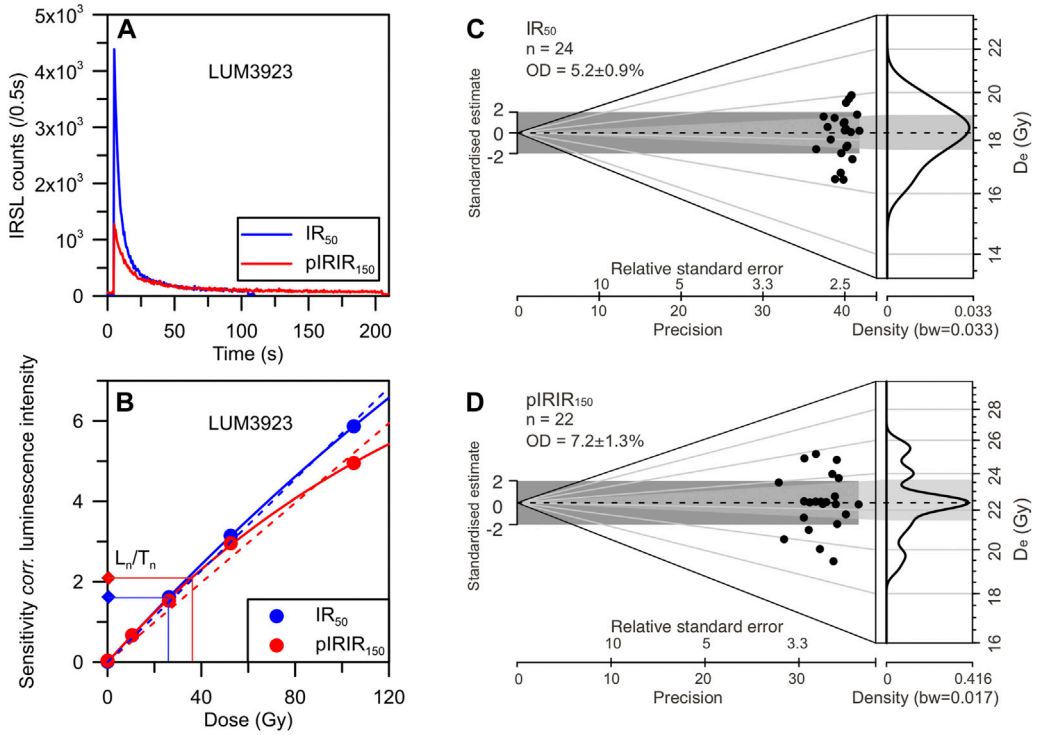

FIGURE 2
Decay curves **(A)**, dose-response curves **(B),** and D_e distribution for the IR$_{50}$ **(C)** and pIRIR$_{150}$ **(D)** signals for one representative sample LUM3923. The dose-response curve was fitted using a linear (dashed line) and one saturating exponential (dashed line) equation in Figure 2B, respectively.

TABLE 3 Results of $pIRIR_{150}$ dating for all the samples.

Sample ID	Signal	*g* (%/decade)	Individual DRC			sDRC			
			De (Gy)[a]	Apparent age (ka)	FC age (ka)[b]	De (Gy)[a]	Apparent age (ka)	FC age (ka)[b]	FC age (ka)[c]
LUM3769	$pIRIR_{150}$	1.94 ± 0.38	37.36 ± 0.46	9.5 ± 0.4	11.4 ± 0.6	36.42 ± 0.43	9.0 ± 0.4	10.8 ± 0.5	10.9 ± 1.4
	IR_{50}	7.51 ± 0.74	33.58 ± 0.47	8.5 ± 0.4	26.3 ± 7.3	33.56 ± 0.45	8.3 ± 0.3	25.6 ± 10.0	25.3 ± 5.5
LUM3770	$pIRIR_{150}$	3.10 ± 1.59	45.79 ± 0.58	12.5 ± 0.5	17.0 ± 4.6	44.24 ± 0.53	10.9 ± 0.5	14.8 ± 3.2	16.3 ± 2.3
	IR_{50}	7.16 ± 0.20	41.38 ± 0.52	11.3 ± 0.5	32.4 ± 2.7	41.45 ± 0.52	10.2 ± 0.4	29.0 ± 2.0	31.5 ± 2.9
LUM3751	$pIRIR_{150}$	1.89 ± 0.58	16.98 ± 0.79	4.2 ± 0.3	5.0 ± 0.5	18.42 ± 0.44	4.5 ± 0.2	5.3 ± 0.5	5.3 ± 0.8
	IR_{50}	5.22 ± 0.68	12.97 ± 0.26	3.2 ± 0.2	5.7 ± 0.7	12.94 ± 0.25	3.2 ± 0.1	5.7 ± 0.7	5.8 ± 0.8
LUM3752	$pIRIR_{150}$	1.81 ± 0.31	48.75 ± 0.78	11.9 ± 0.5	14.1 ± 0.7	55.07 ± 0.86	13.6 ± 0.6	16.1 ± 0.8	15.6 ± 2.0
	IR_{50}	5.33 ± 0.16	41.39 ± 0.57	10.1 ± 0.4	19.2 ± 1.0	41.85 ± 0.56	10.3 ± 0.4	20.0 ± 1.0	19.5 ± 1.6
LUM3917	$pIRIR_{150}$	2.47 ± 0.70	35.29 ± 1.63	9.2 ± 0.6	11.6 ± 1.4	32.95 ± 1.34	8.1 ± 0.5	10.2 ± 1.2	10.8 ± 1.7
	IR_{50}	5.54 ± 0.21	28.59 ± 0.58	7.5 ± 0.3	14.6 ± 0.9	27.65 ± 0.52	6.8 ± 0.3	13.1 ± 0.7	14.2 ± 1.2
LUM3919	$pIRIR_{150}$	1.42 ± 0.66	38.27 ± 0.52	9.8 ± 0.4	11.1 ± 0.8	38.23 ± 0.52	9.4 ± 0.4	10.7 ± 0.9	11.0 ± 1.6
	IR_{50}	6.41 ± 0.41	32.73 ± 0.51	8.4 ± 0.4	19.5 ± 2.2	32.70 ± 0.49	8.1 ± 0.3	18.7 ± 1.6	19.4 ± 2.3
LUM3933	$pIRIR_{150}$	1.28 ± 0.13	39.99 ± 1.09	10.8 ± 0.6	12.1 ± 0.6	39.16 ± 1.04	9.7 ± 0.5	10.9 ± 0.6	11.6 ± 1.5
	IR_{50}	5.32 ± 1.01	26.32 ± 1.74	7.1 ± 0.6	13.2 ± 3.1	26.35 ± 1.73	6.5 ± 0.5	12.1 ± 2.5	13.4 ± 2.8
LUM3758	$pIRIR_{150}$	1.38 ± 0.13	3.89 ± 0.41	0.9 ± 0.1	1.0 ± 0.1	4.09 ± 0.43	1.0 ± 0.1	1.1 ± 0.1	1.1 ± 0.2
	IR_{50}	5.91 ± 0.13	1.06 ± 0.16	0.30 ± 0.04	0.53 ± 0.07	1.08 ± 0.16	0.27 ± 0.04	0.47 ± 0.07	0.52 ± 0.09
LUM3760	$pIRIR_{150}$	1.03 ± 0.48	33.79 ± 0.39	8.2 ± 0.3	9.0 ± 0.5	32.60 ± 0.37	8.0 ± 0.3	8.7 ± 0.5	8.4 ± 1.1
	IR_{50}	4.76 ± 0.12	29.58 ± 0.35	7.1 ± 0.3	12.1 ± 0.5	29.54 ± 0.33	7.3 ± 0.3	12.4 ± 0.6	12.3 ± 1.0
LUM3761	$pIRIR_{150}$	2.13 ± 0.87	36.95 ± 0.65	9.1 ± 0.4	11.1 ± 1.1	34.72 ± 0.56	8.6 ± 0.4	10.5 ± 1.2	10.3 ± 1.7
	IR_{50}	6.00 ± 0.38	31.97 ± 0.48	7.8 ± 0.3	16.5 ± 1.5	31.49 ± 0.47	7.8 ± 0.3	16.5 ± 1.5	16.4 ± 1.8
LUM3764	$pIRIR_{150}$	1.46 ± 0.26	39.48 ± 1.32	8.7 ± 0.4	9.9 ± 0.5	38.74 ± 1.26	9.6 ± 0.5	10.9 ± 0.6	9.5 ± 1.2
	IR_{50}	5.59 ± 0.85	34.51 ± 1.06	7.6 ± 0.4	14.9 ± 2.7	34.88 ± 1.07	8.6 ± 0.4	17.0 ± 2.9	15.1 ± 2.7
LUM3765	$pIRIR_{150}$	2.17 ± 0.60	44.77 ± 1.57	11.5 ± 0.6	14.1 ± 1.1	50.37 ± 1.93	12.4 ± 0.7	15.2 ± 1.3	15.7 ± 2.3
	IR_{50}	8.29 ± 0.53	36.52 ± 0.47	9.4 ± 0.4	39.4 ± 14.0	36.82 ± 0.46	9.1 ± 0.4	37.9 ± 10.6	35.8 ± 6.9
LUM3766	$pIRIR_{150}$	2.15 ± 1.08	34.89 ± 0.46	9.2 ± 0.4	11.2 ± 1.3	33.96 ± 0.43	8.4 ± 0.3	10.2 ± 1.2	10.8 ± 1.9
	IR_{50}	7.88 ± 0.64	31.45 ± 0.52	8.3 ± 0.4	28.9 ± 9.3	31.53 ± 0.50	7.8 ± 0.3	27.0 ± 8.1	27.2 ± 5.7
LUM3767	$pIRIR_{150}$	3.03 ± 0.66	43.68 ± 0.79	11.5 ± 0.5	15.5 ± 1.3	50.93 ± 0.83	12.6 ± 0.5	17.0 ± 1.5	18.1 ± 2.7
	IR_{50}	7.81 ± 0.33	37.10 ± 0.56	9.8 ± 0.4	34.1 ± 4.8	37.33 ± 0.57	9.2 ± 0.4	31.7 ± 4.3	32.2 ± 4.0
LUM3768	$pIRIR_{150}$	2.11 ± 0.56	44.47 ± 1.05	11.6 ± 0.5	14.1 ± 1.1	51.80 ± 1.16	12.8 ± 0.6	15.6 ± 1.2	16.3 ± 2.3
	IR_{50}	8.42 ± 1.22	37.25 ± 0.62	9.7 ± 0.4	43.5 ± 24.1	37.33 ± 0.61	9.2 ± 0.4	40.8 ± 23.5	38.8 ± 16.8
LUM3931	$pIRIR_{150}$	1.32 ± 0.42	23.90 ± 0.71	6.6 ± 0.3	7.4 ± 0.5	24.93 ± 0.67	6.2 ± 0.3	7.0 ± 0.4	7.6 ± 1.0
	IR_{50}	6.80 ± 0.45	20.20 ± 0.35	5.6 ± 0.2	13.8 ± 1.5	20.24 ± 0.35	5.0 ± 0.2	12.2 ± 1.3	13.8 ± 1.8
LUM3932	$pIRIR_{150}$	1.85 ± 0.36	41.26 ± 2.10	11.4 ± 0.7	13.5 ± 1.1	39.84 ± 1.91	9.8 ± 0.6	11.6 ± 0.8	12.9 ± 1.7
	IR_{50}	5.29 ± 0.92	34.98 ± 2.11	9.7 ± 0.7	18.2 ± 3.8	35.87 ± 2.24	9.9 ± 0.7	18.6 ± 3.9	18.4 ± 3.5
LUM3921	$pIRIR_{150}$	2.24 ± 0.46	16.17 ± 1.36	4.2 ± 0.4	5.1 ± 0.5	16.06 ± 1.27	4.0 ± 0.4	4.9 ± 0.5	5.1 ± 0.8
	IR_{50}	6.38 ± 0.10	6.35 ± 1.13	1.7 ± 0.3	3.5 ± 0.7	6.31 ± 1.12	1.6 ± 0.3	3.3 ± 0.7	3.6 ± 0.7
LUM3922	$pIRIR_{150}$	1.79 ± 0.08	25.44 ± 2.62	6.7 ± 0.7	7.9 ± 0.9	27.04 ± 3.00	6.7 ± 0.8	7.9 ± 0.9	8.2 ± 1.3
	IR_{50}	7.80 ± 0.10	12.72 ± 1.99	3.3 ± 0.5	10.0 ± 1.7	12.74 ± 2.01	3.1 ± 0.5	9.3 ± 2.0	10.3 ± 1.8
LUM3912	$pIRIR_{150}$	2.08 ± 0.18	0.97 ± 0.10	0.25 ± 0.03	0.29 ± 0.03	1.03 ± 0.14	0.25 ± 0.04	0.29 ± 0.05	0.32 ± 0.05
(continued)									
LUM3912	IR_{50}	5.95 ± 0.88	0.57 ± 0.03	0.15 ± 0.01	0.25 ± 0.04	0.59 ± 0.02	0.15 ± 0.01	0.25 ± 0.04	0.31 ± 0.06
LUM3913	$pIRIR_{150}$	3.86 ± 0.20	30.58 ± 0.56	7.9 ± 0.4	11.7 ± 0.6	29.46 ± 0.51	7.3 ± 0.3	10.8 ± 0.5	11.4 ± 1.4
	IR_{50}	8.34 ± 1.47	19.53 ± 1.29	5.1 ± 0.4	19.7 ± 7.8	19.30 ± 1.25	4.8 ± 0.4	18.3 ± 8.4	18.2 ± 9.2
LUM3914	$pIRIR_{150}$	0.73 ± 1.38	33.55 ± 0.59	8.7 ± 0.4	9.3 ± 1.4	32.03 ± 0.53	7.9 ± 0.3	8.4 ± 1.1	8.6 ± 1.6

(Continued on following page)

TABLE 3 (*Continued*) Results of $pIRIR_{150}$ dating for all the samples.

Sample ID	Signal	*g* (%/decade)	Individual DRC			sDRC			
			De (Gy)[a]	Apparent age (ka)	FC age (ka)[b]	De (Gy)[a]	Apparent age (ka)	FC age (ka)[b]	FC age (ka)[c]
	IR_{50}	8.21 ± 0.71	21.92 ± 1.35	5.7 ± 0.4	21.3 ± 6.2	21.66 ± 1.31	5.3 ± 0.4	19.6 ± 5.8	19.7 ± 5.0
LUM3915	$pIRIR_{150}$	1.75 ± 0.12	33.23 ± 0.76	8.5 ± 0.4	10.0 ± 0.5	31.10 ± 0.62	7.7 ± 0.3	9.0 ± 0.4	9.2 ± 1.1
	IR_{50}	5.50 ± 0.15	28.30 ± 0.65	7.2 ± 0.3	13.8 ± 0.7	27.26 ± 0.59	6.7 ± 0.3	12.8 ± 0.7	13.5 ± 1.1
LUM3923	$pIRIR_{150}$	2.29 ± 0.46	21.65 ± 0.40	5.7 ± 0.3	7.0 ± 0.5	21.71 ± 0.39	5.4 ± 0.2	6.6 ± 0.4	7.1 ± 0.9
	IR_{50}	5.05 ± 0.27	18.02 ± 0.25	4.8 ± 0.2	8.4 ± 0.5	18.25 ± 0.23	4.5 ± 0.2	7.9 ± 0.5	8.7 ± 0.8
LUM3924	$pIRIR_{150}$	1.75 ± 0.37	43.85 ± 1.08	11.7 ± 0.6	13.7 ± 0.8	42.49 ± 1.02	10.5 ± 0.5	12.3 ± 0.8	13.1 ± 1.7
	IR_{50}	6.44 ± 0.65	34.88 ± 1.17	9.3 ± 0.5	21.9 ± 3.8	34.84 ± 1.16	8.6 ± 0.4	20.1 ± 3.8	21.8 ± 3.6
LUM3754	$pIRIR_{150}$	0.79 ± 0.68	9.31 ± 1.08	2.4 ± 0.3	2.6 ± 0.3	9.10 ± 1.04	2.2 ± 0.3	2.3 ± 0.4	2.4 ± 0.4
	IR_{50}	4.89 ± 0.81	3.82 ± 0.60	1.0 ± 0.2	1.6 ± 0.4	3.86 ± 0.60	0.95 ± 0.15	1.5 ± 0.3	1.7 ± 0.4
LUM3755	$pIRIR_{150}$	0.99 ± 0.03	12.45 ± 1.39	3.5 ± 0.4	3.8 ± 0.4	13.06 ± 1.30	3.2 ± 0.3	3.5 ± 0.3	3.9 ± 0.6
	IR_{50}	4.94 ± 0.67	6.05 ± 0.60	1.7 ± 0.2	2.8 ± 0.4	6.04 ± 0.59	1.5 ± 0.2	2.5 ± 0.4	2.9 ± 0.5
LUM3775	$pIRIR_{150}$	1.78 ± 0.45	16.75 ± 0.99	4.4 ± 0.3	5.1 ± 0.4	17.10 ± 0.87	4.2 ± 0.3	4.9 ± 0.4	5.2 ± 0.7
	IR_{50}	4.95 ± 0.20	10.79 ± 1.00	2.8 ± 0.3	4.7 ± 0.6	10.80 ± 1.00	2.7 ± 0.3	4.6 ± 0.5	4.9 ± 0.6
LUM3756	$pIRIR_{150}$	3.62 ± 0.45	27.84 ± 0.72	7.0 ± 0.3	10.0 ± 0.7	27.08 ± 0.69	6.7 ± 0.3	9.6 ± 0.7	9.8 ± 1.4
	IR_{50}	6.85 ± 0.41	12.48 ± 0.87	3.1 ± 0.3	7.4 ± 0.8	12.48 ± 0.86	3.1 ± 0.2	7.4 ± 0.8	7.7 ± 1.1
LUM3757	$pIRIR_{150}$	2.34 ± 0.80	30.62 ± 2.36	7.2 ± 0.6	8.9 ± 1.2	29.87 ± 2.24	7.4 ± 0.6	9.2 ± 0.9	8.7 ± 1.5
	IR_{50}	7.10 ± 0.28	18.85 ± 1.39	4.5 ± 0.4	11.7 ± 1.3	18.82 ± 1.38	4.6 ± 0.4	12.0 ± 1.1	11.6 ± 1.4
LUM3771	$pIRIR_{150}$	1.83 ± 0.20	11.65 ± 0.53	3.0 ± 0.2	3.5 ± 0.3	11.65 ± 0.50	2.9 ± 0.2	3.4 ± 0.3	3.5 ± 0.5
	IR_{50}	5.24 ± 0.36	6.67 ± 0.35	1.7 ± 0.1	2.9 ± 0.2	6.68 ± 0.34	1.7 ± 0.1	2.9 ± 0.2	3.2 ± 0.3
LUM3772	$pIRIR_{150}$	1.65 ± 0.99	17.43 ± 0.44	4.4 ± 0.2	5.1 ± 0.6	18.31 ± 0.29	4.5 ± 0.2	5.2 ± 0.6	5.3 ± 0.9
	IR_{50}	5.02 ± 0.53	9.36 ± 0.63	2.4 ± 0.2	4.1 ± 0.5	9.36 ± 0.64	2.3 ± 0.2	3.9 ± 0.5	4.1 ± 0.6

[a]D_e value for each sample was determined using the sDRCs, which was fitted by the single saturating exponential function (1EXP).
[b]The FC ages were calculated following Huntley and Lamothe (2001).
[c]The fading corrected (FC) ages were calculated according to Lamothe et al. (2003).

correction using the models of Huntley and Lamothe (2001) and Lamothe et al. (2003) (see Section 6).

Additional 25 samples of charred material, soil organic matter, wood, bone, and plant from nine profiles were collected and dated using the Accelerator Mass Spectrometry (AMS) ^{14}C dating method. The measurements were carried out at Beta Analytic Inc. and Oxford Radiocarbon Accelerator Unit. The dating results are used to evaluate the degree of bleaching of luminescence signals in Section 7. The detailed information on radiocarbon dates was listed in Klinge et al. (2022), which has also been included in Supplementary Table S2.

4 Dosimetry

50 or 700 g of the dried material was measured in sealed Marinelli beakers to determine the activities of the radioactive elements for each sample using high-resolution gamma spectrometry (Table 1). The materials were stored for at least 4 weeks before measurement to secure equilibrium between radon and its daughter nuclides. The calculation of the external beta and gamma dose rate was conducted using the conversion factor in Guérin (2011) and beta attenuation factors in Mejdahl (1979). The *a*-value was set to 0.09 ± 0.02 following Balescu et al. (2007). The cosmic dose rate was calculated for each sample as a function of depth, altitude, and geomagnetic latitude, following Prescott and Hutton (1994). The water content of different types of samples is listed in Table 1 based on field observation and those in the literature (Schwanghart et al., 2009; Lehmkuhl et al., 2011). The uncertainty was used to account for possible moisture alterations in the geological period. For each feldspar sample, an additional internal dose rate was calculated based on a K concentration of 12.5 ± 0.5% (Huntley and Baril, 1997) and a ^{87}Rb concentration of 400 ± 100 ppm (Huntley and Hancock, 2001). Table 1 summarizes the environmental dose rates for all the K-feldspar samples, ranging from 3.60 ± 0.16 to 4.54 ± 0.16 Gy/ka.

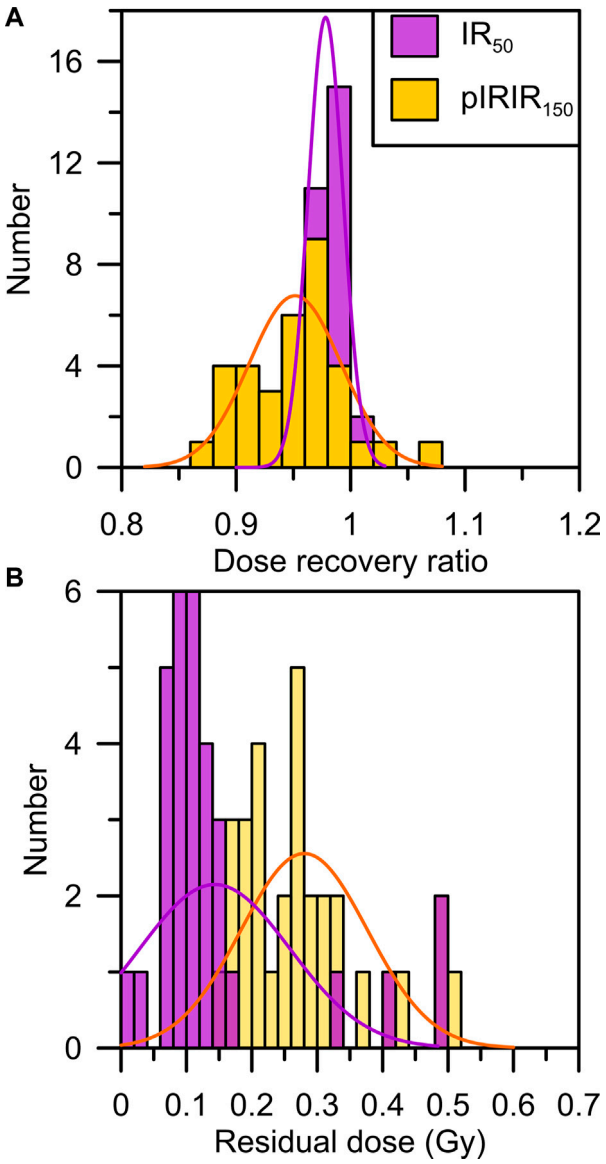

FIGURE 3
Histograms of dose recovery ratios **(A)** and residual dose **(B)** for the IR_{50} and $pIRIR_{150}$ signals for all the samples. The dose recovery ratio and residual dose were determined using three aliquots for each sample.

5 Determination of D_e and apparent age

5.1 Individual DRC

Figure 2 shows the decay curve, DRC, and D_e distribution for the IR_{50} and $pIRIR_{150}$ signals of one representative sample, LUM3923. The DRC was fitted using both the single saturating exponential and linear functions. The natural luminescence intensity (I_n) was projected onto the corresponding DRC to determine D_e for each sample. The equivalent dose and uncertainty were presented as the mean D_e value and standard error of all the D_es with the acceptable recycling ratios (0.9–1.1). The IR_{50} D_e values are between 0.57 ± 0.03 and 41.39 ± 0.57 Gy determined by the single saturating exponential function fitted DRCs, whereas those for the $pIRIR_{150}$ signal range from 0.97 ± 0.10 to 48.75 ± 0.78 Gy. Based on the linear fitted DRCs, the IR_{50} D_e values range from 0.59 ± 0.04 to 41.32 ± 0.57 Gy, whereas the $pIRIR_{150}$ D_es range from 1.04 ± 0.12 to 48.69 ± 0.77 Gy. The overdispersion value for most of the samples is within 10%. The apparent ages were calculated by dividing D_e by the environmental dose rate (Table 3). Figure 3 demonstrates the results of dose recovery tests and residual dose measurements. Although the dose recovery ratios are slightly smaller than 0.90 (0.88–0.90) only for a few samples, the dose recovery ratios for the IR_{50} and $pIRIR_{150}$ signals for most of the samples are within 0.9–1.1. It suggests that the natural doses could be recovered by the $pIRIR_{150}$ measurements within 10% uncertainty. The residual doses are between *ca.* 0.14 and 0.81 Gy for $pIRIR_{150}$, and those are between *ca.* 0.03 and 0.48 Gy for IR_{50}.

5.2 sDRC construction and D_e determination

5.2.1 sDRC construction of intensity re-normalization

sDRCs were constructed following the re-normalization procedure of the sDRC construction (SGC in Li et al., 2015a). The regenerative dose of 10.5 Gy was set as a re-normalization dose. All the I_n and I_x values for each aliquot were first divided by their corresponding $I_{10.5}$ value to eliminate the scatter between aliquots. The re-normalized I_x was then plotted against the corresponding regenerative dose. The sDRCs were fitted using different data and functions ($pIRIR_{150}$: Figures 4A single saturating exponential and Figure 4B-linear; IR_{50}: Figures 4C single saturating exponential and Figure 4D-linear). The fitting equation and the corresponding R-squared value are shown in each diagram. The sDRC for each sample was also constructed and presented using the dashed lines (Figures 4A–D). The sDRC D_e was determined by projecting I_n onto the sDRC using the R package "numOSL" (Peng et al., 2013). Although the IR_{50} sDRCs for the individual samples are identical to the sDRC using all the re-normalized IR_{50} I_xs, the individual $pIRIR_{150}$ sDRCs show two clusters (Figures 4A,B). The upper part shows linear dose growth for each sample, including the individual sDRCs for the samples collected from profiles P-01-02, P-E, P-R, P-K, P-A, P-H, and P-F, whereas those in the lower part are related to the nonlinear dose growth. As the sDRCs of the two clusters are

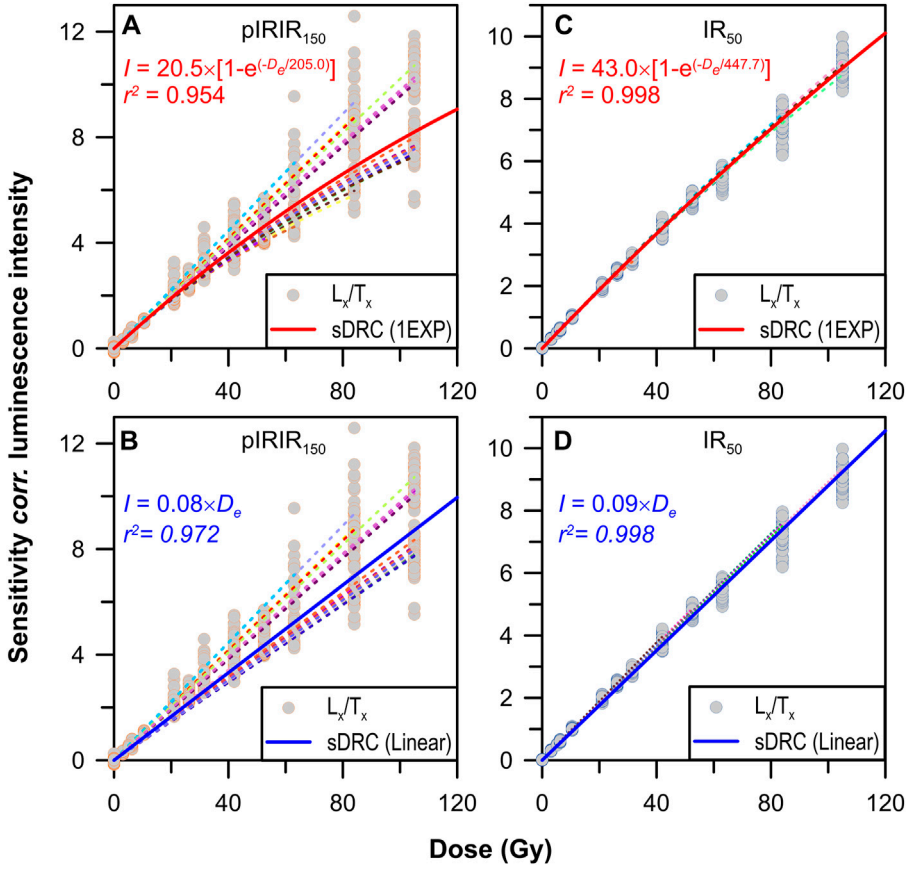

FIGURE 4
Construction and comparison sDRC using data from all the samples following Li B et al. (2015a). **(A,B)** The $pIRIR_{150}$ sDRCs using data of all the samples fitted by the one saturating exponential (1EXP) and linear functions, respectively (solid line). **(C,D)** The IR_{50} sDRCs using data of all the samples fitted by the 1EXP and linear functions, respectively (solid line). The dashed lines show the sDRCs for the individual samples using 12 aliquots.

indistinguishable from each other in aspects of location, age range, and environmental dose rate, further investigations are required to understand the shape discrepancy of the individual sDRCs. D_e and apparent ages determined by the sDRCs are shown in Table 3 (Li et al., 2015a).

5.2.2 sDRC construction of intensity multiplied by test dose

According to Roberts and Duller (2004), the value of I_x in the SAR protocol was first multiplied by the corresponding test dose (T_D) in Gy and then plotted against the regenerative dose. Similar to that in 5.2.1, sDRCs for $pIRIR_{150}$ and IR_{50} were constructed using the single saturating exponential and linear functions, respectively (Figure 5). The fitting equation and the R-squared value are also shown. I_n was then multiplied by the T_D value and projected onto the sDRC to determine the D_e value for each sample (Table 3) (Roberts and Duller, 2004).

5.3 DRC and D_e comparison

It demonstrates that the constructed IR_{50} and $pIRIR_{150}$ sDRCs in this study are comparable within *ca.* 40 Gy, which corresponds to the linear growth region of dose growth, while those show slight discrepancy when *De* is larger than *ca.* 40 Gy. Similarly, the sDRCs constructed using the linear and single saturating exponential functions following Roberts and Duller (2004) are broadly in agreement (Figures 5A,B). Moreover, the characteristic saturation doses (D_0) of the sDRCs after single saturating exponential fitting are comparable by construction using the two approaches of Li et al. (2015a) and Roberts and Duller (2004), indicating that the sDRC in identical shape could be constructed using the two methods, although the normalized luminescence intensities are in a different scale.

D_es determined by the sDRC and individual DRC are compared in Figure 6. For both the $pIRIR_{150}$ and IR_{50} signals, the individual-DRC-determined D_es are generally consistent with the sDRC-determined D_es in the two

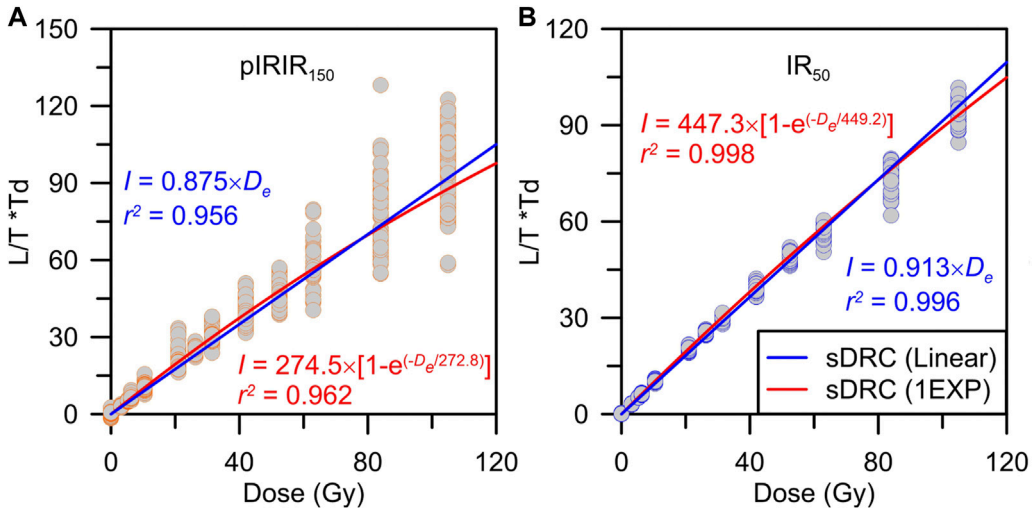

FIGURE 5
sDRC construction using data from all the samples following Roberts and Duller (2004). The sDRCs fitted using 1EXP and linear functions using the $pIRIR_{150}$ **(A)** and IR_{50} **(B)** data, respectively.

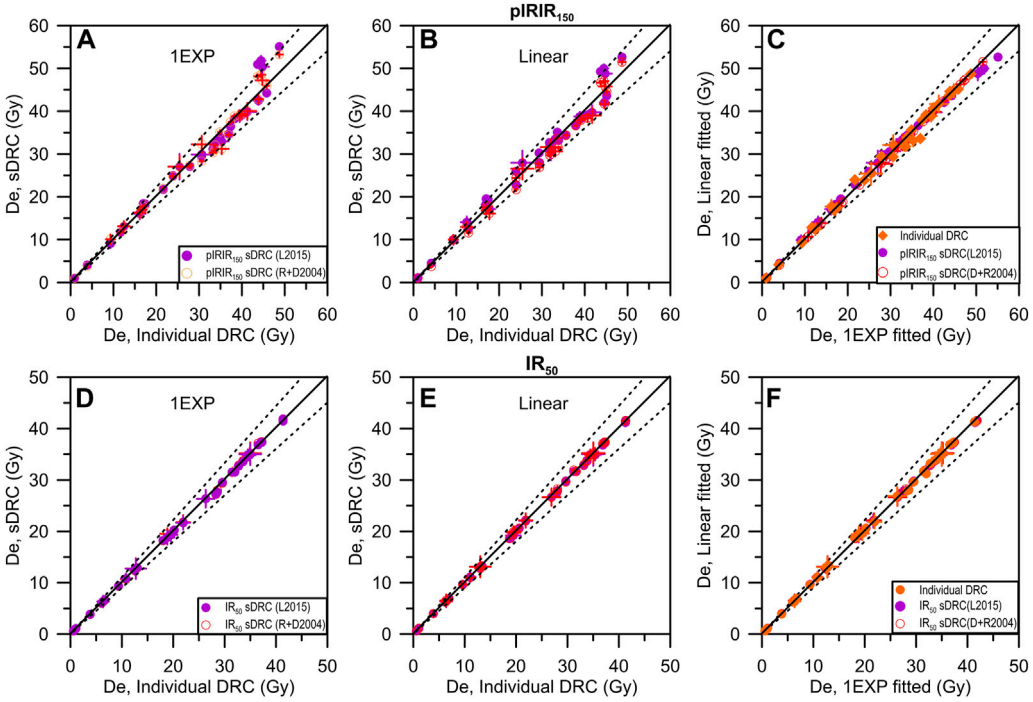

FIGURE 6
Comparisons of D_e determined by the sDRCs and the individual DRC for each sample **(A)** and **(B)**, $pIRIR_{150}$; **(D)** and **(E)**, IR_{50}). The D_e value is presented as the mean D_e of 24 aliquots for each sample. **(A,D)** The results determined using the 1EXP fitted DRCs, and those determined using the linear DRCs are shown in **(B,E)**. **(C,F)** The relationship between D_{es} determined by the 1EXP and linear fitted DRCs.

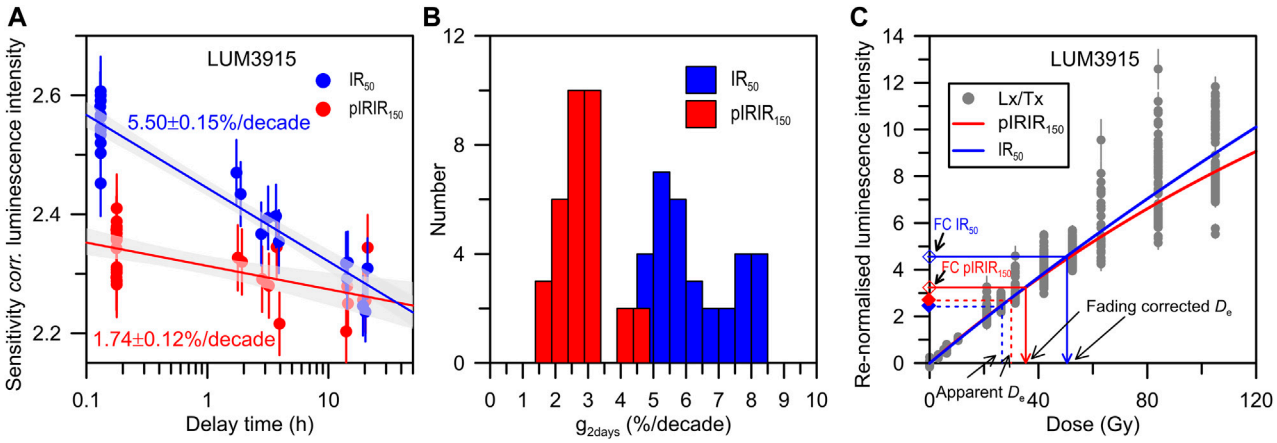

FIGURE 7
Results of fading correction. **(A)** The determination of the fading rates (g, %/decade) of IR_{50} and $pIRIR_{150}$ signals for one representative sample, LUM3915. **(B)** The distributions of the *g* values of IR_{50} and $pIRIR_{150}$ signals for all the samples. **(C)** The fading correction approach for the representative sample LUM3915 following Lamothe et al. (2003).

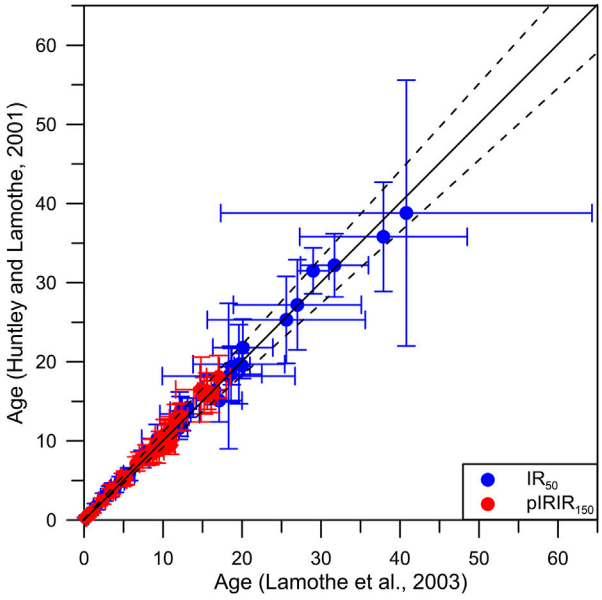

FIGURE 8
Comparisons of the fading corrected ages following Huntley and Lamothe (2001) and Lamothe et al. (2003).

approaches (Figures 6A,B,D,E). For the $pIRIR_{150}$ signal, although the sDRC determined D_es of approximately 50 Gy are slightly larger than those yielded by the individual DRCs, they are still comparable within 10% uncertainty (Figures 6A,B). Meanwhile, the sDRCs fitted using single saturating exponential and linear functions result in D_es in agreement (Figures 6C,F). They imply that both the single saturating exponentially and linearly fitted sDRCs could yield reliable D_e for the studied Mongolian samples within *ca.* 20 ka, which is applicable for D_e measurement with high efficiency. The D_e values determined using the sDRCs fitted by the single saturating exponential function for the two signals following Li et al. (2015a) were used for fading correction below.

6 Fading correction of the K-feldspar luminescence ages

In order to eliminate the underestimation of the K-feldspar luminescence ages by anomalous fading, the numerical models proposed by Huntley and Lamothe (2001) and Lamothe et al. (2003) were applied and compared in this study. The sDRC fitted using the single saturating exponential function and the yielded apparent ages were used for fading correction. The fading rates of *ca.* 4.76–8.42%/decade for IR_{50} and *ca.* 0.73–3.86%/decade for $pIRIR_{150}$ were determined (Figures 7A,B). Table 3 summarizes the outcomes of the fading rates and the fading corrected ages. The fading corrected $pIRIR_{150}$ ages following Huntley and Lamothe (2001) are between 0.29 ± 0.05 and 17.0 ± 1.5 ka, and the IR_{50} ages after fading correction range from 0.25 ± 0.04 to 40.8 ± 23.5 ka (Table 3). Following the fading correction model of Lamothe et al. (2003), the initial luminescence intensity I_0 was first corrected for fading and then projected onto the sDRC to yield the fading corrected D_e (Figure 7C). The fading corrected $pIRIR_{150}$ ages determined by the fading corrected D_e and the environmental dose rate are 0.32 ± 0.05–18.1 ± 2.7 ka. For the

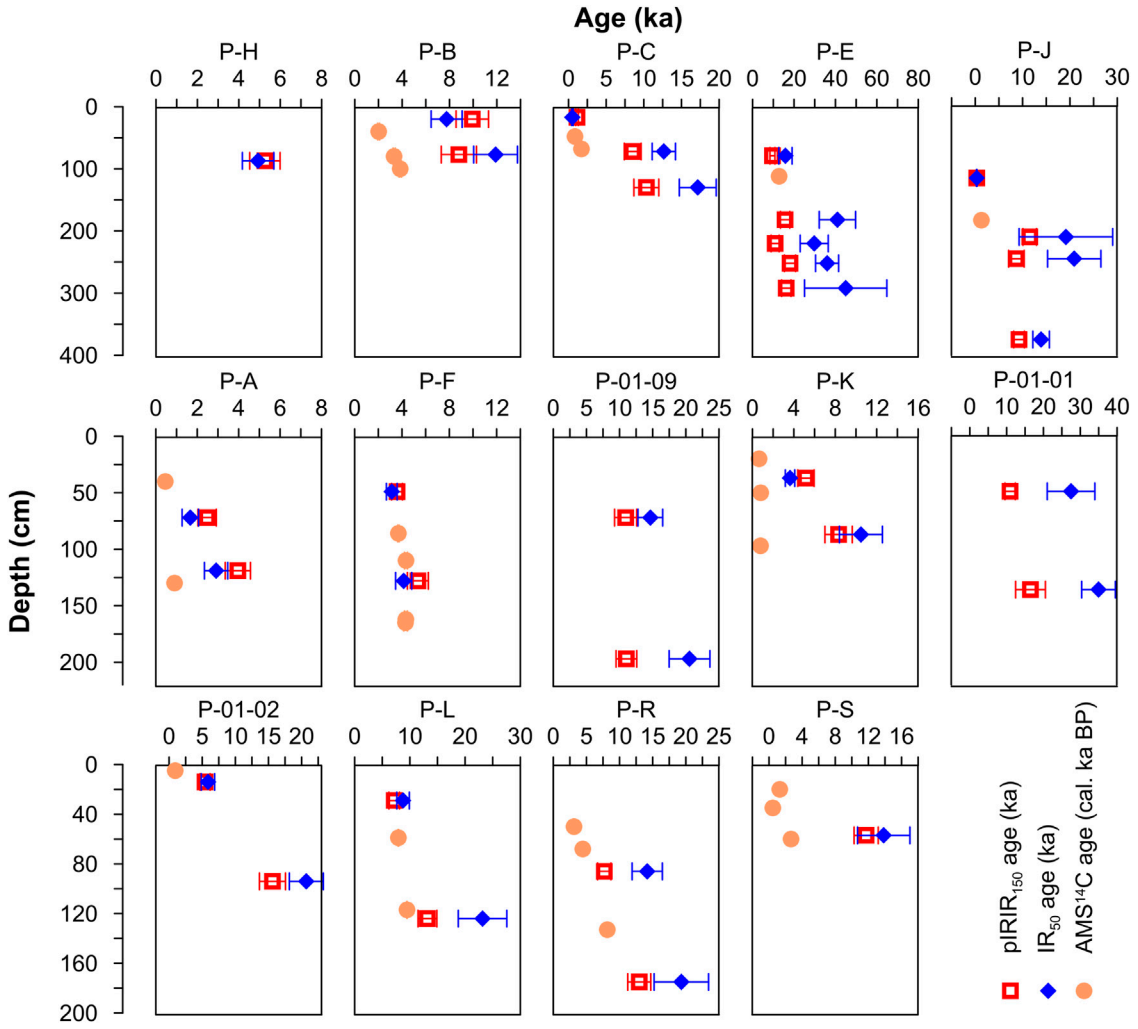

FIGURE 9
Comparison between the luminescence ages and the radiocarbon dates for each profile. The fading corrected $pIRIR_{150}$ and IR_{50} ages were determined using the sDRC fitted by a single saturating exponential function and fading corrected following Lamothe et al. (2003).

IR_{50} signal, the fading corrected ages range from 0.31 ± 0.06 to 38.8 ± 16.8 ka.

Figure 8A shows that the fading corrected ages following Huntley and Lamothe (2001) are generally consistent with those after correction following Lamothe et al. (2003). Specifically, the $pIRIR_{150}$ ages corrected by the two models are perfectly consistent with each other. The fading corrected IR_{50} ages agree with each other within 10% uncertainty. Meanwhile, a tendency of slight underestimation with the increase in age has been observed for those after Huntley and Lamothe (2001) to the corresponding ages after Lamothe et al. (2003). One possible explanation is to associate the fading corrected IR_{50} ages of > *ca.* 30 ka with the nonlinear region of dose growth, for which the fading corrected ages after Huntley and Lamothe (2001) start to be underestimated.

7 Degree of signal bleaching and luminescence chronology

As the IR_{50} signal is bleached much faster than the $pIRIR_{150}$ signal (e.g., Reimann et al., 2012; Tsukamoto et al., 2017), the $pIRIR_{150}$ signal would be well bleached if the $pIRIR_{150}$ are consistent with the IR_{50} ages (Murray et al., 2012; Reimann et al., 2015; Li et al., 2018b). In order to assess the degree of bleaching for the luminescence signals, radiocarbon dates, the fading corrected IR_{50}, and $pIRIR_{150}$ ages are compared. The fading corrected ages using the approach of Lamothe et al. (2003) were employed. Radiocarbon dates are used as a reference to evaluate the reliability of luminescence ages.

The fading corrected IR_{50} and $pIRIR_{150}$ ages of each profile are shown in Figure 9. Some of the IR_{50} ages agree with the

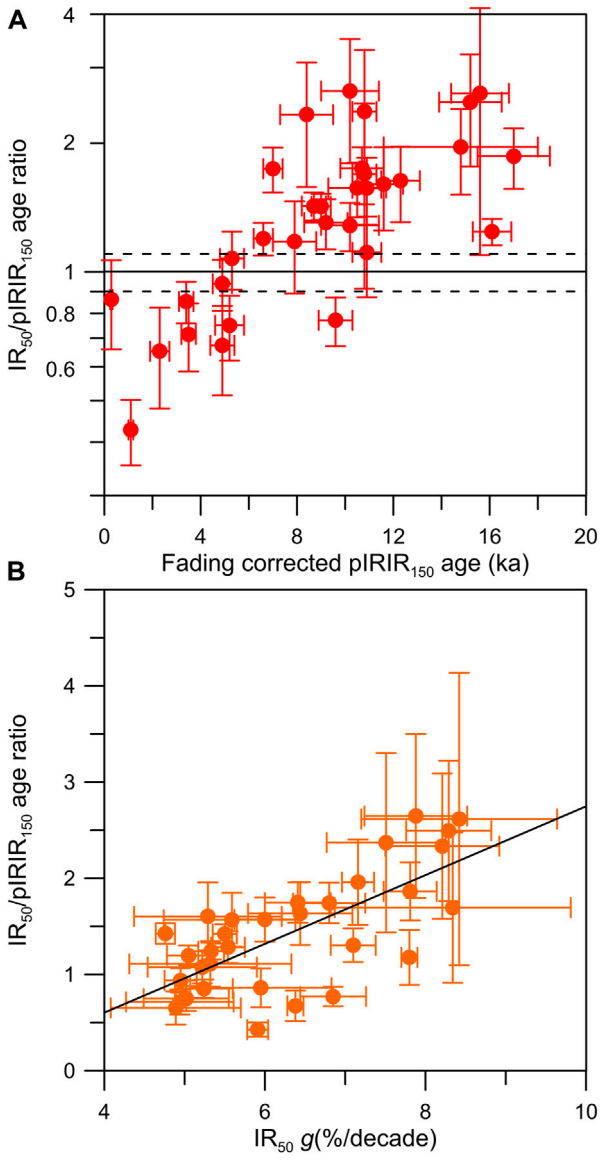

FIGURE 10
Comparison between the IR_{50} and $pIRIR_{150}$ ages. **(A)** The relationship between the $IR_{50}/pIRIR_{150}$ age ratio and the fading corrected $pIRIR_{150}$ ages. The IR_{50} and $pIRIR_{150}$ ages used for calculating the age ratios are fading corrected following Lamothe et al. (2003). **(B)** Relationship between the $IR_{50}/pIRIR_{150}$ age ratio and *g* values for the IR_{50} signal with the trendline (black solid line).

corresponding $pIRIR_{150}$ ages, whereas the IR_{50} ages tend to overestimate the associated $pIRIR_{150}$ ages for a large portion of samples. In order to explore the tendency and potential reason for age discrepancy, the $IR_{50}/pIRIR_{150}$ age ratios were calculated and plotted against the $pIRIR_{150}$ ages (Figure 10A). The age ratio varies from *ca.* 0.5 to 3.0. Although the $pIRIR_{150}$ ages overestimate the corresponding IR_{50} ages for the samples younger than *ca.* 6 ka (e.g., those in profile P-A), the IR_{50} ages tend to overestimate the $pIRIR_{150}$ ages for the relatively old samples (Figure 10A). The $pIRIR_{150}$ age is larger than the IR_{50} age for the younger samples due to partial bleaching of the $pIRIR_{150}$ signal, which is relatively severe for the young sample. However, this could not explain the overestimated IR_{50} ages for the older samples. The overestimation of the IR_{50} ages may be related to the age over-correction by the large fading rate. The relationship between the $IR_{50}/pIRIR_{150}$ age ratio and the associated IR_{50} fading rates is demonstrated in Figure 10B. It shows that the IR_{50} age is overestimated with the increased *g* value. Fading rates larger than *ca.* 6%/decade have yielded unacceptable corrected ages (Thomsen et al., 2008; Tsukamoto and Duller, 2008; Li et al., 2017). The comparison between the reference chronology of Chinese loess and the corresponding fading corrected ages using the two models (Lamothe et al., 2003; Kars et al., 2008) also suggested that fading over-correction happened with *g* values larger than *ca.* 4–5%/decade using the Lamothe et al. (2003) model (Li et al., 2018a). In this study, some of the fading rates of up to *ca.* 8.42%/decade were determined for the IR_{50} signal (Figure 7B), suggesting that the fading rates are overestimated, therefore yielding the over-corrected IR_{50} ages.

The chronology of the soil and aeolian in the north slope of Khangai Mountain was subsequently established based on the degree of luminescence signal bleaching and comparison between the luminescence age and radiocarbon dates. The luminescence age of *ca.* 5 ka (sample LUM3775) is determined for the soil in profile P-H, broadly consistent with the fading corrected IR_{50} ages, indicating the $pIRIR_{150}$ signal was well bleached. The IR_{50} fading rate is 4.95%/decade, suggesting that the IR_{50} age is not problematic concerning fading over-correction (Figure 9). The $pIRIR_{150}$ and IR_{50} ages largely overestimate the radiocarbon dates younger than *ca.* 4 ka in profile P-B. The IR_{50} ages are likely over-corrected by the fading rates of 6–7%/decade. The $pIRIR_{150}$ signal was probably poorly bleached, shown by slight anti-stratigraphic order and overestimation of the corresponding IR_{50} ages. The radiocarbon dates of P-B might be underestimated because they are still younger than the fading uncorrected IR_{50} ages, especially for the lowermost two ages (Figure 9). Similarly, the underestimated radiocarbon dates and the overestimated luminescence ages are observed in profile P-K. The radiocarbon dates in profiles P-S and P-A are also likely underestimated, but the $pIRIR_{150}$ and IR_{50} ages are broadly in agreement (Figure 9), for which the fading corrected IR_{50} ages are reliable if taking 6%/decade as the lower boundary of fading over-correction. In profile P-F, the $pIRIR_{150}$ and IR_{50} ages are consistent within the uncertainty, agreeing with the radiocarbon dates in stratigraphic order. The consistency of the $pIRIR_{150}$ ages and radiocarbon dates in stratigraphic order are observed for profiles P-E, P-J, P-01-02, and P-R, whereas the corresponding IR_{50} ages are overestimated due to fading over-correction. The IR_{50} ages are also over-corrected in profiles P-C,

P-01-09, P-01-01, and P-L. The luminescence chronology based on the $pIRIR_{150}$ ages reveals that the investigated sediment profiles record the sedimentation and environmental information on the north slope of Khangai Mountain after the Last Glacial Maximum (LGM).

8 Conclusion

In this study, 32 K-feldspar samples from the north slope of Khangai Mountain, Mongolia, were dated using the $pIRIR_{150}$ protocol. The applicability of the standardized dose-response curve (sDRC) and the fading correction models were evaluated. The degree of bleaching for the applied luminescence signals was assessed by comparing the associated ages with the radiocarbon dates. The timing of sedimentation in explored profiles from the north slope of Khangai Mountain was finally determined. The main conclusions are drawn as follows:

- The sDRCs, constructed for both the K-feldspar $pIRIR_{150}$ and IR_{50} signals according to the re-normalization and test dose-standardization procedures, could yield a consistent D_e value compared to the individual DRC within *ca.* 40 Gy, suggesting that the sDRC is applicable for more effective D_e measurement of the Mongolian sediments.
- The fading corrected ages following Huntley and Lamothe (2001) and Lamothe et al. (2003) are broadly in agreement for the IR_{50} and $pIRIR_{150}$ signals. With the increase in age and/or fading rate, the fading corrected age using the model solely for the linear region of dose growth may underestimate that corrected by the model appliable for the full dose region.
- Some of the fading corrected IR_{50} ages are overestimated, most likely resulting from fading over-correction, whereas the overestimation of several $pIRIR_{150}$ ages is derived from partial bleaching.

Data availability statement

The original contributions presented in the study are included in the article/Supplementary Material. Further inquiries can be directed to the corresponding author.

Author contributions

Conceptualization and methodology, YL and MF; formal analysis, YL, ST, MK, DS and MF; original draft preparation, YL and ST; and review and editing, YL, ST, MK, DS and MF. All authors have read and agreed to the published version of the manuscript.

Funding

YL is financially supported by the National Natural Science Foundation (no. 41907376), the Excellent Chinese and Foreign Young Scientist Exchange Program of CAST, and the 111 Project (no. B20011). The field work was supported by the Deutsche Forschungsgemeinschaft (DFG. no. 385460422).

Acknowledgments

Sabine Mogwitz in S3 LIAG is thanked for sample preparation in the laboratory.

Conflict of interest

The authors declare that the research was conducted in the absence of any commercial or financial relationships that could be construed as a potential conflict of interest.

Publisher's note

Supplementary material

The Supplementary Material for this article can be found online at: https://www.frontiersin.org/articles/10.3389/feart.2022.939852/full#supplementary-material

References

Balescu, S., Ritz, J. F., Lamothe, M., Auclair, M., and Todbileg, M. (2007). Luminescence dating of a gigantic palaeolandslide in the Gobi-Altay mountains, Mongolia. *Quat. Geochronol.* 2, 290–295. doi:10.1016/j.quageo.2006.05.026

Böhner, J. (2006). General climatic controls and topoclimatic variations in Central and High Asia. *Boreas* 35, 279–295. doi:10.1111/j.1502-3885.2006.tb01158.x

Buylaert, J. P., Murray, A. S., Gebhardt, A. C., Sohbati, R., Ohlendorf, C., Thiel, C., et al. (2013). Luminescence dating of the PASADO core 5022-1D from Laguna Potrok Aike (Argentina) using IRSL signals from feldspar. *Quat. Sci. Rev.* 71, 70–80. doi:10.1016/j.quascirev.2013.03.018

Buylaert, J. P., Murray, A. S., Thomsen, K. J., and Jain, M. (2009). Testing the potential of an elevated temperature IRSL signal from K-feldspar. *Radiat. Meas.* 44, 560–565. doi:10.1016/j.radmeas.2009.02.007

Colarossi, D., Duller, G. A. T., Roberts, H. M., Tooth, S., and Lyons, R. (2015). Comparison of paired quartz OSL and feldspar post-IR IRSL dose distributions in poorly bleached fluvial sediments from South Africa. *Quat. Geochronol.* 30, 233–238. doi:10.1016/j.quageo.2015.02.015

Feng, Z. D., Wang, W. G., Guo, L. L., Khosbayar, P., Narantsetseg, T., Jull, A. J. T., et al. (2005). Lacustrine and eolian records of holocene climate changes in the Mongolian plateau: Preliminary results. *Quat. Int.* 136, 25–32. doi:10.1016/j.quaint.2004.11.005

Feng, Z. D., Zhai, X. W., Ma, Y. Z., Huang, C. Q., Wang, W. G., Zhang, H. C., et al. (2007). Eolian environmental changes in the Northern Mongolian Plateau during the past ~35, 000 yr. *Palaeogeogr. Palaeoclimatol. Palaeoecol.* 245, 505–517. doi:10.1016/j.palaeo.2006.09.009

Fowell, S. J., Hansen, B. C. S., Peck, J. A., Khosbayar, P., and Ganbold, E. (2017). Mid to late Holocene climate evolution of the Lake Telmen Basin, North Central Mongolia, based on palynological data. *Quat. Res.* 59, 353–363. doi:10.1016/s0033-5894(02)00020-0

Fu, X., Li, B., Jacobs, Z., Jankowski, N. R., Cohen, T. J., and Roberts, R. G. (2020). Establishing standardised growth curves (SGCs) for OSL signals from individual grains of quartz: A continental-scale case study. *Quat. Geochronol.* 60, 101107. doi:10.1016/j.quageo.2020.101107

Fu, X., and Li, S.-H. (2013). A modified multi-elevated-temperature post-IR IRSL protocol for dating Holocene sediments using K-feldspar. *Quat. Geochronol.* 17, 44–54. doi:10.1016/j.quageo.2013.02.004

Fuchs, M., and Owen, L. A. (2008). Luminescence dating of glacial and associated sediments: Review, recommendations and future directions. *Boreas* 37, 636–659. doi:10.1111/j.1502-3885.2008.00052.x

Guérin, G. (2011). Dose-rate conversion factors update. *Anc. TL* 29, 5–8.

Guo, Y., Li, B., Zhang, J., Yuan, B., Xie, F., and Roberts, R. (2016). Luminescence ages for three 'Middle Palaeolithic' sites in the Nihewan Basin, northern China, and their archaeological and palaeoenvironmental implications. *Quat. Res.* 85, 456–470. doi:10.1016/j.yqres.2016.03.002

Huntley, D. J., and Baril, M. R. (1997). The K content of the K-feldspars being measured in optical dating or in thermoluminescence dating. *Anc. TL* 15, 11–13.

Huntley, D. J., and Hancock, R. G. V. (2001). The Rb contents of the K-feldspars being measured in optical dating. *Anc. TL* 19, 43–46.

Huntley, D. J., and Lamothe, M. (2001). Ubiquity of anomalous fading in K-feldspars and the measurement and correction for it in optical dating. *Can. J. Earth Sci.* 38, 1093–1106. doi:10.1139/e01-013

Kars, R. H., Wallinga, J., and Cohen, K. M. (2008). A new approach towards anomalous fading correction for feldspar IRSL dating — Tests on samples in field saturation. *Radiat. Meas.* 43, 786–790. doi:10.1016/j.radmeas.2008.01.021

Klinge, M., Schneider, F., Li, Y., Frechen, M., and Sauer, D. (2022). Variations in geomorphological dynamics in the northern Khangai Mountains, Mongolia, since the Late Glacial period. *Geomorphology* 401, 108113. doi:10.1016/j.geomorph.2022.108113

Klinge, M., Lehmkuhl, F., Schulte, P., Hülle, D., and Nottebaum, V. (2017). Implications of (reworked) aeolian sediments and paleosols for Holocene environmental change in Western Mongolia. *Geomorphology* 292, 59–71. doi:10.1016/j.geomorph.2017.04.027

Klinge, M., and Sauer, D. (2019). Spatial pattern of Late Glacial and Holocene climatic and environmental development in Western Mongolia - a critical review and synthesis. *Quat. Sci. Rev.* 210, 26–50. doi:10.1016/j.quascirev.2019.02.020

Lai, Z. (2006). Testing the use of an OSL standardised growth curve (SGC) for determination on quartz from the Chinese Loess Plateau. *Radiat. Meas.* 41, 9–16. doi:10.1016/j.radmeas.2005.06.031

Lamothe, M., Auclair, M., Hamzaoui, C., and Huot, S. (2003). Towards a prediction of long-term anomalous fading of feldspar IRSL. *Radiat. Meas.* 37, 493–498. doi:10.1016/s1350-4487(03)00016-7

Lamothe, M., Forget Brisson, L., and Hardy, F. (2020). Circumvention of anomalous fading in feldspar luminescence dating using Post-Isothermal IRSL. *Quat. Geochronol.* 57, 101062. doi:10.1016/j.quageo.2020.101062

Lamothe, M. (2016). Luminescence dating of interglacial coastal depositional systems: Recent developments and future avenues of research. *Quat. Sci. Rev.* 146, 1–27. doi:10.1016/j.quascirev.2016.05.005

Lehmkuhl, F., Hilgers, A., Fries, S., Hülle, D., Schlütz, F., Shumilovskikh, L., et al. (2011). Holocene geomorphological processes and soil development as indicator for environmental change around Karakorum, Upper Orkhon Valley (Central Mongolia). *Catena* 87, 31–44. doi:10.1016/j.catena.2011.05.005

Lehmkuhl, F., Klinge, M., Rother, H., and Hülle, D. (2016). Distribution and timing of Holocene and late Pleistocene glacier fluctuations in Western Mongolia. *Ann. Glaciol.* 57, 169–178. doi:10.3189/2016aog71a030

Lehmkuhl, F., Nottebaum, V., and Hülle, D. (2018). Aspects of late quaternary geomorphological development in the Khangai mountains and the gobi altai mountains (Mongolia). *Geomorphology* 312, 24–39. doi:10.1016/j.geomorph.2018.03.029

Li, B., Jacobs, Z., Roberts, R. G., and Li, S.-H. (2018). Single-grain dating of potassium-rich feldspar grains: Towards a global standardised growth curve for the post-IR IRSL signal. *Quat. Geochronol.* 45, 23–36. doi:10.1016/j.quageo.2018.02.001

Li, B., and Li, S.-H. (2011). Luminescence dating of K-feldspar from sediments: A protocol without anomalous fading correction. *Quat. Geochronol.* 6, 468–479. doi:10.1016/j.quageo.2011.05.001

Li, B., Roberts, R. G., Jacobs, Z., Li, S.-H., and Guo, Y.-J. (2015b). Construction of a 'global standardised growth curve' (gSGC) for infrared stimulated luminescence dating of K-feldspar. *Quat. Geochronol.* 27, 119–130. doi:10.1016/j.quageo.2015.02.010

Li, B., Roberts, R. G., Jacobs, Z., and Li, S.-H. (2015a). Potential of establishing a 'global standardised growth curve' (gSGC) for optical dating of quartz from sediments. *Quat. Geochronol.* 27, 94–104. doi:10.1016/j.quageo.2015.02.011

Li, Y., Shang, Z. W., Tsukamoto, S., Tamura, T., Yi, L., Wang, H., et al. (2018b). Quartz and K-feldspar luminescence dating of sedimentation in the North Bohai coastal area (NE China) since the late pleistocene. *J. Asian Earth Sci.* 152, 103–115. doi:10.1016/j.jseaes.2017.10.036

Li, Y., Tsukamoto, S., Hu, K., and Frechen, M. (2017). Quartz OSL and K-feldspar post-IR IRSL dating of sand accumulation in the lower liao plain (liaoning, NE China). *Geochronometria* 44, 1–15. doi:10.1515/geochr-2015-0051

Li, Y., Tsukamoto, S., Long, H., Zhang, J., Yang, L., He, Z., et al. (2018a). Testing the reliability of fading correction methods for feldspar IRSL dating: A comparison between natural and simulated-natural dose response curves. *Radiat. Meas.* 120, 228–233. doi:10.1016/j.radmeas.2018.06.025

Long, H., Haberzettl, T., Tsukamoto, S., Shen, J., Kasper, T., Daut, G., et al. (2015). Luminescence dating of lacustrine sediments from Tangra Yumco (southern Tibetan Plateau) using post-IR IRSL signals from polymineral grains. *Boreas* 44, 139–152. doi:10.1111/bor.12096

Long, H., Lai, Z., Fan, Q., Sun, Y., and Liu, X. (2010). Applicability of a quartz OSL standardised growth curve for De determination up to 400Gy for lacustrine sediments from the Qaidam Basin of the Qinghai-Tibetan Plateau. *Quat. Geochronol.* 5, 212–217. doi:10.1016/j.quageo.2009.05.005

Long, H., Shen, J., Tsukamoto, S., Chen, J., Yang, L., and Frechen, M. (2014). Dry early Holocene revealed by sand dune accumulation chronology in Bayanbulak Basin (Xinjiang, NW China). *Holocene* 24, 614–626. doi:10.1177/0959683614523804

Madsen, A., Buylaert, J.-P., and Murray, A. (2011). Luminescence dating of young coastal deposits from New Zealand using feldspar. *Geochronometria* 38, 379–390. doi:10.2478/s13386-011-0042-5

Mejdahl, V. (1979). Thermoluminescence dating: Beta-dose attenuation in quartz grains. *Archaeometry* 21, 61–72. doi:10.1111/j.1475-4754.1979.tb00241.x

Mercier, N., Martin, L., Kreutzer, S., Moineau, V., and Cliquet, D. (2019). Dating the palaeolithic footprints of 'le rozel' (normandy, France). *Quat. Geochronol.* 49, 271–277. doi:10.1016/j.quageo.2017.12.005

Murray, A. S., Thomsen, K. J., Masuda, N., Buylaert, J. P., and Jain, M. (2012). Identifying well-bleached quartz using the different bleaching rates of quartz and feldspar luminescence signals. *Radiat. Meas.* 47, 688–695. doi:10.1016/j.radmeas.2012.05.006

Nalin, R., Lamothe, M., Auclair, M., and Massari, F. (2020). Chronology of the marine terraces of the Crotone Peninsula (Calabria, southern Italy) by means of infrared-stimulated luminescence (IRSL). *Mar. Petroleum Geol.* 122, 104645. doi:10.1016/j.marpetgeo.2020.104645

Peck, J. A., Khosbayar, P., Fowell, S. J., Pearce, R. B., Ariunbileg, S., Hansen, B. C. S., et al. (2002). Mid to Late Holocene climate change in north centralMongolia as recorded in the sediments of Lake Telmen. *Palaeogeogr. Palaeoclimatol. Palaeoecol.* 183, 135–153. doi:10.1016/s0031-0182(01)00465-5

Peng, J., Dong, Z., Han, F., Long, H., and Liu, X. (2013). R package numOSL: Numeric routines for optically stimulated luminescence dating. *Anc. TL* 31, 41–48.

Prasad, A. K., Poolton, N. R. J., Kook, M., and Jain, M. (2017). Optical dating in a new light: A direct, non-destructive probe of trapped electrons. *Sci. Rep.* 7, 12097. doi:10.1038/s41598-017-10174-8

Prescott, J. R., and Hutton, J. T. (1994). Cosmic ray contributions to dose rates for luminescence and ESR dating Large depths and long-term time variations. *Radiat. Meas.* 23, 497–500. doi:10.1016/1350-4487(94)90086-8

Reimann, T., Notenboom, P. D., De Schipper, M. A., and Wallinga, J. (2015). Testing for sufficient signal resetting during sediment transport using a polymineral multiple-signal luminescence approach. *Quat. Geochronol.* 25, 26–36. doi:10.1016/j.quageo.2014.09.002

Reimann, T., and Tsukamoto, S. (2012). Dating the recent past (<500 years) by post-IR IRSL feldspar–examples from the North Sea and Baltic Sea coast. *Quaternary Geochronology* 10, 180–187.

Reimann, T., Tsukamoto, S., Naumann, M., and Frechen, M. (2011). The potential of using K-rich feldspars for optical dating of young coastal sediments – a test case from Darss-Zingst peninsula (southern Baltic Sea coast). *Quat. Geochronol.* 6, 207–222. doi:10.1016/j.quageo.2010.10.001

Roberts, H. M., and Duller, G. A. T. (2004). Standardised growth curves for optical dating of sediment using multiple-grain aliquots. *Radiat. Meas.* 38, 241–252. doi:10.1016/j.radmeas.2003.10.001

Roberts, H. M. (2008). The development and application of luminescence dating to loess deposits: A perspective on the past, present and future. *Boreas* 37, 483–507. doi:10.1111/j.1502-3885.2008.00057.x

Schwanghart, W., Frechen, M., Kuhn, N. J., and Schütt, B. (2009). Holocene environmental changes in the Ugii Nuur basin, Mongolia. *Palaeogeogr. Palaeoclimatol. Palaeoecol.* 279, 160–171. doi:10.1016/j.palaeo.2009.05.007

Telfer, M. W., Bateman, M. D., Carr, A. S., and Chase, B. M. (2008). Testing the applicability of a standardized growth curve (SGC) for quartz OSL dating: Kalahari dunes, South African coastal dunes and Florida dune cordons. *Quat. Geochronol.* 3, 137–142. doi:10.1016/j.quageo.2007.08.001

Thiel, C., Buylaert, J.-P., Murray, A., Terhorst, B., Hofer, I., Tsukamoto, S., et al. (2011). Luminescence dating of the Stratzing loess profile (Austria) – testing the potential of an elevated temperature post-IR IRSL protocol. *Quat. Int.* 234, 23–31. doi:10.1016/j.quaint.2010.05.018

Thomsen, K. J., Jain, M., Murray, A. S., Denby, P. M., Roy, N., and Bøtter-Jensen, L. (2008). Minimizing feldspar OSL contamination in quartz UV-OSL using pulsed blue stimulation. *Radiat. Meas.* 43, 752–757. doi:10.1016/j.radmeas.2008.01.020

Thrasher, I. M., Mauz, B., Chiverrell, R. C., and Lang, A. (2009). Luminescence dating of glaciofluvial deposits: A review. *Earth. Sci. Rev.* 97, 133–146. doi:10.1016/j.earscirev.2009.09.001

Tsukamoto, S., and Duller, G. A. T. (2008). Anomalous fading of various luminescence signals from terrestrial basaltic samples as Martian analogues. *Radiat. Meas.* 43, 721–725. doi:10.1016/j.radmeas.2007.10.025

Tsukamoto, S., Kataoka, K., Oguchi, T., Murray, A. S., and Komatsu, G. (2014). Luminescence dating of scoria fall and lahar deposits from Somma–Vesuvius, Italy. *Quat. Geochronol.* 20, 39–50. doi:10.1016/j.quageo.2013.10.005

Tsukamoto, S., Kondo, R., Lauer, T., and Jain, M. (2017). Pulsed IRSL: A stable and fast bleaching luminescence signal from feldspar for dating quaternary sediments. *Quat. Geochronol.* 41, 26–36. doi:10.1016/j.quageo.2017.05.004

Wallinga, J., Bos, A. J. J., Dorenbos, P., Murray, A. S., and Schokker, J. (2007). A test case for anomalous fading correction in IRSL dating. *Quat. Geochronol.* 2, 216–221. doi:10.1016/j.quageo.2006.05.014

Wallinga, J., Murray, A., and Wintle, A. G. (2000). The single-aliquot regenerative-dose (SAR) protocol applied to coarse-grain feldspar. *Radiat. Meas.* 32, 529–533. doi:10.1016/s1350-4487(00)00091-3

Wallinga, J. (2002). Optically stimulated luminescence dating of fluvial deposits: A review. *Boreas* 31, 303–322. doi:10.1111/j.1502-3885.2002.tb01076.x

Wintle, A. G., and Murray, A. (2000). Quartz OSL: Effects of thermal treatment and their relevance to laboratory dating procedures. *Radiat. Meas.* 32, 387–400. doi:10.1016/s1350-4487(00)00057-3

Yi, S., Buylaert, J. P., Murray, A. S., Thiel, C., Zeng, L., and Lu, H. (2015). High resolution OSL and post-IR IRSL dating of the last interglacial-glacial cycle at the Sanbahuo loess site (northeastern China). *Quat. Geochronol.* 30, 200–206. doi:10.1016/j.quageo.2015.02.013

Zhang, J., and Li, S. H. (2019). Constructions of standardised growth curves (SGCs) for IRSL signals from K-feldspar, plagioclase and polymineral fractions. *Quat. Geochronol.* 49, 8–15. doi:10.1016/j.quageo.2018.05.015

Frontiers in Earth Science

Investigates the processes operating within the major spheres of our planet

Advances our understanding across the earth sciences, providing a theoretical background for better use of our planet's resources and equipping us to face major environmental challenges.

Discover the latest Research Topics

See more →

Frontiers

Avenue du Tribunal-Fédéral 34
1005 Lausanne, Switzerland
frontiersin.org

Contact us

+41 (0)21 510 17 00
frontiersin.org/about/contact